UNIVERSITY OF LONDON THESIS

Degree PhD Year 2007 Name of Author KATHERINE JOY

Studies in Lunar Geology and Geochemistry Using Sample Analysis and Remote Sensing Measurements

A thesis submitted to the University of London
For the degree of Doctor of Philosophy
By

Katherine Helen Joy

Department of Earth Sciences
University College London
Gower Street
London
WC1E 6BT

March 2007

ProQuest LLC
789 East Eisenhower Parkway
P.O. Box 1346
Ann Arbor, MI 48106-1346

Abstract

The thesis reports the results of an investigation into the geochemistry and petrology of lunar meteorites and synthesises this knowledge with research into the calibration and interpretation of lunar X-ray spectroscopy from the D-CIXS instrument.

I present the mineralogy, bulk composition and petrography of two lunar regolith breccia meteorites (DaG 400 and MET 01210), and a launch paired group of mare basalt meteorites (LAP 02205/02224/02226/02436/03632). Individual sample geochemistry is interpreted and geological models proposed to account for the meteorites' formation histories and subsequent impact related processes. These are compared to previously studied Apollo, Luna and meteorite lunar samples in order to understand how these new samples fit within the context of existing theories of lunar evolution. I have also utilised currently available geochemical remote sensing datasets to try and constrain possible meteorite launch localities, thus relating the microscopic perspective of lunar geological processes from the sample collection back to the 'big-picture' of global remotely sensed datasets.

I review the scientific findings of the UK-built D-CIXS X-ray spectrometer, which flew to the Moon on the SMART-1 mission between 2003 and 2006. I present an overview of the instrument and discuss various hardware and software problems the mission encountered. Results of laboratory calibration work and of theoretical X-ray fluorescence modelling are also presented. This thesis introduces the first detailed examination and interpretation of D-CIXS data recorded by the instrument during lunar science phase activities in 2005. These datasets focus on X-ray flux recorded during periods of strong solar activity (i.e. solar flare associated events), with particular attention to an observation of the lunar far-side feldspathic highlands and the South Pole-Aitkin Basin, which records an X-ray flux difference between the two lithological terrains indicative of a marked variation in surface composition.

This work will help to lay the groundwork for understanding and interpreting data from the new C1XS instrument, which will fly to the Moon in 2008 aboard the Indian Chandrayaan-1 mission.

Acknowledgements

This thesis would simply not have been possible without the unwavering kindness, support and extreme patience of my supervisor, Ian Crawford. He has been enthusiastic and helpful throughout every stage of my research, and has helped me above and beyond the 'call of lunar duty'. I will be forever grateful that I have had the opportunity to be his student (and I am especially proud that I have been his first Planetary Science student!).

I have to express also my gratitude to the help given to me by my hoard of 'official' and 'unofficial' Supervisors. Chris Howe for putting up with my general stupidity, and also for giving me a place to stay whilst I have embarked on my RAL adventures. Hilary Downes for trusting me to teach Birkbeck students Planetary Volcanism – a brave decision all round! Barry Kellett for embarking on the formidable task of teaching me how to programme in IDL, and for then enduring the following years of IDL and DCIXS related questions (sorry!). Sara Russell for introducing me to Moon rocks, and for then putting up with my plethora of enquiring meteorite-related emails. I could not have completed this thesis without any of you, so many thanks.

I also especially thank Anton Kearsley, John Spratt, Terry William, Ben Williamson, Sarah James and Teresa Jeffries from the Natural History Museum London, and Andy Beard and Adrian Jones from UCL, for all of their help with analytical instrumentation and advice about igneous petrology. Thanks to David Lawrence and David Heather for help with IDL programming problems at various stages in my research programme. Thanks to Vera for great chats about the Moon.

Thank you to my Mum and Dad for being interested in my work and being loving and supportive throughout my life. Thanks also to 'the little ones': Elizabeth, Sarah and James, to my Grandmothers Lydia Joy and Violet Bye, and to the rest of the Joy and Bye Clan who are still here, and those that are not.

Thanks to all my friends and especially to my current housemates Pete, Emma, Dan all the others from all the past few years who have been inflicted with all the Moon-related talk. Cheers to the RPIF crew for taking care of me as well. Thanks go Su for being such a fantastic cubby-mate, Dom for all the help and advice, Emily, Helen, Claire, Joyce, Ollie, John, Ellen, Emma, Terry and Roberto etc. for making me coffee, making me laugh and generally humouring my lunch-time babbling.

Thanks to PPARC and CCLRC RAL for paying for me to complete this research and supporting my extensive travelling over the past three and a half years! I would also like to thank the Royal Astronomical Society, the UCL Graduate School, the Barringer Crater Company, the Natural History Museum London and the Wilhelm and Else Heraeus Trust for subsidising me with additional funding resources to attend a range of exciting conferences, seminars, courses and field-trips.

My thanks also go out to my examiners Prof. Lionel Wilson and Dr. Mahesh Anand for their extremely thorough reading of this thesis. Your thoughts and suggestions are much appreciated.

This Thesis is dedicated to my grandfather Kenneth Joy, on whose knee I sat in 1986, to watch Halley's Comet on the television, and to all those who told me that the moon was made of cheese!

"The Moon - is it a flat disc of light in the sky, put there in order to illuminate the trysts of lovers? Or is it a celestial body of such overwhelming power that it can pull thunderous tonnages of water from one side of the world to the other - a body deserving of careful study and immense respect?"

Robert Fitzroy to Charles Darwin in the book *This Thing of Darkness* by Harry Thompson: A story of adventure, tragedy and a voyage that changes the world.

Contents

Chapter 1: Introduction to Lunar Geology and Evolution

Chapter 2: Meteorite Samples and Methods

Chapter 3: Dar al Gani 400 - A Lunar Feldspathic Regolith Breccia

Chapter 4: Lunar Meteorite Regolith Breccia MET 01210

Table Contents

Figure Contents

1.1 Introduction to Lunar Geology and Lunar Evolution

The Moon is our closest planetary neighbour (Fig. 1.1). It is the only place in the solar system, other than our own planet, that human-kind has visited, marking the first exciting steps in exploring the solar system.

The scientific importance of the Moon arises from the fact that it has an extremely ancient surface, mostly older than 3 billion years, with some areas extending almost all the way back to the origin of the Moon at ~4.5 billion years ago. It therefore preserves a record of the inner Solar System environment from billions of years ago that bodies such as the other 'terrestrial' planets like the Earth, Venus and Mars have long lost by virtue of their subsequent geological, atmospheric or biological activity. With the possible exception of the much less accessible surface of Mercury, this record is unlikely to be preserved anywhere else in the Solar System. Studies of the Moon are therefore important for improving our understanding of the early history of the Earth-Moon system, as well as the Solar System as a whole.

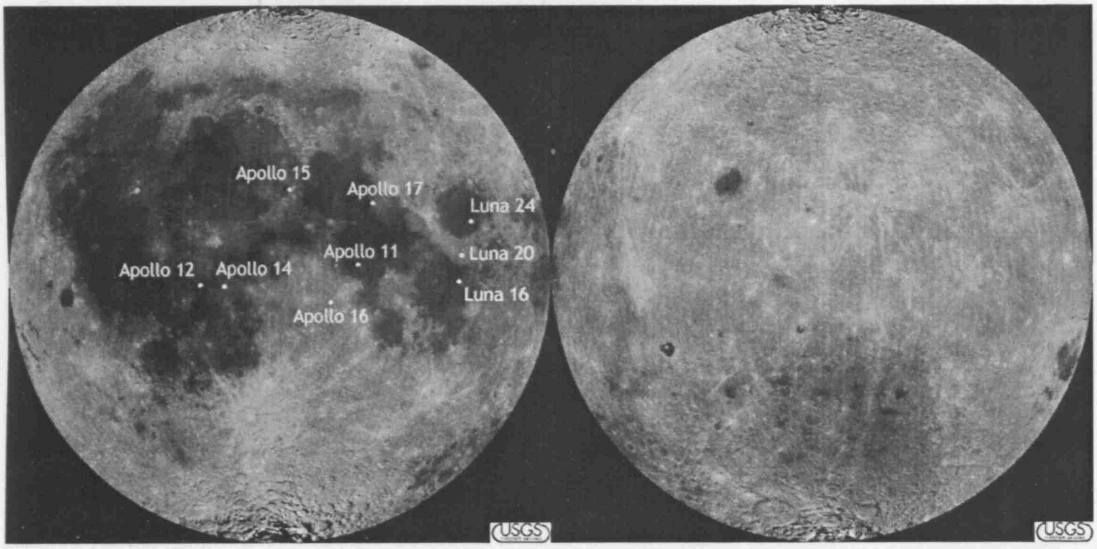

Fig. 1.1. The Moon: an old view and a new perspective. Lunar albedo maps compiled from 750 nm waveband from the Clementine mission (USGS images). The left image shows the well known view of the near-side of the Moon, with the Apollo mission and Luna landing sites illustrated. The right image shows the far-side of the Moon, unseen to the human eye before 1959. By comparison to the near-side, the lunar far-side has very few outcrops of dark (low-albedo) mare basalt deposits.

Lunar Sample Analysis. The NASA 'Apollo' manned missions and Russian 'Luna' sample return missions from 1969-1976 retrieved ~382 kg of lunar rock and soil samples (Vaniman et al. 1991) from a total of nine landing sites situated in broadly equatorial areas of the lunar near-side (Fig. 1.1). These samples have provided valuable first-order information about the age and composition of the Moon. Understanding the geological history of the Moon requires a

synthesis of many different disciplines. Integration of geochemical, isotopic, seismic and geophysical datasets has helped answer many questions about its formation, differentiation and subsequent history, but many questions remain to satisfy a coherent model of the lunar evolution. In this chapter, after introducing the fundamentals of lunar geology, I will present the latest theories about lunar evolution and subsequent modification processes by impact events. I will also review what research from the study lunar meteorites has contributed to our understanding of the Moon, and what new insights have arisen from the interpretations of data taken from remote sensing missions.

Lunar Geology. At first glance the Moon can be broadly divided into two geological units: the high albedo ancient, heavily cratered, lunar 'terrae' or highlands, and the low-albedo, younger, less heavily cratered basaltic 'maria' plains that have infilled rounded impact basins and topographic lows, predominantly on the lunar nearside (Fig. 1.1). The original naming of terra and mare relates back to early astronomical interpretations of basaltic plains being seas, or maria, and the highlands being the land, or terra.

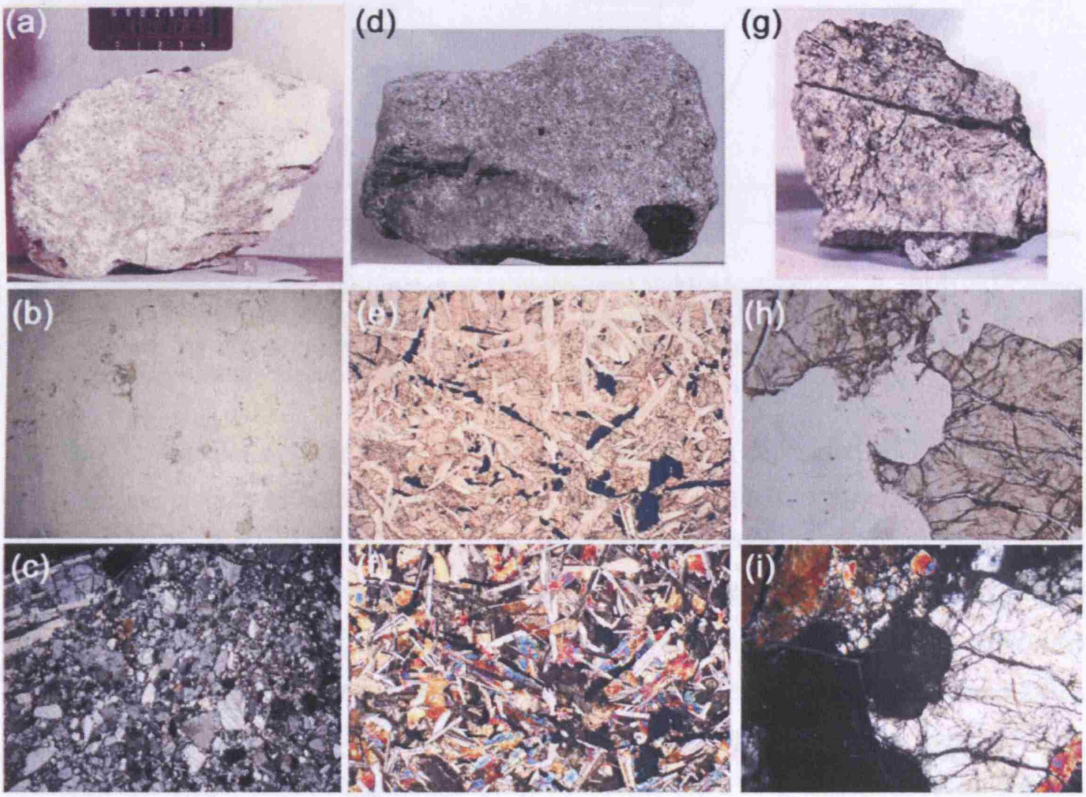

Fig. 1.2. Apollo lunar rock samples. (a) Anorthositic, Apollo 16 highland rock sample 60025 hand specimen. (b) Plane polarised light (ppl) thin section microphotograph of 60025. (c) Cross polarised light (cpl) thin section microphotograph of 60025. (d) Mare basalt sample 12046 from the Apollo 12 landing site. Sample is 7 cm across. (e) ppl of thin section of 12046. (f) cpl of thin section of 12046. (g) Hand specimen of norite sample 78235 from the Apollo 17 landing site. Sample is 5 cm across. (h) ppl of thin section of 78235. (i) cpl of thin section of 78235. Field of view in all thin section images is ~3 mm.

Sample return allowed a detailed study of these geological regions. The lunar highlands were found to be generally anorthositic in composition (Fig. 1.2 a,b,c); they are dominated by lithologies rich in the pale-whitish mineral calcium-plagioclase ($CaAl_2Si_2O_8$). These are crustal rocks that have been radiometrically dated to ~4.5 Ga (i.e. 4.5 billion years) and are thought to represent some of the earliest products of lunar differentiation. Samples from the lunar highlands are often referred to as the ferroan anorthosite or FAN suite, as in addition to plagioclase phases samples contain a minor proportion of mafic (Mg/Fe-rich) phases such as olivine ($[Mg,Fe]_2SiO_4$) and pyroxene ($[Ca,Mg,Fe]_2Si_2O_6$). The 'ferroan' part of the FAN name arises from the mafic mineral phases having somewhat Fe-richer compositions relative to the most Mg-rich pyroxenes or olivines found on the Moon. FAN rocks are generally comprised of a combination of these three principal mineral phases (Fig. 1.3), but always dominated by anorthitic plagioclase.

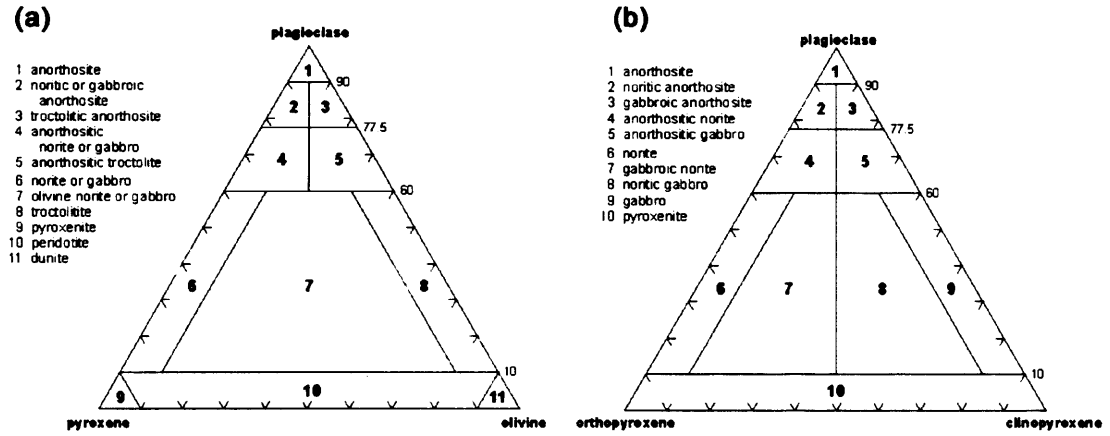

Fig. 1.3. Classification scheme for igneous rocks in the lunar highlands (Stöffler et al. 1980). (a) Ternary classification based on the plagioclase ($CaAl_2Si_2O_8$) – **pyroxene** ($[Ca,Mg,Fe]_2Si_2O_6$) – olivine ($[Mg,Fe]_2SiO_4$) system. (b) Ternary classification based on the plagioclase ($CaAl_2Si_2O_8$) – **orthopyroxene** ($[Mg,Fe]_2Si_2O_6$) – **clinopyroxene** ($[Ca,Mg,Fe]_2Si_2O_6$) system.

The dark lunar plains or 'maria' are composed of basaltic lava deposits (Fig. 1.2d,e,f). These maria are the product of partial melting of the lunar mantle that were erupted onto the lunar surface between ~3.8 and 2.9 Ga ago (e.g. Nyquist and Shih, 1992; Stöffler and Ryder, 2001; Fagen et al. 2002; Borg et al. 2004). They are exposed over 17% of the lunar surface (~30% of the near-side and ~2% of the far-side: Wilhelms, 1982), but are believed to have only contributed to <1% of the lunar crustal volume (Shultz and Spudis, 1983; Head and Wilson, 1992). Estimates of relative age dating using the crater counting statistic technique (e.g. Hiesinger and Head, 2006), suggests that some flows may have been erupted as recently as 1.1 Ga ago in Oceanus Procellarum. Mineralogically, mare basalts are primarily composed of pyroxenes, plagioclase, olivine and ilmenite ($FeTiO_3$; which is the dominant carrier of titanium on the Moon), with minor contributions of spinel ($[Fe,Mg][Cr,Al,Fe,Ti]_2O_4$), silica ($SiO_2$) and accessory troilite (FeS), native FeNi metal, whitlockite/merrillite ($Ca_{16}[REE],[Mg,Fe]_2[PO_4]_{14}$),

apatite ($Ca_5[PO_4]_3[OH,F,Cl]$), tranqillityite ($[Fe,Ca]_8[Y,Zr]_2Ti_3Si_3O_{24}$), armalcolite [$(Fe_{0.5}Mg_{0.5})Ti_2O_5$], baddeleyite ($ZrO_2$) and rutile ($TiO_2$) (Papike et al. 1998).

Other Major Lithologies. In addition to the lunar FAN and mare basalt suites other lunar rocks are generally classified as belonging to the Magnesian-Suite (Mg-Suite or HMS), the High Alkali-Suite (HAS) and the KREEP Basaltic Suite (KREEP standing for potassium [K], REE elements and phosphorus [P]). Outcrops of these suites seem to be concentrated on the lunar near-side and are likely related to early plutonic intrusion events (see section 1.1.1). The HMS group of rocks includes a range of magnesian mafic mineral-rich norites (Fig. 1.2g,h,i), gabbros and troctolites (see Fig. 1.3 for the mineralogical classification). The HAS group is comprised of small fragments of evolved granites/felsites and alkali-anorthosites (rich in alkali-feldspar [$NaAlSi_3O_8$] and incompatible elements).

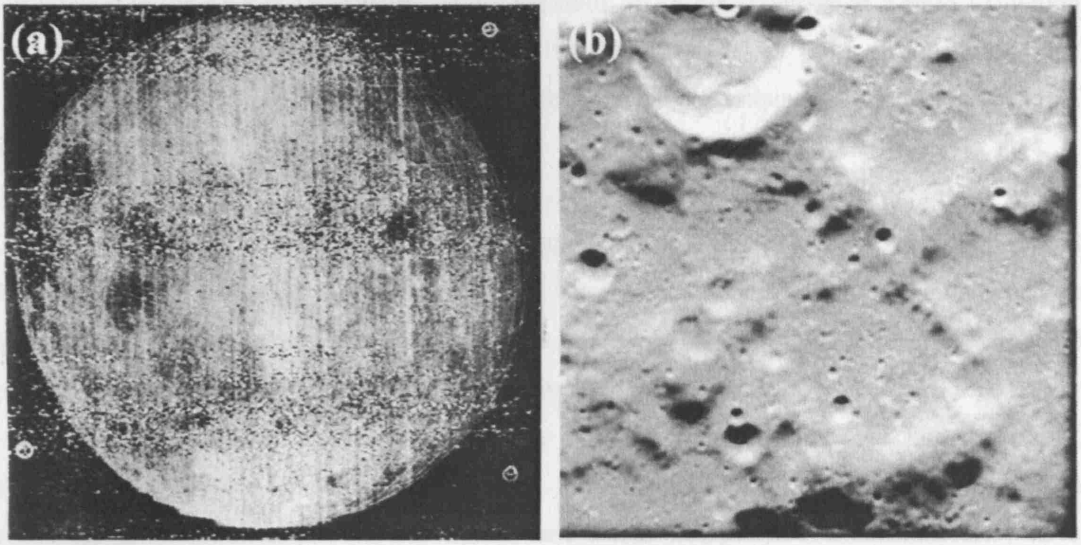

Fig. 1.4. The changing view of the lunar surface. (a) Frame 35 returned from the Luna 3 mission taken in 1959 showing the first grainy views of the farside of the Moon (Website 1.1). (b) Frame from SMART-1's AMIE camera image (Josset, 1999) taken in 2005 of the lunar farside highlands with a resolution of 124 m per pixel.

Remote Sensing. "Remote sensing is the determination of the physical or compositional state of a surface without physical contact" (Lucey et al. 2006). Observations and mapping of the near-side of the Moon from Earth based telescopes initiated much of the drive to study the Moon as an exciting planetary object. The first scientific description and the first detailed maps of the lunar surface were made as early as 1609 by Galileo Galilei. Other early astronomers mapped the near-side surface using progressively more advanced telescopes, naming many of the features as we know them today. The middle part of the twentieth century heralded the rocket age where the Moon was closely explored for the first time. The first investigation of the lunar surface by an orbiting spacecraft occurred in 1959 when the Russian Luna 2 craft flew past the Moon. Luna 3, flown later the same year, successfully returned the first photographs of the

lunar farside (Fig. 1.4a) revealing a high albedo landscape nearly devoid of basaltic mare. Since this ground-breaking achievement progressively more sophisticated camera technology (on the Zond, Ranger, Lunar Orbiter, Luna, Clementine and SMART-1 [Fig 1.4b] spacecrafts) has imaged the Moon in a range of wavelengths, and X-ray and Gamma-ray experiments have made direct measurements of the composition of the lunar surface (Vaniman et al. 1991).

Geochemical Observations. Prior to the return of geological samples by the Apollo and Luna missions, scientists could only theorise about what the Moon was made of, how it was formed and how it has evolved as a planetary body. Interpretation of the returned samples and analysis of surface-based experiments allowed huge advances to be made in understanding the composition of different geological terranes and their relationship to lunar geological history. However, these samples were collected from localised geographical horizons (from only a few centimetres in the case of Luna return lander missions, to ~8 km traverses at Apollo 17) within broadly equatorial latitudes on the near-side of the Moon (Fig. 1.1). Thus, from the returned Apollo and Luna sample collection alone we actually have a rather restricted perspective of lunar geological variability.

Global geochemical information is thus a requirement for understanding the complex and diverse nature of a differentiated planetary body. Through the understanding of the composition and variation of the lunar surface environment, a detailed view of lunar heterogeneity and geological variability is better understood. In the words of Lucey et al. (2006) "our understanding of the interior of the Moon is derived from surficial, but not superficial, information, coupled with geologic reasoning". Geochemical and other remote sensing data obtained by the Apollo, Galileo, Clementine and Lunar Prospector missions therefore have significantly contributed to the current understanding of the distribution of specific rock types, and what they tell us about the Moon's geological history and evolution.

1.1.1 Formation of the Moon and Early Differentiation

A better understanding of how the Moon formed, differentiated and evolved has been born out of the detailed petrological, isotopic and geochemical studies of the rocks and remote sensing data discussed above. Models have been formulated to account for accretionary and differentiation processes, and to explain similarities and differences between the major lithological suites.

Theories of Lunar Formation. There are four prominent theories of how the Moon came to exist. (1) Rotational fission: George Darwin (1880) first proposed that the Moon was formed, or indeed 'spun-off', from an early rapidly spinning Earth. (2) Binary accretion: that the Moon was formed from the 'left-overs' of Earth's proto-planetary material. (3) Capture: that the Moon formed in an orbit similar to the Earth and was 'captured' by its gravity into a stable orbit. (4) Giant Impact: that the Moon was formed in a catastrophic impact event between a large (Mars-sized?) body and an early Earth (Hartmann and Davis, 1975; Canup and Agnor, 2000) approximately 50 million years after the start of the solar system (Halliday and Lee, 1999). It is most widely (although not unanimously) accepted that the giant impact scenario best accounts for a diverse range of geochemical, geophysical and orbital dynamic evidence. This model hypothesises that the rock fragments that formed the Moon would have coalesced over a relatively short period of time (e.g. on the scale of 1 month to 100 years depending on the model: Shearer et al. 2006 *and references therein*), and theoretically formed a large molten body of magma encompassing at least the outer layers, and possibly all of the proto-Moon.

Magma Ocean Models. Models of lunar primordial differentiation focus around the subsequent history of the Moon after this formation event. Early theories favoured the idea that the rapid accretion of the Moon gave rise to a magma ocean (MO) that encompassed the whole (or at least the vast majority) of the lunar interior. Observations of crustal heterogeneity and modelling of ferroan anorthosite (FAN) rock systems suggest a complex differentiation history (e.g. Jolliff and Haskin, 1995; Snyder et al. 1995, Shearer and Floss, 2000; Longhi, 2003, Shearer et al. 2006 and Fig. 1.5, 1.6). Petrological studies indicate that a MO would have a crystallisation sequence similar to that of terrestrial layered igneous intrusions: olivine → opx±olivine → olivine+cpx±plag → cpx+plag → cpx+plag+ilmenite (p. 394, Shearer et al. 2006). From this it has been theorised that an early, anhydrous, MO rapidly fractionally crystallised a Moon-wide series of mafic/ultramafic cumulate piles that 'sank' to form a deep lunar mantle (Taylor, 1982; Warren, 1985, 1990; Papike et al. 1998; Shearer and Papike, 1999; Shearer et al. 2006), with plagioclase floating to form an anorthositic crust (Fig. 1.5)

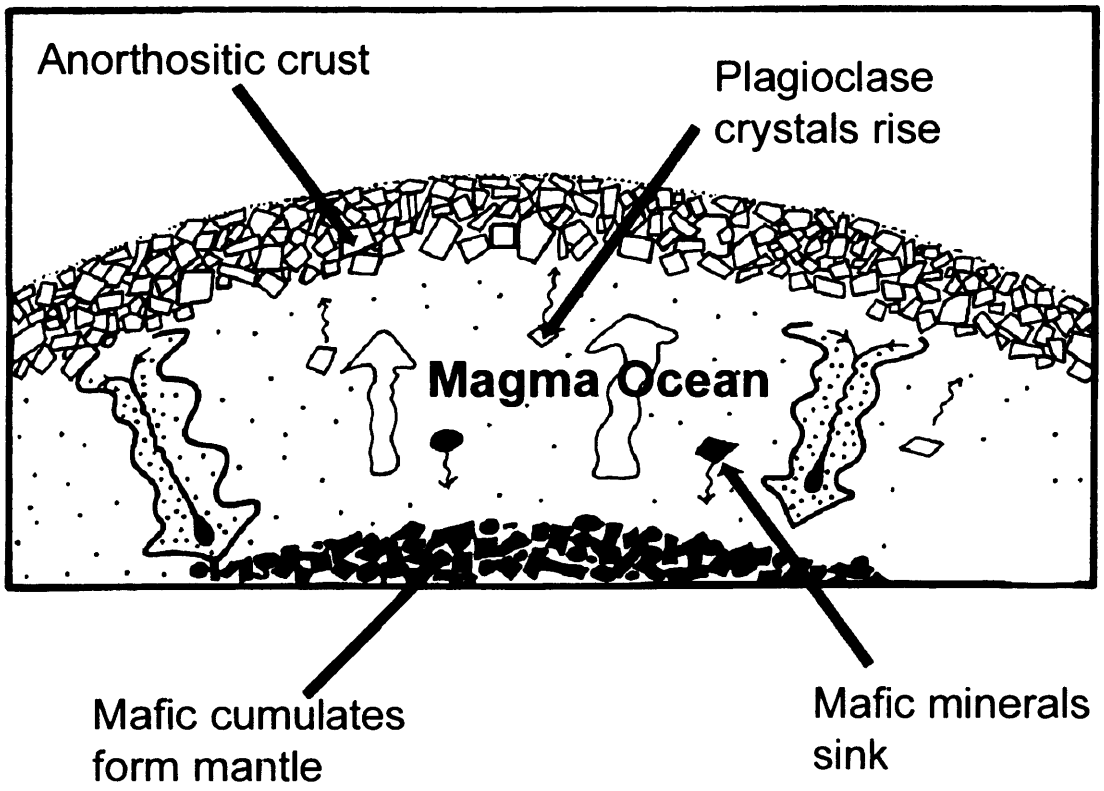

Fig. 1.5. Simplistic cartoon of lunar plagioclase flotation from a magma ocean, with dense mafic phases sinking to form a mafic mantle. Adapted from Walker (1983).

In a manner similar to those in terrestrial igneous systems, Rare Earth Elements (REE) in the lunar MO melt should have existed in a trivalent state, making them behave as incompatible trace elements (ITE) that do not easily substitute into mineral phases. Europium, however, under such low oxygen fugacity conditions, is present in a divalent state (Eu^{2+}) and so is easily accepted into the plagioclase crystal structure in place of Ca^{2+} (p 188, Taylor et al. 1991).

It has been calculated by Snyder et al. (1995) that depending on the original MO Al-content, plagioclase would become a liquidus phase (i.e. started to crystallise) after between 57% (if initial Al_2O_3 was 7%) to 80% (if initial Al_2O_3 was <5%) of total MO crystallisation. Upon formation, this plagioclase overcame a density contrast with dense comagmatically crystallising mafic phases by buoyantly rising and migrating towards the lunar surface. Plagioclase thus accumulated to form a crust 30 to 150 km thick. This crystal separation also removed Eu from the MO melt, and provided the anorthositic crust with a positive chondrite normalised ($_{cn}$) Eu-anomaly ($Eu_{cn} / \sqrt{(Sm_{cn} + Gd_{cn})} > 1.0$), and a composition low in ITE.

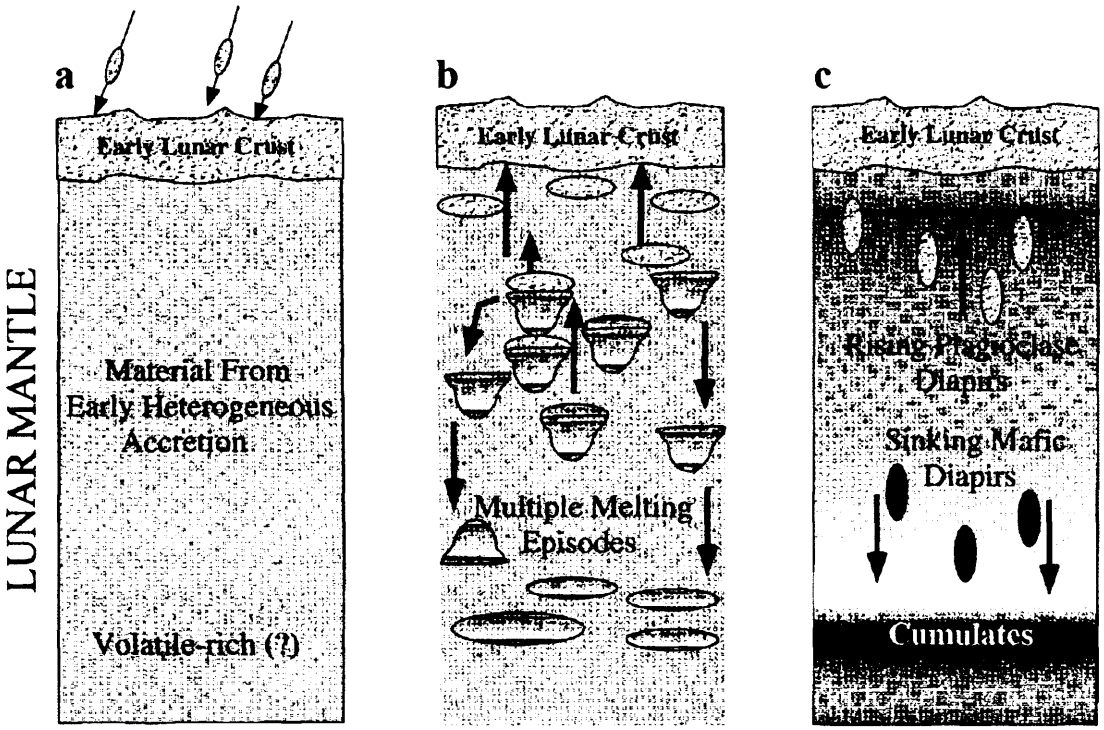

Fig. 1.6. Three models of early lunar evolution taken from Shearer and Papike (1999): (a) A crust formed from the accumulation of cosmic sediment (e.g. Walker, 1983) protecting and overlying an undifferentiated lunar mantle. (b) Lunar differentiation processing caused a process of serial magmatism where multiple episodic melting occurred in the lunar mantle (e.g. Longhi and Ashwal, 1984; Walker 1983). (c) Magma ocean differentiation model in which crystallising plagioclase diapirs buoyantly rise to form a thick lunar crust (e.g. Taylor, 1982; Warren, 1985).

Alternative crustal evolution models. According to a magma ocean model the lunar crust should form a comagmatic, monogenetic suite of rocks (Walker, 1983). However, many petrological and remote sensing observations have identified that the lunar highlands are actually composed of a heterogeneous suite of lithologies that cannot be petrologically related, and therefore cannot have been emplaced co-magmatically. Alternative models of early lunar evolution must therefore account for the contribution of other magmatic products to the lunar crust (Fig, 1.6). Several of the principal MO alternative models theories are outlined below:

Wetherill (1975) proposed that after lunar accretion, primordial differentiation took place in regional magma chambers all over the Moon, as there was not enough accretional heating to trigger a Moon-wide melting event forming a MO. Large-scale impacts would have been very common throughout early lunar evolution and he argued that these would have formed several (up to ~60) localised, near-surface differentiated plutons, each forming layered intrusions with plagioclase floatation and mafic mineral sinking. Weaknesses in this model have been identified by Warren (1985) and Shearer et al. (2006), who point out that this type of localised melting would not produce the diversity of mantle source cumulates to account for the compositional variation of mare basalts seen in the sample collection. Additionally, when comparing this

model with terrestrial analogues, most of the large layered intrusions found on Earth do not have such thick anorthosite units.

The observation that the majority of rocks from the lunar highlands have a positive Eu-anomaly (and that the lunar mare basalts have a corresponding negative Eu-anomaly) supports the lunar MO model. This argument has been criticised by investigators such as Walker (1983) and O'Hara (2000a,b) who argue that the lunar highlands actually have a negligible Eu-anomaly based on estimates of bulk crust composition and remote sensing evidence. Walker (1983) uses this evidence to invoke an early crust that was formed by episodic serial magmatism, although does not completely exclude the possibility of a global MO event. O'Hara however is very critical of the total Moon-wide anhydrous melting model, and prefers a history purely involving serial volcanism to explain the crust's formation. He advocates that early lunar evolution was driven by partial melting in the presence of water, with hydrated mineral phases being massively dehydrated as they are violently erupted into a vacuum environment. This model involving a hydrous mantle does seem somewhat implausible, however, as no investigator has reported a meaningful abundance of hydrous minerals or high concentrations of highly volatile elements in any lunar sample (water concentrations in lunar samples have been recently discussed by Saal et al. 2007).

Longhi (2003) presents an argument for post-MO melting to account for lunar ferroan anorthosite crustal formation, using evidence from Sm-Nd isotopes in FAN samples. He theorises that primitive accreted materials would have likely formed a magma ocean topped by an insulating impact breccia crust (Fig. 1.7: left). This would have led to a scenario of crystallised mafic and ultramafic cumulates experiencing density instability, triggering two-layer convection. This convection advected the heat necessary for partial melting, generating FAN-like plagioclase saturated liquids. It was from these melts (and not the original MO products) that crystallising plagioclase buoyantly rose from the residual crystal mush to form upwelling anorthositic diapirs (Fig. 1.7: centre). Evidence for this model is apparently provided by Sm/Nd isotopic systematics in Apollo 16 ferroan anorthosites. The isotope systematics in these primitive samples suggests that they crystallised at ~4.56 Ga from a melt source that was light REE-depleted (with positive εNd values i.e. $\{[^{143}Nd/^{144}Nd_{\text{ in the sample}}] / [^{143}Nd/^{144}Nd_{\text{ in the chondrite uniform reservoir}}]-1\} \times 10^4$). This LREE-depletion is inconsistent with the Moon having an initial chondritic composition (e.g. Rankenburg et al. 2006) as the MO would not have dramatically fractionated Sm/Nd ratios throughout crystallisation. Therefore, according to this argument a secondary partial melt had to be responsible for the fractionation and crystallisation of the FAN-suite.

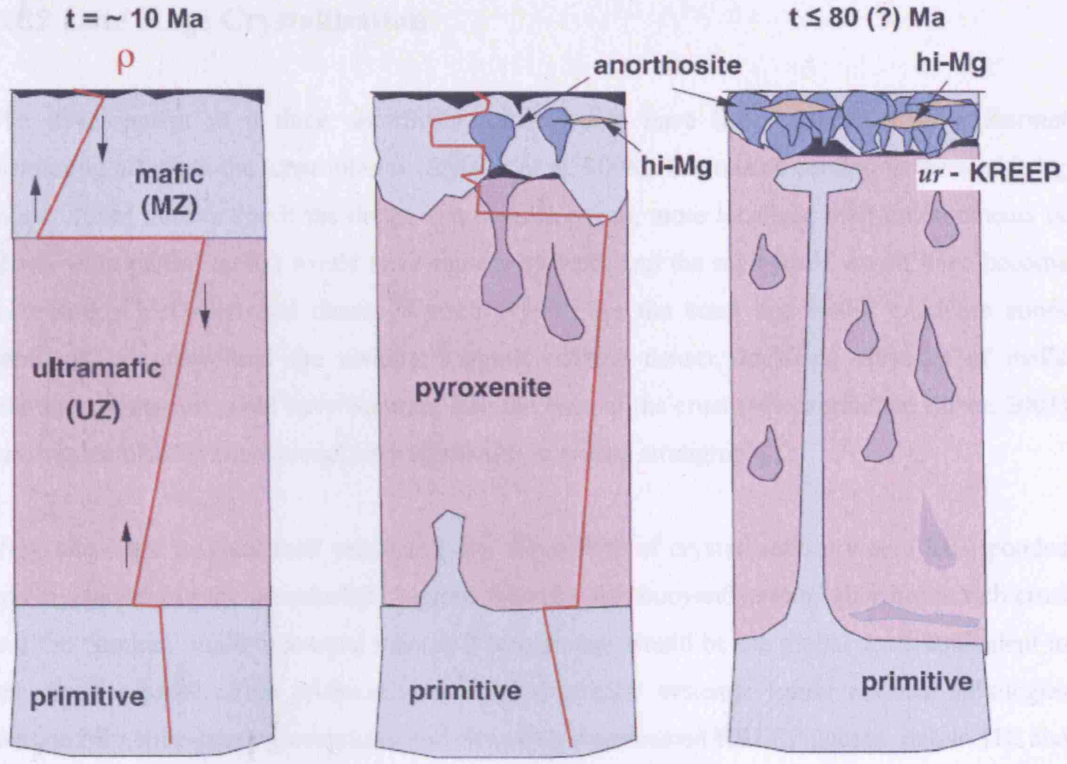

Fig. 1.7. Longhi (2003) model of lunar ferroan anorthosite evolution in which a fractionally crystallising magma ocean forms a thin, insulting crust (possibly composed of mafic/ultramafic impact melt breccias [Longhi and Ashwal, 1984]) overlying mafic (MZ) and ultra-mafic (UZ) zones (left). There was an unstable density contrast between the MZ and UZ zones because of the upwards decrease in Mg# which resulted in two-layer convection. Heating of the mafic cumulate piles resulted in large-scale partial melting and the formation of FAN-like melts (central). Plagioclase crystallising from these melts buoyantly rises as diapirs and slowly forms a thickened crust. Finally conductive heating from above or radioactive decay causes plumes to partially melt large areas of the mantle, generating upwelling Mg-suite diapirs that are serially, and co-magmatically, intruded into the FAN highlands. Time (t) is given in million years from Moon formation.

Lunar Crust Formation. Whatever differentiation process occurred it is likely to have formed a thick pile of anorthositic-noritic plutons, or 'rockbergs', in the upper crust, displacing and assimilating any original MO products and forming the lunar crust as we observe today. These plutons potentially would have consisted of cumulus plagioclase and an intercumulus melt phase. Upon isolation from the MO system these also experienced fractionation, mineral separation and settling to an extent that they formed small scale cumulate piles of increasing mafic content and Mg# (molar Mg/Mg+Fe) with depth. Jolliff and Haskin (1995) estimated that the isolated diapir intercumulus melt associated with cumulus plagioclase phases had ~7 to 9 times chondritic REE abundances and a small positive Eu-anomaly (compositions similar to the lunar meteorite MAC 88104/88105: Jolliff and Haskin, 1995).

1.1.2 Late Stage Crystallisation

The development of a thick anorthosite crust would have likely caused a large thermal blanketing effect on the lunar interior (Shearer et al. 2006). The rate of cooling in the remaining molten lunar interior (be it the dregs of a magma ocean, more localised melt environments or Moon-wide partial melts) would have rapidly slowed, and the melt itself would have become increasingly FeO-rich and dense (Warren, 1990). As the crust and mafic cumulate zones continued to grow, and the residual magma became denser, localised episodes of mafic cumulate floatation could have occurred into the base of the crust (Wieczorek and Zuber, 2001) causing localised compositional heterogeneities in crustal stratigraphy.

Very late-stage residual melt products (after 90 to 95% of crystallisation) would have ponded and crystallised in the intermediate regions between the 'buoyantly risen' anorthosite rich crust and the 'sunken' mafic cumulate mantle. These phases would be the global scale equivalent to late stage crystallisation products in normal magmatic systems. Lunar residual lithologies included ilmenite-bearing cumulates and extremely fractionated KREEP phases, rich in ITE and heat-producing elements like U and Th.

1.1.3 The Formation of the Plutonic Suite

The lunar near-side highlands, as sampled by the Apollo missions, are rich in a range of endogenic igneous plutonic lithologies. These have been classified into the petrologic subgroups: Magnesian-Suite (Mg-Suite or HMS) rocks and alkali-rich plutonic rocks (HAS) and KREEP-basalts (Section 1.1 and Fig. 1.8a). All of these lithologies are ancient (radiometrically dated to be 4.5 Ga to 3.85 Ga), and are believed to have been emplaced by contemporaneously serial magmatism, probably derived from a common petrologic source. Several lunar feldspathic meteorites (Section 1.1.5) that may have been derived from the lunar farside, are notably lacking in these HMS lithologies – suggesting that the HMS rocks are derivatives of KREEP-related near-side magmatism.

Compared with estimated FAN parental melt composition, HMS parental magmas have typical KREEPy geochemical signatures suggesting that Mg-Suite cumulates must have been formed after the formation of KREEP, and therefore after MO closure. A range of models has been postulated to account for the petrological range of plutonic rocks in the sample collection (see Shearer et al. 2006 for a discussion). Geochemical modelling requires that the plutonic suite was generated by the melting of deep, early-crystallised, magma ocean mafic cumulates and the

assimilation of KREEP. To account for the very magnesian olivines identified in some HMS troctolites (Fo_{92}), Hess (1994) proposed either that the melted mantle had to be heterogeneous in composition (variable Mg#), or that cumulate source regions would have had to have experienced large (>25%) amounts of fractional melting to generate Mg-melts in equilibrium with crystallising Mg#-rich olivine phases.

The cause of this mantle melting is somewhat disputed. It is possible that it could have been caused by radioactive decay (Hess, 1994) or by decompression melting as a result of cumulate overturn (Hess and Parmentier, 1995), or possibly by a combination of both mechanisms. Longhi (2003) proposed that the HMS parental melts could have been generated by mantle plume processes, triggered as a consequence of density instabilities and melting from radioactive decay (Fig. 1.7: right). On the other hand, O'Hara (2000a) has argued that lunar plume processes are unlikely to be a cause of early mantle melting as there is no evidence of large-scale surface crustal deformation; however, it is possible that any surface expressions may have been completed removed by subsequent basin generation. Whatever the cause, these melts would have been transported up through the mantle, possibly melting and reacting with KREEP-rich lithologies at intermediate stratigraphic horizons, to gain a range of ITE enrichment.

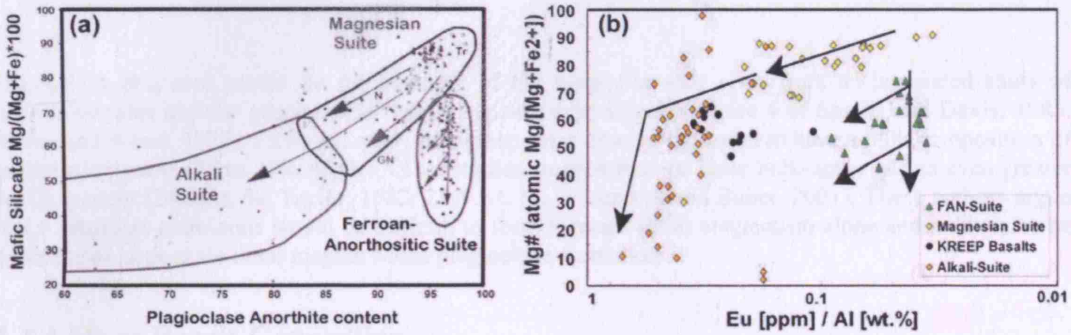

Fig. 1.8. (a) Mg# in all mafic silicates vs. coexisting plagioclase An-content for intrusive highland igneous rock suites and eruptive KREEP basalts. Crystallisation trends (arrows) depict the petrological relationships between the Mg-Suite and Alkali-Suite rocks, and petrological variations between specific groups (norites, gabbronorites, troctolites) within the Mg-Suite. Diagram taken from Fig. 3.2 in Wieczorek et al. (2006) using the data complied by Warren (1993) and Papike et al. (1998). (b) Bulk rock compositions exhibit a similar trend in Mg# vs. bulk Eu/Al content (data complied from Papike et al. 1998 and Wieczorek et al. 2006).

The presence of a KREEPy-ITE signature and isotopic systematics suggest that there is a petrologic link between the HMS rocks and other plutonic samples (Shearer and Floss, 2000; Shearer et al. 2006). They are either likely to represent a continuum of crystallised products (Fig. 1.8) of parental magmas with compositions similar to the KREEP basalts (Snyder et al. 1995), or to represent a more complex scenario with KREEP magmas assimilating different

amounts of crustal ferroan anorthosites and/or magma mixing (Shervais and McGee, 1998, 1999).

In accordance with isotopic dating of highland lithologies (Nyquist and Shih, 1992; and see Papike et al. 1998 and Shearer et al. 2006 for a discussion) magmas representing the plutonic magmatic suite were periodically intruded into the overlying crust (Fig. 1.9), where they crystallised at depths of ~10 to 50 km (Herzberg and Baker, 1979; Schwartz and McCallum, 1999).

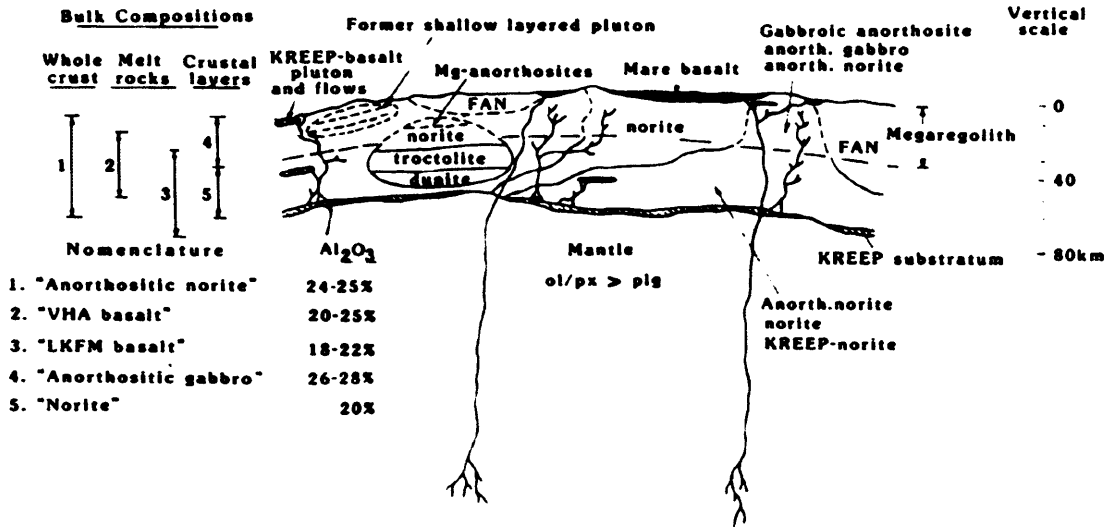

Fig. 1.9. A proposed model for the structure of the lunar near-side crust from an integrated study of Apollo samples and the geochemical remote sensing experiments (Figure 4 of Spudis and Davis, 1985. Ryder and Wood, 1977). From this study the upper lunar crust is estimated to have a bulk composition of anorthositic norite (24 to 25% Al_2O_3). Other studies suggest that the lunar bulk-upper has an even greater Al_2O_3 content (24.6 wt. %: Taylor, 1982; 28.5 wt. %: Wieczorek and Zuber, 2001). These authors argue that a crust this aluminous would be difficult to form through serial magmatism alone and is likely to be evidence of large-scale lunar magma ocean plagioclase formation.

1.1.4 Mare Basalt Generation

Existing petrogenesis models. After 90 to 95% of magma ocean crystallisation, FeO-rich silicate (fayalite, Fe-pyroxenes etc.) and TiO_2-oxide mineral phases (ilmenite, ulvöspinel-spinel) began to be precipitated. These phases have a high density and will sink, piling up on Mg-rich phases (olivine and pyroxene-bearing cumulates) already settled out at depth. A situation of dense mineral phases overlying less dense mineral phases is intrinsically gravitationally unstable and it has been theorised that a large-scale mantle overturn occurred, sinking the FeO and TiO_2 phases to deep mantle horizons (Neal and Taylor, 1992; Shearer et al. 2006). It is possible that an overturn would have entrained very late stage KREEPy residual material, sinking heat-producing elements down into the mantle. This concentration of Th and U buried at depth therefore provides a plausible heat-source for subsequent melting of now buried

gravitationally stable, and compositionally heterogeneous, mantle cumulates (p. 467, Shearer et al. 2006). It is debatable whether this down-welling of KREEP material occurred on a global scale, or was concentrated in mantle regions on the lunar near-side (Wieczorek and Philips, 2000). This later scenario could be used to account for the preferential eruption of lunar mare basalts in near-side rather than far-side basins.

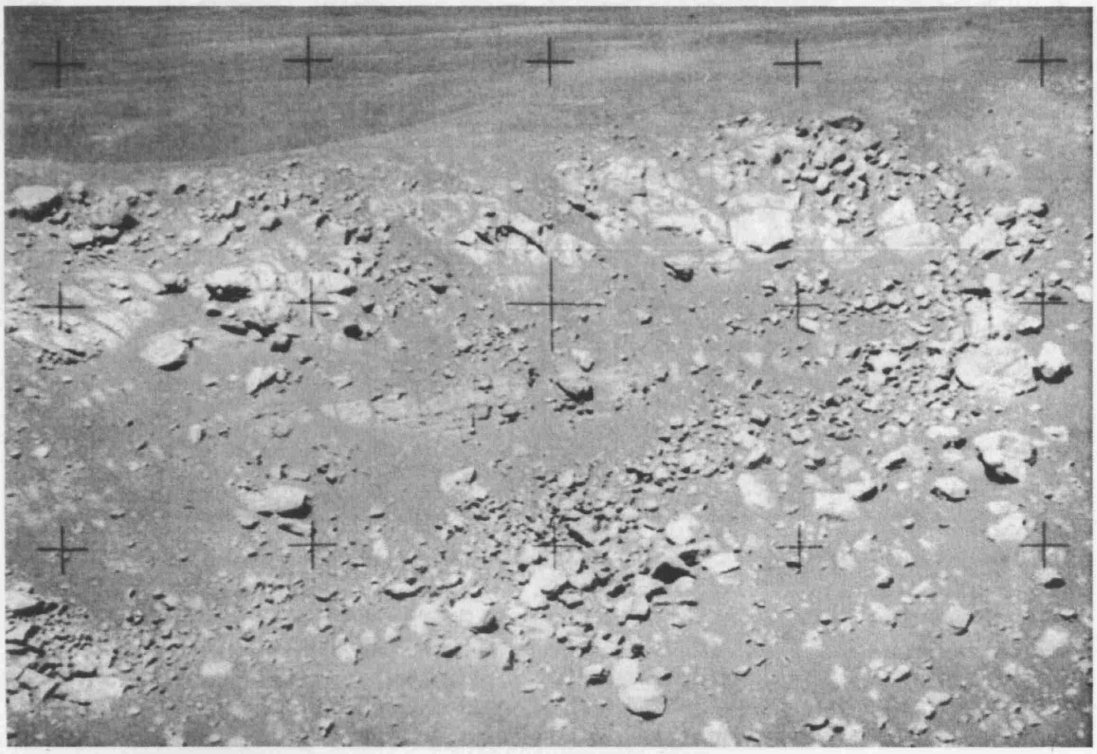

Fig. 1.10. Wall of the Hadley Rille collapsed lava channel photographed on the Apollo 15 mission (A15 frame H-12115: NASA). Possible thin, gently dipping, layers of flood mare basalts (~a few metres thick) can be seen in the centre of the image. These layers are the only bedrock outcrops to be identified at Apollo landing sites.

Mare basalts are the erupted volcanic products (Fig. 1.10) of the partial melting of these mantle cumulates from depths estimated to be 100 to 500 km (Shearer and Papike, 1993; Shearer et al. 2006). Basalts were preferentially erupted into large basins and low-topographic features on the lunar near-side (Fig. 1.1a) with some minor outcrops occurring in younger basins and craters on the lunar farside (Fig. 1.1b). Although mare deposits are typically associated with these large impact structures, it is not thought that the basin generation itself directly gave rise to significant partial melting to cause mare basalt generation (Hiesinger and Head, 2006). The principal evidence for this is that there is often a significant period of time (several hundred millions years) between the basin generation event and the age of infilling mare basalt deposits. Moreover, the South Pole Aitkin Basin, the largest and most ancient impact basin on the Moon, contains only a small quantity of mare basalt outcrops; this is not consistent with long-lived, localised decompression mantle melting (Shearer et al. 2006). The asymmetry of mare basalt

volcanism is therefore not related solely to crustal thickness, but is perhaps more importantly related to the heterogeneous extent of heat-producing elements in the lunar mantle.

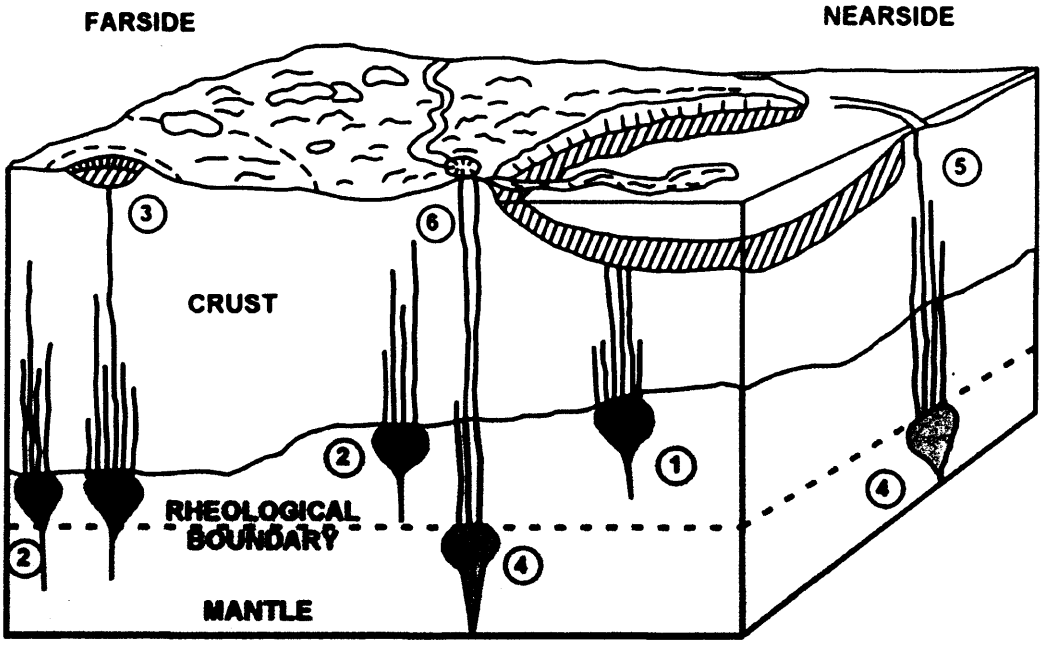

Fig. 1.11. Magma transport from ponded reserves in neutral buoyancy zones (Head and Wilson, 1992). Diapirs of mantle partial melts pond at the base of the lunar crust (1), (2). Partial melts may also be generated from deeper mantle horizons (4). If melt is generated on the lunar farside, it could potentially be retarded by thick crustal units and so may become trapped at depth in dykes (2) with only minor infilling of the largest and deepest basins (3). As basins are infilled lavas preferentially erupt at rim (5). Cooling of the lunar interior over time reduces melt availability from deeper mantle reserves. As a consequence lava effusion rate falls causing more localised young eruptions (6).

The large geographical extent of near-side basalt outcrops, and the sustained time scale on which they were erupted, suggests that mare basalts were probably erupted in highly effusive eruptions with some occasional fire-fountain events (Head and Wilson, 1992, Wieczorek et al. 2006 *and references therein*). Evidence of this fire-fountaining comes from the findings of spherical pyroclastic glass beads in the Apollo samples (Shearer and Papike, 1993), and from remote sensing observations of dark mantling deposits and possible fissure vent sites (Wilhelms, 1982; Head and Wilson, 1992, 2002). Lava was transported from sub-crustal magma-chambers to these eruptive centres by a network of feeder dykes (Fig. 1.11) that probably in many cases exploited sub-basin fracture/fault structures. Upon eruption, low-viscosity lavas flooded topographically low horizons forming thick sequences of thin flood basalt flows (Fig. 1.10). Less frequent episodes of higher viscosity basaltic lava created lobate flows (up to 40 m in height: Wilhelms, 1982) that flowed for up to as much as 1200 km in some maria (Wilhelms, 1982). Volumetrically, most of the basalts were erupted in the Late Imbrium Period between ~3.7 and 3.3 Ga with effusion rates diminishing after this period as the lunar interior cooled and mantle melting slowed (Fig. 1.11).

Mare basalts display a wide range of textures as a result of different cooling regimes, exsolved gas content (vesiculation) and post-emplacement shock history. They also exhibit a wide range of igneous textures from vitrophyric (glassy) through to sub-ophitic to poikilitic and to porphyritic gabbros, indicating the variable nature of emplacement and lava flow thickness.

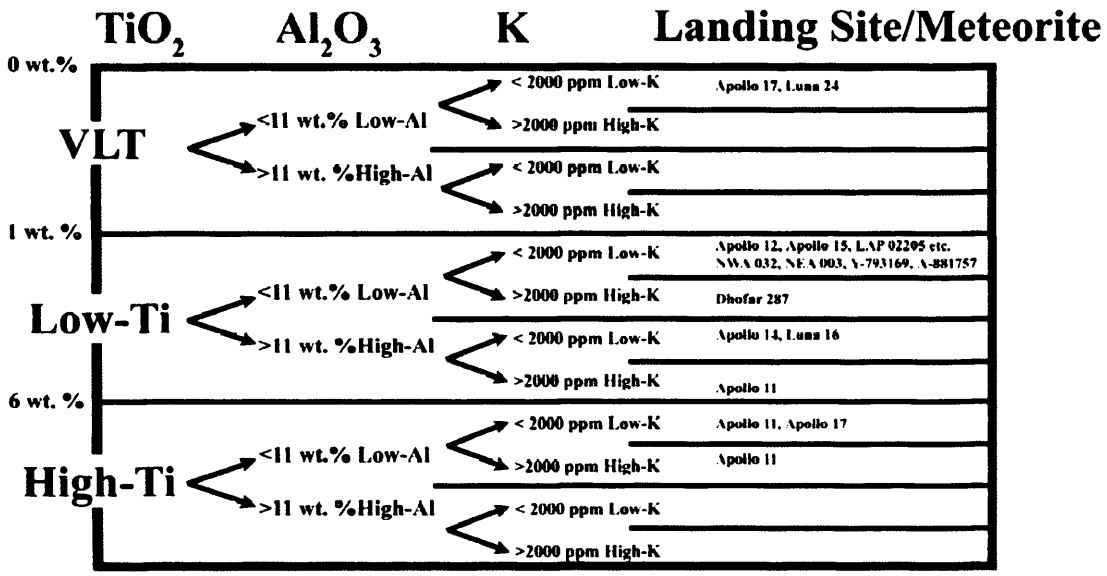

Fig. 1.12. Lunar mare basalt classification scheme adapted and updated from Neal and Taylor (1992). The low-Ti group is then often sub-classified according to specific mineralic lithologies at the different landing sites e.g. olivine basalts (A12, A15), pigeonite basalts, (A12, A15), quartz-normative basalts (A15), ilmenite basalts (A12), feldspathic basalts (A12). Classifications of lunar meteorites come from reference material listed on Website 1.2.

Classification. We have samples of mare basalt lavas from all of the Apollo landing sites (even from the 'highland' Apollo 16 landing site, e.g. Ziegler et al. 2006). These exist either as large hand specimens or as clasts within breccias. Petrologic analysis of this material has revealed that, relative to terrestrial basalts, mare basalts exhibit a diverse range of compositions (e.g. BVSP, 1981; Taylor et al, 1991; Papike et al. 1998; Shearer et al. 2006, Wieczorek et al. 2006). Mare basalts have greater concentrations of FeO and Fe/Mg and less Al_2O_3 compared with terrestrial basalts. Lunar basalts also have low bulk K_2O + Na_2O meaning that they have much lower alkali-contents than basalts on Earth. Neal and Taylor (1992) presented a classification scheme, shown in Figure 1.12, of mare basalts based on sample bulk TiO_2, Al_2O_3 and K composition.

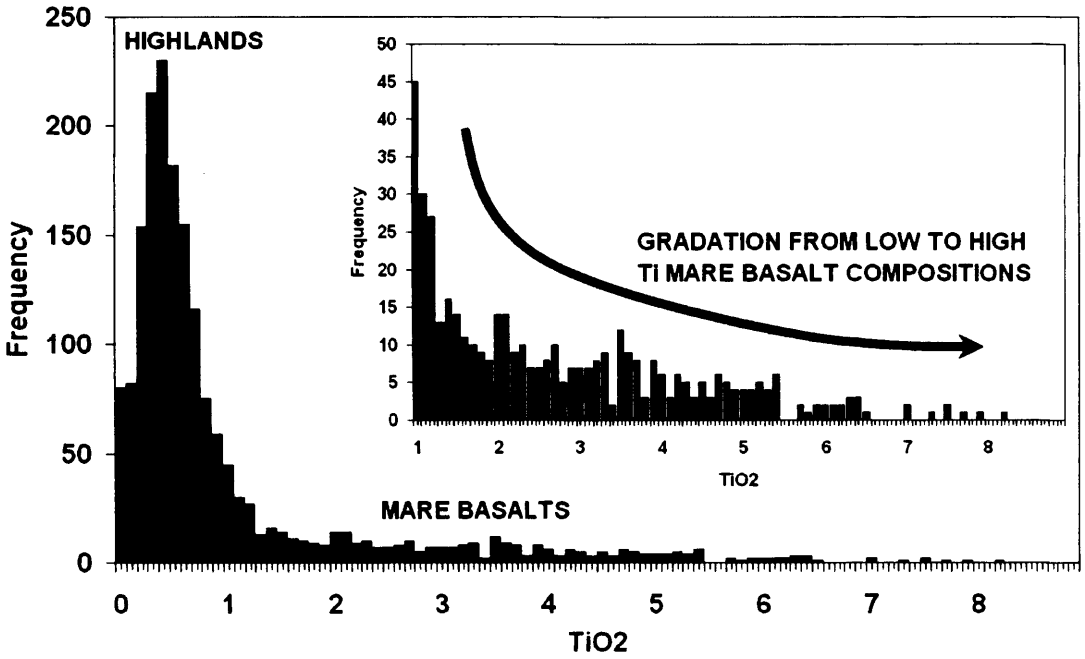

Fig. 1.13. Frequency of Lunar Prospector 2° TiO_2 dataset (Prettyman et al. 2006) illustrating the remotely sensed continuum of soil TiO_2 compositions. The remotely sensed datasets do not show the same bi-modal distribution of TiO_2 content as the sample collection; good evidence of the petrologically limited nature of the rock collection. These data illustrate the widespread nature of the Low-Ti basalts compared to outcrops of high-Ti basalts. This trend has also been observed in the lunar meteorite collection (Fig. 1.12): to date we only have meteorites containing low-Ti or VLT material – no high-Ti basalts have ever been identified. Inlay shows the frequency of pixels with compositions >1 wt.% TiO_2.

The Apollo and Luna sample collections show a bimodal distribution between low and high-Ti basalts with no/few compositions having bulk TiO_2-contents between 5.5 and 8 wt.% (see Fig. 4.35 in Shearer et al. 2006). This bimodality has also been correlated with radiometric age dates, with high-Ti basalt groups having older crystallisation ages (3.8 to 3.5 Ga) than low-Ti groups (<3.5 Ga to 2.8 Ga) (Nyquist and Shih, 1992). This evidence was used to theorise that upper mantle sources (ilmenite-rich) were preferentially melted in early events with High-Ti basalts being erupted. Through time the mantle melt source increased in depth with progressively poorer Ti reserves being melted, and forming the Low-Ti basalt suite. However, remote sensing information has led to the development of a much more complicated mare petrogenesis scenario. TiO_2 data (e.g. Prettyman et al. 2006) from the Lunar Prospector mission (Fig. 1.13) have shown that there is a near continuum between low and high Ti soil compositions. Lava flow crater counting relative age determination by a number of authors (e.g. Hiesinger et al. 1998, 1999, 2000a, 2000b, 2003; Shinsuke and Yasushi 2003; Hackwill et al. 2006) agrees that generally throughout time there is a decrease in basalt Ti-content with age. However, deposits in individual basins show no correlations, with low and high-Ti flows erupting simultaneously in different places suggesting that mare basalts are fed from a heterogeneous source region.

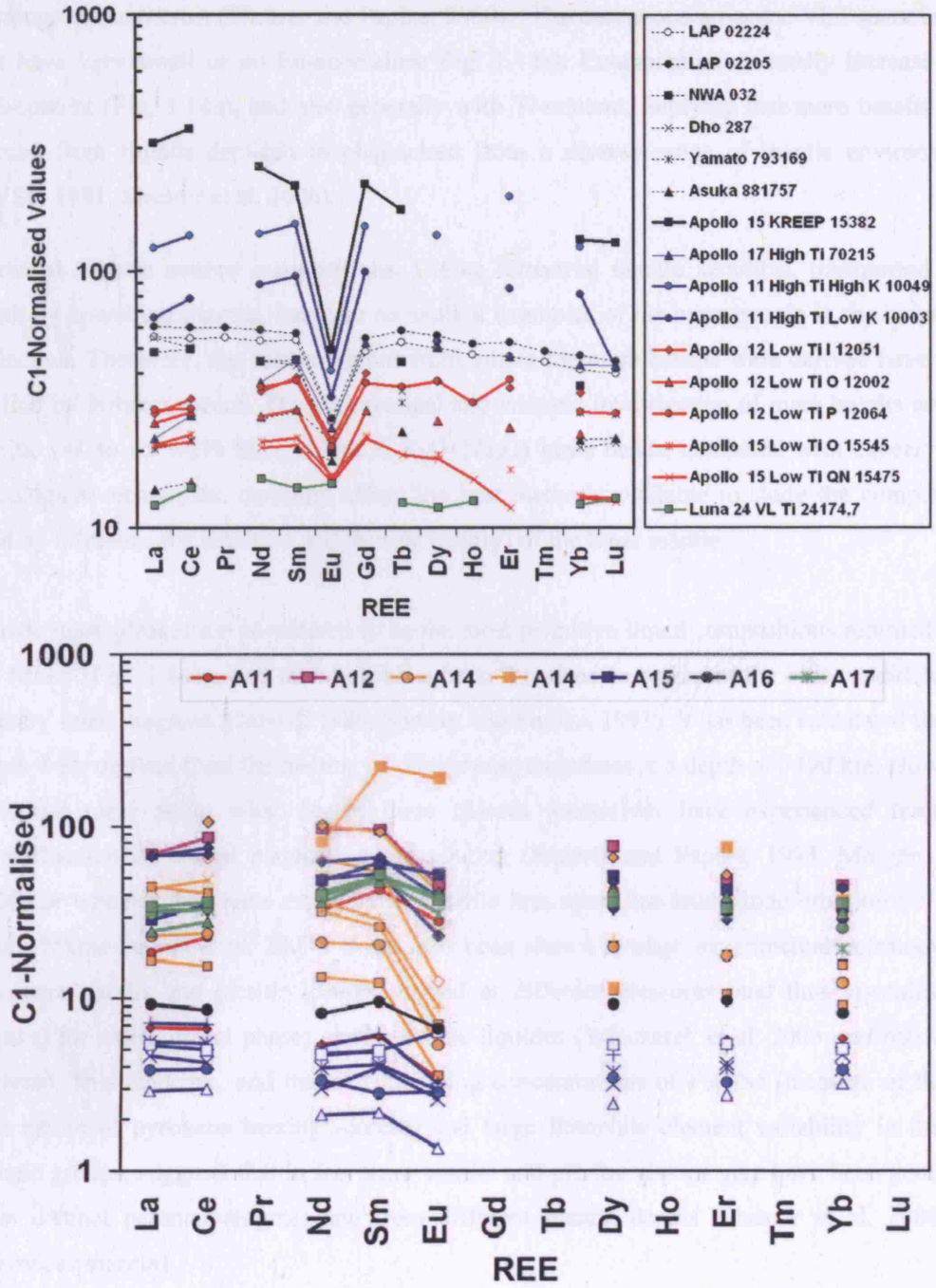

Fig. 1.14. (a) Top: Range of Apollo and Luna mare basalt bulk sample REE compositions (from data compiled in BVSP, 1981) normalised to C1-chondrites (Anders and Grevesse, 1989). The higher the Ti-content of the basalt generally the higher the ITE-content. Mare basaltic meteorites LAP 02205 & 02224 (Joy et al. 2006b), Dhofar 287 (Anand et al. 2003b), NWA 032 (Zeigler et al. 2005), Y-793169 and A-881757 (Warren and Kallemeyn, 1993; Koeberl et al. 1993) are illustrated for comparison. (b) Bottom: REE-compositional data from picritic glasses normalised to chondrites. Data compiled by Shearer et al. (2006).

Trace element chemistry. Nearly all mare basalts have a negative europium anomaly (Fig. 1.14a), believed to have been inherited from a common plagioclase-understaturated source region, complementary with a region that had experienced fractionation of plagioclase whilst

forming the lunar crust (Shearer and Papike, 2000). (The exceptions are some VLT mare basalts that have very small or no Eu-anomalies: Fig. 1.14a). Eu-anomalies generally increase with ITE-content (Fig. 1.14a), and also generally with Ti-content, implying that mare basalts were formed from liquids depleted in plagioclase from a diverse range of mantle environments (BVSP, 1981, Shearer et al. 2006).

Parental mantle source compositions. Unlike terrestrial mantle xenoliths, transported from depth by upwelling magma, there are no explicit examples of the lunar mantle in the lunar rock collection. Therefore, the source regions from where the mare basalts were derived have to be studied by indirect means. The geochemical and isotopic investigation of mare basalts and the picritic (41 to 45 wt.% SiO_2, <3 wt.% K_2O+Na_2O) glass beads, combined with experimental petrological techniques, currently afford the best methods available to study the composition (and by inference the structure and thermal history) of the lunar mantle.

Picritic mare glasses are considered to be the most primitive liquid compositions returned from the Moon (Fig. 1.14b), and therefore have been theorised to represent the best candidates for primary lunar magmas (Delano, 1986; Shearer and Papike, 1993). It has been calculated that the beads were derived from the melting of olivine-opx cumulates at a depth of >400 km. However, it is not clear as to what degree these glasses themselves have experienced fractional crystallization or crustal plagioclase assimilation (Shearer and Papike, 1993; Morgan et al. 2006) or whether they have experienced volatile loss upon fire-fountaining eruption (O'Hara, 2000; Elkins-Tanton et al. 2003). It has also been shown through experimental petrology that the mare basalts and picritic glasses formed at different pressures (and thus crystallisation depths) for when crystal phases appear on the liquidus (Wieczorek et al. 2006 *and references therein*). This evidence, and that of contrasting concentrations of FeO/Sc (measure of the Fe-rich nature of pyroxene bearing sources) and large lithophile element variability in the two sample groups, suggests that in fact mare basalts and picritic glasses may have been generated from distinct parental magmas and from different mantle depths (Shearer et al. 2006 *and references therein*).

Several authors have therefore suggested that the best representation of a parent magma composition can be estimated from the Apollo vitrophyre basalt samples i.e. those samples that were rapidly cooled and quenched upon eruption (e.g. Rhodes et al. 1977; Neal et al. 1994a, 1994b). Neal et al. (1994b) used vitrophyric samples in the Apollo 12 Low-Ti pigeonite, olivine and ilmenite suite to model potential crystallisation sequences and fractionation pathways. Interpretation of these pathways suggests that the different basalt suites were generated from non-modal batch melting from distinct magma reserves that experienced either closed-system

fractional/cumulate crystallisation or assimilation-fractional crystallisation of a plagioclase rich source. The fact that these lavas were emplaced in close proximity to each other from three distinct mantle reservoirs tells of the complicated heterogeneous nature of melting in the lunar mantle.

1.1.5 Impact Processes and the Lunar Regolith Environment

The Moon preserves a record of its impact history for at least the last 4 billion years. Its scarred surface has become the calibration system for defining the cratering record of the inner solar system, and the age dating of other planetary surfaces. Craters are ubiquitous on the lunar surface. They range in size from micro-pits (<50 μm) on glass beads in the sample collection, to the South Pole-Aitkin basin, the largest impact basin in the solar system (2500 km diameter). The lunar cratering flux through time has been calibrated using radiometrically dated samples returned from specific site localities and the crater abundance within the geological units at these sites (Stöffler et al. 2006 *and references therein*). This flux, when extended to other geological units across the Moon, can be used to interpret the geological history of the lunar surface and to provide estimates of the ages of the largest basins that pock-mark the near and far-side of the Moon. According to Wilhelms (1982) there were 30 multi-ringed basins formed between 4.2 and 3.92 Ga and 12 basins formed between 3.92 and 3.85 Ga (with the Orientale basin marking the youngest impact at ~3.8 Ga). From 3.8 Ga onwards, no large basin-forming impacts occurred on the lunar surface, and the overall flux of Moon-crossing bodies impacting the lunar surface rapidly declined.

Impact Deposits. An impact into any planetary surface, on any scale, will generate shock-induced thermal metamorphism. Impacts larger than a few centimetres in scale will also cause shock pressure induced metamorphic effects. Evidence of these processes will be seen in mineral and rock samples, at the micro and hand specimen scale, and in large-scale crater morphological features (Fig. 1.15).

Assuming the lunar crust has a stratigraphic structure like that shown in Figure 1.9, impact melt will be generated from the homogenised products of an anorthositic upper crust and lower crust mafic lithologies such as magnesian-anorthosites (e.g. gabbros and norites). Large basin-forming impactors with diameters >100 km have the potential to have penetrated through the lower crust excavating trapped KREEP products and, possibly even melting and incorporating rocks from the upper mantle (Stöffler et al. 2006).

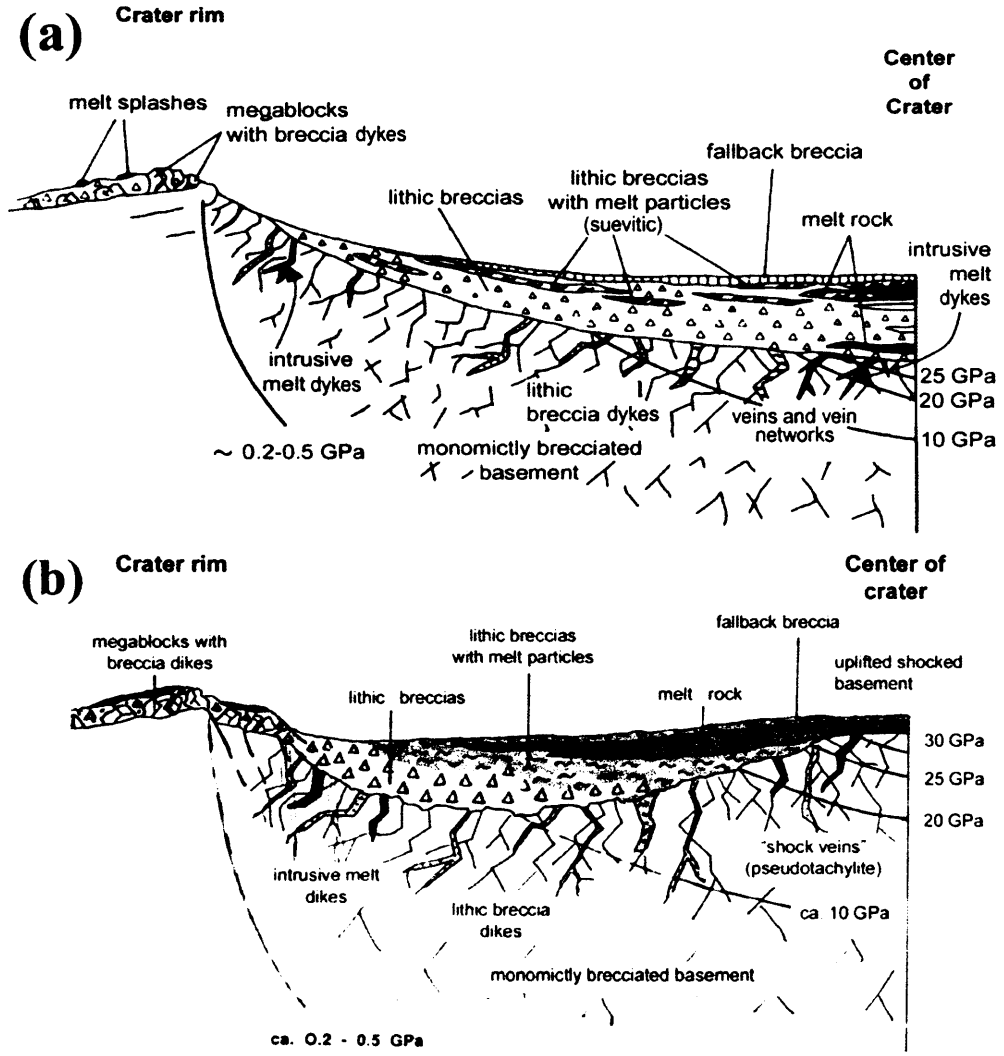

Fig. 1.15. Geological environment at (a) a complex crater and (b) a simple crater. Different crater settings will produce different textured melt rocks/breccias (Fig. 1.16). Shock wave isobars are given in GPa (Diagrams taken from Fig. 5.10 in Stöffler et al. 2006).

There are generally four types of impact breccias (Fig. 1.16) identified by Stöffler et al. (1979) that can be ascribed to different geographical settings in an impact environment (Fig. 1.15). Additional thermal metamorphic effects, i.e. deformation features in mineral grains, granulisation of rocks, annealing of mineral boundaries etc., have been seen in the majority of lunar samples, indicative of the pervasive shock processes that occur on the Moon.

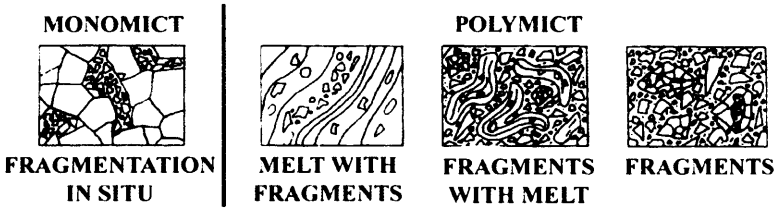

Fig. 1.16. Illustration of typical textures displayed in impact breccias (adapted from Stöffler et al. 1979). Monomict rocks include cataclastic (heavily fragmented) crystalline rocks. Polymict breccias include three subgroups: (a) Melt with fragments: breccia with glassy crystalline matrix. (b) Fragments with melt: breccias with clastic matrix and melt particles (glassy or crystalline). (c) Fragments: breccia with a clastic matrix.

The Regolith Environment. "The lunar surface is composed of igneous rocks and their impact-metamorphosed and impact weathered derivatives" (O'Hara, 2000a). The lunar regolith forms a boundary layer between the lunar crust and the solar-space environment. It is formed from unconsolidated fragmental rocky material that completely covers the underlying bedrock and is our main source of information about the geology and geochemistry of the Moon. All direct remote sensing measurements have been made from the very upper layers of its surface, and most of the samples returned by the Apollo and Luna missions were also plucked from just the surficial portion. Not only does it preserve a record of local lunar geology processed vertically by a gardening exhumation mechanism, but it contains a record of distal geology introduced by impact ejecta, and of external rocky fragments introduced from impacting meteorites. It also contains a record of solar and galactic implanted particles throughout the early history of the solar system (Lucey et al. 2006). Horz et al. (1991) theorised a stratigraphic section through the lunar crust (Fig. 1.17), illustrating the makeup of the thick regolith (mega-regolith) that covers the lunar surface and underlying bedrock environment. Impacts into the regolith have in many cases caused it to fuse into regolith breccias. These contain a diverse range of lithologies typical of the environment in which it was fused and are important samples of the lunar crust, providing evidence of the heterogeneous nature of the regolith environment.

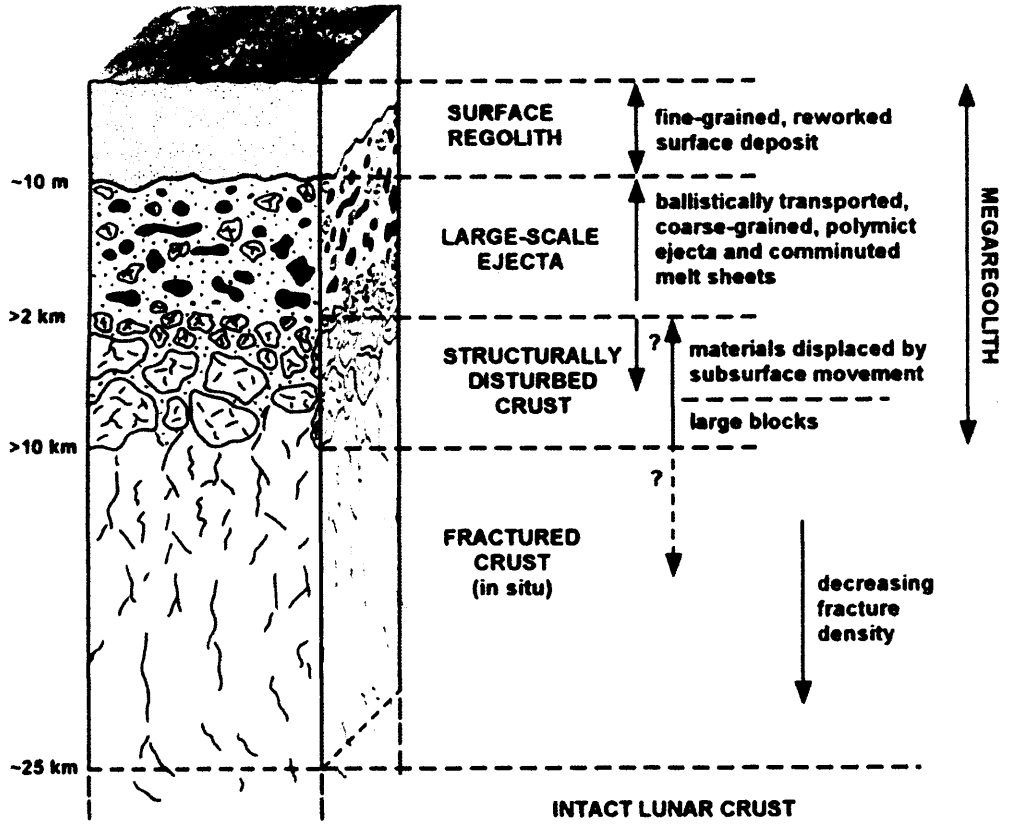

Fig. 1.17. Theorised cross-section through the mega-regolith. The effects of lunar gardening process and reworking can be clearly seen in the fine grain-size of the upper unit. Variations at depth are dependent on regional impact and basin processes (adapted from Horz et al. 1991, and are taken from Hiesinger and Head, 2006).

1.1.5 Lunar Meteorites

Manned and unmanned missions to the Moon have returned about 382 kg of lunar rocks and soils (Vaniman et al. 1991). These were all collected from rather atypical regions on the lunar near-side, within and around the Procellarum KREEP Terrane (Fig. 1.1), or from equatorial latitudes on the eastern limb. Therefore interpretations of the nature of the lunar crust and mantle have been made from a dataset from geographically restricted areas of the Moon. Lunar meteorites, in contrast, are derived from random sample sites on the surface, and thus provide a wealth of new information about the nature of the Moon, even though their precise provenance is as yet unknown. To date there have been ~98 individual stones of lunar material collected that can be related through compositional, mineralogical or isotopic similarities to form 44 groups of landing-paired stones [Website 1.2]. It has been estimated this material has been launched (launch-paired) from at least 27 separate localities on the Moon (Lucey et al. 2006).

Lunar Origin. Proof of lunar origin can be taken from several lines of evidence. (1) The presence of a fusion crust suggests that the sample is of meteoritic origin and has passed through the Earth's atmosphere causing frictional melting of the peripheral surface. (2) The rock has an anhydrous 'simple' mineralogy that suggests an extraterrestrial origin. (3) An oxygen isotope ratio corresponding that of the Earth-Moon fractionation trend. (4) Typical bulk rock elemental ratios are similar to those of the Apollo and Luna Moon samples (i.e. most lunar rocks sit on a trend between FeO and Al_2O_3). (5) Typical mafic mineral Mn/Fe ratios are indicative of the volatile poor nature of lunar samples that trend on a 'lunar line' distinct from terrestrial rocks and samples from Mars and asteroids (Section 2.3; Papike, 1998; Papike et al. 2003).

All lunar meteorites are thought to have been launched from the Moon in the last 20 million years (Korotev, 2005). As there are believed to have been no large craters generated on the Moon during this period, it is assumed that all lunar meteorites are launched from craters only a few kilometres in diameter (all craters in the last 1 million years or so are thought to be <3.6 km in diameter: Warren, 1994). This implies that lunar meteorites have been ejected from relatively shallow depth provenances, implying some selectivity in their being representative of lunar crustal material.

Lunar meteorites can be broadly classified according to their bulk aluminium content into three groups: the feldspathic meteorites (>26 wt. % Al_2O_3), the 'mingled' meteorites (13 to 26 wt. % Al_2O_3) and the basaltic meteorites (<13 wt. % Al_2O_3) [Website 1.2]. Each group contains important lithological information about the lunar crust at the site from which it was ejected.

Feldspathic Meteorites. These are classified as having bulk compositions with >26 Al_2O_3 wt.% and being composed of either fragmental feldspathic material or impact melt. They are particularly fascinating in that they represent new samples of the lunar highlands crust. Prior to lunar meteorite studies, the majority of our information about the lunar crust had been extrapolated from the petrological investigations of Apollo 16 samples. These new samples are statistically more likely to have been launched from terranes on the far-side of the Moon (Korotev et al. 2003; Korotev, 2005), and therefore are potentially the only true samples we have of the lunar crust that has not been contaminated with material from the Imbrium impact. These meteorites are therefore the best representation we have of the geochemistry of the most ancient lunar terrane, and our best insight into early lunar crustal evolution processes. They have provided new views on the composition and diversity of the lunar crust, and led to the identification of new anorthosite-magnesian lithologies (e.g. magnesian granulitic breccias) that may form an important part of the lunar crust not previously studied (Korotev, 2005; Lucey et al. 2006).

Mare Basalt Meteorites. This class of lunar meteorites are either composed entirely of crystalline mare basalt material, or are consolidated mare basaltic fragmental/impact melt breccias. They are classified as having a bulk compositions with <11 wt. % Al_2O_3. To date there are only 8 paired groups of basaltic lunar meteorites, including: Yamoto-793169, Asuka-881757, LAP 02205/02224/02226/02436/03632/04841, NWA 032/079, Dhofar 287, NEA 003, NWA 733/2700/2727/2977/3160/3333 and MIL 05035. There are suggestions that NWA 032 and the LAP-basalt (Zeigler et al. 2005; Day et al. 2006; Joy et al. 2006) may be launch paired and that Y-793169, A-881757 and MIL 05035 are paired (Korotev, 2005; Joy et al. 2007) suggesting that these basaltic meteorites were launched from at least 5 difference localities on the Moon.

Regolith Breccia Meteorites. This sub-classification is comprised of fragmental breccias that were consolidated in a lunar regolith environment. They encompass fused regolith material from a range of regolith environments: e.g. feldspathic, mare, or mixed ('mingled') mare-feldspathic regoliths. On the evidence of cosmic-ray exposure studies many of the regolith breccia samples are believed to have been derived from shallow to very shallow stratigraphic horizons (2 m to >100 m; Warren, 1994). For this reason they can provide a remote sensing calibration for the composition of the upper regolith. In particular lunar feldspathic regolith breccia meteorites have been used to calibrate remote sensing information from the lunar highlands (Warren, 2005; Prettyman et al. 2006; Joy et al. 2006a), and have been used to inform discussions of lunar anorthosite petrogenesis and crustal evolution (Jolliff and Haskin, 1995; Shearer and Floss, 2000; Longhi, 2003; Warren et al. 2005).

1.2 Lunar Remote Sensing: Introduction to X-ray Fluorescence Spectroscopy

Supplemental to the Apollo ground-based scientific payloads were a series of remote sensing experiments mounted onto the scientific instrument module (SIM) on the orbiting command-service module (CSM). As part of this science package the Apollo 15 and 16 missions carried successfully operating X-ray fluorescence (XRF) and gamma-ray experiments, which together mapped more than 9% of the lunar surface.

1.2.1 Theory of the X-ray Fluorescence Technique

X-rays are electromagnetic radiation with wavelengths in the range of 0.005 to 10 nm. At the short wavelengths they overlap with gamma-rays and at longer wavelengths they have similar wavelengths to ultraviolet radiation (Markowicz, 2002). Since the 1950s X-ray fluorescence (XRF) spectroscopy has been refined as a powerful technique for defining the elemental composition of materials.

Electrons within atoms are arranged in an ordered sequence of shells - K, L, M etc. (Fig. 1.18) - surrounding the nucleus out to a final valence shell, with inner shells having the higher binding energies. Element-characteristic spectra are produced when inner shell electrons are excited by incoming radiation (charged particles or X-rays) of a sufficient energy (Fig. 1.18a). When an inner shell electron is ejected from its orbital position, an electron from an outer shell will be transferred ("fall in") to the vacant position (Fig. 1.18a,b,c). During this transition a photon is radiated with energy equal to the energy difference of the two shells. These energies are specific to individual atoms, and by measuring the energy of the emitted X-ray it is possible to determine the element involved (Yin et al. 1993; Fitton 1997; Markowicz, 2002).

The intensity (number of X-rays emitted) is proportional to the amount of element in the material being analysed. When counts are collected over a period of time by an X-ray spectrometer they are observed as peaks (in a perfect instrument these peaks would be perfectly resolved lines). By measuring the counts in different X-ray lines it is possible to determine the elemental composition of the analysed materials.

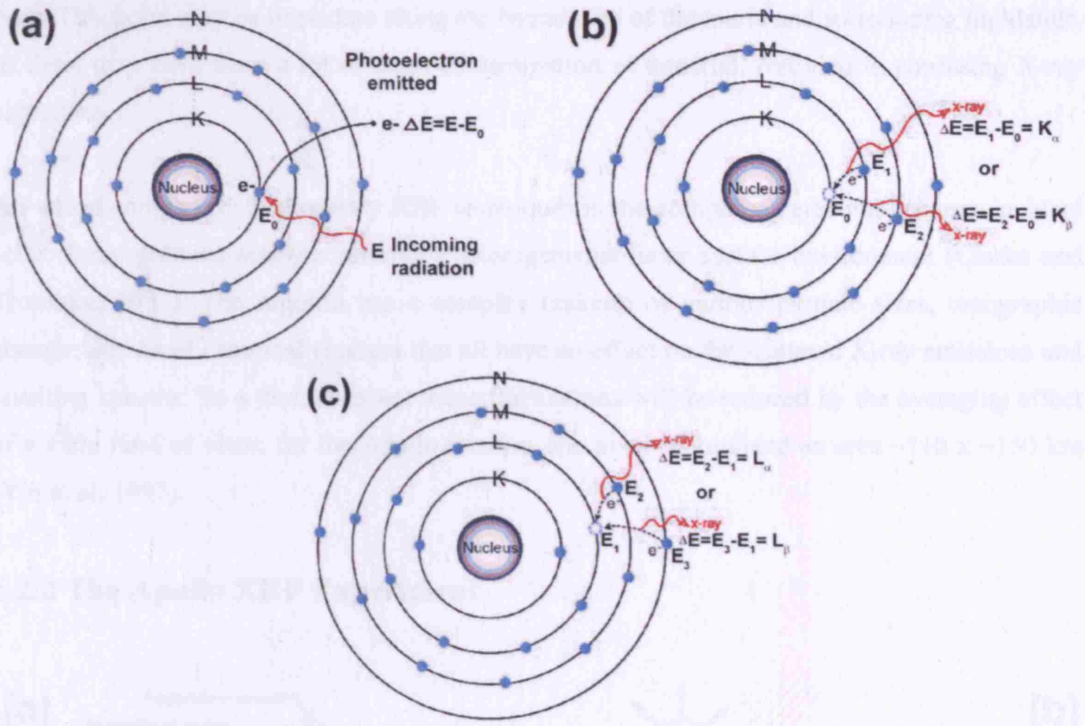

Fig. 1.18. Theory of X-ray fluorescence generation (see text for details). Adapted from Website 1.3.

In the laboratory environment a stabilised, and well characterised, electron beam is generated to provide the necessary energy for atom excitation and X-ray emission. Stars are the main source of excitation of X-rays from planetary surfaces. As stars like the Sun experience different cycles of activity, they can be considered to be a variable emission source of X-ray photons. Typical levels of solar intensity will result in the excitement of low atomic number elements, including the rock-forming minerals Mg, Al and Si. In periods of intense activity of X-ray emission (solar flares), excitement of heavier elements like Fe, Ti, Ca, P, Na, Co, Mn and K will occur (Adler et al. 1971, 1972a,b; Yin et al. 1993; Dunkin et al. 2003).

Planetary XRF observations can only be carried out on the inner solar system bodies like the Moon, Mercury and asteroids, where there are no atmospheres present to absorb the low energy incident and fluorescent X-rays, and additionally where the solar flux is high enough to cause detectable X-ray flux (Yin et al. 1993). It is important to realise that the incident solar X-rays will only penetrate into the upper few micrometers of a planetary surface, only producing fluorescent X-rays from very shallow depths (Adler et al. 1972d; Yin et al. 1993; Clarke and Trombka, 1997). It therefore has to be assumed that this surface regolith material is representative of the geological units at buried stratigraphic horizons. It is however possible that material could have physically been brought in from distal lithologies by impact processes, and that the measured chemical signature reflects this exotic material and not the localised bedrock

type. This point may be important along the boundaries of the maria and surrounding highlands, as there may have been a lot of cross-contamination of material, resulting in confusing X-ray signatures.

An added complexity to planetary XRF techniques is the complex interaction between incident solar X-ray photons and the texturally heterogeneous lunar surface environment (Clarke and Trombka, 1997). The regolith has a complex makeup of various particle sizes, topographic changes and local chemical changes that all have an effect on the scattered X-ray emissions and resulting spectra. To a certain extent these fluctuations will be reduced by the averaging effect of a wide field of view: for the Apollo mission one pixel represented an area ~110 x ~150 km (Yin et al. 1993).

1.2.2 The Apollo XRF Experiment

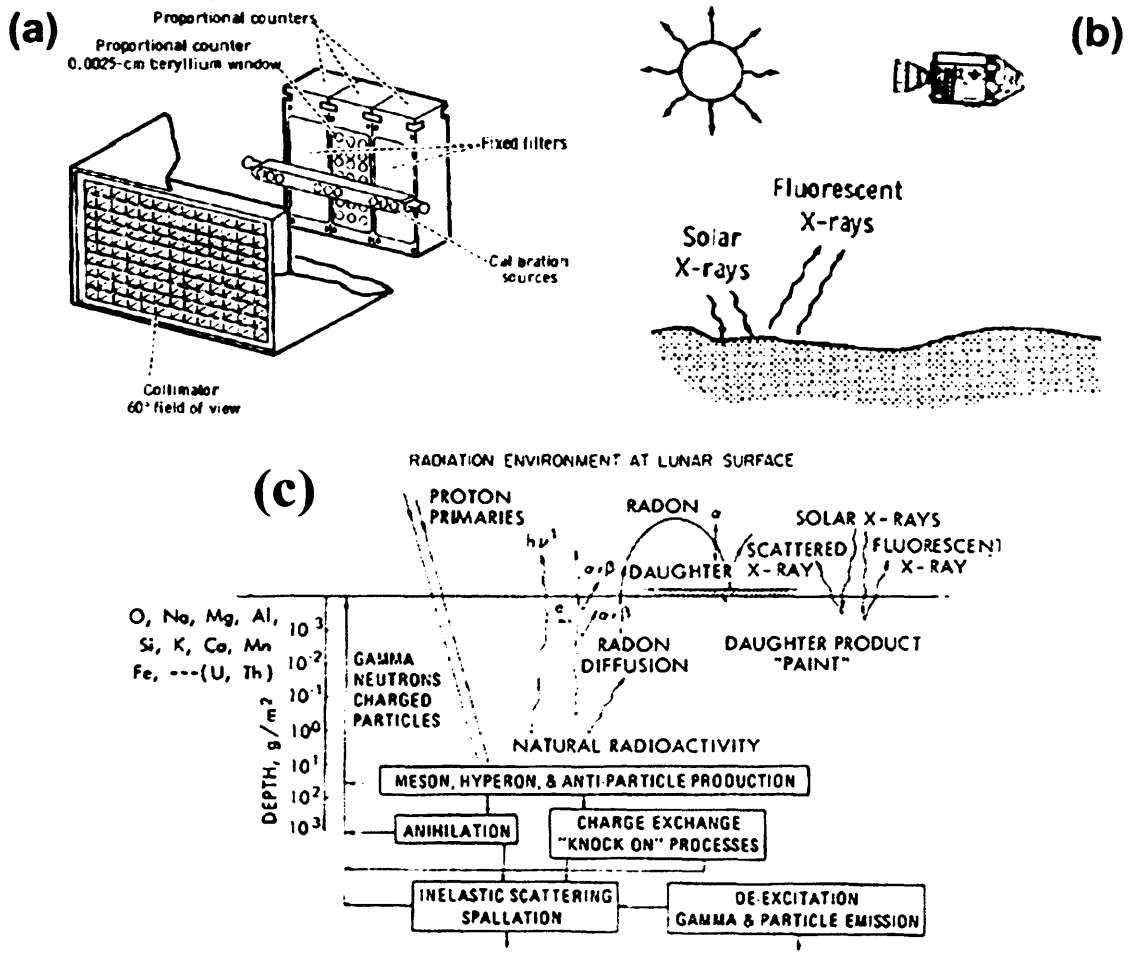

Fig. 1.19. (a) Schematic of the Apollo XRF instrument showing the collimator assembly mounted in front of three proportional counters. (b) Diagram of Apollo XRF experiment (adapted from Adler et al. 1971). (c) Model of high energy X-ray (right) and Gamma-ray (left and central) interactions with the regolith of airless planetary bodies (Clark and Trombka, 1997).

Lunar X-ray fluorescence was first successfully detected by the Russian Luna 12 mission in 1968 (Adler et al. 1972d). The Apollo 15 and 16 XRF payloads were the first attempt to conduct compositional XRF spectrometry on a planetary scale (Fig. 1.19). A simple proportional counter instrument was used on both missions (Fig. 1.19a). The front-end detection system consisted of three large area counters mounted behind filters (Mg-foil, Al-foil and no filter) for the selective detection of different energy X-ray lines. This ensured that only the photons from a specific rock-forming element were identified per counter. By comparing the count rate between the detectors intensity ratios could be calculated for selected elements. The surface resolution of the device was defined by a single large-area collimator assembly (Adler et al. 1972a,b,c,d,e) ensuring the same field of view (FOV) for all three detectors. In-flight calibration was conducted every 16 minutes by rotating a calibration rod with two radioactive sources (Mg and Mn K radiation) in front of the proportional counters. Data were handled by an electronic pulse height analyser, clocking data through to the telemetry system for return to Earth (Adler et al. 1972c). Raw data were returned as intensity (count) values measured (integrated) over a defined period of time. The Apollo XRF experiments covered ~9% of the lunar surface as they were limited by orbital constraints and by the location of sunlit regions of the Moon.

Solar X-ray photon flux is not constant, but throughout the Apollo 15 and 16 missions levels of solar energy were relatively similar with some minor flare events. Photon activity from the sun was measured simultaneously with a proportional counter solar monitor, mounted on the opposite side of the CSM. Thus, solar flux measurements (Fig. 1.20) could be made to accurately map changes in the solar energy intensity affecting the lunar X-ray emission response. In periods when increased solar flux occurred there was also preferential excitement of the Si emission line (higher energy) over lower energy Al and Mg lines – resulting in the detection of disproportional X-ray counts (Yin et al. 1993). The solar monitor device tracked these changes and normalization of the data could be made to account for Si enhancement.

Data gathered from the XRF experiments were initially presented as intensity ratios of Al/Si and Mg/Si. Magnesium and aluminium counts were both divided by the intensity of Si, as Si varies very little (no more than 5%) over the lunar surface, providing a good consistent normalising factor (Yin et al. 1993).

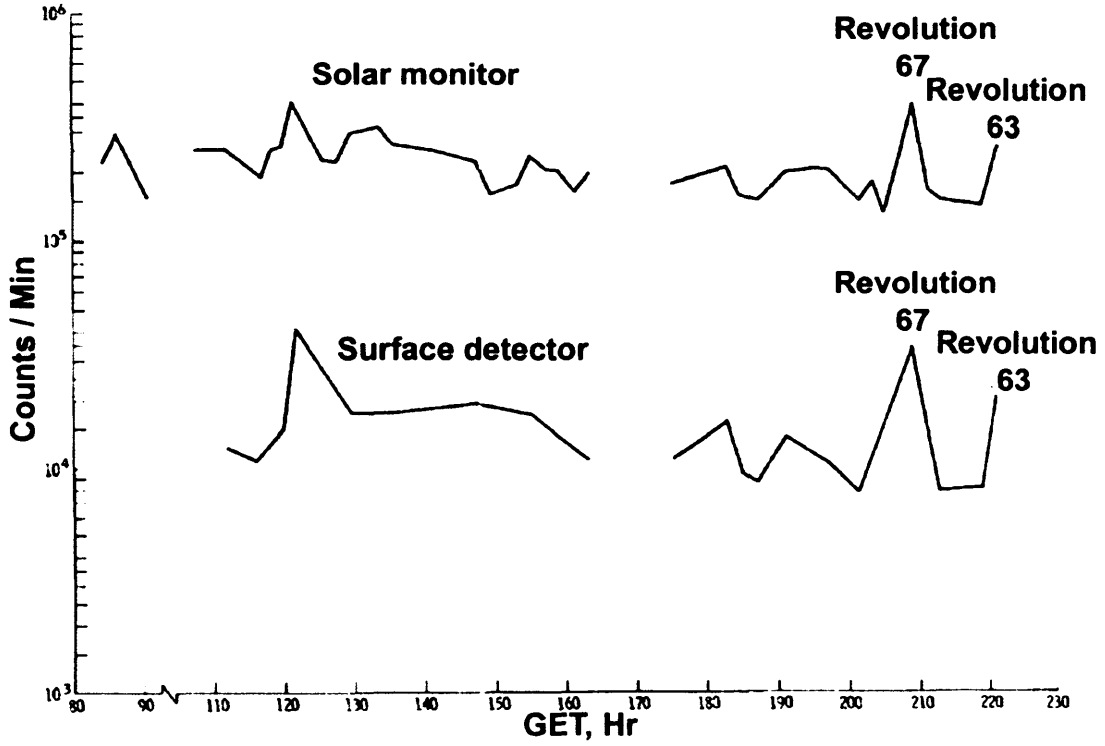

Fig. 1.20. Comparison between the integrated incident solar X-ray flux measured by the solar monitor and the X-ray flux from the lunar surface as measured by the XRF detectors during Apollo 15. The solar flux stayed fairly constant but there was a noted increase in activity on orbit 67 and 63. (Adapted from Adler et al. 1971). Ground elapsed time (GET) in hours.

These intensity ratios were useful in very early analysis as they allowed basic geochemical information to be obtained about the nature of the lunar surface. After initial analysis they were converted into concentration ratios to give accurate relationships between elements in the lunar crust over a ground footprint. Concentration ratios of Mg/Si and Al/Si were derived from calibration using in-flight Mn and Mg X-ray sources, theoretical calculations and ground truthing (comparing the compositions of lunar landing site soils to remote XRF spectra). A linear relationship between intensity and concentration ratios was produced (Alder et al. 1972a) using a calculated projection of X-ray lines for an average solar coronal temperature of 4 x 10^6 K (similar to those conditions observed by the solar monitor) and then using projected X-ray yields of measured samples to calculate the fluxes of X-ray emissions from elements on the lunar surface (Alder et al. 1971; 1972a,b; Yin et al. 1993).

The validity of this analysis was supported by comparing the Al/Si concentration with the average Al/Si concentration ratios in the samples analysed from over-flown Apollo sites. The two values derived (orbital observed and ground truths) were found to agree to within 10 % (Adler et al. 1972a). Moreover, the results obtained for areas over the Apollo 15 and 16 ground tracks overlapped and agreed to within 10% (Adler et al. 1972d). Figure 1.21 shows the elemental ratio maps produced to provide a visual interpretation of levels of concentration ratios

across the Moon. These footprints illustrate the limited regional coverage of the Apollo XRF experiment.

The main geological interpretations of the lunar regolith made from elemental concentration relationships mapped by the Apollo XRF experiments are:

- In both experiments the Al/Si and Mg/Si concentration ratios show an inverse relationship (Adler et al. 1972d). Thus the chemistry of the relatively Mg-rich mare and Al-rich highland regions can be tracked from these remote XRF experiments.
- Evidence that the lunar highlands are very aluminous supports the magma ocean model of early lunar evolution and differentiation whereby an anorthositic crust was crystallised out of and floated above a magma-sphere body.
- Al/Si concentrations in the Smythii region of the Moon in the far-side western highlands shows relatively higher values than the near-side central highlands; evidence of the heterogeneous nature of the lunar crust (Andre et al. 1977; Clark and Hawke, 1991)
- Despite the large Apollo field of view, compositional variations were measured between relatively large scale features like large impact craters and mares/highland contacts. For example, concentric patterns of Al/Si enrichment around the Crisium basin have been inferred as possible impact rings from a multi-ringed system (Andre et al. 1977) and the high Al/Si tracks of an ejecta blanket from the Langrenus crater have been tracked.
- Areas of dark halo craters within Mare Smythii corresponding to high Mg/Si intensity values (Clark and Hawke, 1991), and dark mare regions in Mare Crisium with low Al/Si intensity values (Maxwell et al. 1977), are good evidence of the excavation of Mg-rich, mare material that are likely to be deposits of pyroclastic glass.

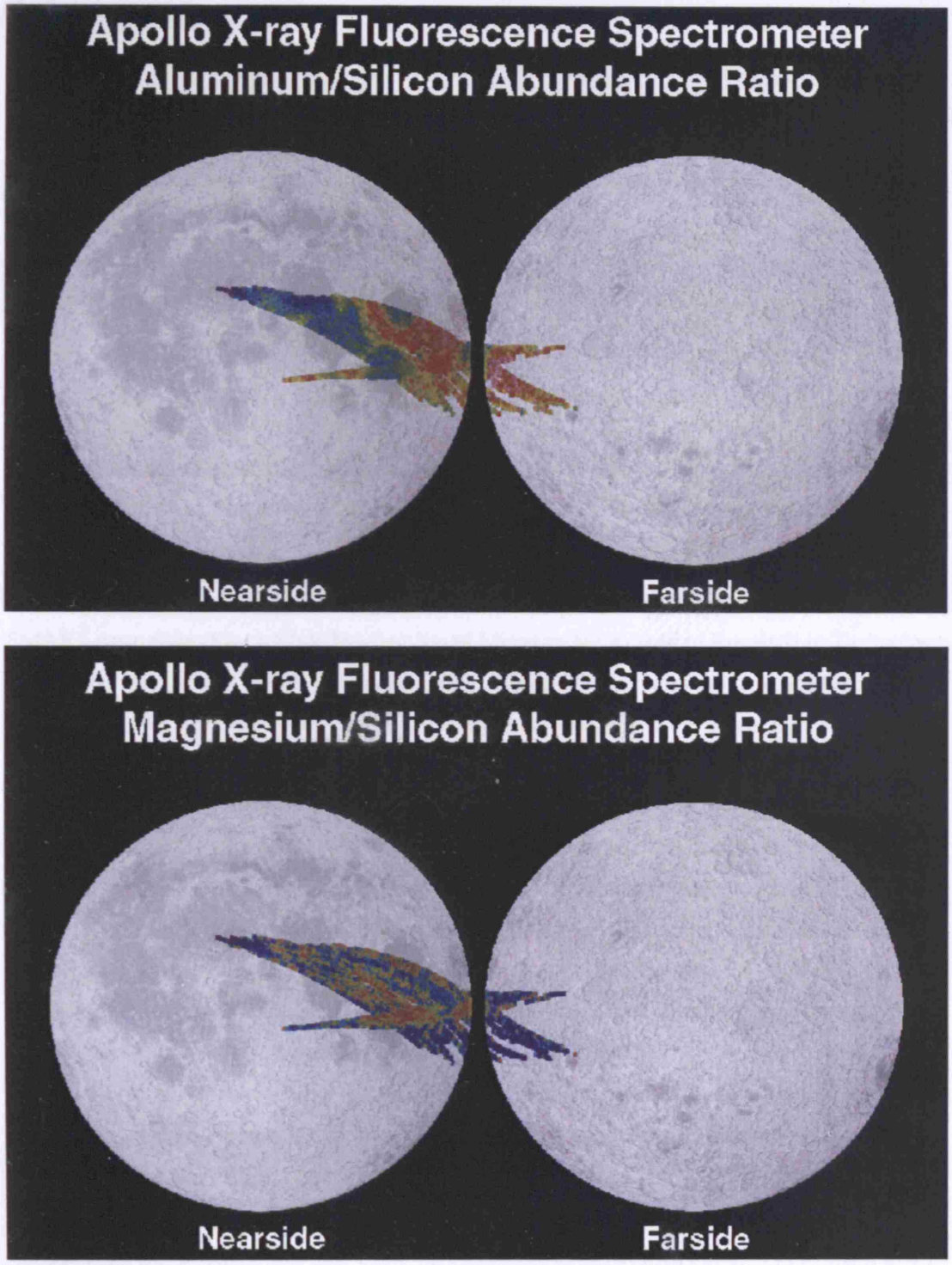

Fig. 1.21. Lunar maps produced from processed XRF data illustrating averaged elemental concentration ratios. Top image shows map of Al/SI ratio. Lower image shows map of Mg/Si ratio. Red areas in both maps reflect high ratio values i.e. in Al/Si map reds reflect anorthositic highland terranes and in Mg/Si map reds represent mare basalt compositions. Blue colours correspond to low ratio values i.e. the opposite correlation. Green colours represent intermediate ratio values likely to be surface compositional mixing between mare and anorthositic terranes. Images taken from Website 1.4.

1.2.3 SMART-1

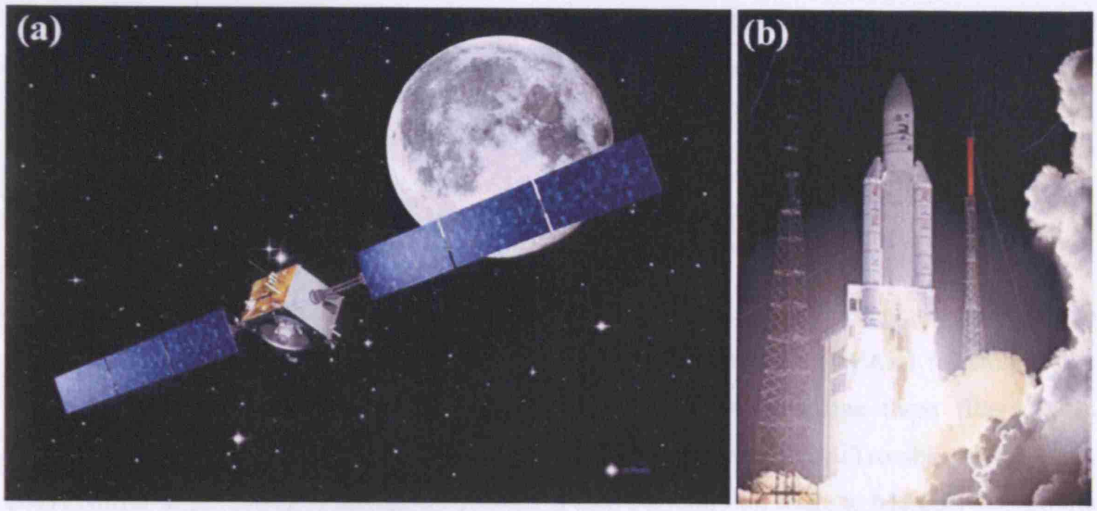

Fig. 1.22. (a) Artist's illustration of the SMART-1 spacecraft on its way to the Moon. (b) SMART-1 launched on ESA's Ariane 5 launch vehicle in French Guinea in 2003.

The latest space mission to conduct orbital XRF investigations of the lunar surface was ESA's SMART-1 satellite (Fig. 1.22a). The first Small Missions for Advanced Research in Technology (SMART-1 for short) is the European Space Agency's first mission to the Moon. It was launched on the 27th September 2003 (Fig. 1.22b) and travelled to the Moon over an 18 month cruise period whilst testing an innovative solar-electric propulsion (ion) drive. The spacecraft carried seven technology demonstrator miniaturised instruments, designed for scientific investigations of the Moon and the surrounding space environment (Racca et al. 2002; Huovelin et al. 2002; Grande et al. 2003; Foing et al. 2003). The principal instruments included:

- DCIXS: Demonstration of a Compact Imaging X-ray Spectrometer: an innovative XRF mapping instrument designed to detect X-ray flux in the 1 to 10 keV range at a nominal resolution of 180 eV, enabling the mapping of the major rock forming elements Mg, Al and Si (Grande et al. 1999; Dunkin et al. 1999; Grande et al. 2007).
- XSM: a monitor of the solar flux and an integral part of the D-CIXS package that provided measurements of the solar input spectrum necessary for X-ray data calibration (Huovelin et al. 2002).
- AMIE: Advanced Moon micro-Imager Experiment. A high resolution (30 to 80 m/pixel) CCD visible and near infra-red electronic camera (Josset et al. 1999; Shkuratov et al. 2003).
- SIR: an infra-red spectrometer mapper designed to observe in very high resolution the mineral content of the lunar surface (Basilevsky et al. 2004).

SMART-1 spent 18 months mapping the surface of the Moon and was crashed onto its surface on the 3rd September 2006. First results from the D-CIXS instrument were reported by Grande et al. (2007a,b) and XRF data collected by D-CIXS will be discussed in detail in Chapter 6 of this thesis.

1.2.4 Other Planetary XRF Experiments

X-ray fluorescence technology has been employed, or will be used in the future, to study a range of different planetary targets. The Near Earth Asteroid Rendezvous (NEAR) mission to the asteroid Eros carried with it an XRF experiment, based on the same three filtered, gas proportional counter system employed on the Apollo XRF instruments (Trombka et al. 2000, 2001; Nittler et al. 2001). A similar instrument is also currently on route to Mercury aboard the MESSENGER mission. When it arrives there in 2011 it will provide the first global geochemical dataset of the Mercurian surface (Starr et al. 2001). The Japanese mission Hayabusa/MUSES-C to the asteroid Itokawa has used a CCD based X-ray Spectrometer to study the composition of the asteroid's surface, and was able to study lunar X-ray abundance during its cruise phase (Okada et al. 1999, 2002, 2006a). Future CCD/SCD based XRF experiments will fly to the Moon aboard the Japanese mission SELENE (Ogawa et al. 2006b) and the Indian mission Chandrayyan-1 (Grande et al. 2006), and it is hoped that a UK-built CCD X-ray spectrometer will also fly to Mercury aboard the European Bepi-Columbo mission (Grande and Dunkin, 2003).

1.3: Lunar Remote Sensing: Introduction to Other Forms of Remote Sensing

1.3.1 Multi-Spectral Analysis: Clementine

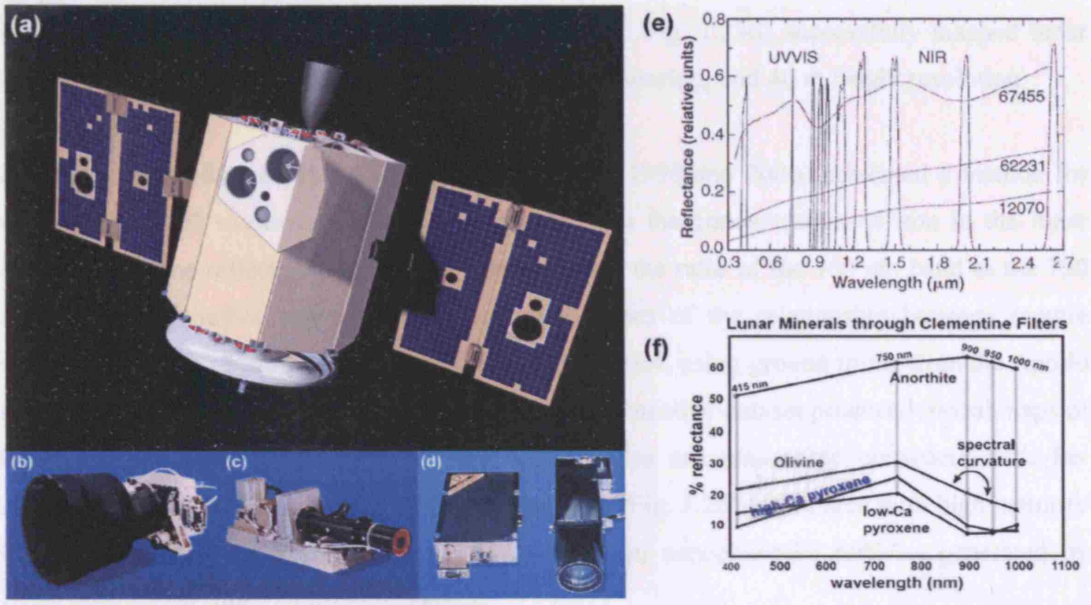

Fig. 1.23. (a) Artist's interpretation of the Clementine spacecraft. (b) The UVVIS CCD camera system. (c) The near-IR imaging system. (d) The LIDAR multi-spectral imager and laser altimeter instrument. (e) Lab. reflectance spectra of lunar samples 67455 (feldspathic breccia), 62231 (mature feldspathic soil) and 12070 (a mature basaltic soil) superimposed onto the Clementine filter wavelengths of the UVVIS and near-IR cameras (Fig 2.47 of Lucey et al. 2006). (f) Taken from Figure 2 of Robinson and Riner (2005) showing the basic principal of mineral identification using bandwidth ratios and spectral curvature profiles as developed by Tompkins and Pieters (1999).

The Clementine mission (Fig. 1.23a) was a small (140 kg) satellite launched on 25th January 1994. It was a joint collaboration between NASA and the Ballistic Missile Defence Organisation to test the space-worthiness of a range of advanced sensors for military satellite operations. Clementine was designed to enter lunar orbit, map the Moon's surface, and then travel onto an asteroid target for extended mapping operations. The satellite successfully completed two months of mapping at the Moon, but upon leaving lunar orbit on May 3rd 1994 a software failure resulted in the firing of the altitude-control thrusters, causing the spacecraft to spin uncontrollably. The mission was finally abandoned and Clementine did not rendezvous with its asteroid target (Spudis et al. 1994).

Clementine carried a suite of instruments designed to investigate the mineralogy and topography of the lunar surface. Multi-spectral imaging packages included a UVVIS CCD camera (Fig. 1.23b) that used a filter wheel to map the Moon in five wavelengths: 415, 750,

900, 950 and 1000 nm (Fig. 1.23e) and a near-IR CCD imager (Fig. 1.23c) that was filtered to map the Moon at 1100, 1250, 1500, 2000, 2600 and 2780 nm (Fig. 1.23e). Near-complete global multi-spectral channel mapping was completed at an average resolution of 200 m/pixel, and selected areas of the Moon were imaged in high resolution at 25 m/pixel for the visible wavelength bands (Robinson and Riner, 2005). In addition to these important scientific multi-spectral datasets the on-board laser altimeter (LIDAR: Fig. 1.23d) successfully mapped lunar topography at a resolution of 1 to 2 km along track monitoring, and 40 m height resolution.

Elemental Abundance Method: Lucey et al. (1995, 1998 and 2000) presented a method for using the UVVIS multi-spectral datasets to determine the concentration of iron in the lunar surface using the reflectance of the 750 nm band, and the ratio of the 950 nm band to the 750 nm band. The method employed empirical calibrations of the relationship between sample maturity, FeO concentration and spectral reflectance ratios, using ground truths from the Apollo landing sites. Applying this technique to the global Clementine dataset produced global maps of FeO abundance (e.g. Fig. 1.24b, 1.25b). These maps are reasonably consistent with Fe-abundances mapped by the Lunar Prospector mission (Fig. 1.26) but in area with high maturity indexes there may be problematic contamination from nanophase-Fe particles generated by space weathering (micro-gardening) effects.

The relationship between UV/VIS colour ratios and the Ti content of silicate minerals, glasses and opaque phases (Hapke et al. 1975) was also exploited and used to produce maps of lunar Ti content (Blewett et al. 1997; Lucey et al. 1998, 2000). These Ti-concentration datasets rely on the assumption that all the Ti occurs within ilmenite ($FeTiO_3$) phases in the regolith (dark, spectrally neutral). However, it is known from study of the lunar rocks that spinel (particularly ulvöspinel; also an opaque, Ti-rich mineral phase) does occur in lunar basaltic material, albeit at much lower modal abundances than ilmenite (Riner et al. 2005).

The algorithms (Lucey et al. 1998) responsible for the production of the FeO and TiO_2 maps are given below (Equation 1 to 4). In the following equations, R(750) refers to Clementine reflectance at 750 nm, ratio_IR refers to the ratio of the reflectance at 950 nm to the reflectance at 750 nm, and ratio_UV refers to the ratio of the reflectance at 415 nm to the reflectance at 750 nm:

FeO:

Iron parameter, theta (Fe) = $\tan^{-1}\{[ratio\_IR - y0] / [R(750) - x0]\}$ *Equation 1*
where x0 = 0.08
where y0 = 1.17

wt.% FeO = {15.522 * [theta(Fe)]} - 3.724 *Equation 2*

TiO_2:

Titanium parameter, theta(Ti) = $\tan^{-1}\{[ratio\_UV-y0] / [R(750) -x0]\}$ *Equation 3*
where x0 = -0.02
where y0 = 0.425

wt.% TiO_2 = 5.550 * [theta(Ti) ^ 5.684] *Equation 4*

Another significant problem with elemental data derived using the UVVIS waveband ratio technique is that associated with topographic shading (Lucey et al. 1998). Crater walls and other features of steep local slope introduce errors associated with shadow or extreme albedo brightness affecting the 750 nm reflectance band. This causes a particular issue at high phase angle observations and/or oblique lighting conditions where shadowed regions appear to have large apparent elemental concentrations compared with bright reflectance features that have apparent low elemental concentrations (Fig. 1.24).

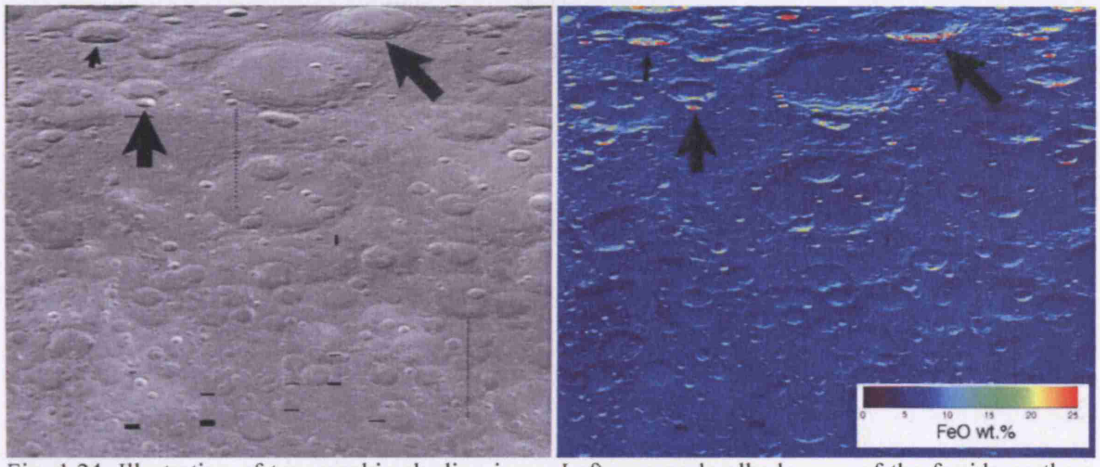

Fig. 1.24. Illustration of topographic shading issue. Left: greyscale albedo map of the farside northern lunar highlands as taken with the 750 nm reflectance band. Large craters and basins contain regions of shadow and regions of bright solar reflectance. Right: Concentrations of FeO in this region derived from *Equation 1 & 2.* Shaded regions give anomalously high concentrations of FeO (>15 wt.%) and bright crater walls give anomalously low concentrations (<3 wt.%) compared with surrounding anorthositic highlands.

These complexities, and additional problems associated with particle size considerations (Riner et al. 2006b), introduce errors in fully understanding the UVVIS reflectance relationships and Clementine Ti-abundance (Riner et al. 2006). Lucey et al. (2006) have suggested therefore that these Ti abundances may be imprecise to as much as 5 wt.%, accounting for the difference

between Clementine UVVIS Ti-abundances and those measured by Lunar Prospector (Riner et al. 2005). Despite these uncertainties, the Clementine UVVIS remote sensing datasets are by far the best resolution *global* mineralogical and (calculated) elemental mapping that has been conducted on the lunar surface to date. Clementine datasets utilised in this thesis were originally created using UVVIS data processed by the U.S. Geological Survey (USGS) and released in 1998 as ISIS data cubes. The data were radiometrically calibrated, and orbit and phase angles were reconciled between the two months of spacecraft operation by the USGS. The maps used for work in this thesis (e.g. Section 2.4) have a 1 km per pixel resolution and extend from 70 degree north to 70 degree south latitude, encompassing all 360 degrees of longitudinal data in a cylindrical projection.

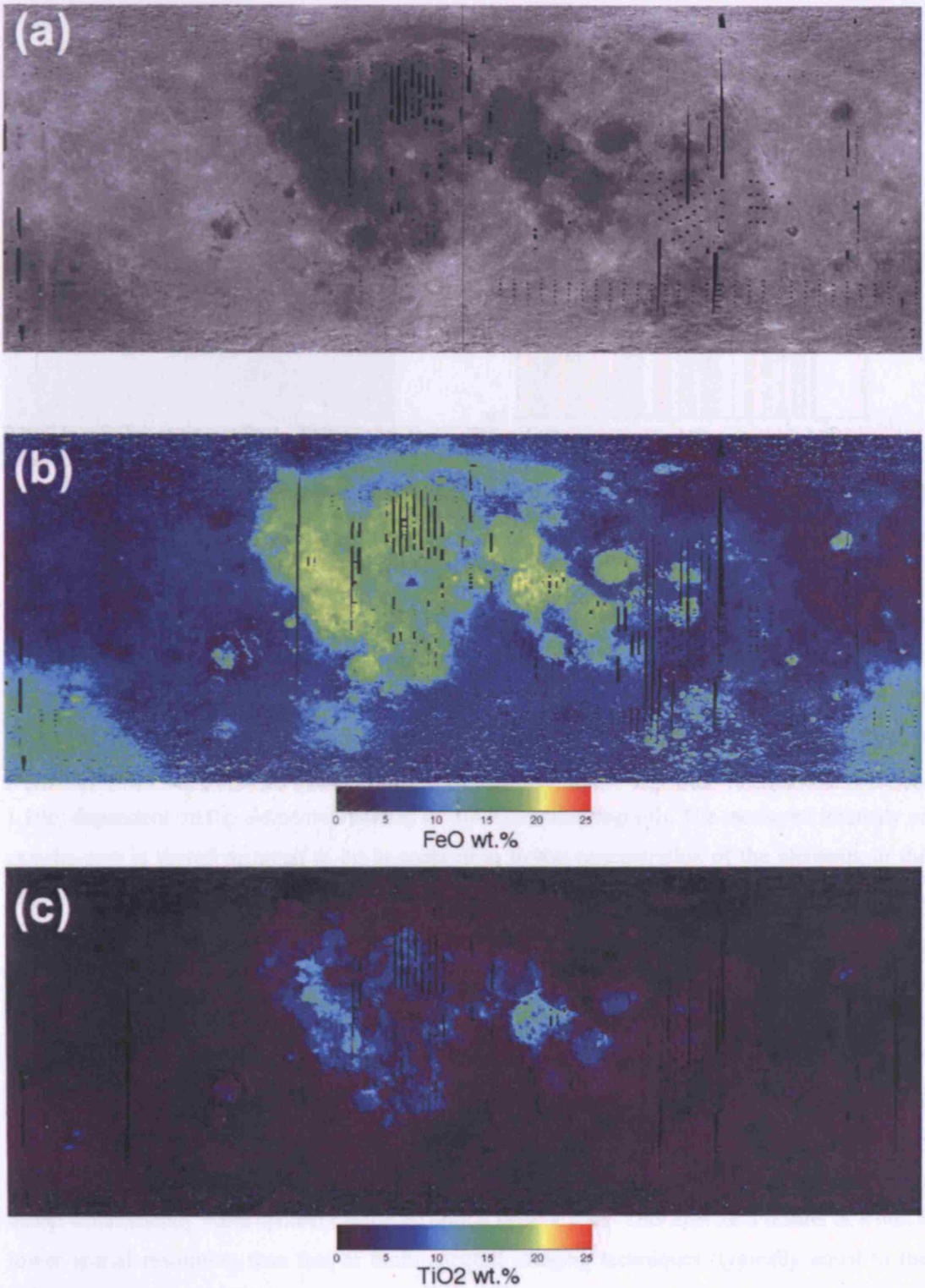

Fig. 1.25. Clementine high resolution compositional datasets where one pixel corresponds to 1 km on the Moon. (a) Albedo map derived from 750 nm band-width. (b) FeO wt.% abundance as calculated using the algorithms of Lucey et al. (1998). (c) TiO_2 wt.% abundance calculated using the algorithms of Lucey et al. (1998).

1.3.2 Gamma and Neutron Spectroscopy: Lunar Prospector

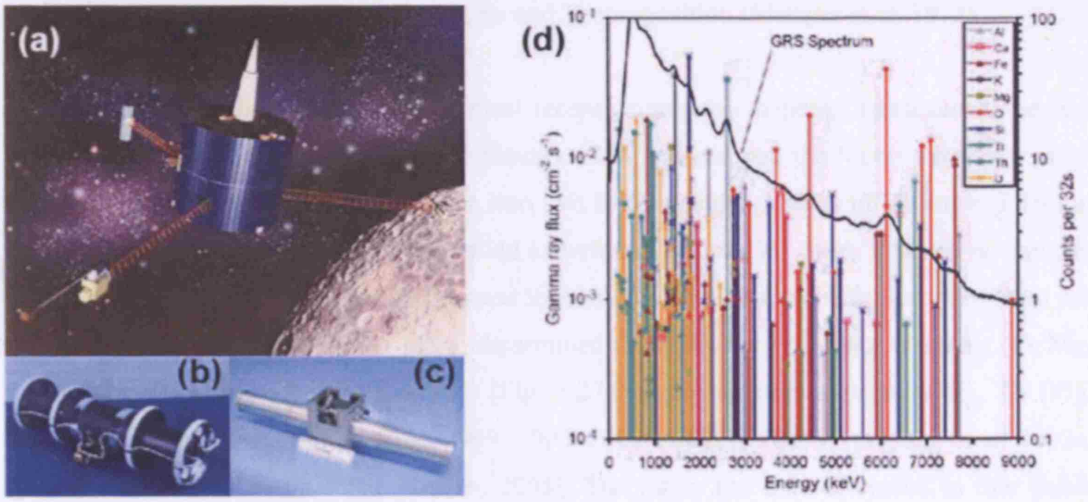

Fig. 1.26. (a) Artist's impression of the Lunar Prospector Spacecraft. (b) The gamma-ray experiment. (c) The neutron spectrometer experiment designed to map the abundance of hydrogen (and therefore possibly water) on the lunar surface. (d) Typical LP GRS co-added spectrum (thick black line) with individual elemental characteristic line features: diagram taken from Figure 3 of Prettyman et al. (2006).

Gamma-ray production is initiated by the interaction of galactic cosmic rays (GCR) colliding with a planetary surface or from the decay of naturally occurring radioactive elements like ^{40}K, Th, and U (Fig. 1.19c). Gamma-rays are either absorbed or scattered in the lunar regolith to depths of orders of a few cm. GCR interaction triggers a cascading sequence of lower energy particles including neutrons. These neutrons in turn cause a series of radiation emission (Fig. 1.19c) dependent on the elemental makeup of the interacting regolith. The measured intensity of gamma-rays is therefore taken to be in proportion to the concentration of the elements in the lunar surface and the flux of GCR particles that cause the nuclear reactions to occur (Adler et al. 1972d; Prettyman et al. 2006).

The measurement of elemental composition by gamma-ray spectroscopy (GRS) therefore requires an accurate measurement of the gamma ray intensity, and knowledge of the flux of neutrons within the surface. Short wavelength photon emissions from the Moon (i.e. X-ray and gamma-ray) are far weaker than those emitted in the UV/VIS wavelengths. Because of this low-count rate, gamma-ray spectrometers (GRS) have to employ a broad counting area in order to detect a statistically valid spatially resolved signal (Fig. 1.26d). This approach results in a much lower spatial resolution than that of multi-spectral imaging techniques (typically equal to the altitude of the spacecraft).

Gamma-ray spectroscopy of the Moon was originally conducted by the Apollo 15 and 16 command modules as part of the Apollo orbital science package. These experiments ran in conjunction with the XRF packages discussed in Section 1.2 but because gamma-ray production

does not rely on a solar input spectrum, lunar coverage was much larger with >20% of the surface being successfully mapped in Th, Fe and Ti composition (Metzger et al. 1973).

Lunar Prospector (Fig. 1.26) carried the most recent gamma-ray mapping instrument to be sent to the Moon. It was launched on the 6th January 1998 and mapped the Moon for a year at an altitude of 100 km before being dropped into two lower mapping orbits of 30 km and 10 km before crashing into the Moon in a controlled experiment on July 31st 1999. Gamma-ray spectra (Fig. 1.26d) measured by the Lunar Prospector mission, and corrected with flux rates from the neutron spectrometer, have been used to determined the abundance of major elements (O, Mg, Al, Si, Ca, Ti [Fig. 1.27, 1.28,], and Fe [Fig. 1.27a]) and radioactive elements (K, Th [Fig. 1.27b], and U) [Lawrence et al. 1998, 1999, 2000, 2002a, 2002b, 2003; Prettyman et al. 2002a, 2002b, 2006; Gillis et al. 2004; Warren, 2005]. The maps and data discussed in this thesis originate from the following datasets and were loaded into IDL using software developed for this thesis by K. Joy and B. Kellett. The 5 degree datasets were displayed (Fig. 1.28) using the IDL programme make_grid_2deg.pro (Website 1.5: Lawrence, 1998) and coloured using the IDL ITools software.

Half Degree Thorium and Iron Abundance Data: The LP gamma ray spectrometer (Feldman et al.. 1999) half degree absolute abundances of thorium (ppm) and iron (weight percent) (Fig. 1.27) is taken from the low-altitude portion of the LP mission. Prior to release datasets were reduced using the methods of Lawrence et al. (2002a,b). Half degree map bin size is 15 km by 15 km.

5 Degree Elemental Abundance Data Products: Elemental abundance values for O, Si, Ti, Al, Fe, Mg, Ca (weight percent) and Th, U and K (ppm) were derived from LP gamma ray spectrometer observations acquired during the high-altitude portion of the LP mission (Fig. 1.28). The data were derived using the latest Prettyman et al. (2006) full modelling and response function analysis. Five degree map bin size is 150 km by 150 km.

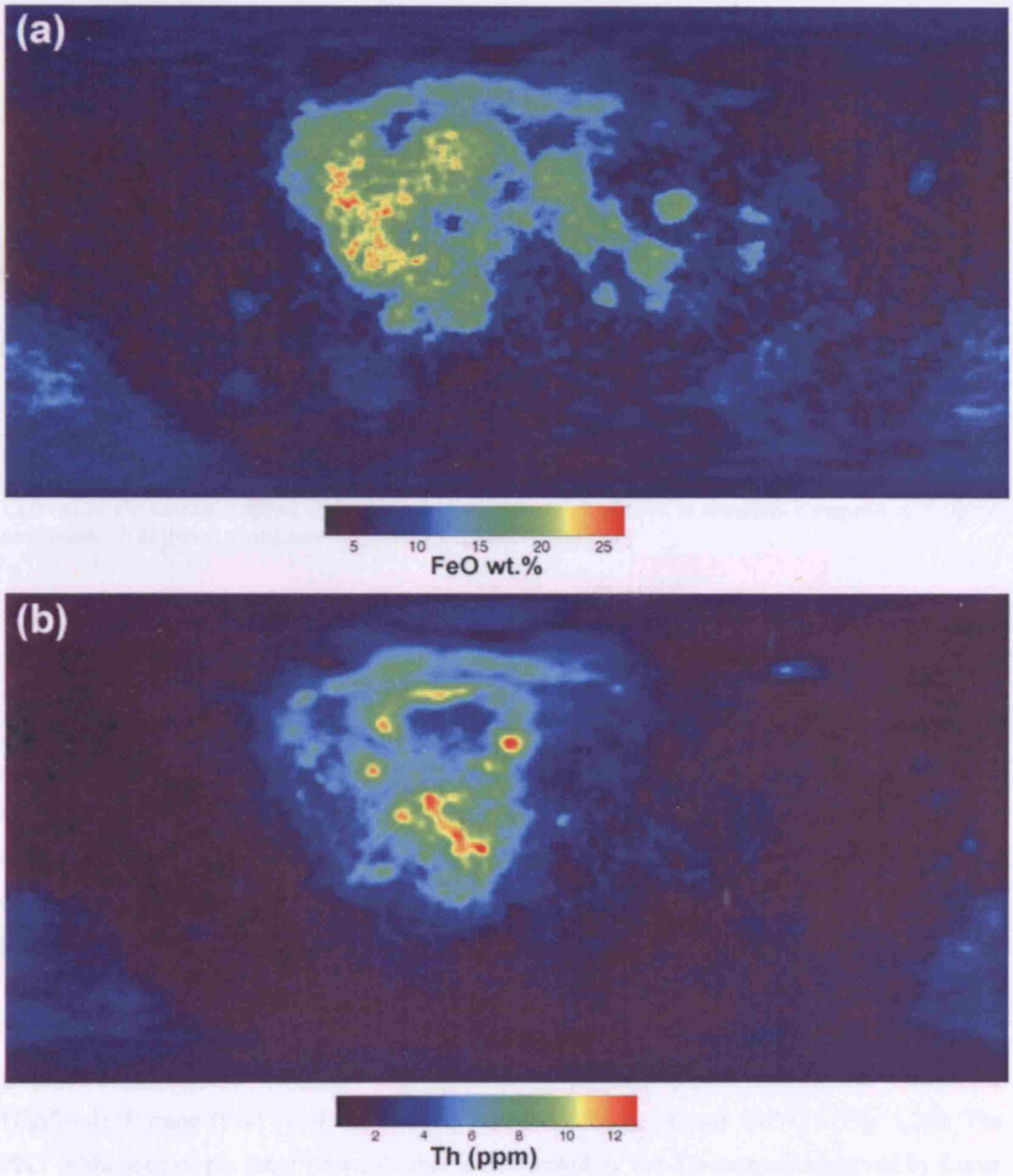

Fig. 1.27. Lunar Prospector high resolution 0.5 degree resolution datasets where one pixel corresponds to 15 km on the Moon. (a) FeO wt.% abundance Lawrence et al. (2002b). (c) Th abundance in parts per million (ppm) Lawrence et al. (2002a). This Th map shows the intense concentration of radioactive elements (carried by KREEP-rich lithologies) concentrated in and around the Imbrium basin.

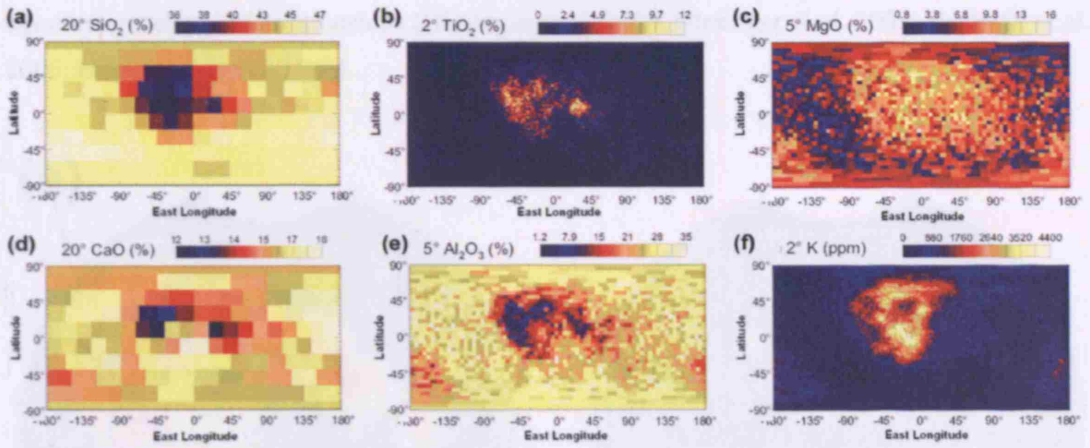

Fig. 1.28. Lunar Prospector major element abundance global maps. All diagrams are taken from Prettyman et al. (2006). (a) SiO_2 wt.% abundance mapped at a resolution of 20° pixels. (b) TiO_2 wt.% abundance mapped at 2 °/pixel resolution. (c) MgO wt.% abundance mapped at 5 °/pixel resolution (d) CaO wt.% abundance mapped at 20 °/pixel resolution. (e) Al_2O_3 wt.% abundance mapped at 5 °/pixel resolution. (f) K [ppm] abundance mapped at 2 °/pixel resolution.

1.4 Integrating Results of Lunar Sample and Remote Sensing Studies

Theories of lunar evolution born out of petrological investigations of the Apollo and Luna sample were greatly refined by the global geochemical and mineralogical datasets provided by Clementine and Lunar Prospector. Simplistic models of a Moon-wide plagioclase floatation event were simply not consistent with the heterogeneous nature of the lunar crust, and the dichotomy between near, and far-side geochemistry. Thus global remotely-sensed datasets have forced a re-examination of lunar geochemical history.

Jolliff et al. (2000) first introduced the notion that the Moon can be broadly divided in three geochemically distinct 'terranes': the Procellarum KREEP Terrane (PKT), the Feldspathic Highlands Terrane (FHT) and the South Pole-Aitkin Basin Terrane (SPAT) (Fig. 1.29). The PKT is the area of the lunar near-side that is dominated by the Th-anomaly observed by Lunar Prospector (Fig 1.27b). It is dominated by mafic lithologies that have incorporated a 'KREEPy' signature. As KREEP is the dominant carrier of radioactive elements, this suggests that a large portion of the Moon's heat-producing elements have been retained within just ~10% of the lunar crustal volume (Jolliff et al. 2000; Wieczorek and Phillips, 2000). This may have triggered widespread partial melting of the lunar mantle (Wieczorek and Phillips [2000] modelled melting depths up to 600 km), generating a massive eruption of basalts over a long period of time. The mare basalts of Oceanus Procellarum and the Imbrium, Humorum and Nubium maria are the surface expressions of this relatively localised heating. Detailed geological mapping of these maria has been conducted by a number of authors in order to constrain individual flow eruption

ages and geochemical relationships (Hiesinger et al. 2000; Hiesinger et al. 2003; Hackwill et al. 2006; Bugiolacchi et al. 2006).

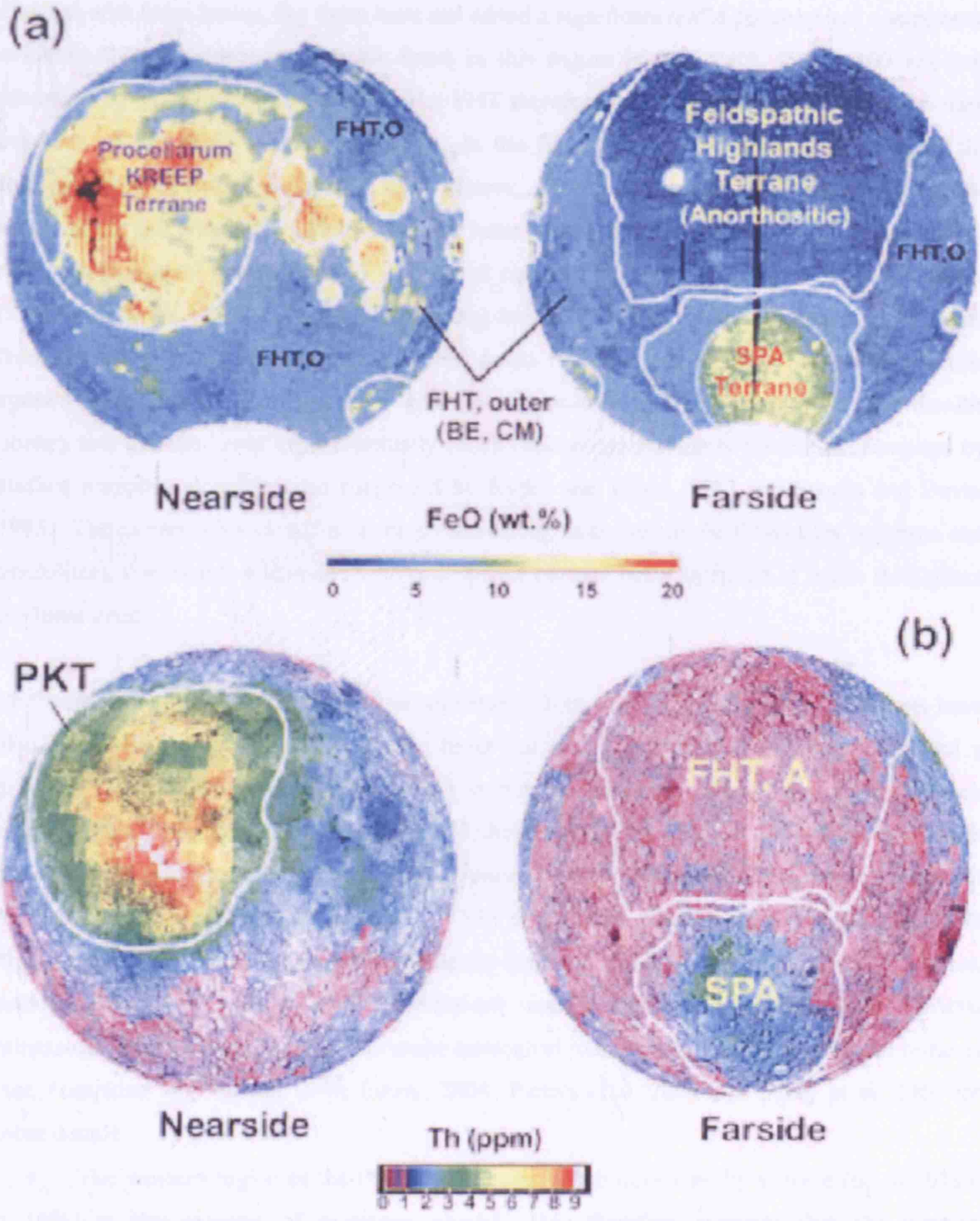

Fig. 1.29. Surface expressions of major lunar crustal terranes proposed by Jolliff et al. (2000). This figure is taken directly from Plate 1 of Jolliff et al. (2000). Terranes are projected onto (a) Clementine FeO map of the Moon prepared using the Lucey et al. (1995) algorithm and (b) a Th-abundance map of the Moon merged with a shaded topographic projection. PKT: Procellarum KREEP Terrane, FHT: Feldspathic Highlands Terrane, SPA: South-Pole Aitkin basin.

The Feldspathic Highlands Terrane is an area dominated by anorthosite-rich rock types, encompassing most of the northern portion of the lunar far-side, with outer FHT portions including the near-side central and southern highlands (Fig. 1.29). The terrane is heavily cratered with large basins, but these have not added a significant mafic geochemical component; evidence that the upper anorthositic crust in this region is very thick (60 to 100 km was modelled by Wieczorek et al. [2006]). The FHT therefore probably best represents the primary products of the lunar magma ocean and is the likely launch provenance of most of the feldspathic meteorites. Tompkins and Pieters (1999) developed a technique to probe stratigraphic mineralogical variations in the lunar crust using Clementine. They classified the spectrally dominant mineralogies of 109 impact central peak features with low maturity indexes (thus limiting the effects of space weathering) in order to study material vertically excavated from the lower crust. Profiles of the central peaks revealed that the crust increases in mafic content with depth (anorthosite → gabbroic-noritic-troctolitic anorthosite → anorthositic norite), and that the lower crust is actually much more compositionally diverse than implied by surface mapping alone (as also suggested by Ryder and Wood, 1977 and Spudis and Davis, 1985). The survey also identified craters excavating 'massive' mafic lithologies (gabbros and troctolites), consistent with models of widespread plutons being intruded at depth throughout the lunar crust.

Methods of identifying mineral spectral signatures from the Clementine UVVIS datasets have also been applied to the whole of the lunar surface. Lucey (2004) initially automated a procedure using radiative transfer modelling to make global maps of the relative concentrations of plagioclase, olivine, clinopyroxene and orthopyroxene, in areas of the Moon with a low maturity index. Pieters et al. (2006 *and references therein*) developed an alternative empirical method of estimating mineralogy from UVVIS data. These calculations were used to model high resolution (15 km/pixel) modal abundance maps of specific pyroxene (pigeonite, augites, orthopyroxene and Fe-pyroxene) distributions across the lunar surface. Such surficial mineralogical maps have been used to make geological interpretations of different lunar terranes (see Tompkins and Pieters, 1999; Lucey, 2004; Pieters et al. 2006 and Lucey et al. 2006 for more detail):

- The western region of the PKT is particularly rich in olivine by volume (up to 50% ± 10%) at the expense of pyroxene phases. This therefore suggests that the western Procellarum is dominated by Fe-rich, olivine basalts.
- Olivine is probably very low by volume (<10%) in the SPA Basin. This suggests that the SPA has probably not exposed significant amounts of the lunar mantle, but has more likely just excavated the pyroxene-rich lower crust.

- The eastern-rim of the SPA is also particularly rich in orthopyroxene compared with the rest of the Moon. This possibly indicates that the lower-crust is dominated by a noritic lithology, not exposed at the surface in significant volumes anywhere else on the Moon.
- Olivine is present, and is the most dominant mafic phase (<20% modal abundance), in the FHT anorthositic lithologies, evidence of their primitive nature, and is consistent with lunar meteorite magnesian-rich lithologies not associated with rock-types seen in the Mg-Suite. This observation has also been made in petrological investigations into feldspathic lunar meteorites, believed to have been mostly derived from the FHT.

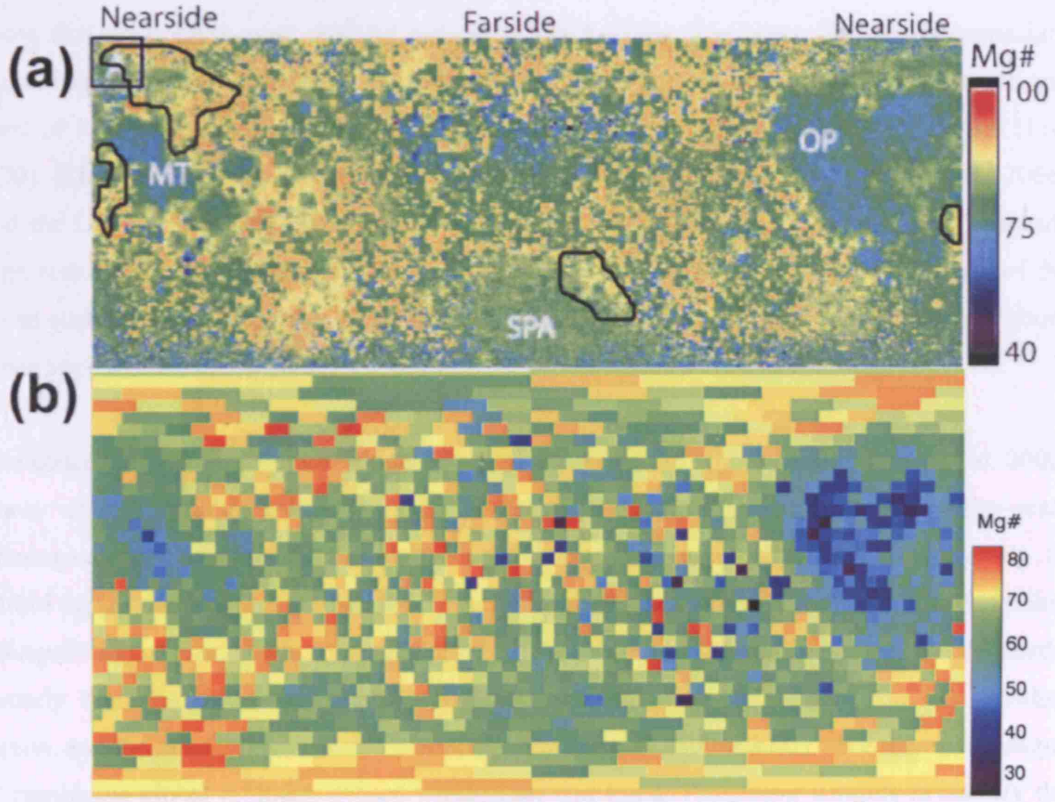

Fig. 1.30. Global Mg# variations. (a) Map of lunar Mg# as published by Cahill et al. (2005) calculated using a best-fit spectral look-up table of possible variations of mineral grain-size and different Mg# compositions. The authors estimate a mean error of ± 7. Moon-wide Mg# estimates using this technique has a range from 40 to 90 that is very similar to the range exhibited by the lunar meteorite collection. The black circled areas (with the exception of the square in the upper left hand corner) outline identified plagioclase-poor, Mg#-rich lithologies, possibly corresponding to outcrops of HMS intrusions. (b) Mg# as derived from the Prettyman et al. (2006) two degree MgO and FeO datasets. Moon-wide Mg# estimates using the LP datasets has a range from 22 to 83 Mg#.

Magnesium-number, or Mg#, is an important geochemical discriminator in understanding petrological sequences and crustal evolution. It is determined by the atomic ratio of Mg to the sum of Mg plus Fe (that occurs on the Moon in the 2+ state): i.e. Mg# = 100*(Mg/[Mg+Fe^{2+}]). Typically, the Mg# of mafic mineral phases or the bulk sample provides an indication of

petrological 'evolutionary state', with the most primitive minerals/rocks having high Mg#, and most evolved minerals/rocks having a very low Mg#. Mapping the distribution of Mg# on the lunar surface is therefore important for understanding the spatial diversity of lunar rock types (Lucey et al. 2004). Lunar surface magnesium has not yet been mapped at high resolution (Fig. 1.30c), and so global estimates of Mg# have either been made from low-resolution Lunar Prospector datasets (see Lucey and Cahill, 2006) or from theoretical modelling of mineral compositions using the Clementine UVVIS datasets (Fig. 1.30a) (Lucey et al. 2004; Cahill et al. 2005, Lucey and Cahill 2006). These datasets have provided further evidence that magnesian feldspathic material is widespread throughout the FHT. This technique has also been used to show that plagioclase-poor (<60%) and Mg#-rich (>70%) lithologies like High-Magnesian-Suite (Mg-Suite or HMS) rocks are spatially concentrated on the lunar nearside to the north and west of Serenitatis, in the central-western highlands, and to the north rim of the SPAT (Fig. 1.30). It is hoped that the X-ray Spectrometer abroad the Selene mission (Ogawa et al. 2006) and the C1XS instrument aboard the Chandrayaan mission (Grande et al. 2006) will provide high resolution (50 km/pixel) mapping of magnesium and Mg# across much, if not all, of the lunar surface, and from these datasets detailed, localised, interpretations can be made about lunar Mg# variability.

The concept of subdividing the Moon into similar geochemical terranes (e.g. Jolliff et al. 2000, Lucey et al. 2006) is efficient in that it allows an easy distinction between large-scale lithological environments. However, there are many localized regions that do not easily fit within these three broad classifications: e.g. the mare regions to the east of the PKT (including Tranquillitatis, Fecunditatis, Nectaris, Crisium, Smythii and Marginis), the near-side north-easterly highland areas (potentially composed of magnesian rich lithologies), the Schiller region, and the large Mare Australe basin, etc. Spudis et al. (2000, 2002) have used a technique of combining global remotely-sensed Clementine and Lunar Prospector datasets to classify the lunar surface using detailed petrological constraints. Their ternary space Ti-(Fe-Ti)-Al global maps (Fig. 1.31) reveal that the Schiller region, Mare Australe and a significant portion of the SPA, are in fact likely to represent areas of ancient buried mafic mare deposits (corresponding to 'unit 8' colour scheme). The scheme clearly subdivides different mare basalt flows according to their Ti-content, with VLT, Fe-rich basalts occurring in the northern Mare Frigoris, to high Ti-basalts outcropping in Mare Tranquillitatis and Oceanus Procellarum. Significantly the near-side highlands regolith (as sampled by Apollo 16) appears to be composed of a mixture of 'units 9, 13' lithologies that are atypical of much of the far-side highlands regions. The FHT is divided by this elemental classification into a complicated mixture of pure anorthosite regoliths ('unit 15'), and soils with mixtures of highland and low-Ti mafic lithologies ('unit 14 and 13') with some more localised regoliths rich in 'unit 9'. The main limitation of this method is that the 'Al'

elemental parameter is not a direct measurement of Al-atoms in the lunar surface, but is based on the known anti-correlation between FeO and Al_2O_3 from the Apollo soil and rock sample collection.

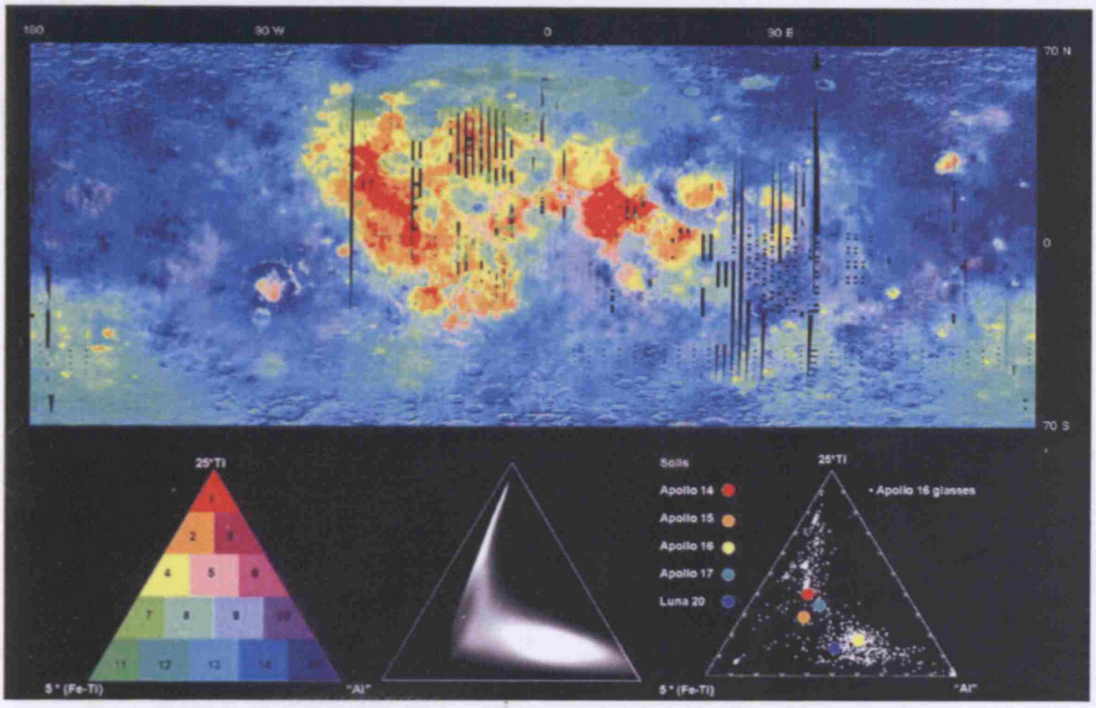

Fig. 1.31. Taken from Spudis et al. (2002): petrologic map of the Moon based on the compositional systematics of the Ti – (Fe-Ti) – "pseudo-Al" ternary system. Plots at bottom are in atomic proportion. At left is the (arbitrary) breakdown of units in ternary space. The scattergram in the middle shows the distribution of compositional pixels in the global image. At right is a ternary plot of Apollo 16 impact glasses (white dots) and the average soil compositions from highland Apollo and Luna landing sites (colour dots).

1.5 Aims of This Project

The aims of this study are to integrate geological interpretations from the petrographic and petrologic investigation of lunar meteorites with geochemical information from remote sensing missions, and to use remote sensing datasets to try to relate lunar meteorites back to their launch provenances on the Moon. To achieve these goals I present data from mineralogical and geochemical investigations of thin sections and small chips of lunar meteorites. I will describe my involvement in the SMART-1 mission to the Moon, and discuss preparatory and calibration work done to help the interpretation of D-CIXS data. I will also discuss actual lunar XRF data, as measured by the D-CIXS instrument, and discuss the problems associated with the datasets. I will outline plans that may help in the interpretation of lunar geochemical data from D-CIXS and what the future holds for the next generation of planetary XRF instrumentation.

Chapter 2: Meteorite Samples and Methods

2.1 Meteorite Samples

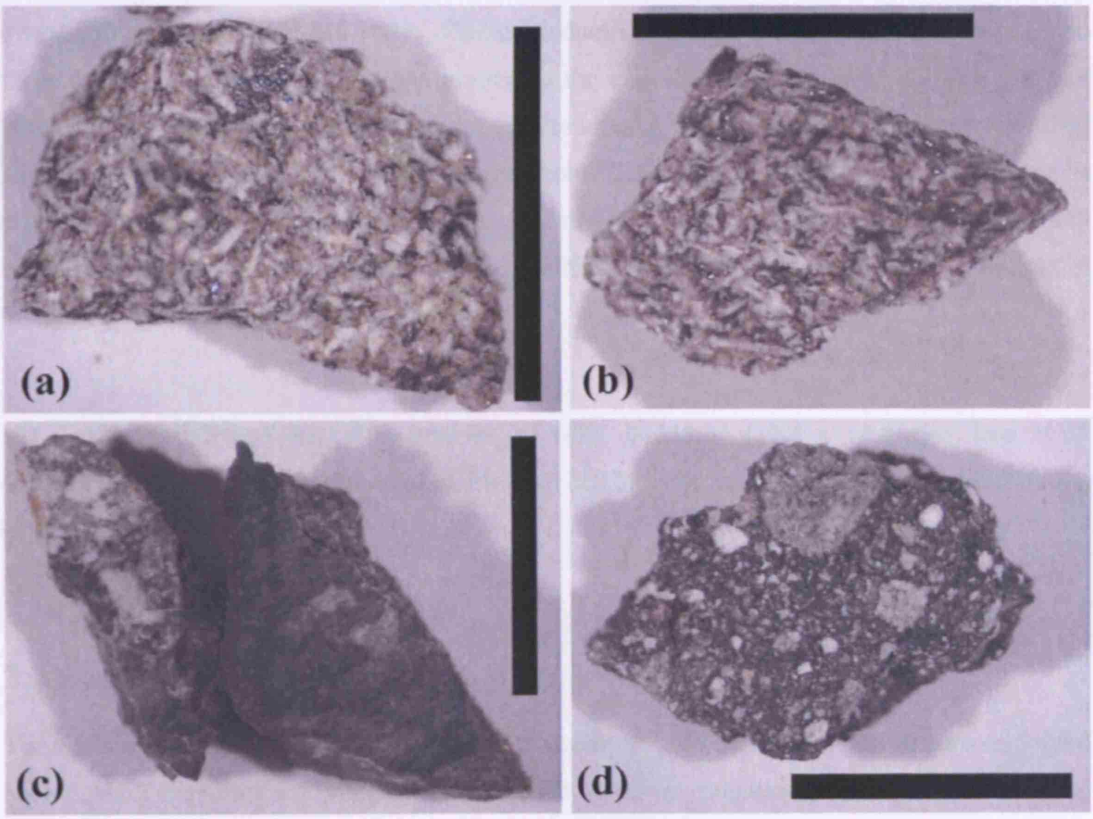

Fig. 2.1. Photographs of chips of lunar meteorites used in bulk composition investigations. In all images scale bar = 5 mm. (a) Main mass of LAP 02224,34 illustrating the crystalline nature of the sample. Plagioclase lath-like mineral grains (white) stand out against the pyroxene (brown-green phases) and ilmenite (black phases) groundmass. (b) Main mass of LAP 02205,13. (c) DaG 400 chips removed from main mass slab held at the NHM. Rocklet is rich in dark grey impact melt matrix enclosing small anorthositic white clasts/minerals. (d) Half of mass of MET 01210,25 This rocklet has a diverse range of mineral fragments (brown components are pyroxene phases, bright white components are plagioclase grains) and anorthositic and basaltic lithic clasts.

The following lunar meteorites have been studied for work in this thesis:

Unbrecciated meteorites:

LAP 02205/02224/02226/02436/03632: Polished thin sections of LAP 02205,32 (10 x 12 mm), LAP 02224,35 (5.5 x 14.1 mm), LAP 02226,25 (5.8 x 8.4 mm), LAP 02436,27 (8.1 x 13.2 mm) and LAP 03632,19 (8.9 x 7.35 mm) were provided by NASA's Meteorite Working Group (MWG). The MWG also provided two chippings: (Fig. 2.1a, b) LAP 02205,13 (original mass: 209 milligrams [mg]) and LAP 02224,31 (original mass: 216 mg) for bulk chemical investigations.

Regolith Breccias:

DaG 400: I was provided with a polished thick section block of DaG 400 from the Vatican Observatory Collection. The sample had previously been studied for trace element investigations by LA-ICP-MS (laser ablation inductively coupled mass spectrometry) and so there was some scarring of clasts and matrix on the exposed surface by laser ablation pits and pit ejecta. In order to gain precise quantitative reproducible results measurements were not taken from areas up to 150 μm from these damaged zones. The section was repolished to remove as much deposited material as possible before analysis was conducted. A small portion of DaG 400 was also removed from the main slab held at the Natural History Museum London to be used in bulk composition investigations (Fig. 2.1c).

MET 01210: Polished thick-thin sections of MET 01210,21 (10.4 x 14.6 mm) and MET 01210,27 (8.6 x 13.1 mm), and chip of MET 01210,25 (Fig. 2.1d), were also provided by the MWG.

2.2 Analytical Techniques

The analytical procedures used for studying the compositions of lunar meteorites are described below. All of the thin/thick polished sections used in this investigation were initially studied and imaged using optical microscopy and were then coated with carbon for electron microprobe investigations.

2.2.1 Mineral Major and Minor Element Chemistry

Major and minor element concentrations in the constituent phases of the meteorite sections were determined using a Cameca SX50 wavelength dispersive electron microprobe (EMP) at the Natural History Museum, London (NHM). The Cameca was operated at a 20 keV accelerating voltage with a 20 nA beam current with a focused beam analysis for 10 to 30 s count time per element, and employed well-characterized silicate, oxide and metal standards. In spinel investigations, results were corrected for an instrumental V, Ti peak overlap, and in metal and sulphide investigation, results were corrected for the Fe, Co overlap.

X-ray maps and supplementary mineral composition data were determined by electron dispersive spectrometry using a JEOL 5900LV SEM and a LEO 1455VP SEM at the NHM,

both fitted with an Oxford Instruments INCA energy dispersive X-ray microanalyzer system and operated at a 20 kV accelerating voltage and 2 nA beam current. Both instruments were calibrated with well characterized samples. X-Ray maps were taken at a resolution of 256 by 256 pixels and at a magnification of x200 - x250 for large whole sample maps, and at higher magnification (x200 - x1000) for individual area studies.

2.2.2 Mineral Minor and Trace Element Chemistry

The concentration of trace elements in mineral phases in DaG 400 and LAP 02205 was determined by time-resolved analysis using laser ablation inductively coupled plasma mass spectrometry (LA-ICP-MS) at the NHM. The instrument was a VG Plasma Quad VG PQ3, coupled to a New Instrument UP-213 nm laser. Carrier gases were a mix of Ar and He. Data taken at the NHM were reduced using the LAMTRACE software programme. Measurements were made for 120 s, during which time the abundance of 36 elements was monitored. Background conditions were monitored for 60 s and the laser ablated the sample for 60 s.

Trace element investigations in MET 01210 were conducted using an Agilent LA-ICP-MS system coupled to a New Instrument 213 nm laser system at University College London (UCL). Data taken at UCL were reduced using the Glitter software programme. Carrier gases were a mix of Ar and He and the system was purged between each analysis with He to reduce background contamination. Measurements were made for 60 s, during which time the abundance of 36 elements was monitored. Background conditions were monitored for 30 s and the laser ablated the sample for 30 s.

Analyses on both instruments were performed in situ, with variable sized laser ablation pits depending on the target mineral or clast. The ablated volume allowed compositional information to be obtained for individual mineral phases and clast regions. The external standard also used on both instruments was NIST 612 (a synthetic doped glass) that was ablated under the same conditions as the sample being analysed. The relative standard deviations of the NIST 612 measurements were between 1 and 10% precision for the elements analyzed. As an assessment of accuracy, the average relative error for the NHM/UCL NIST 612 compared with the Pearce et al. (1997) NIST 612 reported concentrations was always <10% for all elements. Calcium was used as an internal standard by comparing the CaO abundance in minerals also measured previously by EMP. I ensured that the laser was directed to the centre of the mineral grain/clast area to avoid contamination from surrounding crystals or from terrestrial contamination deposits in fractures. There is a risk that in 3-dimensions the laser beam can penetrate to the glass slide,

however the raster process reduces this risk and the glass slide has distinctive HREE patterns that ensure that any sampling errors can be removed in the time-resolved calibration process.

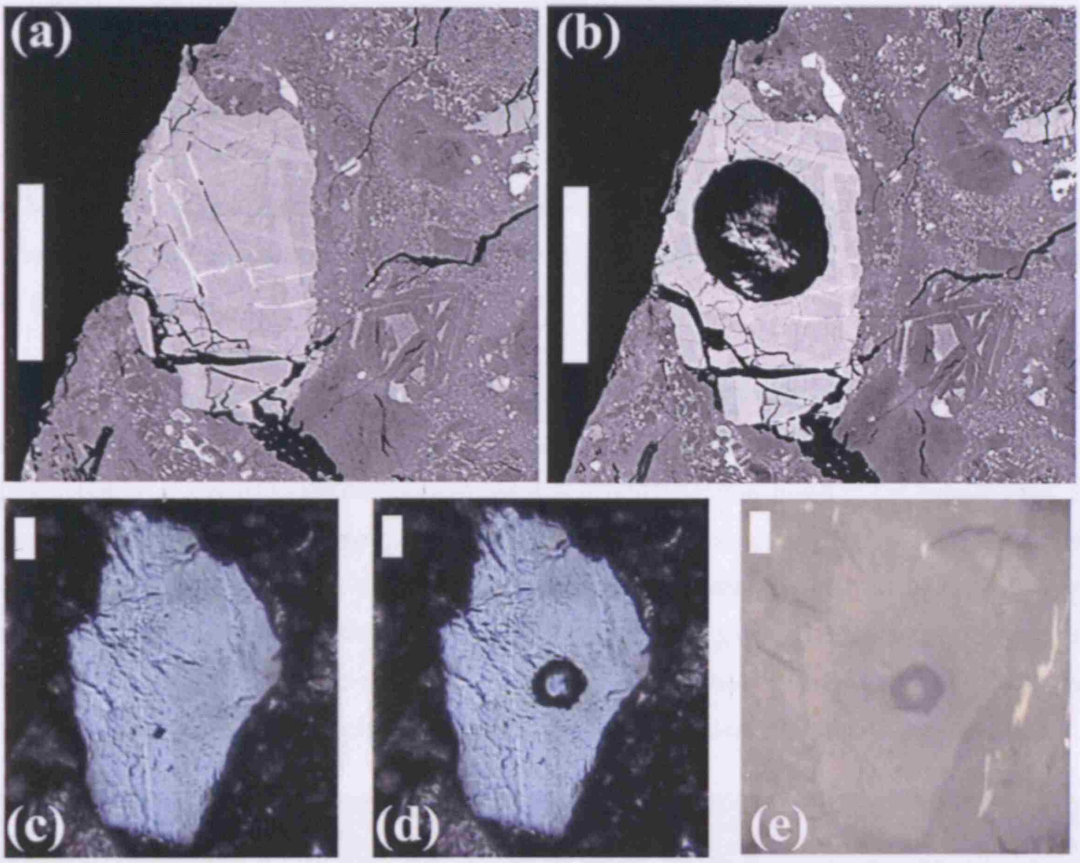

Fig. 2.2. Photo-micrographs showing the investigation into mineral trace and minor element chemistry. Scale bar in all images is 100 µm. Back scattered electron images showing exsolved pyroxene in DaG 400 (a) before and (b) after laser ablation analysis. Plagioclase grain in MET 01210 (c) before analysis (cross polarised light) and (d) (e) after analysis. (e) Debris ejecta can be seen around the pit in reflected light image of plagioclase grain.

2.2.3 Bulk Clast Analytical Techniques

An investigation of the bulk composition of individual lithic fragments was conducted for clasts in DaG 400 and MET 01210. Major element geochemistry was estimated using broad-beam measurements on the JEOL 5900LV SEM coupled with INCA software. Three to five measurements of each investigated clast were made for a counting time of 60 s. The results of these measurements were averaged, and their values were normalised to their analytical total. (This normalisation helped to correct the problem of broad-beam analysis low analytical totals). The standard deviations between the individual measurements were used as a measure of error of the technique.

Trace and minor element concentrations were made using LA-ICP-MS, following the technique described in section 2.2.2. As lithic material is predominately heterogeneous in composition a large laser head size or a rastered elongate pit was used to ablate as much of the sample away as possible, thus providing a measure of the bulk composition of several phases within just one clast (Fig. 2.3). In most clasts laser measurements were collected for 3 or more points. Larger clasts were targeted for up to five or six tracks, and smaller fragments for one or two tracks (the number of measurements will be listed in tables of composition). Standard deviations between these analyses were used as a measure of the range of geochemical diversity in these clasts.

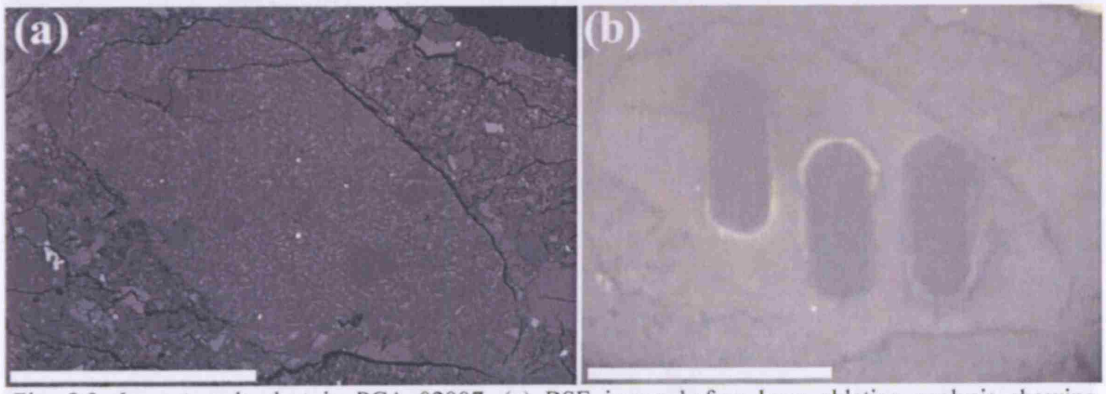

Fig. 2.3. Impact melt clast in PCA 02007. (a) BSE image before laser ablation analysis showing heterogeneous texture of plagioclase chadacrysts included in a matrix of recrystallised plagioclase and mafic melt. (b) Reflected light image of the same clast after trace element investigation by LA-ICP-MS, clearly showing laser tracks of ablated material. Scale bar is 300 μm in both images.

2.2.4 Modal Mineralogy

Modal mineralogy in the basaltic LAP meteorites was calculated using the Oxford Instruments INCA Phasemap tool. This software allows the identification of mineralogical phases (Fig. 2.4a) using ternary element plots of specific pixel information from montaged X-ray maps of the samples (Fig. 2.4b). The major source of uncertainty in this determination of mineral modes is because of difficulties in determining exact phase boundaries, but by combining several of these plots representative mineral proportions can be made (Fig. 2.4c).

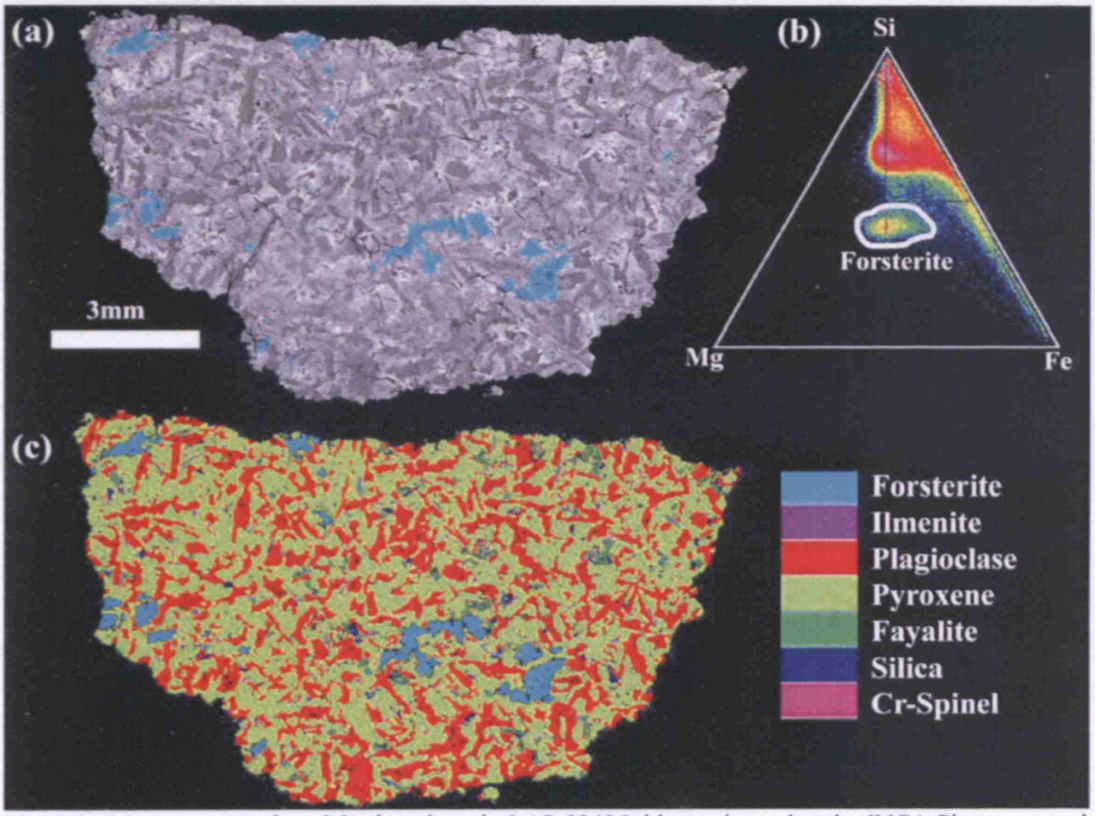

Fig. 2.4. Measurement of modal mineralogy in LAP 02436 thin section using the INCA Phasemap tool. (a) Backscattered electron image shows location of forsteritic olivine phases in the sample. (b) Three element ternary plot illustrating technique of geochemically constraining individual mineral phases from combination X-ray maps [note colours in this plot do not relate to colours in image (c)]. Ternary plot illustrated corresponds to pixels corresponding to forsterite olivine. (c) Composite of all of the compositional phases identified in the study for LAP 02436. The modal proportions of these phases are taken as the modal proportions of minerals in the section.

2.2.5 Bulk Sample Composition Analytical Techniques

Whole-rock major, minor and trace element composition of lunar meteorite chippings (Fig. 2.1) were determined using Inductively Coupled Plasma - Atomic Emission Spectrometry (ICP-AES) and Inductively Coupled Plasma - Mass Spectrometry (ICP-MS) at the NHM. The instruments used were a Varian VISTA PRO Axial ICP-AES and a Varian ICP-MS. Prior to analysis the chippings were photographed, weighed and crushed using an agate pestle and mortar in a clean room environment. For the major elements 40 mg of powdered material was fused with $LiBO_2$ flux and then dissolved in dilute HNO_3. For the trace elements, a $HF/HClO_4/HNO_3$ dissolution was undertaken using 100 mg of sample. Both dissolution methods were based on those of Thompson and Walsh (2003). Five analyses were completed for each sample to determine measurement precision. Major elements were determined by ICP-AES, and the instrument was calibrated with NHM certified reference materials (CRMs; Mica-Fe, NIM-D, NIM-N, NIM-P). Selected trace elements were also determined by ICP-AES after calibration using the standard NHM synthetic standards, and matrix corrected with CRMs (W1, BHVO-1, BCR-1). Remaining trace elements were determined by ICP-MS, again calibrated with synthetic standards, using Rh and In as internal standards, and with CRMs (BCR-1, BHVO-1) used to check the data quality. Some minor and trace elements were measured by both techniques and are generally in good agreement.

2.3 Evidence of Meteorites having a Lunar Origin

The recognition of the lunar meteorites as having originated from a non-terrestrial environment, and being launched from the Moon, is based on several lines of evidence:

(1) All of the stones collected were originally coated with glassy fusion crusts suggesting that they have an extraterrestrial origin. The crust developed as the samples were frictionally heated as the meteorites passed through the Earth's upper atmosphere.

(2) Lunar mineralogy is distinct from that of terrestrial samples in that all of the mineral phases were crystallised in an anhydrous magmatic environment and display no signs of aqueous alteration. The presence of FeNi metal, troilite (FeS), ilmenite with a Ti-richer composition (Raymond and Wenk, 1971) and the lack of ferric iron and hydrous mineral phases suggests that they were formed in a highly-reducing environment such as those typically associated with lunar magmatic conditions as seen in the Apollo and Luna rock collections.

(3) Oxygen isotope compositions of material derived from the Moon sits on the terrestrial fractionation line (TFL). LAP 02205 has isotopic compositions of $\delta^{18}O$ of +5.6 ‰ and $\delta^{17}O$ of +2.7‰ (Satterwhite, 2003) and falls just below the TFL trend (Fig. 2.5).

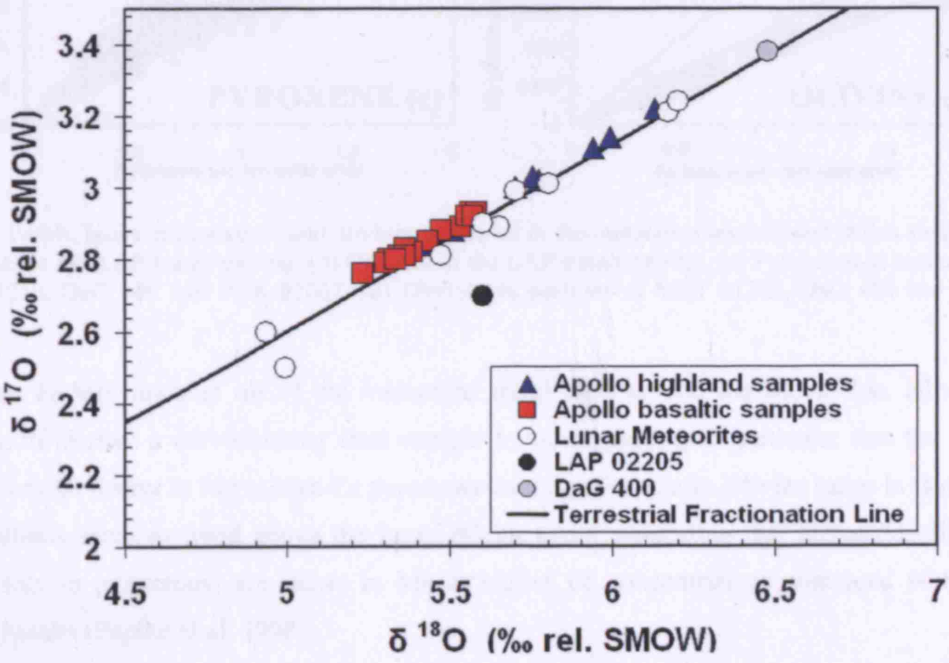

Fig. 2.5. Oxygen isotope compositions of lunar samples compared with the TFL. Apollo values are taken from Weichert et al. (2001). LAP 02205 values taken from Satterwhite (2003), DaG 400 value taken from Zipfel et al. (1998). Lunar meteorite values taken from Bischoff et al. (1998), Fagan et al. (2001), Weichert et al. (2001), Kaiden and Kojima (2002), Anand et al. (2003b) and Cahill et al. (2004).

(4) The ratios of Fe to Mn in pyroxenes and olivine can be a powerful tool in determining planetary origin. This relationship will vary among planetary bodies because of differences in the state of initial accreted material, planetary thermal dynamic history and differentiation and differing oxygen fugacity conditions (Papike 1998, Papike et al. 2003). Lunar pyroxenes and olivines exhibit strongly differentiated Fe/Mn ratios compared with the Earth, Mars, Vesta-like bodies and chondrites, probably as the result of volatile loss in an early Moon-forming event (Papike et al. 1998). Fe/Mn ratios in pyroxenes and olivines measured in the meteorites investigated in this study are shown in Figure 2.6.

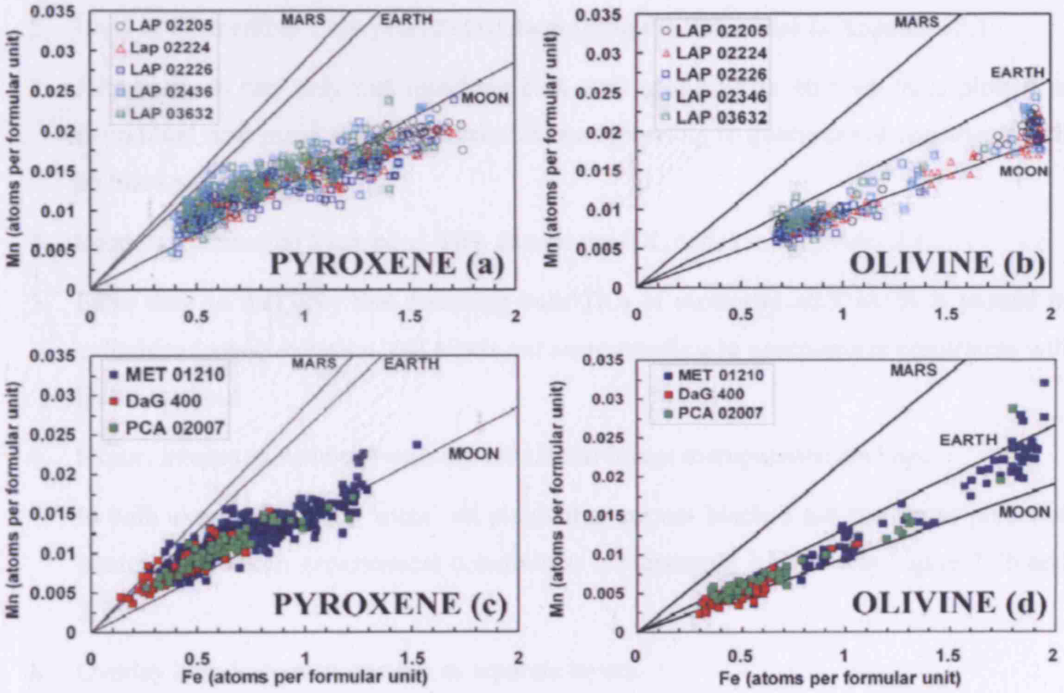

Fig. 2.6. Fe/Mn ratios in pyroxenes and olivines measured in the meteorites investigated in this study. (a) Pyroxenes in the LAP basalt pairing. (b) Olivines in the LAP basalt pairing. (c) Pyroxenes in sections of MET 01210, DaG 400 and PCA 02007. (d) Olivines in sections of MET 01210, DaG 400 and PCA 02007.

Pyroxene Fe/Mn ratios in all of the meteorites trend well around the Moon line, although seeming to display a curved rather than straight trend suggesting in particular that the LAP basalts may be poorer in Mn at high-Fe pyroxenes than Apollo basalts. Olivine ratios in fayalitic compositions seem to trend above the lunar olivine trend suggesting that meteorite olivines (conversely to pyroxenes) are richer in Mn at higher Fe concentrations compared with the Apollo basalts (Papike et al. 1998).

2.4 Technique to Identify Provenance of Lunar Meteorites

Data from remote sensing missions have been integrated with that from lunar meteorites in an attempt to identify soil compositions that best match the compositions of the lunar meteorites; thus constraining likely meteorite launch localities. I have developed such a method, which is outlined below:

1. Derive bulk chemical composition of meteorite (requires FeO, TiO_2, Th). Regolith breccias will provide the best type of sample for this study because they already represent the heterogeneous soil compositions sampled by remote sensing missions.
2. Load in Clementine 1 km/pixel FeO dataset using the IDL codes in Appendix 2.1.
3. Filter data so that only that matching bulk FeO of meteorite ±0.5 wt. % is plotted in cylindrical map projection. All pixels not corresponding to geochemical constraints will be blacked out.
4. Load in Clementine 1 km/pixel TiO_2 dataset the IDL codes in Appendix 2.1.
5. Filter data so that only that matching bulk TiO_2 of meteorite ±0.5 wt. % is plotted in cylindrical map projection. All pixels not corresponding to geochemical constraints will be blacked out.
6. Export images to Adobe Photoshop (or similar image manipulation package).
7. In both exported images 'clear' all pixels that are not blacked out (i.e. those pixels of interest that match geochemical constraints). An example is shown in Figure 2.7b and 2.7c.
8. Overlay both images in one file as separate layers.
9. On the resulting multilayered image any pixels that are clear/not black (i.e. can be see on a coloured background) correspond to best fit of FeO and TiO_2 constraints for the meteorite to ±0.5 wt. %.
10. Load in LP Th ppm 0.5 °/pixel FeO dataset from 70° north to 70° south latitude using codes in Appendix 2.2.
11. Filter data so that only that matching bulk Th of meteorite ±1 ppm is plotted. All pixels not corresponding to geochemical constraints will be blacked out.
12. Export dataset as an image and 'clear' all pixels that are not blacked out e.g. Figure 2.7a.
13. Overlay this image with that already made at stage 9. This will result in a combination multi-element constrained plot. Any pixels that are clear/not black (i.e. can be see on a

coloured background) correspond to best fit of FeO and TiO_2 constraints for the meteorite to ±0.5 wt. % and to best fit Th to ±1 ppm.

This technique provides a first order qualitative assessment of soils compositions most similar to the bulk compositions of meteorites analysed in this study. To be truly accurate the best-fit geochemically constrained regions should also be cross-correlated with radiometric age dates of samples and crater count statistics of regions of interest.

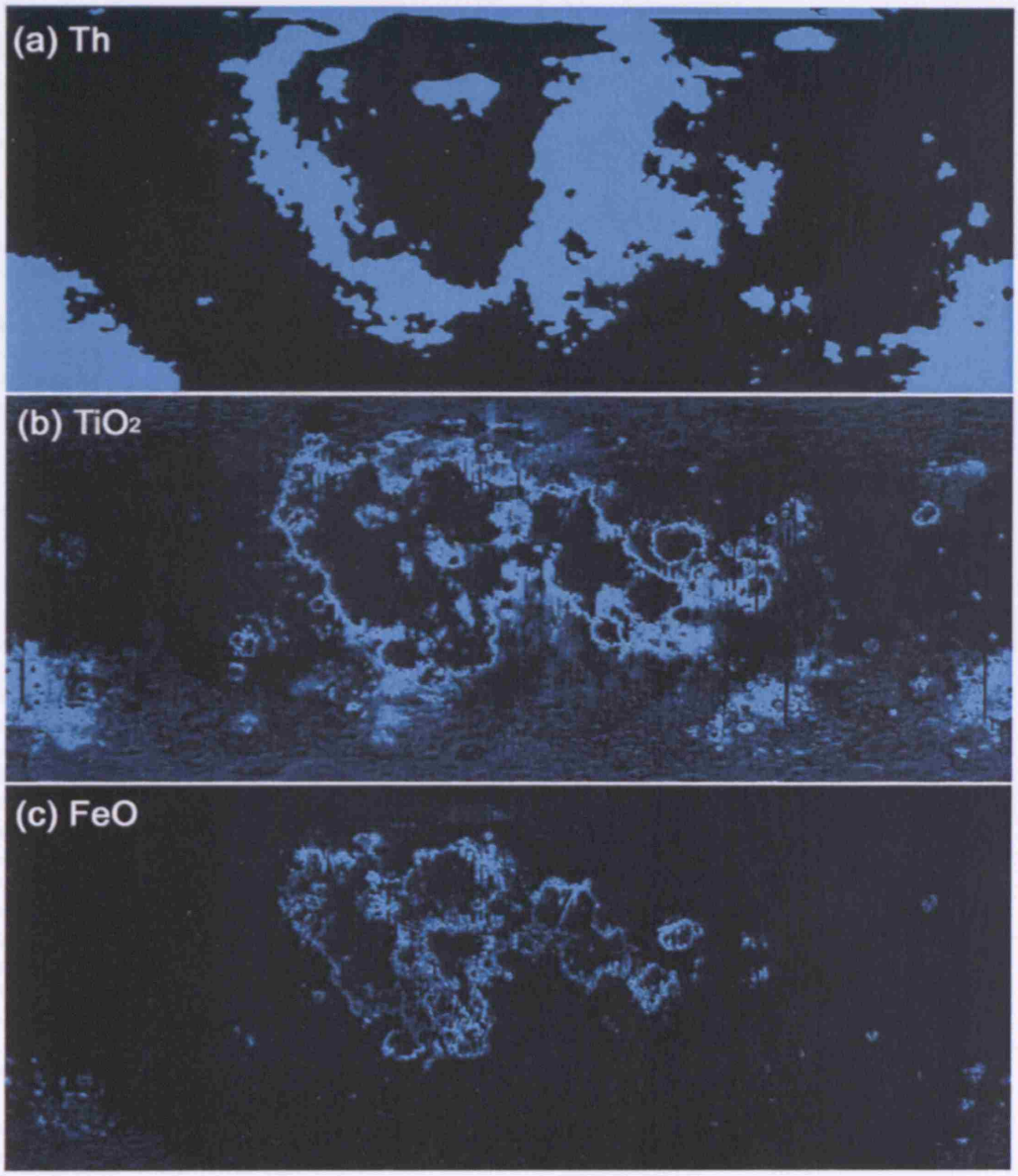

Fig. 2.7. MET 01210 geochemical constraint outputs. (a) Pixels of Th [ppm] corresponding with <1- <4 ppm Th using half degree LP datasets Lawrence et al. (2002a,b). (b) Pixels of TiO_2 [wt.%] from 1 km resolution UVVIS datasets of Lucey et al. (1998). (c) Pixels of FeO [wt.%] from 1 km resolution UVVIS datasets of Lucey et al. (1998). Note that this method does not consider latitudes 30° from each pole because complete Clementine datasets do not exist for this region. The blue areas in all three plots correspond with 'similar' compositions to the meteorite discussed. It is only when all three images are combines that they can be used as a useful multi-element geochemical constraint map of possible lunar meteorite regolith ejection localities.

Appendix 2.1. Example of IDL code used to load in Clementine elemental and albedo datasets. Code has been split into two columns. With thanks to Dave Heather and Barry Kellet for help with developing code.

```
Pro Clementine_extraction_LAP
;NAME: Clementine_extraction
; PURPOSE:
; Extract Clementine FeO and TiO2 information
; Plot Clementine FeO and TiO2 information
; CALLING SEQUENCE:
; INPUTS:
; east_feo, west_feo, east_tio2, west_tio2
; OPTIONAL INPUTS:
; KEYWORD PARAMETERS:
; OUTPUTS:
; data plots
;
; CAUTIONS:
;MODIFICATION HISTORY:
;Created by Katherine joy
;Date: 20th Sept 2006
;-----------------------
; Extract Clementine FeO and TiO2 information
; Plot Clementine FeO and TiO2 information
; CALLING SEQUENCE:
; INPUTS:
; east_feo, west_feo, east_tio2, west_tio2
; OPTIONAL INPUTS:
; KEYWORD PARAMETERS:
; OUTPUTS:
; data plots
;
; CAUTIONS:
;MODIFICATION HISTORY:
;Created by Katherine joy
;Date: 20th Sept 2006
;-----------------------------------------------------------------------
;Set up Graphics parameters
device, decomposed = 0
loadct,12
;-----------------------------------------------------------------------
;set up four element array to hold all datasets
;Moon = fltarr(4,10916,4245)
;-----------------------------------------------------------------------
;Albedo Maps load in code
albedo_east = bytarr(5458,4245)
albedo_west = bytarr(5458,4245)
;
openr,1,"D:\Katherine Joy\Clementine files\west_750"
readu,1,albedo_east
close,1
;
openr,1,"D:\Katherine Joy\Clementine files\east_750"
readu,1,albedo_west
close,1
;-----------------------------------------------------------------------
;Read in albedo map into filter, add together and then flip so that correct geometry
moon_albedo = fltarr(10916,4245)
moon_albedo(0:5457,*) = albedo_east
moon_albedo(5458:10915,*)= albedo_west
albedo_flip = moon_albedo /500
albedo= reverse (albedo_flip,2)
;
close,1
;-----------------------------------------------------------------------
;Read in albedo map into filter, add together and then flip so that correct geometry
moon_albedo = fltarr(10916,4245)
moon_albedo(0:5457,*) = albedo_east
moon_albedo(5458:10915,*)= albedo_west
albedo_flip = moon_albedo /500
albedo= reverse (albedo_flip,2)
;
;plot up image into window and then into ITOOLS
tvscl,congrid (albedo,545,424)
iimage, albedo
;-----------------------------------------------------------------------

;FEO MAP Load Inputs

fe_east = bytarr(5458,4245)
fe_west = bytarr(5458,4245)
openr,1,"D:\Katherine Joy\Clementine files\west_feo"
readu,1,fe_east
close,1
openr,1,"D:\Katherine Joy\Clementine files\east_feo"
readu,1,fe_west
close,1
;Read in FeO map into filter, add together and then flip so that correct geometry
moon_fe = fltarr(10916,4245)
moon_fe(0:5457,*) = fe_east
moon_fe(5458:10915,*)= fe_west
feo_flip = moon_fe /10
feo= reverse (feo_flip,2)
;-----------------------------------------------------------------------
;Select compositional limit parameters
;wz = where (feo gt 20)
;LAP = 0.0 * feo
;LAP (wz) =  feo ( wz )
wx = where ((feo ge (21.43-0.5)) and (feo le (21.43+0.5)))
LAP_feo_1 = 0.0 * feo
LAP_feo_1  (wx) =  feo (wx)
;-----------------------------------------------------------------------
;TiO2 MAP Inputs
ti_east = bytarr(5458,4245)
ti_west = bytarr(5458,4245)
openr,1,"D:\Katherine Joy\Clementine files\east_tio2"
readu,1,ti_east
close,1
openr,1,"D:\Katherine Joy\Clementine files\west_tio2"
readu,1,ti_west
close,1;
;Read in TiO2 map into filter, add together and then flip so that correct geometry
moon_ti = fltarr(10916,4245)
moon_ti(0:5457,*) = ti_west
moon_ti(5458:10915,*)= ti_east
tio2_flip = moon_ti /10
tio2= reverse (tio2_flip,2)
;-----------------------------------------
;discriminating tio2 regions of interest
wx = where ((tio2 ge (3.32-0.5)) and (tio2 le (3.32+0.5)))
LAP_tio2_1 = 0.0 * tio2
LAP_tio2_1  (wx) =  tio2 (wx)
```

```
;-----------------------------------------------
;Plotting in ITOOLS
iimage,feo
iimage,tio2
;-----------------------------------------------
;Plotting in normal plot window
;window,0
;tvscl,congrid (feo,545,424)
window,1
tvscl,congrid (al2o3,545,424)
;window,1
;tvscl,congrid (tio2,545,424)
;-----------------------------------------------
End
```

Appendix 2.2. Example of IDL code used to load in Lunar Prospector high resolution 2 degree Th and FeO datasets. Code has been split into two columns.

```
Pro LP_mapping
;
;NAME: Lunar_Prospector_extract
; PURPOSE:
; CALLING SEQUENCE:
; INPUTS:
; OPTIONAL INPUTS:
; KEYWORD PARAMETERS:
; OUTPUTS:
; CAUTIONS:
; MODIFICATION HISTORY:
;Created by Katherine joy
;Date: 4th October 2006
;-----------------------------------------------
;READ IN PROSPECTOR DATA FROM FILES
;x=number of index values in the original array you are reading in
x = 259200
;
;the names of the different column information in the luanr prospector file
lat_minf = fltarr(x)
lat_maxf = fltarr(x)
lon_minf = fltarr(x)
lon_maxf = fltarr(x)
feo_values = fltarr(x)
;
; open text file with Lunar Prospector Data
openr,1,"D:\Katherine Joy\Luna _Prospector\ironhd_v1.txt"
;
;set up a string variable
a=' '
; i needs to have an L after is as it is a long variable integer as there are more
;than 32768 (2 to the power 8 - 1!) values in the array
;
i = 0L
;
;instruction to read in every row of data until the end of file is encountered
while not eof ( 1 ) do begin
   readf, 1, a
   lat_minf(i) =  float ( strmid ( a, 2, 6 ) )
   ;set up a 2-d array to read in the Th values so that you can make a bmp
feo = fltarr(720,360)
z = 720
p = 0L
q = 1L
for i = 0,360-1 do begin
feo (*,i) = feo_values ((z*p):(z*q)-1)
 q = q + 1L
endfor
;-----------------------------------------------
;the names of the different column information in the luanr prospector file
lat_mint = fltarr(x)
lat_maxt = fltarr(x)
lon_mint = fltarr(x)
lon_maxt = fltarr(x)
Th_values = fltarr(x)
; open text file with Lunar Prospector Data
openr,1,"D:\Katherine Joy\Luna _Prospector\thoriumhd_v1.txt"
;set up a string variable
a=' '
; i needs to have an L after is as it is a long variable integer as there are more
;than 32768 (2 to the power 8 - 1!) values in the array
i = 0L
;instruction to read in every row of data until the end of file is encountered
while not eof ( 1 ) do begin
   readf, 1, a
   lat_mint(i) =  float ( strmid ( a, 2, 6 ) )
   lat_maxt (i)=  float ( strmid ( a, 13, 6 ) )
   lon_mint (i)=  float ( strmid ( a, 24, 6 ) )
   lon_maxt (i)=  float ( strmid ( a, 35, 6 ) )
   Th_values (i)=  float ( strmid ( a, 48, 6 ) )
;control for increasing loop by 1 every time
   i = i + 1L
endwhile
;close the file
close,1
;----------------------------------------------- ;set up a 2-d array to read in
the Th values so that you can make a bmp
Th = fltarr(720,360)
```

```
  lat_maxf (i)= float ( strmid ( a, 13, 6 ) )
  lon_minf (i)= float ( strmid ( a, 24, 6 ) )
  lon_maxf (i)= float ( strmid ( a, 35, 6 ) )
  feo_values (i)= float ( strmid ( a, 48, 6 ) )
;
;control for increasing loop by 1 every time
  i = i + 1L
Endwhile
;close the file
close,1
;-------------------------------------------------------------
```

```
z = 720
p = 0L
q = 1L
for i = 0,360-1 do begin
Th (*,i) = Th_values ((z*p):((z*q)-1))
;Th (*,1) = Th_values ((z*1):((z*2)-1))
;Th (*,2) = Th_values ((z*2):((z*3)-1))
  p = p + 1L
  q = q + 1L
endfor
;-------------------------------------------------------------
;sorting to see which areas have similar compositions as DaG 400
wx = where ((Ratio ge (DaG_ratio - DaG_ratio_var)) and (Ratio le (DaG_ratio +DaG_ratio_var)))
dag = 0.0 * Ratio
dag (wx) = Ratio (wx)
;-------------------------------------------------------------
iimage, dag
window,0
tvscl, dag
End
```

Chapter 3: Dar al Gani 400 - A Lunar Feldspathic Regolith Breccia

3.1 Introduction

Dar al Gani (DaG) 400 is classified as a feldspathic lunar regolith breccia meteorite (Grossman et al. 1998). It was collected in the Libyan desert in 1998 (Fig. 3.1). The meteorite was partially coated with a brown fusion crust (Zipfel et al. 1998) and is one of the largest masses (1.43 kg) of lunar material collected anywhere on Earth (exceeded only by the Botswanan regolith breccia Kalahari 009 (Russell, 2005) that had an exceptional collective mass of 13.5 kg). DaG 400 is classified according to the lunar rock type classification scheme of Stöffler et al. (1994) as a polymict consolidated regolith breccia. There has been some suggestions in past literature (e.g. Korotev et al. 2003, Warren et al. 2005) that the sample is in fact an impact melt breccia (Bukovansk et. al. 1999), because the majority of its constituent rock fragments have an impact melt origin. However, based on the presence of crystalline lithic clasts, large relict mineral fragments and impact melt spherules (Zipfel et al. 1998; Warren et al. 2005), the rock has a similarity to regolith breccias returned by Apollo missions (Simonds et al. 1977; McKay et al. 1986; Korotev et al. 1996). The present investigation into a sub-sample of Dag 400 did not find any spherules or remnants of a fused soil component, suggesting that the sample had been thermally disintegrated and/or annealed by shock metamorphic processes.

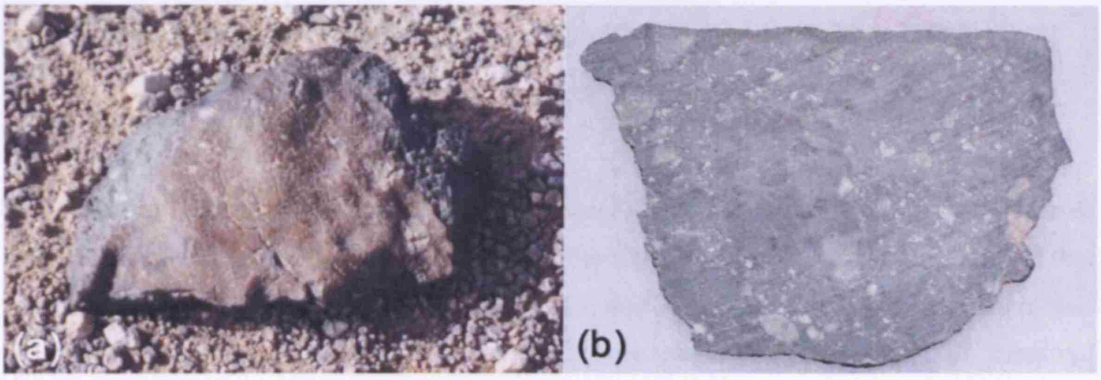

Fig. 3.1. (a) DaG 400 stone photographed on discovery in the Libyan strewn fields. (b) Large slab of DaG 400 9 cm across. Feldspathic lithic clasts can be clearly distinguished from the pale glassy / impact melt rich matrix. A large impact melt clast sits just off centre left of the image and is estimated to be ~ 4 cm in diameter. (Images: Website 1.2).

DaG 400 is a polymict breccia, containing a mixture of lithic and mineral fragments with a seriate grain size distribution that are fused in a glassy pale gray matrix. From photographs of different DaG 400 sub-splits it is clear that some lithic clasts may be as large as 5 cm (Fig. 3.1b) with many being ~1 cm. This size distribution of clastic material, and general lack of agglutinates, suggest that this sample must have been fused in a very immature regolith environment. Most clasts display very sharp contacts with the surrounding matrix, indicating

that they have crystallised in a remote environment and then been brought in, as clasts, to the regolith that formed this breccia. Some of the fragments (particularly the impact melt breccias) have glassy rims that appear to merge into the sample matrix, indicating that their margins have been partially melted by the pervasive shock process that welded the original regolith together.

It is essential to understand the complicated makeup of the lunar regolith in order to maximise our understanding of mineralogical and geochemical global remote sensing datasets. If we are to interpret trends in crustal geological variations we need to understand the significance of how regolith geochemistry is controlled by variations of clast and mineral composition and lithological affiliation. By examining the clasts and minerals in DaG 400 I can investigate the composition and mineralogy of the individual components and hypothesise what bedrock sources were included in the original regolith environment. This information can then be used to address the following questions:

- Is the sample chemically and texturally heterogeneous or homogeneous?
- What components form DaG 400, and in what proportions?
- What does this imply about the nature of the regolith at time of consolidation?
- How does DaG 400 compare to other lunar meteorites and is it a good representation of the lunar crust in the region where it was consolidated?
- What does this analysis imply about the nature of the ancient lunar regolith and how is this relevant today for remote sensing projects?

3.1.1 Terrestrial Contamination

DaG 400 is a hot desert find and has therefore been exposed to terrestrial contamination from water interaction since it entered the Earth's atmosphere. Nishiizumi et al. (2002) reported that DaG 400 has a terrestrial exposure age of <50 ka, and a recalculated age by Nishiizumi was reported by Crozaz et al. (2003) to be 17 ± 2 ka. Generally the amount of terrestrial contamination mineralization (for example; barites, celestite, calcite (Fig. 3.2), gypsum and opal) is related to sample porosity and internal fracturing. It has been suggested these weathering deposits begin to form rapidly after the meteorite is introduced to the desert environment and that the rate of mineralization decreases as available pore and fracture spaces are infilled through time (Cahill et al. 2004). Thus similar low-porosity feldspathic lunar meteorites like DaG 262, which have longer exposure histories, may well have a similar degree of contamination (Crozaz et al. 2003).

The DaG 400 subsection studied in this investigation is cross-cut by calcite-rich veins and small pores (Fig. 3.2, 3.3) that occur randomly throughout the rock. Oxidation of iron is seen in some of the larger veins and is a visible sign of terrestrial weathering (Fig. 3.3c). Additionally small (<10 μm) barium sulphate ($BaSO_4$) crystals cluster around vein rims and have sometimes crystallized in nearby fractures, pores and individual mineral fractures.

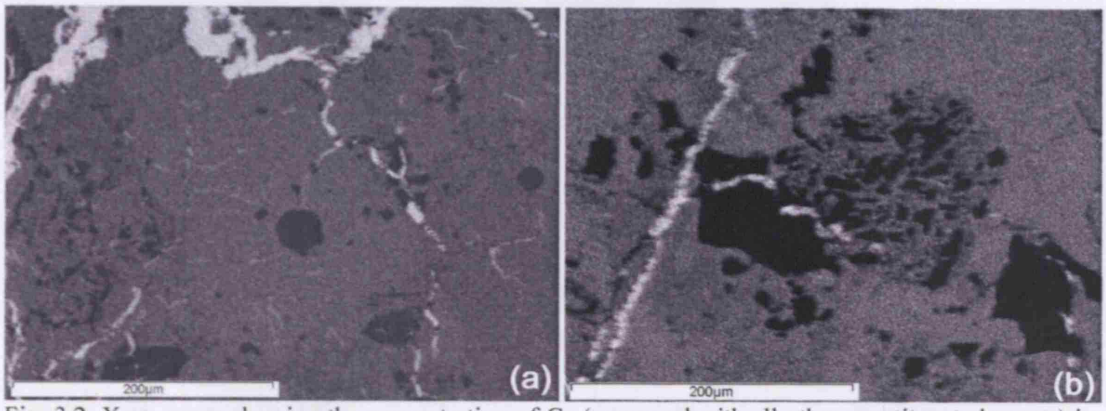

Fig. 3.2. X-ray maps showing the concentration of Ca (compared with all other constituent elements) in two small regions of DaG 400. Terrestrial deposited Ca is concentrated in veins and fractures throughout.

3.2 Petrography and Detailed Clast Investigation

DaG 400 is very well consolidated, with small pale-cream coloured clasts set in a very fine grained grey to dark grey matrix. In the section studied for this investigation the largest clast is elongate, has a sub-rounded rim and is ~5 mm by ~2 mm. There are no large vesicles in the section and thus the rock has a very low porosity. The section is crossed and cut by veins, probably formed through impact melt injection, and fractures that have been infilled with terrestrial $CaCO_3$. Lithic clasts greater than approximately 100 μm form ~70% of the rock and are cemented by a glassy clast-rich matrix that is also rich (~8 %) in remnant mineral fragments. Lithic clasts range from subophitic and fine-grained crystalline lithics to intergranularly recrystallised anorthosites and large individual mineral fragments. Impact melt clasts are distributed throughout and show a range of textures grading from clastic melt breccias to recrystallised microporphyritic crystalline forms. The whole rock is cemented together in a matrix of crushed impact melt, lithic and mineral fragments, bound by a glassy substrate that was fused together by impact induced thermal sintering.

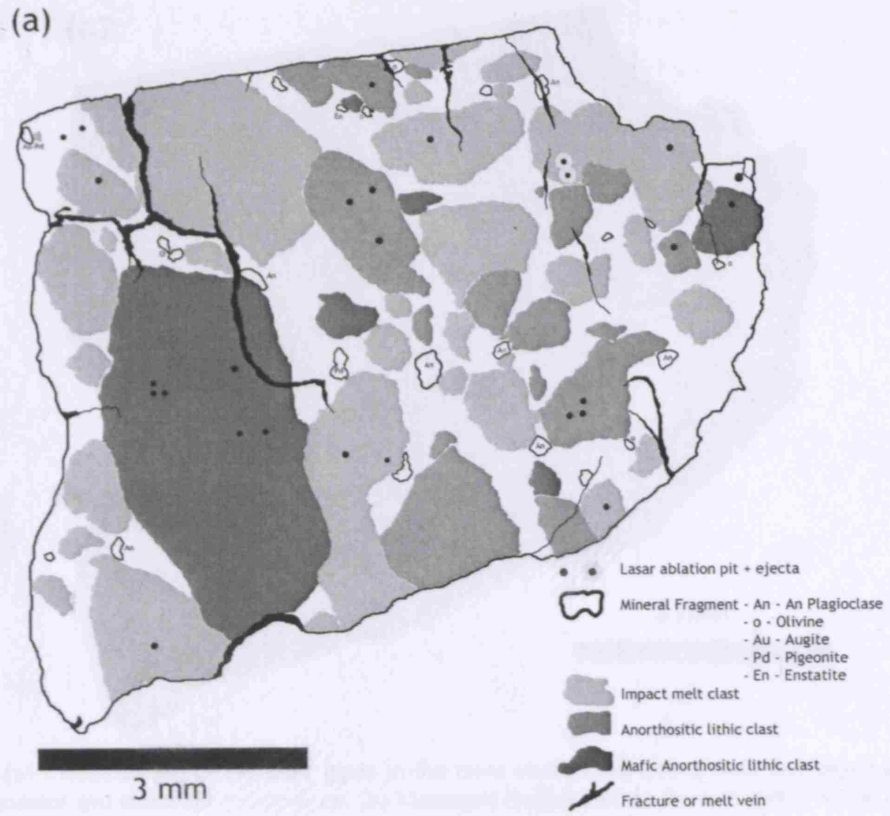
(a)
3 mm
Lasar ablation pit + ejecta
Mineral Fragment - An - An Plagioclase
- o - Olivine
- Au - Augite
- Pd - Pigeonite
- En - Enstatite
Impact melt clast
Anorthositic lithic clast
Mafic Anorthositic lithic clast
Fracture or melt vein

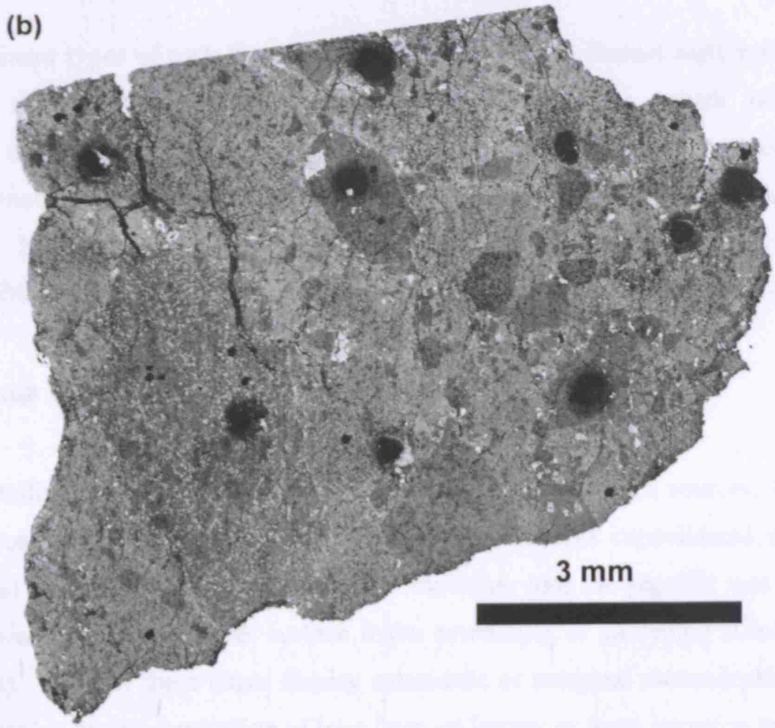
(b)
3 mm

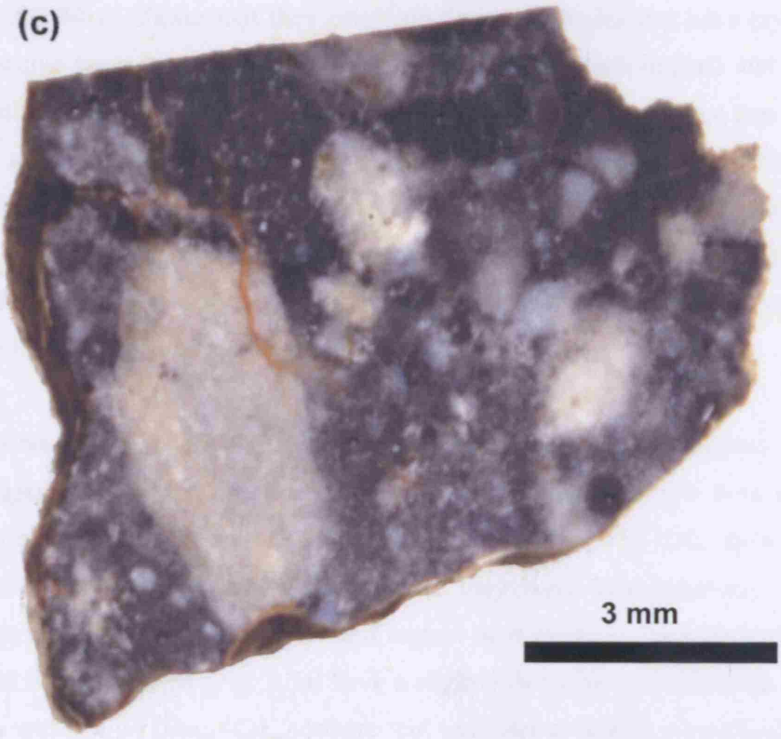

Fig. 3.3. (a) Classification of the clast types in the main studied section of DaG 400 based on texture, mineral content and chemical composition. (b) Montaged back-scattered electron (BSE) image of the sub-section. (c) Scanned true-colour image of section showing red discolouration in fractures as a result of terrestrial mineralization. White clasts are easily identified as being anorthosite rich.

Two predominant types of rock fragments occur in DaG 400 – impact melt derived clasts and lithic clasts that crystallised in an endogenic igneous process, which have then been subsequently altered (but not completely melted) by secondary thermal processes (either shock or regional metamorphic). From modal mineral count (Table 3.3) lithic clasts of all size fractions and lithologies form 78 % of the sample, and represent 99.7 % of the >500 μm fraction, 78.6% of the <500 μm - 20 μm fraction and 2.2% of the <20 μm fraction.

3.2.1 Igneous crystalline lithic clasts

Igneous crystalline lithic clasts (Fig. 3.4) have originated from bedrock sources. These probably originated close to the area where the DaG 400 regolith was consolidated and have been excavated and disseminated by impact events. Inclusion into the regolith was probably as a result of lateral mixing and upper surface insitu reworking or gardening (Gault et al. 1974; Morris, 1978). Most of these clasts display cataclastic or marginal metamorphic textures as a result of alteration by the conduction of heat from an impact or local intrusion events, although all of them (except for one hornfelsic anorthosite clast) have low concentrations of Ni (<100 ppm) and ITEs (<1 ppm). The mineral chemistry and bulk elemental concentration of these

clasts (Fig. 3.5/6/7/8) indicate that they originate from lithologies that have crystallised from different primitive lunar magmas. The majority of crystalline clasts in DaG 400 are associated with the primitive crustal FAN highland suite of rocks (Fig. 3.6): evidence that DaG 400 was consolidated in a lunar highlands environment that contained abundant anorthositic material. Pristine FAN crustal rocks are classified in four subgroups (James et al. 1989; Floss et al. 1998) on the basis of mineralogy and mineral composition. Clasts in DaG 400 can be classified as being typical of either the anorthositic ferroan (AF) FAN or mafic magnesian (MM) FAN suites. This will now be discussed in detail.

A. Anorthositic Ferroan FAN clasts: Rock fragments are predominately composed of anorthitic plagioclase, contain minor pyroxene grains and, in this section, have estimated bulk compositions of >30% Al_2O_3 and <2.5% FeO (Table 3.1, 3.4; Fig. 3.6). Bulk trace element analysis of these anorthositic clasts reveals that they have low (generally <1 ppm) ITE concentrations compared with MM FAN and impact melt clasts in the section (Fig. 3.6, 3.7). CI-normalised REE patterned (Fig. 3.7a) have a slightly decreasing LREE slope, large positive Eu anomalies with $Eu_{cn}/\sqrt{(Sm_{cn}\times Gd_{cn})}$ (where 'cn' indicates chondrite normalised) values in the range 6 to 30, and variable low concentrations of HREE. These clasts fit within the typical FAN trend of REE concentration (Floss et al. 1998) even though the clasts have often been thermally annealed and cannot be considered to be 'pristine' (Warren and Wasson, 1978).

Pyroxenes in the clasts in the anorthositic FAN suite have a limited range of Mg-Fe contents (Fig. 3.5) suggesting that they originated from a petrogenetically similar magmatic source region. Pyroxenes have higher Fe-contents (and have thus experienced greater fractionation) than the MM FAN varieties discussed below, indicating that AF FAN rock types originated from an Fe-richer, REE-poorer magmatic source. Olivines do not generally occur in these FAN clasts with the exception of micro-inclusions (Fo_{57}) within pyroxenes in an anorthositic norite clast. AF FAN clasts in DaG 400 are described in detail in Table 3.1 and can be subdivided into the following rock-types based on modal mineral composition:

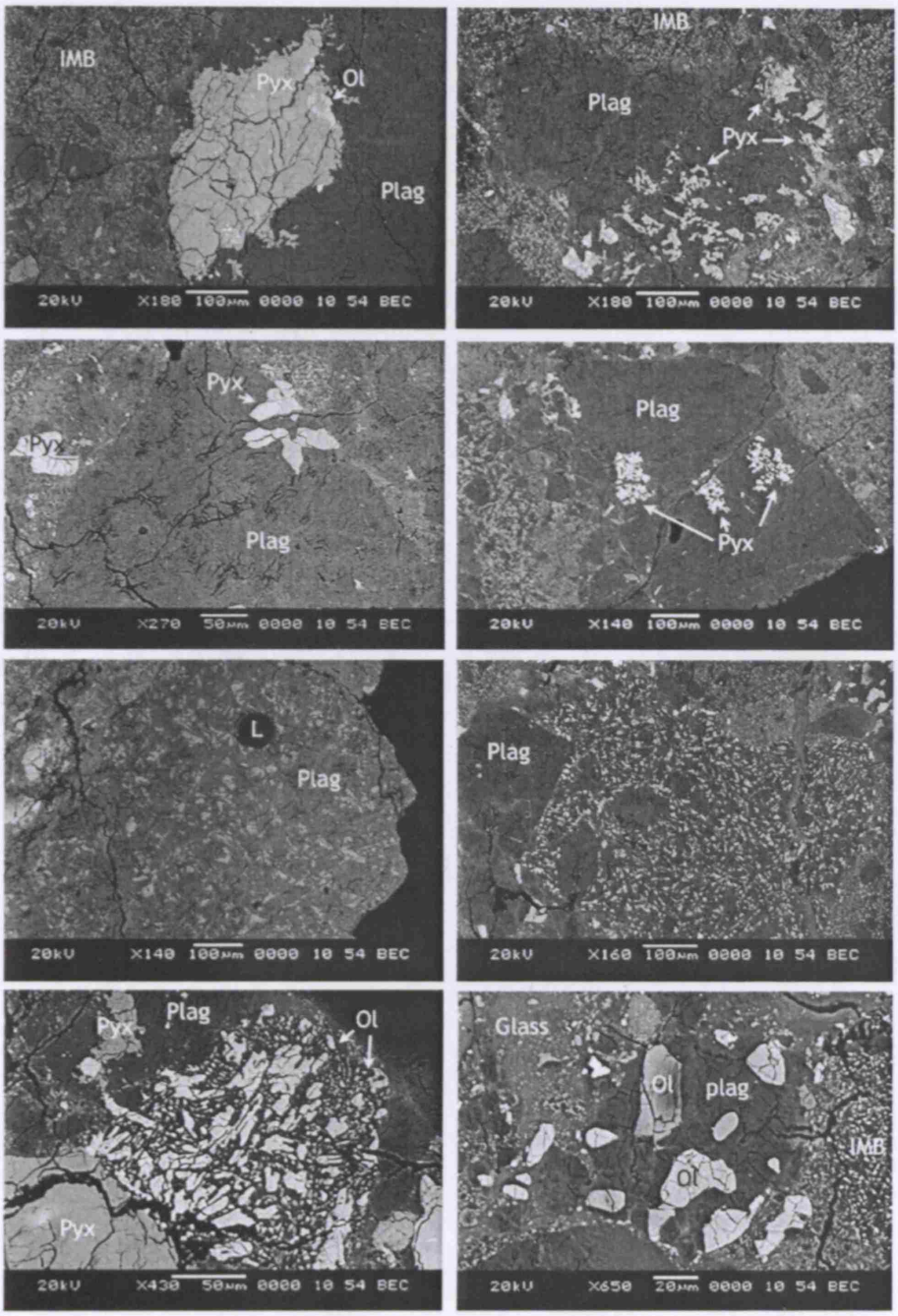

Fig. 3.4. BSE images of clasts in section of DaG 400. See Table 3.4 and Table 3.5 for corresponding description. Abbreviations used are anorthositic norite (AN), anorthositic gabbronorite (AGN), anorthositic gabbro (AG), troctolite (T), anorthositic troctolite (AT), hornfelsic anorthositic troctolite (HAT) and norite (N). (a) AF FAN clast: image of detail in large pyroxene-olivine-spinel complex mineral fragment in AN 1. Mineral edge has undergone partial re-absorption into anorthosite groundmass; clast itself is surrounded by clastic impact-melt breccia (left of image). (b) AF FAN clast: AN 2 containing partially melted pyroxenes in a plagioclase / vitric plagioclase groundmass. (c) AF FAN clast: large ANG clast containing relatively unaltered pyroxene phenocrysts in a shocked and fractured plagioclase groundmass. (d) AF FAN clast: AG clast with large strange digested pigeonites. (e) MM FAN clast: AT 2 with a visible laser ablation pit. (f) MM FAN clast: HAT with larger plagioclase fragments in a bead-like olivines and small plagioclase groundmass. (g) MM FAN clast: small T 1 thermally annealed clast. (h) MM FAN clast: small T 2 containing rounded olivine phenocrysts of varying compositions. L= laser pit. Ol = olivine. Pyx = pyroxene. IMB = impact melt breccia.

Clast	Clast Dimension (mm)	Mineral Modes	Clast Description	Plag	Pyroxene	Olivine
Ferroan Anorthosite FAN						
AN1	1.8 x 1.0	80% An,	Large elongate clast, creamy white in hand specimen. Contains one large pyroxene fragment (A) with minor inclusions of forsteritic olivine and Al-titanium chromite ($(Ti,Al,Cr,Fe)_3O_4$) and several separate small bundles of pyroxene (B) – olivine complexes. None of these pyroxene crystals retain a recognisable crystal form, but all have a cuneiform texture with the groundmass. The clast has minor fractures generally following a preferred orientation throughout the plagioclase groundmass and more regular fractures in the larger pyroxene phenocryst	An_{96-97}	A $En_{56}Fs_{31}Wo_{12}$ B $En_{55}Fs_{33}Wo_{10}$	Fo--
AN2	0.45 x 0.3	60% An, 40% OPX	Pyroxenes display quench textures from thermal degradation/partial melting to form small blebs and subhedral fractured forms. Again the clast is heavily fractured and displays internal variation in the plagioclase, suggesting area of alteration to a glassy state	An_{92-97}	$En_{46.5}Fs_{27.40}Wo_{6.23}$	
AO	1.2 x 0.9	90% An, 5% CPX, 5% OPX	Pyroxenes (>100μm) are subedral and appear not to have undergone any impact annealing (as in the case of the two anorthositic norites discussed above). The pyroxenes plot with slightly Mg enriched trend with a CPX - OPX miscibility gap implying magmatic co-crystallisation	An_{94-97}	CPX $En_{39.42}Fs_{16.23}Wo_{37.41}$ OPX $En_{57.60}Fs_{38.23}Wo_{5.9}$	
AG	0.8 x 0.6	90% An, 10% Pig	A small clast of 60% anorthosite which is partially cataclastic with an annealed texture and enclosing (40 % of clast) remnant Ca-pyroxenes. These have a 'digested' texture, where the pyroxene has been reduced to small blebs and irregular fragments, but generally still preserve a rough outline of their original subhedral crystal shape as a consequence of thermal annealing. This partial melting of the mineral grain edges is a typical feature of multi-mineral phase rocks that have been metamorphosed by conduction of heat from an impact event (Cohen et al 2004)	An_{95-97}	PIG $En_{31.38}Fs_{26.41}Wo_{21.30}$	
Mafic Magnesian FAN						
AT1	4 x 1.5	70% An, 20% Ol, 10% PYX	The largest clast in the subsection is an elongate fragment in size which ~17% of the sample by mode. Micro-crystalline lathe shaped phenocrysts of plagioclase radiate from larger nuclei subhedral plagioclases. Plagioclases subophitically enclose intergranular grains of olivine and pyroxenes. Cl-normalised REE element trends shows that the clast fits well within the field of recognised FAN lithologies (Floss et al. 1998) and three different targeted points show that there are slight changes in REE concentration within the one clast. Generally there is enrichment in LREE over HREE, and a large positive Eu anomaly associated with the clast's plagioclase-rich nature	An_{95-97}	CPX $En_{50.55}Fs_{12.17}Wo_{32.38}$ OPX $En_{68.70}Fs_{17.19}Wo_{10.12}$	$Fo_{73.78}$
AT2	0.75 x 0.8	70% An, 20% Ol, 10% PYX	Clast has a similar texture to anorthositic T1 but with ~70% plagioclase and ~30% olivine. It also has similar trace element chemistry and it is very possible that is a smaller fragment of anorthositic AT1	An_{96}		Fo_{79}
HAT	0.5 x 0.7		This is a unique clast in the section with fine grained subhedral bead-like olivine micro-phenocrysts (<5μm) intergrown with small (<10μm) plagioclase grains. The hornfels encloses angular plagioclase fragments (~30-200 um) similar to hornfels clasts discussed by McGee (1989). The intergrowth between the olivine and plagioclase groundmass suggests a high temperature metamorphic event that caused mineral annealing. The precursor lithology to this sample was probable an anorthositic troctolite	An_{94-97}		Fo_{69-75}
GrN	0.4 x 0.2	50% An, 45% PYX, 5% Ol	Small fragment composed of subedral anorthite crystals subophitically enclosing intergranular mafic minerals with a precursor norite lithology. Bulk Clast Mg# is high (Mg#83.5) reflecting the Mg-rich nature of the pyroxenes and olivines and suggesting that this fragment was crystallised from the most Mg-rich melt compared to other clasts closely studied in the section	An_{95-96}	CPX $En_{54}Fs_{10}Wo_{34}$ OPX $En_{75}Fs_{15}Wo_{8}$	Fo_{73-85}
T1	0.17 x 0.15	40% An, 60% Ol	Small clast with anorthite subophitically enclosing olivine. Olivines are subedral and have an unusual bleb-like and wormy texture as a result of thermally induced solid state recrystallisation of the mineral boundaries. This clast has enriched trace element composition with a relatively flat REE profile and a positive Eu anomaly	An_{97}		Fo_{70-71}
T2	0.1 x 0.15	50 % An, 50 % Ol	Olivines are small <30μm and are rounded with several individual phenocrysts displaying a zonation from Mg-richer cores to Fe-rich rims	An_{97}		Fo_{73-86}

Table 3.1. Detailed description of Clasts of the AF FAN and MM FAN suites in DaG 400 section. Mineralogical abbreviations are anorthositic norite (AN), anorthositic gabbronorite (AGN), anorthositic pigeonite (AP), troctolite (T), anorthositic troctolite (AT), hornfelsic anorthositic troctolite (HAT) and granulitic norite (GrN).

Cataclastic anorthosites are lithic clasts containing >95 % plagioclase (An_{95-97}) that constitute about 9% of the subsection bulk (based on modal clast counting). They often enclose very small (<1 μm) inclusions of mafic or sulphide minerals. These clasts contain minerals that are not pristine (Warren and Wasson, 1978) and have been fractured, maskelynised and thermally annealed by impact-related processes.

Gabbroic and noritic anorthosites are a chemically and texturally diverse range of the AF FAN group (James et al. 1989). They contain a proportion of mafic minerals that have textures that vary from well preserved phenocrysts to thermally annealed varieties. This range of mineral textures illustrates that different clasts within DaG 400 have undergone different thermal histories. Pyroxene compositions vary from clast to clast (Fig. 3.4) but actually occupy a relatively narrow Mg-Fe field (Fig. 3.5a), suggesting that they all crystallised out from a compositionally similar, primitive, parental magma.

B. Mafic Magnesian FAN Clasts and Magnesian Suite Clasts

Mafic magnesian (MM) FAN clasts have estimated bulk compositions <30% Al_2O_3 and >2.5% FeO, with flat Cl-normalised REE patterns having $(La/Lu)_{cn}$ ratios of 0.86 to 1.79 (Fig. 3.7). The clasts have positive Eu anomalies, with Eu/Eu* (i.e. $Eu_{cn}/\sqrt{(Sm_{cn}\times Gd_{cn})}$) values in the range of 3 to 9. MM FAN clasts have a greater proportion of mafic minerals and higher REE concentrations compared with the anorthositic FAN clasts discussed above, contain Mg-rich olivines (Fig. 3.5b), and have more primitive pyroxene compositions (Fig. 3.5a). MM FAN clasts in DaG 400 are described in detail in Table 3.1. These types of rock include:

Anorthositic troctolites, Norites and Troctolites. These clasts have bulk major chemical compositions that trend towards the more mafic magnesian FAN and Mg-suite range of highland lithologies (Fig. 3.6). Collectively their pyroxene content suggests that they crystallised from a more Mg-rich primitive magmatic source than their AF FAN counterparts discussed above.

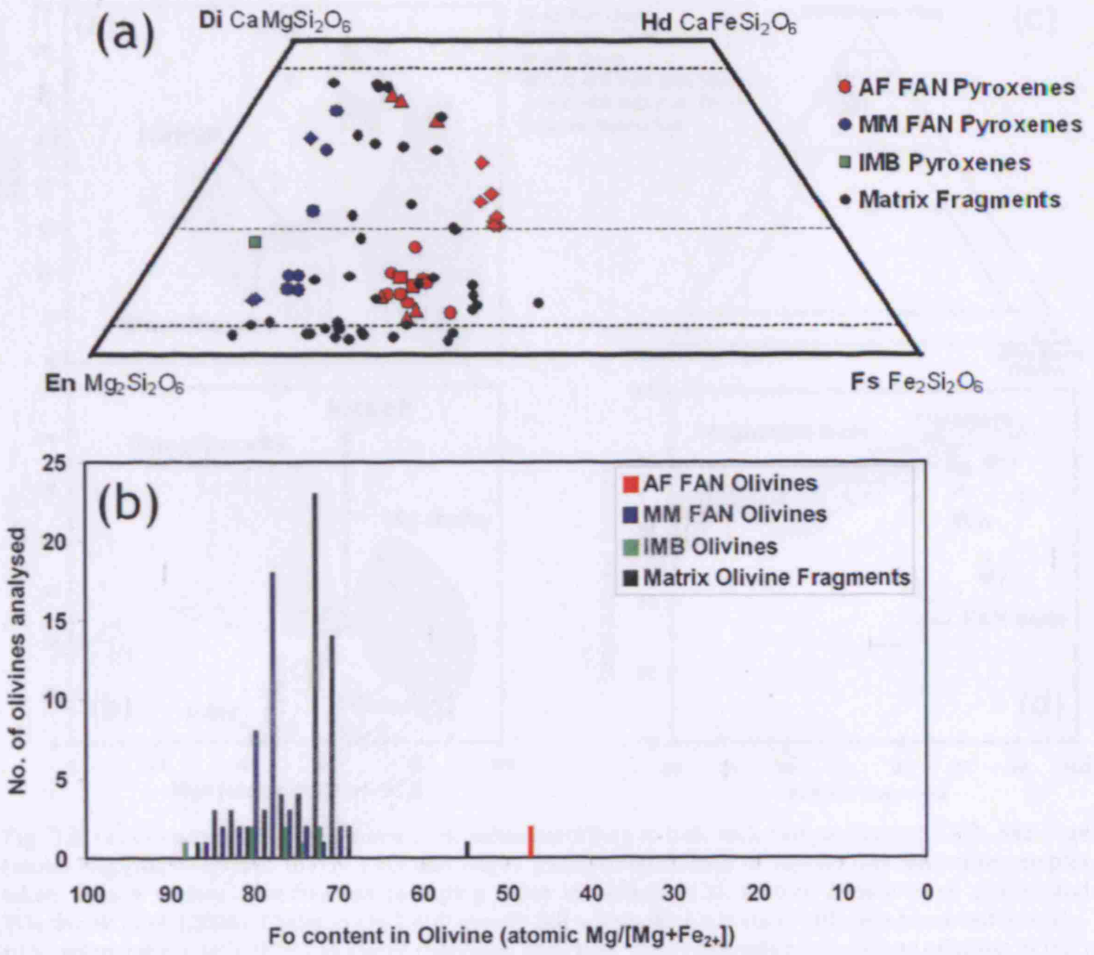

Fig. 3.5. (a) Plot of pyroxenes in the various clast types. MM FAN clasts (troctolites, anorthositic troctolites [blue circles] and norites [blue diamonds]) have Mg-richer pyroxenes, whereas AF FAN clasts (anorthosites and anorthositic norites [red circles], anorthositic pigeonites [red diamonds], anorthositic gabbronorites [red triangles]) contain compositionally more evolved pyroxene varieties. The pyroxene fragments that were randomly distributed throughout the section show a divided variation between Ca-rich and Ca-poor varieties and a similar range in terms of Fe-Mg content as the pyroxene in the AF FAN and more MM FAN clasts. Semenova et al. (2000) reported similar pyroxene compositions in a different section of DaG 400. They also report Fe-augites and pigeonites grains with a mare basalt affinity. (b) Comparison of Olivine compositions in mafic igneous and melt clasts and in monomineralic fragments in DaG 400. The olivines in MM FAN igneous clasts show a rough Gaussian spread with the peak at Fo_{79}. This trend suggests that the mafic FAN clasts originate from a more Mg-rich source than the many of the random mineral fragments in DaG 400 implying that the magmatic source of the random olivine fragments is more evolved than the source of the MM FAN lithics. Cross correlating this with the pyroxene interpretation (a) it is possible to infer that most of these random pyroxenes probably originated from predominantly an AF FAN bedrock source with a contribution from minor MM FAN source. Olivine grains included as fragments in impact melt clasts have compositions that span the range of clast olivine compositions.

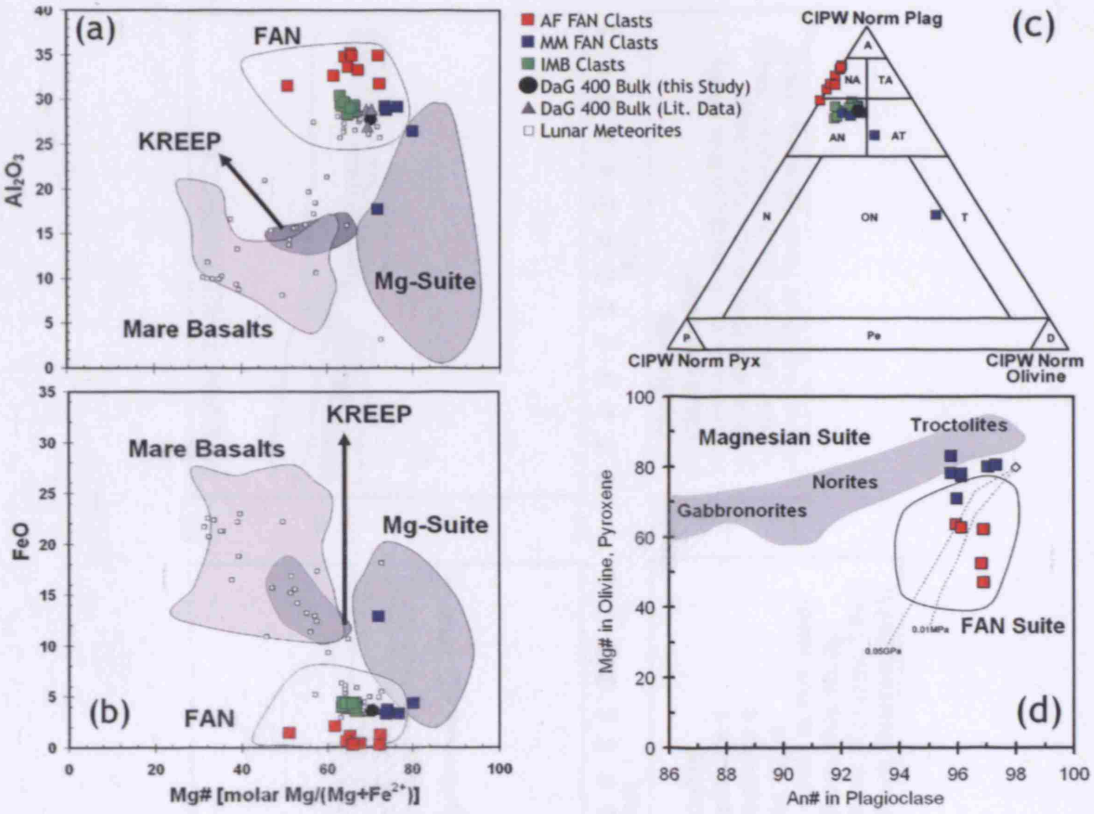

Fig. 3.6. (a) Division of the main lunar rock suites according to bulk rock composition of Al_2O_3 and Mg# (molar Mg/[Mg+Fe]) and (b) by FeO and Mg#. Bulk compositions of Apollo and meteorite samples taken from a variety of references including those in Heiken et al. (1991), Papike et al. (1998) and Wieczorek et al. (2006). Clasts in DaG 400 mostly fall within the FAN suite, although trend towards Mg-rich end members. (c) CIPW calculated (Milliken and Basu, 2000) normative mineralogy of clasts in DaG 400 (idealised mass fraction based on clast bulk chemistry). Non-mare rock fields are taken from those described in Lucey et al. (2006): A: anorthosite; NA: noritic (gabbroic) anorthosite; TA: troctolitic anorthosite; AN: anorthositic norite (gabbro); AT: anorthositic troctolite; N: norite; ON: olivine norite; T: troctolite; P: pyroxenite; Pe: peridotite; D: dunite. (d) Comparison of the average An# (molar Ca/Ca+ K + Na) in plagioclase and Mg# in pyroxene and olivine grains in lithic clasts in DaG 400.

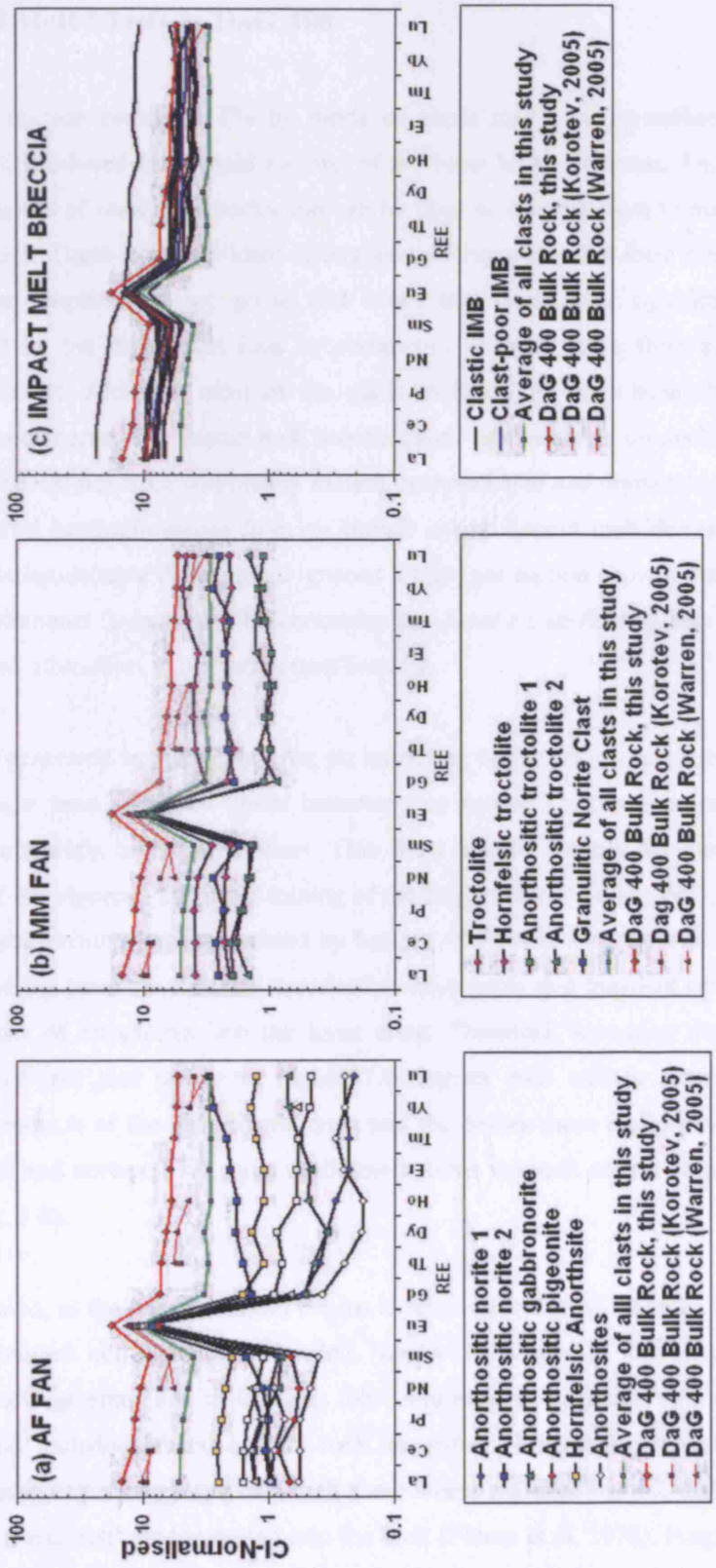

Fig. 3.7. Average REE compositions of clasts in DaG 400. Results are normalised to the C1-chondrite values of Anders and Grevesse (1989) values. (a) AF FAN clasts, (b) MM FAN clasts and (c) impact melt breccia clasts.

3.2.2 Impact Melt Clasts in DaG 400

The DaG 400 section contains 41% by mode of clasts that have crystallised from impact generated melts, produced from rapid melting of the lunar highlands crust. These impact melt clasts are fragments of melt sheet rocks and can be used as a comparison to macro-scale lunar impact lithologies. There is a significant difference between rocks that form directly from melt generated in an impact pressure pulse and rocks that have been significantly internally metamorphosed by the transfer of heat by conduction through rocks from an impact event (Cohen et al. 2004). Although most of the clasts in DaG 400 have been altered by shock processes to some degree, the 'impact melt breccia clasts' are the direct products of impact melt where the lunar crust has been completely melted, recrystallised and reassembled as a result of the shock-induced heating/pressure from an impact event. Impact melt derived fragments in DaG 400 are distinguishable from altered igneous lithics (see section above); they are often rich in siderophile elements from meteoritic contamination, have a significant glassy components or glass matrix, and often form multi-component breccias.

Impact melt is generated immediately after an impacting bolide begins to excavate a transient cavity. The target area is melted under instantaneous pressure decompression, generating a superheated, turbulently mixed melt sheet. This sheet will be chemically homogeneous as a consequence of the vigorous and rapid mixing of the target rocks (Spudis, 1993; French, 1998). Large-scale basin-forming impacts created by bolides >10 km in size, such as those that have typically shaped the lunar far-side, are theorised to have excavated transient cavities extending to depths of tens of kilometres into the lunar crust. Therefore, assuming the Moon has an internal structure like that shown in Figure 1.9, impact melt will be generated from the homogenised products of the anorthositic crust and the deeper more mafic lithologies such as Mg-anorthosites and norites. This more mafic melt forms the melt matrix construct in impact melt clasts (Fig. 3.8).

In crater formation, as the transient crater begins to rebound and grow laterally, the superheated melt sheet encounters non-melted, un-shocked, 'cooler' lithologies at shallower depths. These lithologies were fragmented and included as lithic and mineral fragments to form a breccia of impact melt and included crustal country-rock xenoliths. Fragment-rich melts would have formed at the base or periphery rim of a melt sheet where material was thermally eroded from the country rock and easily incorporated into the melt (Floren et al. 1976). Fragment-poor melt clasts are likely to be examples of the internal portion of melt piles that did not encounter any country-rock (Fig. 3.8f). These different impact melt regimes may have experienced a regime of

cooling conditions (dependent on pile depth, proximity to surface, reheating by subsequent impacts, etc.), sometimes resulting in the re-crystallisation of several generations of plagioclase microcrysts within the matrix, thus producing the texturally diverse lithologies evident in impact melt breccia clasts in DaG 400.

As DaG 400 contains feldspathic impact melt varieties it is most analogous to the feldspathic impact-melt and melt breccias collected from the Apollo 16 landing region. Impact melt breccias in DaG 400 can be classified using a combination of the existing classification schemes of Stöffler et al. (1979) and Stöffler and Grieve (1994) that categorise macro-breccia samples (Table 3.2).

Clastic Nature	**Overall Texture of Clasts / Crystal Component**	**Detailed Texture of Clasts / Crystal Component**
Clastic microporphyritic crystalline impact melt breccia (>40% clastic material) Seriate clasts of (normally) rounded to sub-rounded anhedral (digested or eroded edge texture) plagioclase or secondary mafic mineral fragments (pyroxene, olivines, spinels, troilite, metals etc) or xenolith material	Xenocrysts or xenoliths (chadacrysts) set into a matrix of single-generation microcrystalline (aphanitic) melt. Melt matrix consists of euhedral microcrystalline plagioclases laths with interstitial cryptocrystalline mafic-rich glass phases.	Intergranular (several matrix crystals subophitically enclosing plagioclase micro-phenocrysts)
		Poikilitic (one matrix mineral plagioclase micro-phenocrysts)
	Chadacrysts set in a matrix with multi-generation large recrystallised plagioclase laths and an aphanitic melt matrix with plagioclase microcrysts and mafic glass phases.	Intergranular
		Poikilitic
Clast-poor (cryptocrystalline) impact melts (<40 % clasts)	Subophitic ophitic glassy melt phase enclosing euhedral-subhedral clastic material (<40 clasts) or recrystallised phenocrysts.	Intergranular
		Poikilitic
		Intersertal crystalline form generally lacking in any clastic component. Skeletal plagioclase laths often containing cores of more mafic glass melt
		Devitrified texture – laths of euhedral plagioclase and interstitial cryptocrystalline pyroxene-rich melt ophitically Often microcrysts appear to have nucleation points

Table. 3.2 Classification of textures of impact melt clasts in DaG 400 based on the schemes of Stöffler et al. (1979) and Stöffler and Grieve (1994).

Clast-rich Impact Melt Breccias have a hyalopilitic texture where relict fragments of plagioclase (chadacrysts) are poikilitically enclosed by a matrix of mafic glass and seriate recrystallised feldspars (<10 μm - >100 μm). These plagioclase chadacrysts are often euhedral tablets, either disaggregated or having rounded/sub-rounded grain boundaries as a result of resorption into the impact melt (Simonds et al. 1973; Powell et al. 1975), and most have experienced partial maskelynisation. Plagioclase compositions within the chadacrysts are generally more refractory (Ca-rich: $An_{95.5-97.5}$) than the melt recrystallised microcrysts ($An_{94.5-96.8}$): evidence that the relict

plagioclases are xenocryst fragments as they are not chemically equilibrated with the impact melt that crystallised the matrix feldspars (Stöffler et al. 1979; Simonds et al. 1973).

Mafic mineral fragments have also been included into some of the breccias. These mafic inclusions are always rare (<5% of clastic component), small (<50 μm) and are normally forsteritic olivine (Fo_{69-78}). Olivines (and a single pyroxene grain) in this compositional range are similar to those measured in mafic magnesian FAN lithic fragments (Fig. 3.5). This implies that the bedrock component incorporated into the clastic impact melt breccias was dominated by more magnesian FAN crustal suite lithologies, possibly representing lower crustal material.

Minor spinels and blebs of troilite and FeNi (<10 μm) also occur heterogeneously throughout some of the more mafic impact melt clasts. Pyroxene fragments are noticeably missing from inclusions within these clastic impact breccias and two theories exist to account for this discrepancy. It was initially thought that any included pyroxenes must have been preferentially partially melted during interactions with the impact melt (e.g. Simonds et al. 1973). However, if this hypothesis is correct then why would so much plagioclase be preserved as clastic debris, rather than be reabsorbed, as it generally has a melting point comparable to or lower than that of pyroxene? Moreover, included olivine fragments do not exhibit resorption rims indicative of significant thermal annealing effects. An alternative theory proposed by Spudis et al. (1991) argues that the basin-scale impact events that are likely to have generated these sorts of impact melt breccias created melt piles that must have just included shallow level material from the upper anorthositic crust that is significantly lacking in small pyroxene fragments and/or pyroxene-bearing lithologies.

Clast-Poor Cryptocrystalline Impact Melt breccias are components of DaG 400 that do not contain a significant (>45%) clastic component. These were generated as part of the central region of an impact melt pile (i.e. did not include cooler material from the surrounding country rock). As discussed above these breccias show a district range of textures as a consequence of variable cooling effects. Intersertal breccias contain large, skeletal recrystallised plagioclases (50 to 250 μm) with mafic glassy cores and enclosed by phases of a very fine grained mafic glass phase (Fig. 3.8d). Other more quenched melt textures with striated textures (similar to those in DaG 400 and DaG 262 discussed by Cohen et al. (1999, 2005) include clasts with micro-needles (<50 μm) of plagioclase enclosed by mafic interstitial glass (Fig. 3.8f). Recrystallised plagioclases often have radiating patterns from mineral fragment inclusion nucleation sites (Fig. 3.8e).

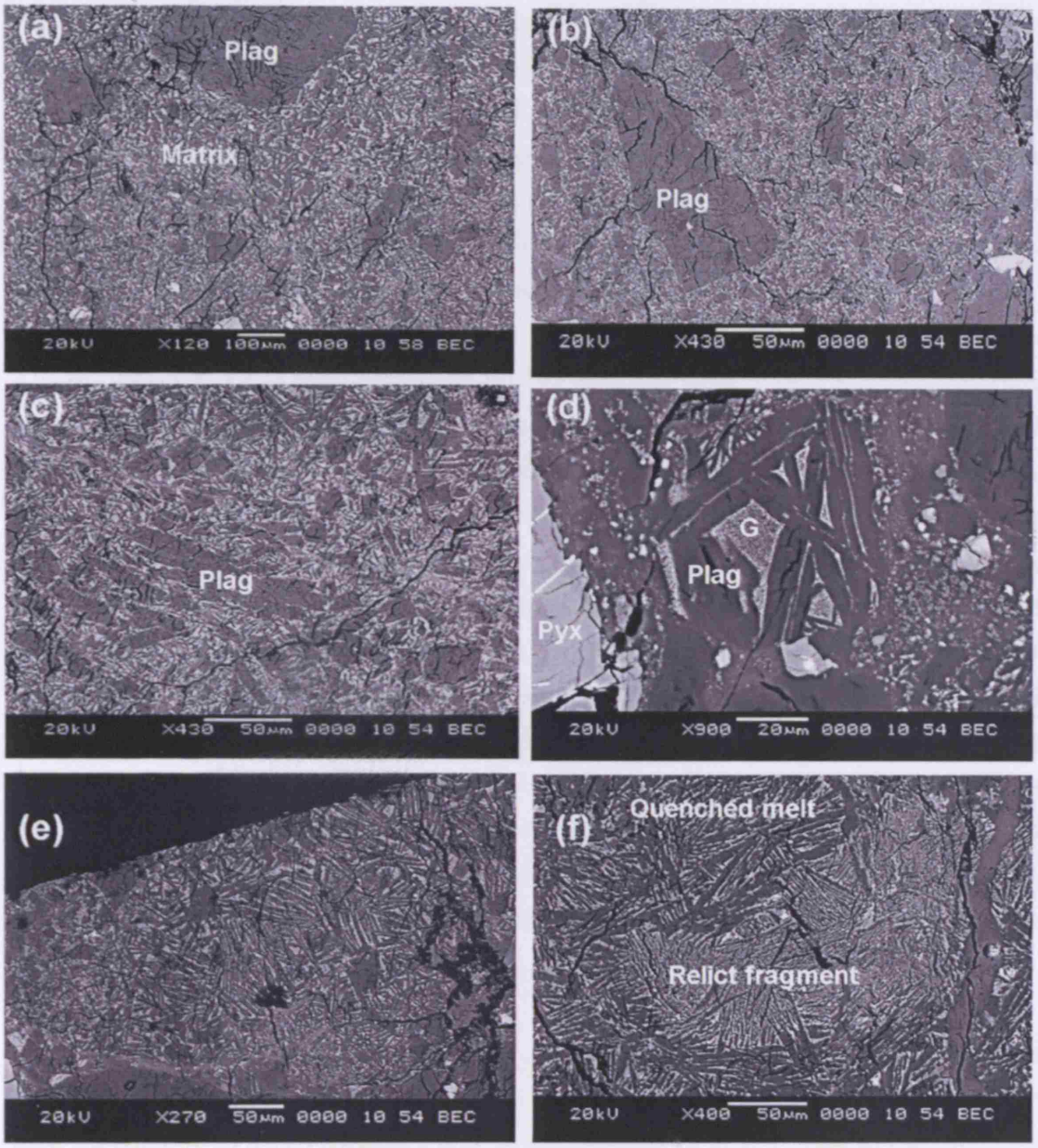

Fig. 3.8. BSE images of varieties of impact melt clasts in DaG 400. (a) Clastic single generation melt with large inclusions of plagioclase and minor olivines with rounded grain boundaries from thermal erosion in the melt. There is evidence of melt flow around the larger clasts with oriented melt minerals. (b) Clastic single generation melt, again with large plagioclase inclusions and a fine grained melt matrix. (c) Multi-generational melt with small rounded clasts of plagioclase in a matrix of large recrystallised plagioclase laths and a much finer melt matrix with small plagioclase and crypto-pyroxene melt. (d) Small intersertal melt clast with large plagioclase laths optically enclosing mafic glassy melt pockets. (e) Non-clastic clast with small aligned laths of melt minerals nucleating off rare small plagioclase remnant fragments – clast is richer in incompatible elements than any of the other studied melt clasts. (f) Non-clastic quenched clast with very small melt crystals radiating from nucleation points. A ghost mafic mineral fragment outline is preserved by a region of devitrified mafic glass. G = glass. Plag = plagioclase. Pyx = pyroxene.

All of the impact melt breccia clasts, regardless of texture, have bulk major element compositions that are classified as picro-basalts (41 to 43% SiO_2; 0.3 to 0.6 $Na_2O + K_2O$) and fall within the compositional range of the FAN suite (Fig. 3.6). They are classified as ITE-poor (<8 ppm Sm concentrations), feldspathic impact-melt breccias following the criteria of Korotev (1996, 1997) based on studies of impact melt rocks from the Apollo 16 site. The IMB clasts have limited bulk Mg# compositions (63.4 to 66.9 Mg#), evidence that they were generated in a very similar, if not the same, impact melt regime that essentially homogenised Mg# variations.

All DaG 400 impact melt breccia clasts are Al-rich, reflecting the high abundance of plagioclase phases in both the relict fragments (chadacrysts) and as recrystallised microcrysts in the melt itself. However they have a smaller Eu anomaly (Eu/Eu*: 2.57 to 4.22) than the igneous lithic fragments discussed above because they contain greater proportions of crypto-pyroxene-rich glass phases and relict olivine grains that are not preferential substitution sites for plagiophilic Eu. A plot of bulk clast Sc/Sm (Fig. 3.9) shows the comparison of IMB clasts in DaG 400 and those impact melt samples collected from the Apollo 16 landing site (Korotev et al. 1994). Several compositional groupings and sub-groupings exist for the Apollo 16 suite as defined by Floren et al. (1976), McKinley et al. (1984) and developed by Korotev (1994). Compositionally the impact melt clasts measured in DaG 400 in this investigation have Sm values most similar to the Group 4 'feldspathic' (fragment laden) and 'microporphyritic' melt breccias, but they are also Sc-richer, suggesting that the impact source area was comparatively KREEP-poor but rich in pyroxene-rich (Sc-compatible mineral phase) lithologies and ilmenite compared with the Apollo 16 site.

REE patterns are similar in all the IMBs with concentrations x3 to x20 chondritic abundances (Fig. 3.7c). These concentrations are similar to the feldspathic impact melt breccia clasts in lunar meteorite ALH 81005 (Goodrich et al. 1984). Impact melt breccia clasts in DaG 400 have enriched LREE patterns ($[La/Lu]_{cn}$: 14.23 to 25.33), a small Eu anomaly, and depleted HREE. The similarities between the REE profiles suggest that most of the melt from which these clasts were derived (except for one ITE-rich clast) was similarly fractionated in incompatible elements. On the basis of the similarities between IMB clast major, minor and trace elemental concentrations, I propose that the majority of them originated from a single chemically homogeneous impact melt sheet in the feldspathic crustal highlands.

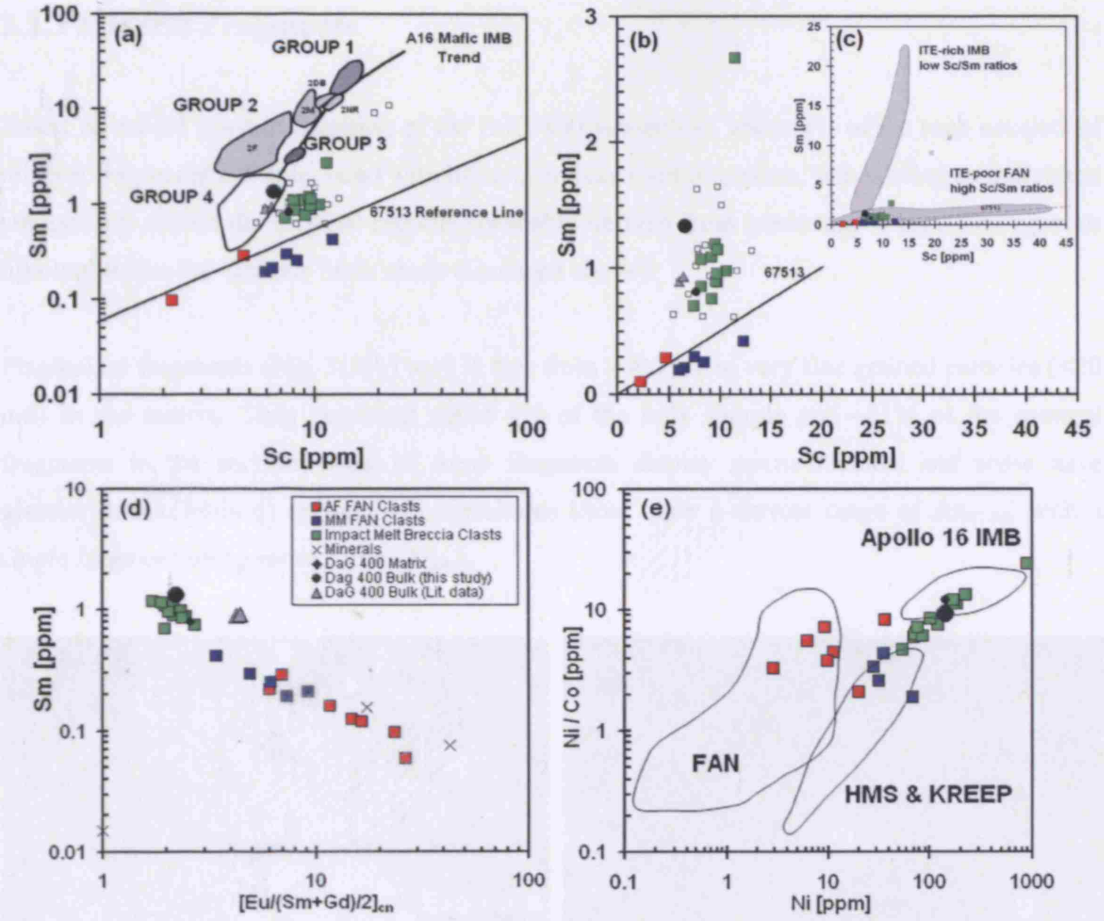

Fig. 3.9. (a) Average Sm and Sc concentrations in melt clasts, FAN clasts and the DaG 400 bulk rock composition. Superimposed are the 4 compositional impact melt groups identified by McKinley et al. (1984) and Korotev (1994). This classification of Apollo 16 rock types includes: Group 1 (dark grey area); Apollo 16 LKFM varieties and KREEPy basalts, Group 2 (pale grey areas); VHA basalts, impact-melts splashes and bombs, Group 3 (small medium grey area); Anorthositic basalts, FAN rocks, Group 4 (white area; Feldspathic (fragment laden) melt breccia, intergranular breccias and feldspathic microporphyritic melt breccias. The Apollo 67513 sub-sample reference line is taken from Jolliff and Haskin (1995) for comparison. DaG 400 melt clasts are richer in Sc (pyroxene phases) than their feldspathic Group 4 counterparts. (b) Clasts in DaG 400 compared with the ITE-poor portion of the Sc-Sm field of Apollo 16 samples. (c) DaG 400 clasts compared with the Apollo 16 sample trends for IMB and FAN rock samples (Jolliff and Haskin 1995); all of the DaG 400 and most feldspathic lunar meteorite samples plot in the plagioclase-rich, ITE-poor portion of the Apollo fields. (d) Compositional variations among clasts investigated in DaG 400; chondrite normalised (cn) values are taken from CI chondrite composition reported by Anders and Grevesse (1989). (e) Measure of meteoritic siderophile element contamination in clasts in DaG 400 compared with the siderophile element values in pristine rocks from the Apollo Suite; fields are taken from Norman et al. (1995).

3.2.3 Mineral Fragments

Based on modal mineral counting of the DaG 400 subsection, about 8% of the rock consists of mineral fragments not associated with lithic or impact melt fragments, but existing as individual components within the original regolith (probably derived from gardening of precursor igneous lithologies like the igneous lithic clasts discussed above).

Plagioclase fragments (Fig. 3.10b) vary in size from >500 μm to very fine grained particles (<20 μm) in the matrix. They represent about 4% of the bulk sample and ~61% of the mineral fragments in the section. Most of these fragments display micro-fractures and some have glassier (maskelynised) regions. Compositions show quite a narrow range of An_{97-95}, with a single fragment being more sodic (An_{90}).

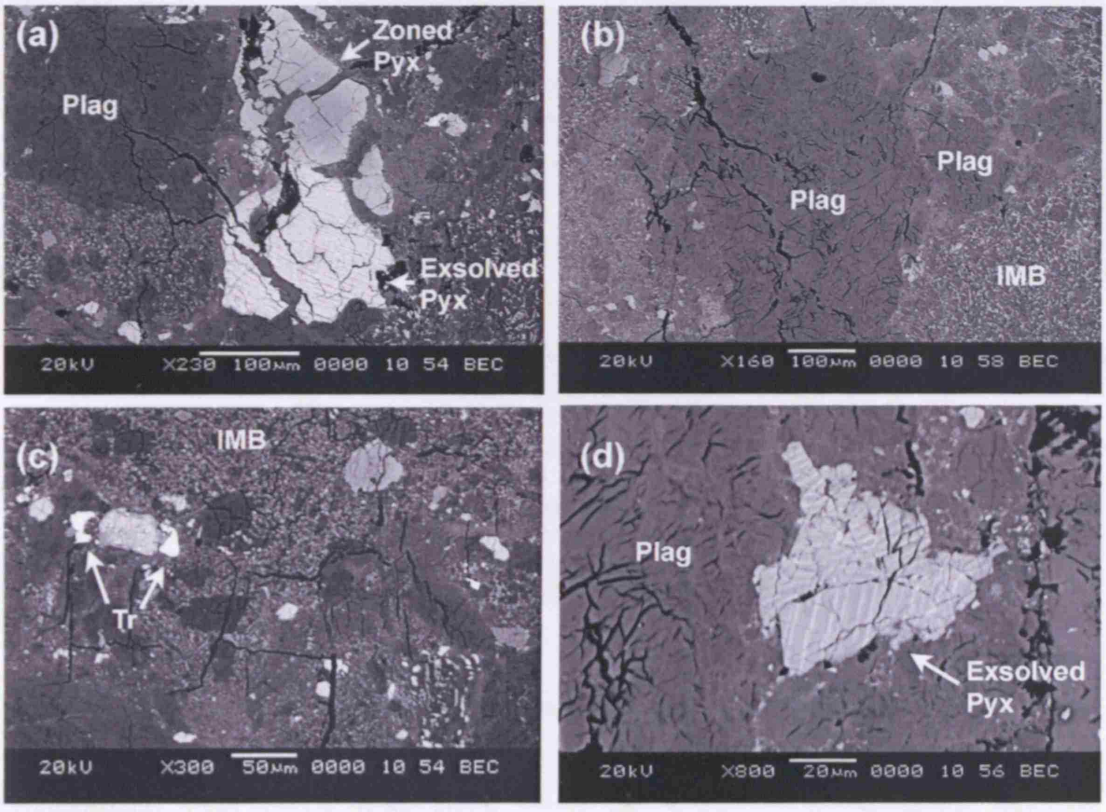

Fig. 3.10. BSE images of a variety of mineral fragments in DaG 400. (a) Two pyroxene fragments – the upper grain is zoned from a Mg-core to Fe-rim and the lower grain displays exsolution lamellae. (b) Plagioclase fragments of varying sizes and alteration. (c) Mineral fragments in the matrix of DaG 400; a bright troilite fragment has been fractured in two and surrounds a pyroxene mineral fragment. (d) Shocked and fragmented pyroxene with multiple offset exsolution lamellae. IMB = impact melt breccia. Pyx = pyroxene. Tr = troilite.

Although no plagioclases in DaG 400 can be considered as 'pristine' (Warren and Wasson, 1978), as they have all been shock processed, trace element concentrations in two investigated grains (Table 3.6) are typical of lunar anorthosite compositions (Fig. 3.11). REE concentrations in these plagioclases are at near chondritic abundances and have a sloping LREE trend (1.4 - 2.0 $[La/Sm]_{cn}$) with a large positive Eu anomaly (8.7 Eu/Eu*). The composition of the melt that crystallised these plagioclases can be reconstructed by applying the lunar distribution coefficients compiled by Snyder et al. (1995). The DaG 400 plagioclase melt LREE trends: 0.6 to 0.8 $[La/Sm]_{cn}$, are identical to those reconstructed from Apollo 16 FAN plagioclases reported by Papike et al. (1998): 0.6 to 0.9 $[La/Sm]_{cn}$.

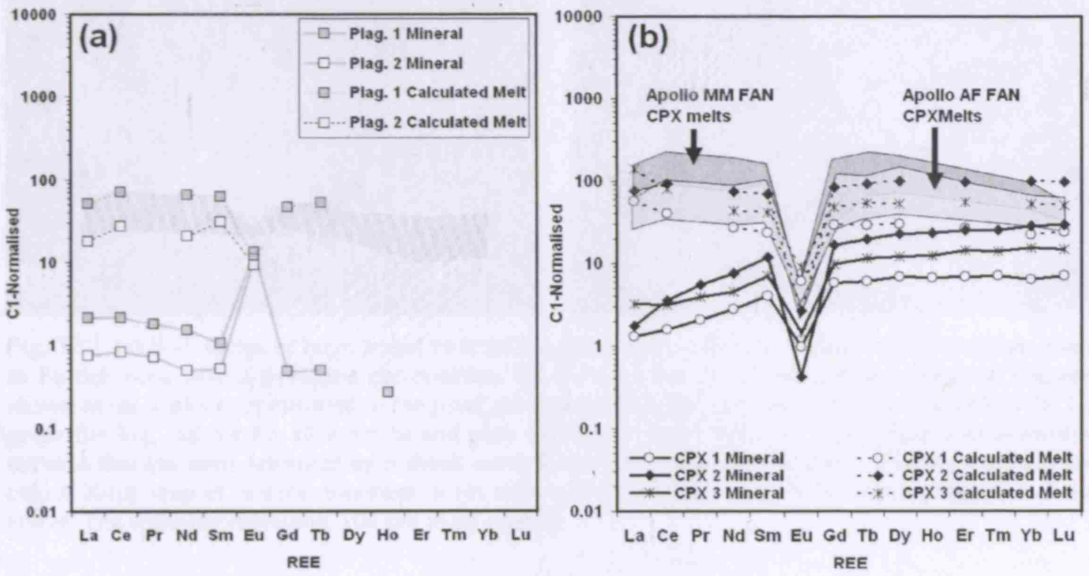

Fig. 3.11. REE CI-normalised (Anders and Grevesse 1981) profiles of (a) plagioclase and olivine mineral grains and (b) opx and two cpx grains in DaG 400. The reconstructed equilibrium melt compositions of the individual mineral phases (as calculated using the distribution coefficients listed by Snyder et al. (1995)) are also plotted in dashed lines. The shaded areas show the reconstructed melt compositions (using the same distribution coefficients) of Apollo 16 (a) plagioclases (Papike et al. 1997) and (b) Apollo 16 high-Ca pyroxenes (Floss et al. 1998) from anorthositic ferroan FAN and mafic magnesian FAN suites for comparison.

Mafic mineral fragments are quite diverse and show a range of textures and compositions, reflecting the diverse nature of minerals in the lunar highland regolith. Olivines have a range in compositions from Fo_{69-78} (Fig. 3.5b). There are texturally diverse grains including homogeneous varieties and ones that display gradual zonation from core (Fo_{71-78}) to Fe-rich rims (Fo_{69-73}). One grain (Fig. 3.12a,b) is zoned from an Mg-rich olivine core (Fo_{70}) to a pyroxene-rich rim ($En_{67}\,Fs_4\,Wo_{28}$), suggesting that it crystallised out of equilibrium with the changing melt composition.

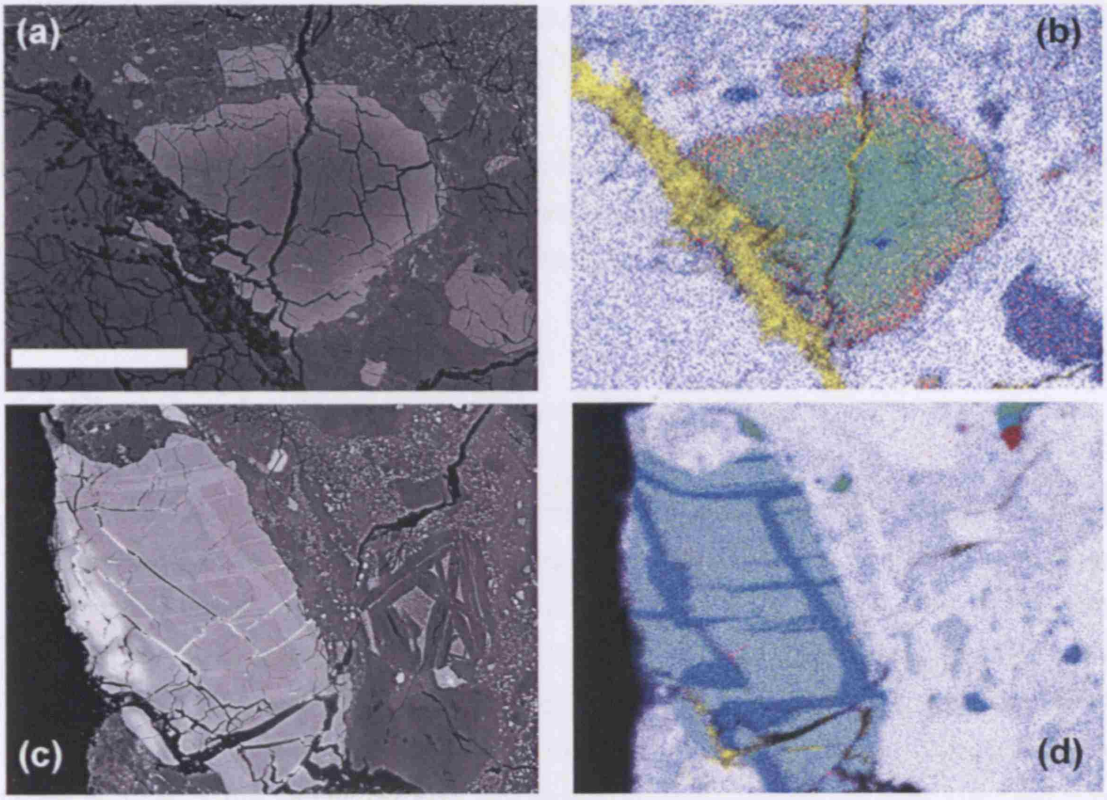

Fig. 3.12. (a) BSE image of large zoned mineral fragment with a Mg-rich olivine core composition zoned to Fe-rich rims with a pyroxene composition. (b) False colour X-ray map of same mineral fragment shown in (a). Colours correspond to the pixel strength of different elements (white for Al, yellow for Ca, green for Mg, red for Fe, blue for Si and pink for Ti). (c) BSE image of a pyroxene with exsolution textures that has been deformed by a shock event to show exsolution in a variety of directions. (d) False colour X-ray map of mineral fragment in (c) with colours corresponding to the same elements as listed above. The scale-bar represents 100 μm in all images.

Pyroxene fragments (Fig. 3.10, 3.12) vary in texture from compositionally diverse homogeneous grains (En_{38-81} Fs_{2-42} Wo_{8-49}) that are typical of FAN suite pyroxene compositions, to grains that have ~2 μm exsolution lamellae. One exsolved fragment (75 μm by 200 μm: Fig. 3.12c,d) shows an unusual pattern of relatively Al-rich cpx (En_{48-51} Fs_{14-16} Wo_{29-31} Al_{2-4} [where Al represents Al substitution]) enclosing Mg-rich opx (En_{66} Fs_{29} Wo_1 Al_2) lamellae that have an unusual deformed structure suggesting that the fragment has experienced high levels of shock deformation.

REE concentrations were measured in three clinopyroxenes (cpx) grains (Fig. 3.11b, Table 3.6). All three grains have flat HREE patterns with 5 to 10 times chondritic abundances, negative Eu-anomalies (0.01 to 0.10 Eu/Eu*) and sloped LREE profiles (0.15 to 0.46 $[La/Sm]_{cn}$). The melts that produced these grains have been reconstructed using the lunar cpx distribution coefficients of Snyder et al. (1995). The reconstructed cpx melts have REE concentrations of ~20 to 100 x chondritic for most elements except Eu and have relatively flat REE patterns (0.8 to 2.8 $[La/Lu]_{cn}$). These melt compositions are very similar to those in equilibrium with Ca-rich

pyroxene compositions from the Apollo MM FAN and AF FAN suites reported by Floss et al. (1998).

Sulphide and metal fragments are distributed heterogeneously throughout the matrix. These grains are normally very small (<20 μm) and are predominately troilite ($Fe_{49-50}S_{49-50}$: Fig 3.10c). There are also small fragments of metal ($Fe_{90}Ni_{10}$) derived from meteoritic sources incorporated into the breccia when it was lithified.

3.3 Clast Populations

Characterisation of clast populations within the subsection of DaG 400 provides important information about the nature of the ancient lunar regolith that can be extrapolated to allow interpretation of the nature and composition of the regional geology from where this regolith formed. Frequency distribution was calculated through modal counting of clast/mineral types from a grid of 2296 spots lain over a montaged BSE image. There is a distinct possibility of human error and bias involved in this method, and there are certain difficulties with the fact that some portions of this section are very fine grained (even on a highly detailed map) and it is difficult to distinguish regions of anorthosite, very fine grained impact melt material and glassy phases. To counter this, clasts of anorthosite were considered different from plagioclase fragments in that they contained noticeable mineral inclusions, were cataclastic and re-annealed or did not exhibit a typical plagioclase euhedral/subhedral texture. Glass in the SEM BSE image appeared in a paler tone of grey in comparison with plagioclase material. If it could not easily be distinguished, because of its fine grained nature, material was classified as unknown or fine grained impact melt.

The abundance of lithic clasts, impact melt clasts, mineral fragments, fractures and pores etc. is given in Table 3.3. About 15.5% of the subsection consists of fine grained material <20 μm in size. Most of this fraction is attributed to very fine grained matrix and glass, and small mineral fragments including plagioclases, mafic minerals and unidentifiable sulphides, oxides and metals.

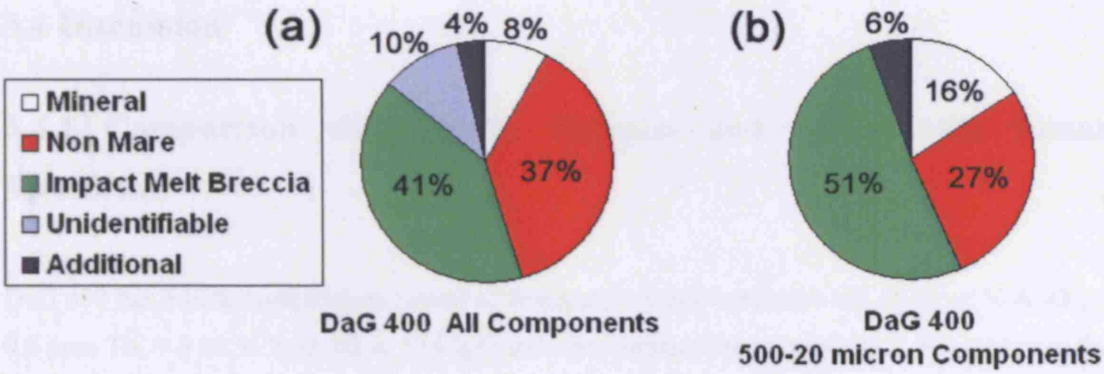

Fig. 3.13. Modal clast breakdown in DaG 400. Detailed list of modal mineral counts in Table 3.3.

Modally 54.9% of our section consists of material >500 μm in size. This mode is much higher than that of material in the Apollo 16 breccias studied by McKay et al. (1986) and reflects the diversity of size fractions within lunar highland regolith breccias. It is also evidence that the coarseness of material in DaG 400 represents material that has undergone less gardening than that returned from the Apollo 16, site and represents a more immature burial environment. As is true for past studies of lunar breccias (e.g. McKay et al. 1986), lithic fragments of all varieties make up the majority (modally 99.7%) of material >500 μm in size. In this size fraction several clasts dominate the point-count abundance, and it is because of this sampling bias that these results should be viewed with caution. The data on the 20 to 500 μm size fraction are taken to be more representative as it encompasses a wider range of clast and mineral types that are not over-represented or under-represented by the modal point counting sampling technique. More than 660 points from the sample fell into this size fraction category (Fig. 3.13). In this intermediate size fraction the most abundant components are the impact melt clasts that make up 51% of the section. Crystalline lithic clasts (including anorthosites, noritic anorthosites etc.) make up 27.4% of this size fraction, with mineral fragments of all varieties contributing modally to 15.8% of the section. Fractures, laser ablation pits (caused by LA-ICP-MS investigations), melt veins etc. form 5.6% of the sample at this size fraction. These abundances provide evidence that the original regolith was rich in lithic fragments crystallised from impact melt environments relative to relict bedrock crystalline fragments and minerals.

3.4 Discussion

3.4.1 Comparison with Apollo Samples and Anorthositic Lunar Meteorites

DaG 400 has a bulk composition typical of feldspathic lunar meteorites (25 to 36 wt.% Al_2O_3, < 0.6 ppm Th, < 6 wt.% FeO, 62 to 75 Mg#) and also similar to the composition of samples in the Apollo FAN suite (Fig. 3.6). DaG 400 is one of 21 recognised different feldspathic lunar meteorites (including paired stones: Website 1.2, Fig. 3.14). It is most similar in composition to the regolith breccias DaG 262 and MAC 88104/88105, the granulitic breccia Dhofar 026, the fragmental breccia Yamato 86032 and the impact melt breccia NWA 482, although it is not paired with any of them on the basis of radionuclide analysis and age dating. The bulk composition of DaG 400 measured for this study (Table 3.8, Joy et al. (2006), Fig. 3.14), is similar to compositions reported from other chips of DaG 400 using different geochemical techniques (Zipfel et al. 1998; Korotev et al. 2005; Warren et al. 2005). It is slightly enriched in incompatible elements compared with these studies (Table 3) and with the average composition of the lithic anorthositic clasts (Fig. 3.7). This suggests that I may have sampled a subsection of DaG 400 that was dominated by ITE enriched impact melt breccia clasts.

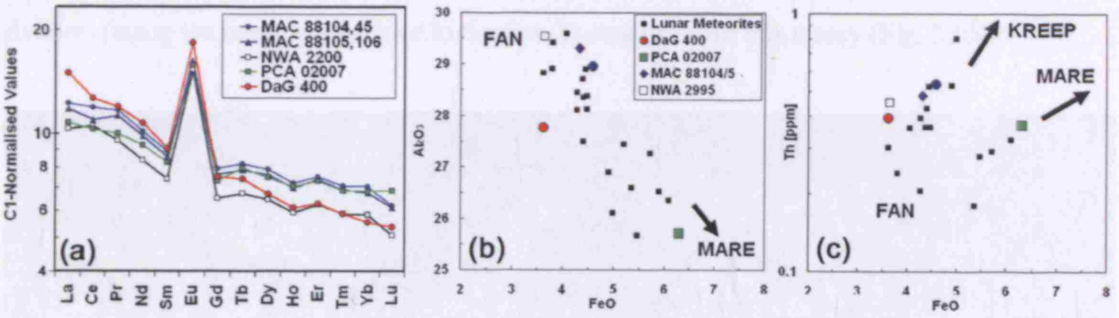

Fig. 3.14. (a) C1-normalised REE values of DaG 400 compared with other feldspathic lunar meteorites measured using the same instrumentation at the Natural History Museum London (Joy et al. 2006 and unpublished data). DaG 400 bulk composition compared with literature lunar meteorite data assessing relationship to (b) mare basalts and (c) KREEP compositions.

3.4.2 Lunar Provenance

The Moon is geologically diverse. We know from studies of Apollo samples that there are three main groups of 'typical' lunar lithologies including the FAN and High Magnesia / High Alkali suites (HMS, HAS) of highland rocks, the mare basalt suite and the KREEPy impact melt breccia suite, with each group containing several sub-classifications of rocks. Remote sensing

missions that have mapped the geochemistry of the lunar surface (FeO and TiO_2 by the Clementine mission (Section 1.3.1) and Th (a proxy for other incompatible elements), FeO and TiO_2 by Lunar Prospector (Section 1.3.2)) have advanced our knowledge of the geographical extent of heterogeneities in the uppermost parts of the lunar crust.

DaG 400 is a highly anorthositic regolith breccia with individual rock components being contributed from anorthositic ferroan and mafic magnesian FAN lithologies, with a few fragments having a more magnesian mafic mineralogy and bulk composition, suggesting a possible origin from the HMS suite. Lithic components have low concentrations of incompatible trace elements and therefore do not have a KREEPy signature. Clast compositions within DaG 400 (Fig. 3.6) are much more limited than the range of compositions observed in regolith breccias at the Apollo 16 site (Cohen et al. 2005). This restricted compositional diversity suggests that the rocks that make up DaG 400 must have crystallised in a particularly anorthosite-rich environment that did not have an appreciable contribution from HMS, KREEP or mare basalt lithologies. As the near-side sampled regolith of the Moon is typically dominated by these non-FAN rock-types and, according to remote sensing observations, the lunar far-side is dominated by Th-poor (KREEP-poor) FAN-like rocks, it has been proposed by Semonova et al. (1998), Korotev et al. (2003) and Cahill et al. (2004) that it is most likely that DaG 400 (in addition to many other feldspathic lunar meteorites) was launched from the far-side within the Feldspathic Highlands Terrane (FHT: Jolliff et al. 1998) and my analysis of remote sensing datasets (using the methods outlined in Section 2) concurs with this theory (Fig. 3.15).

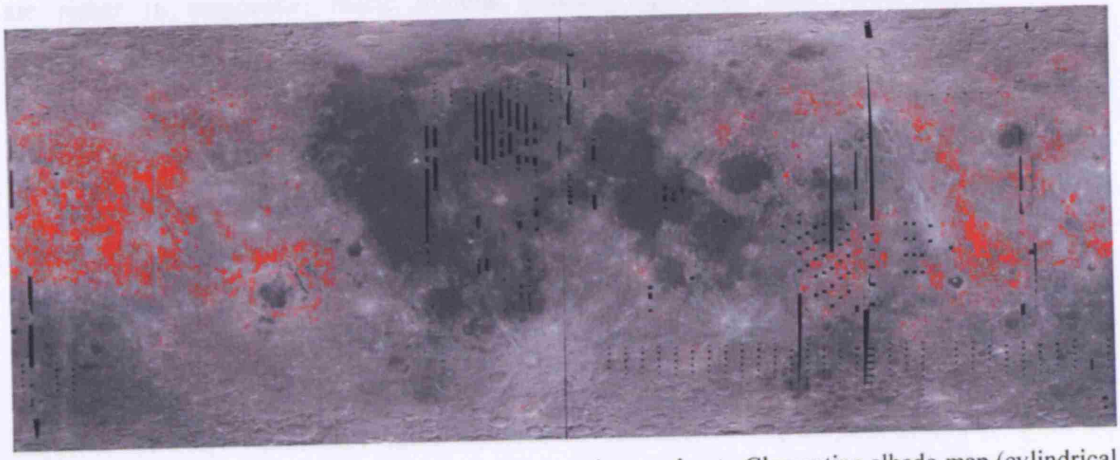

Fig. 3.15. Potential launch localities for DaG 400 superimposed onto Clementine albedo map (cylindrical projection 70° N to 70° S Longitude). Red areas represent the most similar regolith compositions (within 0.5 wt.%) to DaG 400's bulk composition (Table 3.8) based on data from the Clementine 1 km resolution UV/VIS TiO_2 and FeO datasets (based on the algorithms of Lucey et al. 2000) .

3.4.3 Feldspathic Clast Origins

Petrogenesis of the ferroan anorthosite suite has been discussed in detail by James et al. (1989), Warren (1990), Norman et al. (1995), Jolliff and Haskin (1995), Floss et al. (1998), and by the authors mentioned in the introduction to this thesis. As most of the lithic fragments in DaG 400 are not pristine (i.e. mineral phases may have experienced thermal annealing and/or elemental sub-solidus re-equilibration as a consequence of impact metamorphism) it is difficult to make accurate correlations with their parental melt compositions, and therefore fully examine how FAN clasts relate directly to models of lunar evolution (as was alluded to by Consolmango et al. 2004). However, some observations and interpretations can be made, and are discussed below:

All of the anorthositic ferroan FAN (AF FAN) clasts are lunar-CIPW (Milliken and Basu, 2000) plagioclase normative (>78%) and pyroxene-normative (11-24%) (Fig. 3.6c). The bulk composition and mineral compositions of AF FAN clasts in DaG 400 are consistent with anorthositic noritic and gabbroic lithologies generated in primitive magma-ocean FAN cumulate environments (Fig. 3.6, 3.7, 3.9), although are not truly 'anorthositic' in the *sensus strictus* definition: i.e. >90% anorthositic plagioclase.

Mafic magnesian (MM) FAN are classified as being noritic-anorthosite to troctolitic-anorthosite normative, with a single troctolitic clast having a more olivine-rich olivine-norite normative composition more typical of rocks in the High-Mg Suite (Fig. 3.6). MM FAN lithic fragments are richer in magnesian mafic mineral phases (Fig. 3.5), have more magnesian bulk compositions (Fig. 3.6) and generally are also more REE-rich than the AF FAN clasts discussed above suggesting that they may have crystallised from a more evolved melt environment, despite being more magnesian. This correlates well with the observations of Floss et al. (1998) who concluded that plagioclase in pristine MM FAN rocks had a more evolved parentage (REE + Na-content) than that in AF FAN rocks.

The conclusions reached by Floss et al. (1998) and other workers (e.g. Snyder et al. 1992) implies that the petrogenesis of the ferroan anorthosite crust is complicated, and that a fractional sequence of FAN rocks may have crystallised at different depths and pressures from an extensive evolving crystallising magma ocean affected by continual impact perturbations. It may even imply that some of these more mafic FAN rocks may have been generated through the assimilation and mixing of more magnesian HMS cumulate intrusions (Mg-rich, REE-rich) with plagioclase-rich rocks from the FAN Suite.

3.4.4 Impact Melt Clast ITE Signature

The impact melt breccia clasts in DaG 400 are feldspathic with a basaltic bulk composition and have normative modal mineral contents representing anorthositic norite-normative assemblages. The breccias have low-ITE contents compared with most IMB from the Apollo 16 site (Fig. 3.7, 3.9). However, in comparison to other clast components in DaG 400, they have an enriched ITE signature (Fig. 3.6, 3.7, 3.9). This enrichment implies that the melt component of these clasts has been derived from a rapidly melted mixture of target rocks that are likely to have included a range of protolith crustal FAN suite lithologies similar to those discussed above, the impactor/s (of unknown composition) and deeper crustal mafic lithologies that could possibly have entrained ITE from mixing with small quantities of disseminated KREEP pockets/layers. By rapidly combining these components in an impact event there was little time for fractional crystallisation to occur and so the resultant melt from a single impact event is similarly rich in incompatible trace elements compared with the upper crust, unmelted FAN protolith material.

Impact melt breccias in DaG 400 have relatively uniform REE patterns (Fig. 3.7c) and similar absolute elemental abundances (Fig. 3.6, 3.9) with exception of one ITE-richer clast (~2.8 ppm Sm). I propose that the majority of these impact clasts, despite the variance in their textures and modal abundance of chadacryst clasts, were likely to have originated from impacts into similar depths of the lunar crust and, on the evidence of very similar trace element concentrations, that they were generated in a single impact event. Several impact melt clasts in a different portion of DaG 400 have been radiometrically dated by Cohen et al. (2005) using ^{40}Ar-^{39}Ar step-heating techniques. The investigations found that whilst IMB material had similarly restricted major element compositional variations, their geochronology was somewhat more varied with three groups of IMB material being dated to 2590 ± 447 Ma, 3035 ± 214 Ma and 3358 ± 143 Ma. Cohen et al. (2005) did not however report trace element concentrations for the clasts they measured and so relationships cannot be hypothesised between the age dates and similarities/differences in trace element content in impact melt clasts in DaG 400. This would be a good line of enquiry for future work if firm conclusions could be drawn on the numbers of impact events with contributed material to the regolith environment from where DaG 400 was consolidated.

DaG 400's impact melt breccia clasts are vastly different from the Apollo 15 low-K Fra Maura (LKFM) impact melts (Spudis et al. 1991) that are plagioclase clast-poor and do not contain a clastic FAN contribution. In this case, impact melts are assumed to have been formed from the melting of an aluminous-poor region, which was completely lacking in a FAN crust, or from a region dominated by Mg-suite intrusions, or alternatively from a very large impact melting of

the lower portion (40 to 80 km) of the lunar crust (Spudis, 1993). However, like IMB material from the Apollo 16 highland site, the feldspathic nature of DaG 400 IMB clast component is evidence of the highly plagioclase-rich nature of the protolith that was disassembled and included into the impact melt. Although IMBs in DaG 400 have low-ITE contents and are most comparable to the Group 4 feldspathic (fragment laden) melt breccias, intergranular breccias and feldspathic microporphyritic melt breccias (Korotev, 1994), the DaG 400 material is consistently richer in Sc (Fig. 3.9). This trend has also been observed in impact melt clasts from within other feldspathic lunar meteorites (see Jolliff and Haskin, 1995 Fig. 15 and references therein; Taylor, 1991). This enrichment suggests that the DaG 400 impact melt originated from a plagioclase (aluminous) region (presumably the upper lunar crust), which has experienced minimal KREEP (ITE) contamination, and that is rich in pyroxene phases compared with the crust that was melted to form the Group 4 Apollo 16 impact melts. This inference is important, because if it is assumed that the rock fragments in DaG 400 were consolidated on the farside of the Moon, then in comparison to the nearside crust sampled at the Apollo 16 site, the lunar farside at similar stratigraphic horizons (depths?) has lithologies that are pyroxene-rich, possibly noritic lithologies.

3.5 Summary

DaG 400 is an anorthositic regolith breccia which was consolidated in a feldspathic highlands environment. It contains a range of mineral fragments and lithic clasts that are compositionally and texturally heterogeneous. These components are fused together in a glassy, fine grained matrix. The lithic clast portion of DaG 400 includes rock fragments from the AF FAN suite (Al_2O_3-rich, REE-poor), the MM FAN suite (Mg-rich, REE-richer) and impact melt basalt breccias (ITE-richer). Impact melt clasts have a range of textures from chadacryst clast-rich to crypto-crystalline (clast-poor), but the majority have very similar major element and trace element bulk compositions, suggesting that they were all (except for one) generated in a single impact event. This impact excavated and melted material from a relatively shallow crustal region in the feldspathic highlands of the Moon in a locality that was highly aluminous in nature.

The different lithic and mono-mineralic fragments were mixed together by meteoritic lunar gardening processes into a regolith that was dominated by local (possibly basin-generated) impact melt-rich rocks and feldspathic FAN material. The regolith became fused into a highly consolidated glassy breccia by a subsequent impact event. Because of the extremely welded nature of the sample this probably occurred before the impact event which actually spalled the

DaG 400 breccia off the Moon because if the regolith was poorly consolidated the individual fragments would probably not have survived the launch event and subsequent entry through Earth's atmosphere.

	Point Counts				Percentage %			
	> 500 µm	500 - 20 µm	<20 µm	All fractions	> 500 µm	500 - 20 µm	<20 µm	All Fractions
Mineral								
Plagioclase	4	61	47	112	0 17	2 66	2 05	4 88
Olivine	0	21	2	23	0 00	0 91	0 09	1 00
Pyroxene non zoned	0	24	3	27	0 00	1 05	0 13	1 18
Unidentified mafic mineral phase	0	1	20	21	0 00	0 04	0 87	0 91
subtotal	4	107	72	183	0 17	4 66	3 14	7 97
Non Mare								
cataclastic anorthsoite	87	18	1	106	3 79	0 78	0 04	4 62
Anorthosite (contains other mineral	24	68	4	96	1 05	2 96	0 17	4 18
Anorthositic norite	15	23	0	38	0 65	1 00	0 00	1 66
Anorthsoitic gabbro	45	7	0	52	1 96	0 30	0 00	2 26
Anorthositic troctolite	488	23	0	511	21 25	1 00	0 00	22 26
Norite	0	36	0	36	0 00	1 57	0 00	1 57
Troctolite	5	10	1	16	0 22	0 44	0 04	0 70
subtotal of non mare lithics	664	185	6	855	28 92	8 06	0 26	37 24
Impact MeltBreccia								
Individul clast surrounded by melt	0	18	0	18	0 00	0 78	0 00	0 78
Clastic (>80%) aphantic melt	192	191	1	384	8 36	8 32	0 04	16 72
Clastic (>80%) aphantic melt +plag	364	119	1	484	15 85	5 18	0 04	21 08
Vitrophylic (fine lathes)	33	15	0	48	1 44	0 65	0 00	2 09
Intersertial	4	3	0	7	0 17	0 13	0 00	0 30
subtotal	593	346	2	941	25 83	15 07	0 09	40 98
Unidentifiable								
Unidentifiable	0	0	235	235	0 00	0 00	10 24	10 24
subtotal	0	0	235	235	0 00	0 00	10 24	10 24
Additional								
Pore	0	0	0	0	0 00	0 00	0 00	0 00
Lasar ablation pit hole	0	6	0	6	0 00	0 26	0 00	0 26
surface flaw	0	1	4	5	0 00	0 04	0 17	0 22
Infilled fracture	0	21	16	37	0 00	0 91	0 70	1 61
Fracture	0	6	18	24	0 00	0 26	0 78	1 05
Melt vein	0	4	6	10	0 00	0 17	0 26	0 44
subtotal	0	38	44	82	0 00	1 66	1 92	3 57
Total	1261	676	359	2296	54 92	29 44	15 64	100 00

Table 3.3. Modal mineral fragments (monomict clasts) and lithic clast (polymineralic clasts) counts for DaG 400 generated using the technique outlined in Chapter 2.

	Norefelsic Anorthosite	Anorthositic norite 1	Anorthositic norite 2	Anorthositic gabbronorite	Anorthositic pigeonite	Anorthosite	Anorthosite
	AF FAN	AF FAN	AF FAN	AF FAN	AF FAN	AF FAN	AF FAN
Na_2O	0.53 ± 0.05	0.40 ± 0.03	0.43 ± 0.03	0.53 ± 0.10	0.30 ± 0.04		
MgO	1.80 ± 0.05	1.19 ± 0.11	1.92 ± 0.08	0.46 ± 0.01	0.84 ± 0.06		
Al_2O_3	31.73 ± 0.29	33.64 ± 0.12	32.65 ± 0.30	33.30 ± 0.17	31.52 ± 0.17		
SiO_2	42.52 ± 0.59	42.39 ± 0.42	43.74 ± 0.33	41.20 ± 0.67	41.05 ± 0.30		
K_2O	0.10 ± 0.03	b.d.	0.10 ± 0.03	b.d.	b.d.		
CaO	21.83 ± 0.41	21.04 ± 0.11	18.73 ± 0.22	24.00 ± 0.30	24.69 ± 0.39	21.31	21.31
TiO_2	0.19 ± 0.01	0.04 ± 0.01	0.41 ± 0.01	0.05 ± 0.06	0.02 ± 0.01		
FeO	1.22 ± 0.10	1.12 ± 0.28	2.11 ± 0.16	0.40 ± 0.18	1.44 ± 0.26		
Total	99.91	99.82	100.09	99.95	99.86		
Mg#	72.50	65.30	61.81	67.61	51.12		
No.	3	3	3	3	3		
Sc	4.71	<2.81	n.m.	<2.37	2.20	n.m.	n.m.
V	10.70	3.82	44.42	3.34 ± 0.01	b.d.	2.43	5.13
Mn	208 ± 32	46 ± 2	1102	82 ± 112	34	43	95
Co	15.00 ± 10.46	0.88 ± 0.52	9.68	1.30 ± 2.27	0.39	4.49	2.66
Ni	171.5 ± 161.2	2.9 ± 0.2	20.2	9.3	b.d.	37.1	9.9
Cu	4.57 ± 3.34	2.03	2.76	1.10	b.d.	0.93	1.75
Zn	2.14 ± 2.55	1.00 ± 0.48	5.37	1.11	b.d.	0.45	1.15
Rb	0.45 ± 0.04	0.23 ± 0.06	1.40	0.33 ± 0.20	0.21	0.17	0.38
Sr	339 ± 77	270 ± 134	187	238 ± 106	184	198	266
Y	1.67 ± 0.13	0.42 ± 0.08	2.92	0.52 ± 0.61	0.31	0.25	0.95
Zr	3.95 ± 0.56	1.75 ± 0.20	13.40	0.54 ± 0.39	0.73	0.12	2.11
Nb	0.42 ± 0.01	0.18 ± 0.05	0.57	0.06 ± 0.02	0.08	0.02	0.25
Mo	0.12	0.08 ± 0.00	0.38	0.05		0.10	0.08
Ba	429 ± 162	226 ± 155	166	167 ± 76	157	132	108
La	0.57 ± 0.08	0.23 ± 0.02	0.22	0.29 ± 0.08	0.16	0.14	0.37
Ce	1.57 ± 0.18	0.65 ± 0.07	0.63	0.80 ± 0.05	0.51	0.34	0.95
Pr	0.21 ± 0.03	0.09 ± 0.00	0.09	0.10 ± 0.03	0.06	0.05	0.13
Nd	0.99 ± 0.11	0.44 ± 0.10	0.51	0.38 ± 0.26	0.26	0.21	0.56
Sm	0.29 ± 0.01	0.12 ± 0.01	0.22	0.12 ± 0.01	0.10	0.06	0.16
Eu	0.68 ± 0.08	0.56 ± 0.10	0.48	0.61 ± 0.02	0.43	0.57	0.64
Gd	0.31 ± 0.07	0.10 ± 0.05	0.26	0.10 ± 0.04	b.d.	0.07	0.18
Tb	0.04 ± 0.01	0.01	0.06	0.02 ± 0.01	b.d.	0.01	0.03
Dy	0.33 ± 0.02	0.08 ± 0.03	0.45	0.09 ± 0.07	b.d.	0.04	0.21
Ho	0.06 ± 0.02	0.02 ± 0.02	0.10	0.03	b.d.	0.01	0.03
Er	0.17 ± 0.03	0.04	0.33	0.08	b.d.	0.04	0.10
Tm	0.03 ± 0.01	0.01 ± 0.02	0.05	0.01	b.d.	0.01	0.01
Yb	0.23 ± 0.04	0.04	0.45	b.d.	b.d.	0.04	0.08
Lu	0.03	0.01	0.07	0.02	b.d.	0.01	0.01
Hf	0.10 ± 0.02	0.03	0.23	0.03	b.d.	0.06	0.05
Ta	0.01	0.01	0.00	0.01	b.d.	0.01	0.01
Pb	0.12 ± 0.02	0.05 ± 0.02	0.08	b.d.	b.d.	0.02	0.03
Th	0.04	0.06	0.01	0.01	0.59	0.02	0.04
U	0.16 ± 0.17	0.11 ± 0.03	0.04	0.08 ± 0.01	0.14	0.06	0.14
No.	2	2	1	2	1	1	1

*except if no 2σ standard deviation reported: in which case only one laser point measured concentration (due to problem in setting up element list for analysis)

Table 3.4. AF FAN clast bulk compositions in DaG 400. See Table 3.1 for description of specific clasts.

	Anorthositic troctolite	Anorthositic noritic hornfel	Anorthositic troctolite	Noritic hornfel	Troctolite	Troctolite
	MM FAN	MM FAN	MM FAN	MM FAN	MM FAN	MM FAN
Na_2O	0.39 ± 0.05	0.36 ± 0.02	0.31 ± 0.08	0.36 ± 0.05	0.21 ± 0.04	0.19 ± 0.01
MgO	5.15 ± 0.12	5.95 ± 0.50	6.18 ± 0.12	5.95 ± 0.14	9.78 ± 0.15	18.63 ± 0.39
Al_2O_3	29.21 ± 0.45	28.81 ± 0.55	29.19 ± 0.18	28.81 ± 0.35	26.45 ± 0.28	17.70 ± 0.59
SiO_2	41.83 ± 0.13	41.56 ± 0.09	42.67 ± 0.16	41.56 ± 0.52	41.49 ± 0.40	42.03 ± 0.41
P_2O_5	b.d.	b.d.	b.d.	b.d.	b.d.	b.d.
K_2O	b.d.	0.04 ± 0.05	0.10 ± 0.02	b.d.	0.07 ± 0.05	b.d.
CaO	19.79 ± 0.43	19.19 ± 0.32	17.82 ± 0.23	19.19 ± 0.33	17.43 ± 0.22	9.95 ± 0.13
TiO_2	0.16 ± 0.25	0.30 ± 0.23	0.19	0.42	0.02	0.28
Cr_2O_3	0.01 ± 0.02	0.07 ± 0.04	0.06 ± 0.10	0.07 ± 0.09	0.07 ± 0.06	0.07 ± 0.16
MnO	0.07 ± 0.07	0.02 ± 0.03	0.06 ± 0.10	0.02 ± 0.00	0.02 ± 0.02	0.13 ± 0.02
FeO	3.26 ± 0.15	3.71 ± 0.09	3.34 ± 0.07	3.71 ± 0.17	4.33 ± 0.31	12.88 ± 0.19
Total	99.88	100.02	99.93	100.10	99.86	101.86
Mg#	73.78	74.07	76.74	74.07	80.12	72.07
No.						
Sc	5.97 ± 4.53	7.49	6.45	8.40	b.d.	12.30
V	10.07 ± 18.88	26.44			0.85	
Mn	280 ± 509	477 ± 180	305	465	19	1459
Co	8.37 ± 15.24	12.18 ± 6.72	8.25	11.53	0.50	35.56
Ni	28 ± 35	32 ± 51	36	75	2	68
Cu	2.25 ± 5.13	3.23 ± 2.70		3.83	0.50	6.86
Zn	2.58 ± 6.18	4.06 ± 3.22	2.16	3.51	0.23	12.16
Rb	0.23 ± 0.06	0.21 ± 0.06	0.30	0.30	0.08	0.34
Sr	200 ± 35	236 ± 40	168	236	102	241
Y	1.50 ± 2.28	3.01 ± 2.42	1.58	3.20	0.30	5.43
Zr	4.00 ± 6.69	8.03 ± 7.95	4.32	8.58	0.65	15.63
Nb	0.31 ± 0.50	0.42 ± 0.47	0.29	0.57	0.07	0.49
Mo	0.09 ± 0.16	0.24		0.19	0.05	0.37
Ba	172 ± 59	247 ± 12	194	326	67	368
La	0.45 ± 0.19	0.49 ± 0.19	0.35	0.59	0.13	0.92
Ce	1.21 ± 0.30	1.39 ± 0.72	1.13	1.58	0.36	2.35
Pr	0.15 ± 0.09	0.20 ± 0.09	0.15	0.21	0.06	0.35
Nd	0.65 ± 0.39	1.02 ± 0.63	0.64	1.25	0.24	1.65
Sm	0.19 ± 0.26	0.30 ± 0.23	0.21	0.25	0.08	0.42
Eu	0.49 ± 0.01	0.57 ± 0.06	0.59	0.62	0.28	0.58
Gd	0.22 ± 0.26	0.43 ± 0.25	0.17	0.38	0.06	0.64
Tb	0.04 ± 0.05	0.07 ± 0.07	0.04	0.08	0.01	0.14
Dy	0.26 ± 0.42	0.56 ± 0.52	0.25	0.54	0.04	0.98
Ho	0.06 ± 0.08	0.12 ± 0.11	0.05	0.12	0.01	0.22
Er	0.15 ± 0.24	0.35 ± 0.29	0.20	0.36	0.02	0.59
Tm	0.03 ± 0.04	0.06 ± 0.07	0.03	0.05	0.00	0.11
Yb	0.20 ± 0.34	0.33 ± 0.41	0.19	0.45	0.02	0.80
Lu	0.03 ± 0.05	0.05 ± 0.03	0.04	0.06	0.01	0.11
Hf	0.11 ± 0.23	0.20 ± 0.24	0.10	0.22	0.01	0.40
Ta	0.02 ± 0.03	0.03 ± 0.01		0.03	0.00	0.03
Pb	0.08 ± 0.09	0.18 ± 0.10	0.06	0.15	0.01	0.49
Th	0.04 ± 0.07	0.11	1.88	0.33	0.01	0.18
U	0.08 ± 0.03	0.12 ± 0.02	0.07	0.12	0.03	0.13
No	4	2				

*except if no 2σ standard deviation reported, in which case only one laser point measured concentration

Table 3.5. MM FAN Clast bulk composition. See Table 3.1 for description of specific clasts.

	Matrix	Melt Vein	Plag. 1	Plag. 1	Pyx. 1	Pyx.2	Pyx. 3
SiO_2			43.31 ± 0.27	44.54 ± 0.27	50.40 ± 0.31	55.53 ± 0.34	
TiO_2			b.d	0.15 ± 0.01	0.39 ± 0.01	0.49 ± 0.01	
Al_2O_3			34.99 ± 0.09	30.53 ± 0.08	3.56 ± 0.01	1.50 ± 0.01	
Cr_2O_3			b.d	0.09 ± 0.01	0.64 ± 0.01	0.50 ± 0.01	
FeO			0.24 ± 0.01	2.76 ± 0.03	16.41 ± 0.19	11.49 ± 0.13	
MnO			0.06 ± 0.01	0.05 ± 0.01	0.35 ± 0.01	0.20 ± 0.01	
MgO			0.25 ± 0.01	3.68 ± 0.01	16.76 ± 0.01	18.91 ± 0.02	
CaO			20.21 ± 0.37	17.68 ± 0.33	11.30 ± 0.21	11.23 ± 0.21	
Na_2O			0.32 ± 0.01	0.39 ± 0.01	0.11 ± 0.01	b.d.	
K_2O			0.03 ± 0.01	0.05 ± 0.01	0.01 ± 0.01	b.d.	
P_2O_5			0.05 ± 0.01	0.03 ± 0.01	b.d.	b.d.	
Total			**99.46**	**99.94**	**99.93**	**99.85**	
Mg#			**64.36**	**70.41**	**64.56**	**74.59**	
Sc	7.65 ± 0.05	n.m	2.22 ± 0.01	n.m	106.32 ± 0.19	49.29 ± 0.09	64.72 0.46
V	n.m	101 ± 1	n.m	n.m	n.m	n.m	n.m
Mn	330 ± 3	3601 ± 10	34 ± 1	34 ± 1	4009 ± 3	1111 ± 1	4002 ± 32
Co	11.97 ± 0.10	44.73 ± 0.21	0.74 ± 0.01	0.49 ± 0.01	33.46 ± 0.07	11.17 ± 0.02	36.52 ± 0.32
Ni	145 ± 1	95 ± 0.47	14 ± 1	b.d.	16 ± 1	5 ± 1	15 ± 1
Cu	4.26 ± 0.03	41.95 ± 0.33	2.52 ± 0.03	b.d.	7.71 ± 0.04	2.34 ± 0.01	6.21 ± 0.04
Zn	2.44 ± 0.04	137.19 ± 1.76	0.46 ± 0.01	b.d.	13.46 ± 0.03	5.83 ± 0.01	10.51 ± 0.16
Rb	0.55 ± 0.01	60.18 ± 0.51	b.d	0.18 ± 0.01	b.d.	0.23 ± 0.01	1.11 ± 0.01
Sr	215 ± 1	2475 ± 13	193 ± 1	192 ± 1	53 ± 1	96 ± 1	188 ± 1
Y	6.91 ± 0.05	25.51 ± 0.10	0.47 ± 0.01	0.23 ± 0.01	31.98 ± 0.09	9.85 ± 0.03	18.92 ± 0.13
Zr	26.25 ± 0.07	111.71 ± 0.37	0.32 ± 0.01	b.d.	56.75 ± 0.01	4.98 ± 0.01	22.75 ± 0.06
Nb	1.80 ± 0.01	14.15 ± 0.03	0.07 ± 0.01	0.03 ± 0.00	1.71 ± 0.01	0.11 ± 0.01	0.38 ± 0.01
Mo	b.d	2.21 ± 0.02	b.d	b.d.	0.60 ± 0.01	0.24 ± 0.01	0.71 ± 0.01
Ba	430 ± 4	16666 ± 70	60 ± 1	89 ± 1	222 ± 1	1212 ± 7	580 ± 6
La	1.99 ± 0.01	20.69 ± 0.10	0.50 ± 0.01	0.18 ± 0.01	0.42 ± 0.01	0.31 ± 0.01	0.77 ± 0.01
Ce	4.58 ± 0.03	58.09 ± 0.19	1.29 ± 0.01	0.50 ± 0.01	2.17 ± 0.01	0.96 ± 0.01	1.89 ± 0.01
Pr	0.72 ± 0.01	5.59 ± 0.03	0.16 ± 0.01	0.06 ± 0.01	0.49 ± 0.01	0.19 ± 0.01	0.35 ± 0.01
Nd	3.29 ± 0.02	21.08 ± 0.14	0.70 ± 0.01	0.22 ± 0.01	3.49 ± 0.01	1.28 ± 0.01	2.07 ± 0.01
Sm	0.81 ± 0.01	5.00 ± 0.03	0.16 ± 0.01	0.08 ± 0.01	1.75 ± 0.01	0.59 ± 0.01	1.04 ± 0.01
Eu	0.79 ± 0.01	2.84 ± 0.02	0.75 ± 0.01	0.62 ± 0.01	b.d.	0.06 ± 0.01	0.08 ± 0.01
Gd	1.08 ± 0.01	4.81 ± 0.02	0.10 ± 0.01	b.d.	3.33 ± 0.03	1.14 ± 0.01	1.91 ± 0.01
Tb	0.16 ± 0.01	0.72 ± 0.01	0.02 ± 0.01	b.d.	0.72 ± 0.01	0.22 ± 0.01	0.42 ± 0.01
Dy	1.32 ± 0.01	4.50 ± 0.03	b.d	b.d.	5.60 ± 0.04	1.68 ± 0.01	2.95 ± 0.02
Ho	0.25 ± 0.01	0.92 ± 0.01	0.02 ± 0.01	b.d.	1.31 ± 0.01	0.38 ± 0.01	0.70 ± 0.01
Er	0.73 ± 0.01	2.45 ± 0.02	b.d	b.d.	4.07 ± 0.01	1.11 ± 0.01	2.29 ± 0.02
Tm	0.11 ± 0.01	0.38 ± 0.01	b.d	b.d.	0.61 ± 0.01	0.17 ± 0.01	0.34 ± 0.01
Yb	0.62 ± 0.01	2.71 ± 0.02	b.d	b.d.	4.70 ± 0.05	1.05 ± 0.01	2.50 ± 0.03
Lu	0.12 ± 0.01	0.38 ± 0.01	b.d	b.d.	0.72 ± 0.01	0.17 ± 0.01	0.36 ± 0.01
Hf	0.56 ± 0.01	2.58 ± 0.01	b.d	b.d.	1.88 ± 0.01	0.20 ± 0.01	0.44 ± 0.01
Ta	0.09 ± 0.01	0.82 ± 0.01	b.d	b.d.	0.09 ± 0.01	0.00 ± 0.01	b.d.
Pb	0.17 ± 0.01	8.94 ± 0.03	0.03 ± 0.01	b.d.	0.14 ± 0.01	0.13 ± 0.01	0.33 ± 0.01
Th	0.26 ± 0.01	4.61 ± 0.04	0.25 ± 0.01	0.23 ± 0.01	0.13 ± 0.01	0.17 ± 0.01	0.14 ± 0.01
U	0.06 ± 0.01	4.79 ± 0.02	b.d	0.05 ± 0.01	0.16 ± 0.01	0.07 ± 0.01	0.17 ± 0.01

Table 3.6. Composition of mineral grains, matrix and melt vein composition in DaG 400 as measured by LA-ICP-MS. Note the extreme Ba-enrichment of vein composition as a result of terrestrial desert mineralisation.

Precision for major elements are reported as 2 sigma standard deviations calculated from the variation of basalt glass standard measured on the Cameca SX50. Errors for trace elements are 2 sigma standard deviations calculated on the basis of standard deviation variation of measurements of NIST 6121 standard. n.m. = not measured. b.d. = below detection limits

	Vitric		Clastic		Clastic		Clastic		Clastic		Clastic		Clastic		Clastic		Clastic	
	IMB		IMB		IMB		IMB		IMB		IMB		IMB		IMB		IMB	
Na_2O	0.37	0.02	0.43	0.03	0.43	0.14	0.46	0.04	0.42	0.07	0.42	0.10	0.51	0.06	0.33	0.14	0.53	0.10	0.36	0.03	0.45	0.03	0.48	0.03
MgO	4.30	0.15	3.90	0.17	3.86	0.04	4.16	0.14	4.05	0.01	3.91	0.10	4.90	0.17	4.59	0.22	4.41	0.32	4.35	0.01	4.30	0.22	4.44	0.21
Al_2O_3	28.25	0.19	29.51	0.45	29.58	0.12	28.51	0.32	29.17	0.35	30.31	0.30	28.63	0.14	28.35	0.42	29.24	0.10	29.34	0.26	29.63	0.22	29.05	0.43
SiO_2	42.48	0.26	43.71	0.51	43.43	0.31	42.92	0.23	42.12	0.64	43.33	0.66	43.28	0.13	41.86	0.35	43.42	1.02	42.76	0.59	43.63	0.21	43.49	0.43
P_2O_5	b.d		b.d		b.d		b.d		b.d		0.01	0.07	b.d		0.01	0.02	b.d		b.d		b.d			
K_2O	b.d		0.01	0.01	0.01	0.01	0.01	0.01	0.03	0.05	b.d		b.d		0.01	0.01	0.10	0.05	0.06	0.03	b.d			
CaO	19.66	0.06	17.72	0.31	18.27	0.34	18.16	0.19	19.16	0.20	17.16	0.19	18.23	0.13	19.75	0.05	17.10	0.07	18.11	0.22	17.51	0.12	17.09	0.11
TiO_2	0.44	0.02	0.39	0.12	0.44	0.02	0.35	0.05	0.35	0.11	0.42	0.01	0.47	0.01	0.30	0.01	0.35	0.01	0.37	0.01	0.40	0.01	0.58	0.01
Cr_2O_3	0.14	0.11	0.13	0.06	0.02	0.03	0.08	0.08	b.d		0.11	0.11	b.d		0.08	0.06	0.13	0.03	b.d		b.d		b.d	
MnO	b.d		0.18	0.11	b.d		0.13	0.03	0.11	0.13	0.05	0.04	b.d		b.d		b.d		0.05	0.08	b.d		0.04	0.01
FeO	4.20	0.15	3.83	0.19	3.36	0.24	4.40	0.04	3.58	0.05	4.08	0.16	4.38	0.06	4.33	0.10	4.46	0.45	3.88	0.11	4.34	0.12	4.32	0.19
Total	100.13		99.94		100.15		99.79		100.21		99.98		100.41		99.87		99.91		99.93		100.40		99.72	
MgO#	65.04		64.52		63.46		65.67		66.85		63.43		64.61		65.11		63.63		66.67		64.33		65.91	
No.	3		3		3		3		3		3		3		3		3		3		3		3	
Sc	9.61		9.75		9.17		8.11		9.16		10.65		9.53		7.41		8.14		9.12		9.76		11.62	
V	18.35		15.22		11.37		16.67		14.41															
Ni	414	31	464	100	497	31	384	155	426	125	501		540		473		436		425		524		541	
Co	11.74	4.43	16.39	1.70	15.61	7.45	14.36	4.98	12.07	0.21	11.67		14.26		16.03		10.71		12.07		11.41		11.24	
Cu	55	10	106	72	175	178	172	14	71	15	73		86		120		78		102		859		223	
Cs	3.04	1.28	5.21	2.67	4.42	2.19	5.13	0.20	4.04	0.46	2.90		3.92		5.07		3.54		3.84		11.43		3.61	
Zn	3.93	0.77	3.31	0.70	4.20	1.41	3.73	3.75	2.91	0.56	3.12		3.26		3.54		3.91		3.31		3.64		2.65	
Rb	0.65	0.04	0.63	0.02	0.75	0.11	0.62	0.27	0.52	0.21	0.51		0.52		0.52		0.76		0.53		0.62		1.51	
Sr	250	24	205	40	263	85	263	12	251	23	288		264		215		241		230		263		275	
Y	7.02	0.45	6.43	3.18	7.58	0.85	7.93	3.01	5.19	3.77	8.65		8.52		5.52		5.90		8.22		8.27		11.30	
Zr	23.85	1.00	21.5	12.06	29.90	7.34	28.31	10.36	20.05	12.93	30.41		31.31		19.54		21.77		28.86		28.36		15.38	
Nb	1.37	0.03	1.12	1.06	2.37	0.67	2.05	0.72	1.53	0.66	1.81		2.46		1.62		1.73		1.82		1.62		1.63	
Mo	0.14	0.07	0.16		0.15	0.06	0.22		0.14	0.05	0.20								0.10		0.11		0.17	
Ba	206	4	193	42	241	97	335	19	285	27	240		244		290		260		632		624		334	
La	1.34	0.19	1.86	1.22	2.26	0.27	2.33	1.18	1.63	0.90	2.06		2.43		1.58		1.76		2.04		2.10		5.71	
Ce	5.11	0.45	4.64	2.55	5.83	1.15	5.47	2.82	4.15	2.07	4.75		5.73		4.25		4.82		4.82		4.55		14.33	
Pr	0.68	0.09	0.65	0.34	0.83	0.15	0.78	0.42	0.57	0.23	0.66		0.84		0.55		0.65		0.67		0.64		1.36	
Nd	3.12	0.25	2.85	1.51	3.52	0.28	3.46	1.88	2.50	1.12	3.36		3.50		2.74		2.93		3.03		3.36		8.31	
Sm	0.83	0.11	0.83	0.41	1.03	0.32	1.07	0.47	0.76	0.43	0.98		1.19		0.70		0.86		0.96		1.14		2.61	
Eu	0.63	0.00	0.74	0.16	0.74	0.03	0.82	0.54	0.73	0.21	0.85		0.88		0.51		0.63		0.70		0.73		0.81	
Gd	1.04	0.11	0.92	0.53	1.15	0.00	1.25	0.52	0.88	0.55	1.23		1.18		0.83		0.91		1.13		1.19		2.58	
Tb	0.18	0.03	0.17	0.08	0.19	0.03	0.21	0.10	0.15	0.07	0.21		0.22		0.14		0.15		0.19		0.20		0.45	
Dy	1.21	0.34	1.15	0.45	1.33	0.11	1.50	0.75	1.05	0.63	1.55		1.46		1.05		1.15		1.36		1.42		3.18	
Ho	0.27	0.02	0.24	0.11	0.28	0.001	0.30	0.16	0.22	0.16	0.31		0.31		0.22		0.20		0.30		0.29		0.60	
Er	0.78	0.08	0.63	0.23	0.82	0.01	0.84	0.43	0.65	0.44	0.92		0.90		0.62		0.66		0.83		0.95		1.95	
Tm	0.11	0.03	0.10	0.05	0.12	0.05	0.13	0.08	0.09	0.05	0.14		0.12		0.09		0.09		0.13		0.12		0.27	
Yb	0.73	0.12	0.70	0.25	0.87	0.11	0.89	0.31	0.62	0.44	0.83		0.87		0.68		0.63		0.93		0.79		1.90	
Lu	0.11	0.03	0.10	0.02	0.13	0.03	0.13	0.04	0.10	0.06	0.15		0.10		0.10		0.09		0.12		0.13		0.26	
Hf	0.53	0.14	0.50	0.18	0.68	0.19	0.73	0.34	0.52	0.33	0.70		0.62		0.47		0.54		0.69		0.66		1.66	
Ta	0.09	0.01	0.08	0.06	0.10	0.03	0.10	0.05	0.07	0.06	0.10		0.10		0.08		0.07		0.09		0.09		0.23	
Pb	0.18	0.05	0.12	0.05	0.23	0.13	0.32	0.30	0.11	0.07	0.23		0.22		0.22		0.23		0.25		0.33		0.32	
Th	0.30	0.01	0.22	0.03	0.34	0.11	0.33	0.21	0.26	0.24	0.41		0.34		0.23		1.61		0.33		0.31		0.83	
U	0.14	0.02	0.09	0.03	0.12	0.03	0.14	0.11	0.11	0.04	0.13		0.10		0.13		0.13		0.16		0.21		0.23	
No.	2		2		2		3		2															

Table 3.7. Impact Melt Breccia (IMB) bulk clast composition in DaG 400.

	Jog et al. 2006		Zipfel et al. 1998	Semenova et al. 2000	Korotev et al. 2003	Warren et al. 2005
SiO_2	41.42 ± 0.13	†	44.93	43.40	43.48	43.00
TiO_2	0.17 ± 0.01	†	0.18	0.23	0.18	0.14
Al_2O_3	27.76 ± 0.05	†	28.91	28.60	28.83	27.02
Cr_2O_3	0.08	†			0.08	0.07
FeO	3.61 ± 0.04	†	3.78	3.52	3.62	3.72
MnO	0.07 ± 0.01	†	0.05	0.06	0.07	0.07
MgO	4.84 ± 0.02	†	5.14	3.80	4.62	4.81
BaO	1.34	†			0.03	
CaO	17.24 ± 0.12	†	17.35	18.70	18.44	19.87
Na_2O	0.39 ± 0.01	†	0.32	0.33	0.34	0.32
K_2O	0.08 ± 0.01	†	0.07	0.10	0.09	0.08
P_2O_5	0.43 ± 0.01	Δ	0.11		0.22	
Total	97.43		100.85	98.74	100.00	99.10
Mg #	68.24		70.80	65.82	69.52	69.76
Li	6.22 ± 0.02					
Be	0.29 ± 0.04					
Sc	5.68 ± 0.19		5.4		5.39	6.40
V	18.14 ± 0.02					23.00
Cr	527 ± 4	†	550		520	
Cr	432.0 ± 1.6		113		132	160
Co	15.3 ± 0.1					
Ni	142.6 ± 1.4		14.0		13.8	15.1
Cu	15.64 ± 0.11					
Zn	5.37 ± 0.04				33.80	
Ga	3.66 ± 0.11					
Br	n.d.				1.00	3.60
As	2.78 ± 0.15				0.79	1.02
Rb	0.68 ± 0.03				<2	3
Sr	451.5 ± 3.5	†	190		268	300
Sr	440 ± 18					
Y	9.56 ± 0.07					
Zr	39.85 ± 0.18				28.00	<24
Nb	2.26 ± 0.11					
Mo	0.94 ± 0.04					
Ag	n.d.				0.12	
Sb	n.d.				0.15	72.00
Cd	0.16 ± 0.01					
Cs	0.02 ± 0.01				0.04	0.07
Ba	1203 ± 3	†	140		257	820
La	3.52 ± 0.10				2.22	2.50
Ce	7.62 ± 0.17				5.52	5.30
Pr	1.07 ± 0.02					
Nd	4.85 ± 0.03				3.30	2.60
Sm	1.33 ± 0.03				0.89	0.93
Eu	1.02 ± 0.03				0.72	0.78
Gd	1.48 ± 0.05					
Tb	0.27 ± 0.01				0.18	0.21
Dy	1.62 ± 0.07					1.36
Ho	0.34 ± 0.01					0.25
Er	1.00 ± 0.03					
Tm	0.14 ± 0.01					
Yb	0.90 ± 0.01				0.69	0.73
Lu	0.13 ± 0.01				0.10	0.08
Hf	0.69 ± 0.04				0.63	0.65
Ta	0.20 ± 0.04				0.12	0.11
W	b.d.				2.00	
Ir (ppb)	n.d.		4		4.20	5.30
Au (ppb)	n.d.				26.00	2.30
Th	0.39 ± 0.02				0.30	0.37
U	0.47 ± 0.02				0.29	0.58
Pb	1.35 ± 0.02					
Bi	0.05 ± 0.01					
Mass (mg)	140				20	146
Technique	ICP-AES† and ICP-MS		XRF and INAA	Broad Beam	EMP and INAA	INAA

Table 3.8. Bulk rock compositions of different sub-sections of DaG 400. Abbreviation for my analysis: b.d. = below detection limits. n.m. = not measured using this technique. † = measured using ICP-MS. Δ = measured using ICP-AES.

Chapter 4: Lunar Meteorite Regolith Breccia MET 01210

4.1 Introduction

The lunar meteorite 'Meteorite Hills 01210' (from hereon in referred to as MET 01210 or MET) was collected in the cold desert Meteorite Hills region of Antarctica by the 2001 ANSMET field excursion. The original stone was quite small with a mass of only 22.83 g and dimensions of ~4.0 x 2.2 x 1.7 cm. It was found with a black/brown fusion crust (Fig. 4.1a) covering approximately 30% of its surface area (Satterwhite et al. 2004). The meteorite was originally classified as being a basaltic bearing anorthositic breccia by McCoy et al. (2004), but in fact the meteorite is actually an anorthosite bearing basaltic lunar regolith breccia (Arai et al. 2005; Huber and Warren, 2005; Zeigler et al. 2005; Day et al. 2006; Joy et al. 2006a,b).

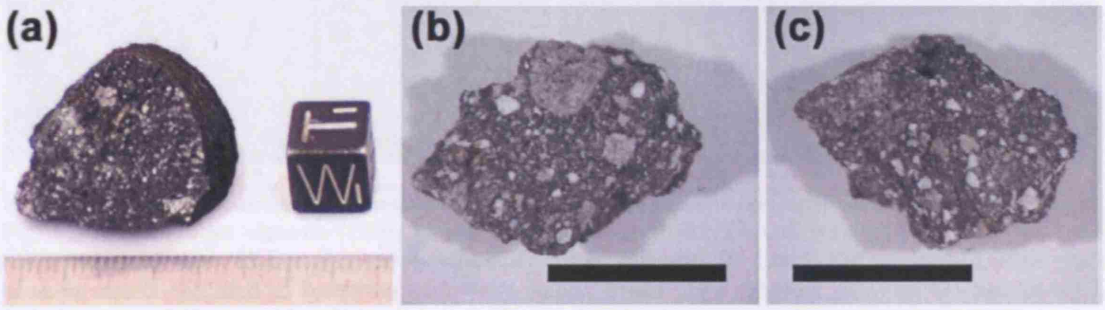

Fig. 4.1. (a) Photograph of hand specimen of MET 01210 taken in the meteorite curatorial facilities at JSC (Website 1.2). Scale cube is 1 cm by 1 cm. (b)(c) Different view of MET 01210,25 chip provided by the MWG. Black line scale bar is 5 mm.

MET 01210 comprises a dark grey matrix enclosing small white, grey and brown mineral fragments (Fig 4.1). The MWG thins sections (MET 01210,21 and MET 01210,27) studied in this investigation both have vesicular fusion crusts and are samples of an immature polymict regolith (Stöffler et al. 1979) that formed a consolidated breccia with rock (<4 mm) and mineral fragments (<2 mm) fused together in a fine grained crystalline and glass matrix. The lithic fragment size is generally small (compared especially to DaG 400), with a few clasts being as large as 0.5 cm in size, but with the majority being <<1 cm (Fig. 4.1a). All of these lithic and mineral fragments have very sharp contacts with the surrounding matrix indicating that they have been incorporated into the regolith that formed this breccia, but not significantly remelted by any subsequent impact process. MET is classified as being a breccia consolidated in a regolith environment as it contains a component of small impact melt spherules (Fig. 4.2a,b,c), rounded glass agglutinates and glassy melt aggregates. By examining the clasts and minerals in MET 01210 I aim to investigate the composition and mineralogy of the individual components and conduct a provenance study of the bedrock sources that were included in the original regolith environment.

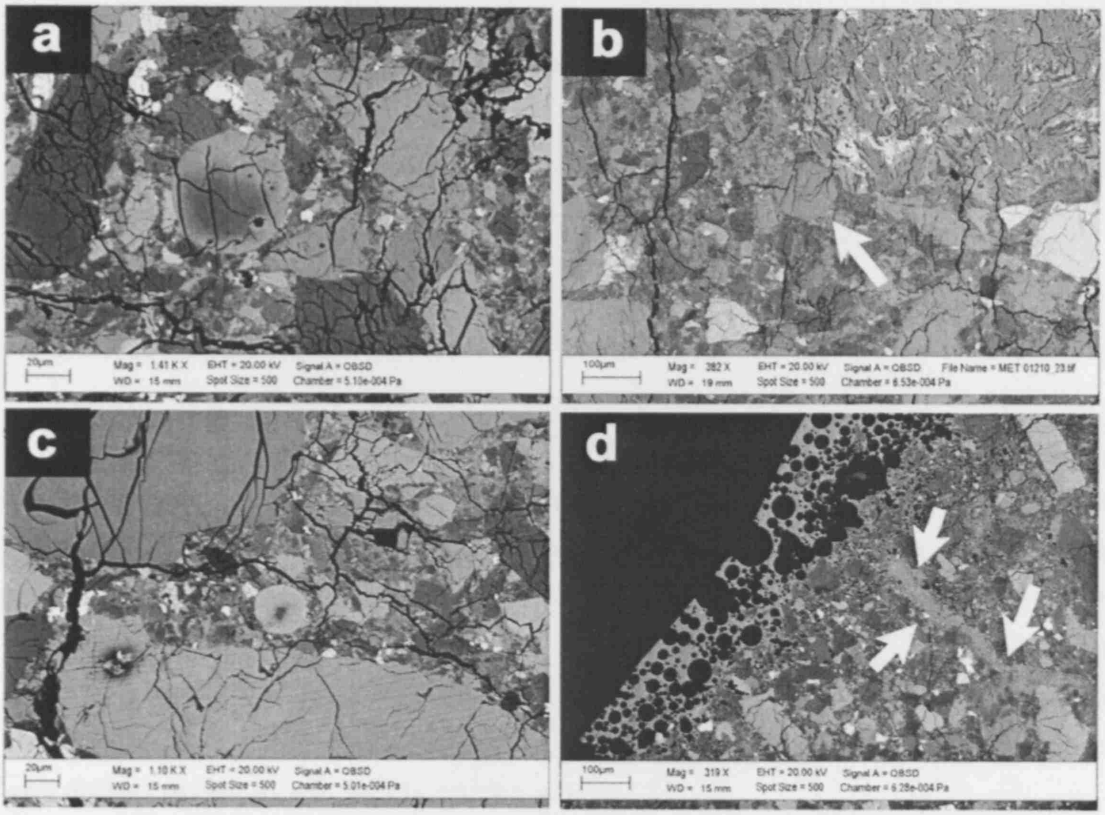

Fig. 4.2. Back-scatter electron (BSE) images of regolith and matrix component of MET 01210,21 and MET 01210,27. (a) ~45 µm glass compositionally zoned spheroid. (b) Large 100 µm homogenous glass bead in matrix (pointed to by arrow). (c) Very small 20 µm glass spheroid. (d) Fusion crust in MET 01210,27. Small glassy melt veins cross cut region (pointed to by arrows) often melting and incorporating localised mineral fragments.

4.2 Petrography and Detailed Clast Investigation

MET 01210 is reasonably well consolidated, with small lithic and monomineralic clast assemblages set in a dark grey matrix (Fig. 4.1, 4.3). The largest visible lithic clast in the two sections is an irregular-shaped meta-clastic anorthositic fragment in section 27, with dimensions of ~4 x 3 mm (Fig. 4.3c). The sample contains few vesicles and as has a relatively low porosity. Both thin sections studied are cross-cut with variable sized fractures that have a preferred left to right orientation in the photomicrographs (Fig. 4.3). These have not been infilled with terrestrial contamination products like the hot desert meteorite DaG 400: evidence of the reduced effects of terrestrial mineralisation processes occurring in cold desert regions. Lithic clasts in MET include examples of a texturally distinct range of mare basalts including intergranular subophitic varieties and some with fine grained feathery plumose textures. There is a significant anorthositic highlands component with small granulites and intergranularly recrystallised anorthosites in addition to more mafic norite and troctolite clasts. Anorthositic impact melt breccia (IMB) clasts are distributed throughout and show a range of textures along a gradation from clastic melt breccias to completely recrystallised microporphyritic crystalline

varieties. Individual monomict mineral fragments are more abundant than lithic fragments by mode (Table 4.1). These include compositionally diverse pyroxenes, plagioclases, olivines (both forsteritic and fayalitic), ilmenite and large silica grains. The whole rock is cemented together in a matrix of crushed impact melt, lithic and mineral fragments, bound by a glassy substrate that was fused together by impact-induced thermal sintering.

4.2.1 Clast Populations

To assess the modal mineralogy and clast content variability in MET 01210, spot point counting classification surveys were conducted on both thin sections following the procedures described in Chapter 2. 1024 individual points were studied in section MET 01210,27 and 771 points were counted in section MET 01210,21. The comparative data from this investigation are listed in Table 4.1 and are also illustrated in Figure 4.4. For all the material studied (of any sized mineral or clast fragment) 44 to 53% of the sections were composed of unidentifiable very small matrix material. This matrix is composed of glassy melt or very small mineral fragments <10 μm that were difficult to classify as a specific mineral species.

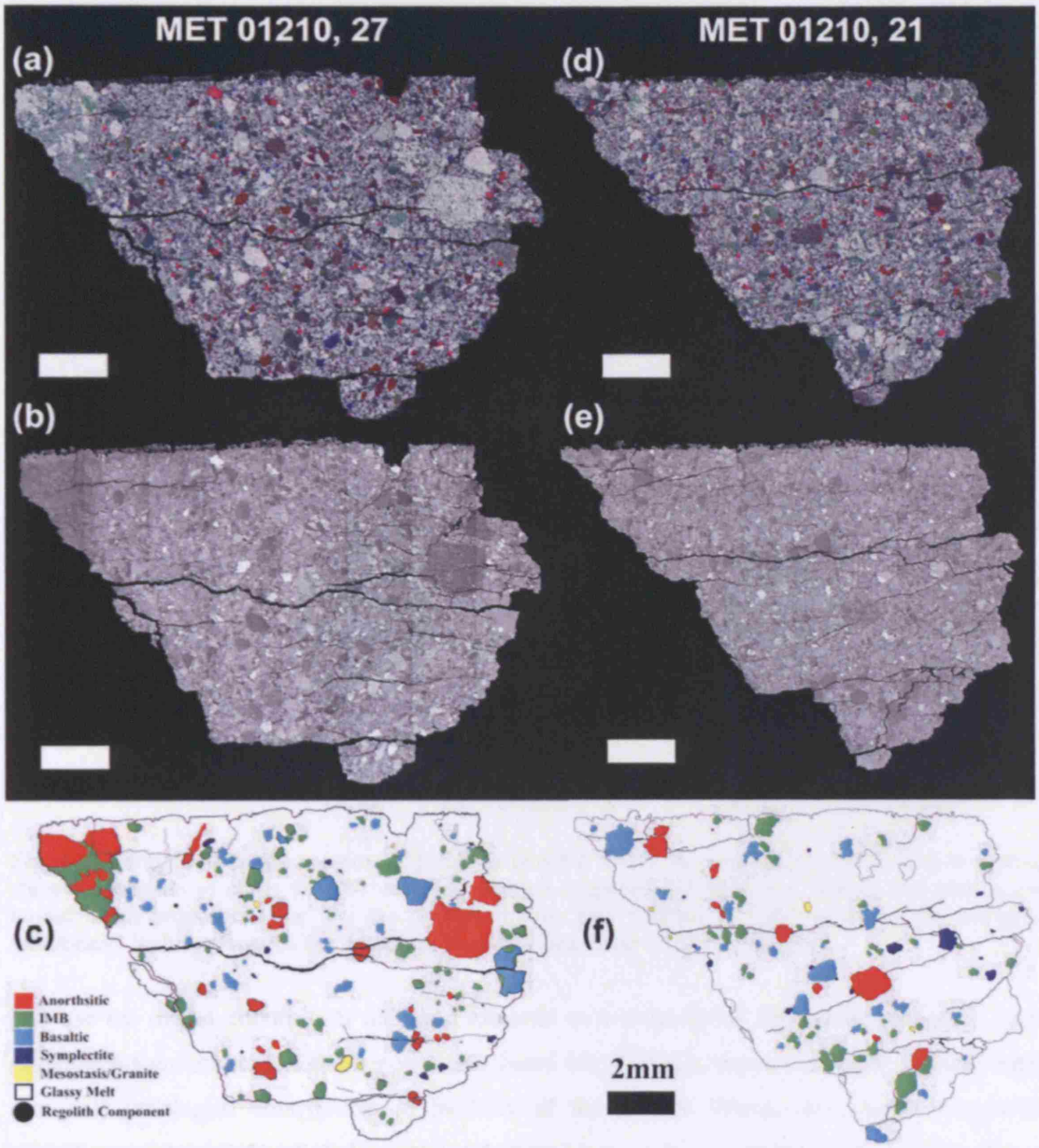

Fig. 4.3. Images of the two thin sections investigated. Scale bar in all images is 2 mm. (a) False colour x-ray map image of MET 01210,27 where different colours refer to concentrations of different elements (Al = white, Ca = yellow, Si = blue, Mg = green, Fe = red and Ti = pink). (b) BSE image of the same section. (c) Clast classification of lithic fragments in this section. (d) False colour image of MET 01210,21 with same colour scheme used in (a). (e)BSE image of MET 01210,21 and (f) clast classifications in MET 01210,21.

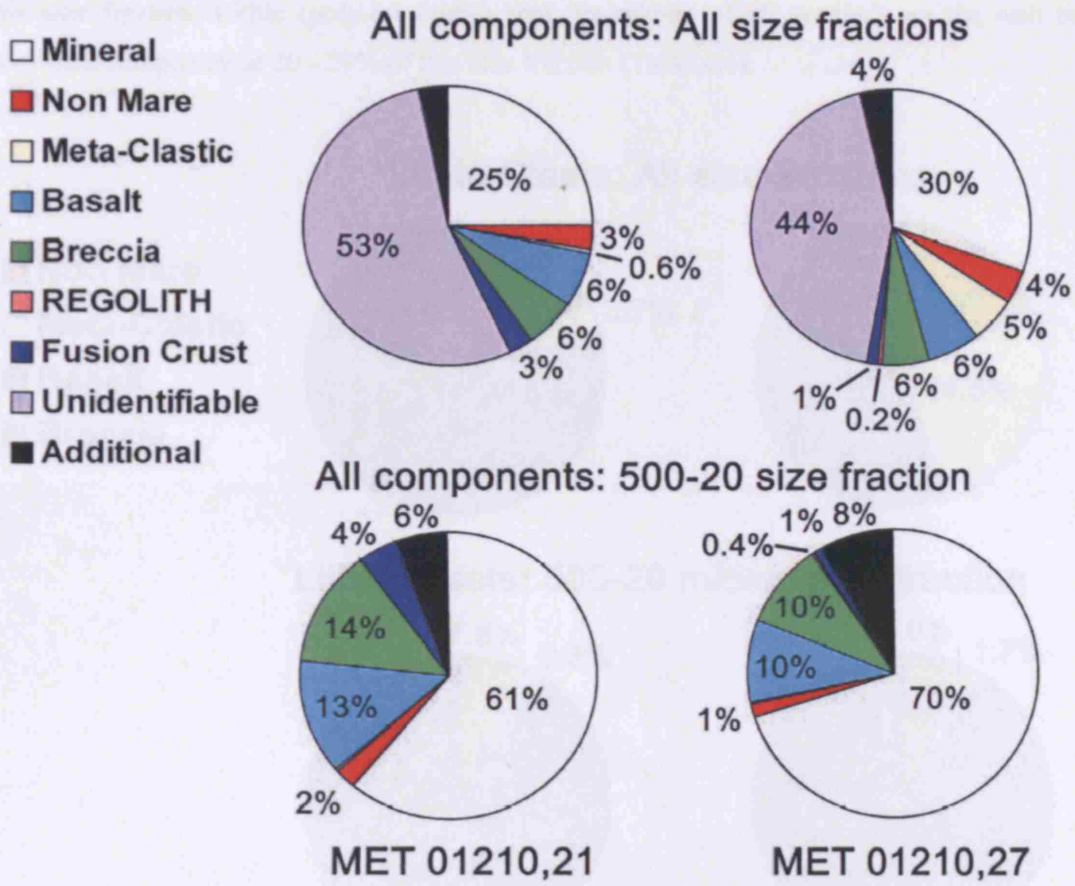

Fig. 4.4. Normalised modal component fractions in MET 01210 for sections 21 and 27. Top two plots show comparison of clasts for all the points counted, regardless of clast size. Bottom two plots show modal count proportions for just the 500-20 micron size fraction in both sections. The category 'additional' includes features like fractures; pores etc (see Table 4.1 for a full list).

If I use the modal counting of all sized material as a measure of what individual lithic rock components contributed to the regolith that fused MET 01210, then anorthositic (or non-mare material) lithologies contributed 26 to 28% of the sample lithics, mare basalt fragments contributed 38 to 66% of the sample and meta-clastic lithics contributed 6 to 35%. These proportions vary widely between the two sections studied and from this it is difficult to actually assess whether the rock is a basaltic or anorthositic regolith breccia. Therefore, as discussed in the DaG 400 clast population section (Section 3.3), the data counted from the 20 - 500 μm size fraction is taken to be more representative of the general makeup of the original lunar regolith as it encompasses a wider range of clast and mineral types that are not over-represented, or under-represented by the modal point counting sampling technique (McKay et al. 1986). For MET 01210,21 273 spot-points or 35.4% of the sample fell into this size category. For MET 01210,27 405 spot-points or 38.1% of the sample was categorised as being part of this size range (Fig. 4.4, 4.5). Of these counts the most modally abundant component in both sections are individual mineral fragments (plagioclases, pyroxenes, ilmenite, olivine etc.) that make up 61 to 70% of

this size fraction. Lithic (poly-mineralic) rock fragments (of all species) are the next most dominant component at 20 - 29% of this size fraction (Table 4.1).

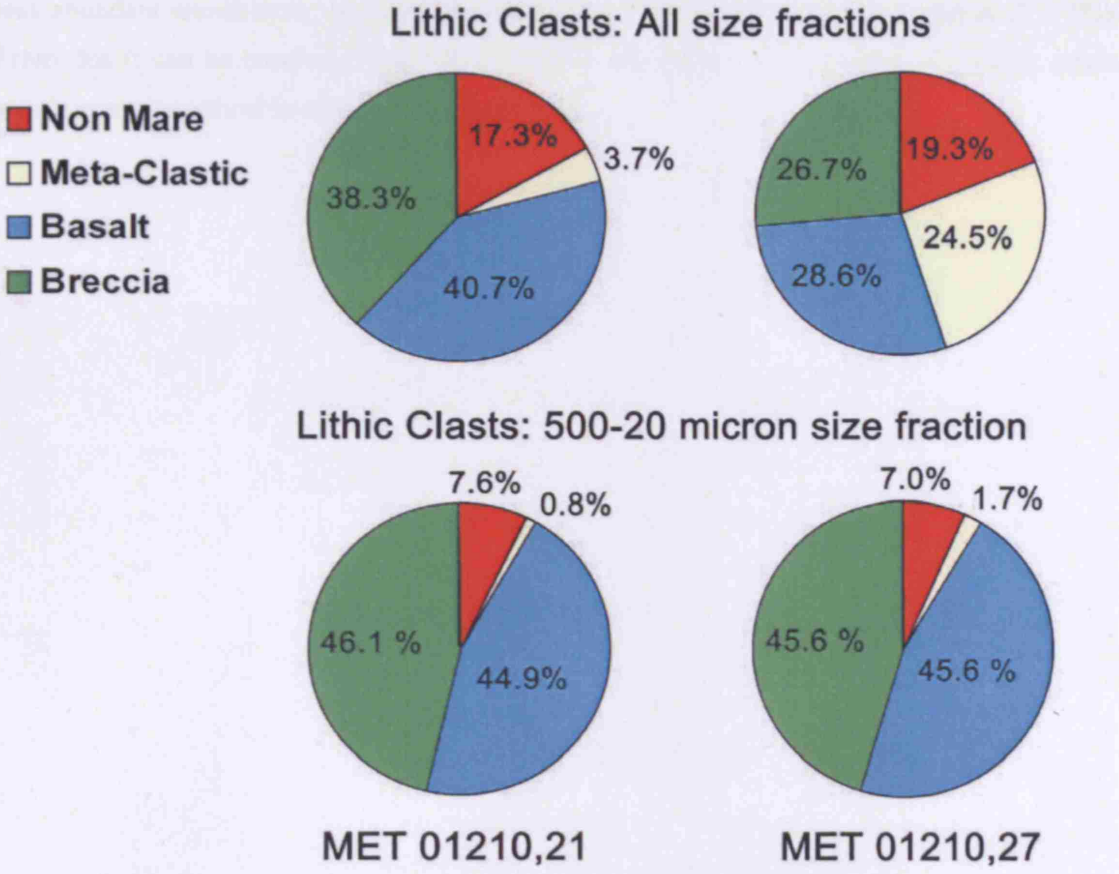

Fig. 4.5. Normalised modal lithic clast fractions in MET 01210 for sections 21 and 27. Top two plots show comparison of clasts for all the points counted, regardless of clast size. Bottom two plots show count clast proportions for just the 500 -20 micron size fraction in both sections; at this representative size fraction there is a remarkable similarity in proportion of lithics between the two sections investigated for this study.

Lithic Clast Component. Fragments of local bedrock in the sections studied here are all <4 mm in size. A comparison of all clasts counted in the study (Fig. 4.5: top) actually shows a similar proportion of basalt and highland-sourced lithic clast fragments in the sample. This however, is likely to be biased towards several very large anorthositic clasts in the sections. Clast species within the 500-20 μm modal count fraction (Fig. 4.5: bottom) suggests that the two thin sections contain similar modal clast proportions and are in fact dominated by impact melt breccia (46.1 - 45.6%) and basalt clast lithologies (44.9 - 45.6%).

This study shows that, despite the variability of large lithic clast components between the two thin sections (and presumably the heterogeneity of the original lunar regolith environment that was fused to form this breccia), there is a remarkable similarity between the proportions of

polymict clast lithologies that contribute to the intermediate size fraction of material. Ignoring the impact melt breccia component, which is a common feature of most regolith breccias, basalt fragments in this representative size fraction make up 83 - 84% of the sample compared with less abundant anorthositic derived fragments (13 - 14%) and meta-clastic material (2 - 3%). From this it can be concluded that MET 01210 is indeed a regolith breccia of basaltic origin with a minor anorthositic contributing component.

4.2.2 Basaltic Clast Assemblage

Basaltic fragments in MET 01210 have a range of textures (Fig. 4.6, 4.7) suggesting variable source environment cooling conditions:

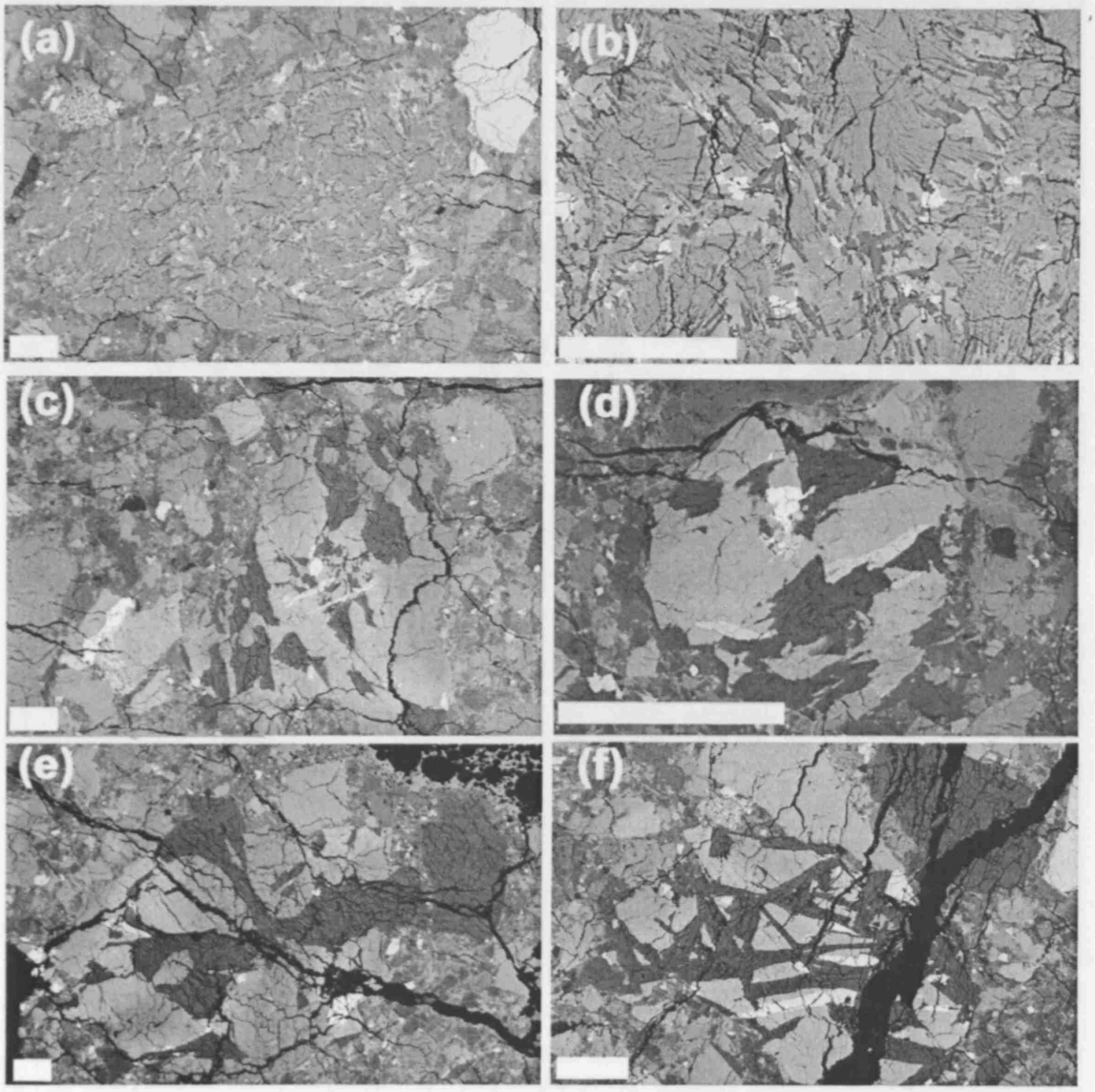

Fig. 4.6. BSE images of different mare basalt fragments in MET 01210. (a) Large plumose fine grained basalt fragment with sub-rounded rim. (b) Close up of the plumose basalt shown in (a) illustrating the texture of feathery intergrowth of plagioclase and pyroxenes with interstitial ilmenite grains. (c) Large intergranular basalt fragment with coarse-grained compositionally zoned pyroxene phases subophitically enclosing small plagioclase aggregates; ilmenite laths and small mesostasis pockets with a large troilite grain at centre. (d) Small intergranular basalt fragment. (e) Large intergranular basalt clast similar to that described in (c); evolved basalt with lath shaped plagioclase crystals and elongate small ilmenite phases, and ulvöspinel aggregates. (f) Subophitic basalt with lath-like, elongate plagioclases.

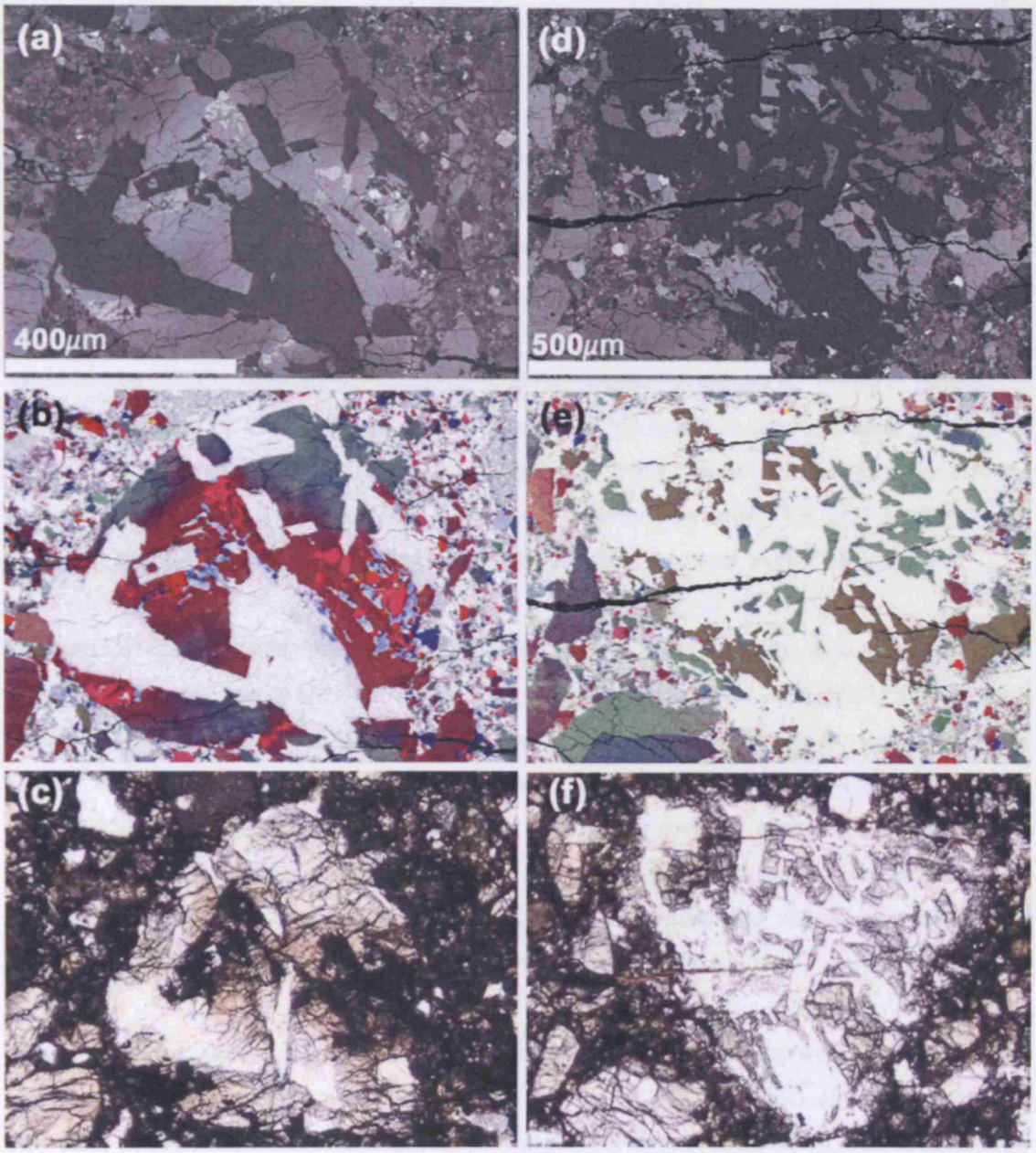

Fig. 4.7. Detailed examination of two basalt fragments in MET 01210,27. (a) BSE image of an evolved low-Ti intergranular basalt fragment. (b) False-colour X-ray montage image of the clast shown in (a). Colours correspond to concentrations of difference elements where white = Al, yellow = Ca, pink = Ti, blue = silica, green = Mg, red = Fe and turquoise = Cr. This image illustrates nicely the complex zonation of pyroxene mineral phases from Mg-rich core areas to Fe-rich, Ca-poor rims associated with mesostasis aggregates of Si-rich glass, fayalite, silica and ulvöspinel. (c) Plane polarised light image of intergranular basalt in (a) and (b). (d) BSE image of feldspathic, Very Low Titanium (VLT), subophitic basalt clast. (e) False-colour X-ray montage image of the clast shown in (d) Colour scheme is as described above. Green phases in the clast correspond to more primitive clinopyroxenes with Mg# in the range of 55 to 63. Brown phases are co-crystallised forsteritic olivines. (f) Plane polarised light image of VLT basalt shown in (d) and (e).

Intergranular basalts. These clasts are holocrystalline fragments of a relatively coarse grained mare ferro-basalt lava flow (Fig. 4.6c,d,e, Fig. 4.7a,b,c). These clasts appear to be similar in appearance to 'Clast A' as discussed by Day et al. (2006) and intergranular basalts described by Arai et al. (2005). They generally are composed of large (<800 μm) zoned pyroxenes (Fig. 4.10a) with Mg-pigeonitic/augites cores zoned to extremely Fe-rich rims (En_{1-47} Fs_{27-86} Wo_{10-30}). Subhedral plagioclase grains have a serrate size range (700 - <20 μm) and have compositions typical of the range seen in mare basalt samples: An_{89-98} Al_{2-10} $Or_{0-0.4}$ (Fig. 4.11). The most sodic of these plagioclases are often associated with small late stage symplectic mesostasis assemblages (silica, ulvöspinel, fayalite, K-glass, apatite, whitlockite, troilite). Ilmenite is present in all of the clasts as an accessory phase (<10 %) as either small elongate grains (Fig. 4.6c,d) or small anhedral grains (Fig. 4.6a,e; Fig. 4.7a). Estimates of bulk sample major element composition (Table 4.2) suggest that they have a low-Ti affinity (1.6 to 3.4 wt.% TiO_2) following the recommended classification of mare basalts (Neal and Taylor, 1991).

Bulk minor and trace element composition (Fig. 4.18b, Table 4.2) was also measured in the small intergranular basalt clast shown in Figure 4.6d using in-situ LA-ICP-MS. Its bulk REE composition is plotted in Fig. 4.8b and it has a similar flat LREE, negative Eu-anomaly and flat HREE trend (albeit at an increased REE composition) to the evolved mare basalts LAP 02224/02205. It appears to be very rich in Th (Table 4.2: 6 ppm). However, this fragment is very small, and possibly samples only a late-stage mineral assemblage; therefore it may be under-representative of the complete basalt bulk composition, and should be viewed with caution as being representative of the Th-concentration of this lava flow.

Trace element compositions (Table 4.3) of pyroxenes and plagioclases were investigated in a single intergranular basalt clast pictured in Figure 4.7a,b,c. CI-normalised (Andres and Grevesse, 1989) REE concentrations are illustrated with their reconstructed melt compositions in Figure 4.8. The pigeonites investigated (Mg-core composition [PYXB] to an evolved near rim compositions [PYXC]) have positive LREE trends, negative Eu-anomalies and flat HREE trends. Plagioclases have slightly negative LREE trends, large positive Eu-anomalies, and relatively flat-slightly negative HREE profiles. These compositions are very similar to ion probe compositions for basalts in MET 01210 reported by Day et al. (2006) and are also similar to mineral compositions measured using LA-ICP-MS in the evolved ferro-basalt meteorite LAP 02205 (Joy et al. 2006). Reconstructed melt REE profiles suggest a crystallisation from a basaltic melt with REE concentrations x 100 to x 2000 chondritic (Fig. 4.8a). The plagioclases grains analysed seem to have crystallised out at a slightly earlier stage (REE-poorer source melt) than analysed pyroxene grains, with later co-crystallisation of the two mineral species.

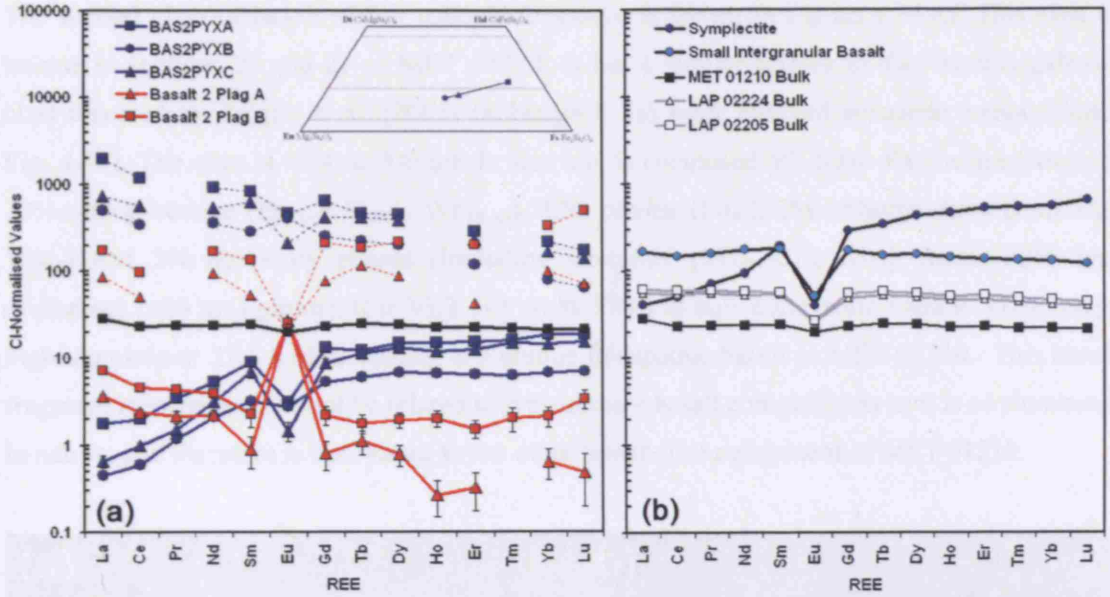

Fig. 4.8. (a) REE compositions of plagioclases and pyroxenes (Table 4.3) from intergranular basalt shown in Figure 4.7a,b,c measured in situ using LA-ICP-MS. Melt REE-concentrations (dashed lines) have been calculated using the distribution coefficients collated by Snyder et al. (1998). Inlay shows the compositions of pyroxenes investigated. (b) Bulk REE composition of symplectites clast (Table 4.4) and small intergranular basalt clast (Fig. 4.6d). Bulk clast analysis is compared with bulk MET 01210 analysis (Table 4.5) and bulk element concentrations of low-Ti evolved basaltic meteorites LAP 02224 and 02205 (Table5.2) as reported by Joy et al. (2006). All elemental concentrations have been normalised to CI-chondrites (Anders and Grevesse, 1989).

Plumose basalts. Plumose basalts include rapidly-crystallized fine-grained clasts that have a distinctive feathery or plumose texture with a low-Ti mare basalt affinity (Fig. 4.6a,b). Some early-formed pyroxene microcrysts (<400 μm) display zonation from Mg-rich cores to Fe-rich rims and appear to have been crystallised before a secondary quenching event where pyroxene microcrysts (<100 μm) were co-crystallised with feathery (<50 μm) plagioclase needles. Accessory phases include small fayalite, ilmenite, chromite and ulvöspinel grains distributed interstitially to the pyroxene microcrysts. These textures are similar to quenched basaltic textures identified by Day et al. (2006) in MET 01210 and in the Low-Ti lunar meteorite NWA 032 (Zeigler et al. 2005; Day et al. 2007).

Subophitic basalts. There are two distinct types of subophitic basalts identified in MET 01210. The first is illustrated in Fig. 4.6f and is very similar to 'Class AA' discussed by Day et al. (2006). It has narrow, elongate euhedral plagioclase phases (<500 μm: An_{95}) subophtically enclosed by large zoned pyroxene phases (Fig. 4.10) that have rims with extreme Fe-enrichment: En_{1-41} Fs_{47-80} Wo_{11-28}. Accessory phases include ilmenite laths, ulvöspinel grains and troilite blebs (<50 μm). They are likely associated with the low-Ti mare basalt suite described above.

The second class of basalt with a subophitic texture is shown in Figure 4.7d,e,f. This clast is unique in sections 21 and 27 of MET 01210. Is has a similar texture to the 'basaltic-gabbro' clast reported by Zeigler et al. (2005) (although it has more evolved pyroxene compositions: Fig. 4.10). The clast is ~900 x 900 μm in size and is composed of ~50% plagioclase (An_{93-97}), 22% clinopyroxene (En_{41-44} Fs_{25-27} Wo_{28-33}), 22% olivine (Fo_{49}), 3% orthopyroxene (En_{45} Fs_{45} Wo_{11}) and 2% accessory phases (including Cr-spinel [$2Ti_{49}$ Cr_{39} Al_{13}], minor FeNi and ulvöspinel [<20 μm] grains). It is VLT (<1 wt.% TiO_2) in bulk composition and is VHA (very-high aluminium: 27.4 wt.%), making it a unique feldspathic basalt in MET 01210. This basalt fragment is interpreted to not be related to typical mare basalt compositions as it is so aluminous in nature, and therefore is not related to the other basalt clast component of MET 01210.

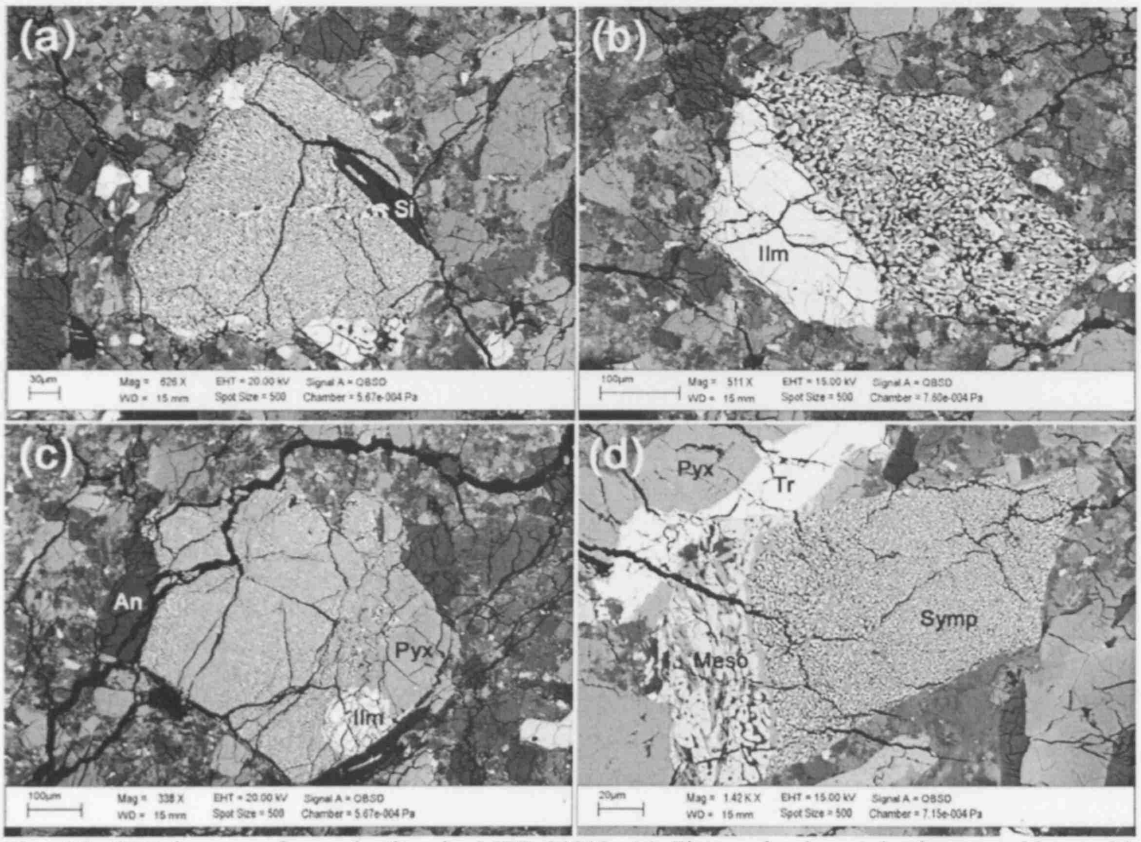

Fig. 4.9. BSE images of symplectites in MET 01210. (a) Fine grained symplectite assemblage with coexisting larger grains of primary crystallised silica, fayalite and Fe-rich pyroxene (i.e. typical mesostasis assemblage). (b) Coarser, granulised, symplectites aggregate with co-existing large subhedral ilmenite grain. (c) Fine grained variety. (d) Fine grained symplectite in contact with late-stage mesostasis assemblage rich in K-rich glass, fayalitic olivine and silica. An = anorthite. Symp = symplectite. Meso = mesostasis. Ilm = ilmenite. Si = silica. Pyx = pyroxene. Tr = troilite.

Symplectites. These small clasts (Fig. 4.9) have a texture of either very fine grained or granular-like intergrowths of silica, fayalite (Fo_{6-7}) and hedenbergite (En_{2-32} Fs_{34-94} Wo_{2-40}). They are often found in an association with ilmenite and ulvöspinel grains. These clasts represent the collective break-down products of late-stage unstable pyroxferroite or ferrosilite (Oba and

Kobayashi, 2001) and I interpret them to be originally formed in association with the large monomict pyroxene fragments that are seen throughout the matrix of MET 01210 (some containing small regions of symplectic breakdown). The bulk composition of three symplectite clasts is listed in Table 4.4. They have very Fe-rich (39 to 46 wt.% FeO) compositions similar to the composition of their original pyroxene state (although they have slightly excessive SiO_2 in a similar manner to those described by Oba and Kobayashi, 2001 in Asuka-881757). Bulk REE concentrations are typical of a very-evolved pyroxene composition (Fig. 4.8b, Table 4.4) with a positive C1-normalised LREE trend, a negative Eu-anomaly and a flat HREE profile.

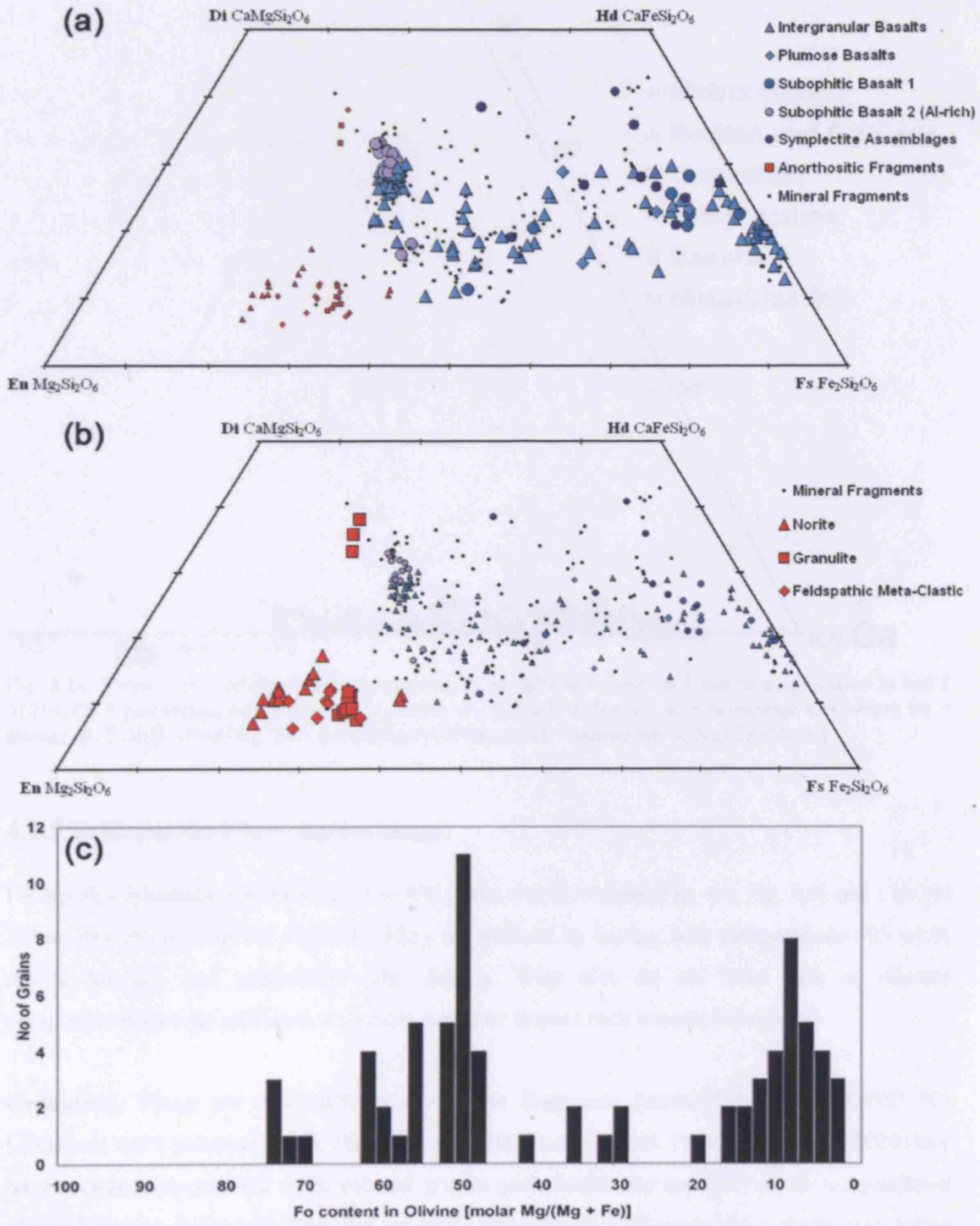

Fig. 4.10. (a) Pyroxene composition variation in the different lithic and monomineralic clasts in MET 01210. Basaltic clast types are highlighted in (a). Anorthositic clast species are highlighted in (b). (c) Histogram of range of olivine compositions in MET 01210.

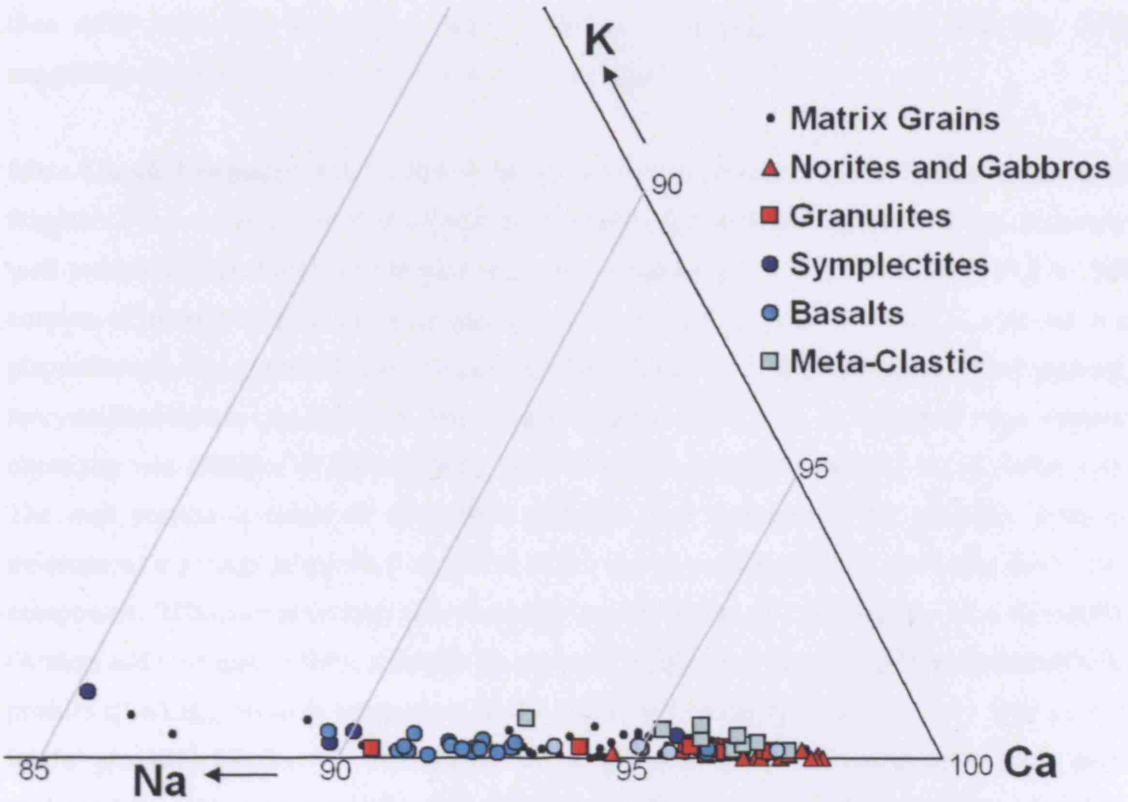

Fig. 4.11. Ternary plot of plagioclase compositions in different clasts and matrix plagioclases in MET 01210. Ca = percentage An# where An = atomic wt. % Ca/[Ca+Na+K]. K = percentage Or# where Or = atomic wt. % K/[Ca+Na+K]. Na = percentage Al# where Al = atomic wt. % Na/[Ca+Na+K].

4.2.3 Feldspathic Clast Assemblage

Feldspathic igneous clasts make up 3 to 4% of the whole sample (Fig. 4.3, Fig. 4.4) and 1 to 2% of the 500-20 μm fraction: Fig. 4.4). They are defined by having bulk compositions >25 wt.% Al_2O_3, $Mg\#_{40-80}$ and plagioclase with An_{94-98}. They also do not have bulk or mineral compositions that are affiliated with mare basalt or impact melt breccia lithologies.

Granulites. These are recrystallised crystalline fragments (metamorphosed to >1000 °C: Lindstrom and Lindstrom, 1986; Papike et al. 1998; Cushing et al. 1999, Cohen et al. 2004) that have rounded-sub-rounded mafic mineral phases granoblastically enclosed within recrystallised plagioclase (Fig. 4.12a,b,c). They are generally fine-grained with mafic phase chadacrysts being <30 μm in size. Compositions in mafic mineral phases have been reequilibrated, are of near constant composition (olivine = Fo_{60-61} and pyroxene = En_{45-60} Fs_{18-32} Wo_{8-35}), and are unzoned. Plagioclases show a compositional range of An_{90-97}. Bulk compositions (Table 4.6) of granulites are the equivalent of anorthositic-norite troctolitic or anorthositic troctolitic ferroan anorthosites. Bulk REE-profiles in one large investigated clast (Fig. 4.12a,b,c, Table 4.6) are relatively flat ($[La/Lu]_{cn}$ = 0.9) with a positive Eu-anomaly (Eu/Eu* = 3.6). REE concentrations are higher

than most FAN-suite samples (compare with clasts investigated in DaG 400: Fig. 3.7), suggesting a contribution from a non-pristine FAN source.

Meta-Clastic Fragment. MET 01210,27 is dominated by a large triangular shaped meta-clastic fragment (~3 x 4 mm). The clast consists of two texturally differing regions. A relict, relatively well preserved granulitic textured portion (appears translucent in PPL microscopy: Fig. 4.12d) consists of intergrown annealed pyroxene (En_{58-68} Fs_{23-34} Wo_{6-12}) and olivine (Fo_{69-73}) phases in a plagioclase (An_{93-97}) groundmass. These granulitic regions are held together in a fine grained, recrystallised matrix (appears dark, brown opaque phase in PPL: Fig. 4.12d). Bulk trace element chemistry was obtained of the two lithic portions of this annealed clast (Fig. 4.14a, Table 4.4). The melt portion is richer in siderophile elements than measured in the granulitic portion: evidence of a greater proportion of melted mafic phases and possibly an additional meteoritic component. REE-concentrations are reasonably similar in the two portions at ~10 x chondritic (Anders and Grevesse, 1989), although the granulite portion has poorer-LREE and richer-HREE profiles ($[La/Lu]_{cn}$ =0.6) in comparison to the impact melt portion($[La/Lu]_{cn}$ = 1.1). This profile in the granulitic portion is evidence for the presence of abundant pyroxene phases. Both portions have very similar positive EU-anomalies (Eu/Eu* = 3.5 to 3.7), suggesting a similarly fractionated proportion of plagioclase between the two components.

This large fragment is interpreted as being very similar to the granulite material discussed above, but has not experienced as high temperature / pressure metamorphic regimes. It therefore represents a rock at an intermediate stage between being a relic igneous anorthositic noritic troctolite bedrock fragment and being a highly altered granulite (similar to that shown in Fig 4.12a).

Cataclastic Troctolite. MET 01210,27 contains a small, heavily fractured and cataclastic clast of troctolitic material (55% plagioclase, 42% olivine). Its bulk composition is indicative of being affiliated with rocks in the HMS-suite.

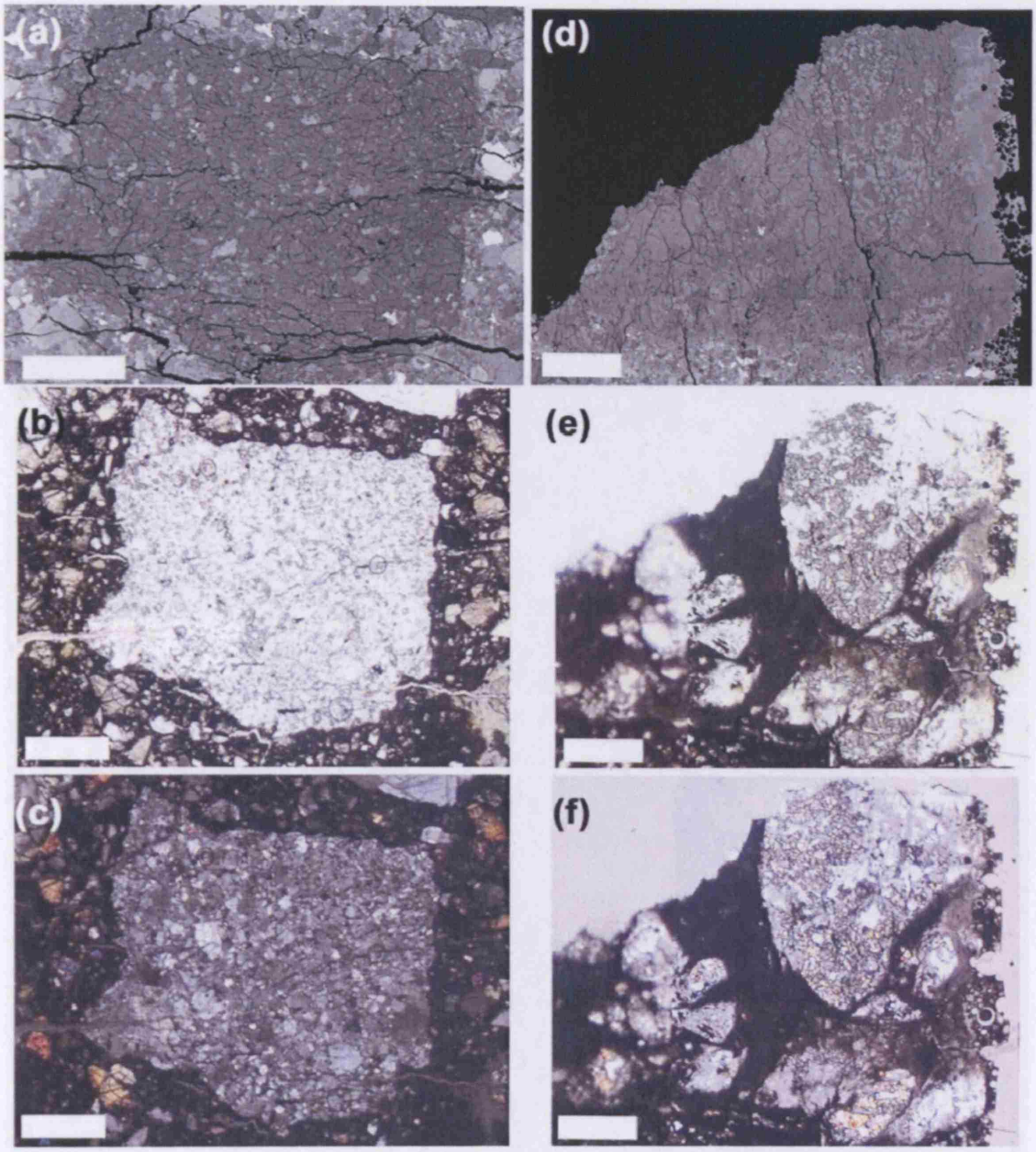

Fig. 4.12. Feldspathic clasts in MET 01210. (a) BSE image of large granulite in MET 01210,27; small thermally annealed olivine and pyroxene grains are poikiloblastically enclosed in anorthosite groundmass. (b) Plane and (c) cross polarised light microphotograph images of same clast. (d) Large meta-igneous anorthositic clast in MET 01210,27; remnant thermally annealed anorthositic troctolite fragments are enclosed by dark glassy regions that have been completely melted by impact thermal metamorphism. (e) Plane and (f) cross polarised light microphotographs of the clast in (d) illustrating the relationship between melt regions and surviving igneous clast fragments. Scale bar = 400 μm in all images.

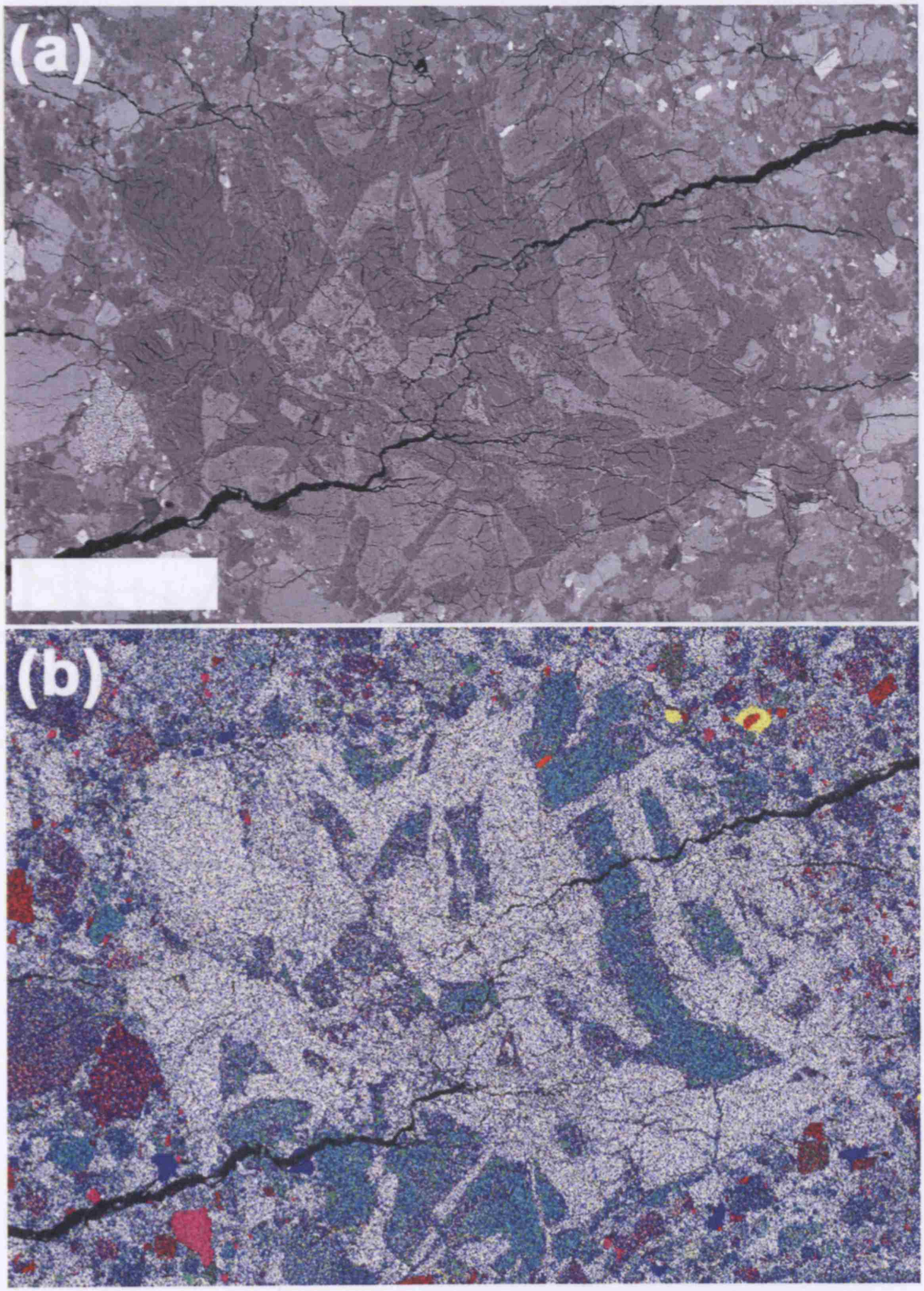

Fig. 4.13. (a) BSE image of norite clast in MET 01210,21. (b) False colour image of same clast with the same colour scheme as in Fig. 4.3. Pyroxenes in clast (dark green phases) are the most Mg-rich of any studied in the sections. Scale bar = 400 μm in both images. Bright yellow phases = apatite grains. Bright pink = ilmenite.

Norite. This large clast (1.5 x 1 mm) in MET 01210,21 (Fig. 4.13) is evidence of the presence of mafic-magnesian FAN material in MET 01210 (MM FAN). Large plagioclase (60%: An_{94-97}) masses (400 to 600 μm) and smaller lath-shaped plagioclases (100 to 500 μm) enclose magnesian orthopyroxene (~40%: <500 μm) phases that are zoned from Mg-rich cores to more Fe-rich rims (Fig. 4.13b; En_{58-72} Fs_{20-25} Wo_{7-18}). The plagioclase grains are cross-cut by Fe-rich glass melt veins (<10 μm across) and some of the pyroxene rims have break-down/melt textures indicating that the clast must have experienced a powerful shock event.

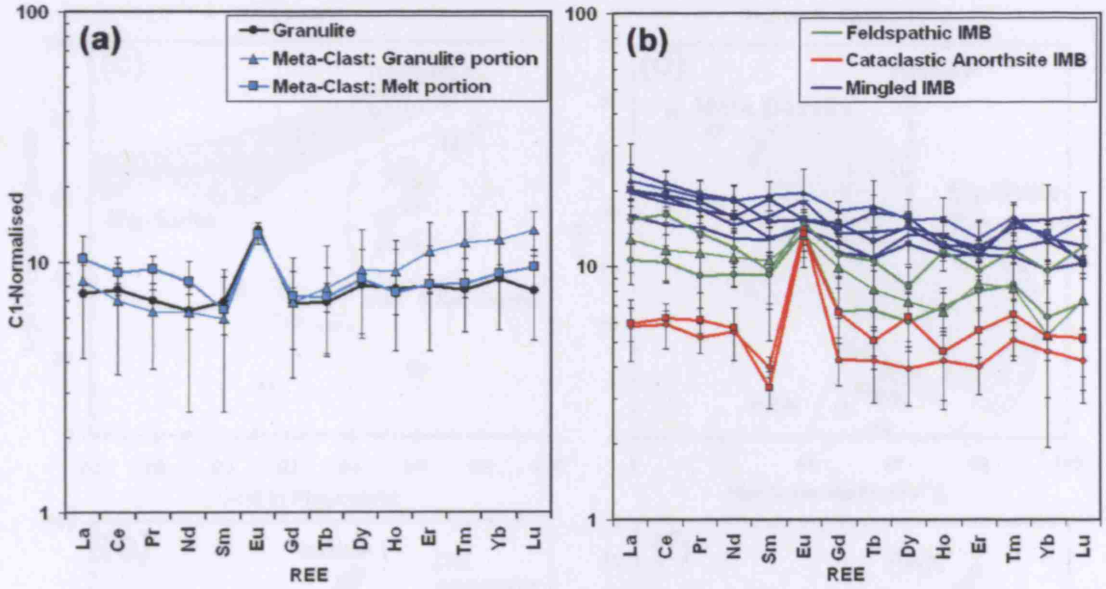

Fig. 4.14. (a) REE concentrations normalised to C1-chondrites (Anders and Grevesse, 1989) in feldspathic clasts in MET 01210,27. Errors bars represent the standard deviation from the 2-5 spots measured in each clast (see Table 4.7 and 4.8 for elemental concentration list). (b) REE-C-1 normalised profiled in impact melt clasts in MET 01210,27. There is a clear difference between those clasts with a feldspathic or mingled affinity.

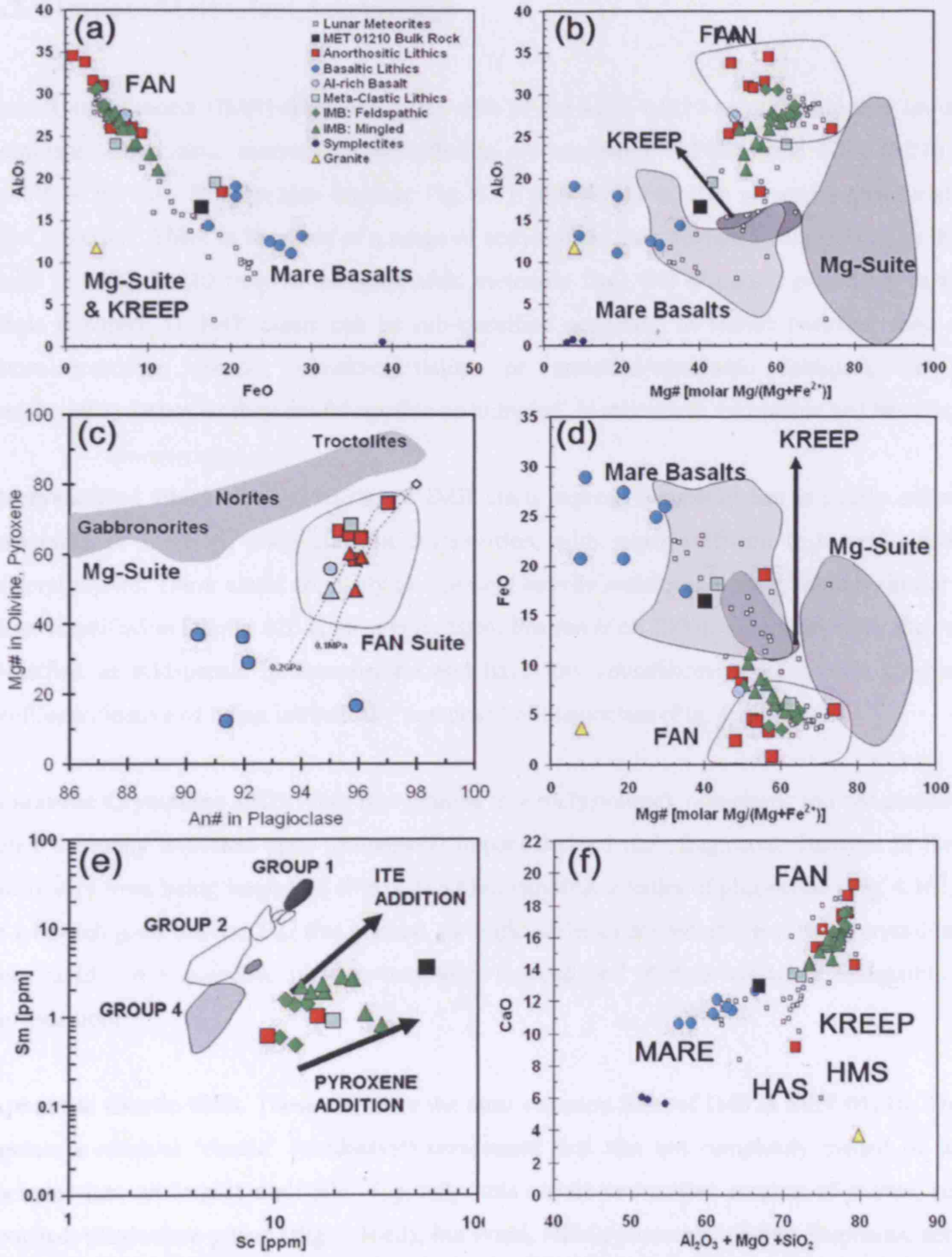

Fig. 4.15. Elemental variability among clasts in MET 01210. Clast compositions are listed in Table 4.2, 4.4, 4.6, 4.7 and 4.8. Bulk rock element chemistry is listed in Table 4.5. (a) Clasts compared with lunar meteorite trend between Al_2O_3-rich FAN lithologies and FeO-rich mare basalt compositions. (b) Mg# vs. Al_2O_3 (c) Mafic mineral Mg# vs. plagioclase An# illustrating relationship between FAN rocks and Mg-Suite samples; circles represent Mg# in olivine grains, triangles represent pyroxene Mg# for the same grains. (d) Mg# vs. FeO. Apollo bulk rock fields and lunar meteorite compositions are taken from a number of sources including Heiken et al. (1991), Papike et al. (1998) and Wieczorek et al. (2006) and references therein. (e) Comparison of IMB clasts (and feldspathic clasts) to Apollo 16 IMB groups. (f) Clasts in MET 01210 plotted on an elemental plot showing a mixing of three end-member compositions (mare basalts, FAN samples and KREEP/HMS/HAS samples). Most clasts plot on the mixing trends between FAN and mare basalts. The troctolite clast investigated in this work is grouped with more Mg-suite (HMS) lithologies and the granite clast (section 4.2.5) is similar to evolved Apollo HAS rock types.

4.2.4 Impact Melt Clast Assemblage

Impact melt breccia (IMB) fragments form ~6% of the MET 01210 regolith, and they are the dominant lithic clastic assemblage identified in sections MET 01210,21 and MET 01210,27 (~46% of the 20 - 500 μm size fraction: Fig. 4.5): they are even more numerous than basaltic clast material. There is far more of a range of textures and bulk chemical composition in IMB clasts in MET 01210 than in the feldspathic meteorite DaG 400 discussed previously in this thesis (Chapter 3). IMB clasts can be sub-classified according to texture (whether they are micro-crystalline, clastic, clastic-crystalline or annealed/cataclastic feldspar), or by geochemistry (whether they are feldspathic or 'mingled' [a mixture of feldspathic and basaltic]).

Recrystallised Plagioclase IMB. Some IMB clasts represent material that is nearly entirely cataclastic or remelted plagioclase in composition, with minor (difficult to identify) mafic mineral phases. These clasts are likely to represent heavily metamorphosed granulites similar to those identified in Dhofar 026 (Cohen et al. 2004; Warren et al. 2006). Compositionally they are classified as feldspathic in composition and have low abundances of REE, with C1-norm profiles indicative of being intrinsically composed of plagioclase (Fig. 4.14b).

Aphanitic Crystalline IMB. Very fine grained (microcrystalline), non-clastic (do not contain a relict thermally annealed clast component) impact derived melt fragments. Textures in these clasts vary from being intersertal (Fig. 4.16a,b) to variolitic needles of plagioclase (Fig. 4.16c,d) in a Fe-rich glass matrix. The fine grained variolitic varieties are indicative of being crystallised very rapidly in a quenched melt environment. Typically all of these clasts are feldspathic in composition.

Aphanitic Clastic IMB. These clasts are the most common form of IMB in MET 01210. They contain a residual 'clastic' (chadacryst) component that was not completely melted or was included into an impact melt pile. Typically, this clastic component consists of serrate, sub-rounded, plagioclase grains (Fig. 4.16e,f), but small, relict pyroxenes, olivines fragments, and a small noritic granulite clast have been observed in IMB in the sections discussed here. Some of the more feldspathic varieties of clastic IMB contain a matrix with recrystallised micro-laths of plagioclase. Whether any given clast can be defined as feldspathic or mingled is dependent on the proportion of impact melt to plagioclase clast/crystal component (Fig. 4.14b). The more mafic (or 'mingled') clasts always have an enriched REE signature, and smaller or no Eu-anomalies.

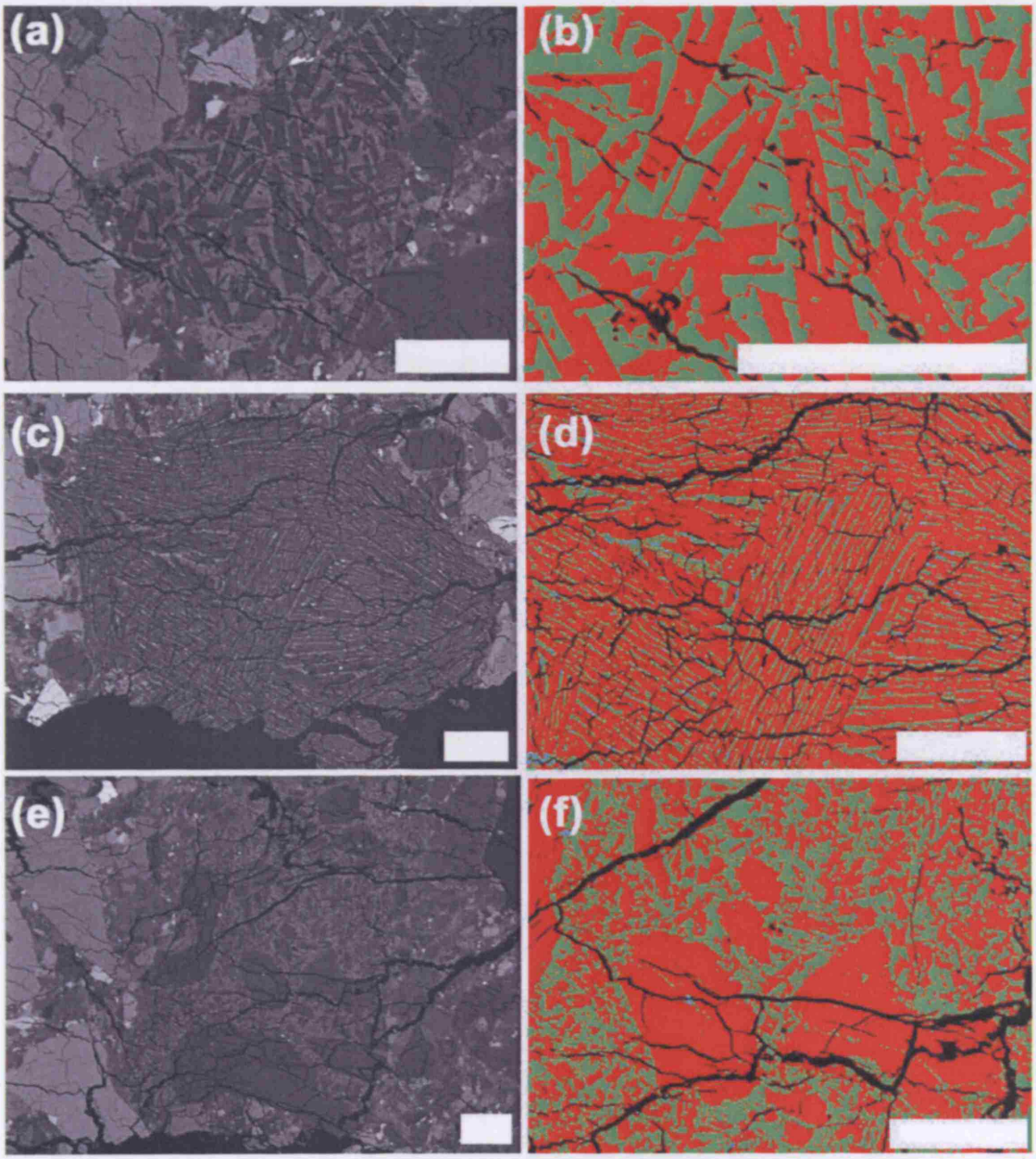

Fig. 4.16. Study of impact melt breccia (IMB) clast textures in MET 01210,27. (a) BSE image of microcrystalline intersertal impact melt clast where plagioclase has been devitrified from the glassy melt phase to form small (<100 μm) equant laths (some caution is needed as this may be a small fragment of the matrix of a clastic breccia). (b) False colour image of the texture of IMB shown in (a). Red corresponds to BSE dark grey phases (plagioclase), green to BSE mid-tones (mafic impact melt), black to BSE black tones (fractures) and turquoise to BSE white tones (troilite or FeNi blebs). (c) BSE image of an aphanitic feldspathic IMB with barred micro-laths of plagioclase enclosing very fine grained interstitial mafic melt. (d) False colour image of the texture of IMB shown in (c) with same colour scheme as described above. (e) BSE image of a clastic-feldspathic impact melt clast with seriate annealed anorthosite chadacrysts enclosed in a vitrophyric mafic melt matrix. (f) False colour image of the texture of IMB shown in (e) with same colour scheme as described above. Scale bar = 100 μm.

4.2.5 Monomict Mineral Fragment Assemblage

Pyroxenes. Monomict pyroxene clasts span a size distribution from large grains (<800 μm) to tiny matrix component material (<20 μm). Larger sized grains are indicative of extremely slow cooling conditions from a shallow intrusive setting, or from the deep interior of a thick lava flow. Matrix pyroxene compositions span the spectrum of typical basaltic compositions (Fig. 4.10a), even to very Fe-rich pyroxene compositions and to Fe-hedenbergite compositions typically affiliated with symplectite associated pyroxene phases. A minority of grains are more Mg-rich and are affiliated with the feldspathic suite discussed above.

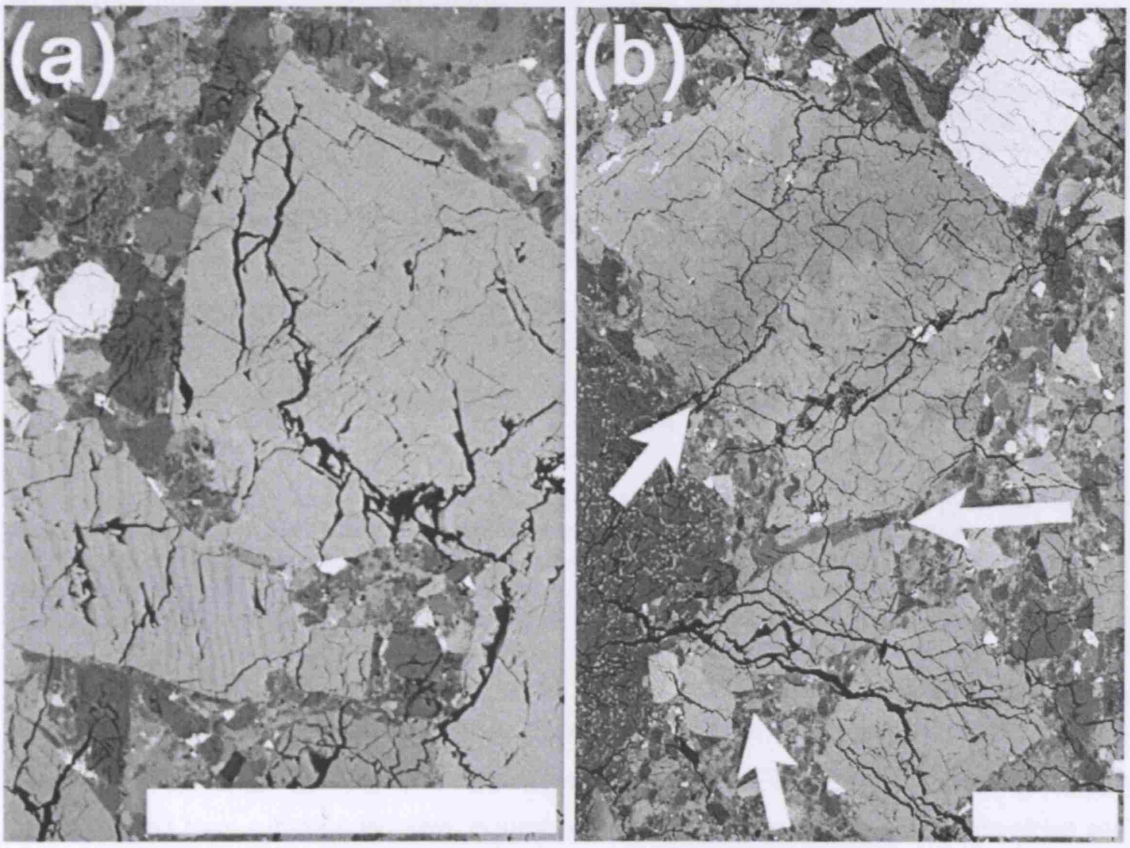

Fig. 4.17. (a) Equilibrated pyroxene fragments with differing thicknesses of exsolution lamellae in MET 01210. (b) Mineral aggregate of large unequilibrated zoned pyroxene (top arrow: enclosing small breakdown fayalite-silica micro-grains), bordering small plagioclase grain (central arrow: elongate, thin grain) and coexisting exsolved pyroxene fragment (bottom arrow). Scale bar = 100 μm in both images.

Pyroxene textures vary widely throughout the sample. Some are completely homogenous, whilst others display complex, and not-continual, zonation from Mg-rich cores to Fe-rich rims (Fig. 4.17b). Fractionated grains, like that shown in Figure 4.17b, also contain small grains of silica and fayalitic olivine along Fe-rim boundaries: evidence of the onset of ferrosilite breakdown and conversion to symplectite assemblage phases (Fig. 4.9). Exsolved pyroxene grains (typically cpx lamellae in opx/pigeonite host) are commonly distributed throughout the sections. Lamellae vary in width (<1 to 5 μm) depending on orientation of the grain orientation in the thin

section. These equilibration features have been also discussed by Huber and Warren (2005) and Day et al. (2006).

Trace elements have been measured in a number of matrix pyroxene grains (not associated with lithic clasts) throughout MET 01210,27 (Table. 4.9, Fig. 4.18a,b). Compositions in some grains are similar to those measured in core pyroxenes from the basalt clast shown in Figure 4.8. More REE-rich composition (Fig. 4.18b), are akin to compositions measured in pyroxenes in ferro-basalt LAP 02205 (Fig. 5.6), indicating that pyroxenes included into the MET 01210 regolith are sourced from a highly-fractionated magmatic basaltic environment.

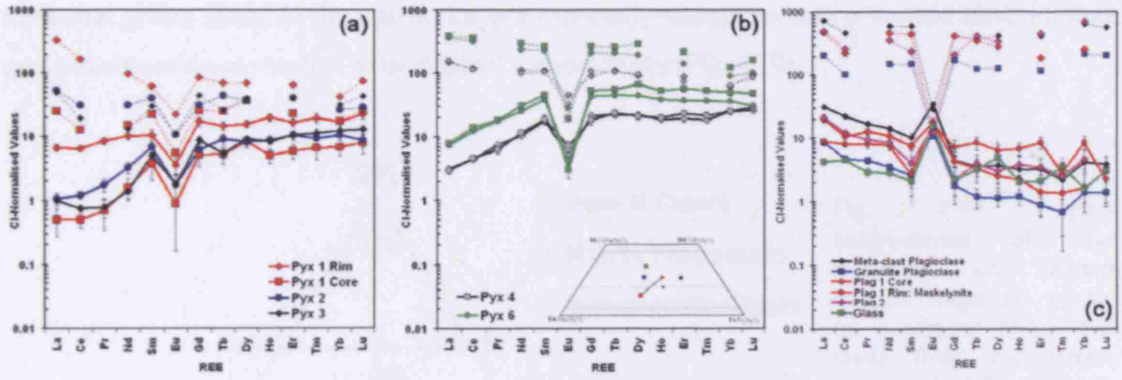

Fig. 4.18. Chondrite normalised (Anders and Grevesse, 1989) REE-profiles in (a) (b) pyroxenes and (c) plagioclases in MET 01210. Also shown are the mineral's reconstructed melt compositions; mineral-melt distribution coefficients are taken from those compiled by Snyder et al. (1995). Inlay in (b) displays ternary pyroxene plot for grains investigated by LA-ICP-MS. (c) Plagioclase and glass fragment REE measured in MET 01210,27. Error bars represent 1 sigma error calculated from variance of standard NIST 612 measured (provided by Glitter software). See Table 4.9 and 4.10 for a full element list.

Plagioclases. These are heterogeneously distributed as large (>700 μm) monomict clastic fragments and as smaller fragments throughout the matrix of MET (Fig. 4.20a). They are subhedral and have sub-rounded rims, typical of material that has undergone communition and fragmentation in regolith gardening processes. The majority of grains also no longer display relict twinning, and have experienced differing degrees of conversion to shock glass ('maskelynisation'). Monomict plagioclase fragments are compositionally diverse (Fig. 4.11: An_{86-98}) and match the range measured within lithic clasts associated plagioclase from both the feldspathic and mare basalt suites represented in MET 01210. Trace element investigations of large plagioclase fragments (Table, 4.10, Fig. 4.18c) suggest that they were sourced from compositions akin to, but more evolved than, those grains investigated in the basalt clasts discussed above (Fig. 4.8).

Olivine. Olivine fragments distributed throughout the MET matrix vary from Mg-rich compositions affiliated with anorthositic lithologies ($Mg\#_{48-58}$), to those fayalitic varieties

($Mg\#_{2\text{-}20}$) that are likely derived from late-stage crystallisation of an evolved mare basalt/gabbroic parentage (Fig. 4.20d). Olivines with an intermediate range of composition ($Mg\#_{30\text{-}48}$) are likely also to have been derived from mare basalt/gabbro lithology and maybe represent fragments (rims?) of more forsteritic olivines, associated with an earlier crystallisation heritage of the fayalitic grains discussed above.

Oxides. Monomict clasts of ilmenite (50 to 54% TiO_2, 42 to 47% FeO) occur frequently in the matrix of MET 01210, providing evidence that the original regolith environment was dominated by mare basalts/gabbros with a low-Ti affinity. These grains are occasionally large (<500 μm: Fig. 4.20d), and have characteristic parallel to sub-parallel fractures. Spinel fragments are far rarer, and grains found in the matrix (i.e. not especially associated with a basaltic clast) all have evolved chromian-ulvöspinel to ulvöspinel compositions (Fig. 4.19).

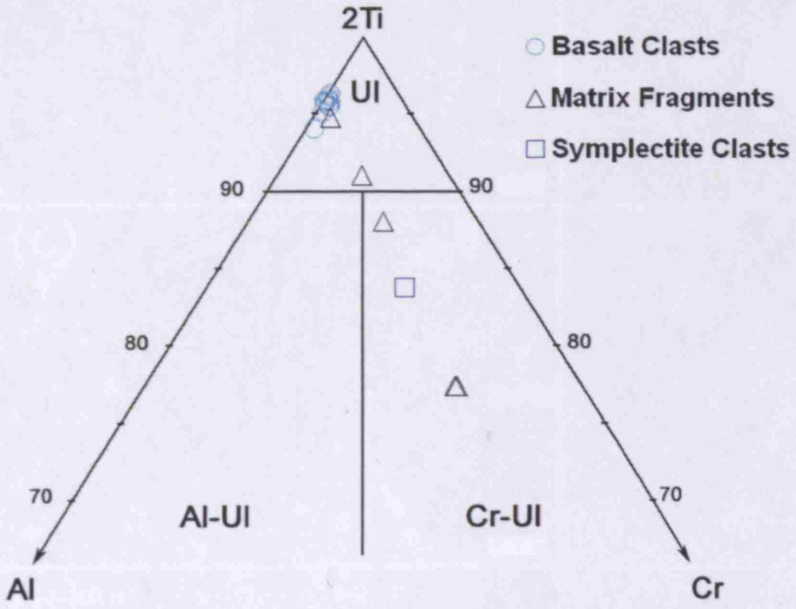

Fig. 4.19. Spinel compositions of clast associated and random mineral fragments plotted on a ternary spinel plot made from end-member ulvöspinel (2Ti), Chromite (Cr) and Hercynite (Al). Abbreviations in plot: Al-Ul = aluminous-ulvöspinel, Cr-Ul = chromian-ulvöspinel, Ul = ulvöspinel

Silica. Silica grains (e.g. Fig. 4.20c) are heterogeneously distributed throughout MET (Fig. 4.3a,d: blue coloured mineral phases). They are remarkably large in places (up to 400 μm) and display a seriate grain size down to small matrix fragments (<10 μm). They were likely formed as part of the late-stage mineral assemblage in the mare gabbroic lithologies described above (similar to that reported in lunar mare gabbro meteorite MIL 05035: Joy et al. 2007). One particular large fragment (400 x 200 μm) in MET 01210,27 (mapped on Fig. 4.3c as 'mesostasis/granite' and listed in Fig. 4.15 as 'granite'), represents a residual mesostasis aggregate and is intimately intergrown with K-rich glass, mafic glass veins, K-rich feldspar and small blebs of troilite and ulvöspinel.

Accessory Phases. Minor mineralogical phases identified in MET 01210 include troilite (Fe_{60-63} S_{34-37}) and metal fragments (Fe_{83-95} Ni_{2-14}). Late-stage phases such as apatite (Fig. 4.20f), whitlockite/merrillite (Fig. 4.20e) and tiny grains (<10 μm) of baddelyite (Fig. 4.20e) have also been identified and have been used to provide radiometric dating of the basaltic/gabbroic phases by Terada et al. (2007). Assuming that these phosphate grains were originally formed as part of the low-Ti basaltic crystallised assemblage, these age dates suggest that lava flows that emplaced these constituent basalts were crystallised at 3904 ± 86 Ma Terada et al. (2007)), and therefore represent some of the oldest radiometrically age dated lunar basalt complexes (Hiesinger and Head, 2006).

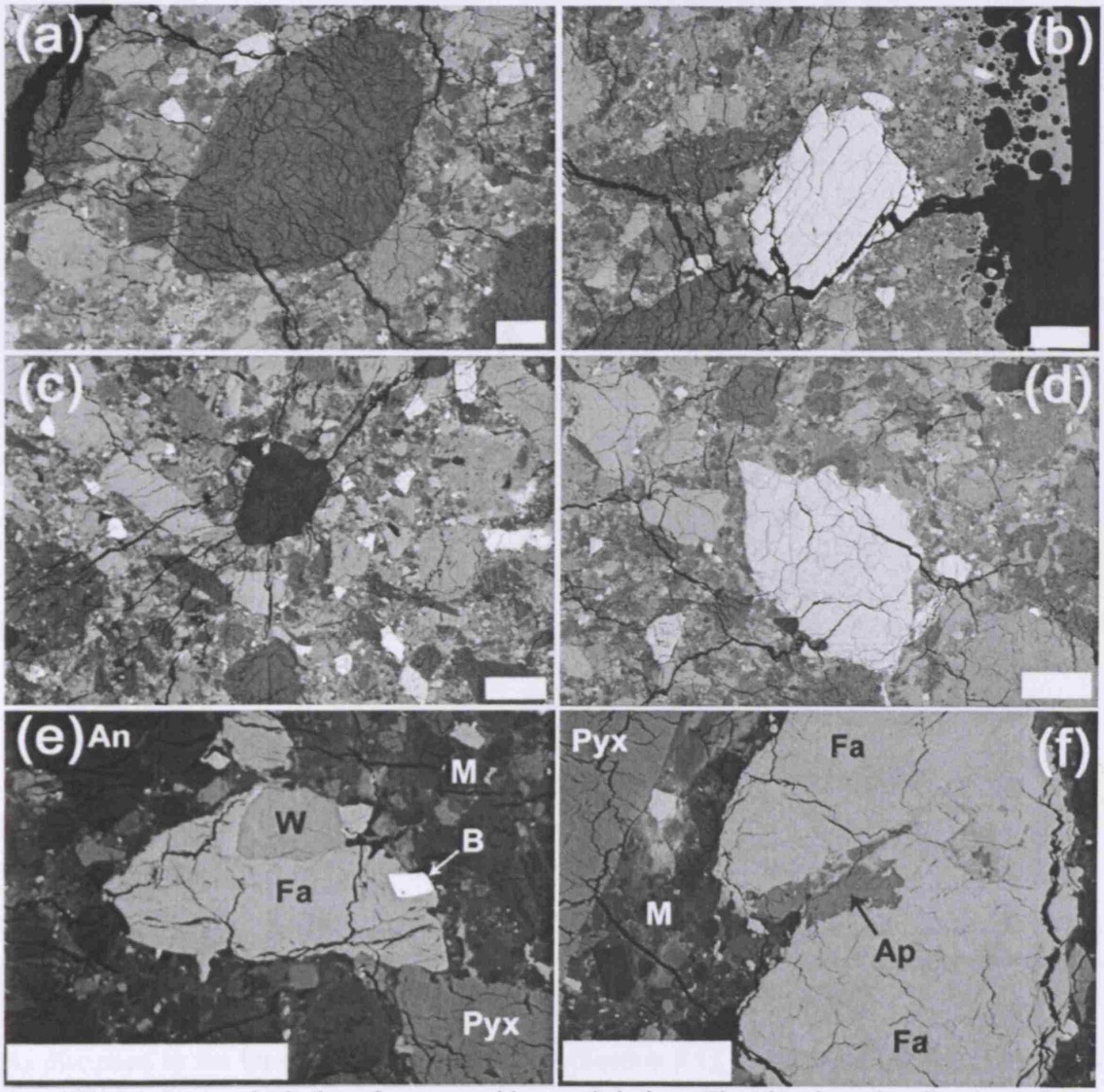

Fig. 4.20. (a) Large plagioclase fragment with rounded rims. Clast has been heavily shocked and fractured. (b) Ilmenite monomict fragment; late-stage crystallisation mineral phases in matrix of MET 01210: (c) Large silica fragment and (d) fayalite grain. (e) Accessory phase whitlockite hosted within a fayalite grain, and co-existing with a small baddeleyite grain. (f) Apatite mass hosted within fayalite grain. M = matrix, An = anorthite, Pyx = pyroxene, B = baddelyite, W = whitlockite, Fa = fayalite and Ap = apatite. Scale bar in all in images = 100 μm.

4.2.6 Glass Beads

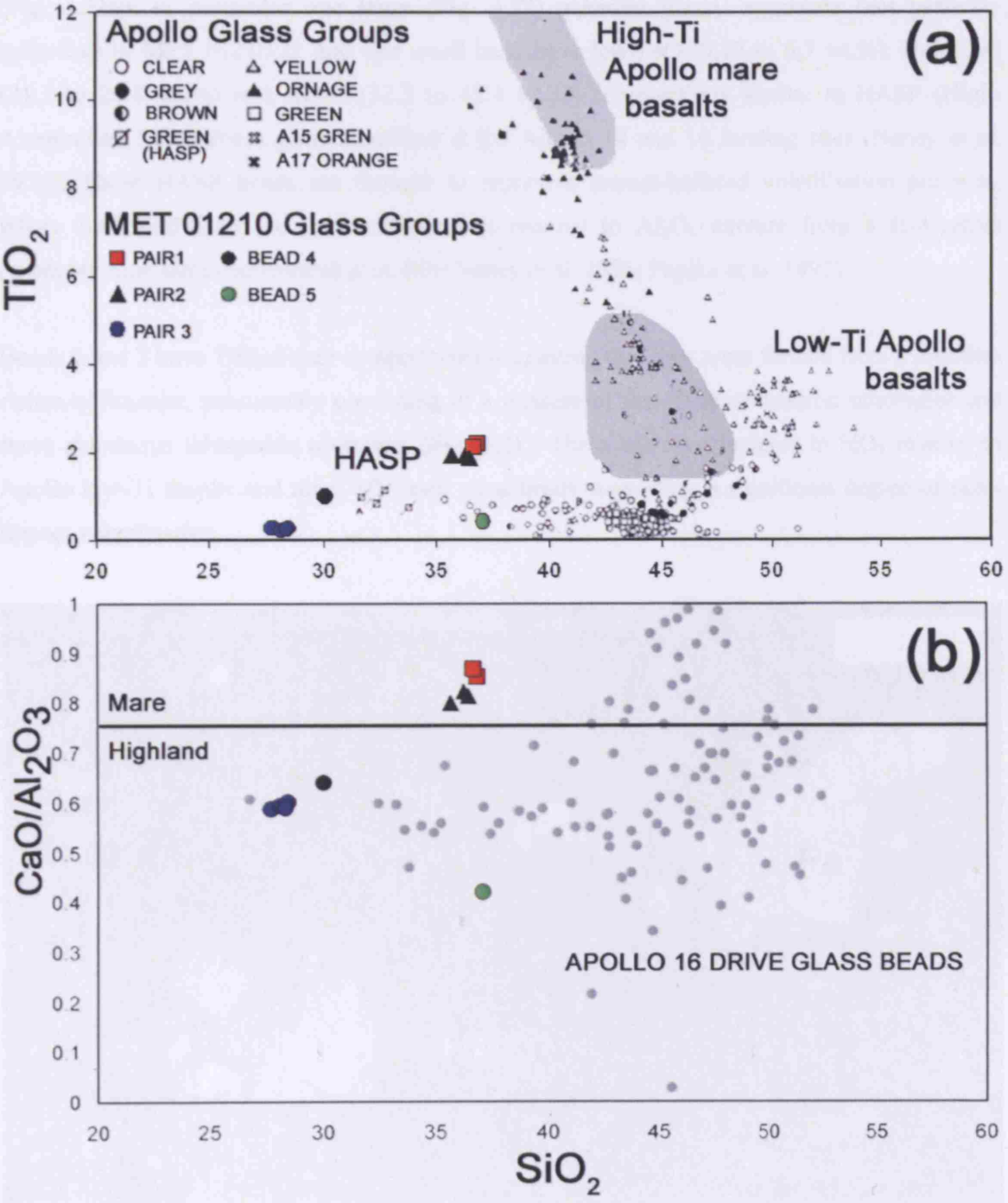

Fig. 4.21. Comparison of glass beads found in matrix of MET 01210 compared with (a) Apollo 16 soil and regolith glass fragments as reported in Figure 3 of Naney et al. (1976), and (b) glass beads identified in the Apollo 16 drive-shaft tube as reported by Kempa and Papike (1980).

As discussed in the introduction to this chapter (Section 4.1), glass fragments and glass beads are distributed heterogeneously throughout the matrix of MET 01210 (Fig. 4.2). Spherical beads (i.e. those not fragmented by communition processes) range in size from <20 to 100 μm and those analysed are all aluminous in nature (Fig. 4.21) and most similar in composition to low-Ti beads from the Apollo 16 (Naney et al. 1976, Kempa and Papike, 1980). These beads have

compositions that are depleted in SiO_2 relative to beads collected at the Apollo landing sites (Fig. 4.21a). In particular one large (Fig. 4.22) anhedral glassy aggregate (not perfectly spherical) in MET 01210,21 and one small bead have low-FeO (0.17 to 6.7 wt.%), high-CaO (21.1 to 25.1 wt.%) and Al_2O_3 (32.3 to 42.4 wt.%) compositions similar to HASP (High-Aluminium, Silica-Poor) glass identified at the Apollo 14 and 16 landing sites (Naney et al. 1976). These HASP beads are thought to represent impact-induced volatilisation products, where SiO_2 and FeO are preferentially lost relative to Al_2O_3 content from a feldspathic (probably near-pure anorthosite) protolith (Naney et al. 1976; Papike et al. 1997).

Beads 1 and 2 have TiO_2-richer compositions suggesting that they were formed from a protolith richer in ilmenite, presumably consisting of a mixture of low-Ti mare basaltic lithologies and more aluminous feldspathic protoliths (Fig. 4.21). These are also depleted in SiO_2 relative to Apollo low-Ti basalts and mare affiliated glass beads suggesting a significant degree of post-impact volatilisation.

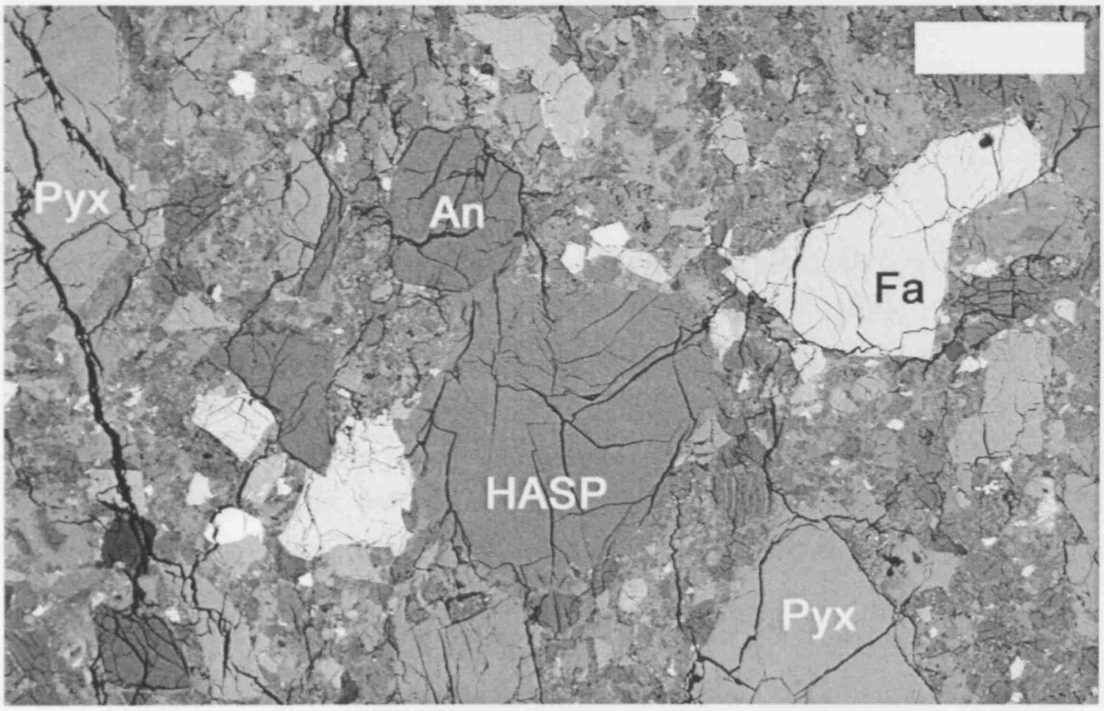

Fig. 4.22. Amorphous HASP glass fragment in MET 01210,21. Pyx = pyroxene, An = anorthite, Fa = fayalite. Scale bar = 100 μm.

4.3 Discussion

MET 01210 is a lithified, polymineralic lithic clast and monomineralic clast-rich regolith breccia. The regolith was consolidated in a mare basalt environment as ~45% of both sections are comprised of basalt clastic material (for the representative 20 to 500 μm size fraction). The feldspathic lithic clast component (~10%) is comprised of anorthositic rock fragments including granulites, meta-clastic rocks and a minor component of norite and troctolite material (Fig. 4.12, 4.13). Feldspathic, ITE-poor (Fig. 4.14, 4.15), impact melt breccias form the remaining 45% of the lithic clast component for this size fraction.

A seriate range of mineral fragments is heterogeneously distributed throughout the sample matrix. These include large zoned and exsolved pyroxene grains affiliated with a gabbroic VLT/low-Ti magmatic heritage. Large silica, fayalite and ilmenite grains indicative of a slow-cooling regime are likely to be from the same evolved gabbroic deposit. Mg-rich pyroxenes, forsteritic olivines and large anorthositic plagioclase fragments are more likely to have been sourced from highland lithologies.

4.3.1 Basalt Clast Parentage

I theorise that that the intergranular basalts and plumose basalt clasts originate from the same fractionally crystallised lava flow/pond as they have a similar low-Ti affinity (1.7 to 3.5 TiO_2 wt.%) and have similar mineral components and chemistries (Fig. 4.8, 4.10, 4.11, 4.23). Textural differences among the clasts and associated mineral fragments simply represent differences in cooling regimes: i.e. plumose textures were rapidly cooled and crystallised in proximity to flow margins, and coarser grained intergranular basalt clasts were thermally insulated within a flow/pond that cooled relatively slowly forming mineral grains in excess of 500 μm in size.

The extreme Fe-rich nature of the mafic mineral phases and bulk clast composition indicate that these plumose and intergranular fragments represent material from the same lava flow that experiences extreme fractionation from its magma source. They represent highly evolved mare basalt lithologies, poorly sampled by the Apollo mare collection, but similar in composition and mineral chemistry to the low-Ti evolved lunar meteorites LAP 02205/02224/0226/02436/03632 (Anand et al. 2005; Righter et al. 2005; Zeigler et al. 2005; Day et al. 2006; Joy et al. 2006b) and Asuka-881757 / Yamoto-793169 (Warren and Kallemeyn, 1993; Koeberl et al. 1993; Arai et al. 1996).

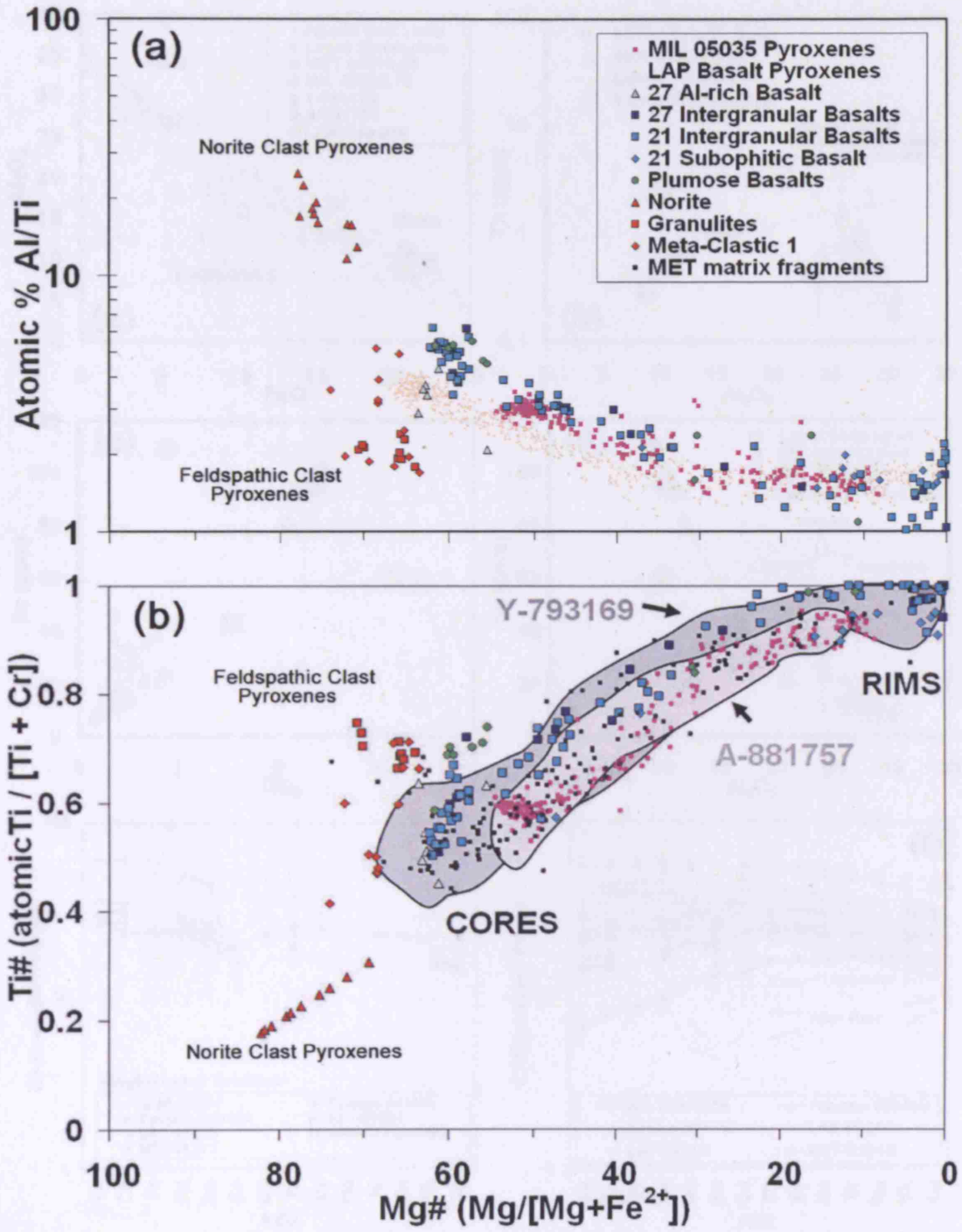

Fig. 4.23. (a) Al/Ti substitution in pyroxenes in basalt and feldspathic clasts in MET 01210, and in pyroxenes in Low-Ti mare basalts LAP (Joy et al. 2006b) and MIL 05035 (Joy et al. 2007). (b) Variations of Ti# in MET 01210 clasts and monomict mineral fragments compared with MIL 05035, and outline trends reported by Arai et al. (1996) in Y-793169 and A-881757.

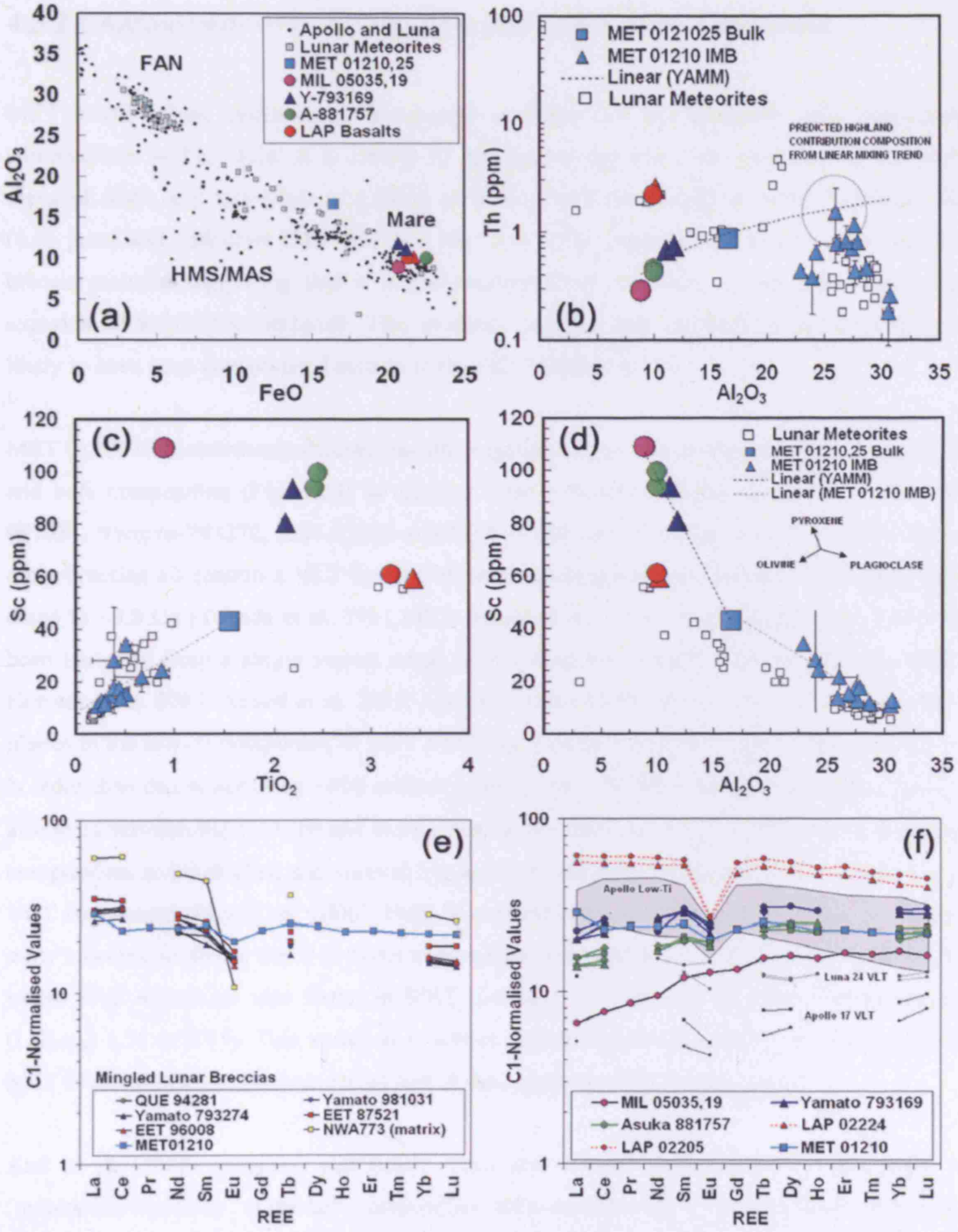

Fig. 4.24. (a)(b)(c)(d) Bulk Composition of MET 01210 (turquoise square) compared with possible paired stones MIL 05035 (pink symbol) (Joy et al. 2007), Asuka-881757 (green symbols) and Yamoto-881757 (dark blue symbols) (Warren and Kallemeyn 1993; Koeberl et al. 1993) and low-Ti lunar meteorite LAP (red symbols); other compositions are taken from a variety of sources. (e) MET 01210 bulk C1-normalised (Anders and Grevesse, 1981) composition compared with other 'mingled' lunar meteorite regolith breccias. (f) REEs compared with lunar VLT and low-Ti basalts and possible paired stones Asuka-881757, Yamoto-793169 and MIL 05035.

4.3.2 Comparison with Apollo Samples and Lunar Meteorites

MET 01210's bulk composition is reported in Table 4.5 and compared with lunar rock compositions in Fig. 4.24. It is similar to typical average mare soil compositions but with elevated Al_2O_3 and less MgO as a result of mixing with anorthositic material. Bulk-rock Th (0.86 ppm) and bulk-clast IMB Th (Th = 0.67 ± 0.37) is comparatively low for mare regolith breccia material suggesting that it is not dominated by clast and mineral components that experienced KREEP assimilation. This evidence suggests that the MET 01210 regolith was likely to have been consolidated distally to the PKT (Section 4.3.3).

MET 01210 is an anorthosite-bearing basaltic regolith breccia and is most similar in appearance and bulk composition (Fig. 4.24) to mingled lunar meteorite breccias QUE-94281, Yamoto-981031, Yamoto-793272, EET-87521 and EET-96008 (Q/E/Y stones: Korotev, 2005). These other breccias all contain a VLT basalt clast/mineral component that has been radiometrically dated to ~3.5 Ga (Takeda et al. 1991,1992; Anand et al. 1999), suggesting that they have all been launched from a single impact event from a common regolith (Arai and Warren, 1999; Korotev et al. 2003; Anand et al. 2003; Korotev, 2006). U-Pb age investigations of phosphate phases in the low-Ti component of MET 01210 by Terada et al. (2007) report that MET 01210 is older than this material by ~400 million years (3904 ± 86 Ma). Geochemical discrepancies also exist between MET 01210 and these other basaltic breccias: MET 01210 has a TiO_2-richer composition, as basalt clast and mineral fragments are affiliated with a low-Ti rather than just a VLT component (Day et al. 2006). Bulk Sc-concentration in MET is also higher than these other breccias, implying that it is richer in pyroxene bearing phases. Bulk C1-normalised REE-trends (Fig. 4.24e) are also flatter in MET (La/Lu_{cn}: 1.31) than in the Q/E/Y paired stones (La/Lu_{cn}: 1.56 to 2.03). This variation in source material ages and geochemistry suggests that MET 01210 should not be included as part of the proposed Q/E/Y launch paring.

Arai et al. (2006) proposed that basalt clasts and mineral grains in MET 01210 have a 'remarkable similarity' to the bulk composition and mineral phases in the mare basalt meteorites Asuka-881757 and Yamoto-793169 (A/Y). New radiometric age dates Terada et al. (2007) also relate basalt fragments in MET 01210 to the ancient ~3.9 Ga year old A/Y mare basalts (Fig. 4.24). The bulk composition of basalt clasts investigated in MET 01210 have a similar range of TiO_2 (1.7 - 3.5 wt.% TiO_2: Table 4.5) to the mare basalt A/Y stones (1.5 to 2.5 wt.% TiO_2: Warren and Kallemeyn 1993; Koeberl et al. 1993). Mare basalt clasts in MET 01210 appear to have a very similar in texture to Y-793169, and have very similar pyroxene minor elemental substitution composition (Fig. 4.23). Individual mineral fragments in MET 01210 are however

more coarsely grained, and have pyroxene compositions similar to pyroxene grains reported for in Asuka-881757 (Fig. 4.23).

Recent investigations of the coarsely grained lunar ferro-gabbroic meteorite MIL 05035 (Joy et al. 2007, Nyquist et al. 2007), also report evidence of a pairing relationship with the A/Y stones and therefore, by inference, MET 01210 (Fig. 4.24, Fig. 4.25)

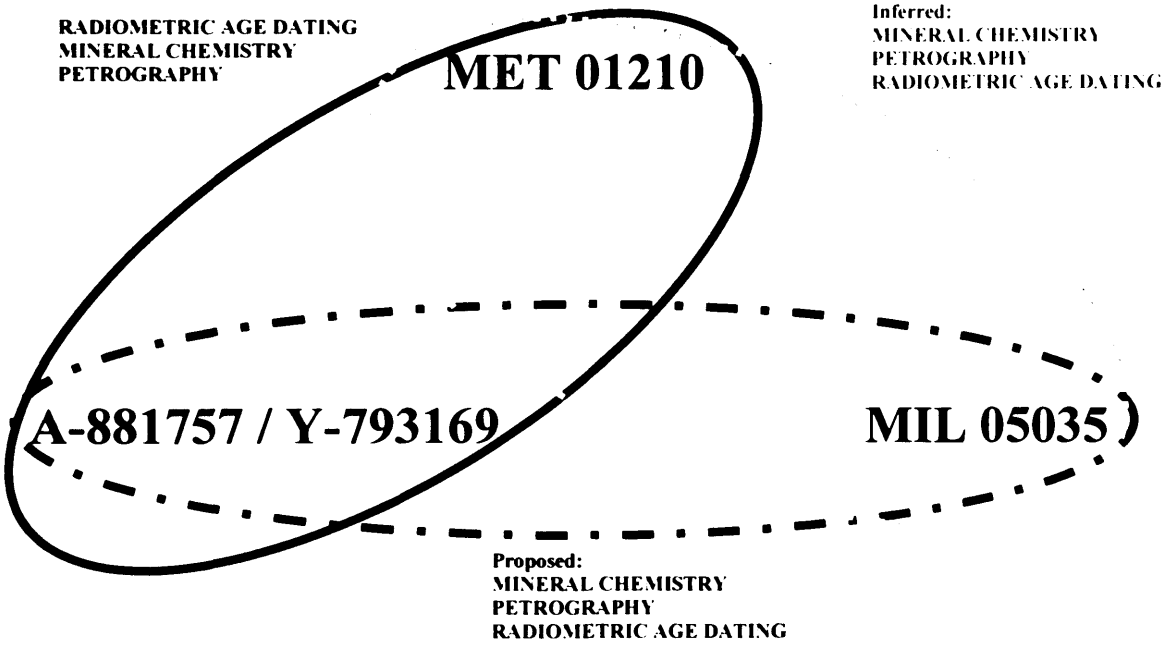

Fig. 4.25. Diagram to explain the evidence of pairing relationships between MET 01210, A-881757, Y-793169 and MIL 05035 to form the YAMM meteorite pairing group.

This petrological relationship theory is further explored in Fig. 4.23. This diagram illustrates the range of element substitution in pyroxenes in MET 01210, compared with pyroxenes in Y-793169, A-881757, MIL 05035 and the low-Ti LAP basalts (Chapter 5). Pyroxenes in Low-Ti basalt *clasts* in MET 01210 (blue/green symbols) appear to have an Al/Ti fractionation trend (between $Mg\#_{30\text{-}60}$) that is higher compared the LAP pyroxene trend (Fig. 4.23a), suggesting that the MET basalt pyroxenes were crystallised from an Al_2O_3-richer, TiO_2-poorer magma compared with the LAP parental melt.

A good correlation exists between the Al/Ti fractionation trend in basaltic pyroxenes in MET 01210 and pyroxenes in MIL 05035 (Fig. 4.23a): evidence that they may be derived from a similarly fractionated magmatic source. Figure 4.23c shows the relationship between Ti and Cr-substitution and Mg# variation in pyroxenes. Normal crystallisation from a fractionating melt will cause a systematic increase in Ti and decrease in Cr with a corresponding depletion in Mg

and enrichment in Fe: this trend in seen in all basalt pyroxene compositions from the different meteorites. There is however a variation between the Ti-contents of basaltic fragments (higher Ti# values) in MET 01210 and in the monomict mineral fragments (relative lower Ti#). These relationships fit well with pyroxene crystallisation in Y-793169 and A-881757 (Arai et al. 1996) and in MIL 05035 (Joy et al. 2007); basalt clast pyroxenes in MET correlate well with higher Ti# pyroxenes in Y-793169, whereas monomict matrix pyroxene fragments correlate well with the Ti#-poorer VLT trends in A-881757 and MIL 05035.

If this pairing relationship is proved to be true by investigating the cosmic ray exposure age of MIL 05035, then collectively the meteorites represent an important insight into the stratigraphic variation of a Low-Ti/VLT mare basalt environment, as illustrated in Figure 4.26:

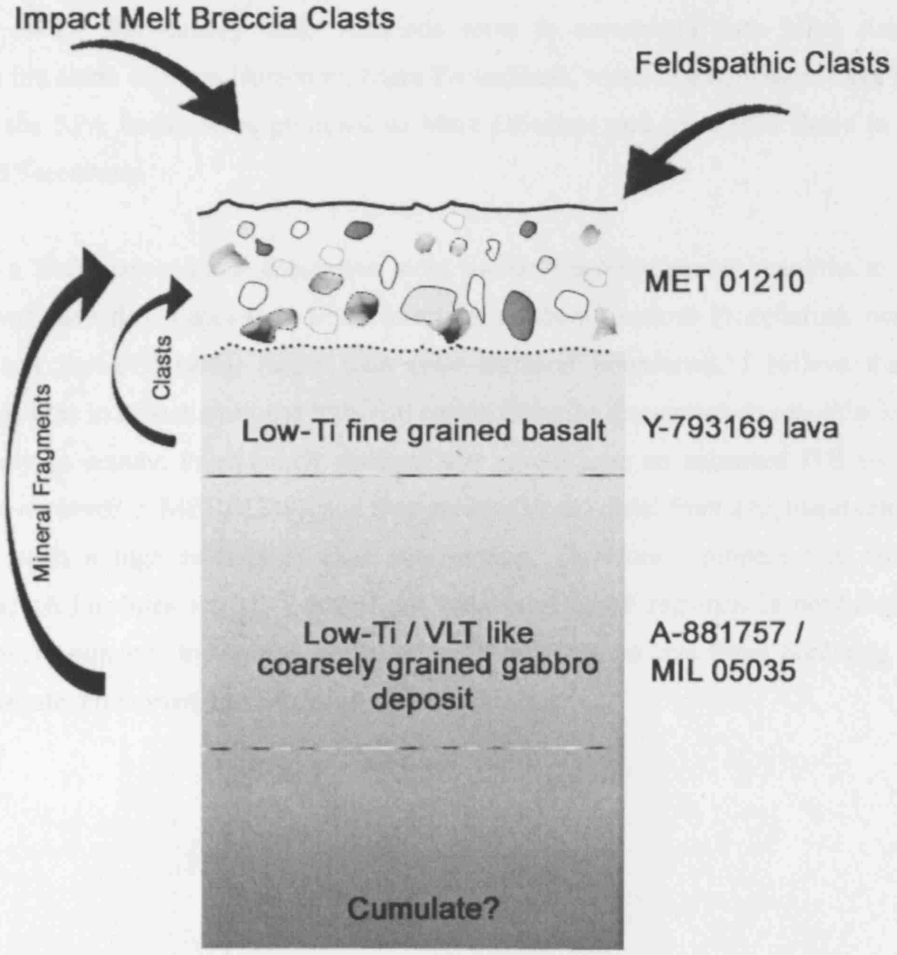

Fig. 4.26. Cartoon of the source environment of MET 01210 and paired stones, Asuka-881757, Yamoto-793169 and new pairing MIL 05035. Basaltic clasts and mineral fragments are preferentially included by vertical and lateral mixing from the underlying Yamoto-like lava flow. Fragmented coarsely grained mineral fragments are also included from deposits represented by the gabbroic Asuka and MIL meteorites. Feldspathic clasts and impact melt breccia fragments are introduced by lateral mixing from proximal deposits. This diagram is intended to be schematic and not scaled.

4.3.3 Lunar Provenance

MET 01210 is a sample of the lunar regolith environment. It represents the type of sample that is typically observed by remote sensing instrumentation, and therefore can be directly related to geochemical information derived from Clementine and Lunar Prospector missions. Figure 4.27a illustrates my attempt to use lunar elemental information to constrain the most similar regolith environments to the bulk composition of MET (Joy et al. 2006, Table 4.5), using limit parameters of plotting pixels that correspond to 1 - 2 wt. % TiO_2 and >1 - <4 ppm Th, and the additional constraints of pixels corresponding to 16 - 17 wt. % FeO (Fig. 4.27b).

Possible launch localities discriminating with just TiO_2 and Th (Fig. 4.27a) are diversely distributed across the lunar surface in localities that border mare basalt settings, generally outside the PKT. Particularly likely locations seem to correspond with Mare Australe, highlands to the south of Mare Humorum, Mare Fecunditatis, Mare Tranquillitatis, mare basalt outcrops in the SPA basin, areas proximal to Mare Orientale and some lava flows in Mare Imbrium and Serenitatis.

Introducing a FeO discriminator constrains most similar candidate parent regoliths to those associated with lava-flow deposits in Mare Imbrium, northern Oceanus Procellarum, northern Serenitatis and the SPA-basin, rather than mare-highland boundaries. I believe that the candidate regoliths in Procellarum and Imbrium can probably be discounted, as regoliths located here are likely to contain impact melt material that would have an enhanced ITE signature (which is not observed in MET 01210), and they seem to be too distal from a highland setting to account for such a high feldspathic clast contribution. Therefore I propose that the best candidate launch localities for MET 01210 are from mare basalt regoliths in northern Mare Serenitatis, mare outcrops in the SPA basin, or small localities on lava flows bordering Mare Crisium, Australe, Humorum, Moscoviense and Smythii.

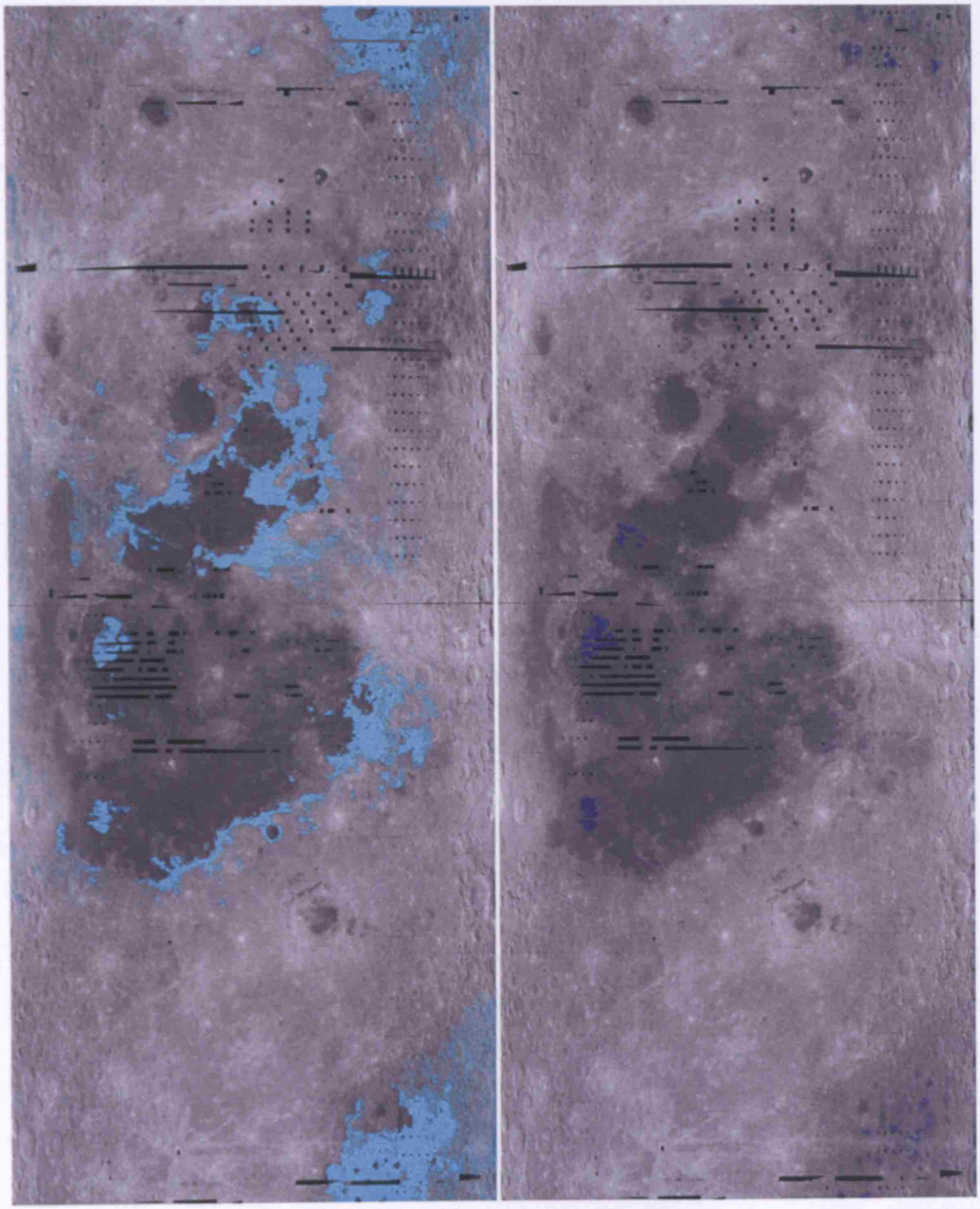

Fig. 4.27. (a) Constraining launch locality using Clementine TiO_2 and Lunar Prospector Th datasets. (b) Further constraining launch locality using Clementine TiO_2, Lunar Prospector Th and Clementine FeO datasets.

4.4 Summary

Lunar meteorite MET 01210 is a regolith breccia that was consolidated in a mare basalt environment. It contains contributions from a diverse range of feldspathic highland lithologies and feldspathic impact melt suggesting that the regolith is likely to have developed in proximity to a mare-highland boundary (Fig. 4.27).

The mare basalt clasts are all petrologically related to each other and originate from a Low-Ti fractionated magmatic source. This regime is possibly representative of a single Low-Ti, Al_2O_3-rich lave flow that experienced different cooling conditions producing a range of textures. These clasts are similar in age Terada et al. (2007) and composition (Fig. 4.24) to lunar meteorite Yamoto-793169. Coarser grained fractionated mono-mineral pyroxene fragments have a slightly different petrologic affiliation and have been sourced from a slowly cooled, Ti-poorer magmatic (Fig. 4.23) environment similar to that of lunar meteorite MIL 05035 and Asuka-881757.

Therefore, I concur with the pairing relationships proposed by Arai et al. (2006) suggesting that MET 01210 is paired to Y-7934169 and A-881757 and I extend this pairing to also include the new lunar VLT gabbroic meteorite MIL 05035 (Joy et al. 2007). This paired group therefore possibly represents an example of lunar stratigraphic variation from a surface regolith, extending down into a mare basalt lava flow that experienced a range of cooling and crystal settling regimes.

MET 01210's bulk chemical composition (Table 4.5) and the composition of impact melt clasts (Table 4.7, 4.8) suggest that the clast and mineral components that were consolidated together in the original regolith environment were KREEP-poor, and likely to have been formed from regions outside the Procellarum KREEP Terrane. An investigation into geochemically constraining the likely launch provenance is non-conclusive, but suggests candidate mare-highland boundary regions in the SPA-basin, northern Serenitatis, and smaller areas bordering Mare Crisium, Australe, Humorum, Moscoviense and Smythii. New, high resolution geochemical remote sensing datasets will be available in the next few years, providing a wider range of elemental constraints that will improve these estimates, and hopefully be used to discover the launch site of MET 01210 and its paired stones.

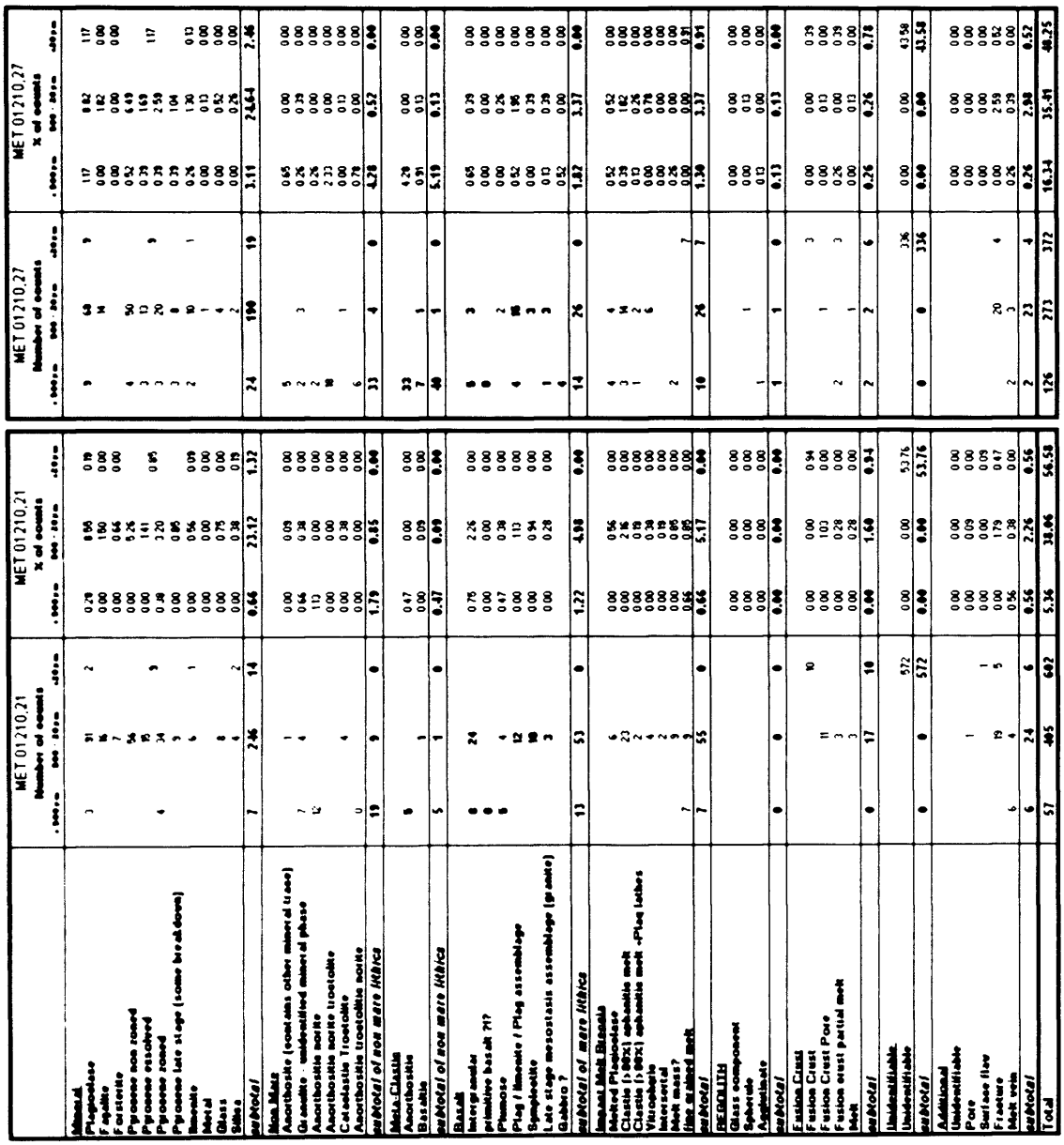

Table 4.1. Modal Mineral counts for MET 01210,21 and MET 01210,27.

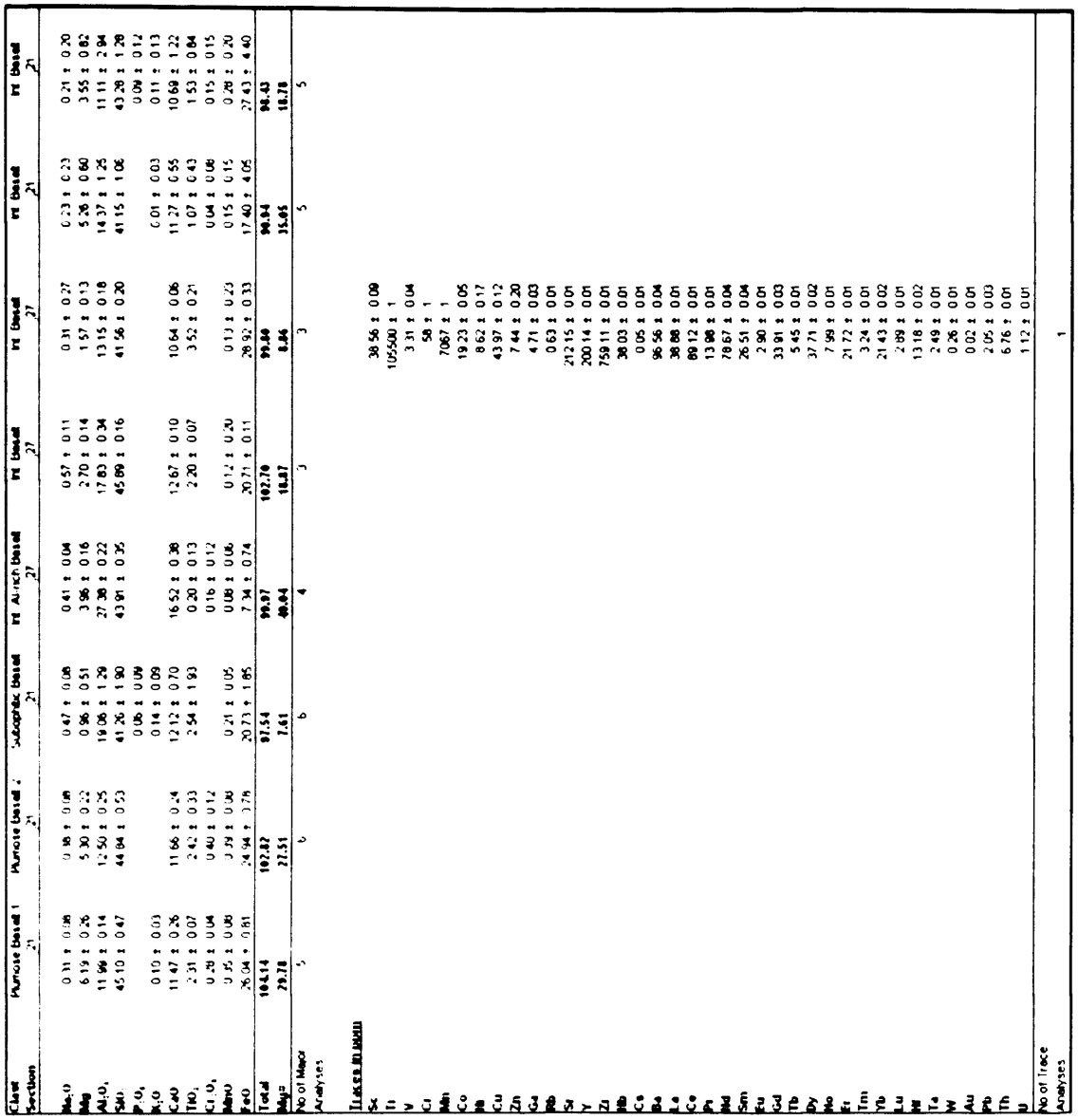

Table 4.2. Bulk compositions of basaltic clasts in MET 01210 calculated from the techniques outlined in Chapter 2. Th concentration in the intergranular basalt is relative high (as noted on page 112) because the clast was very small (Fig 4.6d) and contained an anomalously high quantity of mesostasis.

Standard deviations for the major elements represent the variations in calculating the average bulk chemistry based on the number of samples used to calculate the average. NOTE – the standard deviations on the single basalt analysis are the errors to the NIST 612 standards and not the average sample standard deviation as only one spot point was measured.

	Basalt Plag. A	Basalt Plag. B	Basalt Pyx 1	Basalt Pyx 2	Basalt Pyx 3
SiO_2	48 48 ± 0 15	46 95 ± 0 14	48 73 ± 0 15	44 85 ± 0 14	48 35 ± 0 15
TiO_2	0 05 ± 0 01	0 04 ± 0 01	1 01 ± 0 01	1 69 ± 0 01	0 94 ± 0 01
Al_2O_3	31 35 ± 0 04	30 97 ± 0 04	1 97 ± 0 01	1 48 ± 0 01	1 78 ± 0 01
Cr_2O_3	b d	b d	0 29 ± 0 01	0 08 ± 0 01	0 30 ± 0 01
FeO	0 85 ± 0 01	1 13 ± 0 01	26 71 ± 0 16	34 56 ± 0 20	28 63 ± 0 17
MnO	b d	0 05 ± 0 01	0 50 ± 0 01	0 57 ± 0 01	0 47 ± 0 01
MgO	0 36 ± 0 01	0 26 ± 0 01	12 83 ± 0 01	3 75 ± 0 01	10 89 ± 0 01
CaO	17 71 ± 0 16	17 87 ± 0 16	7 05 ± 0 07	9 62 ± 0 09	7 69 ± 0 07
Na_2O	0 03 ± 0 01	0 03 ± 0 01	b d	0 04 ± 0 01	0 03 ± 0 01
K_2O	0 95 ± 0 01	0 98 ± 0 01	0 02 ± 0 01	b d	0 02 ± 0 01
P_2O_5	b d	b d	0 04	0 03 ± 0 01	0 03 ± 0 01
SO_3	b d	b d	b d	0 02 ± 0 01	b d
Total	99 78	98 28	99 15	96 67	99 12
An=	*91 00*	*90 78*			
Wo=			*15 41*	*23 01*	*17 02*
En=			*39 02*	*12 47*	*33 52*
Fs=			*45 57*	*64 52*	*49 46*
Sc	1 47 ± 0 13	11 30 ± 0 66	110 62 ± 5 45	214 46 ± 11 05	103 28 ± 5 20
Ti	396 ± 72	877 ± 192	16996 ± 3247	16230 ± 3397	5154 ± 1030
V	2 55 ± 0 16	5 79 ± 0 35	16 19 ± 0 82	211 26 ± 11 06	126 67 ± 6 45
Cr	27 ± 3	84 ± 8	348 ± 30	8940 ± 842	6088 ± 551
Mn	83 ± 5	247 ± 16	5790 ± 342	7178 ± 451	2688 ± 164
Co	1 09 ± 0 09	2 77 ± 0 21	16 63 ± 0 97	25 88 ± 1 60	9 58 ± 0 58
Ni	1 39 ± 0 23	3 46 ± 0 52	5 28 ± 0 61	17 55 ± 2 09	10 97 ± 1 25
Cu	1 39 ± 0 16	2 11 ± 0 25	1 41 ± 0 14	0 34 ± 0 08	0 29 ± 0 05
Zn	0 83 ± 0 17	1 86 ± 0 27	2 24 ± 0 21	4 55 ± 0 43	1 95 ± 0 19
Ga	4 52 ± 0 35	5 22 ± 0 46	0 77 ± 0 07	0 87 ± 0 09	0 74 ± 0 07
Pb	0 70 ± 0 08	2 31 ± 0 27	0 02 ± 0 01	b d	b d
Sr	431 4 ± 20 1	282 0 ± 14 5	5 0 ± 0 3	4 9 ± 0 3	22 3 ± 1 1
Y	1 08 ± 0 09	2 60 ± 0 20	20 76 ± 1 28	17 15 ± 1 13	8 92 ± 0 57
Zr	15 64 ± 0 97	44 99 ± 3 04	16 29 ± 1 02	11 82 ± 0 80	6 43 ± 0 42
Nb	0 39 ± 0 04	0 62 ± 0 06	0 07 ± 0 01	1 76 ± 0 11	0 02 ± 0 01
Ba	30 85 ± 2 47	52 42 ± 4 67	1 69 ± 0 20	0 28 ± 0 09	1 34 ± 0 17
La	0 86 ± 0 06	1 70 ± 0 12	0 41 ± 0 03	0 15 ± 0 02	0 11 ± 0 01
Ce	1 43 ± 0 11	2 76 ± 0 22	1 22 ± 0 09	0 60 ± 0 06	0 36 ± 0 03
Pr	0 19 ± 0 02	0 39 ± 0 04	0 31 ± 0 03	0 14 ± 0 02	0 10 ± 0 01
Nd	1 01 ± 0 13	1 80 ± 0 21	2 44 ± 0 19	1 43 ± 0 16	0 96 ± 0 10
Sm	0 13 ± 0 05	0 34 ± 0 10	1 35 ± 0 16	1 03 ± 0 16	0 47 ± 0 08
Eu	1 50 ± 0 12	1 45 ± 0 13	0 18 ± 0 02	0 08 ± 0 02	0 16 ± 0 02
Gd	0 16 ± 0 06	0 44 ± 0 11	2 65 ± 0 24	1 75 ± 0 21	1 05 ± 0 13
Tb	0 04 ± 0 01	0 06 ± 0 02	0 45 ± 0 03	0 41 ± 0 04	0 22 ± 0 02
Dy	0 19 ± 0 05	0 47 ± 0 09	3 71 ± 0 26	3 20 ± 0 27	1 66 ± 0 14
Ho	0 02 ± 0 01	0 11 ± 0 02	0 84 ± 0 06	0 68 ± 0 06	0 38 ± 0 03
Er	0 05 ± 0 02	0 25 ± 0 06	2 49 ± 0 19	2 02 ± 0 18	1 04 ± 0 10
Tm	b d	0 05 ± 0 02	0 39 ± 0 03	0 36 ± 0 04	0 15 ± 0 02
Yb	0 11 ± 0 04	0 35 ± 0 09	3 09 ± 0 27	2 42 ± 0 25	1 12 ± 0 12
Lu	0 01 ± 0 01	0 08 ± 0 02	0 46 ± 0 04	0 38 ± 0 04	0 17 ± 0 02
Hf	0 38 ± 0 06	1 26 ± 0 14	0 94 ± 0 08	0 76 ± 0 09	0 45 ± 0 05
Ta	0 04 ± 0 01	0 04 ± 0 01	b d	0 11 ± 0 02	
W	0 05 ± 0 03	0 02 ± 0 02	b d	b d	b d
Au	b d	b d	b d	b d	b d
Pb	0 24 ± 0 05	0 78 ± 0 11	0 06 ± 0 02	0 04 ± 0 02	b d
Th	0 14 ± 0 03	2 54 ± 0 25	0 03 ± 0 01	b d	b d
U	0 04 ± 0 02	0 08 ± 0 02	b d	b d	b d

Table 4.3. Major, minor and trace element composition from plagioclase and pyroxene fragments in the basalt clast shown in Fig. 4.7a, 4.8a in MET 01210,27. Precision errors for major elements are 1 sigma standard deviations calculated from the variation of basalt glass standard measured on the Cameca SX50. Errors for trace elements are 1 sigma standard deviations calculated automatically by the Glitter software on the basis of variation of measurements of NIST 6121 standard. n.m. = not measured. b.d. = below detection limits

Clast	Meta-Clastic 1	Meta-Clastic 1	Granite	Symplectite 1	Symplectite 2	Symplectite 3
Section	,27	,27	,27	,27	,21	,21
Na_2O	0 33 ± 0 09	0 27 ± 0 05	1 39 ± 0 11			
MgO	5 73 ± 0 32	7 79 ± 0 14	0 18 ± 0 03	1 69 ± 0 11	2 37 ± 0 05	2 24 ± 0 05
Al_2O_3	24 12 ± 0 51	19 55 ± 0 62	11 73 ± 0 09	0 33 ± 0 14	0 55 ± 0 04	0 73 ± 0 11
SiO_2	41 51 ± 0 64	45 11 ± 1 60	67 90 ± 0 48	49 44 ± 0 12	51 61 ± 0 69	49 23 ± 0 74
P_2O_5			0 35 ± 0 11			
K_2O			4 17 ± 0 16			
CaO	13 73 ± 0 13	13 54 ± 0 59	3 72 ± 0 12	6 05 ± 0 10	5 67 ± 0 01	5 90 ± 0 45
TiO_2	0 23 ± 0 08	1 26 ± 0 16	0 73 ± 0 07	0 11 ± 0 18	0 11 ± 0 19	0 46 ± 0 04
Cr_2O_3	0 20 ± 0 09	0 29 ± 0 13				
MnO	0 05 ± 0 06	0 14 ± 0 18		0 71 ± 0 16	0 44 ± 0 05	0 60 ± 0 14
FeO	6 13 ± 0 19	18 19 ± 2 55	3 75 ± 0 11	49 47 ± 0 59	38 79 ± 0 33	51 33 ± 1 01
Total	**92.03**	**106.14**	**93.91**	**107.80**	**99.54**	**110.49**
Mg#	**62.52**	**43.33**	**7.78**	**5.75**	**9.82**	**7.21**
No of Major Analyses	4	3	3	3	5	5
Traces in ppm						
Sc	19 60 ± 3 81			183 14 ± 9 16		
Ti	1611 ± 381			5714 ± 349		
V	30 67 ± 13 09			12 75 ± 1 00		
Cr	1027 ± 383			180 ± 22		
Mn	1783 ± 463			28594 ± 2424		
Co	33 5 ± 24 9			41 0 ± 3 5		
Ni	n s			15 38 ± 1 55		
Cu	4 76 ± 3 76			0 91 ± 0 30		
Zn	17 3 ± 14 1			14 6 ± 2 9		
Ga	3 46 ± 0 40			2 94 ± 0 36		
Rb	0 69 ± 0 46			0 37 ± 0 10		
Sr	127 8 ± 8 2			39 6 ± 3 3		
Y	12 10 ± 3 44			671 7 ± 47 7		
Zr	37 3 ± 15 6			156 4 ± 9 5		
Nb	3 17 ± 1 50			2 43 ± 0 24		
Cs	0 04 ± 0 03					
Ba	41 98 ± 11 96			10 75 ± 1 55		
La	2 19 ± 0 69			9 54 ± 0 71		
Ce	4 84 ± 1 51			30 39 ± 2 36		
Pr	0 70 ± 0 22			6 27 ± 0 55		
Nd	3 31 ± 1 19			42 24 ± 3 62		
Sm	0 91 ± 0 33			28 51 ± 2 69		
Eu	0 73 ± 0 05			2 24 ± 0 28		
Gd	1 40 ± 0 44			56 63 ± 5 24		
Tb	0 27 ± 0 09			12 36 ± 0 64		
Dy	2 17 ± 0 65			106 62 ± 6 29		
Ho	0 47 ± 0 12			26 09 ± 1 51		
Er	1 52 ± 0 43			84 26 ± 7 82		
Tm	0 24 ± 0 08			13 09 ± 1 02		
Yb	1 73 ± 0 47			90 13 ± 8 17		
Lu	0 28 ± 0 07			15 47 ± 1 21		
Hf	1 05 ± 0 42			7 26 ± 0 77		
Ta	0 18 ± 0 07			0 13 ± 0 06		
W	0 05 ± 0 02			0 27 ± 0 15		
Au	0 02 ± 0 02					
Pb	0 70 ± 0 23			0 72 ± 0 21		
Th	0 82 ± 0 51			1 00 ± 0 23		
U	0 27 ± 0 21			0 21 ± 0 09		
No of Trace Analyses	6			1		

Table 4.4. Bulk compositions of meta-clastic, granite and symplectite clasts in MET 01210. Standard deviations represent the variations in calculating the average bulk chemistry based on the number of samples used to calculate the average. n.s. = not significant as standard deviation error is larger than the calculated average value.

	Joy et al. 2006		This study	Day et al. 2006	Zeigler et al. 2005
Section	**MET01210,25**		**MET 01210,27**		
Method	ICP-MS$^{\Delta}$, ICP-AES†		EMPA melt vien	EMPA FC	EMPA FC
	n=5, mass = 140mg		n=26	n=22	
SiO_2	44 03 ± 0 15	†	44 62 ± 1 98	44 80 ± 0 48	44 80
TiO_2	1 55 ± 0 01	†	1 66 ± 0 43	1 64 ± 0 06	1 58
Al_2O_3	16 60 ± 0 04	†	14 86 ± 5 91	16 20 ± 0 19	17 00
Cr_2O_3	0 27 ± 0 01	†	0 24 ± 0 11	0 17 0 04	0 19
FeO	16 46 ± 0 32	†	17 68 ± 4 42	16 90 ± 0 52	16 20
MnO	0 22 ± 0 01	†	0 26 ± 0 08	0 24 ± 0 06	0 26
MgO	6 20 ± 0 02	†	6 96 ± 1 79	6 50 ± 0 14	5 97
CaO	12 96 ± 0 11	†	12 86 ± 1 22	13 00 ± 0 16	13 60
Na_2O	0 32 ± 0 01	†	0 29 ± 0 15	0 28 ± 0 03	0 26
K_2O	0 06 ± 0 01	†	0 06 ± 0 03	0 06 ± 0 02	
P_2O_5	0 13 ± 0 01	Δ	0 06 ± 0 03	0 24 ± 0 04	
Total	**98.80**		**99.54**	**100.03**	**99.86**
Mg #	**40.2**		**41.3**	**40.7**	**39.7**
Li	8 07 ± 0 03	Δ			
Be	1 72 ± 0 09	Δ			
Sc	55 9 ± 0 01	Δ			
Sc	53 4 ± 0 3	Δ			
V	59 8 ± 0 1	Δ			
Cr [1]	1881 ± 16	†			
Cr [2]	1707 9 ± 4 8	Δ			
Co	31 84 ± 0 12	Δ			
Ni	211 9 ± 2 1	Δ			
Cu	23 45 ± 0 05	Δ			
Zn	37 4 ± 0 1	Δ			
Ga	19 09 ± 0 21	Δ			
As	3 62 ± 0 02	Δ			
Rb	1 34 ± 0 08	Δ			
Sr [1]	162 9 ± 0 6	†			
Sr [2]	163 7 ± 4 4	Δ			
Y	36 78 ± 0 04	Δ			
Zr	102 8 ± 0 7	Δ			
Nb	1 07 ± 0 03	Δ			
Mo	12 84 ± 0 15	Δ			
Cd	0 25 ± 0 03	Δ			
Cs	0 09 ± 0 01	Δ			
Ba	80 8 ± 0 2	†			
La	6 69 ± 0 10	Δ			
Ce	13 81 ± 0 21	Δ			
Pr	2 12 ± 0 06	Δ			
Nd	10 66 ± 0 27	Δ			
Sm	3 58 ± 0 06	Δ			
Eu	1 11 ± 0 03	Δ			
Gd	4 54 ± 0 16	Δ			
Tb	0 91 ± 0 03	Δ			
Dy	5 85 ± 0 15	Δ			
Ho	1 26 ± 0 03	Δ			
Er	3 63 ± 0 07	Δ			
Tm	0 53 ± 0 01	Δ			
Yb	3 54 ± 0 05	Δ			
Lu	0 52 ± 0 01	Δ			
Hf	2 37 ± 0 05	Δ			
Ta	0 10 ± 0 01	Δ			
W	0 69 ± 0 10	Δ			
Tl	0 01 ± 0 01	Δ			
Pb	0 55 ± 0 01	Δ			
Bi	0 11 ± 0 01	Δ			
Th	0 86 ± 0 02	Δ			
U	0 32 ± 0 01	Δ			

Table 4.5. Bulk Sample Composition of MET 01210 compared with literature data EMPA fusion crust analysis. Triangular symbol represents concentrations measured by ICP-MS and crosses represent concentrations measured using fused bead ICP-AES.

Normalised Major Elements									
Clast	Granulite	Granulite	Granulite	Granulite	Granulite	Granulite	Granulite	Troctolite	Norite
	ANT	ANT	T	AT	AT	N	ANT		
Section	,27	,27	,27	,27	,27	,27	,21	,27	,21
Na_2O	0.41 ± 0.12	0.37 ± 0.03	0.43 ± 0.09	0.28 ± 0.24	0.41 ± 0.02	1.50 ± 0.10	0.41 ± 0.07		0.41 ± 0.11
MgO	2.84 ± 0.02	2.50 ± 0.28	1.23 ± 0.14	0.66 ± 0.03	8.95 ± 1.46	1.84 ± 0.12	2.84 ± 0.33	13.50 ± 0.35	4.54 ± 1.87
Al_2O_3	31.04 ± 0.28	31.57 ± 0.48	33.82 ± 0.24	34.54 ± 0.09	25.94 ± 0.98	30.26 ± 0.22	30.86 ± 0.86	18.41 ± 0.55	26.11 ± 2.57
SiO_2	43.88 ± 0.33	44.44 ± 0.19	43.43 ± 0.35	44.05 ± 0.29	44.43 ± 1.74	48.14 ± 0.49	44.01 ± 0.26	39.79 ± 0.66	44.58 ± 1.13
P_2O_5									
K_2O				0.02 ±		0.72 ± 0.17			
CaO	17.28 ± 0.14	17.58 ± 0.26	18.84 ± 0.22	19.32 ± 0.03	14.29 ± 0.82	15.16 ± 0.31	17.47 ± 0.25	9.16 ± 0.29	15.40 ± 1.04
TiO_2		0.15 ± 0.12		0.15 ± 0.01	0.13 ± 0.07	0.22 ± 0.07	0.04 ± 0.10		0.34 ± 0.08
Cr_2O_3				0.06 ± 0.06	0.14 ± 0.04				0.19 ± 0.08
MnO					0.15 ± 0.07				0.13 ± 0.05
FeO	4.55 ± 0.05	3.39 ± 0.45	2.36 ± 0.17	0.86 ± 0.03	5.56 ± 0.77	2.15 ± 0.17	4.36 ± 0.63	19.04 ± 0.81	8.15 ± 1.51
Total	100.00	100.00	99.91	99.94	100.00	100.00	100.00	99.91	99.85
Mg#	52.70	56.87	48.11	57.84	74.16	68.43	53.80	55.85	49.83
No of Major Analyses	3	3	3	3	3	3	5	4	7
Traces in ppm									
Sc		16.4 ± 6.0						9.29 ± 1.30	
Ti		2636 ± 2463						783 ± 233	
V		32.2 ± 24.9						9.07 ± 2.05	
Cr		2224 ± 3331						285 ± 131	
Mn		1672 ± 629						1466 ± 573	
Co		12.9 ± 5.8							
Ni		99.0 ± 31.3							
Cu		7.77 ± 1.99							
Zn		13.49 ± 3.75						11.68 ± 1.78	
Ga		3.61 ± 0.34						1.84 ± 0.15	
Rb		0.43 ± 0.04						0.27 ± 0.08	
Sr		144.2 ± 8.4						79.0 ± 6.0	
Y		11.17 ± 4.48						2.93 ± 1.05	
Zr		41.3 ± 23.2						9.57 ± 2.31	
Nb		2.12 ± 1.87						0.66 ± 0.07	
Ba		23.0 ± 0.9						15.43 ± 8.78	
La		1.76 ± 0.06						0.78 ± 0.06	
Ce		4.89 ± 0.26						1.70 ± 0.04	
Pr		0.63 ± 0.07						0.20 ± 0.02	
Nd		2.89 ± 0.46						0.95 ± 0.42	
Sm		1.02 ± 0.27						0.60 ± 0.13	
Eu		0.75 ± 0.05						0.28 ± 0.17	
Gd		1.34 ± 0.46						0.60 ± 0.27	
Tb		0.25 ± 0.09						0.09 ± 0.04	
Dy		1.96 ± 0.78						0.57 ± 0.24	
Ho		0.44 ± 0.19						0.16 ± 0.06	
Er		1.27 ± 0.57						0.41 ± 0.25	
Tm		0.19 ± 0.06						0.10 ± 0.01	
Yb		1.39 ± 0.52						0.47 ± 0.19	
Lu		0.19 ± 0.07						0.11 ± 0.11	
Hf		0.97 ± 0.50						0.24 ± 0.17	
Ta		b.d.						0.05 ± 0.02	
Au		0.02 ± 0.01						b.d.	
Pb		0.47 ± 0.11						0.53 ± 0.08	
Th		0.57 ± 0.32						0.12 ± 0.09	
No of Trace Analyses		5						3	

Table 4.6. Bulk compositions of granulite and feldspathic clasts in MET 01210. Standard deviations represent the variations in calculating the average bulk chemistry based on the number of samples used to calculate the average.

Normalised Major Elements							
Clast	Feldspathic IMB 1	Feldspathic IMB 2	Feldspathic IMB 3	Feldspathic IMB 4	Feldspathic IMB 5	Feldspathic IMB 6	Feldspathic IMB 7
Section	,27	,27	,27	,27	,27	,27	,27
Na_2O	0 37 ± 0 24	0 42 ± 0 10	0 24 ± 0 02	0 46 ± 0 03	0 30 ± 0 08	0 15 ± 0 24	0 42 ± 0 09
MgO	3 04 ± 0 02	2 89 ± 0 05	4 59 ± 0 15	4 70 ± 0 09	5 61 ± 0 08	4 75 ± 0 02	5 20 ± 0 06
Al_2O_3	30 53 ± 0 48	30 69 ± 0 24	28 42 ± 0 02	27 39 ± 0 14	27 69 ± 0 15	28 68 ± 0 48	27 56 ± 0 15
SiO_2	44 85 ± 0 43	44 33 ± 0 12	44 98 ± 0 27	44 60 ± 0 48	44 31 ± 0 23	44 92 ± 0 43	44 63 ± 0 23
P_2O_5							
K_2O							
CaO	17 63 ± 0 18	17 55 ± 0 26	16 89 ± 0 18	16 40 ± 0 18	16 17 ± 0 23	16 73 ± 0 18	16 15 ± 0 19
TiO_2		0 17 ± 0 11	0 14 ± 0 11	0 22 ± 0 06	0 25 ± 0 06	0 11 ± 0 17	0 29 ± 0 07
Cr_2O_3			0 12 ± 0 09	0 21 ± 0 02	0 14 ± 0 03		0 20 ± 0 01
MnO			0 02 ± 0 04	0 07 ± 0 10	0 10 ± 0 03		0 18 ± 0 01
FeO	3 59 ± 0 12	3 89 ± 0 12	4 60 ± 0 27	5 77 ± 0 12	5 43 ± 0 16	4 67 ± 0 12	5 36 ± 0 10
Total	**100.00**	**99.93**	**100.00**	**99.80**	**100.00**	**100.00**	**100.00**
Mg#	**60.19**	**57.00**	**64.06**	**59.20**	**64.83**	**64.44**	**63.38**
No of Analyses	3	3	3	3	3	3	3
Traces in ppm							
Sc	10 60 ± 0 42	12 69 ± 0 61		14 50 ± 0 50	12 58 ± 1 16	11 34 ± 1 09	
Ti	1352 ± 128	1581 ± 25		2110 ± 18	1853 ± 154	1823 ± 448	
V	14 63 ± 0 99	17 27 ± 0 89		29 10 ± 0 24	21 48 ± 2 58	22 65 ± 6 32	
Cr	401 ± 14	534 ± 33		1000 ± 15	718 ± 111	912 ± 609	
Mn	423 ± 62	525 ± 23		685 ± 28	587 ± 63	543 ± 31	
Co							
Ni							
Cu							
Zn	8 32 ± 0 76	5 93 ± 0 14		11 27 ± 1 45	7 57 ± 0 97	12 07 ± 4 33	
Ga	3 20 ± 0 26	2 94 ± 0 23		2 46 ± 0 24	2 28 ± 0 24	3 27 ± 0 59	
Rb	0 46 ± 0 12	0 57 ± 0 01		1 25 ± 0 21	0 36 ± 0 07	0 80 ± 0 50	
Sr	162 ± 3	155 ± 2		145 ± 9	147 ± 5	145 ± 2	
Y	5 93 ± 0 72	7 09 ± 0 35		13 31 ± 0 96	9 62 ± 1 29	9 94 ± 1 32	
Zr	17 55 ± 1 48	24 33 ± 0 30		45 89 ± 1 29	28 61 ± 2 60	38 70 ± 9 09	
Nb	1 70 ± 0 26	1 39 ± 0 33		3 52 ± 0 39	1 99 ± 0 18	2 24 ± 0 54	
Cs		0 05 ± 0 03		0 06 ± 0 00	0 03 ± 0 02	0 06 ± 0 00	
Ba	25 87 ± 2 63	20 14 ± 1 93		48 08 ± 2 76	26 19 ± 1 99	38 42 ± 10 70	
La	1 36 ± 0 37	1 40 ± 0 21		3 60 ± 0 13	2 49 ± 0 49	3 00 ± 0 78	
Ce	3 57 ± 0 73	3 78 ± 0 25		9 68 ± 0 66	6 29 ± 0 99	6 99 ± 1 77	
Pr	0 47 ± 0 06	0 55 ± 0 06		1 20 ± 0 02	0 82 ± 0 29	1 01 ± 0 31	
Nd	2 50 ± 0 59	2 59 ± 0 09		5 36 ± 0 86	4 19 ± 0 42	4 92 ± 1 19	
Sm	0 59 ± 0 06	0 49 ± 0 08		1 42 ± 0 67	1 37 ± 0 32	1 56 ± 0 55	
Eu	0 79 ± 0 04	0 75 ± 0 14		0 83 ± 0 08	0 77 ± 0 09	0 75 ± 0 19	
Gd	0 85 ± 0 18	1 30 ± 0 32		2 20 ± 0 42	1 31 ± 0 49	1 95 ± 0 71	
Tb	0 15 ± 0 05	0 18 ± 0 02		0 38 ± 0 02	0 24 ± 0 10	0 29 ± 0 09	
Dy	0 96 ± 0 27	1 54 ± 0 36		2 02 ± 0 09	1 47 ± 0 51	1 76 ± 0 64	
Ho	0 24 ± 0 07	0 26 ± 0 11		0 65 ± 0 11	0 39 ± 0 07	0 37 ± 0 07	
Er	0 64 ± 0 14	0 89 ± 0 20		1 52 ± 0 22	1 27 ± 0 18	1 36 ± 0 30	
Tm	0 12 ± 0 02	0 16 ± 0 02		0 28 ± 0 10	0 20 ± 0 10	0 20 ± 0 05	
Yb	0 75 ± 0 26	0 86 ± 0 17		1 56 ± 0 17	1 03 ± 0 14	0 87 ± 0 55	
Lu	0 10 ± 0 03	0 13 ± 0 05		0 29 ± 0 07	0 17 ± 0 05	0 18 ± 0 09	
Hf	0 44 ± 0 09	0 82 ± 0 36		1 57 ± 0 34	0 66 ± 0 17	1 09 ± 0 39	
Ta	0 08 ± 0 02	0 09 ± 0 02		0 22 ± 0 12	0 11 ± 0 01	0 19 ± 0 07	
W	0 20	0 11 ± 0 07		0 32 ± 0 01	0 15 ± 0 03		
Au	0 06 ± 0 01			0 10		0 06	
Pb	0 12 ± 0 06	0 27 ± 0 08		0 21 ± 0 12	0 17 ± 0 10	0 40 ± 0 29	
Th	0 18 ± 0 09	0 26 ± 0 06		0 70 ± 0 10	0 43 ± 0 11	0 46 ± 0 12	
U	0 05 ± 0 01	0 05 ± 0 02		0 24 ± 0 04	0 12 ± 0 05	0 13 ± 0 05	
No of Trace Analyses	3	3		3	3	3	

Table. 4.7. Bulk compositions of feldspathic impact melt breccia (IMB) clasts in MET 01210. Standard deviations represent the variations in calculating the average bulk chemistry based on the number of samples used to calculate the average. If value has no standard deviation then only one measurement of this element was made.

Table 4.8. Bulk compositions of mingled impact melt breccia (IMB) clasts in MET 01210. Standard deviations represent the variations in calculating the average bulk chemistry based on the number of samples used to calculate the average.

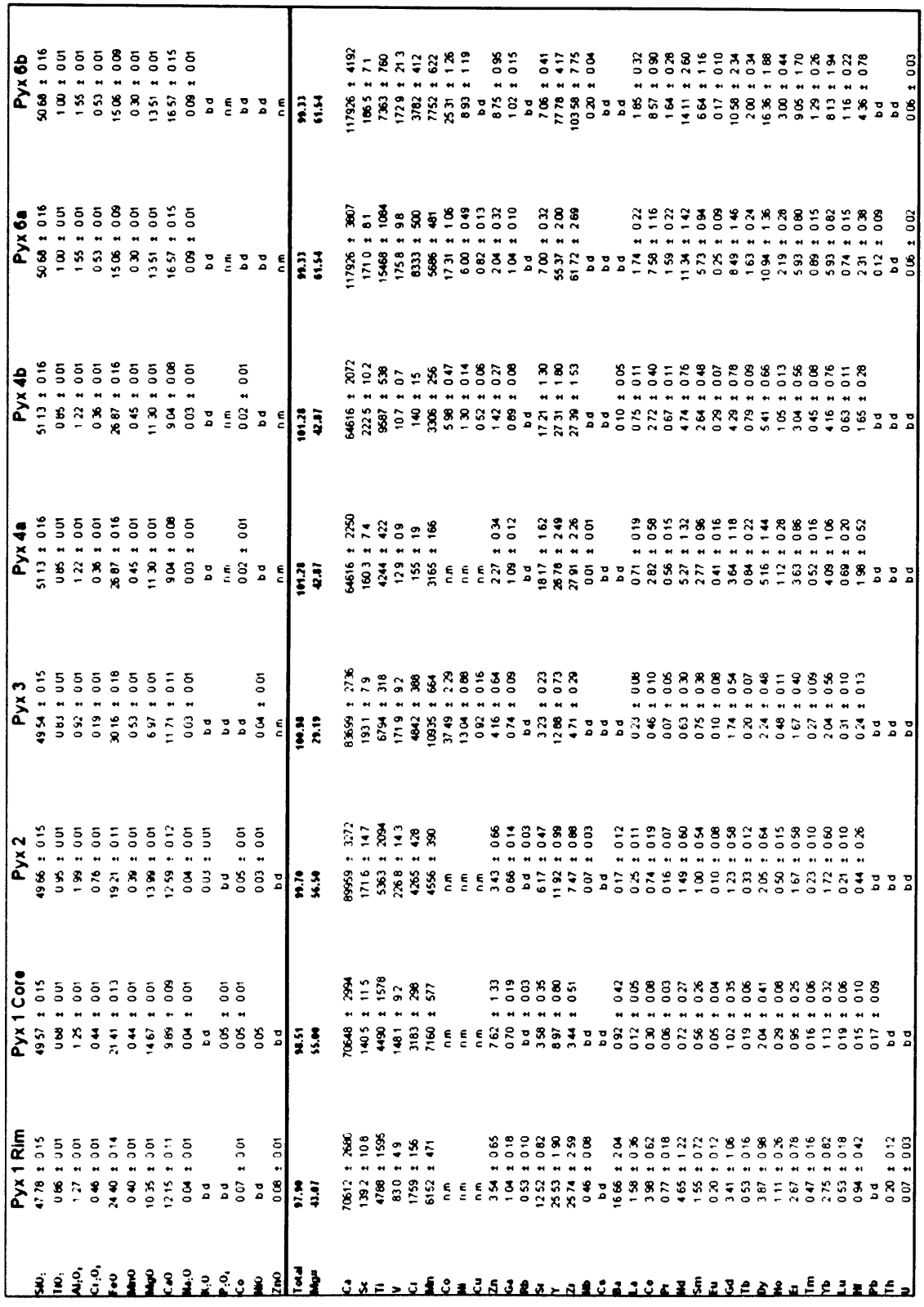

	Pyx 1 Rim	Pyx 1 Core	Pyx 2	Pyx 3	Pyx 4a	Pyx 4b	Pyx 6a	Pyx 6b
SiO_2	47.78 ± 0.15	49.57 ± 0.15	49.66 ± 0.15	49.54 ± 0.15	51.13 ± 0.16	51.13 ± 0.16	50.68 ± 0.16	50.68 ± 0.16
TiO_2	0.66 ± 0.01	0.68 ± 0.01	0.95 ± 0.01	0.83 ± 0.01	0.85 ± 0.01	0.85 ± 0.01	1.00 ± 0.01	1.00 ± 0.01
Al_2O_3	1.27 ± 0.01	1.25 ± 0.01	1.99 ± 0.01	0.92 ± 0.01	1.22 ± 0.01	1.22 ± 0.01	1.55 ± 0.01	1.55 ± 0.01
Cr_2O_3	0.46 ± 0.01	0.44 ± 0.01	0.76 ± 0.01	0.19 ± 0.01	0.36 ± 0.01	0.36 ± 0.01	0.53 ± 0.01	0.53 ± 0.01
FeO	24.40 ± 0.14	21.41 ± 0.13	19.21 ± 0.11	30.16 ± 0.18	26.87 ± 0.16	26.87 ± 0.16	15.06 ± 0.09	15.06 ± 0.09
MnO	0.40 ± 0.01	0.44 ± 0.01	0.39 ± 0.01	0.53 ± 0.01	0.45 ± 0.01	0.45 ± 0.01	0.30 ± 0.01	0.30 ± 0.01
MgO	10.35 ± 0.01	14.67 ± 0.01	13.90 ± 0.01	6.97 ± 0.01	11.30 ± 0.01	11.30 ± 0.01	13.51 ± 0.01	13.51 ± 0.01
CaO	12.15 ± 0.11	9.89 ± 0.09	12.59 ± 0.12	11.71 ± 0.11	9.04 ± 0.08	9.04 ± 0.08	16.57 ± 0.15	16.57 ± 0.15
Na_2O	0.04 ± 0.01	0.04 ± 0.01	0.04 ± 0.01	0.03 ± 0.01	0.03 ± 0.01	0.03 ± 0.01	0.09 ± 0.01	0.09 ± 0.01
K_2O	b.d	b.d	0.03 ± 0.01	b.d	b.d	b.d	b.d	b.d
P_2O_5	b.d	b.d	b.d	b.d	n.m	n.m	n.m	n.m
Co	0.07 ± 0.01	0.05 ± 0.01	0.05 ± 0.01	b.d	0.02 ± 0.01	0.02 ± 0.01	b.d	b.d
NiO	b.d	0.05	0.03 ± 0.01	0.04 ± 0.01	b.d	b.d	b.d	b.d
ZnO	0.06 ± 0.01	b.d	b.d	n.m	n.m	n.m	n.m	n.m
Total	97.90	98.51	99.70	100.98	101.28	101.28	99.33	99.33
Mg#	43.87	55.00	56.50	29.19	42.87	42.87	61.54	61.54
Ca	70612 ± 2660	70648 ± 2994	89959 ± 3372	83699 ± 2736	64616 ± 2250	64616 ± 2072	117926 ± 3807	117926 ± 4192
Sc	139.2 ± 10.8	140.5 ± 11.5	171.6 ± 14.7	193.1 ± 7.9	160.3 ± 7.4	222.5 ± 10.2	171.0 ± 8.1	186.5 ± 7.1
Ti	4788 ± 1595	4490 ± 1578	5363 ± 2094	6794 ± 318	4244 ± 422	9587 ± 538	15468 ± 1084	7363 ± 760
V	830 ± 4.9	1481 ± 9.2	2268 ± 14.3	1719 ± 9.2	1219 ± 0.9	107 ± 0.7	1758 ± 9.8	1729 ± 21.3
Cr	1759 ± 156	3183 ± 298	4265 ± 428	4642 ± 388	155 ± 19	140 ± 15	8333 ± 500	3782 ± 412
Mn	6152 ± 471	7160 ± 577	4556 ± 390	10935 ± 664	3165 ± 166	3306 ± 256	5686 ± 481	7752 ± 622
Co	n.m	n.m	n.m	37.49 ± 2.29	n.m	5.98 ± 0.47	17.31 ± 1.06	25.31 ± 1.26
Ni	n.m	n.m	n.m	13.04 ± 0.88	n.m	1.30 ± 0.14	6.00 ± 0.49	8.93 ± 1.19
Cu	n.m	n.m	n.m	0.92 ± 0.16	n.m	0.52 ± 0.06	0.82 ± 0.13	b.d
Zn	3.54 ± 0.65	7.62 ± 1.33	3.43 ± 0.66	4.16 ± 0.64	2.27 ± 0.34	1.42 ± 0.27	2.04 ± 0.32	8.75 ± 0.95
Ga	1.04 ± 0.18	0.70 ± 0.19	0.66 ± 0.14	0.74 ± 0.09	1.09 ± 0.12	0.89 ± 0.08	1.04 ± 0.10	1.02 ± 0.15
Ge	0.53 ± 0.10	b.d ± 0.03	b.d ± 0.03	b.d	b.d	b.d	b.d	b.d
As	12.52 ± 0.82	3.58 ± 0.35	6.17 ± 0.47	3.23 ± 0.23	18.17 ± 1.62	17.21 ± 1.30	7.00 ± 0.32	7.06 ± 0.41
Se	25.53 ± 1.90	8.97 ± 0.80	11.92 ± 0.98	12.88 ± 0.73	26.78 ± 2.49	27.31 ± 1.80	55.37 ± 2.00	77.78 ± 4.17
Rb	25.74 ± 2.59	3.44 ± 0.51	7.47 ± 0.88	4.71 ± 0.29	27.91 ± 2.26	27.39 ± 1.53	61.72 ± 2.69	103.58 ± 7.75
Sr	0.46 ± 0.06	b.d	0.07 ± 0.03	b.d	0.01 ± 0.01	b.d	b.d	0.20 ± 0.04
Y	b.d	b.d	b.d	b.d	b.d	b.d	b.d	b.d
Zr	16.66 ± 2.04	0.92 ± 0.42	0.17 ± 0.12	b.d	b.d	0.10 ± 0.05	b.d	b.d
Nb	1.58 ± 0.36	0.12 ± 0.05	0.25 ± 0.11	0.23 ± 0.08	0.71 ± 0.19	0.75 ± 0.11	1.74 ± 0.22	1.85 ± 0.32
Cs	3.98 ± 0.62	0.30 ± 0.08	0.74 ± 0.19	0.46 ± 0.10	2.82 ± 0.58	2.72 ± 0.40	7.58 ± 1.16	8.57 ± 0.90
Ba	0.77 ± 0.18	0.06 ± 0.03	0.16 ± 0.07	0.07 ± 0.05	0.56 ± 0.15	0.67 ± 0.11	1.59 ± 0.22	1.64 ± 0.28
La	4.65 ± 1.22	0.72 ± 0.27	1.49 ± 0.60	0.63 ± 0.30	5.27 ± 1.32	4.74 ± 0.76	11.34 ± 1.42	14.11 ± 2.60
Ce	15.55 ± 0.72	0.56 ± 0.26	1.00 ± 0.54	0.75 ± 0.38	2.77 ± 0.96	2.64 ± 0.48	5.73 ± 0.94	6.64 ± 1.16
Pr	0.20 ± 0.12	0.05 ± 0.04	0.10 ± 0.08	0.10 ± 0.08	0.41 ± 0.16	0.29 ± 0.07	0.25 ± 0.09	0.17 ± 0.10
Nd	3.41 ± 1.06	1.02 ± 0.35	1.23 ± 0.58	1.74 ± 0.54	3.64 ± 1.18	4.29 ± 0.78	8.49 ± 1.46	10.58 ± 2.34
Sm	0.53 ± 0.16	0.19 ± 0.06	0.33 ± 0.12	0.20 ± 0.07	0.84 ± 0.22	0.79 ± 0.09	1.63 ± 0.24	2.00 ± 0.34
Eu	0.87 ± 0.98	2.04 ± 0.41	2.05 ± 0.64	2.24 ± 0.46	5.16 ± 1.44	5.41 ± 0.66	10.94 ± 1.36	16.36 ± 1.88
Gd	1.11 ± 0.26	0.29 ± 0.08	0.50 ± 0.15	0.48 ± 0.11	1.12 ± 0.28	1.05 ± 0.13	2.19 ± 0.28	3.00 ± 0.44
Tb	2.67 ± 0.78	0.95 ± 0.25	1.67 ± 0.58	1.67 ± 0.40	3.63 ± 0.86	3.04 ± 0.56	5.93 ± 0.80	9.05 ± 1.70
Dy	0.47 ± 0.16	0.16 ± 0.06	0.23 ± 0.10	0.27 ± 0.09	0.52 ± 0.16	0.45 ± 0.08	0.89 ± 0.15	1.29 ± 0.26
Ho	2.75 ± 0.82	1.13 ± 0.32	1.72 ± 0.60	2.04 ± 0.56	4.09 ± 1.06	4.16 ± 0.76	5.93 ± 0.82	8.13 ± 1.94
Er	0.53 ± 0.18	0.19 ± 0.06	0.21 ± 0.10	0.31 ± 0.10	0.69 ± 0.20	0.63 ± 0.11	0.74 ± 0.15	1.16 ± 0.22
Tm	0.94 ± 0.42	0.15 ± 0.10	0.44 ± 0.26	0.24 ± 0.13	1.98 ± 0.52	1.65 ± 0.28	2.31 ± 0.38	4.36 ± 0.78
Yb	b.d	0.17 ± 0.09	b.d	b.d	b.d	b.d	0.12 ± 0.09	b.d
Lu	0.20 ± 0.12	b.d	b.d	b.d	b.d	b.d	b.d	b.d
Hf	0.07 ± 0.03	b.d	b.d	b.d	b.d	b.d	0.06 ± 0.02	0.06 ± 0.03

Table 4.9. Major, minor and trace element composition from pyroxene fragments in the matrix of MET 01210,27. Errors for major elements are 1 sigma standard deviations calculated from the variation of basalt glass standard measured on the Cameca SX50. Errors for trace elements are 1 sigma standard deviations calculated automatically by the Glitter software on the basis of variation of measurements of NIST 6121 standard. n.m. = not measured. b.d. = below detection limits

	Plag 1 Core	Plag 1 Rim (Maskelynite)	Plag 2	Glass	Meta-Clast Plag	Granulite Plag
SiO_2	34 30 ± 0 11		33 08 ± 0 10	43 38 ± 0 13	42 81 ± 0 13	44 99 ± 0 14
TiO_2	0 03 ± 0 01		0 05 ± 0 01	0 23 ± 0 01	0 05 ± 0 01	0 04 ± 0 01
Al_2O_3	44 85 ± 0 06		44 00 ± 0 06	21 74 ± 0 03	31 60 ± 0 04	34 44 ± 0 04
Cr_2O_3	b d		0 05 ± 0 01	0 10 ± 0 01	b d	b d
FeO	0 21 ± 0 01		0 28 ± 0 01	9 13 ± 0 05	0 09 ± 0 00	0 25 ± 0 01
MnO	0 03 ± 0 01		0 06 ± 0 01	0 11 ± 0 01	0 04 ± 0 01	0 03 ± 0 01
MgO	0 09 ± 0 01		0 06 ± 0 01	8 63 ± 0 01	0 09 ± 0 01	0 09 ± 0 01
CaO	19 27 ± 0 18		18 92 ± 0 17	14 51 ± 0 13	17 25 ± 0 16	19 05 ± 0 18
Na_2O	0 07 ± 0 01		0 05 ± 0 01	0 02 ± 0 01	0 11 ± 0 01	0 04 ± 0 01
K_2O	0 54 ± 0 01		0 73 ± 0 01	0 39 ± 0 01	0 69 ± 0 01	0 45 ± 0 01
P_2O_5	b d		b d	0 05 ± 0 01	0 02 ± 0 01	0 03 ± 0 01
SO_3	b d		b d	2 22 ± 0 01	0 04 ± 0 01	0 09 ± 0 01
Cl	0 05 ± 0 01		0 03 ± 0 01	0 01 ± 0 01	0 25 ± 0 01	0 04 ± 0 01
NiO	b d		b d	0 86 ± 0 01	b d	0 05 ± 0 01
ZnO	n m		0 02 ± 0 01	n m	n m	n m
Total	**99.43**		**97.34**	**101.38**	**93.04**	**99.59**
An#	**94.79**		**93.26**		**92.56**	**95.92**
Sc	4 3 ± 0 6	14 7 ± 1 3	4 6 ± 0 8	8 7 ± 1 0	3 5 ± 0 3	1 7 ± 0 2
Ti	547 ± 141	1823 ± 481	632 ± 261	1153 ± 501	756 ± 108	206 ± 31
V	4 42 ± 0 47	27 24 ± 1 67	3 58 ± 0 50	20 57 ± 1 59	4 09 ± 0 25	2 27 ± 0 15
Cr	29 3 ± 4 8	969 3 ± 73 9	11 7 ± 4 1	546 1 ± 61 7	10 8 ± 1 4	8 4 ± 1 0
Mn	75 7 ± 5 1	658 9 ± 43 1	81 8 ± 7 6	428 9 ± 40 0	72 6 ± 3 7	43 4 ± 2 3
Co	n m	n m	n m	n m	1 52 ± 0 14	1 92 ± 0 15
Ni	n m	n m	n m	n m	9 41 ± 1 01	22 88 ± 2 14
Cu	n m	n m	n m	n m	2 77 ± 0 31	1 70 ± 0 21
Zn	51 0 ± 5 3	5 2 ± 0 9	7 7 ± 1 6	3 9 ± 0 9	3 6 ± 0 5	2 9 ± 0 4
Ga	3 22 ± 0 44	3 41 ± 0 42	5 89 ± 0 76	0 64 ± 0 17	9 05 ± 0 60	2 46 ± 0 20
Rb	4 86 ± 0 48	0 37 ± 0 10	6 27 ± 0 74	0 07 ± 0 05	17 13 ± 1 32	1 42 ± 0 14
Sr	155 ± 8	176 ± 9	185 ± 13	122 ± 8	314 ± 13	160 ± 7
Y	5 75 ± 0 51	9 25 ± 0 72	3 65 ± 0 43	4 92 ± 0 50	5 55 ± 0 34	1 78 ± 0 13
Zr	103 2 ± 8 8	24 9 ± 2 3	105 6 ± 11 9	14 6 ± 1 8	129 3 ± 6 8	30 1 ± 1 7
Nb	1 55 ± 0 22	2 02 ± 0 24	1 52 ± 0 24	1 03 ± 0 15	1 95 ± 0 14	0 50 ± 0 05
Cs	0 14 ± 0 06	0 06 ± 0 04	0 20 ± 0 07	b d	0 38 ± 0 05	0 05 ± 0 02
Ba	75 0 ± 7 1	28 5 ± 3 2	83 6 ± 10 4	16 2 ± 2 4	219 8 ± 14 3	29 7 ± 2 2
La	4 72 ± 0 45	2 08 ± 0 24	4 97 ± 0 56	1 00 ± 0 16	7 36 ± 0 37	2 07 ± 0 13
Ce	6 49 ± 0 49	4 88 ± 0 39	7 34 ± 0 66	2 75 ± 0 28	13 26 ± 0 77	2 89 ± 0 19
Pr	1 14 ± 0 15	0 73 ± 0 11	0 85 ± 0 14	0 26 ± 0 06	1 50 ± 0 12	0 40 ± 0 04
Nd	4 98 ± 0 79	3 52 ± 0 61	3 82 ± 0 77	1 29 ± 0 33	6 53 ± 0 54	1 62 ± 0 21
Sm	1 13 ± 0 39	0 40 ± 0 22	0 60 ± 0 35	0 31 ± 0 19	1 51 ± 0 26	0 38 ± 0 11
Eu	1 00 ± 0 18	0 95 ± 0 17	0 83 ± 0 19	0 86 ± 0 16	1 93 ± 0 17	0 73 ± 0 08
Gd	0 86 ± 0 35	1 44 ± 0 41	0 44 ± 0 26	0 44 ± 0 20	0 88 ± 0 19	0 36 ± 0 11
Tb	0 12 ± 0 05	0 31 ± 0 07	0 15 ± 0 06	0 12 ± 0 04	0 13 ± 0 03	0 04 ± 0 02
Dy	0 62 ± 0 23	1 58 ± 0 35	0 74 ± 0 27	1 23 ± 0 28	0 91 ± 0 16	0 28 ± 0 08
Ho	0 12 ± 0 05	0 38 ± 0 09	0 21 ± 0 07	0 11 ± 0 04	0 18 ± 0 04	0 07 ± 0 02
Er	0 23 ± 0 14	1 36 ± 0 29	0 56 ± 0 22	0 34 ± 0 13	0 52 ± 0 10	0 14 ± 0 05
Tm	0 03 ± 0 03	0 07 ± 0 03	0 06 ± 0 04	0 09 ± 0 04	0 05 ± 0 02	0 02 ± 0 01
Yb	0 27 ± 0 16	1 40 ± 0 34	0 76 ± 0 29	0 26 ± 0 13	0 68 ± 0 15	0 23 ± 0 08
Lu	b d	0 06 ± 0 03	bd	0 08 ± 0 04	0 10 ± 0 03	0 03 ± 0 01
Hf	2 65 ± 0 49	0 51 ± 0 17	2 80 ± 0 63	0 35 ± 0 14	3 71 ± 0 32	0 93 ± 0 12
Ta	0 11 ± 0 05	0 14 ± 0 05	0 15 ± 0 06	0 05 ± 0 03	0 18 ± 0 04	0 05 ± 0 02
W	0 12 ± 0 11	b d	0 15 ± 0 14	0 06 ± 0 06	0 11 ± 0 05	0 04 ± 0 03
Au	b d	b d	bd	b d	0 04 ± 0 03	0 02 ± 0 02
Pb	2 70 ± 0 36	0 23 ± 0 10	2 77 ± 0 42	0 15 ± 0 07	2 06 ± 0 23	0 53 ± 0 09
Th	1 92 ± 0 28	0 36 ± 0 10	1 89 ± 0 31	0 22 ± 0 07	2 01 ± 0 21	0 42 ± 0 07
U	0 31 ± 0 08	0 09 ± 0 05	0 33 ± 0 10	0 08 ± 0 04	0 92 ± 0 12	0 08 ± 0 03

Table 4.10. Major, minor and trace element composition from plagioclase and glass fragments in the matrix, and in two clasts from MET 01210,27. Errors for major elements are 1 sigma standard deviations calculated from the variation of basalt glass standard measured on the Cameca SX50. Errors for trace elements are 1 sigma standard deviations calculated automatically by the Glitter software on the basis of variation of measurements of NIST 6121 standard. n.m. = not measured. b.d. = below detection limits

Chapter 5: A Petrological, Mineralogical and Chemical Analysis of the Lunar Mare Basalt Meteorite: LaPaz Icefield 02205, 02224, 02226, 02436 and 03632

5.1 Introduction

LAP 02205, 02224, 02226, 02436 and 03632 are unbrecciated holocrystalline basaltic lunar meteorites. They are also grouped with a sixth stone, LAP 04841, that is not discussed in this thesis. The meteorites are often cut by fractures and minor black, glassy melt veins (Fig. 5.1). They are quite coarsely grained, with pyroxenes and forsteritic olivine phases sometimes being > 1 mm, and typically exceeding 500 μm, in length. There are some minor differences between the five studied sections (Fig. 5.2, Table 5.2.). LAP 02205,32 the largest of the sections, contains parallel minor fault structures with associated opaque black melt; LAP 02224,35 is slightly coarser grained, and the section is cut by a large (1 mm wide) dark brown melt vein and bound by a fusion crust; LAP 02226,25 is marginally finer grained and the section is cut by small faults that are often in-filled with brown melt; LAP 02436,27, is also slightly coarser grained; LAP 03632,19, is also partially bound by a fusion crust and contains a large (<1 cm) region of green/brown glassy melt.

In all of the stones the major silicate phases are pyroxene and plagioclase, with minor forsteritic and fayalitic olivine and silica (Fig. 5.2). The pyroxenes are intergranularly distributed between the plagioclases and forsteritic olivines. Modal pyroxene contents are 57 to 60 %, whereas plagioclase accounts for 32 to 36 %. Forsteritic olivines are subordinate (modally < 3 %) and generally have an anhedral form subophtically enclosed by pyroxene phases. All stones have very similar mineral proportions (Table 5.1), suggesting that they originated from the same lava flow on the Moon.

Oxide phases include ilmenite and a group of chemically diverse spinels that ranges from titanium-chromite to ulvöspinel. Ilmenite forms about 3 % and spinel phases account for < 1 % of the sections (Table 5.1). Troilite and FeNi grains are dispersed through the samples, particularly associated with residual-melt regions. Mesostasis areas are composed of extremely fractionated liquid-silicate immiscible melt phases including pyroxferroite, fayalite, silica, baddelyite (ZrO_2), apatites, K-Si-rich glasses and Si-rich glasses. Using the combined fayalite and silica modes as an approximate guide to the locate mesostasis areas, the stones are composed of about 0.95 to 2.07 % residual melt.

The results described in this chapter have been published as Joy et al. 2006.

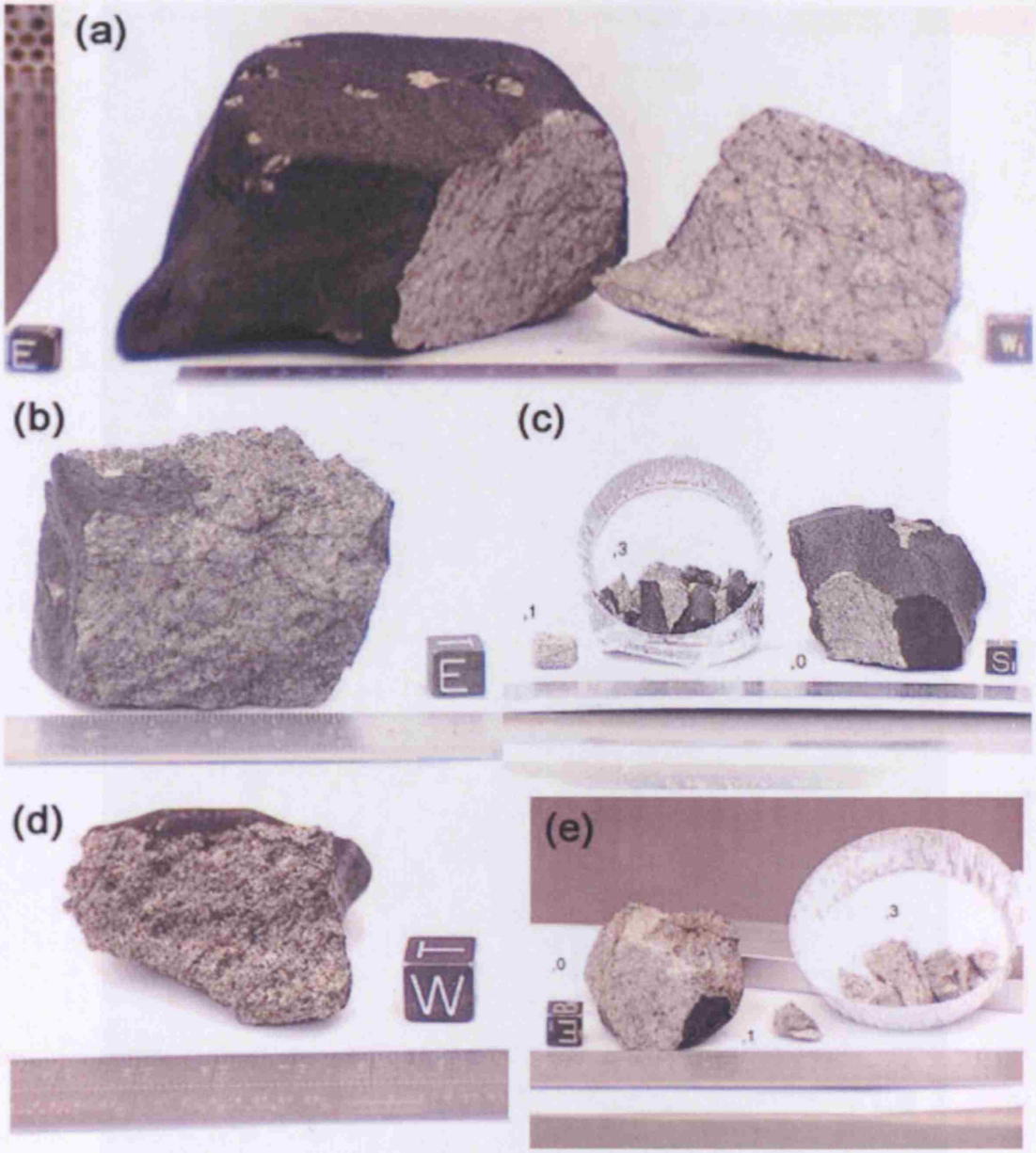

Fig. 5.1. Photographs of (a) LAP 02205, (b) LAP 02224, and (c) LAP 02226 (d) LAP 02436 (e) LAP 03632 meteorite stones in hand specimen. All five stones have a dark brown/black fusion crust. The scale cube is 1 cm on a side. Photographs courtesy of Satterwhite (2003, 2004a) and taken using the links from Website 1.2.

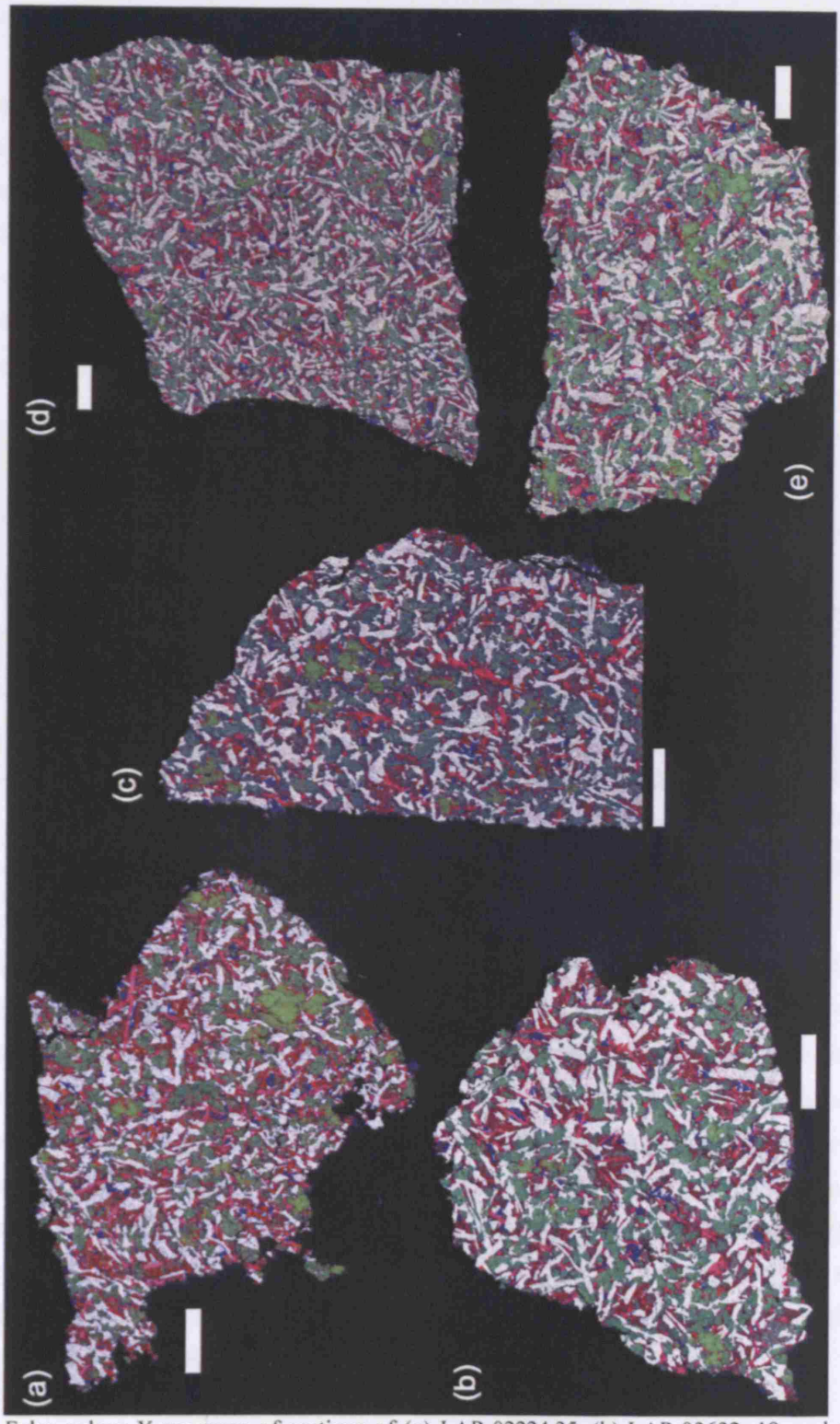

Fig. 5.2. False colour X-ray maps of sections of (a) LAP 02224,35, (b) LAP 03632, 19, and (c) LAP 02226,25 (d) LAP 02205,32, and (e) LAP 02436,27 where white represents Al (plagioclases), yellow represents Ca (plagioclase), red represents Fe (pyroxene rims and fayalitic areas), green represents Mg (pyroxene cores and forsteritic olivines), blue represents Si (cristobalite grains), and pink represents Ti (ilmenite and spinel) rich areas. This technique particularly highlights the location of forsteritic olivine (bright green areas), fayalite (brightest red areas), ilmenite (pink), silica (blue) and plagioclase (white phases).

5.2 Mineral Composition: Silicates

Pyroxene is the most common silicate mineral in all five stones (Table 5.1, 5.3), occurring as large (up to ~1 mm) grains that subophitically enclose other mineral phases. Most of the pyroxene crystals are pristine, with a small fraction showing evidence of shock deformation (Fig. 5.3). The latter are heavily fractured, displaying mosaic extinction in cross polarized light. Moreover, some crystals clearly exhibit parallel internal planar features and these features are interpreted as shock-induced planar deformation features (PDF) and not exsolution lamellae as suggested by Righter et al. (2005).

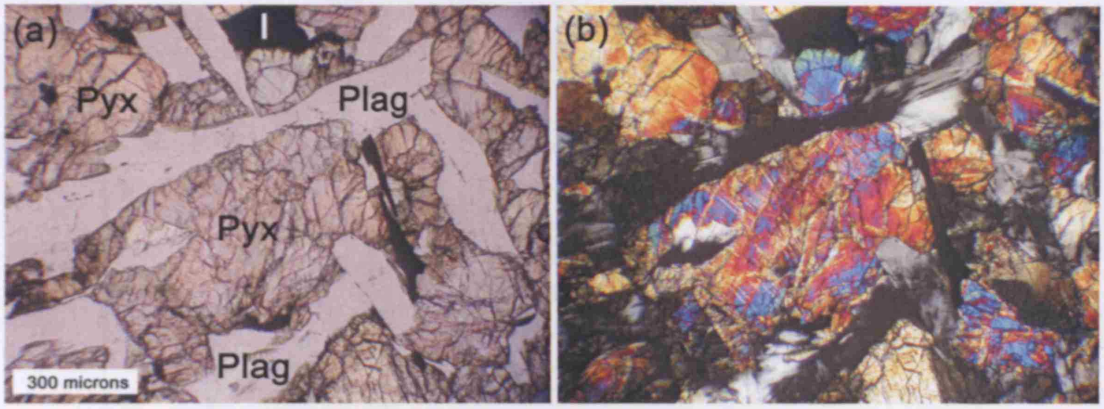

Fig. 5.3. (a) Optical photomicrograph of plane-polarised-light (ppl) view of pyroxene and plagioclase intergrowth in LAP 02205. Pyx = pyroxene, Plag = plagioclase, I = ilmenite. (b) Cross-polarised-light (cpl) view of the same view. The large central pyroxene grain has visible internal planar deformation features that are offset by small faults and cross-cutting fractures.

Pyroxenes show substantial variations (LAP 02205: Fs_{21-90} Wo_{9-41} En_{0-58}; LAP 02224: Fs_{23-86} Wo_{8-39} En_{1-59}; LAP 02226: Fs_{22-87} Wo_{8-40} En_{0-55}; LAP 02436: Fs_{20-81} Wo_{9-43} En_{2-57}; LAP 03632: Fs_{23-82} Wo_{9-37} En_{1-59}; Fig. 5.4), and are nearly all gradually zoned from Mg-rich pigeonites and sub-calcic augite cores to rims that have evolved Fe-rich compositions that in extreme cases are pyroxferroitic (Fig. 5.4). This zonation represents a magmatic history where pyroxene growth developed from an evolving melt that became progressively Mg-depleted with time. Melt fractionation is responsible for late-stage Fe-enrichment in pyroxenes that occur throughout the samples, and in pyroxenes adjacent to mesostasis areas where grains have near-end member compositions (Fig. 5.4). There are a few grains that have sharper core (Mg-rich) - rim (Fe-rich) boundaries that may represent a resorption effort.

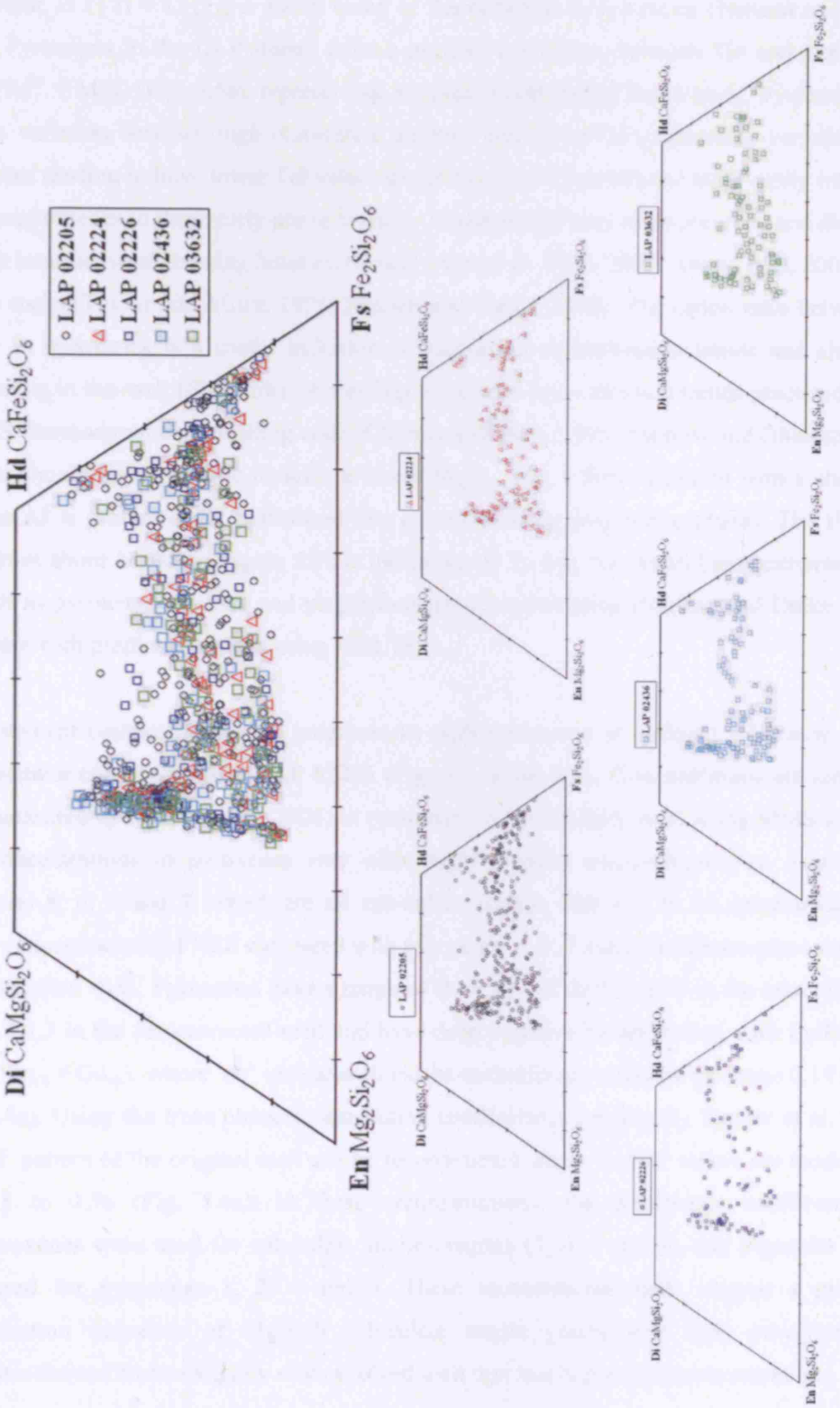

Fig. 5.4. (a) Pyroxene compositions in the LAP basalts plotted on a pyroxene quadrilateral. The five stones show very similar compositional trends with pyroxenes zoned from Mg-rich cores to Fe-rich rims. This similarity is evidence that the stones are geochemically related and are likely to have originated from the same lava flow. Individual stone pyroxene quadrilaterals for (a) LAP 02205,32, (b) LAP 02224,35, (c) LAP 02226,25, (d) LAP 02436,27 and (e) LAP 03632,19.

Ti# (molar Ti / [Ti + Cr]) is a useful index of fractionation in pyroxenes (Nielsen and Drake, 1978). Pyroxenes in the LAP stones show a positive correlation between Ti# and Fe# (molar Fe^{2+} / [Fe^{2+} + Mg]) (Fig. 5.5a), representing a typical fractionating basalt trend. Pyroxene cores show a variation between high (sub-calcic augites) and lower-Ca (pigeonites) varieties, with pigeonites tending to have lower Ti# values suggesting that Ti substituted more easily into high-Ca clinopyroxenes in these early phase crystals. These trends have been observed and discussed in other basaltic/basalt-bearing lunar meteorites (Arai et al. 1996, 2002; Anand et al. 2003a) and Apollo rocks (Taylor and Misra, 1975; Nielsen and Drake, 1978). The cation ratio between Al and Ti in pyroxenes is a useful indicator of concurrent crystallization trends and elemental partitioning in the melt (Fig. 5.5b). According to mineral crystallization trends predicted by the MELTS thermodynamic modelling code (Ghiorso and Sack, 1995; Asimow and Ghiorso, 1998) feldspar should appear on the liquidus at about $Mg\#_{58}$ (Fig. 5.5b); consistent with a change in slope as Al is preferentially partitioned into co-crystallizing plagioclase phases. The flattened slope from about $Mg\#_{40}$ in Figure 5.5b is indicative of Ti, Mg and Al all being extracted from the melt as pyroxene, ilmenite and plagioclase are co-crystallizing (Nielsen and Drake, 1978), consistent with predictions made using MELTS.

Trace element compositions were measured in eight pyroxenes of different sub-calcic augites and pigeonite compositions in LAP 02205 (Fig. 5.6, Table 5.6). Concentrations are similar to those measured by Anand et al. (2006) in pyroxenes in LAP 02205,36/31 using SIMS analysis. REE concentrations in pyroxenes vary with major element composition (Fig. 5.6a insert). Pyroxenes 8, 6, 3 and 7, which are all sub-calcic augites with > 2 % Al substitution, have greater concentrations of REE compared with pyroxenes 1, 4, 5 and 2, which are pigeonites with Al-substitution <1%. Pyroxenes have a range of $(La/Lu)_{cn}$ of 0.05 to 0.78 in the mineral phase, and 20.2-1.3 in the reconstructed melt and have deep negative Eu anomalies, with Eu/Eu* (i.e. $Eu_{cn}/\sqrt{(Sm_{cn} \times Gd_{cn})}$, where 'cn' indicates chondrite-normalized) values in the range 0.14 to 0.17 (Fig. 5.6a). Using the trace element distribution coefficients compiled by Snyder et al. (1995) the REE pattern of the original melt can be reconstructed where Eu/Eu* values are modelled to be 0.18 to 0.36 (Fig. 5.6a). In these reconstructions, the distribution coefficients for clinopyroxenes were used for sub-calcic augites/augites (3, 6, 7 and 8), and pigeonite values were used for pyroxenes 1, 2, 4 and 5. These reconstructed melts suggest a pyroxene crystallization sequence of Mg-rich sub-calcic augite grains with later co-crystallizing pigeonites formed from a slightly more evolved melt that had higher REE concentrations.

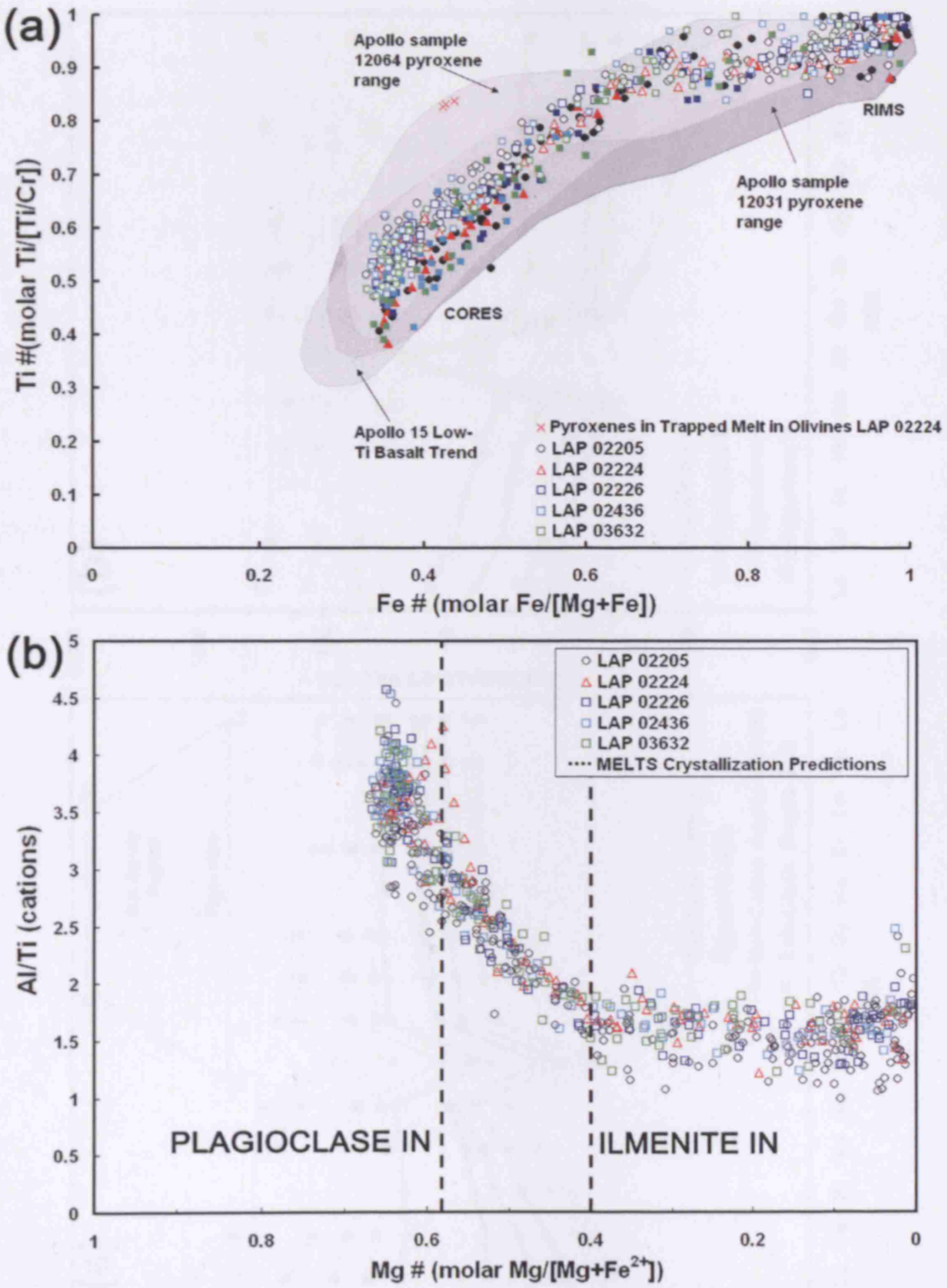

Fig. 5.5. (a) Diagram of Ti# vs. Fe# for pyroxene grains in the LAP stones compared with similar crystallization trends seen in Apollo 15 and 12 low-Ti basalt samples (shaded regions, taken from Nielsen and Drake 1978). Open symbols represent pyroxenes with Ca/ (Ca+Mg+Fe^{2+}) > 20 mol %; closed symbols represent < 20 mol %. (b) Mg# vs. cation ratio of Al/Ti in pyroxenes in LAP stones. Superimposed are predictions using the MELTS thermodynamic modelling code (Ghiorso and Sack 1995; Asimow and Ghiorso 1998) of the point when feldspar ($Mg\#_{58}$) and ilmenite ($Mg\#_{40}$) appeared of the liquidus, and started to co-crystallize with pyroxene grains. These predictions correlate well with observations of depletion in Al when plagioclase is being co-crystallized between ~$Mg\#_{60}$ and ~$Mg\#_{40}$, and a flattening of the trend between ~$Mg\#_{40}$ and ~$Mg\#_{0}$ where Ti, Al and Mg are being partitioned into co-crystallizing ilmenite, plagioclase and pyroxene phases.

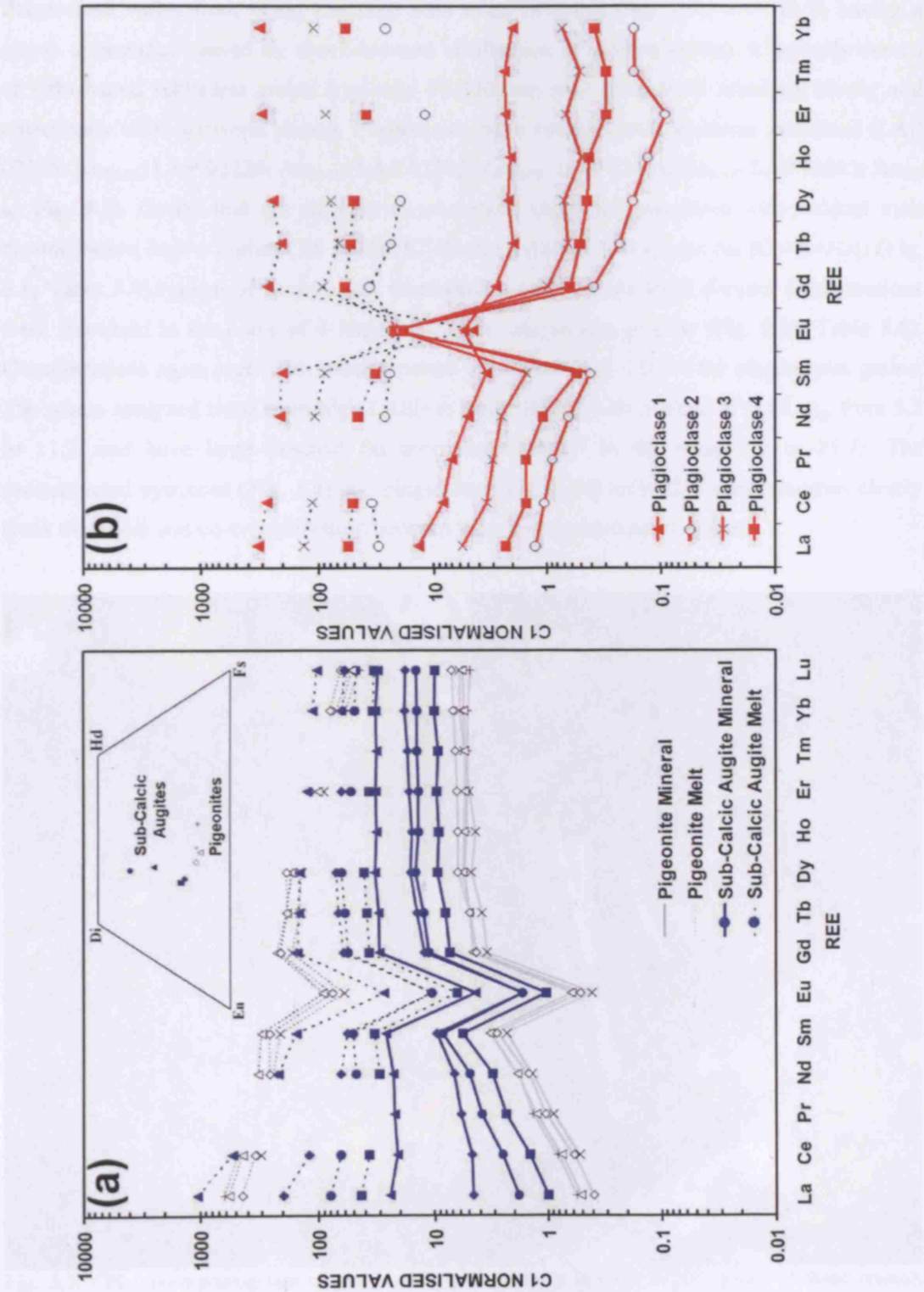

Fig. 5.6. (a) REE composition in LAP 02205 pyroxenes with their reconstructed melt compositions (see text for details), using the lunar distribution coefficients compiled by Snyder et al. (1995) and normalized to the C1 values of Anders and Grevesse (1989). Solid lines are mineral analyses, with pigeonites in grey and sub-calcic augites/augites in black. Dashed lines are their respective reconstructed melt REE concentrations. The inlayed quadrilateral shows the respective pyroxene compositions. (b) REE patterns of plagioclase crystals in LAP 02205 normalized to the C1-Chondrite values of Anders and Grevesse (1989). Dashed lines represent reconstructed melt REE concentrations.

Plagioclase varies from being fractured with relict twinning (Fig. 5.7), to < 40 % having a glassy appearance caused by shock-induced vitrification (maskelynisation). It typically occurs as lath-shaped subhedral grains (typically 50-800 μm) that crystallized relatively slowly and cotectically with pyroxene phases. Plagioclases have complex compositional variations (LAP 02205: An_{81-91}; LAP 02224: An_{84-90}; LAP 02205: An_{84-90}; LAP 02436: An_{82-92} LAP 03632; An_{82-90}: Fig. 5.8). Grains that are adjacent to mesostasis areas and associated with residual melt crystallization have a higher Or# (molar K/[Ca+K+Na]) and Ab# (molar Na/[Ca+K+Na]) (Fig. 5.8; Table 5.4) typical of lunar basalt fractionation trends. Rare earth element concentrations were measured in the cores of 4 large (>500 μm) plagioclase crystals (Fig. 5.6b; Table 5.6). Concentrations agree well with those reported by Anand et al. (2006) for plagioclases grains. The grains analyzed trend from high LREE to lower HREE with a range of $(La/Lu)_{cn}$ from 5.5 to 11.2, and have large positive Eu anomalies (Eu/Eu* in the range 8.9 to 25.7). The reconstructed pyroxene (Fig. 5.a) and plagioclase (Fig. 5.6b) melt REE concentrations clearly show that there was co-crystallization between these two main mineral phases.

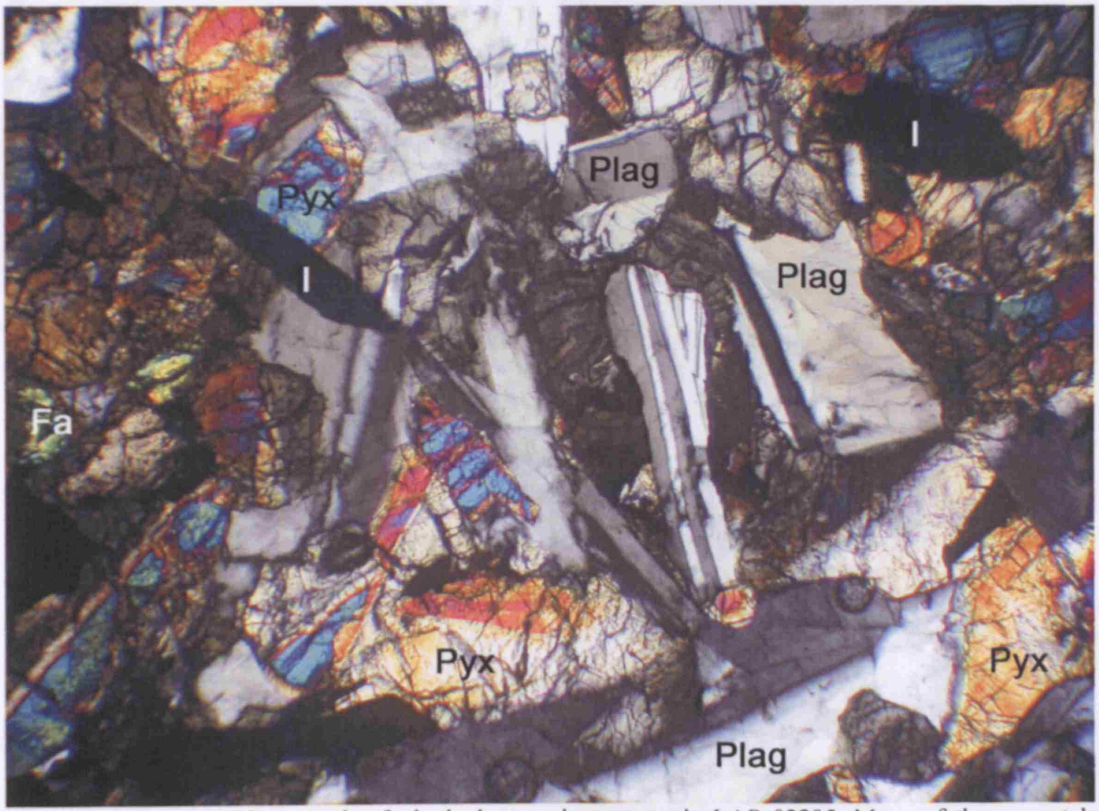

Fig. 5.7. CPL micro-photograph of plagioclase grain textures in LAP 02205. Many of these crystals exhibit relict twinning textures with some becoming blended by shock metamorphic processes. Pyx = pyroxene, Plag = plagioclase, I = ilmenite, Fa = fayalitic olivine.

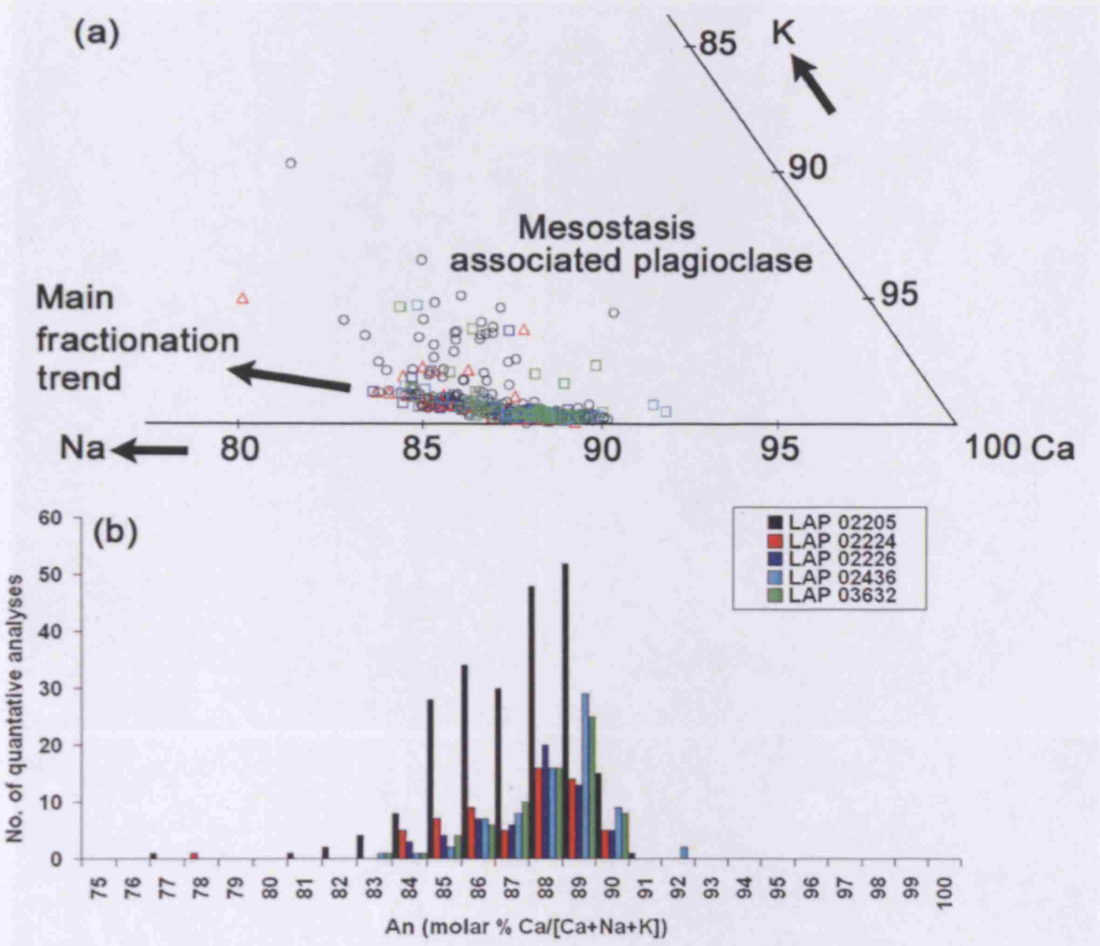

Fig. 5.8. (a) Ternary plot of plagioclase content in LAP 02205, 32, LAP 02224, 35 and LAP 02226, 25 showing typical trend of basalt fractionation (increasing Or and Abs-content with decreasing An-content). K-rich compositions that exhibit a scattered trend representing those plagioclase grains associated with mesostasis areas. (b) Histogram of range of anorthite value among the stones.

Olivine in LAP falls into two main groups (Table 5.4, Fig. 5.9, 5.10). Forsteritic varieties range from large grains (200 µm to 1 mm) to smaller anhedral grains (40 to100 µm). Some of the larger varieties are zoned from relatively Mg-rich (Fo_{64}–Fo_{46}) core compositions to narrow (< 100 µm) Fe-rich rims (Fig. 5.9, 5.10). This Fe-rich rim structure is often incomplete or missing, causing an undulatory contact with surrounding pyroxene phases, indicating that the olivine grains underwent partial resorption to form pyroxene phases during melt cooling. Anhedral, fayalitic (Fa_{87-100}) varieties form part of the groundmass of the mesostasis regions. Olivines in the stones show a similar compositional range to that in Apollo mare basalt samples and lunar basaltic meteorites (Fig. 5.10).

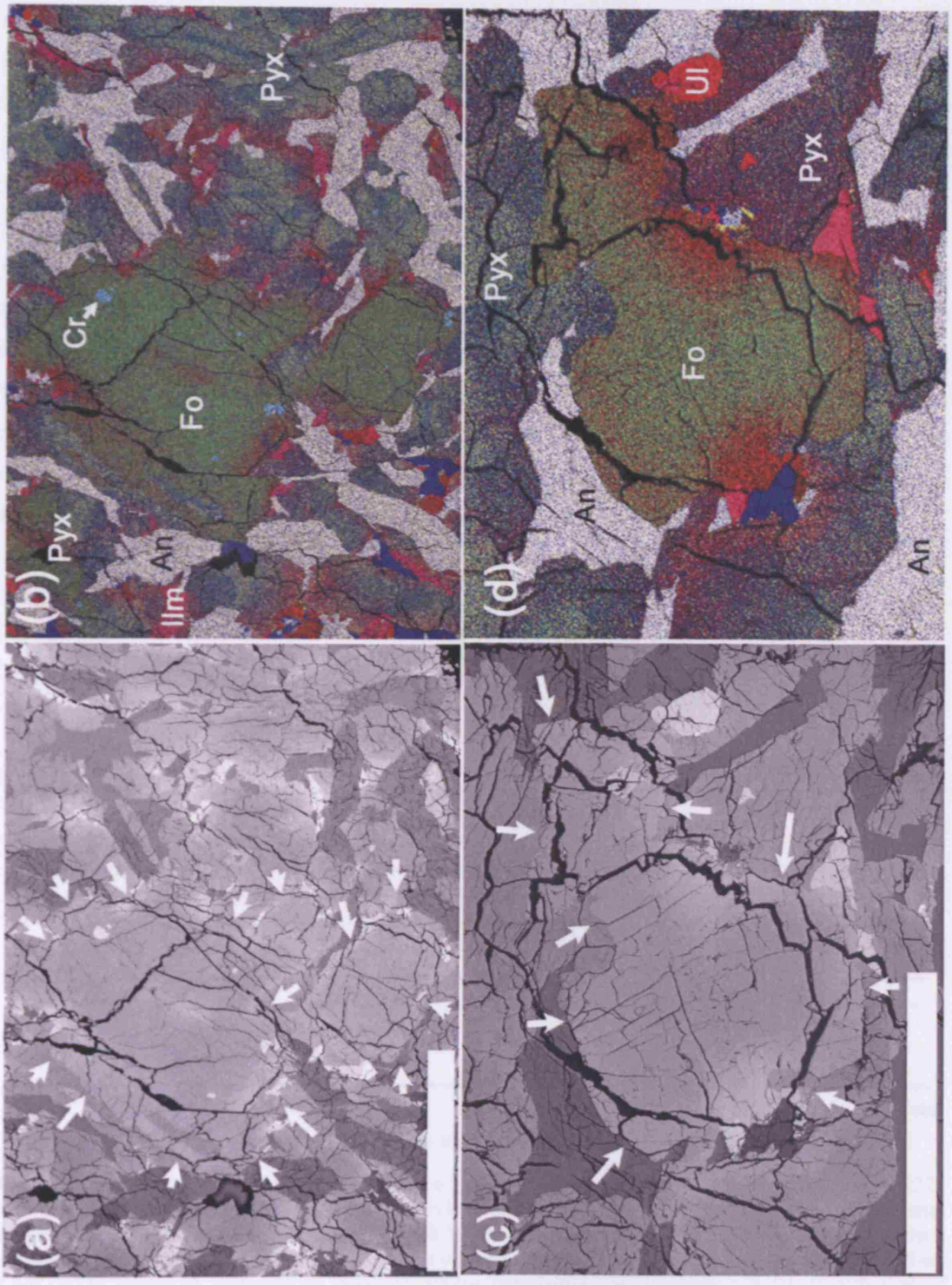

Fig. 5.9. Forsteritic olivine grains in (a) and (b) in LAP 02226 and (c) and (d) in LAP 02224. False colour images are based on the same colour scheme as Figure 5.2. An = anorthite, Pyx = pyroxene, Si = silica, Fo = forsteritic olivine (zoned from Mg-rich cores [bright green], to Fe-rich rims [bright red]), Cr= chromite, Ul = ulvöspinel, Ilm = ilmenite.

A few (< 5 %) large forsteritic olivine grains (Fig. 5.11) contain sub-rounded multiphase inclusions that have sharp boundaries with their host. The melt inclusions contain daughter minerals that include a glass phase (rich in Al and Ca) with microcrysts of a Ti-rich opaque phase intergrown with barred and feathery aggregates (< 5 μm) of pseudo-pyroxene glass (Fig. 5.11b,c) and microcrysts (10 to 20 μm) of near- stoichiometric pyroxene composition (Table 5.3). These phases nucleated from the contact with the olivine where there is a boundary pyroxene layer. They are not an injected melt product, which would be expected to be present in the surrounding fractures and cracks, but are likely to be a primary melt inclusion that was trapped when the olivine crystallized. Similar inclusions have also been observed in olivines from 02224 (Fig. 5.11c), 02226, and in other sections of LAP (Righter et al. 2005). These areas are textually similar to trapped melt areas measured in Apollo 12 and 15 mare basalt samples (as discussed in Weiblen, 1977), and NWA 032 (Fagan et al. 2002), suggesting that this process is typical of lunar low-Ti melt conditions.

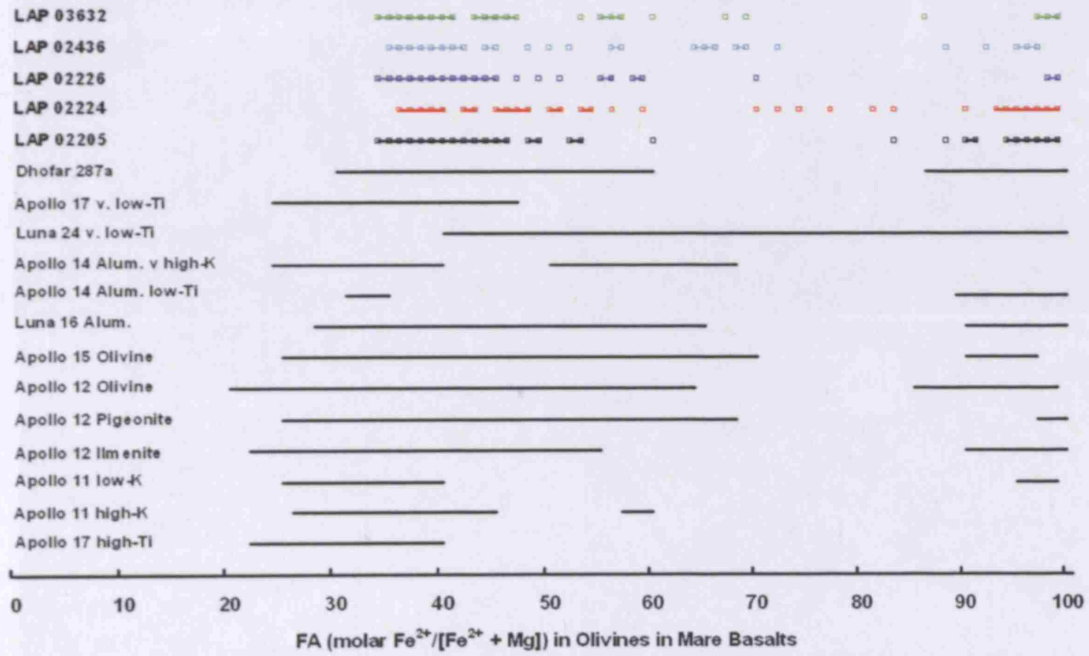

Fig. 5.10. Comparison of olivine Fe# (molar Fe / [Fe + Mg]) compositions in LAP 02205, LAP 02224 and LAP 02226 compared with mare basalt olivine compositions (Papike et al. 1991) and basaltic lunar meteorite Dhofar 287a (Anand et al. 2003b) and NWA 032 (Anand et al. 2006). LAP lunar stones show a similar range to Apollo 12 and 15 basalts, albeit with a higher Fe# value for the most primitive forsterites. LAP 02224 shows an intermediate range of olivine chemistries that correspond to the Fe-rich rims of large olivine crystals.

Fayalite grains are common and all are associated with the mesostasis regions of the samples. These masses are anhedral and form a groundmass containing Al, K-rich glasses, silica, troilite blebs, plagioclases, Fe-rich pyroxenes and ilmenite. It has been suggested (Aramovich et al. 2001, Fagan et al. 2002) that these late-stage olivines could be formed in the breakdown of

pyroxferroite at low pressure into a stable of assemblage of hedenbergite - fayalite - SiO_2. There is evidence for this process in all five stones from the observation of SiO_2 within, and stable pyroxenes adjacent to, the mesostasis regions.

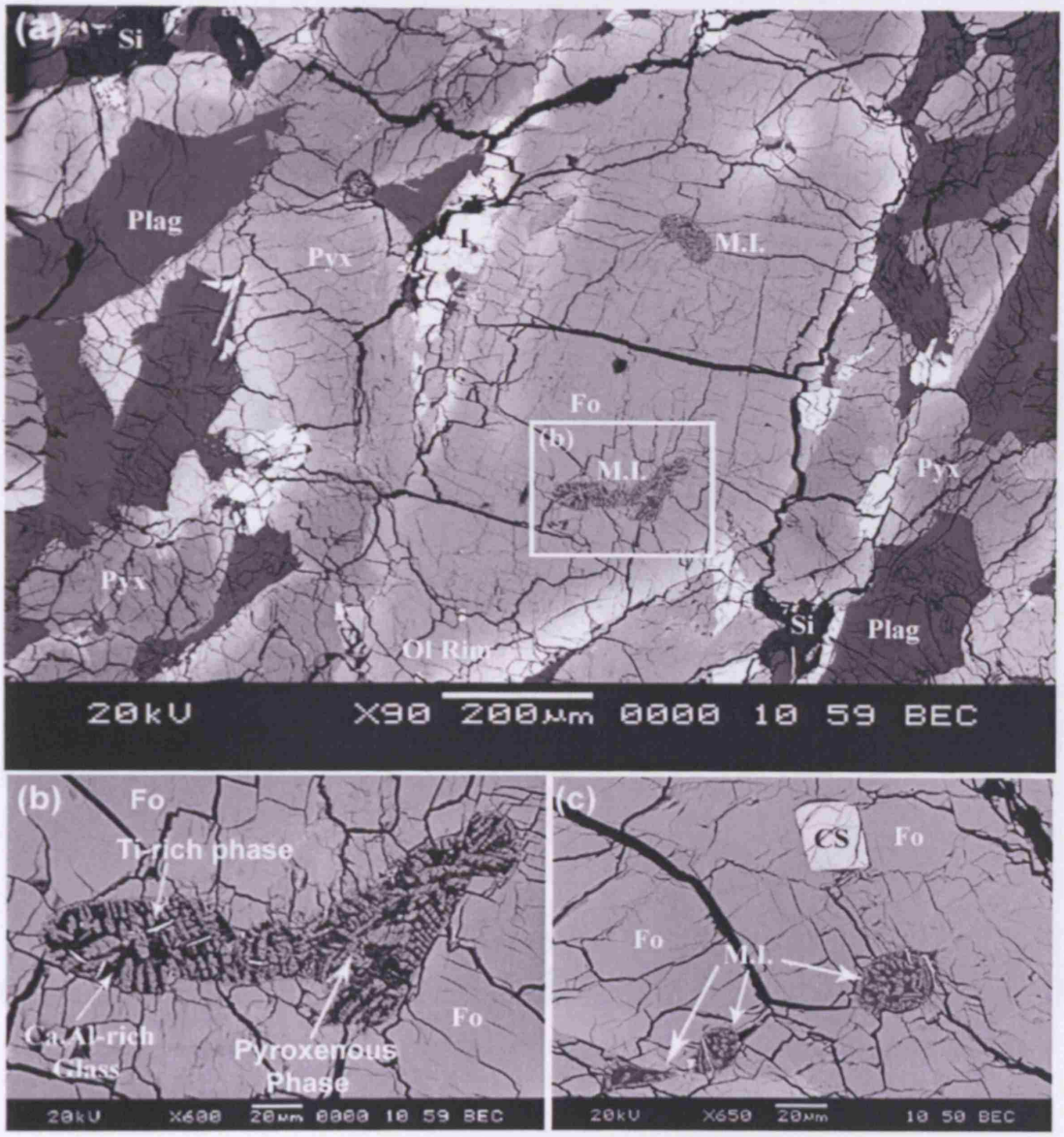

Fig. 5.11 (a) BSE image of large olivine grain in LAP 02205. The mineral is zoned from Fo_{63} core to Fo_{39} rim and contains two small quenched melt areas that have been highlighted. (b) Close-up of the trapped melt with microcrystalline texture in LAP 02205 where daughter barred pyroxene microcrysts sit in a glassy matrix with micro inclusions of a Ti-rich and small S-rich phases (bright albedo). (c) Close-up of small trapped melt inclusions in a single olivine in LAP 02224. Minerals are represented by the following symbols: Pyx = pyroxene; Plag = plagioclase; I = ilmenite; Fo= Forsteritic olivine; CS = chromite-spinel; MI = Melt Inclusion; Si = silica; Ol Rim = olivine rim.

5.3 Mineral Composition: Oxides

Ilmenite (~3 % by mode) is the most common oxide in the LAP stones and occurs as euhedral elongate crystals (typically 100 to 800 μm) distributed interstitially throughout each sample and as more subhedral-anhedral masses (typically < 250 μm) in mesostasis regions (Fig. 5.12). Ilmenite crystals in the stones contain < 0.4 % MgO, 0.25 to 0.45 % MnO, and < 0. 5% Cr_2O_3. The amount of Mg-substitution is generally lower than in other low-Ti Apollo and Luna mare basalt suites but is similar to compositions in A12 pigeonite and olivine basalts (Papike et al. 1991). All five stones show a very similar ilmenite major and minor element composition that is further evidence that the stones originate from the same melt source on the Moon.

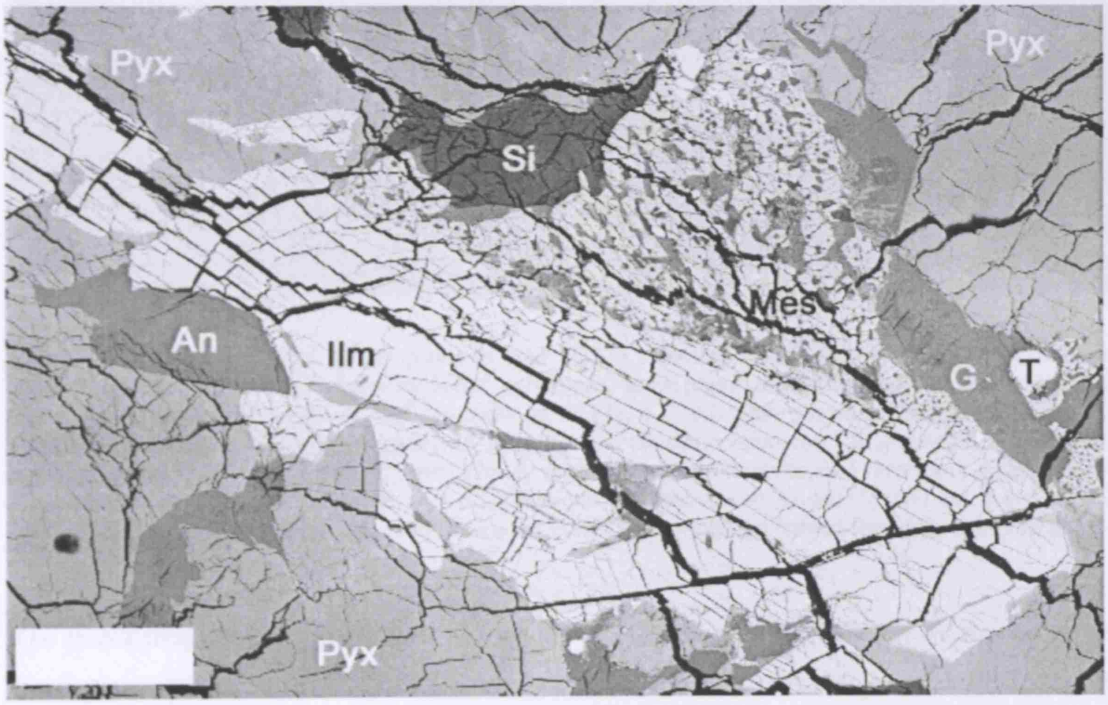

Fig. 5.12. Large, late-stage ilmenite grain in LAP 02224. Pyx = pyroxene; An = plagioclase; Ilm = ilmenite; Si = silica; Mes = mesostasis, G = glass, T= troilite. Scale bar = 100 μm.

Spinel is the second most abundant oxide mineral in LAP (0.3 to 1 % by mode). Small Cr-rich spinel (Al-Ti-Chromite) grains are found as inclusions within forsteritic olivine grains and are related to early crystallization processes. These grains are Mg-rich ($Mg\#_{3-25}$) compared with the late stage ulvöspinel grains ($Mg\#_{0-2}$; Table 5.3). Interstitial spinels follow a narrow fractionation trend (Fig. 5.13a) with an increase in Cr-content/decrease in Ti-content, evolving to ulvöspinel compositions that are often associated with mesostasis area.

Some of the grains display zonation from small Al-Ti-chromite rich cores to sharply defined chromium-ulvöspinel rims (Fig. 5.13). The sharp increase in TiO_2, with a moderate increase in Fe# and a decrease in Cr_2O_3 and Al_2O_3 (Fig. 5.14b,c), represents the 'second' type of spinel zonation as discussed by El Goresy et al. (1976), where early crystallized spinels re-equilibrated with crystallizing melt. Thus the chromite spinels form nucleation cores for later precipitated evolved ulvöspinels. The compositional gap (Fig. 5.14a) between the Cr-rich and Cr-Ti-rich spinels has been interpreted by previous investigators (Arai et al. 1996; Jolliff et al. 2003) to be the result of partial resorption of titian-chromite when melt cooling rates are moderately slow.

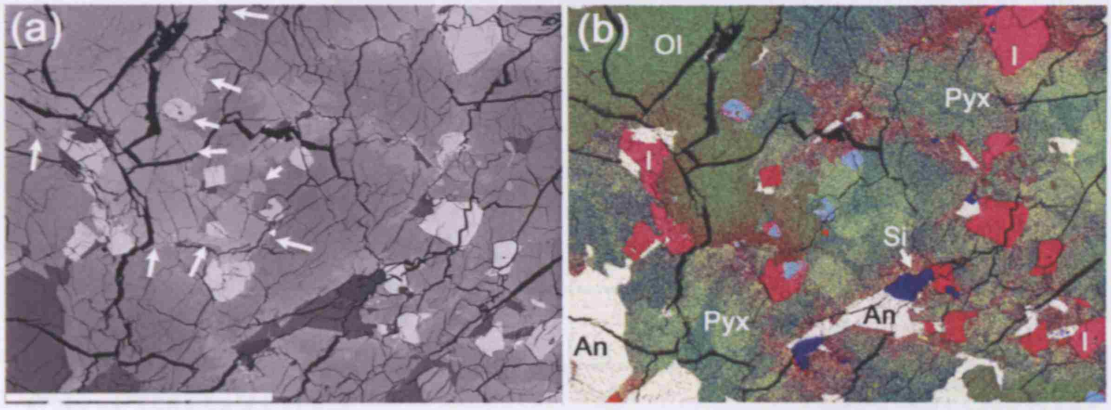

Fig. 5.13. (a) BSE image of spinel grains in LAP 02226 affiliated with a zoned olivine grain (outline indicated by arrows) and a complex of zoned pyroxenes, small plagioclase/silica and ilmenite grains. (b) False colour x-ray map with colours the same as in Fig. 5.2. All pink phases, except those marked I (ilmenite) are spinels. Complex zonation in the pyroxene phases is apparent. Chromite-rich spinel cores are highlighted by turquoise colour; some display gradual zonation to ulvöspinel rims (dark pink colour). One spinel fragment has a chromite core composition, and is then surrounded by (and not zoned to) an ulvöspinel rim. An= anorthite, Pyx = pyroxene, Si = silica, Ol = olivine (zoned from Mg-rich core to Fe-rich rims). Scale bar = 400 µm.

The spinel compositions (Fig. 5.14a) and the Fe# and Ti# trends (Fig. 5.14b,c) are similar to the fractionation trends in some Apollo 12 and Apollo 15 low-Ti basalts (Papike et al. 1991, Anand et al. 2003b), and also those in low-Ti meteorites Yamato 793169 (Arai et al. 1996) and Dhf-287a (Anand et al. 2003b). The LAP stones, however, have more evolved (Ti-rich) ulvöspinel compositions than most Apollo samples and Dhf-287a, another indication that LAP crystallized from a comparatively evolved melt. The five LAP stones have very similar spinel fractionation trends, providing further strong evidence that the stones are petrologically related.

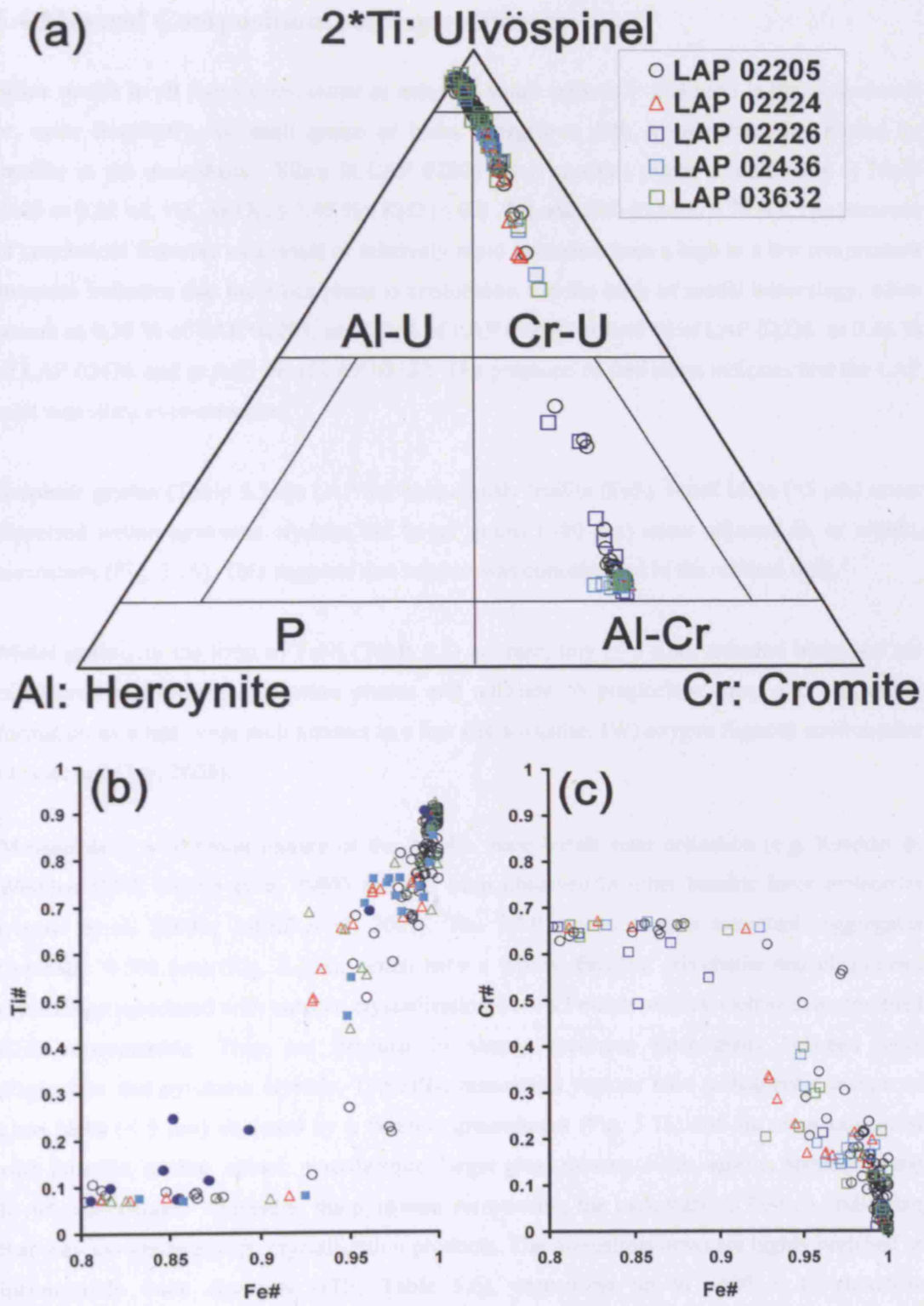

Fig. 5.14. (a) Compositional diagram (2Ti-Cr-Al in mol %) for spinels analyzed in LAP 02205, LAP 02224, LAP 02226, LAP 02436 and LAP 03632. Compositions zones: P = picotite, Al-Cr = aluminous chromite, Al-U = aluminous ulvöspinel, Cr-U = chromian ulvöspinel. (b) Plot of Fe# (molar Fe^{2+} / [Fe^{2+} + Mg]) vs. Ti# (molar Ti / [Ti+Cr+Al]) and (c) Fe# vs. Cr# (molar Cr/ [Al+Cr]) showing crystallization trend of spinels in LAP 02205. Symbols are the same in all three plots.

5.4 Mineral Composition: Accessory Phases

Silica occurs in all five stones, either as anhedral small crystals (< 0.3 mm) in the groundmass or, more frequently, as small grains or blebs intergrown with Al-rich glass and hosted by fayalite in the mesostasis. Silica in LAP 02205 often contains minor contaminants of Na_2O (0.05 to 0.22 wt. %), Al_2O_3 (≤ 1.45 %), K_2O (≤ 0.2 2%) and FeO (0.14 to 0.79 %). The presence of conchoidal fractures as a result of relatively rapid inversion from a high to a low temperature structure indicates that the silica phase is cristobalite. On the basis of modal mineralogy, silica occurs as 0.38 % of LAP 02205, as 0.59 % of LAP 02224, as 0.45 % of LAP 02226, as 0.46 % of LAP 02436 and as 0.61 % of LAP 03632. The presence of free silica indicates that the LAP melt was silica over-saturated.

Sulphide grains (Table 5.5) in LAP are ubiquitously troilite (FeS). Small blebs (<5 μm) occur dispersed within pyroxene crystals, but larger grains (<80 μm) occur adjacent to, or within, mesostasis (Fig. 5.16). This suggests that sulphur was concentrated in the residual melt.

Metal grains, in the form of FeNi (Table 5.5) are rare, tiny (≤ 5 μm), anhedral blebs and are distributed in late-stage pyroxene phases and adjacent to plagioclase rims, also suggesting formation as a late-stage melt product in a low (iron-wustite; IW) oxygen fugacity environment (Taylor and Day, 2005).

Mesostasis is a common feature of the Apollo mare basalt suite collection (e.g. Roedder & Weiblen 1977; Papike et al. 1998) and has been observed in other basaltic lunar meteorites (Anand et al. 2003b; Jolliff et al. 2003). The LAP stones contain mesostasis aggregates (typically < 500 μm) (Fig. 5.16a), which have a typical fayalite, cristobalite and plagioclase mineralogy associated with eutectic crystallization from a Fe-rich residual melt with an enriched REE concentration. They are irregular in shape, occurring interstitially between large plagioclase and pyroxene crystals. Typically, mesostasis regions have a diagnostic texture of glass blebs (< 5 μm) enclosed by a fayalitic groundmass (Fig. 5.16) and are often associated with ilmenite, troilite, spinel, pyroxferroite, larger glass masses, silica, apatite, baddelyite and K-rich plagioclase. Typically, the pyroxene surrounding the mesostasis is Fe-rich, indicating that they too are late-stage crystallization products. The mesostasis areas are highly enriched in incompatible trace elements (ITE; Table 5.6), containing up to ~600 × C1-chondrite concentrations for most REE and with a negative Eu anomaly (Fig. 5.15). Glass bleb inclusions within the fayalitic groundmass represent extreme magmatic fractionation; such evolved glass varieties are essentially the products of the granitic melt portion formed by liquid immiscibility. These form when the melt fractionates to about 95-98% and divided into granitic (K-rich; Table

5.5) and ferrobasaltic (REEP) fractions (Neal and Taylor, 1989). The granitic glass blebs have a range in K_2O contents from 2.3 to 6.3 % (Table 5.4).

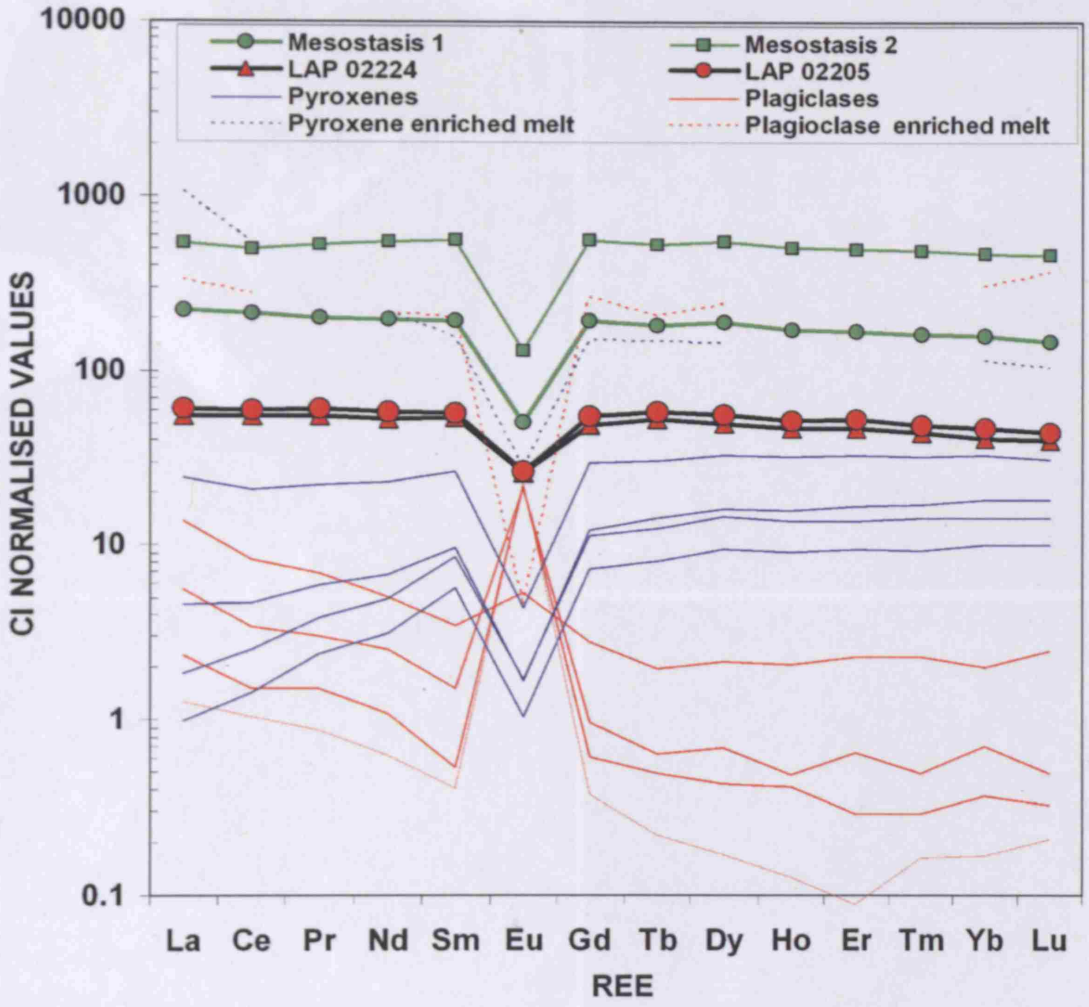

Fig. 5.15. Bulk C1-normalised REE compositions of two mesostasis areas compared with the bulk composition of LAP 02205/02224 and to silicate mineral phases pyroxenes and plagioclase in LAP 02205. The reconstructed melt compositions of the most evolved pyroxene and plagioclase grains (dashed lines) are at very similar concentrations to late-stage melt concentred in the mesostasis areas.

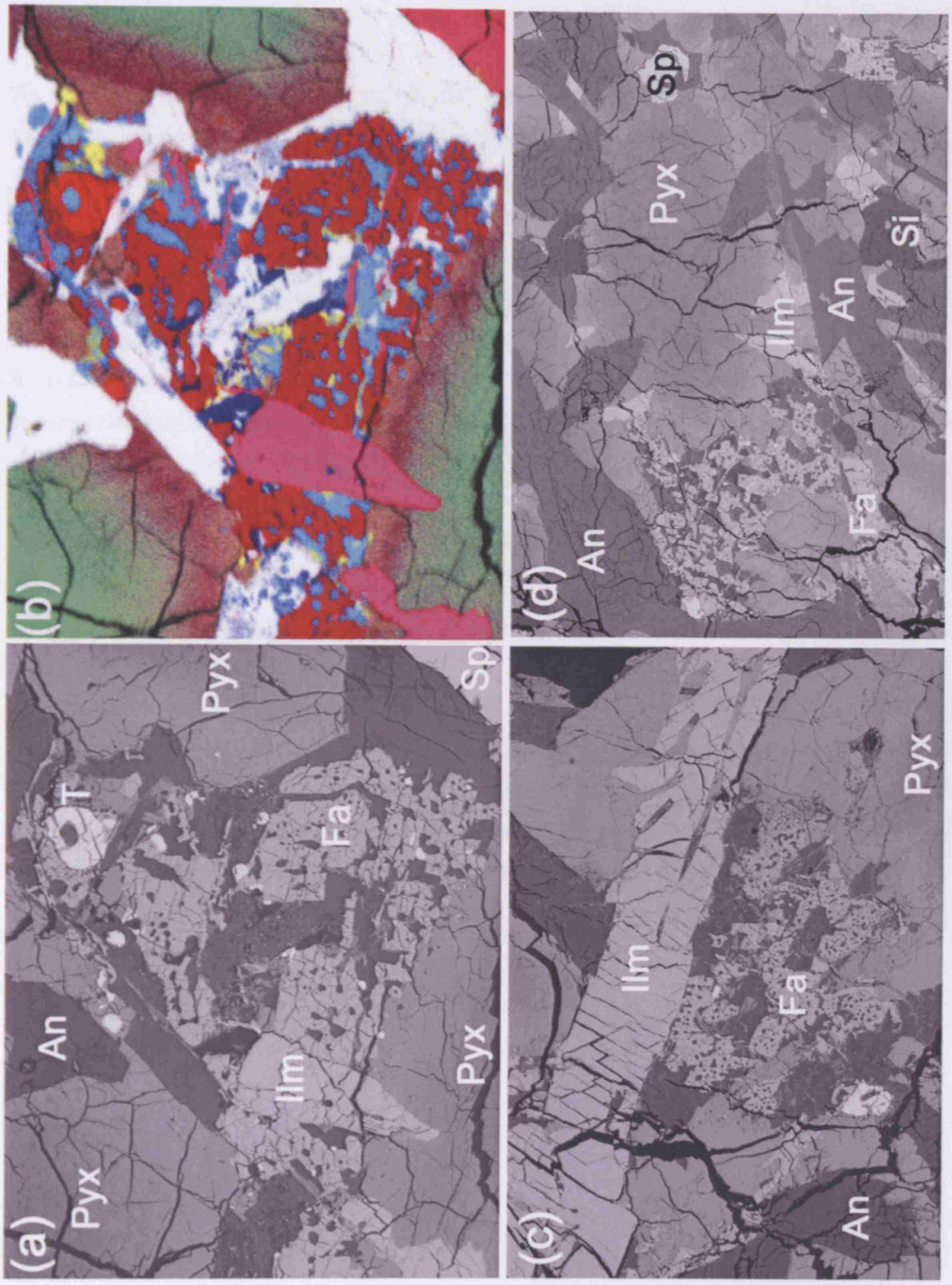

Fig. 5.16. (a) Back scattered electron (BSE) image of a mesostasis area in LAP 02205. Bleb like glass pockets are enclosed by fayalite groundmass and larger glass-rich regions. Mesostasis products enclosed by Fe-rich pyroxenes, ilmenites and plagioclase crystals. (b) False colour X-ray map of same mesostasis area. Colours are as in Fig. 5.2 with the exception that turquoise now represents K-enrichment (i.e. K-rich glass phases). Groundmass (dark red colour) is fayalite. Pyroxene phases exhibit beautiful zonation from Mg-rich cores (green) to Fe-rich rims (pink/red). (c) (d) Mesostasis areas in LAP 02226. An = anorthite, Fa = fayalitic olivine, Si = silica (cristobalite), Ilm = ilmenite, Pyx = pyroxene, T = troilite, Sp = spinel.

5.4 Fusion Crust

As previously reported by Joy at al. (2005a) and Day et al. (2005, 2006), LAP 02224 has a vesicular fusion crust (Fig. 5.17) caused by ablation melting and degassing of the rock's surface as it passed through the Earth's atmosphere. The section of LAP 02436 studied in this investigation also has a vesicular fusion crust. These represent the first examples of a vesicular fusion crust reported for mare basalt meteoritic material, and provide evidence that the sample accumulated solar-wind implanted volatiles in the lunar near-surface environment that have exsolved upon re-melting (Korotev et al. 2005). This suggests that LAP must have been part of a lava flow that was exposed at or near the lunar surface for a significant proportion of its history, allowing the penetration of solar gases. Recent Re-Os isotopic studies (Day et al. 2005) and radionuclide studies (Nishiizumi et al. 2006) of the fusion crust have attempted to constrain the exposure history of the LAP meteorite. Nishiizumi et al. (2006) report elevated ^{26}Al concentrations in the fusion crusts of LAP 02205 and LAP 02224, providing evidence for solar cosmic ray interaction while the rock was in situ on the lunar surface. This confirms a near-surface residence history, as suggested by the presence of a vesicular fusion crust.

The average composition of this fusion crust melt (Table 5.5) in LAP 02224 is unexpectedly poorer in Al_2O_3, and richer in FeO, compared with the bulk sample and melt vein average composition. This difference highlights the problem of using average fusion crust compositions to represent bulk rock composition (as also pointed out by Day et at. 2006), and is presumably because of different minerals being affected differently by the melting associated with fusion crust formation.

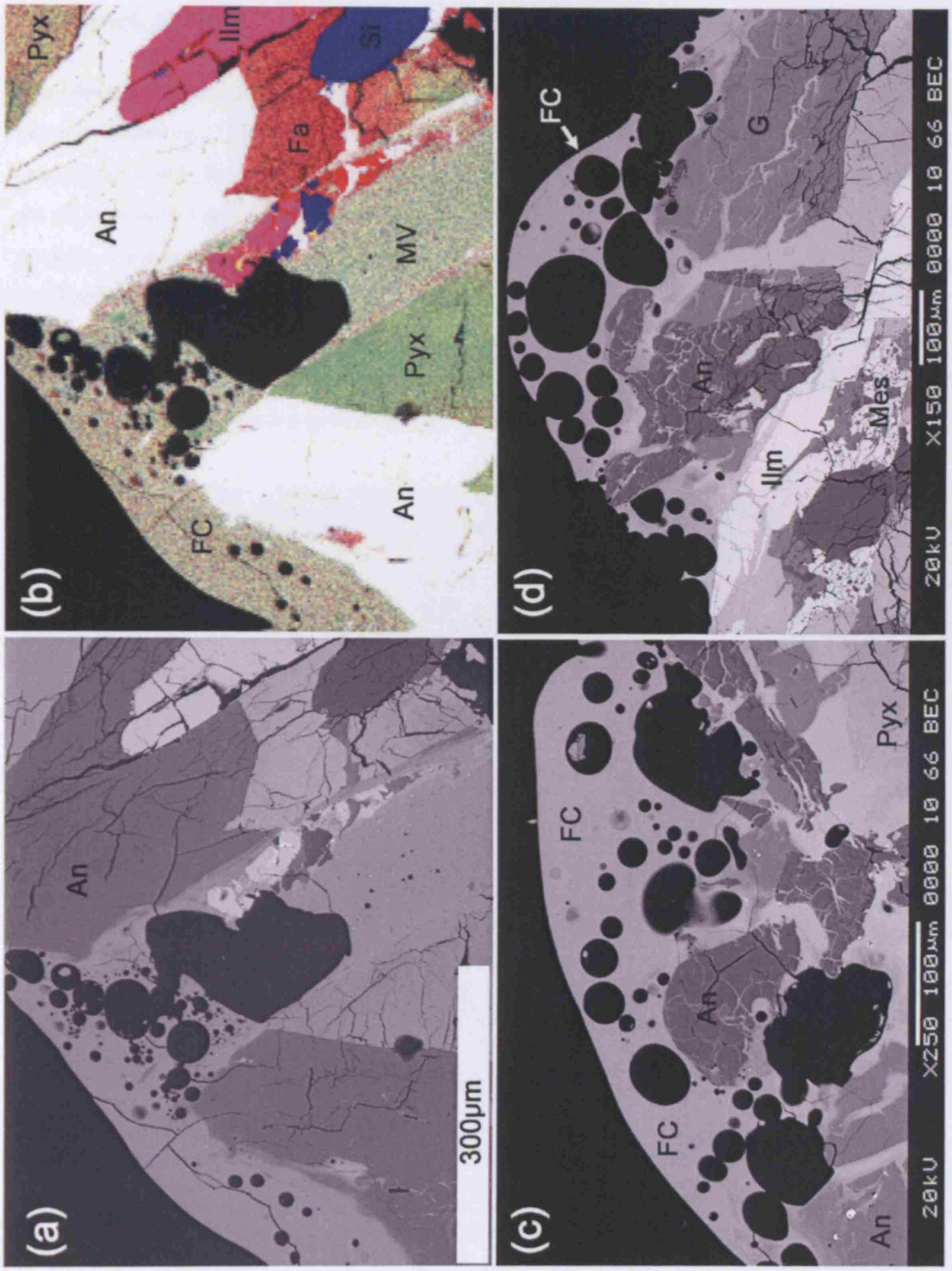

Fig. 5.17. (a) BSE image of area of fusion crust and large melt vein in LAP 02224. (b) False colour X-ray map of same image. Colours are the same as in Fig. 5.2. (c) (d) Other areas of the fusion crust in LAP 02224. Vesicles (black circular regions) are heterogeneously distributed throughout the melted/melting area. Minerals being melted into this zone can be seen at the bottom of the vesiculated region. Minerals are represented by Fa = fayalite, T = Troilite, Mes = mesostasis, G = Glass, Ph = Phosphates, FC = Fusion Crust, An = anorthite, Ilm = ilmenite, Si = silica.

5.5 Shock Effects

The Moon has been subjected to intense bombardment by comets and meteorites throughout its history (Wilhelms, 1987), and the effects of these impacts can clearly be seen in lunar rocks (e.g. Ryder, 1985; Bischoff et al. 1998; Korotev 1991; Anand et al. 2003b). The LAP meteorites are all crystalline basalts with no evident brecciation. However, all of the samples have small pockets, fractures and faults that are partially infilled with black glass (Fig. 5.18), suggesting localized intense shock pressures of greater than 60 GPa (Rubin et al. 1997). An average of 17 melt vein analyses (Table 5.5) is similar to the melt vein compositions reported by Righter et al. (2004) and is of pseudo-bulk rock composition. These regions are therefore interpreted as being derived from localized melting of the basalt.

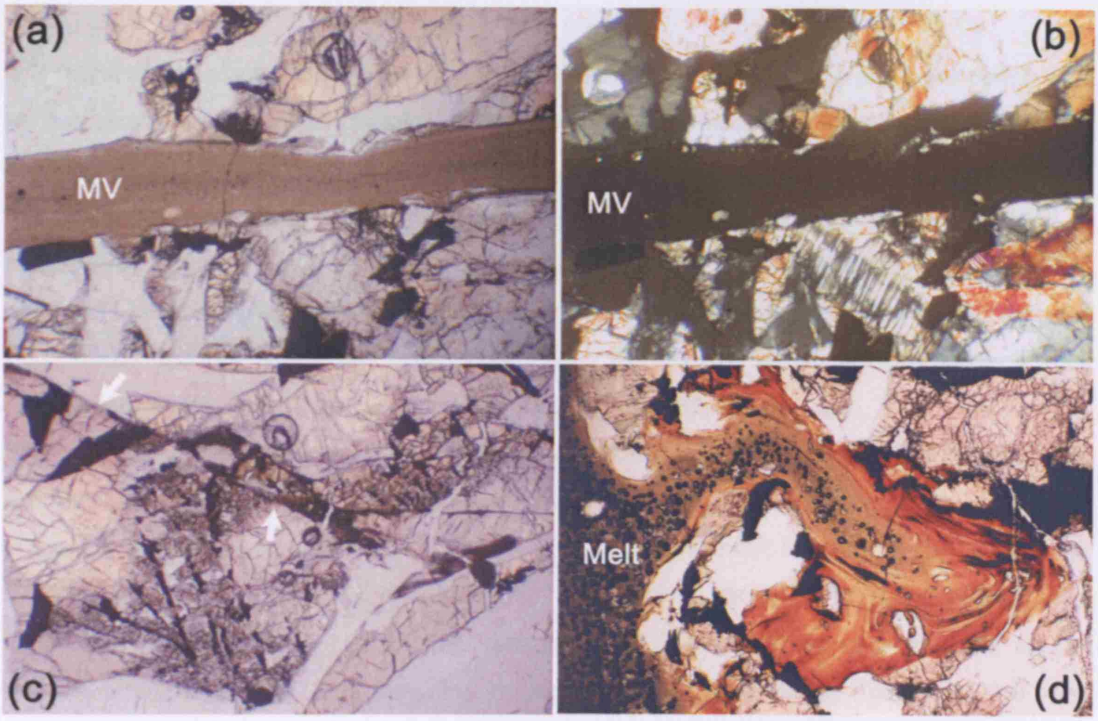

Fig. 5.18. Examples of shock effects in the LAP basalts. Field of view in all photomicrographs is ~ 2 mm. (a) Brown, glassy, melt vein in ppl. (b) Same vein in cpl. Shock deformation features can be seen in pyroxene grain directly under the vein itself. (c) Fault (indicated with arrows) running through and offsetting pyroxene grains and mesostasis areas in LAP 02224. (d) PPL image of brown and orange large vesicular melt vein and pocket cross-cutting into surrounding pyroxene grains.

Minerals in LAP have been affected by different degrees of shock metamorphism, even though they were emplaced in close proximity to each other. Pyroxene grains typically display undulatory extinction with some crystals having weak mosaicism and others displaying shock-induced twinning (Fig. 5.3) and planar deformation features (10 to 30 GPa; Rubin et al. 1997). Forsteritic olivine grains contain irregular fractures, and occasionally show undulose extinction,

suggesting processes of up to S2-3 shock pressures (i.e. > 10 GPa; Stöffler et al. 1991). Plagioclase grains vary in the extent of shock alteration from mildly shocked grains that display clear relict twinning (Fig. 5.7), to those that have undulatory extinction and those that have no internal twinning features and are nearly isotropic in cross-polarized light. The latter implies some degree of conversion to a glass phase (maskelynisation), with shock pressures greater than S5 (30 to 45 GPa; Stöffler et al. 1991). The range of shock metamorphism identified is therefore likely to represent shock pressures that vary from approximately 10 GPa to > 60 GPa throughout the sample.

5.6 Discussion

5.6.1 Comparison with Other Mare Basalts

It is important to place the LAP basalt within the framework of the Apollo and Luna collections, so that petrological and geochemical comparisons can be made and relationships established between site-sampled material and randomly launched meteorites. The LAP stones are important samples as together they are only one of a few lunar meteorites to be classified as mare basalt. Others include Yamato 793169 and Asuka 881757 (Arai et al. 1996), Dhofar 287a (Anand et al. 2003b), and NWA 032/479 (Fagan et al. 2002). A pairing relationship between the LAP stones and NWA 032 has been proposed on the basis of similar mineral and bulk rock compositions (e.g. Koizuni et al. 2005; Righter et al. 2005; Zeigler et al. 2005; Anand et al. 2006). If they are source-related, LAP represents a portion of the melt that has undergone more fractionation than NWA 032, and that cooled more slowly (as it has a larger grain size). Similar young crystallization ages of NWA 032 (Ar-Ar: 2.800 ± 0.020 Ga; Fagan et al. 2002) and LAP 02205 (Ar-Ar: 2.95 ± 0.020 Ga, Nyquist et al. 2005; Rb/Sr: 2.956 ± 0.014 Ga, Rankenburg et al. 2005; and U/Pb: 2.929 ± 0.015 Ga, Anand et al. 2006) help to support these pairing relationships, suggesting that they are examples of the same young mare lava that have undergone slightly different fractionation and cooling histories.

Figure 5.19 and 5.20 summarises the classification of LAP 02205 and LAP 02224 compared with a wide range of Apollo and Luna samples. Figure 5.19b indicates that LAP stones fall towards the Al-rich end of the low-Ti, low-Al classification of Neal and Taylor (1992), and are most similar to the basalts in the Apollo 12 and 15 collections (Rhodes et al. 1973, 1977; Vaniman et al. 1991; Neal et al. 1994a; Papike et al. 1998). However, bulk MgO (5.58 to 6.47 wt. %) and Mg# (31 to 35) is lower than typical values in these low-Ti basalts (Fig. 5.19a, b) and total bulk alkalis ($Na_2O + K_2O$) are much higher (0.51 to 0.54 wt. %). The LAP bulk REE content is shown in Figure 5.20, and is significantly higher than found in basalts collected from

the Apollo 12 and Apollo 15 sites. The LAP REE values are more comparable to Apollo 14 and Luna 16 high-Al basalts rocks, though LAP has a lower bulk-Al_2O_3 content and a different magmatic origin. Elevated REE content also makes LAP distinct from the Y-793169, A-881757 and Dhf-287a meteorites. Th/Sm ratios (Fig. 5.19d: LAP has Th/Sm = 0.275 to 0.297) in LAP are however similar to the proposed paired meteorite NWA 032 (Th/Sm = 0.287 Fagan et al. 2002).

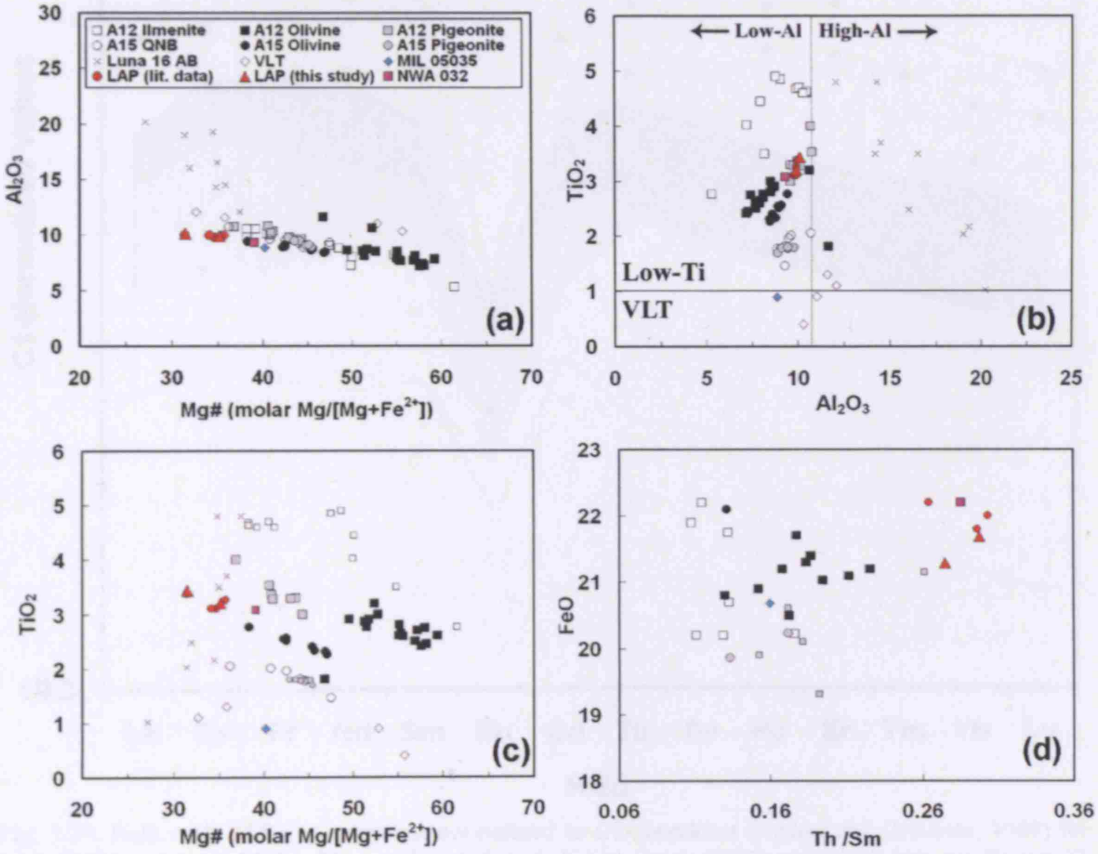

Fig. 5.19. Bulk composition variation diagrams comparing LAP to low-Ti basalts from the A12, A15 and Luna 16 collection. Apollo compositions are taken from Rhodes and Hubbard (1973), Rhodes et al. (1977), BVSP (1981), Neal et al. (1994a), and average bulk composition data for NWA 032 are taken from Zeigler et al. (2005). LAP literature data taken from Anand et al. (2006), Day et al. (2006) and Zeigler et al. (2005). (a) LAP has the lowest Mg# of the low-Al, low-Ti basalts; (b) a plot of TiO_2 against Al_2O_3 shows that the LAP stones are all within the low-Ti, low-Al lunar mare basalt classification as proposed by Neal and Taylor (1992); (c) TiO_2 and Mg# are good distinguishing characteristics for the Apollo basalts – the different olivine, pigeonite, ilmenite and QNB basalts all fall into distinctive groupings, with the LAP stones not easily being fitted into any group; (d) LAP, along with NWA, is Th-rich (and other ITE-rich) compared with the other lunar basalts.

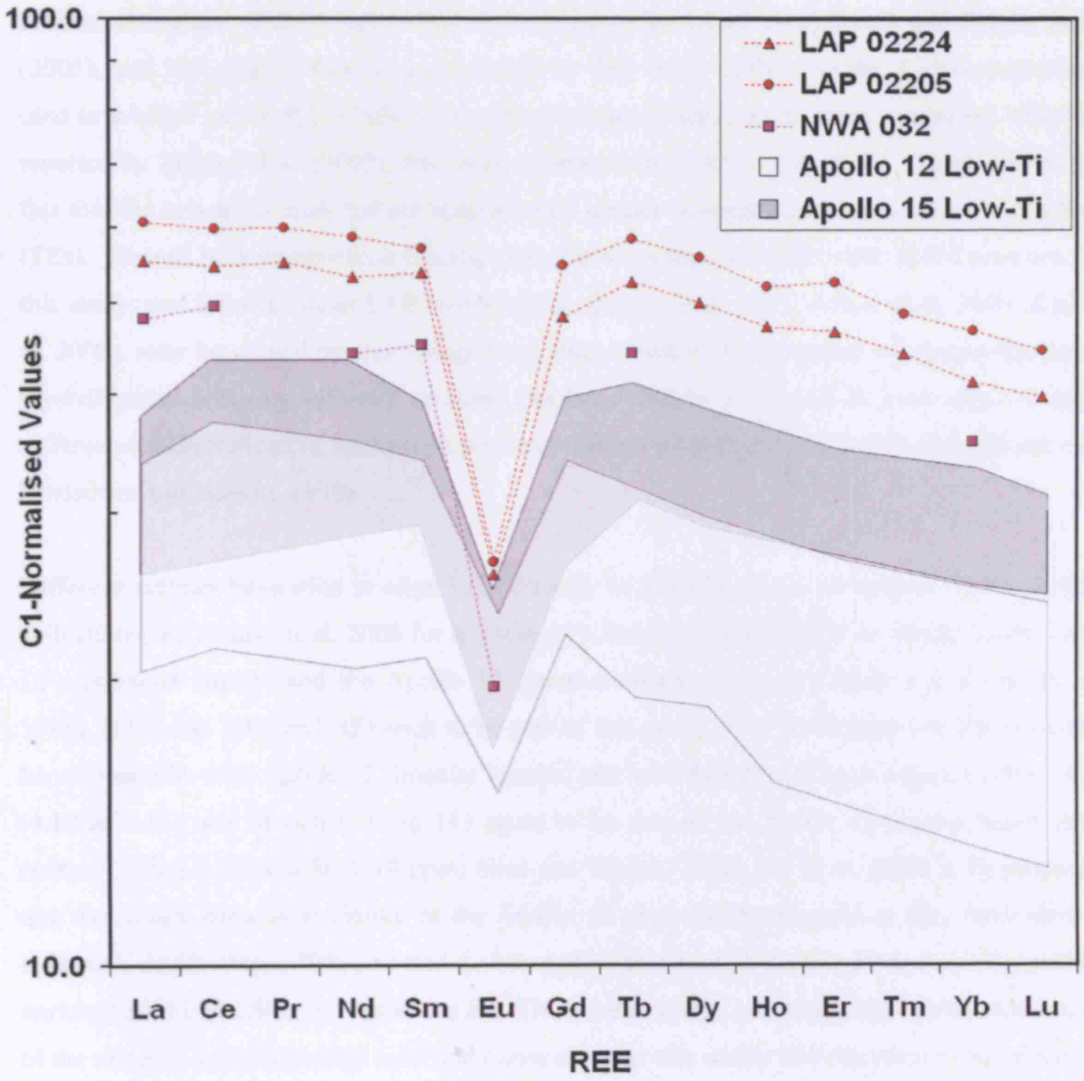

Fig. 5.20. Bulk rock REE concentration normalized to C1-chondrites (Anders and Grevesse, 1989) for LAP 02205 and LAP 02224. The results of this study (Joy et al. (2006) compared with Apollo low-Ti suites and lunar meteorite sample NWA 032. Apollo data fields are taken from Rhodes and Hubbard (1973), Rhodes et al. (1977), BVSP (1981), Neal et al. (1994a); average bulk REE concentrations for NWA 032 are taken from Zeigler et al. (2005). The LAP stones are clearly the most REE-rich low-Ti basalt collected to date.

Whole rock composition for the LAP stones, as determined by ICP-OES/Mass-Spec, fused bead EMPA/ICP-MS, and INAA has recently been reported by Anand et al. (2006), Day et al. (2006) and Zeigler et al. (2005), respectively, and is included in Table 5.2 for comparison. Generally the major elements are within good agreement (to within 1 wt. %), although the FeO reported by Joy et al. (2006) is in better agreement with Day et al. (2006) than with the other two techniques. Figure 5.21 compares the minor and trace element concentrations obtained here (Table 5.2) with other recently published data. It will be seen that the agreement is generally very good, although there are significant discrepancies for Ni, Cu, Zn, Ga, Cs and W. Generally all of the REE concentrations are in good agreement (Fig. 5.21b), although the Joy et al. (2006)

concentrations are 10-20% higher than those reported by Anand et al. (2006) and Zeigler et al. (2005), and 30% higher than those presented by Day et al. (2006). As the K_2O reported here (and to a lesser extent P_2O_5) bulk composition is also elevated, particularly compared with that reported by Zeigler et al. (2005), this small enhancement in REE content may simply reflect the fact that the sub-splits analyzed are samples with greater concentrations of mesostasis (and thus ITEs). Overall bulk composition heterogeneity between the LAP 02205 and 02224 measured in this study, and between other LAP samples (e.g. Zeigler et al. 2005; Anand et al. 2006; Day et al. 2006), may be caused by short-range unmixing, where minerals settled out during fractional crystallization (causing different sections emplaced within a few cm of each other to have different concentrations of mineral phases, and therefore heterogeneous bulk compositions; e.g. Lindstrom and Haskin, 1978).

Different authors have tried to align LAP directly to specific groups of samples in the Apollo collection (see Anand et al. 2006 for a summary). In terms of Mg# LAP is similar to the Luna 16 aluminous basalts and the Apollo 15 quartz-normative basalts (QNBs; e.g. Ryder et al. 1985), but is too TiO_2 and REE-rich to be part of this group. It is too Ti-poor and Rb/Sr rich to be comparable with Apollo 12 ilmenite basalts, and too Mg# poor (Fig. 5.19a,c), Co/Sm poor (4.12 to 4.85) and Sr-rich (135 to 143 ppm) to be part of the Apollo 12 olivine basalt suite (where Co/Sm > 10 and Sr <110 ppm; Neal and Taylor, 1992). Joy et al. (2005 a, b) proposed that the stones were most similar to the Apollo 12 pigeonite basalt suite as they have similar bulk rock Al_2O_3, MgO, TiO_2, Sr and Co/Sm ratios. However, it is now clear that they exhibit enriched LREE profiles, excessive Eu and Th concentrations, and lower Mg# values than most of the samples in the pigeonite suite and I now consider this earlier identification to be unlikely.

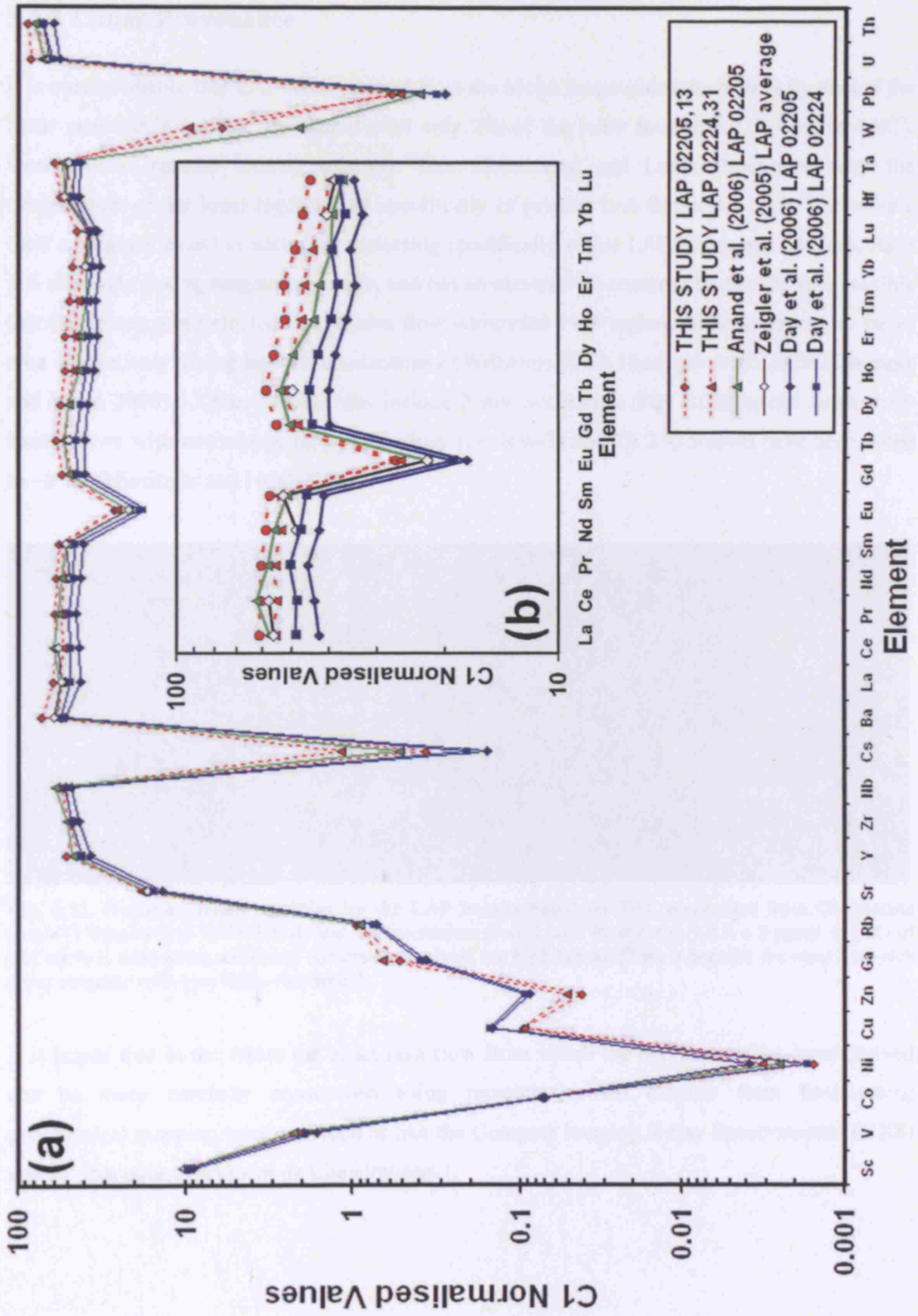

Fig. 5.21. The chondrite-normalized bulk rock concentrations of minor and trace elements for LAP obtained in this study compared with other recently published values. (a) All minor and trace elements; (b) Rare earth elements (REE) only. Note the general agreement, but that the Joy et al. (2006) REE values are systematically higher, presumably reflecting the fact that these sub-splits contain a greater concentration of mesostasis (and thus incompatible trace elements).

5.6.2 Lunar Provenance

It is most probable that LAP was launched from the Moon's near-side (since 30 % by area of the lunar nearside is basaltic, compared with only 2% of the lunar farside; e.g. Wilhelms 1987). Geochemical remote sensing missions like Clementine and Lunar Prospector map the composition of the lunar regolith, not specifically of pristine lava flows like LAP. Therefore a little ambiguity exists in accurately assessing specifically where LAP was launched from. As it is a relatively young magmatic sample, and has an elevated Th content (Table 5.2), it is possible that the stones were ejected from a lava flow within the PKT region, which is known to be an area of relatively young basaltic emplacement (Wilhelms 1987; Hiesinger et al. 2003; Hiesinger and Head 2006). Other possibilities include Mare Serenitatis (Fig. 5.22) where some mare basalt flows with corresponding geochemistry (i.e. low-Ti and Th 2 to 5 ppm) have been dated to ~3 Ga (Hiesinger and Head 2006).

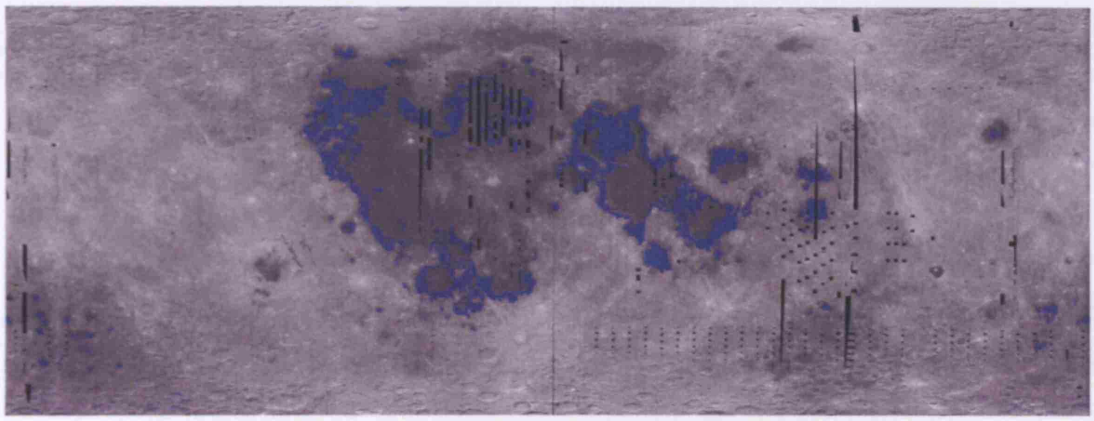

Fig. 5.22. Possible launch localities for the LAP basalts based on TiO_2 constraints from Clementine (Low-Ti Basalts [1-5 wt.% TiO_2]) and Th constraints from Lunar Prospector (LAP ± 3 ppm). If FeO of ~22 wt.% is used as an additional constraint no pixels are highlighted. [This is because the most FeO-rich areas coincide with very TiO_2-rich areas].

It is hoped that in the future the exact lava flow from which the LAP meteorites were derived can be more carefully constrained using remotely sensed datasets from forthcoming geochemical mapping missions, such as like the Compact Imaging X-Ray Spectrometer (C1XS) and M^3 mapping instrument on Chandrayaan-1.

5.6.3 Petrogenesis

The two samples of LAP analyzed for this study have similar bulk major element compositions (Table 5.2, Fig. 5.19, 5.20). Minor differences in MgO (~ 1 %) are probably a consequence of the difference in forsteritic olivine content between the two samples (Table 5.1); LAP 02205 has less forsteritic olivine and therefore less MgO than 02224. Other minor compositional variations (TiO_2, Al_2O_3, and CaO) are a consequence of minor mineralogical heterogeneity. LAP 02205 and 02224 have very similar bulk REE patterns (Fig. 5.20); providing additional evidence that the rocks originate from the same lunar parent melt source. LAP 02205 shows a slight enrichment in REE, probably as a consequence of the measurement of different proportions of incompatible element enriched mesostasis regions in the two stones (Neal et al. 1994a; Day et al. 2006).

The crystallization sequence of minerals in LAP 02205/02224 can be inferred from sample petrography, mineral elemental concentrations, and thermodynamic modelling. There is a discrepancy between petrographic inference and the results of the fractional crystallization modelling using the MELTS modelling code (Ghiorso and Sack 1995; Asimow and Ghiorso 1998). According to petrographic observation the first mineral to be crystallized was Cr-spinel that is enclosed by secondary crystallizing large forsteritic olivine grains. However, using the MELTS software with a system pressure of 1 bar and fO_2 set at 2.0 log units below the IW buffer (Righter et al. 2005; Day et al. 2006), my modelling (Fig. 5.23) predicts that the first mineral to crystallize is chromite (at 1180 °C) followed by pyroxene (at 1137 °C) with *no* forsteritic olivine phases being crystallized *anywhere* in the fractionation sequence. Anand et al. (2006) also report the apparent non-crystallization of Mg-rich olivine in the LAP basalt crystallization sequence, and propose that the forsteritic olivines may be xenocrystic phases that have been incorporated into LAP from mixing in a magma chamber with the fractionated products of an earlier, olivine and Mg-rich melt. My modelling is consistent with this interpretation, and with the petrographic observation that the olivine phases often have embayed or reabsorbed rim structures suggesting a reaction between the existing olivines and crystallizing pyroxene phases from the LAP melt.

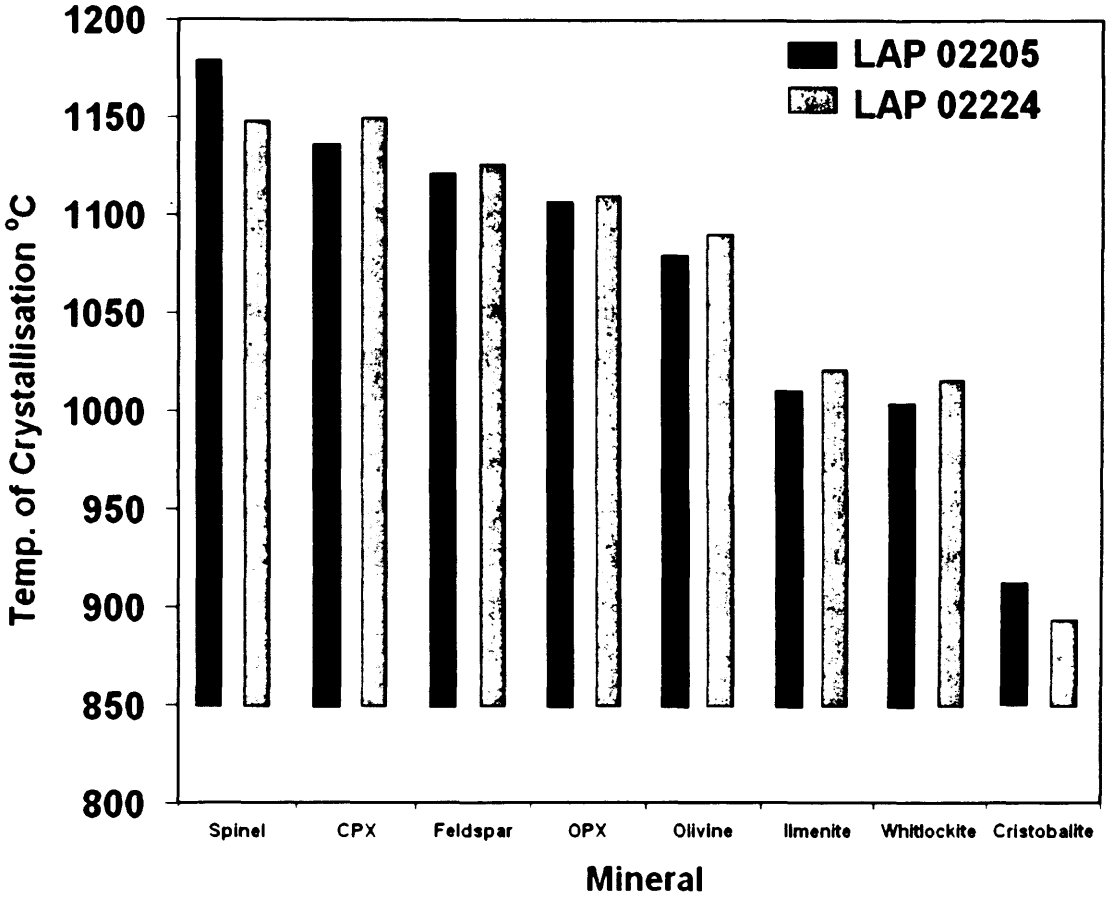

Fig. 5.23. Predicted equilibrium fractional crystallisation trends in LAP 02205 and LAP 02224 estimated by the MELTS thermodynamic software. Appearance of mineral phases (i.e. top of the bar) represents where they first arrive on the liquidus. MELTS predicts that the LAP melt system was closed (~2% residual melt) by ~850°C.

As the melt cooled to ~1124 °C (Fig. 5.23), plagioclase cotectically crystallized with both low and high-Ca pyroxene nuclei grains (core compositions; Fig. 5.4) and spinel (increasing Ti, decreasing Cr; Fig. 5.5). Fayalitic olivine grains ($Mg\#_{30}$) started to co-crystallize at ~1081 °C, and as the residual liquid is depleted in Mg the crystallizing pyroxenes zone to Fe-rich species. Ilmenite arrives on the liquidus after further cooling to ~1012 °C. As compatible elements are substituted into these co-crystallizing phases the melt becomes incompatible element-enriched and silica over-saturated. Late stage crystallization of silica phases occurred from about ~910-890 °C, and Fe-pigeonites, sub-calcic augites and pyroxferroite crystallized as late stage pyroxene rims. Late stage plagioclase became rich in K and Na (Fig. 5.8), and spinel evolved to pure ulvöspinel compositions (Fig. 5.14). Residual melt pockets experienced liquid immiscibility, producing glasses emplaced in a groundmass of fayalitic olivine with associated baddeleyite blebs, FeNi metal grains, and troilite. The parent system had almost wholly crystallized (0.34 % residual liquid) by the time the lava had cooled to <851 °C (Fig. 5.23).

The lunar basalt represented by the LAP meteorite is the product of fractional crystallization from a parental source melt that is similar in composition to the low-Ti source region that produced the Apollo 12 and Apollo 15 low-Ti basalts and low-Ti volcanic glasses, although it cannot be petrologically related to them because of systematic differences in ages between the Apollo and LAP basalts (Day et al. 2006).

Parental melt modelling has been performed by Zeigler et al. (2005) and Righter et al. (2005), who investigated the fractional crystallization trends of a suite of potential melts including lunar low-Ti picritic glass and vitrophyre mare samples. Both groups of authors propose that the Apollo 15 yellow picritic glass would make a good candidate parental melt composition on the basis of major element fractionation trends (particularly CaO, TiO_2). However, Righter et al. (2005) conclude that this cannot be a parental melt for LAP on the basis of ITE modelling, as it would produce fractionates that are too high in Zr and Yb and too-low in Sc. Righter et al. (2005) go on to suggest that modelling from the Apollo 12 olivine basalt suite, and in particular the olivine basalt sample 12009, produces the best candidate compositions that are similar to those of LAP (and NWA 032). However, my calculations using MELTS (Fig. 5.23, 5.24) indicate that the Apollo 12 olivine basalts produce trends that are too TiO_2, CaO and Al_2O_3 rich to truly match with the LAP (and NWA 032) fractionation trend. Moreover, Neal et al. (1994 a, b) showed that, at the Apollo 12 site, the ilmenite, olivine and pigeonite suites are representative of three separate parent magmatic bodies and are independently derived from distinct source regions. This heterogeneity at just one Apollo landing site is indicative of the complexity of mare basalt magmatic generation, and at present the LAP parental source cannot be accurately characterized from available samples in the Apollo collection. It can therefore conclude that the LAP stones represent evolved types of low-Ti, low-Al and low-K basalts that are unique samples of young mare basalt material.

LAP has elevated REE abundances compared with other low-Ti basaltic samples (although it has long been recognized that high-Ti basalts from the Apollo 11 and 17 landing sites, the Luna 16 high-Al basalts, and KREEP basalts exhibit comparable, or higher, REE enrichments; e.g. Beatty et al. 1979, Papike et al. 1998). The elevated REE abundances in LAP in comparison with other low-Ti basalts (Fig. 5.20) resemble those in the comparably 'young' (2.78 Ga, Fernandes et al. 2003; 2.87 Ga, Borg et al. 2004) lunar olivine cumulate NWA 773 (Jolliff et al. 2003; Day et al. 2006). Indeed, comparison of Figure 5.20 with Fig. 7 of Jolliff et al. (2003) shows LAP to be even more REE enhanced. It has been argued by Jolliff et al. (2003) and Borg et al. (2004) that the elevated REE concentrations in NWA 773 are indicative of a KREEP-rich component in the source region, the heat-producing elements of which may have been responsible for maintaining magmatic activity until a relatively late date. In principle, a similar

argument could be constructed for LAP and NWA 032, but only if it can be shown that the enhanced REE abundances cannot be obtained by normal fractionation processes. Day et al. (2006) have investigated the possibility that LAP formed as a result of assimilation fractional crystallization (AFC) processes, whereby mantle derived KREEP material was included into the melt to account for the high REE abundances. However, they concluded that this hypothesis is difficult to reconcile with the REE systematics in pyroxenes, which exhibit a normal fractionation trend – suggesting a closed system and that any ITE assimilation must have occurred prior to the onset of pyroxene crystallization. Clearly, additional samples of young basaltic materials are required to determine whether or not there exists a general trend of increasing ITE concentration with decreasing age, as might be expected if a KREEP component is required to drive late magmatic activity.

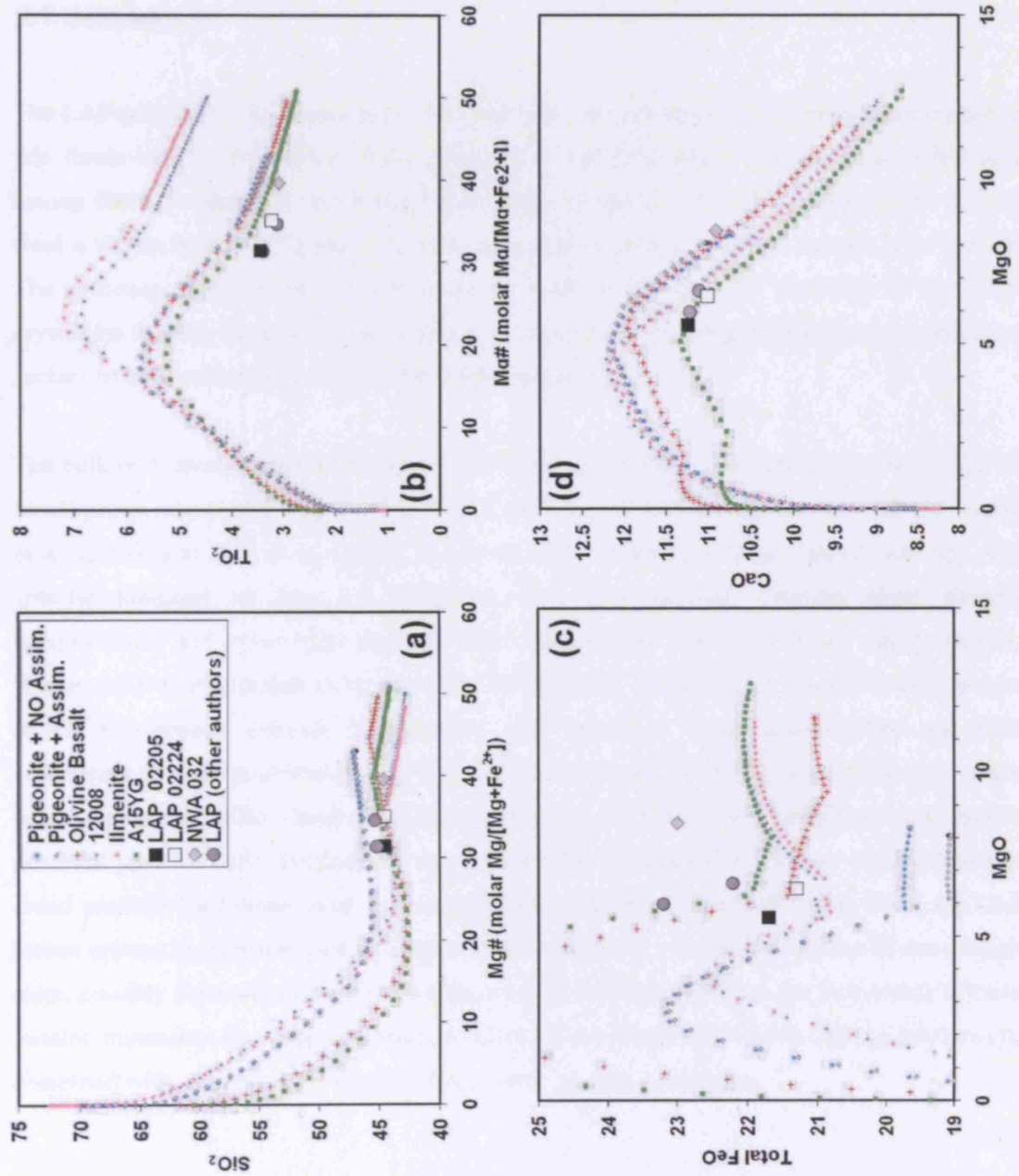

Fig. 5.24. Thermodynamic calculations generation using the MELTS modelling software (Ghiorso and Sack 1995; Asimow and Ghiorso 1998) compared with bulk compositions of the LAP basalts presented by this study and LAP and NWA 032 bulk compositions presented by Zeigler et al. (2005). (a) Comparison of bulk rock Mg# vs. SiO_2 content. (b) Comparison of bulk rock Mg# vs. TiO_2 content: the LAP basalts have significantly less Ti-contents than is predicted by the modelling of vitrophyre ilmenite basalt compositions (Ilmenite + 12008). (c) Comparison of bulk rock MgO vs. FeO content: variable reported LAP FeO values illustrate different best fit modelled melt conditions. (d) Comparison of bulk rock MgO vs. CaO content.

5.7 Summary

The LAP stones are important additions to the lunar rock collection. The five samples studied in this thesis have a very similar bulk composition and mineralogy, and the small differences among them are likely to result from short-range unmixing. Thus, they appear to be derived from a single, relatively young (c.2.9 Ga: Anand et al. 2006), lava flow on the lunar surface. The presence of a vesicular fusion crust on LAP 02224, the first identified in any lunar crystalline basaltic sample, implies that it was at one time located sufficiently close to the lunar surface to have accumulated solar wind implanted gases.

The bulk rock compositions of the LAP stones are most similar to the Apollo 12 low-Ti, low-Al basalt group, concurring with the findings of Zeigler et al. (2005), Righter et al. (2005), Anand et al. (2006) and Day et al. (2006). However, they cannot be directly classed with any site-specific lithology as they are REE-rich, have systematically different major element compositions, and lower Mg# numbers than characterized Apollo and Luna basalt samples. Rather, LAP is interpreted to be a product of fractional crystallization from a Fe-rich source, which experienced extreme fractionation with late-stage liquid immiscibility and REE enrichment in pockets of mesostasis. Thermodynamic modelling by Joy et al. (2006) and others (e.g. Righter et al. 2005, Zeigler et al. 2005, Day et al. 2006) has been used to try to constrain a potential parental melt composition, but as yet there is no identified source composition that could produce fractionates with bulk compositions that match the LAP basalt. Thus, the LAP stones appear to represent part of a previously unsampled, young, low-Al, low-Ti mare basalt suite, possibly from within the PKT. Future work is intended to address the provenance of these basaltic meteorites by using geochemical information from orbital remote-sensing instruments, combined with relative age indicators from crater counting techniques.

Stone	02205	02224	02226	02436	03632
Fayalite	1.69	0.67	0.5	1.00	1.61
Forsterite	1.4	2.71	2.76	0.73	2.90
Pyroxene	59.75	57.93	58.32	57.76	56.55
Plag.	32.04	31.78	32.57	36.10	34.05
Silica	0.38	0.59	0.45	0.46	0.61
Ilmenite	2.74	3.25	2.85	3.31	3.86
Spinels	0.29	0.97	0.27	0.63	0.43
Other	1.72	2.1	2.27	<1	<1
No. of pixels	5.77E+06	7.08E+06	1.28E+07	2.75E+06	2.29E+06

Table 5.1. Estimated modal mineral analysis from the five LAP stones. Other classification = Melt veins, Metal, Glass, Troilite. Number of pixels was calculated from the number of pixels measured in the montaged map.

	Jog et al. 2006 LAP 02224,31	Jog et al. 2006 LAP 02205,13	Anand et al. 2006 LAP	Zeigler et al. 2005 LAP	Day et al. 2006 LAP 02205	Day et al. 2006 LAP 02224
SiO_2	44.57 ± 0.20	44.53 ± 0.14	45.2	45.3	46.00	45.30
TiO_2	3.21 ± 0.02	3.43 ± 0.13	3.38	3.11	3.11	3.27
Al_2O_3	9.93 ± 0.05	10.13 ± 0.03	10	9.79	9.95	9.95
Cr_2O_3	0.290 ± 0.001	0.340 ± 0.002	0.19	0.31	0.29	0.30
FeO	21.29 ± 0.17	21.69 ± 0.18	23.2	22.2	21.80	22.00
MnO	0.276 ± 0.002	0.276 ± 0.002	0.23	0.29	0.32	0.29
MgO	6.47 ± 0.03	5.58 ± 0.02	5.99	6.63	6.32	6.84
CaO	10.99 ± 0.07	11.23 ± 0.11	11.2	11.09	11.40	11.30
Na_2O	0.410 ± 0.002	0.420 ± 0.001	0.33	0.38	0.39	0.38
K_2O	0.110 ± 0.001	0.120 ± 0.001	0.11	0.07	0.10	0.11
P_2O_5	0.110 ± 0.005	0.120 ± 0.001	0.12	0.1	0.17	0.16
Total	97.36	97.53	100	99.28	99.85	99.90
Mg #	35.16	31.45	31.4	34.7	34.09	35.68
Li*	14.00 ± 0.04	13.00 ± 0.11	11.7	-	-	-
Be*	1.18 ± 0.07	1.10 ± 0.09	1.37	-	-	-
Sc*	61.00 ± 0.04	59.00 ± 0.32	58.6	59.2	52.80	57.30
V*	118.00 ± 0.33	107.00 ± 0.11	129	-	92.00	109.00
Co*	38.00 ± 0.26	35.00 ± 0.26	37.3	37	35.40	36.90
Ni*	35.00 ± 0.44	17.00 ± 0.11	27.6	-	42.40	18.50
Cu*	12.00 ± 0.06	12.00 ± 0.12	-	-	18.60	19.40
Zn*	16.00 ± 0.26	13.00 ± 0.34	-	-	27.50	29.60
Ga*	6.68 ± 0.19	5.24 ± 0.18	-	-	3.74	4.07
Rb*	2.15 ± 0.11	2.18 ± 0.07	2.1	-	1.67	1.74
Sr*	143.00 ± 1.17	135.00 ± 1.57	135.3	133	109.0	122.0
Y*	68.00 ± 0.11	80.00 ± 0.10	73.2	-	57.0	64.9
Zr*	198.00 ± 2.12	185.00 ± 2.18	200.3	183	172.0	190.0
Nb*	13.60 ± 0.09	13.20 ± 0.17	14.7	-	11.90	12.90
Cs*	0.220 ± 0.010	0.070 ± 0.003	0.1	-	0.03	0.04
Ba*	136.00 ± 0.54	170.00 ± 0.41	137	145	122.0	131.0
La*	13.000 ± 0.341	14.300 ± 0.339	13.4	13.1	9.97	11.50
Ce*	33.000 ± 0.768	36.200 ± 0.936	37.31	34.7	26.30	29.30
Pr*	4.920 ± 0.146	5.350 ± 0.107	5.15	-	4.04	4.50
Nd*	24.100 ± 0.656	26.500 ± 0.857	25.12	22	19.10	21.50
Sm*	7.310 ± 0.225	8.400 ± 0.146	7.56	7.74	6.05	6.73
Eu*	1.450 ± 0.043	1.490 ± 0.040	1.24	1.24	0.98	1.07
Gd*	9.540 ± 0.340	10.800 ± 0.336	9.95	-	7.81	8.73
Tb*	1.890 ± 0.058	2.100 ± 0.048	1.93	1.79	1.44	1.62
Dy*	12.100 ± 0.404	13.600 ± 0.415	12.08	-	9.35	10.40
Ho*	2.640 ± 0.091	2.910 ± 0.090	2.45	-	2.00	2.21
Er*	7.390 ± 0.231	8.350 ± 0.250	6.71	-	5.40	6.04
Tm*	1.060 ± 0.033	1.170 ± 0.029	0.94	-	0.84	0.94
Yb*	6.720 ± 0.191	7.610 ± 0.211	6.37	6.59	5.30	5.91
Lu*	0.950 ± 0.042	1.070 ± 0.036	0.88	0.92	0.82	0.90
Hf*	4.800 ± 0.129	5.740 ± 0.125	5.39	5.58	4.50	4.92
Ta*	0.750 ± 0.029	0.860 ± 0.035	0.77	0.71	0.60	0.65
W*	0.917 ± 0.110	0.574 ± 0.078	0.2	-	-	-
Tl*	0.047 ± 0.006	0.212 ± 0.019	-	-	-	-
Pb*	1.290 ± 0.020	1.450 ± 0.014	1	-	0.71	0.80
Th*	2.170 ± 0.026	2.500 ± 0.073	2.33	2.04	1.79	2.04
U*	0.580 ± 0.012	0.670 ± 0.004	0.55	0.52	0.45	0.50
Mass	140	140	100	641 (27 - 48 mg per sample)	~30	~30

Table 5.2 Bulk major (oxide weight %), minor and trace element (ppm) composition analyses of LAP 02205 and LAP 02224, obtained using ICP-AES (†) and ICP-MS (*) compared with bulk rock analysis by other authors. The quoted errors are the standard deviations for 5 (major element) and 3 (minor and trace element) independent analyses of each sample. Dashed line "-" = not reported. The reported material mass is the total used for the complete bulk analysis and is given in milligrams (mg).

Pyroxene	02205	02205	02205	02205	02224	02224	02224	02224	02224	02224	02226	02226	02226	02226	Sp Insol	02205	02205
	Pig	Aug	Hd	Fs	Pig	Aug	Hd	Fs	M.I. PYX	Pig	Aug	Hd	Fs			Cr	Ul
Major Elements in wt % by EMPA																	
SiO2	50.53	49.92	46.04	45.40	50.81	50.26	45.92	45.87	48.19	51.34	49.88	45.58	45.75			0.17	0.1
TiO2	0.68	1.4	1.71	0.71	0.58	1.01	1.17	0.62	1.95	0.55	1.42	1.50	0.48			4.89	31.69
Al2O3	1.11	3.11	1.59	0.58	0.93	2.43	1.35	0.53	4.46	1.05	2.79	1.74	0.55			12.16	2.27
Cr2O3	0.41	0.95	0.04	0.02	0.30	0.90	0.03	0.02	0.35	0.36	0.74	0.00	0.01			44.26	0.776
FeO	25.23	13.27	32.29	46.61	25.83	14.69	33.59	47.59	21.69	25.31	16.64	32.44	47.67			31.28	63.89
MnO	0.40	0.27	0.39	0.57	0.42	0.21	0.36	0.55	0.36	0.45	0.27	0.32	0.66			0.29	0.29
MgO	15.78	13.47	0.49	0.33	16.47	15.54	0.66	0.46	15.95	16.20	13.47	0.33	0.17			4.33	0.174
CaO	6.01	17.68	16.95	5.57	5.49	14.98	16.87	5.45	6.92	5.66	15.47	18.23	5.58			nd	0.17
Na2O	0.02	0.07	0.03	0.01	0.00	0.06	0.08	0.03	0.06	0.04	0.06	0.07	nd			nd	0.02
K2O	nd	0.02	nd	0.02	nd	0.01	0.02	0.01	nd	nd	nd	0.01	nd			nd	0.011
V2O3	nd	nd	nd	nd	nd	nd	nd	nd	nd	nd	nd	nd	nd			0.943	nd
Total	*100.17*	*100.16*	*99.51*	*99.82*	*100.83*	*100.08*	*100.05*	*101.12*	*99.92*	*100.95*	*100.73*	*100.20*	*100.66*			*98.32*	*99.39*
Mg#	52.71	64.40	2.62	1.23	53.19	65.35	3.40	1.69	56.72	53.29	59.05	1.79	0.62		**Mg#**	19.79	0.48
En	46.06	40.06	1.58	1.07	47.17	44.98	2.10	1.48	48.20	47.01	39.70	1.05	0.54		**2Ti**	14.77	95.41
Fs	41.32	22.14	58.84	85.78	41.52	23.85	59.57	85.92	36.77	41.20	27.53	57.53	86.89		**Al**	18.37	3.42
Wo	12.62	37.80	39.58	13.14	11.31	31.17	38.34	12.60	15.03	11.79	32.77	41.42	12.57		**Cr**	66.86	1.17
Stoichiometry based on 6 oxygen atoms															**Stoichiometry based on 4 oxygen atoms**		
Si	1.944	1.884	1.922	1.962	1.943	1.895	1.919	1.960	1.838	1.955	1.888	1.900	1.966			0.006	0.004
Ti(4+)	0.020	0.040	0.054	0.023	0.017	0.029	0.037	0.020	0.056	0.016	0.040	0.047	0.015			0.127	0.891
Al	0.050	0.138	0.078	0.030	0.042	0.108	0.066	0.027	0.200	0.047	0.125	0.085	0.028			0.496	0.100
Cr	0.012	0.028	0.001	0.001	0.009	0.027	0.001	0.001	0.011	0.011	0.022	0.000	0.000			1.210	0.023
Fe (2+)	0.812	0.419	1.127	1.684	0.826	0.463	1.174	1.700	0.692	0.806	0.527	1.130	1.713			0.905	1.999
Mn	0.013	0.009	0.014	0.021	0.014	0.007	0.013	0.020	0.012	0.014	0.008	0.011	0.024			0.008	0.009
Mg	0.905	0.758	0.030	0.021	0.939	0.873	0.041	0.029	0.907	0.920	0.760	0.021	0.011			0.223	0.010
Ca	0.248	0.715	0.758	0.258	0.225	0.605	0.756	0.249	0.283	0.231	0.627	0.814	0.248			0.000	0.007
Na	0.002	0.005	0.002	0.001	0.000	0.005	0.006	0.002	0.004	0.003	0.005	0.005	0.000			0.000	0.001
K	0.000	0.001	0.000	0.001	0.000	0.000	0.001	0.000	0.000	0.000	0.000	0.000	0.000			0.000	0.001
V																0.026	0.000
Sum	4.006	3.996	3.986	4.001	4.015	4.012	4.014	4.008	4.003	4.002	4.001	4.014	4.005			2.975	3.044
Tet. Site	*1.994*	*2.022*	*2.000*	*1.991*	*1.985*	*2.003*	*1.985*	*1.986*	*2.039*	*2.002*	*2.012*	*1.985*	*1.993*				
Oct Site	*2.011*	*1.974*	*1.986*	*2.010*	*2.030*	*2.009*	*2.029*	*2.022*	*1.964*	*2.000*	*1.989*	*2.029*	*2.011*				

Table 5.3. Representative compositional data for pyroxenes and spinels in LAP 02205, LAP 02224 and LAP 02226; nd indicates major element concentrations below the detection limit of the instrument. Pig = pigeonite, Aug = augite; Hd = Fe, Ca-rich end-members; Fs = Fe-rich end-members; M.I. Pyx = daughter pyroxene within melt inclusion; Cr = Cr- spinel; Ul = Ulvöspinel. Measurement errors are estimated to be ≤1%, based on multiple measurements of NHM silicate, oxide and metal standards.

Plagioclase	02205	02205	02205	02224	02224	02224	02226	02226
	Core	Na-Rim	K-rim	Core	Na-Rim	K-rim	Core	Na-Rim
Major Element in wt % by EMPA								
SiO2	47.86	47.95	49.23	47.72	42.90	49.26	47.19	49.42
TiO2	0.13	0.06	0.37	0.08	0.08	0.09	0.06	0.05
Al2O3	31.97	31.37	30.43	32.81	31.28	30.58	32.71	31.71
Cr2O3	nd	nd	nd	0.04	0.03	0.02	0.03	0.00
FeO	0.82	0.95	1.67	0.61	1.00	1.80	0.58	0.93
MnO	0.01	0.06	0.04	nd	nd	nd	nd	0.07
MgO	0.22	0.09	0.02	0.18	0.12	0.03	0.31	0.13
CaO	17.44	17.01	16.33	17.95	17.08	16.82	18.01	16.87
Na2O	1.37	1.54	1.64	1.22	1.61	1.11	1.30	1.51
K2O	0.08	0.15	0.41	0.06	0.13	0.62	0.04	0.13
Total	*99.91*	*99.19*	*100.13*	*100.67*	*100.23*	*100.34*	*100.23*	*100.83*
An	87.17	85.13	82.58	88.78	84.77	85.93	88.25	85.40
Al	12.38	13.95	14.97	10.88	14.49	10.28	11.50	13.80
Or	0.46	0.92	2.45	0.34	0.74	3.80	0.25	0.80
Stoichiometry based on 8 oxygen atoms								
Si	2.206	2.227	2.268	2.183	2.245	2.268	2.171	2.251
Ti(4+)	0.005	0.002	0.013	0.003	0.003	0.003	0.002	0.002
Al	1.737	1.717	1.652	1.769	1.693	1.659	1.774	1.702
Cr	0.000	0.000	0.000	0.002	0.001	0.001	0.001	0.000
Fe (2+)	0.031	0.037	0.064	0.023	0.038	0.069	0.022	0.036
Mn	0.001	0.002	0.002	0.000	0.000	0.000	0.000	0.003
Mg	0.015	0.006	0.002	0.013	0.008	0.002	0.021	0.009
Ca	0.861	0.847	0.806	0.880	0.840	0.830	0.888	0.823
Na	0.122	0.139	0.146	0.108	0.144	0.099	0.116	0.133
K	0.005	0.009	0.024	0.003	0.007	0.037	0.002	0.008
Sum	4.984	4.986	4.978	4.984	4.980	4.967	4.998	4.966
Tet Site	*3.944*	*3.944*	*3.921*	*3.953*	*3.938*	*3.927*	*3.945*	*3.954*

Olivine	02205	02205	02224	02224	02226	02226
	Fo	Fa	Fo	Fa	Fo	Fa
Major Element in wt % by EMPA						
SiO2	36.24	29.02	36.58	29.30	36.97	29.30
TiO2	0.03	0.13	0.06	0.15	0.06	0.13
Al2O3	0.05	0.07	0.03	0.05	0.06	0.02
Cr2O3	0.28	nd	0.22	nd	0.18	0.01
FeO	30.71	68.28	33.15	68.78	30.06	68.65
MnO	0.28	0.70	0.31	0.70	0.28	0.62
MgO	31.64	0.62	30.64	1.06	33.11	0.20
CaO	0.37	0.75	0.38	0.74	0.34	1.02
Na2O	nd	0.05	0.04	nd	0.01	nd
K2O	nd	0.05	0.00	nd	nd	nd
Total	*99.60*	*99.66*	*101.40*	*100.77*	*101.06*	*99.95*
Mg#	64.74	1.99	62.23	2.66	66.25	0.52
Fe#	35.26	98.41	37.77	97.34	33.75	99.48
Stoichiometry based on 4 oxygen atoms						
Si	0.990	0.985	0.991	0.982	0.990	0.992
Ti(4+)	0.001	0.003	0.001	0.004	0.001	0.003
Al	0.002	0.003	0.001	0.002	0.002	0.001
Cr	0.006	0.000	0.005	0.000	0.004	0.000
Fe (2+)	0.702	1.938	0.751	1.927	0.673	1.944
Mn	0.006	0.020	0.007	0.020	0.006	0.018
Mg	1.288	0.031	1.237	0.053	1.321	0.010
Ca	0.011	0.027	0.011	0.027	0.010	0.037
Na	0.000	0.003	0.002	0.000	0.000	0.000
K	0.000	0.002	0.000	0.000	0.000	0.000
Sum	3.006	3.013	3.006	3.014	3.007	3.004

Table 5.4. Representative compositional data for plagioclases and olivines in LAP 02205, LAP 02224 and LAP 02226. Fo = Forsteritic olivine; Fa = fayalitic olivine. Measurement errors are estimated to be ≤1%, based on multiple measurements of NHM silicate, oxide and metal standards.

	02205 Ilmenite		02224 Ilmenite		02226 Ilmenite		02205 Chromite		02205 Si-K Glass		02224 M.V. average		02224 Fusion crust	
Number of spots	78		38		25		24		13		17		11	
Major Element in wt % by EMPA														
SiO2	0.05	± 0.04	0.04	± 0.02	0.04	± 0.03	99.52	± 1.07	79.61	± 1.85	44.77	± 0.31	45.28	± 3.39
TiO2	52.68	± 5.08	52.92	± 0.34	52.71	± 0.33	0.26	± 0.05	0.56	± 0.06	3.23	± 0.16	2.91	± 0.77
Al2O3	0.14	± 0.07	0.14	± 0.03	0.16	± 0.03	0.73	± 0.14	11.93	± 0.64	11.83	± 0.25	6.95	± 2.52
Cr2O3	0.11	± 0.07	0.19	± 0.10	0.16	± 0.09	0.01	± 0.01	0.01	± 0.01	0.30	± 0.05	0.32	± 0.22
FeO	46.21	± 4.46	47.00	± 0.61	46.88	± 0.65	0.01	± 0.01	0.01	± 0.02	20.81	± 0.94	25.74	± 7.36
MnO	0.34	± 0.05	0.34	± 0.04	0.32	± 0.04	0.01	± 0.01	0.02	± 0.02	0.25	± 0.03	0.31	± 0.06
MgO	0.06	± 0.17	0.28	± 0.33	0.18	± 0.29	nd		0.01	± 0.01	7.00	± 0.56	7.36	± 3.36
CaO	0.10	± 0.08	0.10	± 0.05	0.10	± 0.05	0.21	± 0.05	1.06	± 0.36	11.22	± 0.19	11.02	± 1.96
Na2O	0.02	± 0.02	0.01	± 0.02	0.02	± 0.02	0.14	± 0.04	0.24	± 0.06	0.46	± 0.04	0.24	± 0.12
K2O	0.01	± 0.01	0.01	± 0.01	0.01	± 0.01	0.03	± 0.02	5.42	± 0.58	0.13	± 0.02	0.09	± 0.05
P2O5	0.02	± 0.02	0.02	± 0.03	0.02	± 0.02	nd		0.14	± 0.05	0.14	± 0.04	0.12	± 0.08
NiO	0.02	± 0.02	0.01	± 0.02	0.02	± 0.02	nd		nd		0.02	± 0.02	0.01	± 0.01
Total	*99.76*		*101.06*		*100.62*		*100.96*		*99.02*		*100.17*		*100.34*	
Mg #											37.52		33.78	

	02205 High-Ni metal		02205 Low-Ni metal		02205 Troilite	
Number of spots	3		2		30	
Element wt % by EMPA						
Si	0.04	± 0.01	nd		0.04	± 0.03
Ti	0.33	± 0.00	0.13	± 0.11	0.09	± 0.09
Cr	0.30	± 0.00	0.23	± 0.10	0.01	± 0.01
Fe	68.85	± 0.95	86.68	± 2.23	62.89	± 1.14
Mn	0.03	± 0.01	0.02	± 0.02	0.02	± 0.01
P	0.01	± 0.01	nd		0.01	± 0.02
Ni	26.20	± 0.40	8.15	± 2.07	0.03	± 0.04
S	0.02	± 0.01	0.08	± 0.06	35.86	± 0.52
Zn	nd		nd		0.02	± 0.02
Co	3.73	± 0.05	1.91	± 0.61	0.04	± 0.02
Total	*99.52*		*97.21*		*99.01*	

Table 5.5. Representative average composition of accessory phases, melt veins and fusion crust. Units are wt %. Errors are standard deviation based on the number of spots analyzed. Melt vein (M.V.) average generated from 17 spots in single melt vein. Fusion crust average generated from 11 spatially diverse spots within crust melt region.

	Pig			Pig			Pig			Pig			SC Aug			SC Aug			SC Aug		
La	0.13	±	0.01	0.24	±	0.02	0.12	±	0.01	0.09	±	0.01	0.43	±	0.04	1.08	±	0.09	0.23	±	0.02	5.74	±	0.47
Ce	0.50	±	0.05	0.32	±	0.03	0.45	±	0.04	0.36	±	0.03	1.54	±	0.14	2.85	±	0.26	0.87	±	0.08	12.69	±	1.16
Pr	0.12	±	0.01	0.08	±	0.01	0.11	±	0.01	0.09	±	0.01	0.35	±	0.03	0.53	±	0.05	0.21	±	0.02	1.99	±	0.17
Nd	0.84	±	0.07	0.63	±	0.05	0.83	±	0.07	0.68	±	0.05	2.26	±	0.18	3.08	±	0.25	1.42	±	0.12	10.33	±	0.84
Sm	0.49	±	0.05	0.34	±	0.03	0.49	±	0.05	0.42	±	0.04	1.27	±	0.12	1.42	±	0.13	0.84	±	0.08	3.88	±	0.37
Eu	0.03	±	0.01	0.02	±	0.01	0.04	±	0.01	0.03	±	0.01	0.10	±	0.01	0.09	±	0.01	0.06	±	0.01	0.25	±	0.02
Gd	0.87	±	0.08	0.69	±	0.06	0.92	±	0.08	0.86	±	0.08	2.21	±	0.20	2.42	±	0.22	1.45	±	0.13	5.91	±	0.54
Tb	0.18	±	0.02	0.14	±	0.01	0.18	±	0.02	0.18	±	0.02	0.46	±	0.04	0.52	±	0.05	0.30	±	0.03	1.11	±	0.10
Dy	1.36	±	0.13	1.16	±	0.11	1.40	±	0.13	1.53	±	0.14	3.58	±	0.33	3.95	±	0.37	2.30	±	0.21	8.04	±	0.75
Ho	0.30	±	0.03	0.25	±	0.02	0.31	±	0.03	0.35	±	0.03	0.78	±	0.07	0.88	±	0.08	0.51	±	0.05	1.78	±	0.16
Er	0.84	±	0.08	0.80	±	0.08	0.88	±	0.08	1.02	±	0.10	2.20	±	0.21	2.66	±	0.25	1.52	±	0.14	5.19	±	0.49
Tm	0.13	±	0.01	0.14	±	0.01	0.13	±	0.01	0.16	±	0.02	0.35	±	0.03	0.42	±	0.04	0.23	±	0.02	0.78	±	0.07
Yb	0.84	±	0.08	0.99	±	0.09	0.91	±	0.08	1.12	±	0.10	2.32	±	0.21	2.96	±	0.27	1.63	±	0.15	5.32	±	0.49
Lu	0.12	±	0.01	0.15	±	0.01	0.14	±	0.01	0.17	±	0.02	0.35	±	0.04	0.44	±	0.04	0.24	±	0.02	0.75	±	0.08
	Plag.			Plag.			Plag.			Plag.			Mesostasis			Mesostasis								
La	3.23	±	0.26	0.30	±	0.02	1.32	±	0.11	0.55	±	0.04	51.82	±	4.22	126.83	±	10.33						
Ce	5.01	±	0.46	0.63	±	0.06	2.06	±	0.19	0.92	±	0.08	128.31	±	11.74	302.63	±	27.69						
Pr	0.62	±	0.05	0.08	±	0.01	0.27	±	0.02	0.14	±	0.01	17.94	±	1.54	47.16	±	4.05						
Nd	2.27	±	0.18	0.29	±	0.02	1.15	±	0.09	0.49	±	0.04	89.19	±	7.23	249.98	±	20.27						
Sm	0.51	±	0.05	0.06	±	0.01	0.22	±	0.02	0.08	±	0.01	28.78	±	2.72	82.55	±	7.81						
Eu	0.30	±	0.03	1.29	±	0.13	1.19	±	0.12	1.22	±	0.12	2.85	±	0.28	7.37	±	0.73						
Gd	0.55	±	0.05	0.07	±	0.01	0.19	±	0.02	0.12	±	0.01	37.85	±	3.47	109.53	±	10.04						
Tb	0.07	±	0.01	0.01	±	0.001	0.02	±	0.002	0.02	±	0.002	6.62	±	0.58	19.29	±	1.69						
Dy	0.52	±	0.05	0.04	±	0.004	0.17	±	0.02	0.11	±	0.01	46.50	±	4.31	134.70	±	12.48						
Ho	0.12	±	0.01	0.01	±	0.001	0.03	±	0.002	0.02	±	0.002	9.66	±	0.87	28.30	±	2.55						
Er	0.36	±	0.03	0.01	±	0.001	0.10	±	0.01	0.05	±	0.004	27.08	±	2.57	80.02	±	7.60						
Tm	0.06	±	0.01	0.004	±	0.001	0.01	±	0.001	0.01	±	0.001	3.96	±	0.37	11.83	±	1.12						
Yb	0.32	±	0.03	0.03	±	0.002	0.11	±	0.01	0.06	±	0.01	25.67	±	2.37	77.23	±	7.13						
Lu	0.06	±	0.01	0.01	±	0.001	0.01	±	0.001	0.01	±	0.001	3.59	±	0.36	11.13	±	1.13						

Table 5.6. Concentrations (in ppm) of REE in minerals as measured by LA-ICP-MS. Errors are based on the standard deviation of four NIST-612 synthetic standard measurements. C1-normalized values illustrating data are shown in Fig. 5.6. Pig = pigeonite; SC AUG = sub-calcic augites; Plag = plagioclase; M= mesostasis bulk area.

Chapter 6: Demonstration of a Compact Imaging X-ray Spectrometer

D-CIXS (Fig. 6.1) is a technology demonstrator of a planetary X-ray spectrometer that flew on ESA's SMART-1 mission to the Moon (Section 1.3.1.3, Fig. 1.20). It was designed and constructed at the Rutherford Appleton Laboratory (RAL), UK, and is an example of miniaturised technology for the purpose of lightweight spaceflight capabilities (Grande et al. 2003, 2007a). In the laboratory environment, X-ray spectrometers are designed for a similar purpose of chemical investigations (albeit on a very much smaller scale) and are often very large and complicated instruments (Potts et al.1995). In comparison, D-CIXS is approximately the size of a kitchen toaster (~30 x 15 x 15 cm) with a front end component of detector arrays and a back-box electronics component.

6.1 D-CIXS: Instrument Design

D-CIXS does not employ the technology of traditional X-ray telescopes whereby photons are focused by mirrors at a grazing incidence angle into detectors, which can either be traditional gas proportional energy counters or silicon diode technology (like the onboard X-ray Solar Monitor: Section 1.2.3). Instead, D-CIXS has been constructed to behave almost like a pin-hole camera, and to detect photons arriving directly on swept charge device (SCD) detector arrays (Lowe et al. 2001; Grande et al. 2003; Holland et al. 2004). The Moon is generally a relatively weak source of X-rays, and so D-CIXS was designed to have a large effective area, collimated to define an accurate field of view. The D-CIXS data collection and signal processing combined new technology, like the collimator stacks and the SCDs, with existing electronic technology. An explanation of data flow through the instrument is presented in Fig. 6.2.

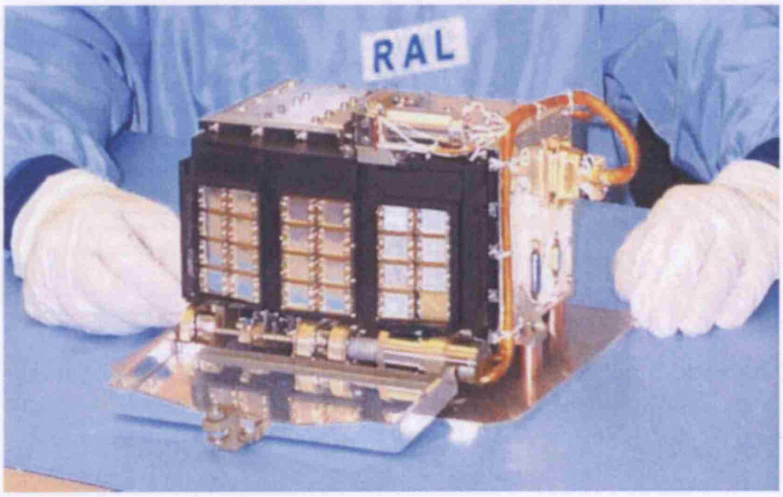

Fig. 6.1. Flight model of the D-CIXS instrument after the completion of pre-flight testing. The door is in the open position and the three facets, each containing an array of 8 detectors, are visible. The right hand facet is the one with mounted magnesium foils and also contains the calibration source detector (bottom row, furthest right: gold colouration: See Figure 6.5c). Photograph courtesy of RAL.

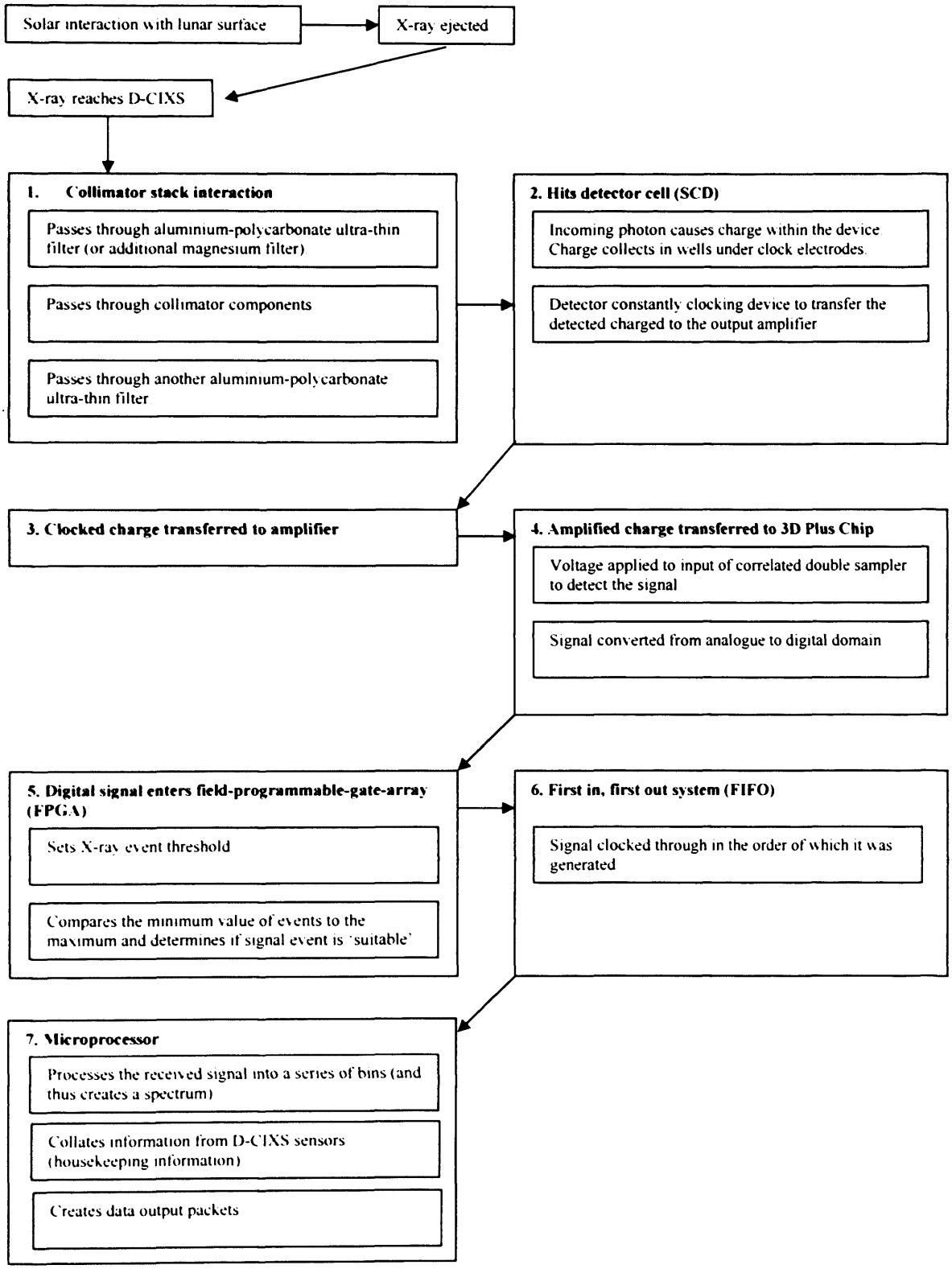

Fig. 6.2. Flow diagram to show the electronic processing of detected X-ray counts to an output of spectral or time-tagged data from the microprocessor system.

6.1.1 Collimator and Filter Assembly

D-CIXS's field of view (FOV) is defined by a collimator assembly, mounted in front of the SCD detector arrays. This assembly has a variable setup dependent upon which facet they are mounted. In both configurations the overall width dimensions of the collimator stack plus mounting is 15.45 x 18 x 2 mm (Fig. 6.3).

The collimators were micro-fabricated to produce low profile devices which were easily mounted in front of the detector arrays (Fig. 6.3, 6.4a,c,d). They are constructed from an epoxy resin (SU-8), supported by a silicon wafer substrate (McBride and Castiglione, 2003) with holes 168 μm wide and walls 30 μm wide; Fig. 6.4a,b. They were designed to only allow X-ray photons to hit the detectors from within a given field of view (Fig. 6.4c). Limiting the X-ray incoming angle provides an accurate data footprint on the lunar surface, or accurate pointings towards specific astronomical targets. The central D-CIXS facet (Fig. 6.1) has an 8° FOV that is defined by 4 collimator elements being stacked on top of each other (Fig. 6.3). The outer two facets in comparison both have a 12° FOV, defined by 3 stacked collimator elements (Fig. 6.3).

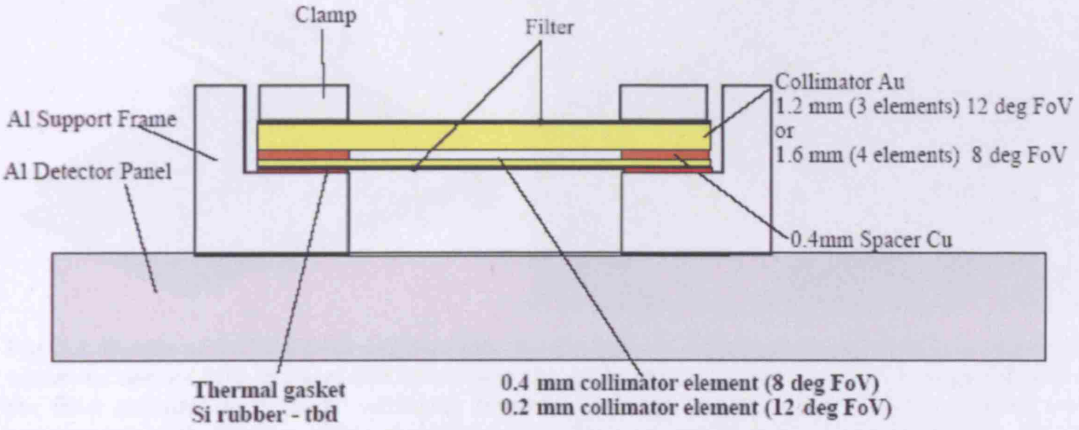

Fig. 6.3. Schematic of a complete collimator stack with mounted Al-filters (RAL Report, 1993)

Both collimator assembly configurations consist of an upper and lower filter made from ultra-thin Al foil (0.2 μm polyimide, 0.2 μm Al) clamped to a collimator component. The filter is in place primarily to prevent any optical light from hitting the SCDs, as having two foils within one stack reduces the chances of both filters being damaged and penetrated. This Al-foil was also designed to attenuate low-energy electrons emitted from the Sun that can cause excessive charge build-up on the SCDs. In addition to this protective filter, detectors housed on the right hand side facet (detectors 16-23) have collimator assemblies with additional magnesium foils mounted to one of the Al-foils; making these stacks slightly larger structures (0.5 μm polyimide,

0.03 μm Al-foil, 6 μm Mg-foil, 0.03 μm Al-foil). The Mg-filter is designed to attenuate X-rays with energies just greater than Mg (in particular Al [1.49 kilo electron Volts] and Si [1.74 keV]). By attenuating these specific lines, the SCDs on facet 3 were designed to be able to distinguish a characteristic Mg-line from complicated low-energy line peaks (Mg+Al+Si). As one of the primary science aims of D-CIXS was to map the Mg-content of the lunar surface this was a particularity important distinction to make.

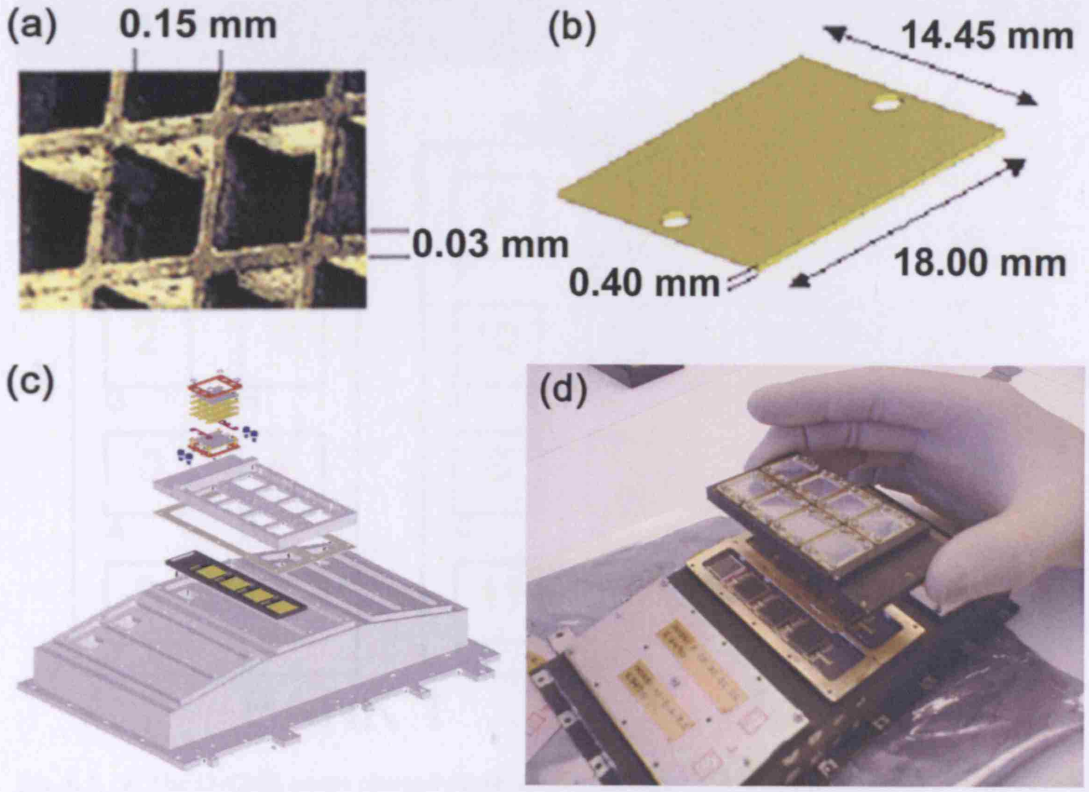

Fig. 6.4. Details of D-CIXS front end assembly. (a) Close up SEM image of one of D-CIXS's collimators where the narrow light passages and interconnecting walls can be clearly seen. (b) Size measurements of the filter mounted to a single collimator element. (c) CAD design of the D-CIXS front-end facet arrangement with detector arrays mounted onto each facet and then overlaid with fixings and the collimator stack assembly. (d) Collimator stacks being mounted in front of the detector arrays in the flight model D-CIXS instrument.

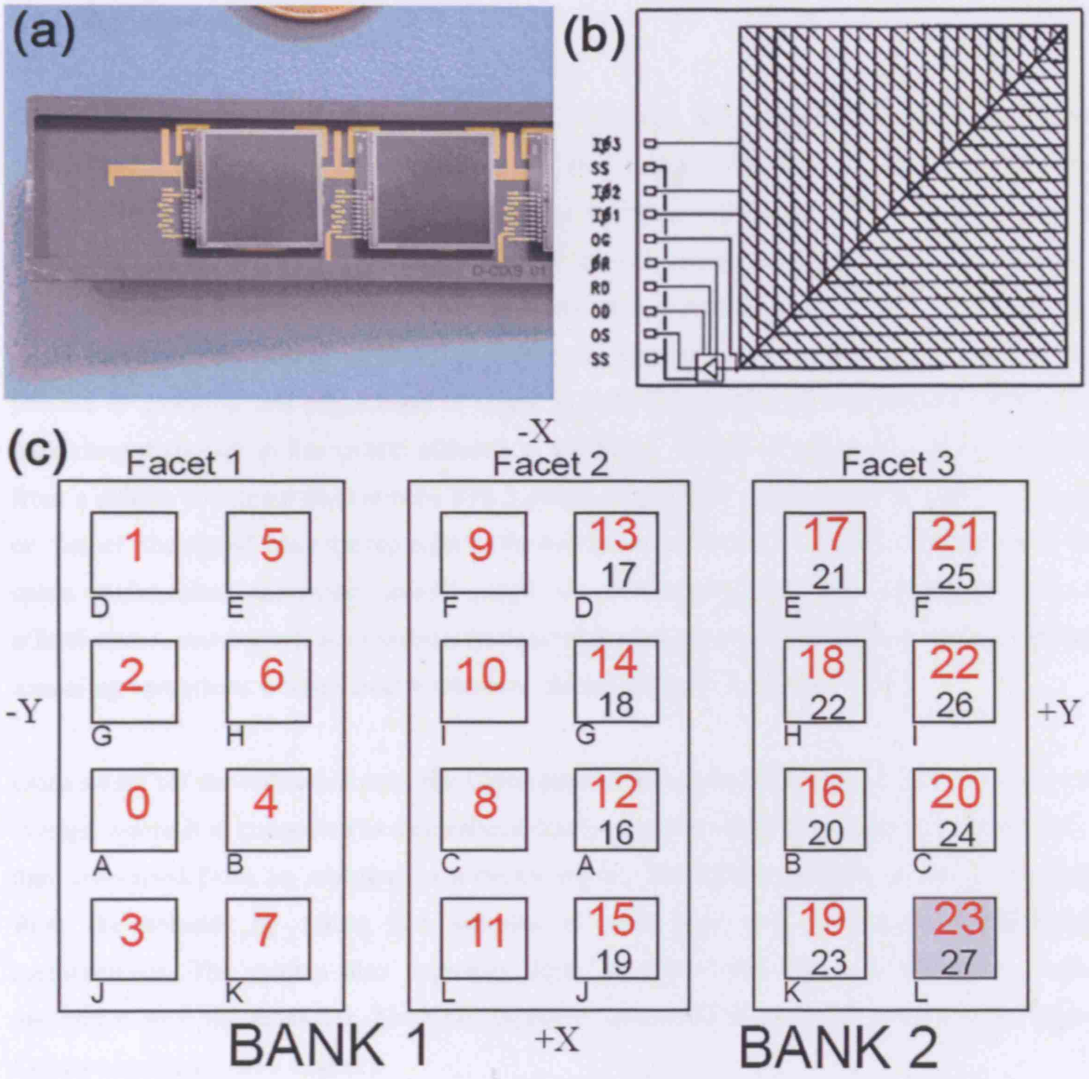

Fig. 6.5. (a) The D-CIXS swept charged device detector arrays: each individual detector is ~1 cm square. (b) Detailed schematic of the electrode makeup of the detectors. Charge is swept from the top right corner to an amplifier at the bottom left of the device. Image taken from Grande et al. (2003). (c) Detector numbering system on the D-CIXS instrument; detector 23 (grey box) represents the calibration unit: a ^{55}Fe radiation source mounted in front of a normal SCD detector. Facet 1 refers to the left hand panel in Fig. 6.2. Facet 2 is the central detector panel, and facet 3 is the right hand set of detectors. Bank 1 and Bank 2 refer to which signal processing system the detectors are connected to.

6.1.2 Signal Processing

Detectors and Signal Clocking. D-CIXS's detectors are designed to allow the rapid accumulation of pixel data, preventing blurring as the spacecraft moves quickly over the lunar surface. They employ SCD technology that is a variation of standard CCD (Charge Coupled Device) imaging detectors. The advancement essentially means that SCD detectors continually clock out charge from the active detector area, rather than reading out data one line at a time as is conducted by traditional CCD detector systems. By only once reading out the charge, the process of clocking and registration of signal is simplified, helping to reduce the build up of dark current (noise) in the system (Grande et al. 2003). The 24 detectors (Fig. 6.5c) are built from a silicon construct that contains 576 3-phase poly-silicon electrodes (Fig. 6.5b) that carry or 'funnel' the signal from the top right to the bottom left of the collecting area. Radiation in the space environment can cause defects in the silicon that trap the charge and reduce readout effectiveness, causing a loss in instrument resolution. In theory this can be corrected by thermal annealing operations where detector temperatures are raised to more than 126 °C.

Once swept off the collection area, the signal passes into an amplifier (Fig. 6.2), is converted to voltage where it is connected to a correlated double sampler (CDS) to extract the signal, and is then converted from an analogue to a digital signal. The CDS essentially extracts the signal from the detector by taking two samples of each pixel and performing a differential measurement. The system also improves signal to noise ratio (S/N) by eliminating noise associated with the amplifier. The CDS output is connected to an ADC (Analogue to Digital Converter) (Howe *pers. comm.*).

The digital signal is then transferred to a field programmable gate array (FPGA) that can be instructed to selectively clock events that occur above a predetermined threshold limit (Fig. 6.6). Quadruple pixel values are clocked through the system according to specific filter systems defined from the ground. For example, the FPGA can be operated in 3 modes:

- *Singles and doubles, use 2nd and 3rd:* selects and sums pixels 2 and 3 provided at least one count is above a threshold limit, and appear between two counts (pixels 1 and 4) that are below the threshold (as shown in Fig. 6.6).
- *Singles and doubles, use 2nd:* employs a filter where pixels 1 and 4 have values below the set threshold and pixels 2 and 3 are above. This time only the value of the pixel 2 is passed into the FIFO.

- *All pixel mode*: All pixels above the threshold are passed to the first-in, first-out (FIFO) memory (1 and 4 do not need to have values below the threshold). All pixels below the threshold level are thrown away.

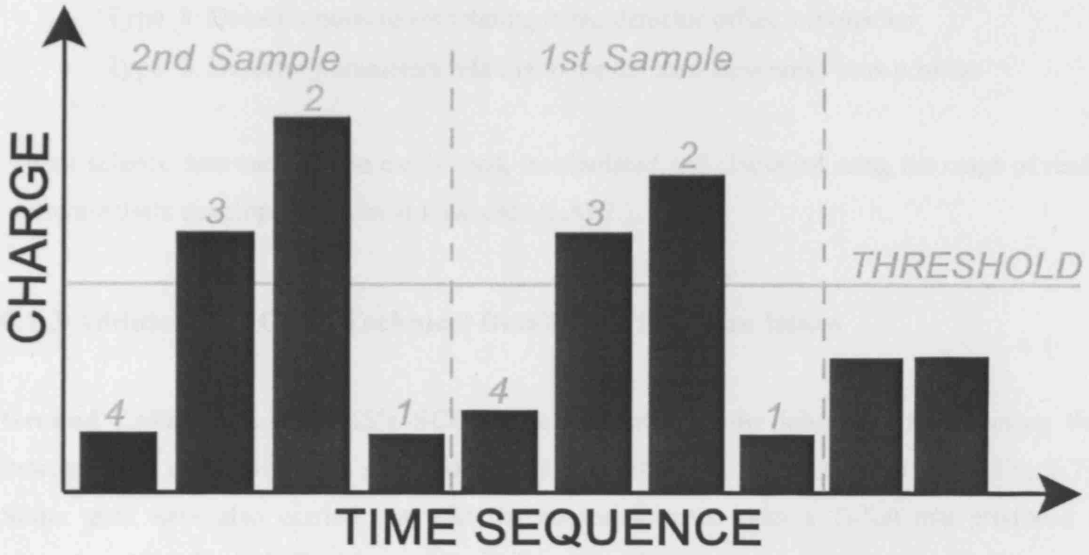

Fig. 6.6. Simplified representation of the FPGA clocking system. Charge is clocked through and is spilt into quadruple samples (pixels) according to levels above or below a threshold level. The differential measurement of this charge is then converted to a digital signal and set to the on-board FIFO and sent to the micro-processor unit.

Data Processing Protocol. In the final stage of on-board processing, the selected signal passes from the FPGA, through a FIFO memory, and into the onboard microprocessor unit. This processor time-stamps the data and converts them into readable output science packets (either stores them as time-tagged count data, or bins counts into a spectrum range per detector per chosen time interval). The processor collates data from sensors distributed throughout the instrument that monitor temperature variations, detector and hardware supplies, operation mode etc. The system stores this information as time-stamped "housekeeping" data packets. Corresponding time-stamped data are also stored from the X-ray Solar Monitor. All of this information is transferred from the instrument to the SMART-1 mass memory, and is then down-linked every few orbits to a terrestrial receiving station and is transferred to ESA's raw-data archive.

Data Archiving. Raw data (S0-level) is collated and then converted into archived level one data (S1) using IDL software developed at RAL. This software collates the science and housekeeping packets into the orbit number in that they were taken, and divides the data into specific data 'types'. Of these data-types the most important to note are:

- Type_0: House-keeping packets
- Type_1: Time-tagged mode packets

- Type_2: Spectral mode packets
- Type_3: High-count mode packets *(redundant, but used for laboratory testing)*
- Type_4: Solar monitor data
- Type_8: Detector parameters relating to the detector offset information
- Type_9: Detector parameters relating to the detector zero noise peak position

These science data can then be easily read, manipulated and displayed using the range of read-software tools developed by David Lawrence (LANL).

6.1.3 Additional D-CIXS Technical Details and Software Issues

Ground Calibration. D-CIXS's SCDs were calibrated in the laboratory by exposing the detectors to a radioactive ^{55}Fe source that emits characteristic ^{55}Mn K α and β peaks (Fig. 6.7). Some tests were also carried out with the source mounted onto a Ti-foil that produced a secondary XRF Ti-peak. Positions of the ^{55}Mn and/or Ti-peaks were monitored to provide a pre-flight assessment of individual detector gain (i.e. spectrum stretching) and variability of channel space offset movement (i.e. how aligned/misaligned the elemental line features occurred on different detectors).

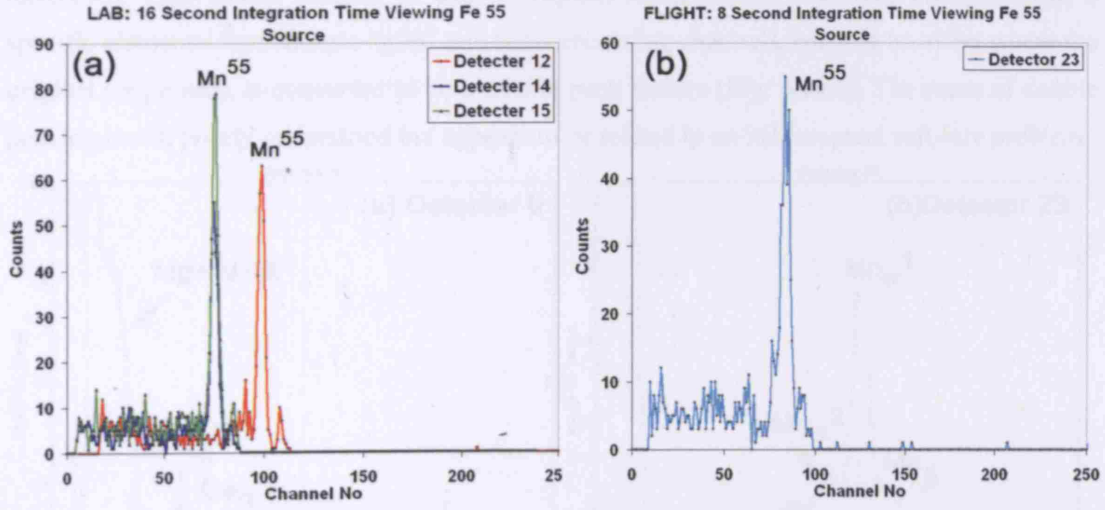

Fig. 6.7. Fe^{55} measurements made on different D-CIXS detectors in (a) the laboratory and (b) in-flight during the early phase of the SMART-1 mission. Note y-axis scale difference.

In-Flight Calibration. After launch, two different methods of onboard calibration were employed. An in-flight ^{55}Fe calibration target was mounted in front of detector 23 (Fig. 6.5), on the lowest row of the right-hand facet. This target was monitored throughout the mission for an assessment of detector operability, energy line resolution degradation, and double peaking

occurrence (see below). This in-flight calibration technique is problematic as it provides a monitor for only one of the 24 detectors. It can therefore be used only to assess the operative status and calibration of all the other individual detectors.

The second method of post-launch calibration operations was to schedule specific instrument pointings towards known X-ray sources, such as X-ray binary targets, the Earth and the Moon.

Elemental Line Resolution Loss. SMART-1 had a long transit time to the Moon (Section 1.2.3) which meant that D-CIXS was exposed to the Earth's radiation belts for more than one year. This extreme radiation dose irrevocably damaged the detector arrays, causing a loss of line-energy resolution (Fig. 6.8a). Pre-flight testing of the detectors (Fig. 6.7a) determined that individual line-peaks would have a FWHM resolution of ~180 eV. After lunar transit and Moon orbit insertion this individual detector resolution had decreased to ~310 to 320 eV (~360 eV when all the detectors on one facet are summed together). This loss in resolution meant that unfortunately the three major low-energy elemental peaks of Mg, Al and Si could not easily be individually resolved, and were blended as a single low-energy line feature (Fig. 6.8a).

Double Peaking Events. One of the most complicated issues that D-CIXS encountered during the whole data collection process was referred to as "double-peaking". This occurred when the instrument experienced periods of data corruption when counts that were affiliated with a specific elemental line became 'split' into the surrounding channels, creating an effect where the original single peak is converted to be a double peak feature (Fig. 6.8a,b). The cause of double peaking is still poorly understood but appears to be related to an instrumental software problem.

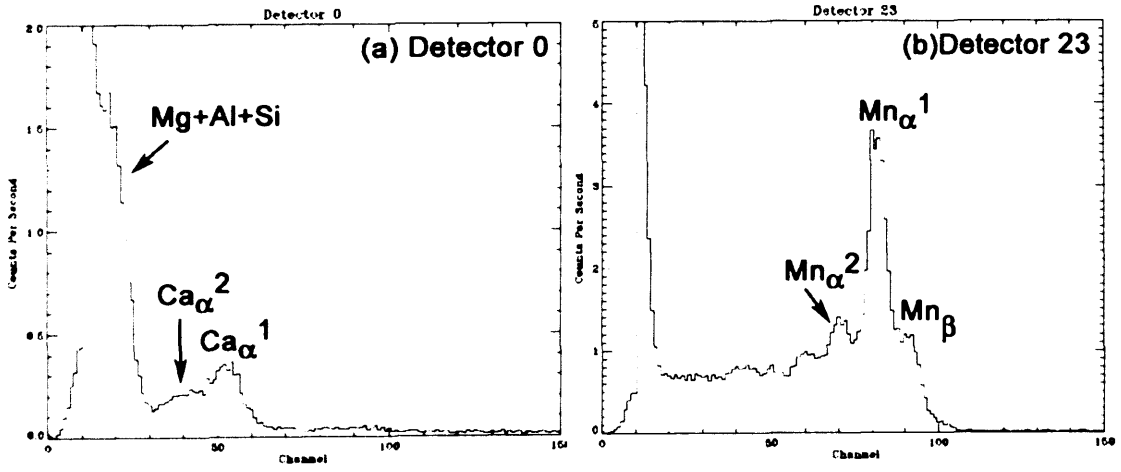

Fig. 6.8 Double peaking events in spectral (mode 2) lunar data taken by D-CIXS. (a) Summed spectrum taken from about 20 min. of observations from detector 0. The Ca-associated peak (Ca_α^1) has become split into a blurred feature (Ca_α^2) to the left of the original peak. (b) More dramatic example from the in-flight calibration target detector 23. The Mn_α^1 line feature (~ channel 80) has been spilt into a smaller, adjacent peak ($^{55}Mn_\alpha^2$).

6.2 D-CIXS: Preparatory Work

6.2.1 D-CIXS Filter Investigation

As part of this thesis, an experiment designed to test the effectiveness of D-CIXS's filters was conducted at the Natural History Museum London, using a JEOL electron dispersive scanning electron microscope (ED-SEM) fitted with INCA Oxford Instruments Analytical software. The investigation was designed to see how an XRF response from a geological sample was effected as it passed through a D-CIXS filter, and in particular to probe to what degree the filters attenuate an X-ray signal from a sample of (relatively) known composition. Additionally, the experiment was designed to test whether the Mg-filter achieve its purpose of completely preventing the transmission of low energy X-ray lines and attenuate the Al and Si X-ray signal (see Fig. 6.12 for expected performance).

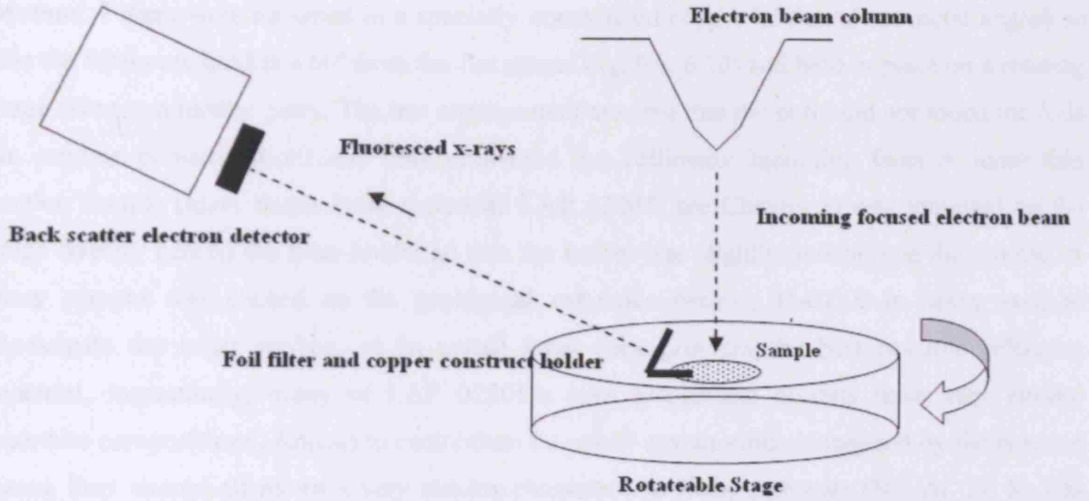

Fig. 6.9 Schematic of the D-CIXS filter test showing direction of incoming generated electron beam, and the path of the detected outgoing fluoresced X-rays (scattered in all directions but only those along the incidence angle of the backscattered detector are measured).

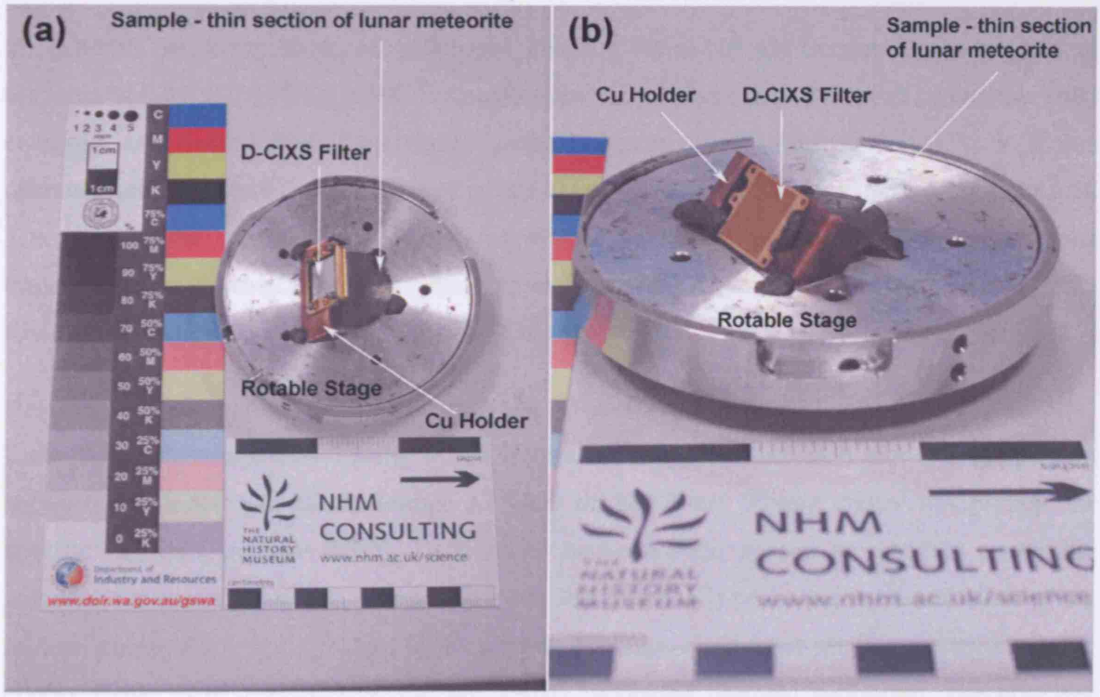

Fig. 6.10 (a) bird's eye view and (b) side view of experimental apparatus sample holder showing mounted Mg foil and copper construct holder at a 60° to the circular lunar sample (partially obscured dark disk). Photograph courtesy of A. Kearsley.

Method. Filters were mounted in a specially constructed copper holder (sheet metal angled so that the filters are held at a 60° from the flat stage: Fig. 6.9, 6.10) and held in place on a rotating stage using conductive putty. The test arrangement ensured that the putty did not touch the foils (to prevent contamination) and only contacted the collimator mounting face. A lunar thin section sample (mare basalt lunar meteorite LAP 02205: see Chapter 5) was mounted on the stage directly behind the filter holder so that the holder was slightly overlapping the sample. A lunar sample was chosen as the geological reference because D-CIXS is being used to investigate the lunar surface, so an actual lunar rock provides the best possible reference material. Importantly, many of LAP 02205's *core* plagioclase crystals have very similar anorthite compositions (An_{85-91}) to each other: i.e. when any anorthite is targeted by the electron beam, they should all return a very similar characteristic X-ray signature (Na, Al, Si, K, Ca-lines). Thus, comparisons between attenuated spectra (when the filter is present) and non attenuated spectra (filter not present: just a typical mineral XRF response) should be easy to interpret.

To generate an X-ray response, a focused electron beam (10 μm diameter) was targeted at minerals in LAP 02205 (Fig. 6.10). Element characteristic spectra are produced when inner shell electrons are ejected from their shell by the incoming X-rays (see section 1.3). It is this characteristic signature that is received in our experiment by the internal JEOL SEM detectors. The comparison of the X-ray signatures when the filters transmit the fluoresced signal transmission, and when there is no filter present, provide information about how the D-CIXS filters attenuate the X-ray signal of different minerals.

Results. The comparison of spectra from the Al and Mg-filters are displayed in Figure 6.11. Each plot is discussed individually in the Figure caption. Note that each plot is a comparison between the individual filters (either Al-filter or Mg-filter) present and/or not present for specific minerals in LAP 02205. Differences between these spectra are used to access the amount of signal attenuation. (Please note that the carbon [C] peaks are not a reflection of the mineral composition but a feature of the sample coating). In all cases the X-axis represents the energy range from 0 to 10 keV and the Y-axis represents detected count-rate. The principal observations of this experiment are listed below, summarised in Table 6.1 and 6.2 and plotted in Fig. 6.12:

- **Al-filter effects:**
  - The Al-filter partially attenuates the X-rays emitted from a plagioclase mineral with high O, Al, Si and Ca.
  - It appears to preferentially impede the lower energy elements like O and the Ca Lα lines (as shown in the expected X-ray transmission plot in Fig. 6.12) than the higher energies signatures like that of Ca and Fe.
  - The transmission of characteristic Si X-rays is blocked by about 10% more than the Al and Ca X-rays. This correlates well with the expected results plotted in Fig. 6.12.
  - These effects are shown in Table 6.1 that indicated the amount of X-ray attenuation by the Al-filter based on differences in elemental peak area size when the filter is present and when there is no filter. These differences are based on plagioclase X-ray fluorescence comparisons. Average transmission of the energy lines is also listed and the data are plotted on Fig. 6.12.
- **Mg-Filter effects:**
  - The Mg-filter completely impedes the low energy X-ray signatures and background (i.e. lower than 0.41 keV).
  - It also essentially stops any transmitted X-rays with energies from 1.3-3.7 keV. Mg characteristic X-rays are however not stopped completely (they are only partially attenuated), which correlates very well with the expected X-ray transmission through the filter as plotted in Figure 6.12.
  - The Mg-filter attenuates the higher energy element signals (Ca, Ti, Cr and Fe) by between 40-60% (Table 6.2), although it is likely that these have also been partially attenuated by the surrounding Al-filters in the Mg-foil arrangement in addition to the Mg-foil itself.
  - The Mg-filter produces an anomalous secondary Mg-peak caused by the foil and not the sample (although this is not too large a secondary peak).

Fig. 6.11a. **Al-filter response.**

Plot of comparison between two plagioclase ($CaAl_2Si_2O_6$) spectra.

The black spectrum represents a plagioclase mineral grain (strong O, Al, Si and Ca peaks) where the resulting X-ray signal has been detected without an Al-filter. There is a large detected background (hidden behind furthest left hand red peak) and strong detected Kα and Kβ lines from the major elements.

The red spectrum represents a plagioclase mineral grain where the X-ray signal has been detected after passing through the Al-filter. It is immediately apparent that there has been count attenuation for all of the elements detected. In particular lower X-ray energy elements like O have had their X-ray counts reduced by more than half. Higher-energy elements like Ca have been attenuated by about a third (~27 peak area difference: Table 6.1). The D-CIXS Al-filters preferentially allow higher energy X-rays through the filter.

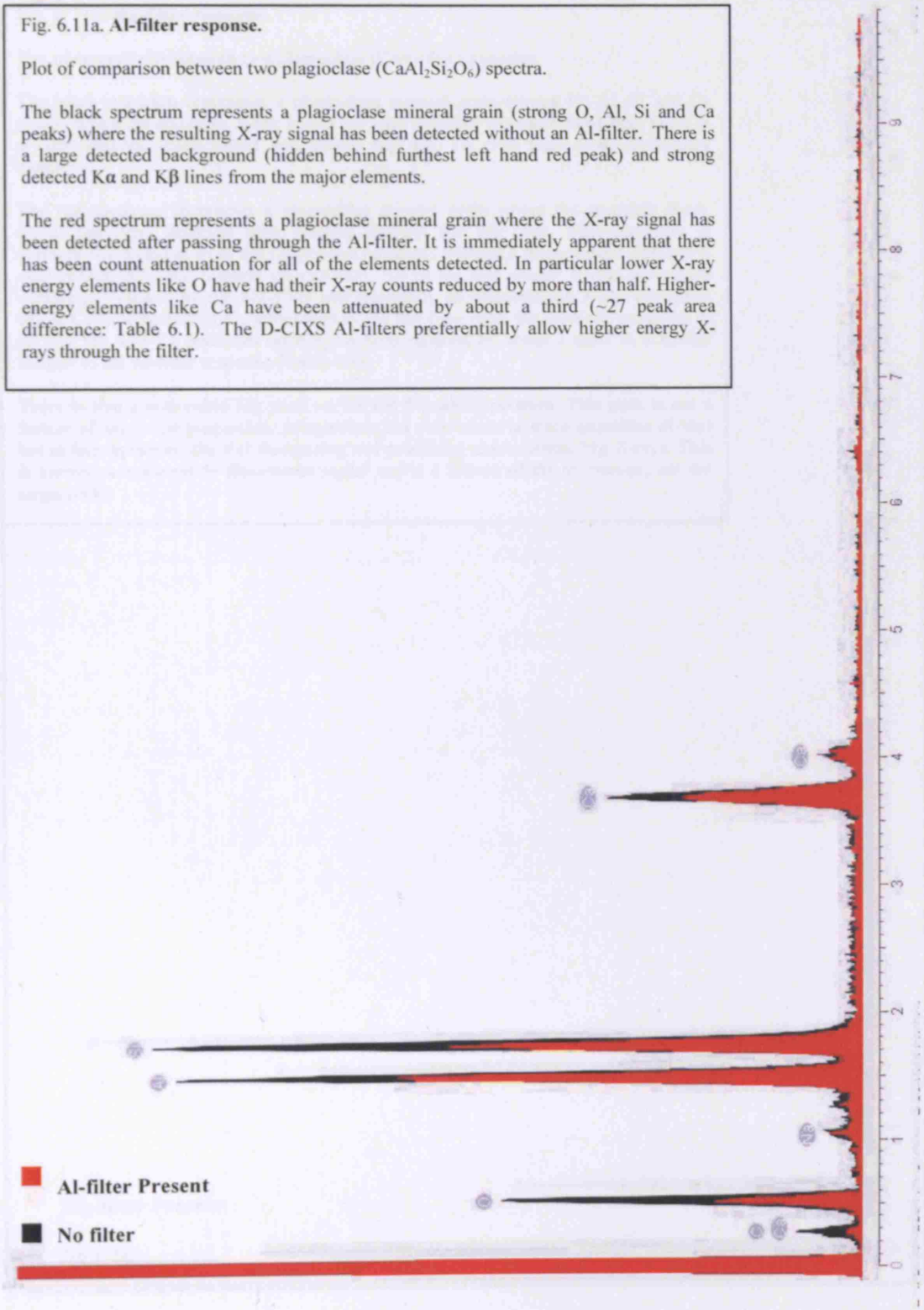

Fig. 6. 11b. **Mg-filter response.**

Plot of comparison between two plagioclase ($CaAl_2Si_2O_6$) spectra.

The black spectrum represents a plagioclase mineral grain (strong O, Al, Si and Ca peaks) where the resulting X-ray signal has been detected without a Mg-filter. There is a large detected background and strong Kα, Kβ, Lα (Fe) lines from constituent elements.

The red spectrum represents a plagioclase mineral grain where the resulting X-ray signal has been detected after passing through the Mg-filter. This spectrum is dramatically different from the plagioclase measured without a filter present although it does reflect the same mineral composition. All of the low energy X-rays have been completely blocked by the Mg-filter and essentially all characteristic X-ray signatures below Ca have been severely attenuated by the Mg-filter (note the dramatic reduction in Al and Si). The Ca peak has once again been reduced by about a third in a similar manner to the Al-filter response (Table 6.2).

There is also a noticeable Mg peak on the red Mg-filter spectrum. This peak is not a feature of Mg in the plagioclase (plagioclase has very minor or trace quantities of Mg) but in fact represents the foil fluorescing and producing characteristic Mg X-rays. This is known as a secondary fluorescent signal and is a feature of the instrument, not the target rock.

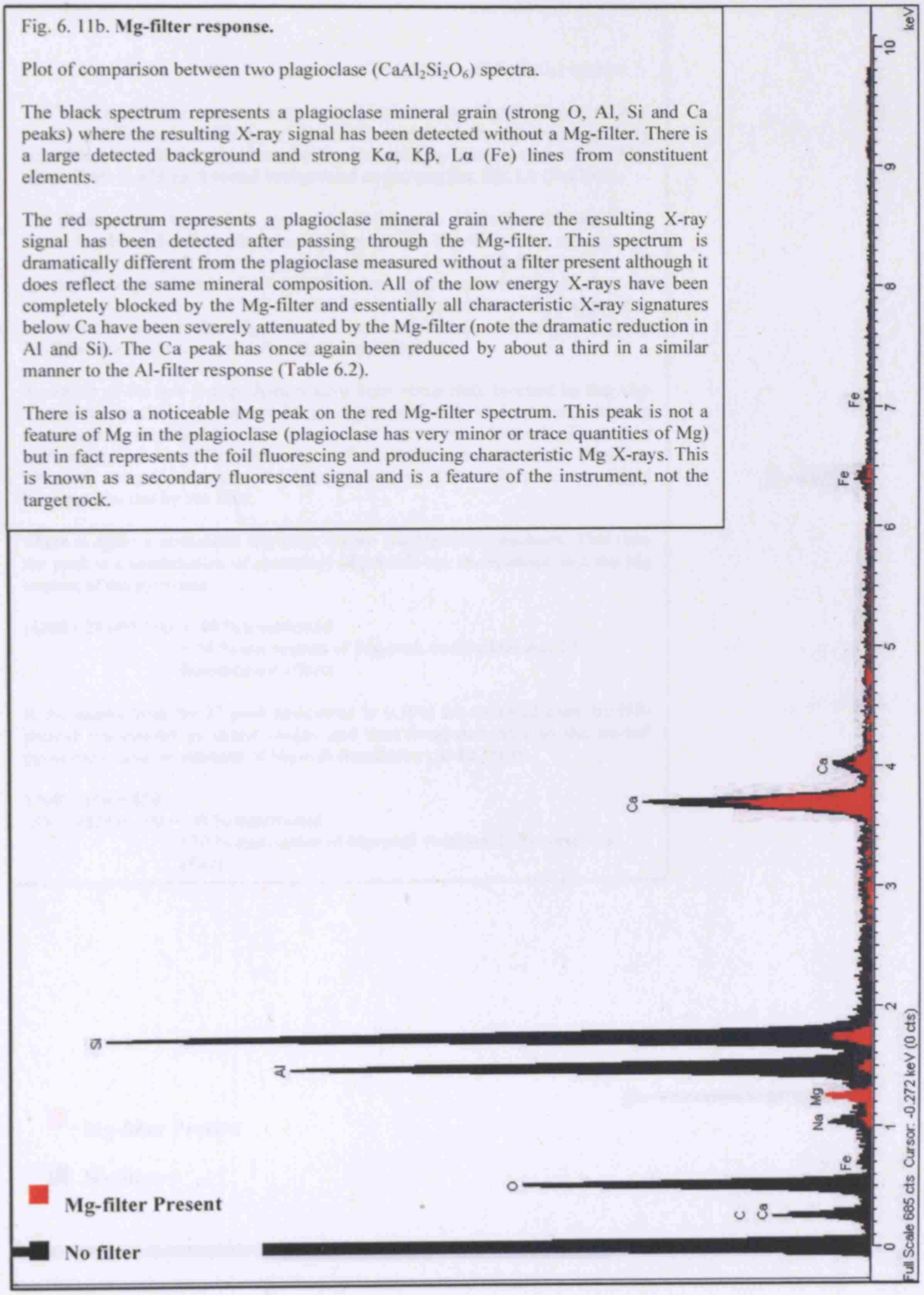

Fig. 6. 11c. **Mg-filter response.**

Plot of comparison between two pyroxene ($CaMgSi_2O_6$ – $CaFeSi_2O_6$) spectra.

The black spectrum represents a pyroxene (augite) mineral grain (strong O, Mg, Si, Ca and Fe peaks with minor Al and Ti peaks) where the resulting X-ray signal has been detected without being attenuated by the presence of the Mg-filter. There is a large detected background and strong Kα, Kβ, Lα (Fe) lines.

The red spectrum represents a pyroxene mineral grain where the resulting X-ray signal has been detected after passing through the Mg-filter. This spectrum is dramatically different from the pyroxene measured without a filter present. *NB pyroxene compositions in LAP 02205 do vary quite substantially as they are zoned between a range of Mg, Fe and Ca rich compositions. We attempted to measure two very similar Mg-rich core regions although invariably there may be difference in the size of the Fe, Al, Ca and Mg peaks.*

Again all of the low energy X-rays have been completely blocked by the Mg-filter and essentially all element X-ray signatures below Ca have been severely attenuated by the Mg-filter. The pyroxene is a good test of how the Fe peak, a high energy (~6.4 keV Kα) element, is affected by the presence of the Mg-filter. The peak comparison seems to suggest that about 50% of its peak area signal has been blocked by the filter.

There is again a noticeable Mg peak on the red Mg-filter spectrum. This time the peak is a combination of secondary Mg-foil X-ray fluorescence and the Mg content of the pyroxene:

(1300 / 2834)* 100 = 46 % transmitted
= 54 % attenuation of Mg-peak (with additional 2^{ry} fluorescence effect)

If the counts from the 2^{ry} peak (discussed in 6.10b) are removed from the foil-present transmitted pyroxene counts and then compared back to the no-foil pyroxene counts an estimate of Mg-foil attenuation can be made:

1300 – 450 = 850
(850 / 2834)* 100 = 30 % transmitted
=70 % attenuation of Mg-peak (without 2^{ry} fluorescence effect)

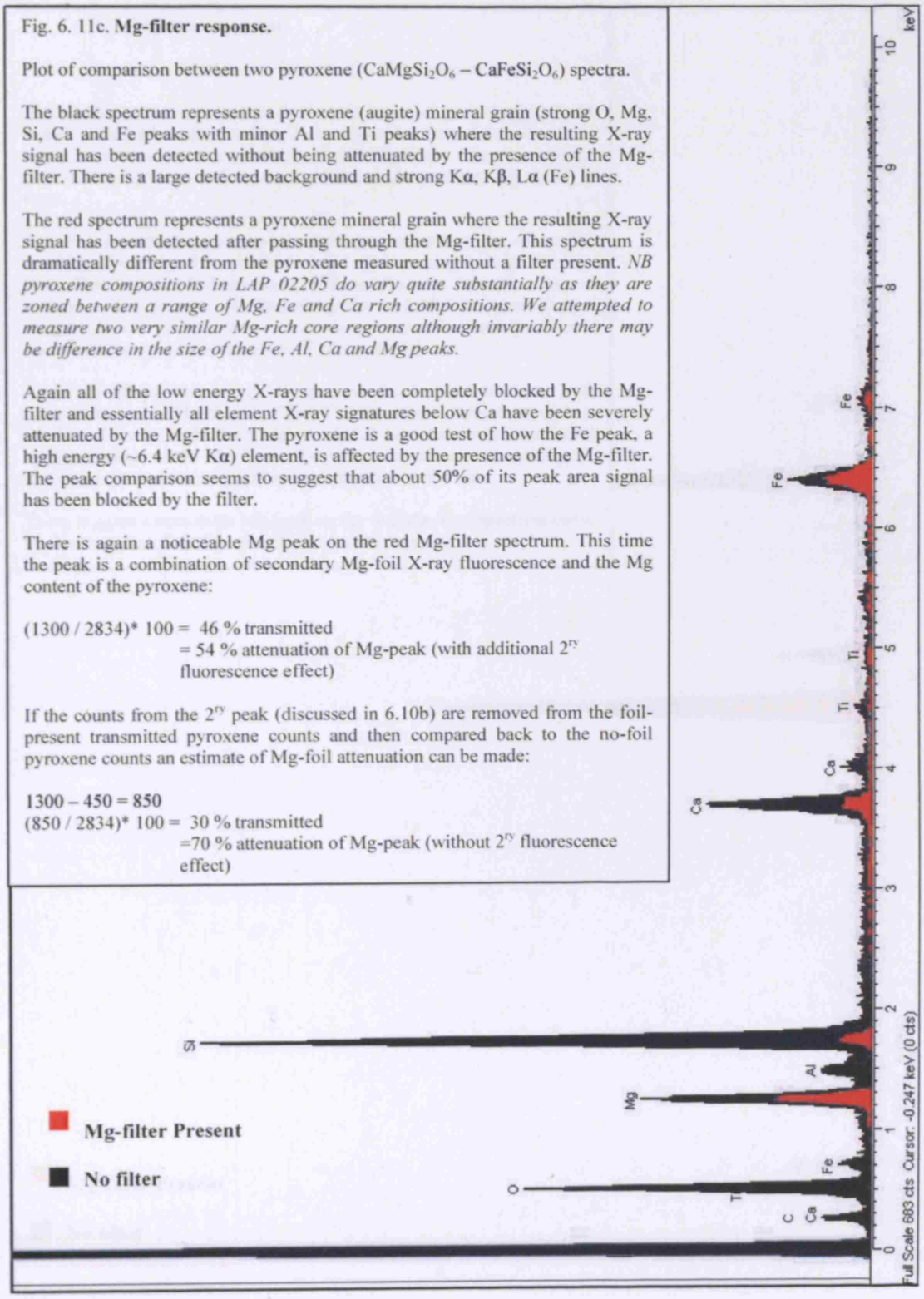

Fig. 6.6. 11d. **Mg-filter response.**

Plot of comparison between two ilmenite ($FeTiO_3$) spectra.

The black spectrum represents an ilmenite mineral grain (strong O, Ti and Fe peaks) where the resulting X-ray signal has been detected without being attenuated by the presence of the Mg-filter. There is a large detected background and strong constituent element Kα, Kβ, Lα (Fe) lines.

The red spectrum represents an ilmenite mineral grain where the resulting X-ray signal has been detected after passing through the Mg-filter. This spectrum is dramatically different from the ilmenite measured without a filter present. *NB Ilmenite grains in LAP 02205 have limited compositional variations it is reasonable to assume that the two minerals measured should have near identical compositions.*

Again all of the low energy X-rays and the background have been completely blocked by the Mg-filter. The ilmenite is a good test of how the Fe and the Ti peaks (both high energy X-ray intensities) are affected by the presence of the Mg-filter. The peak comparisons seem to suggest that about 50% of their signal has been blocked by the filter.

There is again a noticeable Mg peak on the red Mg-filter spectrum cause by fluorescence of the filter itself (and not the sample).

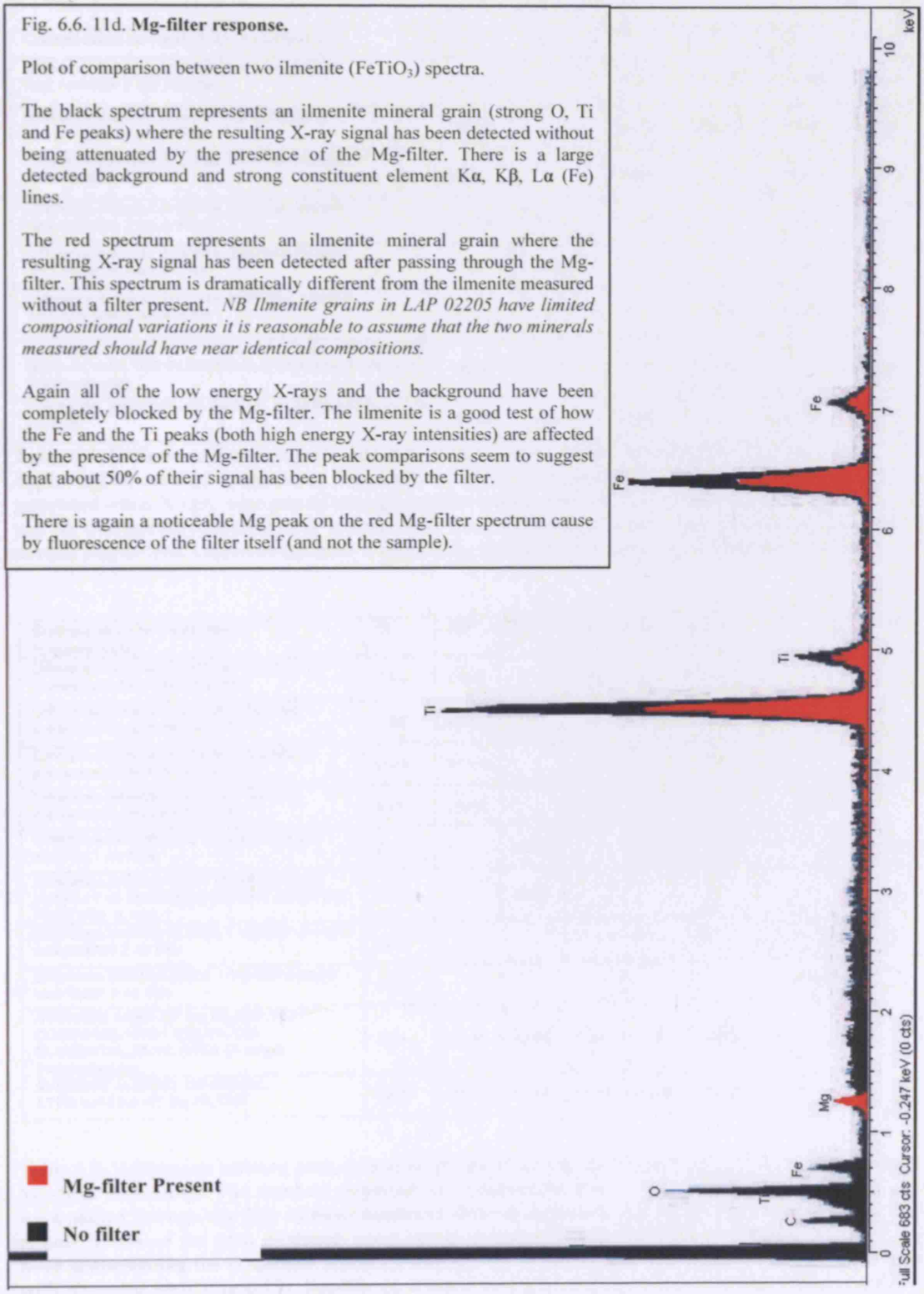

Comparison in Peak Area (counts*keV)	O	Na	Al	Si	Ca	Fe
Difference between Anorthite 1 *Al-Filter present* and Anorthite 3 *No Al-Filter*	40.63		73.67	67.40	71.55	66.03
Difference between Anorthite 1 *Al-Filter present* and Anorthite 4 *No Al-Filter*	39.27		75.08	66.20	72.87	90.61
Difference between Anorthite 1 *Al-Filter present* and Anorthite 5 *No Al-Filter*	39.85		75.14	65.27	73.04	123.51
Difference between Anorthite 2 *Al-Filter present* and Anorthite 3 *No Al-Filter*	37.03	72.56	69.65	57.03	71.02	51.07
Difference between Anorthite 2 *Al-Filter present* and Anorthite 4 *No Al-Filter*	35.79	69.54	70.99	56.01	72.33	70.09
Difference between Anorthite 2 *Al-Filter present* and Anorthite 5 *No Al-Filter*	36.32	75.93	71.04	55.23	72.50	95.54
AVERAGE AREA OF Al-FILTER PEAK COMPARED WITH NON-FILTER ELEMENTAL PEAK AREA (Average Transmission)	**38.52**	**71.05**	**72.91**	**62.39**	**72.16**	**80.26**
AVERAGE AMOUNT OF SIGNAL ATTENUATED BY Al-FILTER	**61.49**	**28.95**	**27.09**	**37.62**	**27.84**	**19.74**

Table 6.1. Differences between peak-area-size in the X-rays emitted from anorthite grains in LAP 02205 depending on Al-filter attenuation. The numbers represent the comparative area of the elemental peaks generated when X-rays were passed through the filter, compared with those unfiltered element signatures, e.g. the average Al-filtered O peak is only 38.51 % of the peak produced when signal is detected from a normal plagioclase. Therefore the filter is attenuating the O element signal on average by 61.49 %.

Comparison in Peak Area (counts*keV)	O	*Na **	*Mg*	Al	Si	Ca	Ti	Cr	Fe
Difference between Anorthite 1 *Mg-filter present* and Anorthite 3 *no filter*	0.79	*26.30*		2.52	5.74	64.72			
Difference between Anorthite 1 *Mg-filter present* and Anorthite 4 *no filter*	0.96	*44.80*		2.79	7.50	76.07			
Difference between Anorthite 2 *Mg-filter present* and Anorthite 3 *no filter*	0.40	*11.70*		1.21	4.18	40.66			
Difference between Anorthite 2 *Mg-filter present* and Anorthite 4 *no filter*	0.48	*19.92*		1.34	5.47	47.80			
Difference between Pyx 1 Mg-filter present and Pyx 1 no filter	0.61		*45.9***		4.28	15.51	21.75	27.15	56.80
Difference between Pyx 1 Mg-filter present and Pyx 1 no filter MINUS EFFECT OF 2nd Mg-PEAK (Fig 6.11c)			***29.98***						
Difference between Ilmenite 1 *Mg-filter present* and Ilmenite 2 *no filter*	1.27						52.71		57.66
Difference between Spinel 1 *Mg-filter present* and Spinel 2 *no filter*	0.78						52.12	58.02	53.62
AVERAGE AREA OF Mg-FILTER PEAK COMPARED WITH NON-FILTER ELEMENTAL PEAK AREA (Average Transmission)	**0.76**	***25.68***	***29.98***	**1.12**	**5.43**	**48.95**	**42.20**	**42.58**	**56.02**
AVERAGE AMOUNT OF SIGNAL ATTENUATED BY Mg-FILTER	**99.25**	***74.32***	***70.12***	**98.88**	**94.57**	**51.05**	**57.80**	**57.42**	**43.98**

Table 6.2. Differences between peak-area-size emitted from various minerals in LAP 02205 depending on Mg-filter attenuation. The numbers represent the comparative area of the peaks generated when X-rays were passed through the filter to those unaltered element signatures, e.g. the average Mg-filtered O peak is only 0.75% of the peak produced when signal is detected from a normal plagioclase. Therefore the filter is attenuating the O element signal on average by 99.24 %. *Na: low signal attenuation compared with observed plots (Fig 6.11). Possible as a result of high counting statistics in the initial plagioclase analysis or an atypical plagioclase analysed. ** Mg - this refers to the secondary fluoresced peak *and* possible difference between the two pyroxenes minerals (they have a variable composition in the sample). As two different pyroxenes were measured this possibly is not a true representation of the signal attenuation or the loss of Mg in pyroxene.

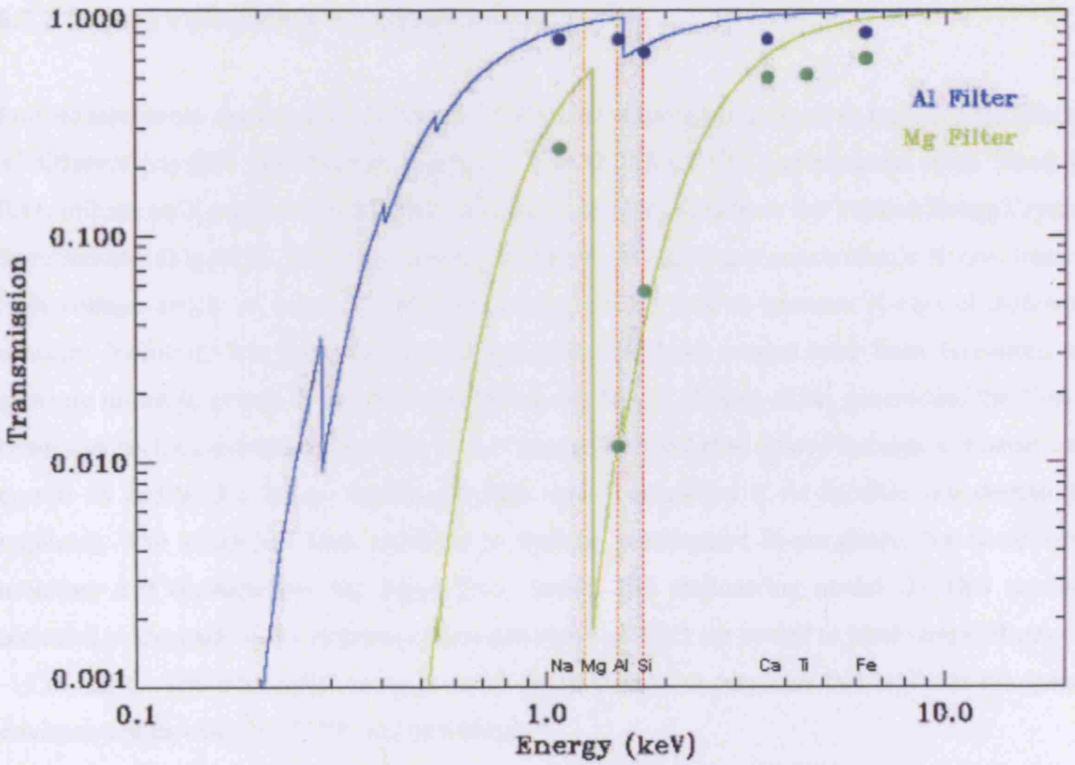

Fig. 6.12. Predicted X-ray transmission (solid lines: calculated by B.J. Kellett) through the D-CIXS filters compared with data from this filter experiment (spot points). Average Transmission from experimental work (Table 6.1 and 6.2) are over plotted where blue points represent Al-filter data and green points represent Mg-filter data. Experimental data correlates well with predicted transmission.

Experiment conclusions. The Al-filter effectively blocks the transmission of low energy X-rays below 1 keV (<61.5% of counts/keV in characteristic elemental peaks are attenuated in the presence of an Al-filter: Fig. 6.11a). It attenuates low-energy signal from Na-Al lines by ~27 to 28% and has the greatest attenuation effect to the Si-line (~38%). This attenuation is matched well to theoretical attenuation predictions made by B.J. Kellett (Fig. 6.12). Higher energy elemental lines (Ca and Fe) do not match the predicted attenuation so well (prediction suggests that nearly 100% of signal should pass through filter, where as measured values are between 72 to 80%: Table 6.1).The Mg-Filter completely impedes X-ray transmission below 1 keV and severely attenuates elemental line signal of Al (99% blocked) and Si-lines (95% blocked). Experimental data correlates well with predicted transmission for this range in energy. As with the Al-filter, the Mg-filter transmission at higher energies does not appear to have such a good correlation between the experimental data and the predicted signal throughput (Fig. 6.12, Table 6.2). The experimental data indicate for both filters that the count-rate was attenuated by more than the model suggests. The results of this experiment need to be included into models of X-ray response prediction for D-CIXS.

6.2.2 Future Laboratory Experimentation

Further laboratory testing of D-CIXS's SCD detector response is planned to measure the effects of different physical and thermal conditions. The D-CIXS/C1XS experimental setup based at RAL utilises an X-ray facility (RESIK) that was modified to calibrate the Yohkoh Bragg Crystal Spectrometer (Fig. 6.13). The large test rig is capable of emitting monochromatic X-rays from a high voltage anode. A range of different anodes can be used to generate X-rays of different energies including Mo, Ho, Ca and Co and some of these anodes have been converted to generate multiple energy X-ray lines (including Al, Mg, K, P, Cu). After generation, the X-ray beam can be focused though a series of collimating slits and then passed through a channel-cut crystal to define the X-ray wavelength (this can be removed if no specific wavelength is required). The setup has been modified to include a calibrated Si-pin diode that accurately monitors and characterises the input X-ray beam. The engineering model D-CIXS can be mounted in the path of the incoming beam and strips of SCD are cooled to ideal temperatures of -15 to -25°C. The whole rig can be pumped down to vacuum pressures that replicate the space environment in which D-CIXS was operating.

After calibration of the C1XS flight model in the summer 2007, the laboratory rig will be made available for SCD calibration and software development. I plan to partake in a variety of laboratory based experiments helping to validate models of lunar XRF conditions that will contribute to help better understand D-CIXS observations and future C1XS observations.

Rock and Mineral X-ray Fluorescence. We plan to modify the experimental setup so that the generated X-ray beam will be focussed on a range of geological samples, to induce secondary X-ray fluorescence. SCD detector arrays will be pointed towards the samples in an effort to detect the emitted X-ray signature. Thus, we can use the setup to irradiate a range of geological samples to provide an "End to End" test of the 'Swinyard' predictive XRF spectra programme (Section 6.3.2) that will be used to convert observed spectra into elemental abundances. This comparison can be used to judge how well the instrument response compares with the prediction from the programme output. Thus if adjustments to the programme are needed, they can be fully addressed before the final analysis of D-CIXS / C1XS lunar data.

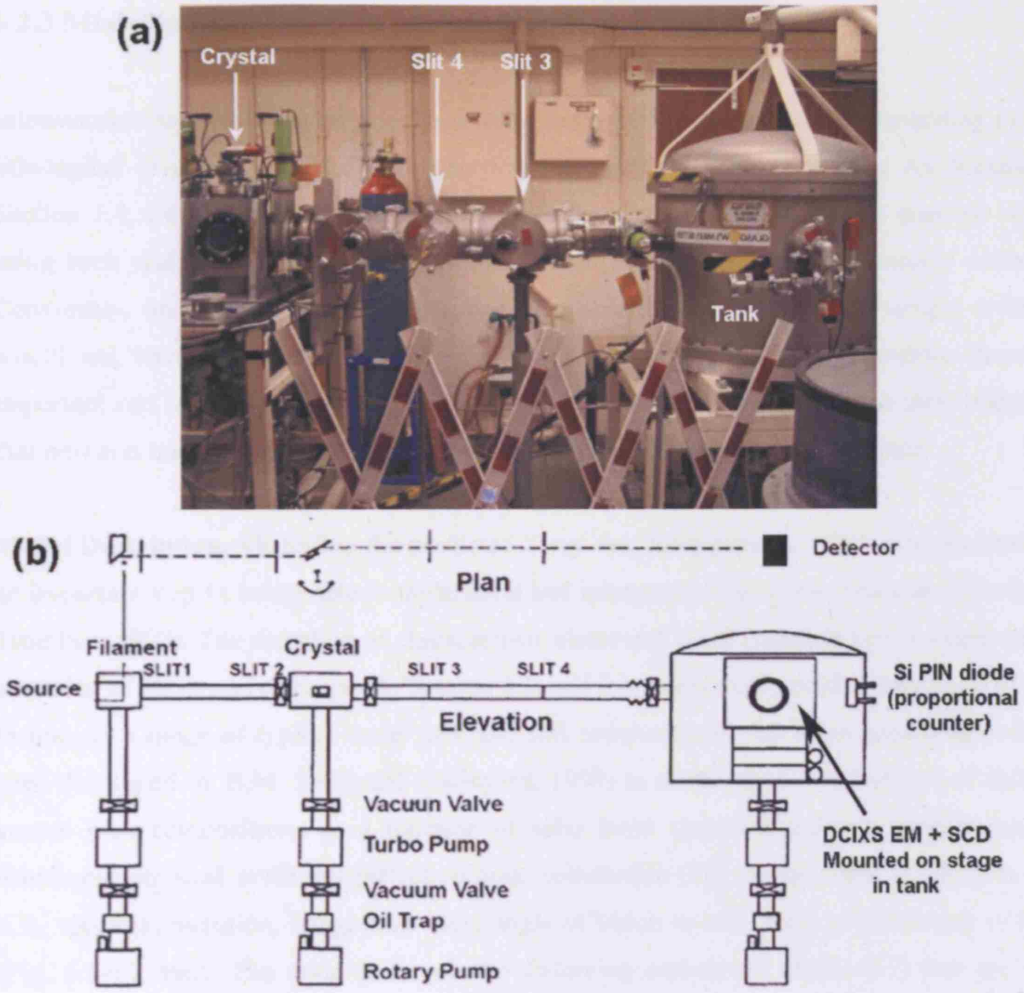

Fig. 6.13. (a) Photograph of the RESIK apparatus available at RAL built for the calibration of the Yohkoh Spectrometer (image courtesy of Emily Baldwin). (b) Schematic diagram of the same apparatus modified from Lang et al. (1993).

Particle Size Investigations. We will perform experiments to quantify the effects of surface roughness upon spectral signature. Prior investigations (Okada et al. 1998; Okada, 2004) have sought to determinate the effects of surface roughness on spectral response. I propose to extend the rock/mineral investigations discussed above to a range of lunar-like regolith analogues with a range of grain-size and porosity. These can be held within a thin box (i.e. 8 μm Kapton walls) to prevent them being scattered during handling or when the chamber is evacuated. A range of samples of known chemical compositions (e.g. 50% plagioclase; 50% olivine; or 100% plagioclase) could be investigated as analogues of porous finely granular regolith. The box could be used to compare X-ray generation from powders of different grain-size and packing with higher density solid materials. Scattering effects, such as elemental line resolution degradation, will hopefully be better understood as a consequence of these experiments.

6.2.3 Modelling XRF Spectra using Lunar Sample Information

Information from geochemical remote sensing has vastly improved our understanding of lunar lithological diversity, and has helped to develop models of lunar evolution. As discussed in Section 1.4, fully exploiting these important datasets would not have been possible without using rock and soil 'ground-truth' calibration from the Apollo and Luna sample collection. Conversely, understanding of the geographical distribution of rocks in the sample collection would not have been possible without the remote sensing datasets. Therefore these two important sets of information are mutually supportive, and it is only through their integration that new and important discoveries can be made about the Moon's geological past.

Model Description. Modelling the predicted X-ray flux from planetary XRF experimentation is an important step in being able to understand and interpret actual returned datasets (Clarke and Trombka, 1997). The detection of characteristic elemental X-ray emission lines is dependent on a number of factors as discussed in Section 1.2, and it is important to predict the effects of these factors on a range of typical lunar rock and soil compositions. An X-ray modelling code has been developed by B.M. Swinyard (Swinyard, 1999) to model the X-ray response of different known rock compositions as a function of solar input spectrum, galactic backgrounds and instrument physical attributes (effective area, collimation (Fig. 6.14a), filter thicknesses (Fig. 6.3), spectral resolution, integration time, angle of Moon to sun, angle of instrument to Moon (Fig. 6.14b), etc.). The code relies on the following parameters (Table 6.3) that are taken directly from Swinyard (1999):

Terms Used for Modelling X-ray Production

Term	Definition & Description
A	The area of the detector(s)
ω	The opening angle of the collimator that defines the half power point
E	MeV: Energy range interpreted this range as being the thickness of material that stops all electrons with energy below E MeV and that all electrons above E MeV pass through unimpeded.
ρ	Density in g/cm3
μ	Total mass absorption coefficient at energy E – the dependence on energy is assumed for clarity
i	Number of elements analysed
C_i	Fractional composition by mass
A_i	Atomic mass
Z_i	Number of each element
θ	The scattering angle
α	Input angle
β	Exit Angle
x	Penetration Depth
N_A	Avogadro's number
r_o	The classical electron radius
I_o	Input Solar flux in photons cm^{-2} s^{-1} keV sr^{-1}
j	Specific Element
Y_l	The fluorescent yield for the line at energy Kline
K_{line}	Line energy in keV
$\mu_j(E)$	The mass absorption coefficient for the j'th element
K_{edge}	The energy of the K-shell absorption for the j'th element
Ω	The solid angle of the collimator
ΔE(E)	The width of the detector resolution element at this energy
$\eta_k(E)$	The detection efficiency for electrons at this energy
$f_c(E)$	The transmission of the filters for electrons at this energy
dN_e	The electron background detected in an observation time t
dN_{xb}	The photon background detected in an observation time t
dN_{xl}	Flux in the line of interest
N_{Dxs}	The scattered x-ray background detected in observation time
N_{Dt}	Total detected counts

Table.6.3. Terms used for modelling X-ray production related to equations 1-4.

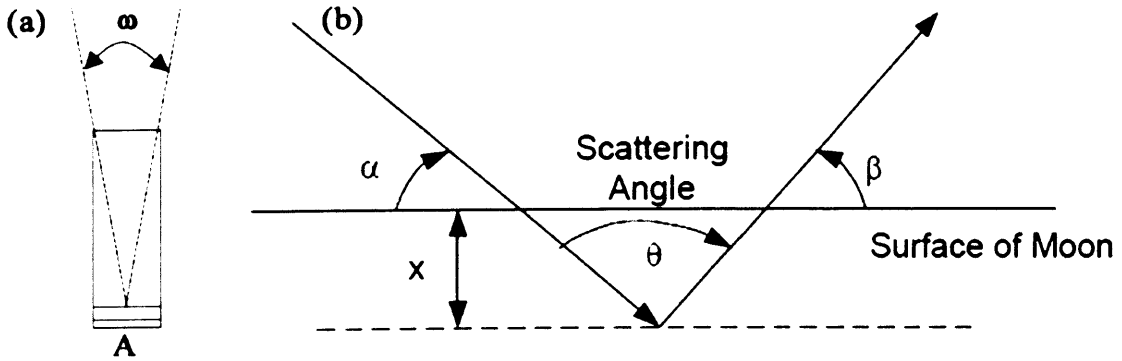

Fig. 6.14. (a) Collimator definition (see text for details). (b) Incident X-rays from the Sun and emergent X-rays from the Moon.

1. Collimator assumptions: The solid angle of the collimator (Fig. 6.14a) is taken as:

$$\omega^2 \qquad \textit{Equation 1}$$

The footprint on the surface of the Moon is given by:

$$2D \tan(\omega / 2) \qquad \textit{Equation 2}$$

where **D** is the distance from the satellite to the lunar surface.

2. Backgrounds (adapted from Swinyard, 1999. See Table 7.1 for description of equation terms): There are two basic sources of background for the case of lunar observations – the low energy solar wind electrons and the scattered solar x-rays from the surface of the moon. The high-energy charged particles and secondary events from the spacecraft structure can be neglected as these will either be discriminated against because they deposit a lot of energy (and will likely swamp the detectors from discriminating any lunar signal), or they will be shielded out by the graded shield surrounding the detector. The background fluxes are written as: $N_e(E)$ electrons $cm^{-2}\ s^{-1}\ keV^{-1}\ Sr^{-1}$ and $N_{xs}(E)$ photons $cm^{-2}\ s^{-1}\ keV^{-1}\ Sr^{-1}$

The electron background is calculated by using a literature electron spectrum (Lin et al. 1995), and then calculating the number of electrons with a sufficient energy to pass through the thickness of the Al-filter in the collimator assembly. The scattered x-ray flux from the lunar surface comes from Thomson scattering of the solar x-rays from the surface of the Moon, integrated over an infinite depth of penetration into the surface, and then substituting for the finite element of solid angle of the instrument (Fig. 6.14b, Swinyard et al. 1999).

3. Flux in the Line of Interest: The flux of energy in the elemental line of interest is written as $N_{xl}(E)$ photons $cm^{-2}s^{-1}\ Sr^{-1}$. (There is no explicit dependence of this quantity on the width of the energy detection band and it is assumed that the line is unresolved). The actual flux expected from a line can be calculated using a modification of Equation 1 in Clarke and Trombka (1997). The expected flux from element j in a substance is given by:

$$dN_{xl} = \frac{C_j Y_j}{\sin\alpha}\frac{d\Omega}{4\pi}\int_{K_{edge}}^{E_{max}} I_o(E)\frac{\mu_j(E)}{\mu(E)/\sin\alpha + \mu(K_{line})/\sin\beta}dE$$

Equation 3

(The photons are assumed to be emitted with equal probability in all directions: i.e. there is no dependence on scattering angle θ).

4. Detected Signal: Hence the total number of detected counts in the detector is:

$$N_{Dt} = N_{\text{Electron background}} + N_{\text{Scattered background}} + N_{\text{Detected counts in the line of interest}} \quad \textit{Equation 4}$$

Thus upon providing an input range of elemental concentration (and series of physical parameters and solar energy), the model will solve these equations (Swinyard, 1999), giving a predicted energy spectrum in eV (x-axis) against photons cm^{-2} s^{-1} Sr^{-1} (y-axis): i.e. spectra in Figure 6.15 of keV as a function of predicted detected flux.

Lunar Compositional Modelling Results. I will now show how lunar sample compositions can be used to empirically relate D-CIXS spectral data back to lunar surface elemental compositions. This technique is entirely reliant on using real lunar soil, rock and meteorite bulk compositions (Appendix 6.4) as a basis for predicting X-ray spectra. Figure 6.15 illustrates the nature of spectra predicted using the Swinyard XRF code, using the following input parameters: a C-class flare event (with no spectral elemental line features), collimators mounted with Al-filters and with a 12° FOV, an optimum viewing geometry of 90° from the instrument to the lunar surface and an optimal 45° angle between the solar position and the lunar surface. These modelled spectra are vital in understanding how sample geochemical variation will affect X-ray signatures from the Moon, and therefore how spacecraft data can be interpreted correctly.

The bulk soil compositions of the various sample-return landing sites have been used as ground-truth calibration targets by the Apollo XRF/Gamma-ray instrumentation, Clementine and Lunar Prospector. Therefore they provide the best starting point in actually having specific lunar targets that D-CIXS and other X-ray instruments could observe during lunar orbit. Lunar meteorites (particularly regolith breccia samples) are also useful tools in calibrating XRF datasets as they provide information about the Moon from localities not visited by sample return missions (Joy et al. 2006a). Figure 6.16 illustrates the same modelling as shown in Figure 6.15, using a range of lunar meteorite bulk compositions, including LAP 02205/02224 (Chapter 5), DaG 400 (Chapter 3) and MET 01210 (Chapter 4) that have been discussed in this thesis.

Figures 6.15 and 6.16 illustrate the problem of loss of resolution of D-CIXS's data: when the model is run with a resolution of ~380 eV FWHM (i.e. Fig. 6.15a,b), it is very difficult to accurately fit Gaussian line fits to the individual elemental peaks, thus making comparative elemental ratios and individual line intensity ratios difficult to determine.

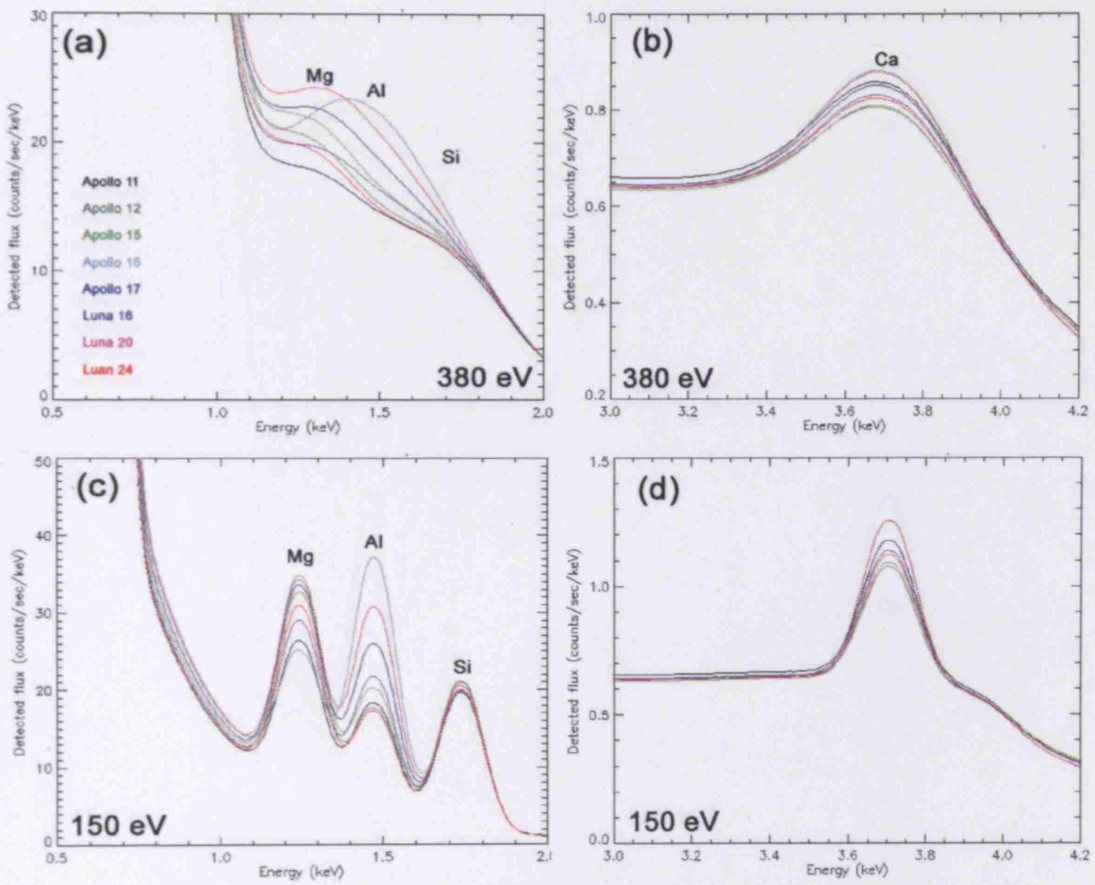

Fig. 6.15. Modelled (Swinyard, 1999) XRF spectra of average Apollo bulk soil compositions (Haskin and Warren, 1991: page 450) for C-class flare conditions, with an energy line resolution of (a)(b) 380 eV FWHM; i.e. D-CIXS line resolution. (c)(d) 150 eV: i.e. predicted C1XS line energy resolution. (Note difference in y-axis scale between line resolution plots).

Figure 6.15c,d and 6.16c,d display the same modelling parameters, for the same rock compositions, with an idealised line resolution of 150 eV FWHM, which is predicted to be the resolution of the new C1XS instrument. It is immediately obvious that the intensity of these well-defined lines can be used to discriminate between the Al-rich Apollo 16 and Luna 20 ('highland') landing sites, and the Mg-richer mare basalt landing soils. Additionally, it also demonstrates the significance of using the Si-peak as a normalisation parameter (as used by the Apollo XRF experiments); despite the 5% SiO_2 difference between the average soil compositions, the Si-peak flux remains relatively constant.

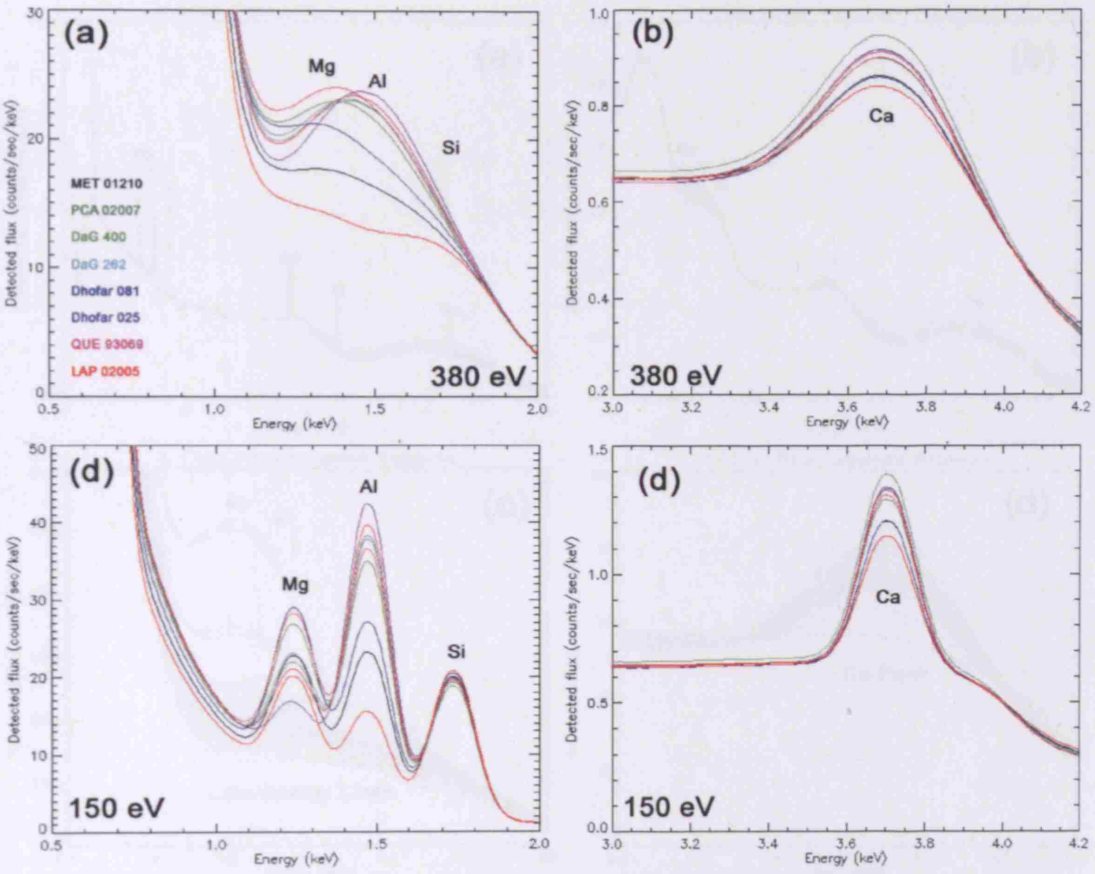

Fig. 6.16. XRF simulated modelling (Swinyard, 1999) of lunar meteorite bulk compositions. (a) (b) 380 eV FWHM: i.e. D-CIXS line resolution. (c) (d) 150 eV: i.e. predicted C1XS line energy resolution. Note difference in y-axis scale between line resolution plots. Data taken from Joy et al. (2006a,b) and Korotev (2003). Mare basaltic meteorites like LAP and MET have very low low-energy peak contributions as their bulk compositions have significant FeO, rather than MgO and Al_2O_3. DaG 400 and DaG 262 have very high Ca-peak features (>0.9 counts/s) because they contain additional $CaCO_3$ from terrestrial contamination (Section 3.2.2).

As a test to check the model validity, 66 lunar rock bulk compositions (including the landing site average soils, lunar meteorites and additional end-member individual rock compositions) were used as input compositions (Appendix 6.4). The samples were chosen as they represent a wide range of compositions (including breccias, plutonic samples, mare basalt and FAN rocks), encompassing many of the regolith lithologies that could potentially be observed by a lunar XRF instrument like D-CIXS/C1XS. Initial modelling was conducted using a scaled-up X-class solar flare input spectrum with no specific line energy contributions (basically a scaled-up C-class flare). An idealised line resolution of 10 eV FWHM were modelled first to predict a near-perfect scenario (Fig. 6.17a). Data from each spectrum was extracted to validate the relationship between spectral output and modelled compositional input. Realistic 'true-resolution' D-CIXS spectra were then modelled under the same conditions with a line resolution FWHM of 380 eV: modelled spectral response is shown in Figure 6.17b, c and d.

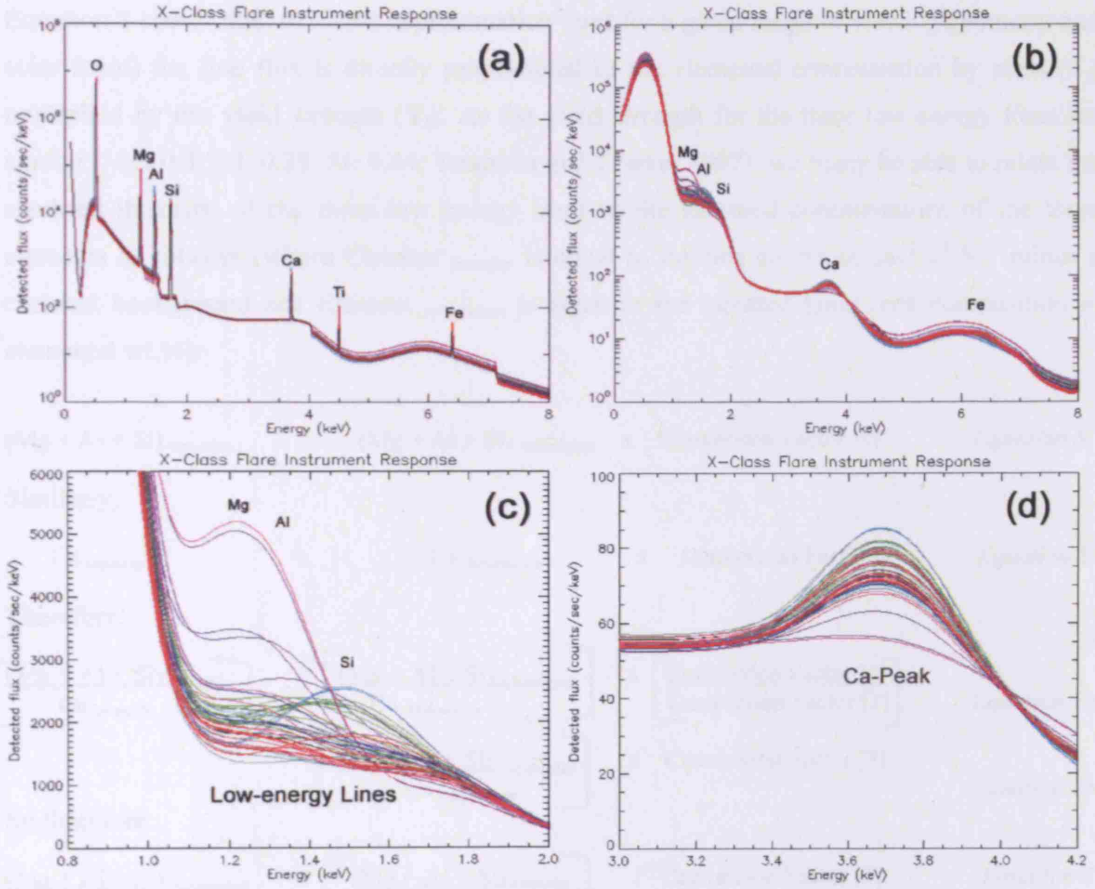

Fig. 6.17. X-class flare (no solar specific line energy input) modelled XRF response function for a range of lunar bulk compositions (see Appendix 6.4). Observation time assumed was 100 seconds. (a) Instrument elemental line resolution response function is set to a very idealistic full-width at half max (FWHM) of 10 eV. (b) Instrument line resolution response function is set to a realistic degraded D-CIXS FWHM of 380 eV. (c) Close up of low energy line variation on a normal scale for a FWHM line resolution of 380 eV. (d) Close up of Ca line variation on a normal scale for a FWHM line resolution of 380 eV.

As noted above, at such degraded spectral line resolution the low energy X-ray peaks of Mg, Al and Si become blended into a broad feature that becomes difficult to deconvolve to the original input composition (Fig, 6.17c). It therefore becomes necessary to try to make scientific inferences from data that are inherently problematic. The Apollo XRF experiments dealt with similar data complexities by ratioing line intensity features against each other, and were able to make geochemical inferences from ratios of Mg/Si and Al/Si (Fig. 1.21). Because D-CIXS has a completely blended low-energy peak it is difficult to deconvolve these line ratios. However, D-CIXS does have an advantage that in times of flare activity (M-class and above), a lunar Ca-line occurs in the spectrum (Grande et al. 2007a), which can be ratioed with the blended low-energy intensity feature. Thus, a geochemical relationship between the low-energy lines and Ca could be used as a calibration between the XRF modelling code, real lunar rock compositions, and data returned from D-CIXS lunar observations (Equations 5-8).

Equation 3 shows that, to a first approximation (and for a given range of viewing geometry and solar input) the line flux is directly proportional to the elemental concentration by mass (C_j) multiplied by the yield strength (Y_j). As the yield strength for the three low energy lines are similar (Mg: 0.3, Al: 0.38, Si: 0.44; Trombka and Clarke, 1997), we many be able to relate the summed intensity of the three low energy lines to the summed concentrations of the three elements as follows (where Element $_{Intensity}$ is equal to the line counts in cm^{-2} s^{-1} Sr^{-1} minus a constant background and Element $_{Abundance}$ is equal to the inputted lunar rock composition in elemental wt.%):

$$(Mg + Al + Si)_{Intensity} \approx (Mg + Al + Si)_{Abundance} \times \text{Conversion Factor [1]} \qquad \textit{Equation 5}$$

Similarly,

$$Ca_{Intensity} \approx Ca_{Abundance} \times \text{Conversion Factor [2]} \qquad \textit{Equation 6}$$

Therefore:

$$\left[\frac{(Mg + Al + Si)_{Intensity}}{Ca_{Intensity}}\right] \approx \left[\frac{(Mg + Al + Si)_{Abundance}}{Ca_{Abundance}}\right] \times \left[\frac{\text{Conversion Factor [1]}}{\text{Conversion Factor [2]}}\right] \qquad \textit{Equation 7a}$$

$$\approx \left[\frac{(Mg + Al + Si)_{Abundance}}{Ca_{Abundance}}\right] \times \text{Conversion Factor [3]} \qquad \textit{Equation 7b}$$

So therefore:

$$\frac{(Mg + Al + Si)_{Abundance}}{Ca_{Abundance}} \approx \left[\frac{(Mg + Al + Si)_{Intensity}}{Ca_{Intensity}}\right] / \text{Conversion Factor [3]} \qquad \textit{Equation 8}$$

Modelled Conversion Factor Calculations. A test was conducted using the near-perfect 10 eV line resolution data to investigate the empirical relationship between X-ray flux $_{Intensity}$ and sample elemental wt.% $_{Abundance}$ (Equations 5-8) for modelled D-CIXS spectral data (Fig. 6.18a,b). The number of counts per line energy (the line intensity) above the spectrum's background was extracted (Fig. 6.18a,b) and directly compared with the elemental wt.% of the sample that was used to originally generate the spectrum (Appendix 6.4). The relationship between this input (elemental ratio) and output (intensity ratio) should therefore define the correction factors in Equation 5-8 for a particular set of solar intensity and viewing geometry parameters.

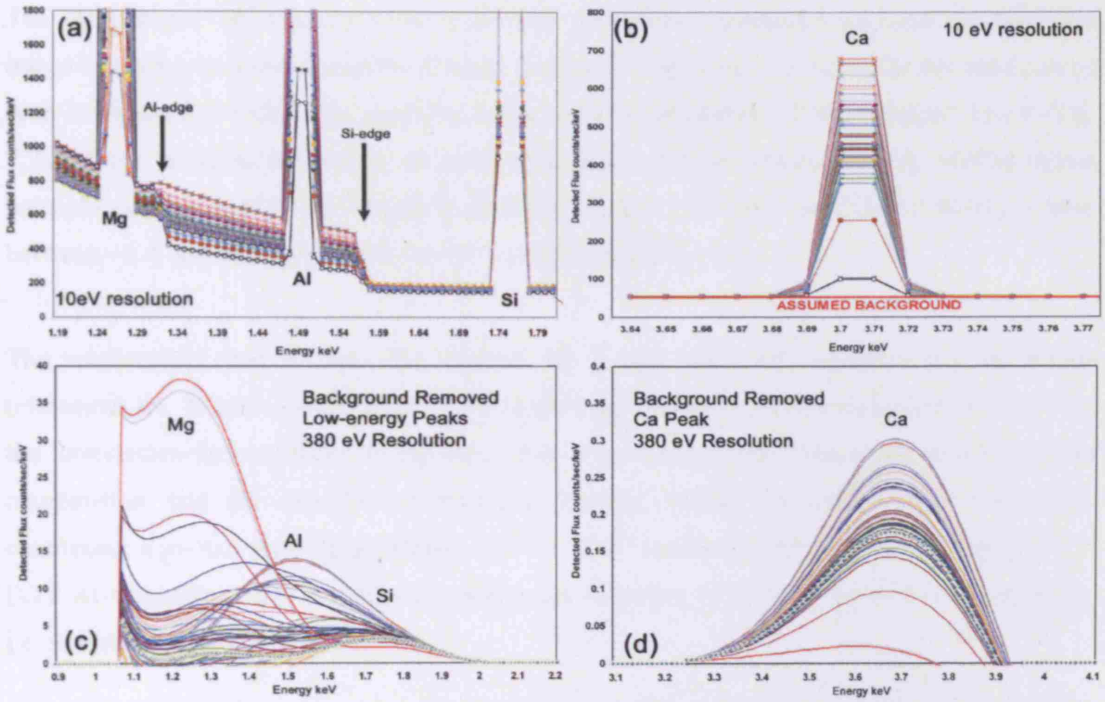

Fig. 6.18. Close up of (a) low energy spectral lines (Mg, Al and Si) and (b) Ca-line energy of XRF (Swinyard, 1999) modelled Apollo, Luna and lunar meteorite compositions (close ups of Fig. 6.17a). Assumed backgrounds for each spectrum were taken as a line extrapolated directly under each peak: e.g. for Ca (b) the line was very similar for each input compositions; however it is highly variable for the low-energy lines (a). The remaining line counts were then used as a measure of the line intensity (Fig. 6.19). (c) Same modelling of low-energy lines and (d) Ca but this time with a line energy resolution of 380 eV. Removed backgrounds were this time constant for all lines

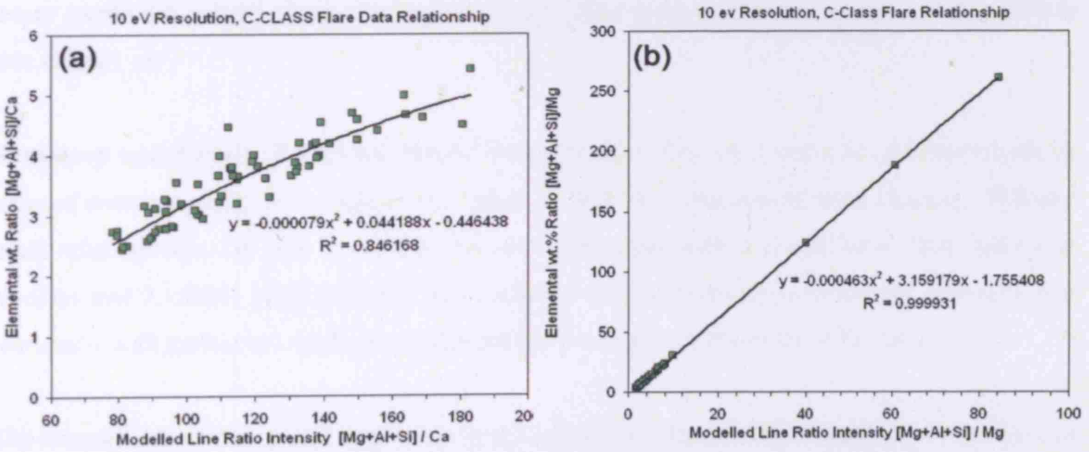

Fig. 6.19 Comparison of low-energy intensity (Mg+Al+Si)/Ca counts to elemental wt. % ratio of (Mg+Al+Si)/Ca. (a) 10 eV FWHM line resolution (background extrapolated for each spectrum). (b) 10 eV line resolution (background extrapolated for each spectrum) for (Mg+Al+Si)/Mg. Line fits are polynomials with no forced fit through 0 point.

The comparison between the input elemental abundance (Appendix 6.4) and the modelled intensity (minus an extrapolated individual spectral background: Fig. 6.18) for this ratio can be seen in Figure 6.19 where the model was run for a line resolution of 'near-perfect' 10 eV (Fig. 7.7a). Rock composition inputs all have elemental wt.% abundance [Mg+Al+Si/Ca] values between ~2.5 and 5.4 ([$MgO+Al_2O_3+SiO_2$]/CaO wt.% = 3.6-7.71), and [Mg+Al+Si/Mg] values between ~3.4 and 123 ([$MgO+Al_2O_3+SiO_2$]/MgO wt.% = 4-150).

The relationship (line of best fit) between the X-axis (modelled intensity) and the Y-axis (elemental wt. % ratio values used in the modelling) therefore defines algorithms for deriving the 'conversion factors' listed in Equations 5-8. For example, the relationship between sample composition and the modelled instrument response whilst observing with C-class flare conditions, a perfect viewing geometry, 10 eV FWHM line resolution and looking through a 12° FOV Al-filter (Fig. 6.19) can be expressed as the following (where x = modelled intensity ratio, i.e. x-axis value in Figure 6.19):

$$Mg+Al+Si / Ca_{\,Abundance} = -0.000079\,x^2 + 0.044188\,x - 0.446438 \qquad \textit{Equation 9}$$

$$Mg+Al+Si / Mg_{\,Abundance} = -0.000463\,x^2 + 3.159179\,x - 1.755408 \qquad \textit{Equation 10}$$

These values will obviously vary for changes in the nature of the input solar spectrum and to a lesser extent for variations in viewing geometry, filter type, collimator opening angle, particle size effects, etc.

Summary and Future Modelling Work. Future work will be carried out to calculate a look-up table of corresponding correction values based on real life variations of these changes. Different input solar spectra will also be used to calculate correction factors for different flare states (i.e. M-class and X-class), with different input spectral line properties (i.e. enhanced elemental line features – with particular emphasis on the effects on solar contributions of Fe and Ca).

The overall aim of this modelling is to provide a method of backward modelling from observed lunar XRF compositions to the original surface composition. I have proposed here that this may be possible by calculating a range of 'conversion factors' (Equations 5-8), rather than developing a library of modelled spectra: i.e. once the solar activity is known, and housekeeping geometry files known, it should be possible to look up a 'best-fit' conversion factor algorithm to apply to the intensity value, calculating back to the original lunar surface elemental abundance ratio. I will attempt to show how this derivation is possible by simulating the relationship

between count intensity and molar abundance [Mg+Al+Si]/Mg and [Mg+Al+Si]/Ca for a C-class event. This work needs to be continued to study the relationship between X-ray line ratios (i.e. Mg/Si, Al/Si and Ca/Si; Fig. 6.20) and changes in the modelled physical state of the observation (solar flux, viewing geometry etc.), with the long-term goal of accurately relating individual line fluxes to elemental abundances (i.e. derivation of absolute abundances). (NB the long-term goal is to adapt the Swinyard code to automate this process and create a look-up table of predicted spectral patterns per solar input and for the full range of predicted viewing geometries. The approach outlined here is designed to provide an initial method to try to determine elemental ratios from D-CIXS spectra).

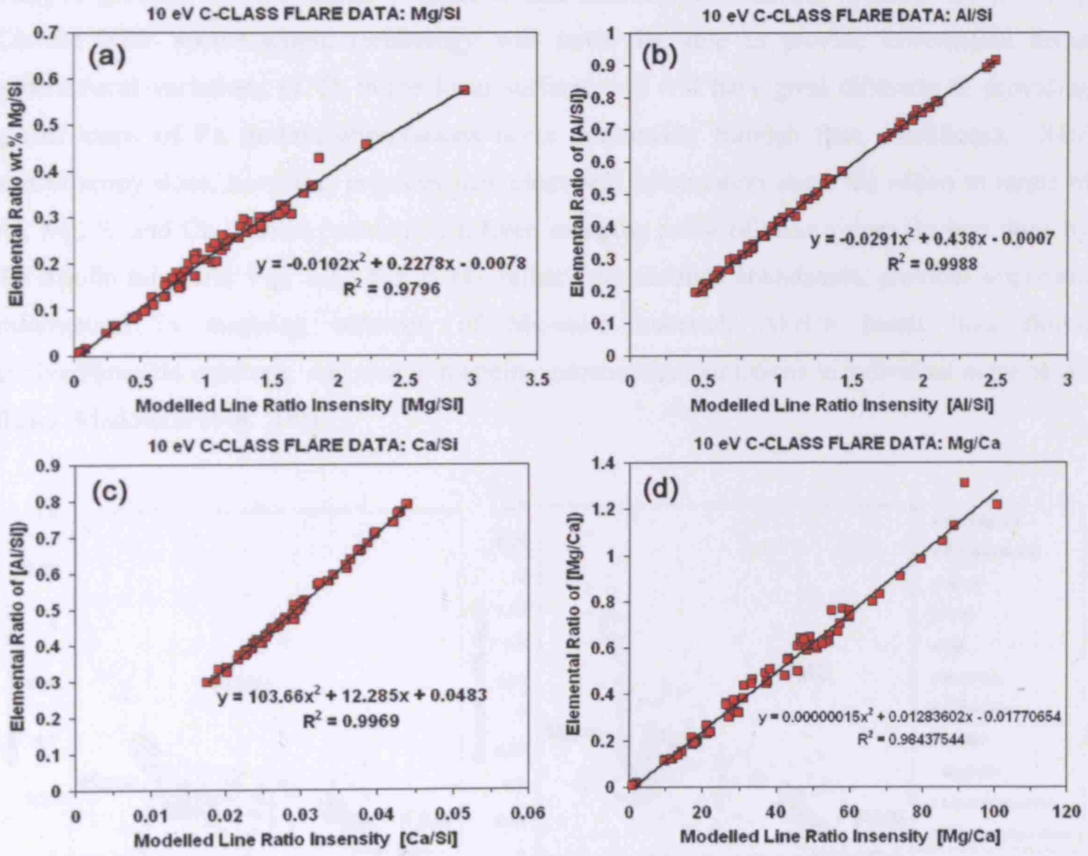

Fig. 6.20. Study of intensity of elemental ratios vs. input molar abundances. X = x-axis value = modelled intensity ratio. Y = y-axis value = input sample elemental composition ratio. (a) Mg/Si where $y = -0.0102\ x^2 + 0.2278\ x - 0.0078$, (b) Al/Si where $y = -0.0291\ x^2 + 0.438\ x - 0.0007$ (c) Ca/Si where $y = 103.66\ x^2 + 12.285\ x + 0.0483$. (c) Mg/Ca where $y = 0.00000015\ x^2 + 0.0128\ x - 0.0177$. These models use the same parameters used for Fig. 6.19 and with an optimal line resolution of 10 eV

6.2.4 Understanding Lunar Lithology Geochemical Variation within the Context of XRF Datasets

The goal of lunar X-ray florescence spectroscopy, or indeed any form of remote sensing spectroscopy, is to map elemental variations in the lunar regolith, and to make interpretations about these variations within the context of lunar geological history. Our current understanding of lunar sample compositional diversity and its geographical distribution was reviewed in Chapter 1. Lunar geological terrains have previously been identified through their variation in FeO and Th-content (e.g. Jolliff et al. 1998; Spudis et al. 2000, 2002). These elements were mapped globally by the Lunar Prospector and Clementine missions (Section 1.4.1, 1.4.2). Current XRF spectroscopic technology will never be able to provide information about geochemical variations of Th in the lunar surface, and will have great difficulty in providing global maps of Fe (unless observations occur continually through flare conditions). XRF spectroscopy does, however, provides new elemental information about the Moon in terms of Al, Mg, Si and Ca content (section 1.3). Even mapping ratios of these values (as was done by the Apollo missions: Fig. 1.21, Fig. 6.21), rather than absolute abundances, provides important information in mapping outcrops of Mg-suite material, Al-rich basalt lava flows, evolved/granitic outcrops, and also in mapping geochemical variations in individual mare basalt flows (Maddison et al. 2006).

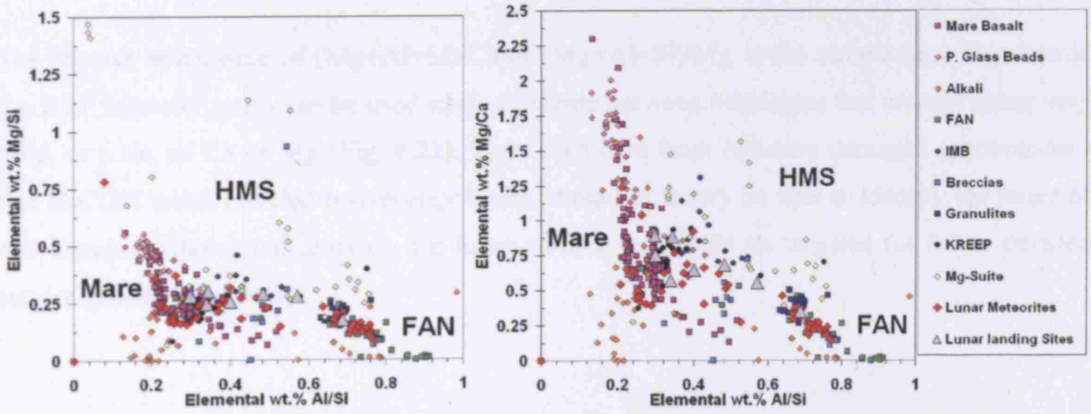

Fig. 6.21. Lunar lithological variations using only Mg, Al, Si and Ca ratios as discriminating elements. Sample literature comes from a range of sources including Haskin and Warren (1991), Papike et al. (1998), BVSP (1981), Wieczorek et al. (2006), Lucey et al. (2006), Korotev (2003), Joy et al. (2006a,b), and unpublished lunar meteorite data.

Spectral data derived from D-CIXS are difficult to interpret as a consequence of loss of spatial resolution due to radiation damage (Section 6.1.3). It is likely that because of the blending of the low-energy line peaks, mapping the ratios of Al/Si and Mg/Si (Fig. 6.21) will be problematic, and the derivation of elemental absolute abundances near impossible. Here, I present a new view of mapping elemental variations using information that theoretically can be best derived from lunar XRF spectroscopy, and its importance for future interpretations of D-CIXS (and CIXS) data.

Assuming that data returned from periods of strong solar activity (i.e. flare events) will always have a distinctive low-energy peak (that is well resolved from the noise peak) and possibly a Ca-peak (which is not experiencing double peaking), and *if* these counts can be corrected for solar effects (ongoing work), then in theory, this information can be used to make important observations about lithological terranes on the lunar surface. Figure 6.22 illustrates that the blended low-energy elemental abundances (Mg+Al+Si) can be used to differentiate compositions from mare basalt, KREEP and highland lithologies, without needing to map Th and FeO concentrations. Samples from the mare basalt and picritic glass beads have the lowest (Mg+Al+Si) values, as these samples carry a dominant Fe-component, and therefore have far lower contributing Mg and Al concentrations. Conversely, the FAN and High-Mg Suite have higher bulk (Mg+Al+Si) values as they are dominated by Al-rich plagioclase and/or Mg-rich olivine phases.

The relative abundance of (Mg+Al+Si)/Ca or (Mg+Al+Si)/Mg in the sample (and therefore in the XRF intensity ratio) can be used to discriminate between lithologies that contain either very little, or a lot, of Ca or Mg (Fig. 6.22). Thus even data from radiation damaged spectrometers like D-CIXS (with blended low-energy lines), should in theory be able to identify the range of end member lithological units on the lunar surface that could be targeted for future detailed remote geochemical study.

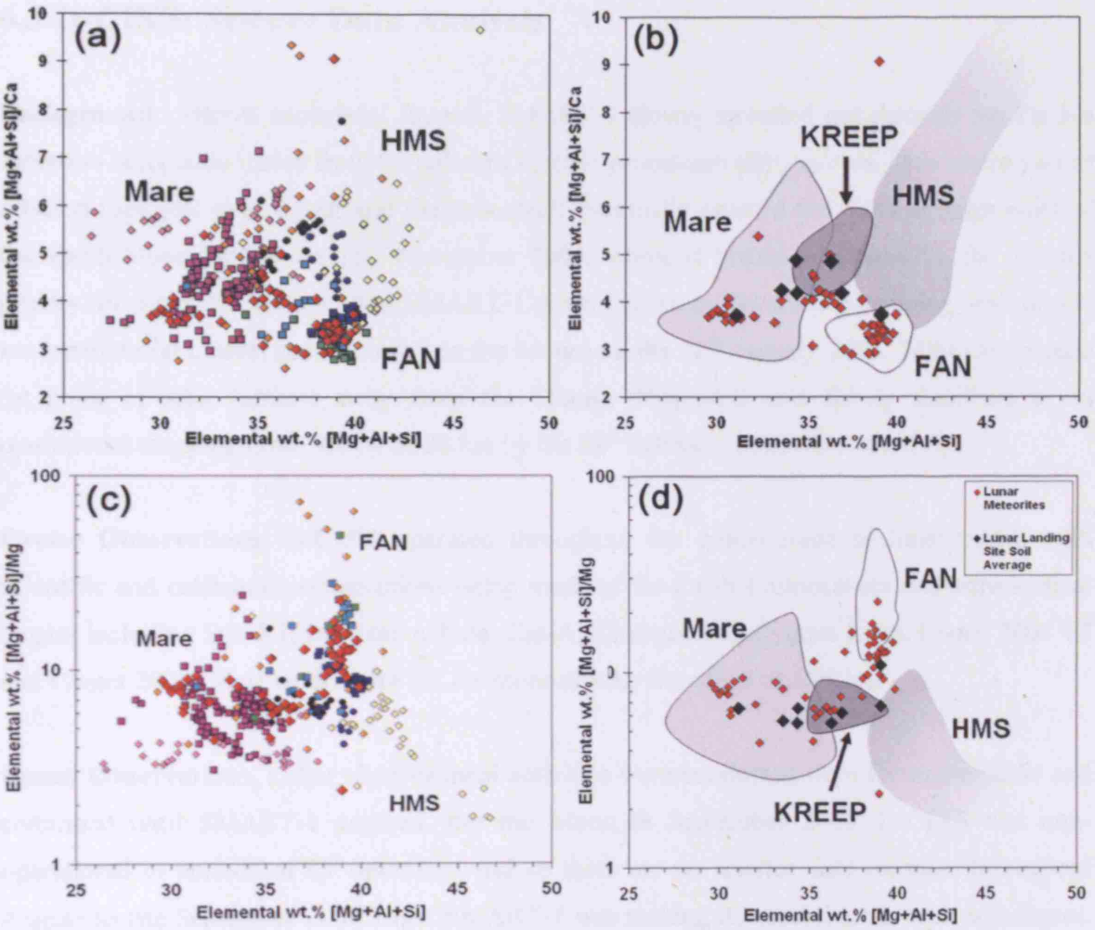

Fig. 6.22. Variations in lunar lithological changes using only the bulk sample abundance of Mg, Al, Si and Ca as discriminating elements. (a) Co-added Low-energy XRF detectable elements (i.e. to replicate the effects of D-CIXS blended line features) compared with the co-added low-energy lines relative to the amount of Ca in the sample; the major lunar lithologies are divided into a ternary mixing trend between mare basalt, FAN and KREEP/HMS/HAS rock samples. (b) Outlines of major lunar rock lithologies for [Mg+Al+Si]/Ca; some HMS-suite samples are located outside the plot area and so are indicated by the fading of outline. Over-plotted are lunar meteorite compositions (red diamond) and bulk landing site soil compositions (black diamonds). (c) Same x-axis as before compared with the co-added low-energy lines relative to the amount of Mg in the sample. (d) Outlines of major lunar rock lithologies for [Mg+Al+Si]/Mg with over plotted lunar meteorite compositions (red diamonds) and bulk landing site soil compositions (black diamonds). Sample literature from same source as Fig. 6.21.

6.3 D-CIXS: Science Data Analysis

Background. After a successful launch, SMART-1 slowly spiralled out through the Earth's radiation belts under drive from its onboard electric propulsion (EP) system. This cruise part of mission took just over a year and the spacecraft eventually crossed the first Lagrange point of the Earth-Moon system on 15th November 2005, where it became captured by the Moon's gravity. Firing of the EP spiralled SMART-1 down into an initial science mapping orbit of 471 km perilune (at closest point in orbit to the Moon) on the 28th January 2005, 2880 km apolune (at point in orbit furthest away from the Moon). This orbit was slowly stabilised to an operational mapping orbit 300 by 3000 km by the 28th February 2005 (Website 1.6).

Cruise Observations. D-CIXS operated throughout the cruise stage of lunar transit with scientific and calibration observations being made of the Earth's atmosphere and astronomical targets including Sco-X1, the Crab nebula, Cas-A, Circinus X-1, Cygnus Loop, Comet 2004 T7 and Comet 2004 Q4. (See Website 1.7 for more details; Grande et al. 2007a).

Lunar Observations. Lunar observational activities were conducted from December 2004 and continued until SMART-1 crashed into the Moon in September 2006. D-CIXS was non-operational in periods of EP operation and so there are no science data recorded throughout August to late September 2005 when SMART-1 was making its second lunar orbit adjustment. An onboard EEPROM software (Electronically Erasable Programmable Read-Only Memory) problem also resulted in operational loss of the instrument between October and early November 2005 when the system was upgraded to version 4.3 of the operating software (Howe, 2006). The problem recurred in December 2005 when few operational science data were also acquired. A solution was finally found in late January 2005, ensuring the successful collection of lunar XRF data throughout 2006.

SMART-1 typically conducted 5 orbital passes around the Moon per one Earth day. One of these orbits was dedicated to down-linking telemetry and science data from the spacecraft to the Earth, and uploading new pointing commands. Spacecraft height, speed and incidence angle are all important factors in achieving the best statistically resolved data from the lunar surface. This information is stored onboard the SMART-1 spacecraft and processed on the ground to produce SPICE (Spacecraft ephemeris Planet Instrument Ckernel Events) files that can be used to extract the exact pointing information of each instrument.

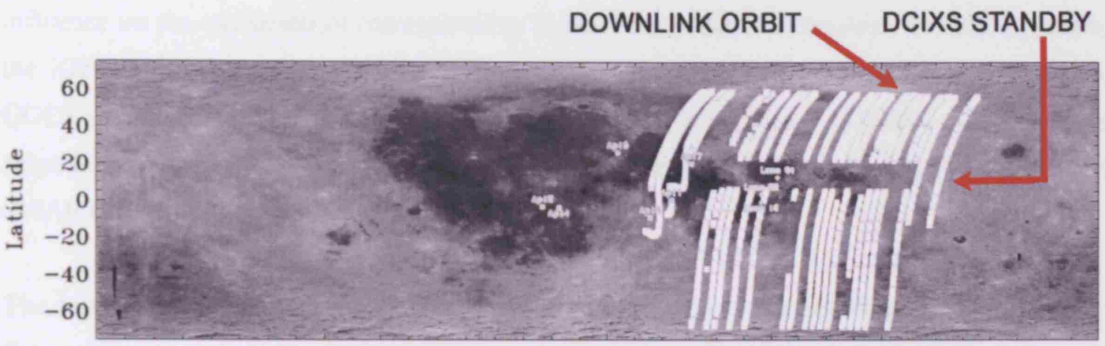

Fig. 6.23. Lunar D-CIXS data coverage ground tracks for facet 1 during the week of 19th March 2005 (right hand side of image where orbit tracks pass over the central far-side of the Moon) until 28th March 2005 (where the orbit tracks pass over Mare Serenitatis on the lunar near-side). Ground tracks are superimposed onto a stretched Clementine albedo map. Missing portions of tracks of the orbit were caused either because the orbit was delegated to data downlink, or because of temperature fluctuations causing the instrument to revert to standby mode (data loss normally in the middle of an orbit).

D-CIXS nominally operated for the other four orbits with science operations primarily being conducted on the illuminated face of the Moon. The SCD detectors are designed for optimal working condition temperatures between -25 to -17 °C. However, in-flight lunar temperature fluctuations for the SMART-1 spacecraft and D-CIXS itself were often higher and more varied than expected, causing the instrument to cease science operations and enter into 'resting' mode until temperatures returned to acceptable limits. Lunar coverage was therefore often compromised, and data loss occurred at intervals throughout the orbital period (Fig. 6.23).

Solar Fluctuations. Planetary XRF production is primarily controlled by the strength of the incoming solar X-ray signal (Chapter 1.3; Yin et al. 1993). Solar activity varies through a cycle from maximum (Solar Max) to minimum (Solar Min) activities (Fig. 6.24a), which can be tracked as a function of number of sunspots on the Sun's surface (Fig. 6.24b). SMART-1 entered lunar orbit in late-2004 to early-2005, coinciding with the last-stage of high solar activity declining into a period of minimal solar activity. This was a very quiet solar activity period (similar to the 1996 trend in Fig. 6.24a) with the majority of activity occurring at class A to B (10^{-8} to 10^{-6} Watts per m^2) with minor class C to M events (10^{-6} to 10^{-5} W/m^2) and very rare X-class events (>10^{-4} W/m^2).

As discussed in the introductory chapter (Section 1.3), it is vital that these solar energy fluctuations are accurately monitored during D-CIXS's scientific observations as XRF outputs from the lunar surface are entirely reliant on the wavelength and strength of the incoming solar photons. For this purpose D-CIXS was coupled to its sister X-ray Solar Monitor (XSM: Huovelin et al. 2002), which was designed to continually measure the solar energy spectrum from 1 keV to 20 keV. This spectral range allowed the monitoring of incoming low-energy X-ray lines (particularly with wavelengths equal to elemental lines of interest) that have a major

influence on the excitation of corresponding X-ray lines in the lunar regolith. For periods when the XSM was not operating, a first order measure of solar activity can be assessed from the GOES solar monitor (Website 1.8). This situation is non-ideal though as GOES only measures solar X-ray flux in a "soft" and "hard" energy band, and not a continuous spectrum like the SMART-1 XSM.

The low solar conditions in 2004-2006 were not ideal for the successful generation of lunar fluorescent X-rays, and so many of the data derived from D-CIXS are 'quiet-time data' with limited elemental line strength information. As a consequence of the data difficulties, this thesis will concentrate on describing data obtained during observation periods coinciding with Class-M flare or above events (> 10^{-5} W / m^2), when the instrument detected a strong, clear X-ray signal with resolvable elemental line features.

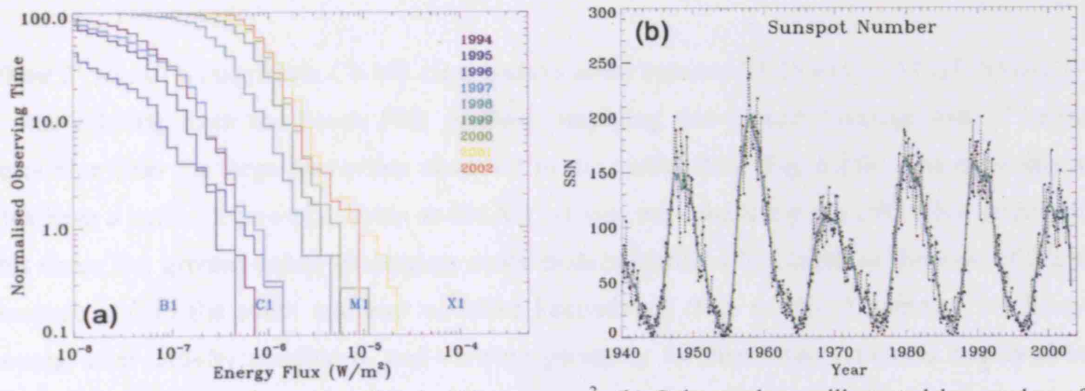

Fig. 6.24. (a) Solar cycle energy flux in Watts per m^2. (b) Solar cycles as illustrated by number of sunspots over the last 65 years. SMART-1 orbited the Moon in 2004-2006 during a period of solar activity decline to solar minimum. *Images courtesy of Barry Kellett (RAL).*

Data Suitability. Archived datasets (Level S1) from the lunar operations part of the mission were analysed for periods of solar flare activity using the IDL programmes '*D-CIXS_moon_summary_map_new.pro*' and '*D-CIXS_moon_sum_facet_new.pro*' written by B. J. Kellet (also utilising other D-CIXS software tools: Website 1.7). For this thesis a library of flare events was developed and orbits / part-orbits selected for their suitability of having data with strong low-energy lines and a Ca-line feature. Upon further investigation, it was often the case that a solar flare event occurred during an observation period, but either the viewing geometry was poor (near the lunar terminator), the SCDs were flooded by incoming particles (electrons, protons, etc.) from the Sun, swamping any lunar XRF signal, or the instrument had left operating mode (and entered 'resting' mode) during the observation because of temperature issues. The following dates and orbits are of primary interest as they coincide with large flares (M-class or above) and have periods of suitable data for initial science analysis.

6.3.1 Observations and Interpretation of XRF Data from the 14th January 2005 Flares

Two significant data intervals occur on this date (Appendix 6.1a,b):

Flare 1: was an M0-M4 Class flare that occurred between 13:54 and 14:21 UT when D-CIXS was over-flying the central-north eastern part of the lunar near-side (Fig. 6.25a). The three facets of the instrument were looking in slightly different orientations as SMART-1 was in the middle of a mid-orbit slew. Facet 1 (Al-foil, 12° FOV) was looking at the highlands to the north of Mare Marginis, onto the lunar far-side, and also covered Mare Humboldtianum in the far north. The central facet (facet 2: Al-foil, 8° FOV) was looking at the highlands just to north-east of Mare Crisium. Detectors on facet 3 (Mg-foil, 12° FOV) collected data from Mare Undarum, the highlands to the south-east of Mare Crisium, and Mare Crisium itself.

Flare 2: was of a magnitude C9-M5 class and occurred between 21:15 and 21:32 UT. SMART-1 was orbiting from the South Pole perilune, implying that ground coverage was of better resolution than the large foot-prints observed in the earlier flare (Fig. 6.25b). The three facets also have a better degree of overlap as SMART-1 was not conducting any mid-orbit slewing at this time. The ground-tracks encompass south-eastern highland lithologies to the west of Mare Australe and to the south and east of Mare Fecunditatis (Fig. 6.25b). A summary of X-ray counts, solar activity conditions, and viewing geometry for these observations is displayed in Appendix 6.1a. Data from both flare observations have a similar problem in that portions are experiencing the 'double-peaking' feature described above and discussed in Grande et al. (2007a, 2007b). Therefore both flare observations can be divided into 2 sub-groups of observations (those that were not experiencing double-peaking, and all the data from the flare regardless of double-peaking events: Fig. 6.26).

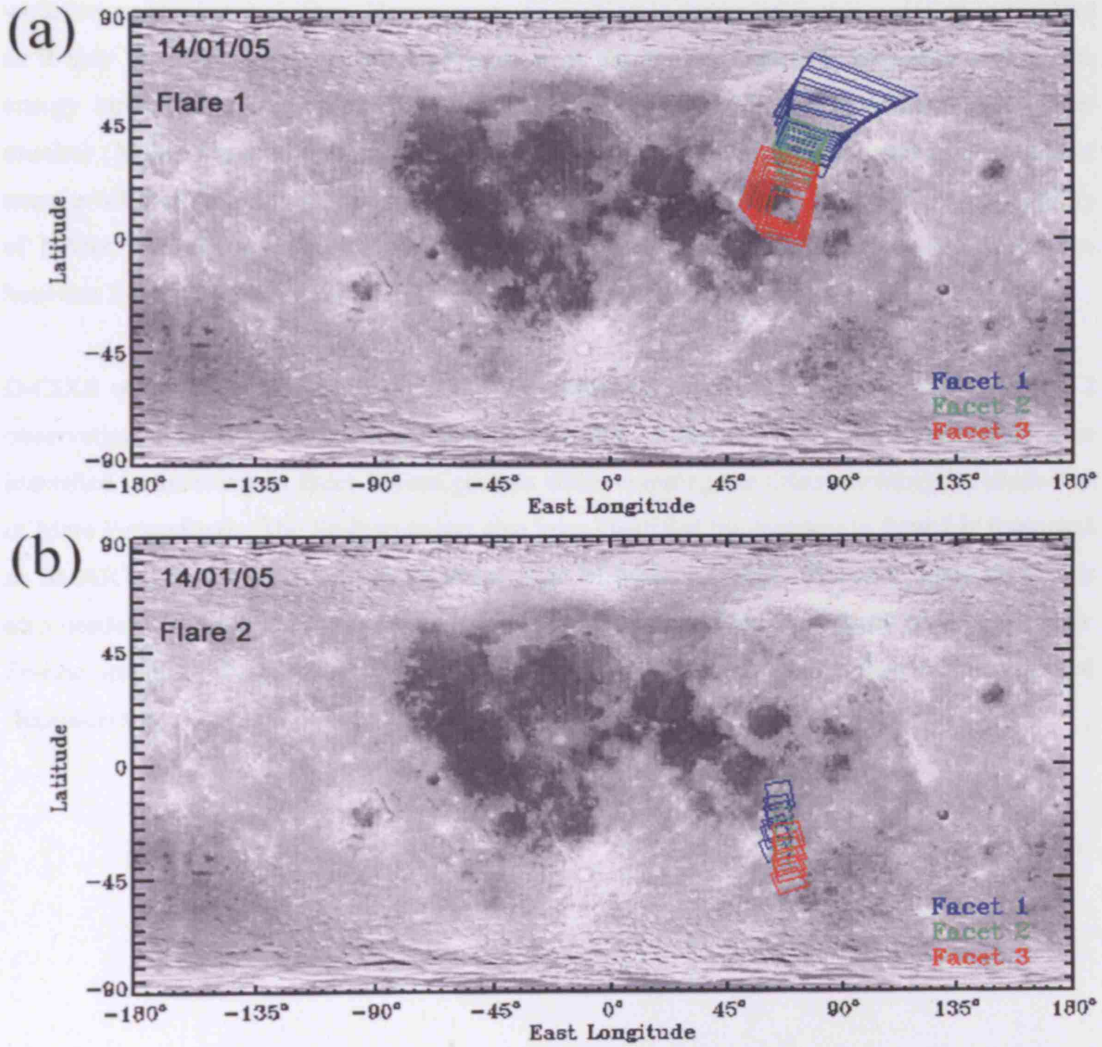

Fig. 6.25. D-CIXS's ground-tracks taken on 14th January 2005. (a) Lunar ground-tracks from the whole of the Flare 1 observation period. (b) Lunar ground-tracks from the whole of the Flare 2 observation period.

Observations. Count rate in the summed detector spectrum for facet 2 (Fig. 6.26b,e) is about 2.25 times less than those counts in facet 1 and facet 3 (Fig. 6.26a,c,d,f). The displayed data are weighted for the length of time the detectors were operating, and therefore are not affected by the fact that only 3 of the 6 detectors for facet 3 were operational. Therefore this reduced count rate is related to the effective area of the summed detectors as the field of view of detectors of facet 2 is only 8°, compared with facet 1 and 3 having an FOV of 12°. This difference between these two areas is a factor of 2.25, equalling the total reduction in observed count rate.

All operating detectors identified an elemental Ca-peak on the lunar surface (Fig. 6.26a,b,c). This Ca-line (3.6905 keV Kα-line) is far-enough removed from the low energy Mg (1.2536 keV Kα-line), Al (1.4866 keV Kα-line) and Si (1.7398 keV Kα-line) lines not to be blended with them. This elemental line feature is likely to be a direct observation of Ca-concentration

variation on the lunar surface. However, some caution in interpreting this variation is required as it may be possible that a small proportion of the Ca-line intensity represents a solar line energy input, rather than lunar fluorescent Ca. Unfortunately D-CIXS's accompanying solar monitor (XSM) was non-operational for this flare, and so we have no accurate measure of the exact profile of the solar spectrum input. Work is in progress, however, to assess the suitability of NASA's RHESSI (Website 1.9) instrument to provide information of the solar spectrum between 3 and 10 keV to provide information about specific solar excitation line energies.

D-CIXS observed a Ca-line feature and an additional Fe-elemental line during the Flare 2 observations in detectors from all three facets (Fig. 6.26d,e,f). This iron feature has been identified in detectors in facet 1 from periods while mapping the areas adjoining the south-east of Mare Fecunditatis. The Fe-feature has also been identified by detectors in facet 3 in footprints as SMART-1 was over-flying the western edge of Mare Australe. However, some caution is also needed in interpreting this Fe-variation as it may be possible that a small proportion of the Fe-line intensity feature represents a solar line energy input, rather than lunar produced fluorescent Fe.

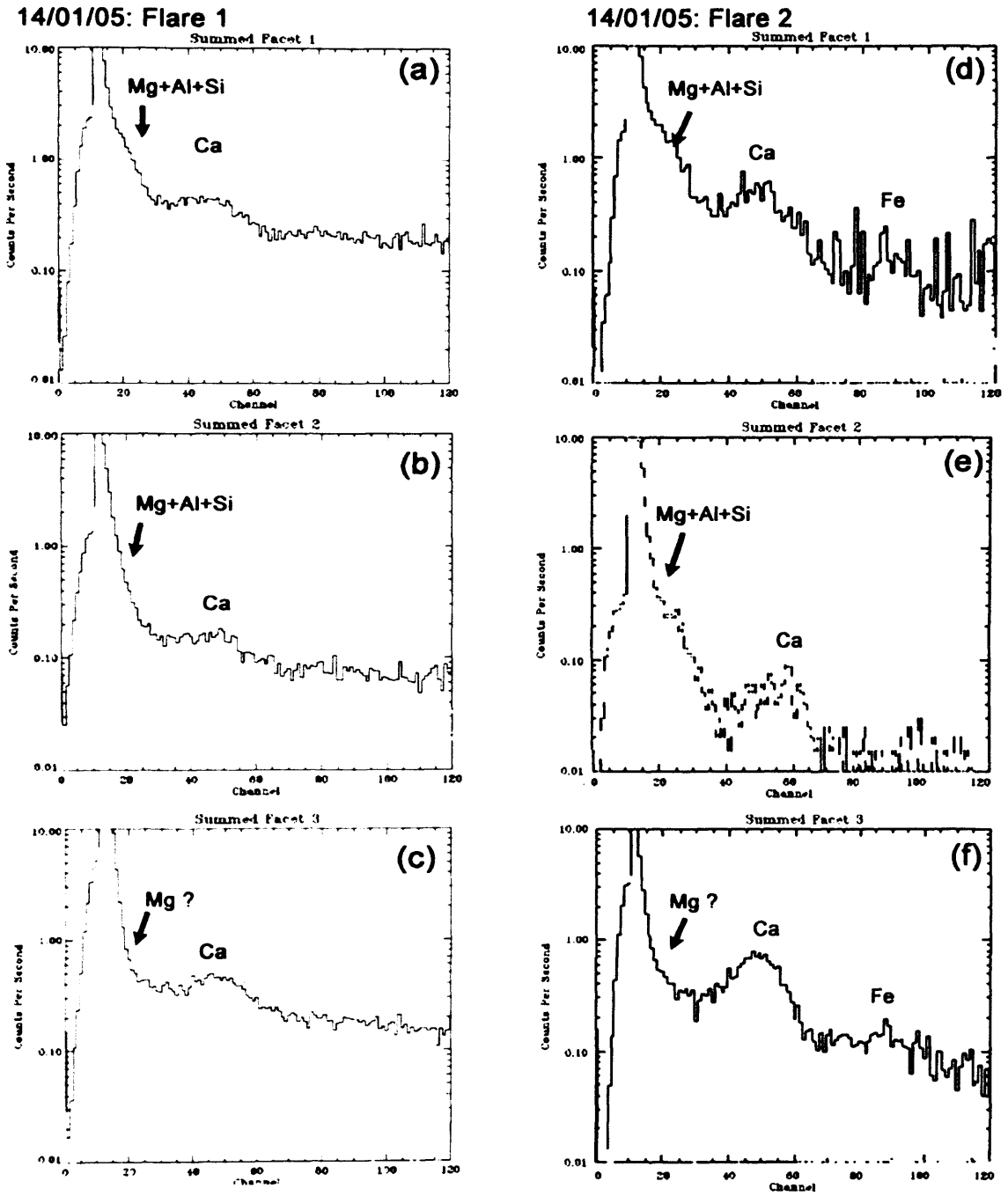

Fig. 6.26. January 14th 2005 Flare 1 summed spectral data. (a) Summary of the summed number of counts / observation seconds for individual detectors (grey spectra) on facet 1 and the total summed facet 1 (thick black spectrum) detector counts. (b) Same plots for facet 2 detectors. (c) Same plots for facet 3 detectors. January 14th 2005 Flare 2 data: (d) Facet 1 detectors. (e) Facet 2 detectors. (f) Facet 3 detectors.

6.3.2 Observations and Interpretation of XRF Data from the 15th January 2005 Flares

Three significant data periods of interest occur on this date. However, two of these periods are very short and so I will concentrate on the main data acquired from an X to M-class flare that occurred between 05:51 and 06:39 (Appendix 6.2). SMART-1 was overlying a similar area (Fig. 6.27a) to that covered during the 14th January 2005 Flare 1 (Fig. 6.25a) around Mare Crisium and the highland area to the north-east of Crisium on the near-side of the Moon, onto the far north-western farside. Data acquired during this observation have also been discussed in Grande et al. (2007a). Unfortunately all of the data that exist for this flare event were experiencing the double peaking phenomenon, and so interpreting variations in the elemental line peaks is additionally complicated.

Despite the double-peaking complications, detectors in facet 3 observed an enhanced Fe-line feature compared with detectors in the other two facets. During these observations facet 3 was pointing towards mare basalt deposits on the lunar eastern near-side, including part of Mare Fecunditatis and the whole of Mare Crisium. These mare regions are much richer in iron than the feldspathic highlands that were simultaneously being observed by facet 1 and it can therefore be interpreted that the difference in Fe-enrichment is directly contributed by the compositions that were over-flown during the flare event, and not as a consequence of a solar Fe-contribution.

Ca-line flux appears to be very similar between facet 1 (Fig. 6.27b) and facet 3 (Fig. 6.27d), suggesting that there may be only a marginal variation between Ca-concentration in the highlands and mare regoliths that were being studied by D-CIXS at this time. As discussed above this may need to be treated with some caution because of lack of information regarding the specific nature of the solar spectral input.

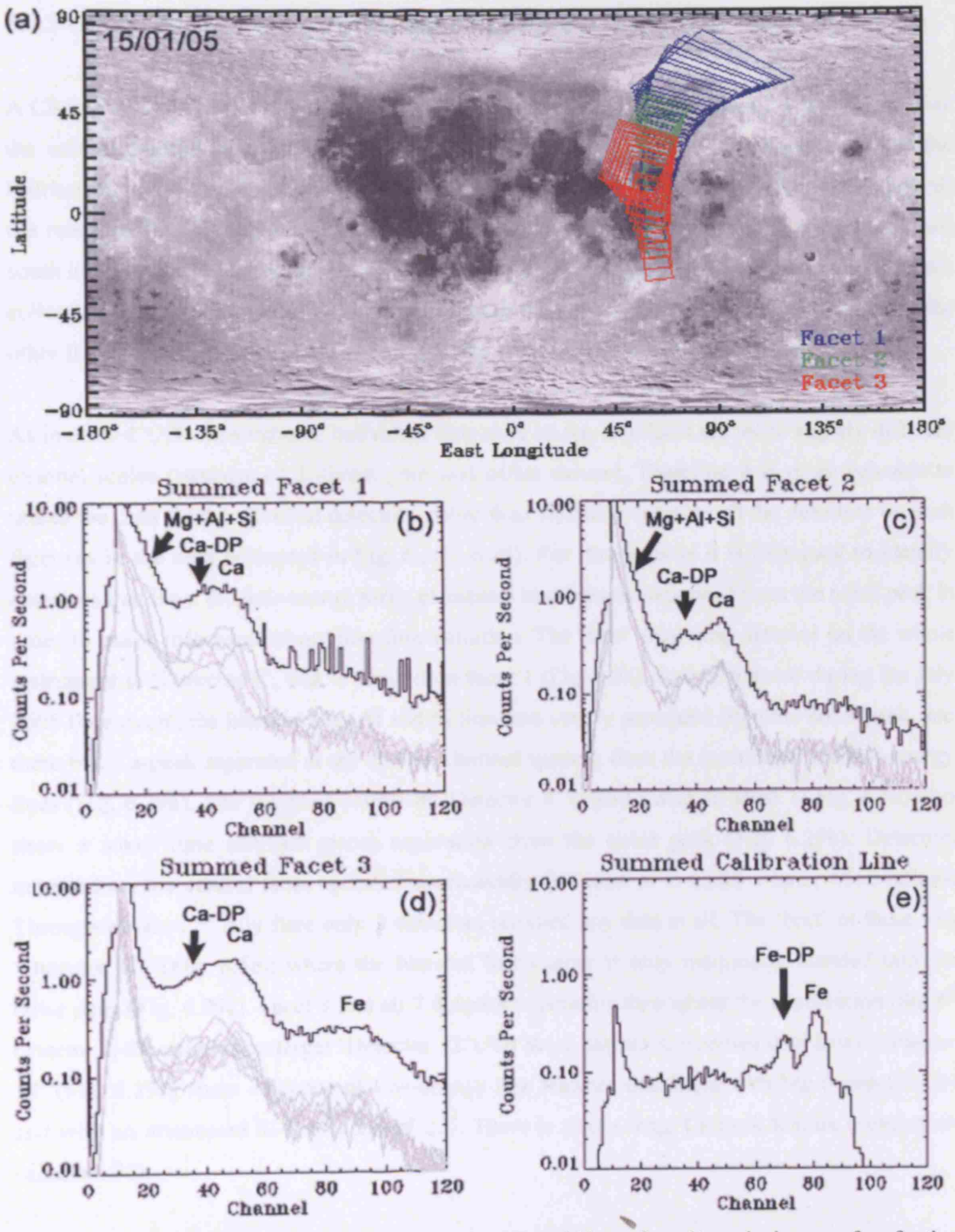

Fig. 6.27. (a) Foot-prints (red = facet 3, green = facet 2, and blue = facet 1) on the lunar surface for the X-M-class flare on 15/01/05. (b) Summary of the summed number of counts / observation seconds for individual detectors (grey spectra) on facet 1 and the total summed facet 1 (thick black spectrum) detector counts. (c) Same plots for facet 2. (d) Same plots for facet 3 detectors. (e). Summed calibration line spectrum from detector 23. Note the individual detectors have not been corrected for individual detector scaling offsets and therefore when summed together in this manner imply a poor-resolution spectra. The blended low-energy line peak is highlighted as Mg+Al+Si. The Ca-elemental peak (channel ~40-60) is identified as Ca, and its double-peaked feature (typically channel ~30-40) is highlighted as Ca-DP. The Fe-elemental peak (channel ~80) is identified as Fe, and its double-peaked feature (typically channel ~70) is highlighted as Fe-DP.

6.3.3 Observations and Interpretation of XRF Data from the 27th July 2005 Flare

A C8 to M4-class flare occurred between 04:42 and 05:30 UT when SMART-1 was flying over the central portion of the lunar farside (Fig. 6.28a, Appendix 6.3). The three facets of the instrument were looking in roughly the same orientation and were initially orientated towards the northern farside highlands feldspathic terrain. As the orbit evolved, observations tracked south into the north-eastern rim of the South Pole-Aitkin Basin impact basin. This period of data collection is very valuable as it did not experience the double-peaking phenomena afflicting the other flare periods, and it did not experience any channel scale offset throughout the period.

As in all D-CIXS observations, individual detectors on any one facet are set to slightly different channel scales (because of different gain and offset values). Therefore it is more valuable to utilise the data from individual detectors rather than summing together all the detectors on each facet (as in the data presented in Fig. 6.26 - 6.28). For this purpose it is important to identify detectors that have the low-energy x-ray elemental line features separated from the noise peak in order to make inferences about line flux variation. The 'best' operating detector on the whole instrument is 'Detector 0', that is located on facet 1 (Fig. 6.5c). In this detector during the July 2005 flare event, the blended Mg, Al and Si lines are clearly separated from the noise peak, and there is a Ca-peak separated at the correct channel spacing from the location of the low-energy lines (Fig. 6.29a). The summed counts in 'Detector 4' (also located on facet 1: Fig. 6.5c) also show a small (one channel space) separation from the noise peak (Fig. 6.29b). Detectors mounted on the central facet operated sporadically for most of D-CIXS's lunar observations. Throughout the 27th July flare only 3 detectors returned any data at all. The 'best' of these was 'Detector 10' (Fig. 6.5c); where the blended low-energy is only marginally blended into the noise peak (Fig. 6.29c). Facet 3 had all 7 detectors operating throughout the observation (the 8th detector is the calibration target 'Detector 23'). Of these detectors, summed data from 'Detector 18' (Fig. 6.29d) show evidence of low-energy line features consistent with Mg (~channel 15) and with an attenuated Si-line (channel 22). There is also a large Ca-peak feature (centred on ~channel 52).

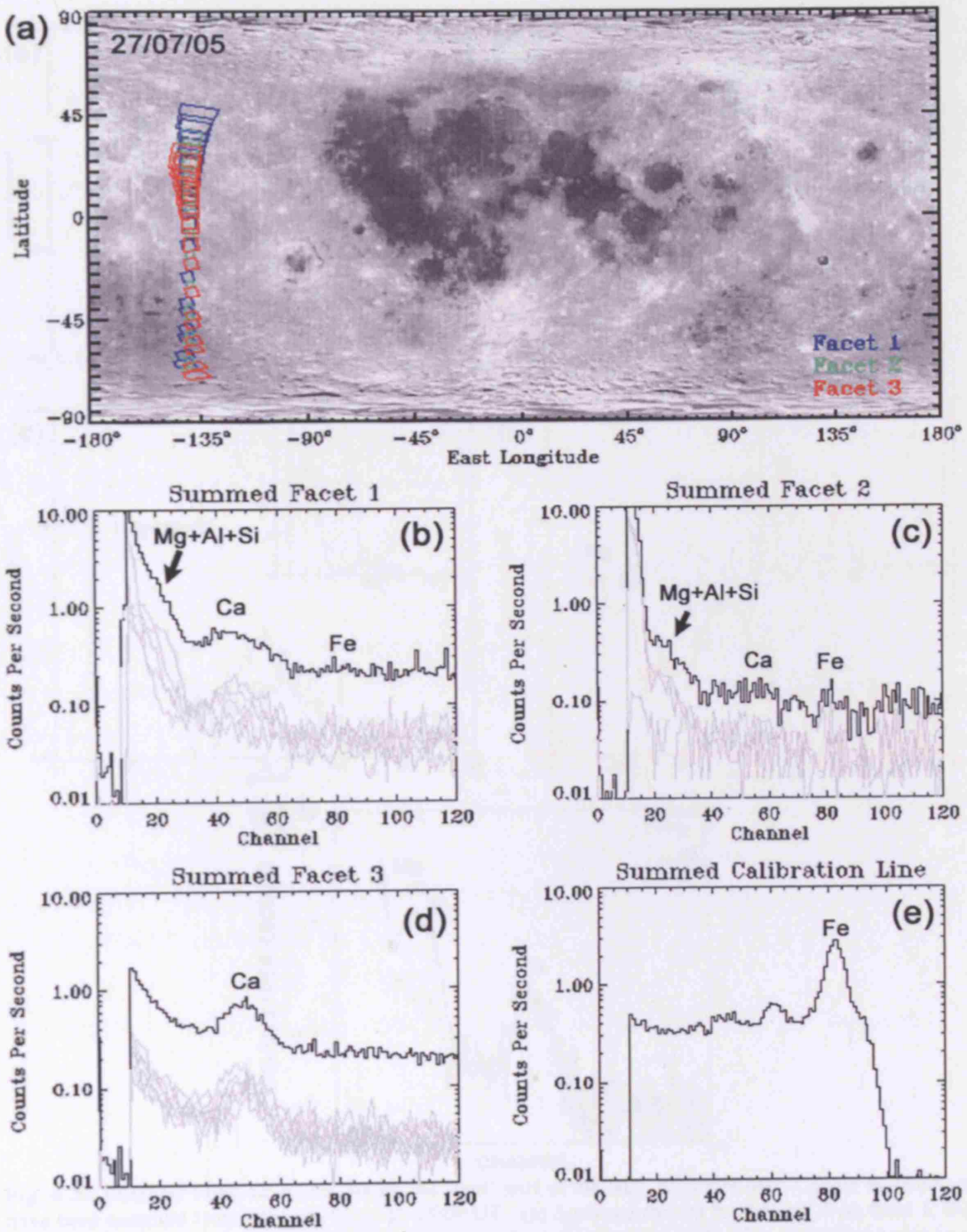

Fig. 6.28. (a) Foot-prints on the lunar surface for the M-class flare on 27/07/05. (b) Summary of the summed number of counts / observation seconds for individual detectors (grey spectra) on facet 1 and the total summed facet 1 (thick black spectrum) detector counts. (c) Same plots for facet 2. (d) Same plots for facet 3 detectors. (e). Summed calibration line spectrum from detector 23. Note the individual detectors have not been corrected for offset against each other. The blended low-energy line peak is highlighted as counts in the Mg+Al+Si channels.

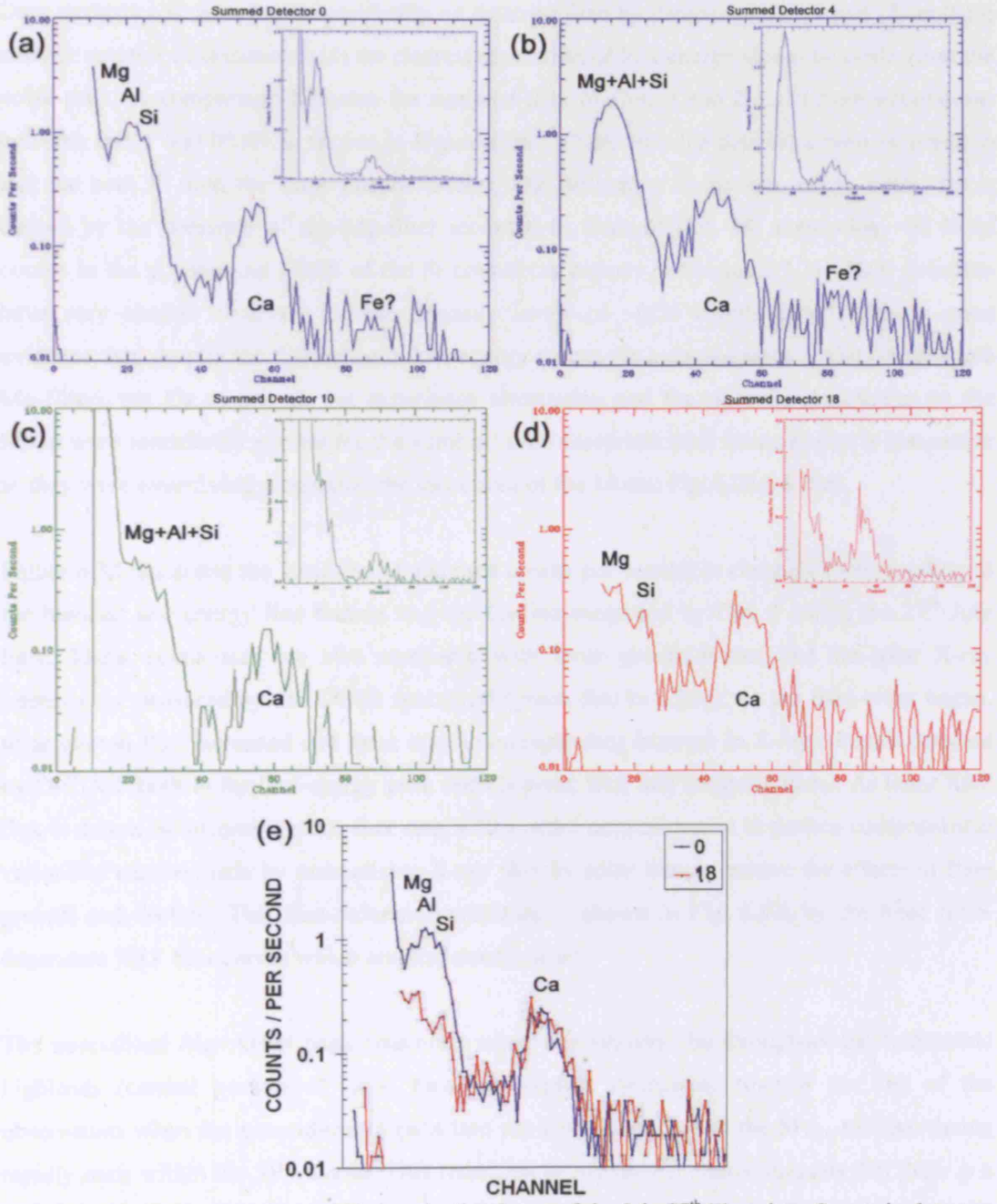

Fig. 6.29. Detailed summed counts during the 'best' part of the July 27th Flare data. Counts in detectors have been summed from between 04:51 to 05:09 UT. (a) Summed spectra for detector 0 on facet 1; the low energy elemental lines are well resolved from the low-energy noise peak. Inlay shows same plot on a non-logarithmic scale. (b) Summed spectra for detector 4 on facet 1; the low energy elemental lines are less well resolved from the edge of the low-energy noise peak. (c) Summed spectra for detector 10 on facet 2; the low energy elemental lines are blended into the edge of the low-energy noise peak, but this represents the best operating detector on the central facet for this time period. (d) Summed spectra for detector 18 on facet 3. The Mg-filter has attenuated all of the X-rays with energies corresponding to Al and the majority of X-ray counts with a Si-energy range. (e) Comparison of spectra from Det. 0 (a) and Det. 18. (d) Overlapped onto the same channel space scale for the flare period.

Data analysis will now focus specifically on data acquired by detectors (Det.) 0 and 18, as these contain spectral information with the clearest separation of low-energy elemental peaks from the noise peak. A comparison between the summed data of Det. 0 and Det. 18 from integrations between 04:51 and 05:09 is shown in Figure 6.29e. (Note that the data have been adjusted so that the both fit onto the same channel scale). The difference in the low-energy count rate is caused by the presence of the Mg-filter mounted in front of Det. 18, attenuating ~98 % of counts in the Al-line and ~95% of the Si counts (as proven in Section 6.2.1). Both detectors have very similar observed Ca-line intensity levels of ~0.25 counts/second. This is good evidence that, despite the difference in low-energy counts (as a consequence of Det. 18 having a Mg-filter), the Ca counts do not experience attenuation and therefore Ca-abundances on the Moon were remarkably similar for the summed orbit footprints (this interpretation is reasonable as they were over-flying essentially the same area of the Moon: Fig. 6.28a, 6.29e).

Figure 6.30 illustrates the variation of summed counts per second in channels corresponding to the blended low-energy line feature and the Ca-line measured by Det. 0 during the 27th July flare. These count-rates are also compared with lunar ground-tracks, and the solar X-ray intensity as measured by the GOES spacecraft (green line in 6.20b). As the flare event began, solar photon flux increased and there was a corresponding increase in X-ray counts/s detected by D-CIXS (both in the low-energy peak and Ca peak; blue and turquoise lines). As lunar XRF flux is driven by incoming solar flux rate, a first-order approximation to surface compositional variability can be made by normalising X-ray flux by solar flux to remove the effects of flare growth and decline. This first-order normalisation is shown in Fig. 6.30c by the three time-dependent XRF flux curves which are discussed below:

The normalised Mg+Al+Si peak count-rate trend is relatively flat throughout the feldspathic highlands (central portion of lunar far-side), slightly decreasing towards the end of the observation when the ground-tracks pass into the eastern portion of the SPA, and decreasing rapidly once within the SPA Basin. This reduction in Mg+Al+Si counts suggests that there is a marked difference in composition between the two terranes. The Ca-flux throughout the observation is more variable with localised changes in count rate. There is a general overall large decrease in Ca-channel flux rate in Southern Highland regions and in the SPA Basin (also seen in Fig. 6.31). The ratio [Mg+Al+Si]/Ca counts/s is shown as the red line in Figure 6.30c. Variations in the ratio are controlled by the noisy Ca-flux.

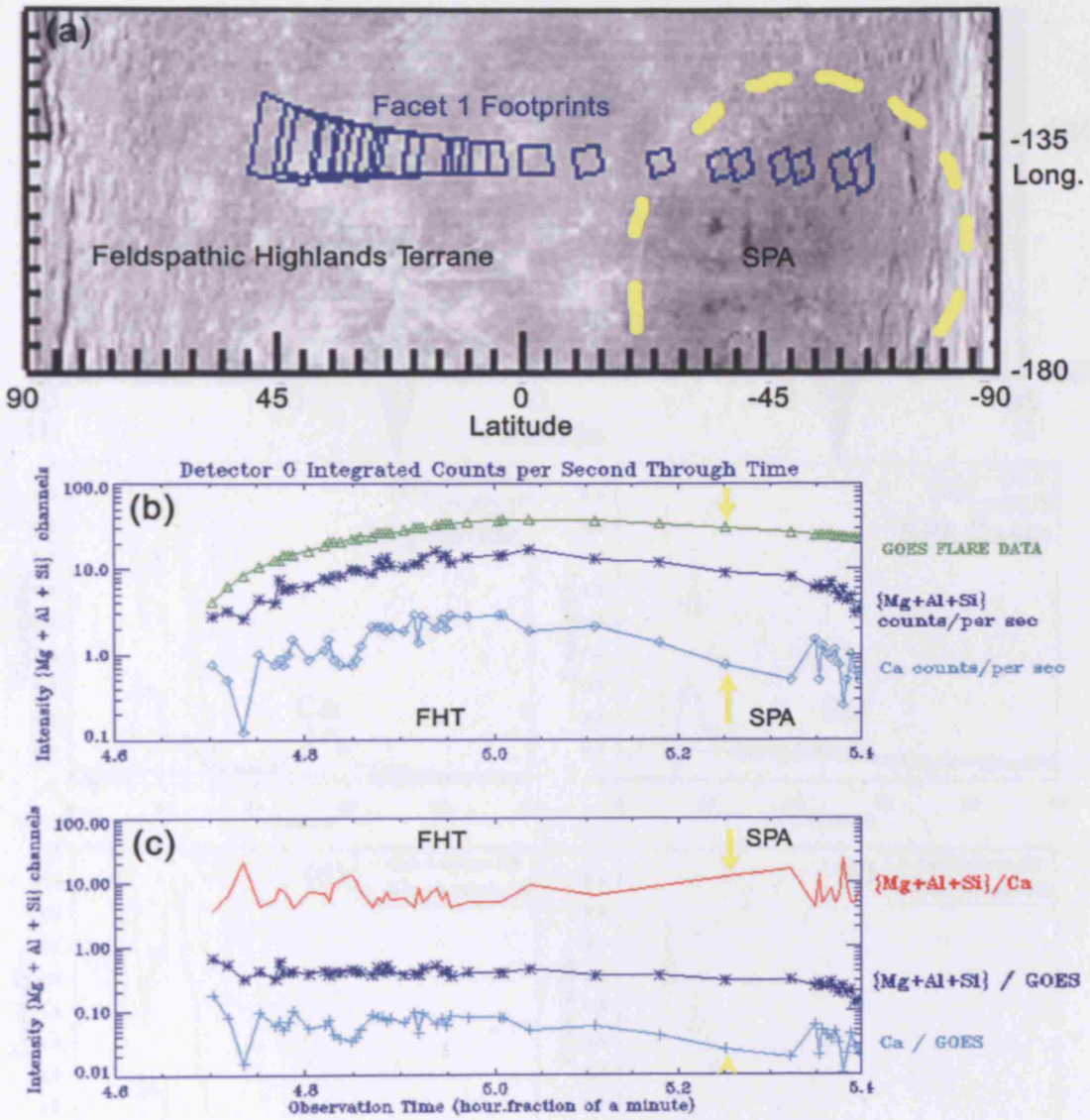

Fig. 6.30. (a) Ground-tracks for the main observation period during the 27th July 2005 flare event. The South Pole-Aitkin Basin is outlined in dashed yellow. (b) Summed energy counts from D-CIXS (blue) and the GOES (green) solar monitor (y-axis) throughout the observation time (x-axis). The dark blue line represents the summed counts per second from the Mg+Al+Si channels, and the turquoise line represents the summed counts/per second from the Ca channels. Yellow arrows mark the transition from the feldspathic highlands terrane to the SPA. (c) D-CIXS count flux normalised to the GOES solar flux in order to 'remove' the effect of solar input. The red line in (c) represents the variation in the ratio of [Mg+Al+Si] / Ca in counts per second through the observation period.

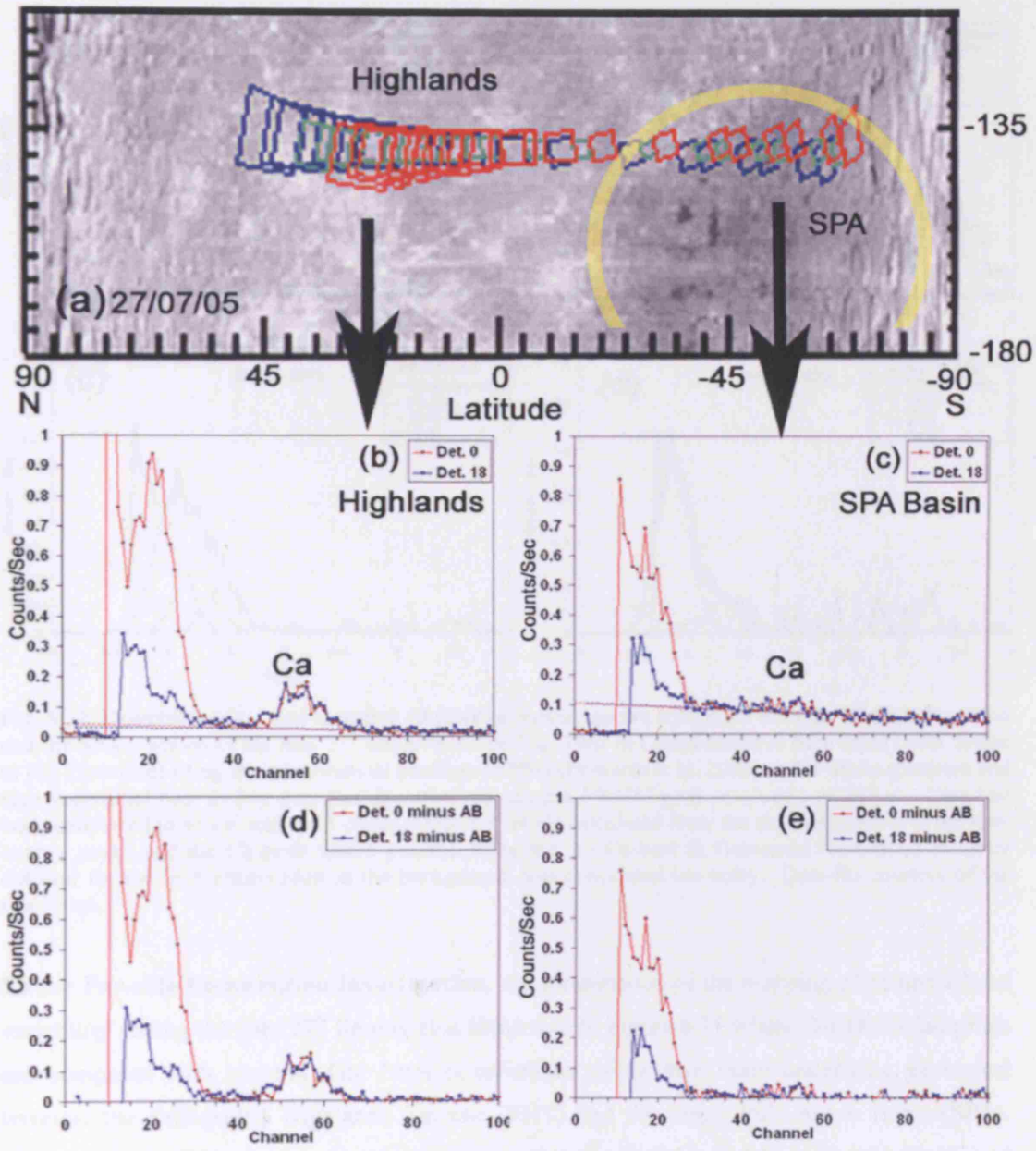

Fig. 6.31. (a) Ground-tracks for all three facets during the main observation period during the 27th July 2005 flare event. (b) Summed count rates for Det. 0 (Al-filter) and Det. 18 (Mg-filter) during the first portion of the flare as SMART-1 was over-flying the far-side Highlands. Dashed lines represent best-fit flat assumed background noise. (c) Summed count rates for Det. 0 and Det. 18 during the second portion of the flare as SMART-1 was over-flying the far-side SPA Basin Integration periods that were excessively noisy or contained no data have been removed from all count-summing. Dashed lines represent best fit flat assumed background noise. (d) Same plot as (b) for the Highlands minus an assumed background (AB). (e) Same plot as (c) for the SPA minus an assumed background (AB).

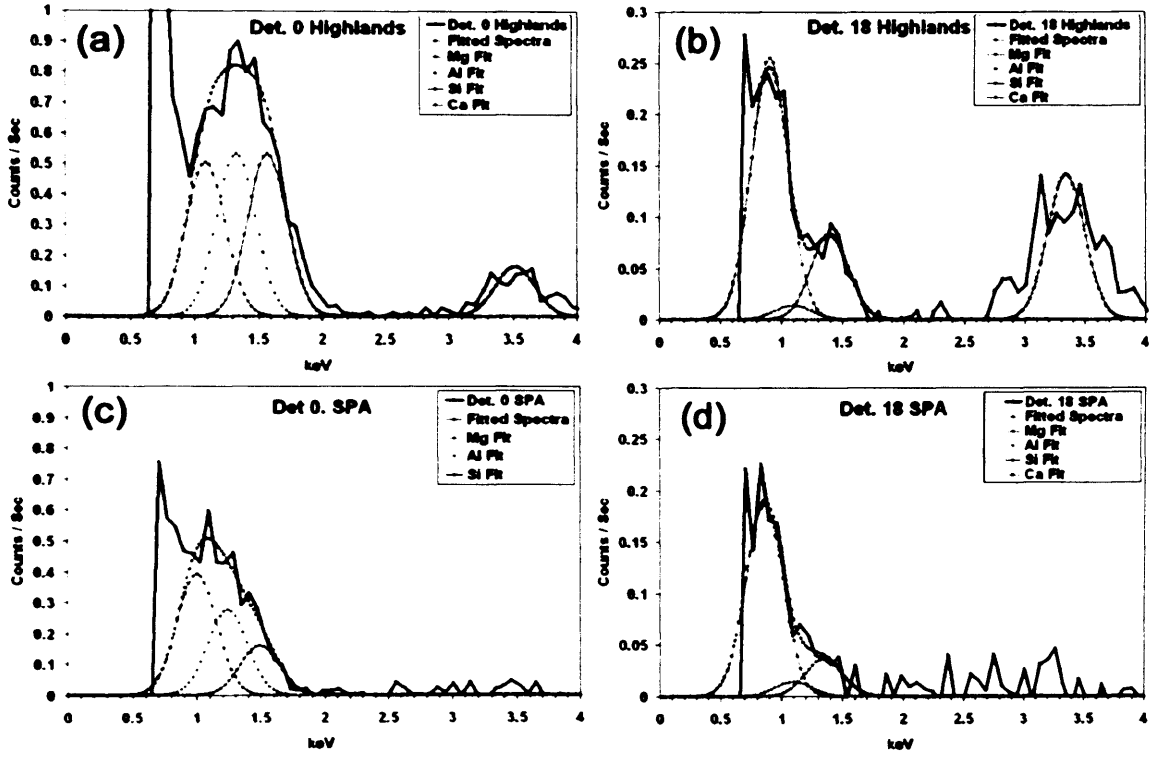

Fig. 6.32. Detector 0 (a)(c) and Detector 18 (b)(d) summed spectra (counts/s) from the Highlands portion and the SPA portions of the July 27th observation period. Best fit Gaussians have been fitted (with thanks to Ian Crawford) using the astronomical package DIPSO (Howarth et al. 2003) to the whole spectrum and then individual best fit line energies deconvolved using a FWHM peak resolution of 360 eV. Data had been converted to an eV scale of 1 channel space = 64 eV calculated from the channel spacing of the low-energy peaks and the Ca-peak where present. Note that no Ca-best fit Gaussians were fitted in either detector for the SPA observation as the background was considered too noisy. Data-fits courtesy of Ian Crawford.

Lunar Far-side Composition Investigation. An examination of the mapping of compositional variability during the July 27th flare is also illustrated in Figure 6.31 where D-CIXS's footprints are compared with spectral data from observations of the two main underlying geological terrains: the Feldspathic Highlands Terrane (FHT) and the South Pole-Aitkin Basin (SPA). Summed X-ray flux spectra are compared from Det. 0 (Al-filter) and Det. 18 (Mg-filter) and exclude any data from integration periods that have large noise peak interferences swamping the lower energy line signal. There is an apparent difference in background count-rate between the two observation periods (indicted by the straight line assumed background in Fig. 6.31b,c) as noise rate increased in the latter part of the flare observation (possibly caused by a decrease in solar photons as the flare began to die off, coupled with the arrival of secondary electrons). A sloping background was extrapolated from higher energy channels and then this background was removed from the four spectra (Fig. 6.31d,e). The data were then converted to an eV scale (see Fig. 6.32 text), and best fit Gaussian profiles were calculated (using the DIPSO routine: Howarth et al. 2003) in order to deconvolve individual line-energy count-rates (Fig. 6.32). These results are listed in Table 6.3 and are interpreted below.

	Line fluxes HIGHLANDS			Line fluxes SPA BASIN			% difference between Highlands and SPA
$Mg_{(Det\ 0)}$	0.194	±	0.011	0.151	±	0.013	22.16
$Al_{(Det\ 0)}$	0.204	±	0.010	0.106	±	0.008	48.04
$Si_{(Det\ 0)}$	0.204	±	0.013	0.062	±	0.012	69.61
$Ca_{(Det\ 0)}$	0.063	±	0.006	n.d.			
$Mg_{(Det\ 18)}$	0.098	±	0.006	0.071	±	0.007	27.55
$Al_{(Det\ 18)}$	-0.004*	±	0.008	0.005	±	0.003	
$Si_{(Det\ 18)}$	0.032	±	0.006	0.014	±	0.006	56.25
$Ca_{(Det\ 18)}$	0.054	±	0.005	n.d.			
RATIO $Mg_{Det\ 0}$ / $Ca_{Det\ 0}$	3.079	±	0.341				
RATIO $Mg_{Det\ 0}$ / $Si_{Det\ 0}$	0.951	±	0.081	2.435	±	0.516	
RATIO $Al_{Det\ 0}$ / $Si_{Det\ 0}$	1.000	±	0.080	1.710	±	0.355	
RATIO Mg+Al+Si / $Mg_{Det\ 0}$	3.103	±	0.146	2.113	±	0.135	
RATIO Mg+Al+Si / $Ca_{Det\ 0}$	9.556	±	0.963				

Table. 6.3. X-ray flux in counts.keV/s for the Gaussian fitted line energies depicted in Figure 6.32 Total line fluxes are determined from the areas of Gaussian fits. Errors on individual line fluxes are calculated depending on the background noise and the best-fit least squares parameters. Ratios errors are propagated through. n.d. = no line detected; *Al data for the Det.18 Highland summed dataset is reported as a negative value according to the Gaussian best-fit function and it should therefore be considered to represent no line detected.

Low-Energy Element Flux. The intensity of Mg+Al+Si counts (the blended low energy lines) varies significantly between the two investigated tracks. Mg+Al+Si count rate is ~52% higher in the Feldspathic Highlands Terrane (FHT) than in the SPA suggesting that either (a) there is a geochemical discrepancy between the two areas; (b) the decrease in solar-flux has caused a reduction in surface X-ray fluorescence; (c) the change is caused by a change in solar-surface phase angle between the northern and southern lunar hemisphere; or (d) the change is caused by a combination of these effects.

The most marked drop in X-ray intensity appears to have occurred on the right hand side of the blended line feature, coinciding with counts associated with the Al (48% decrease in X-ray flux: Table 6.3), and Si peaks (70% decrease in X-ray flux: Table 6.3). I interpret this change to represent a decrease in Al-content and, by inference, anorthositic plagioclase, as D-CIXS moved from the FHT into the SPA Basin. Figure 6.33 illustrates that this is consistent with mapping by Lucey et al. (2006: pg. 185 and Plate 2.10) of a high abundance of plagioclase outcrops in the far-side lunar highlands, and a much lower abundance of plagioclase occurring in the regolith of the SPA Basin.

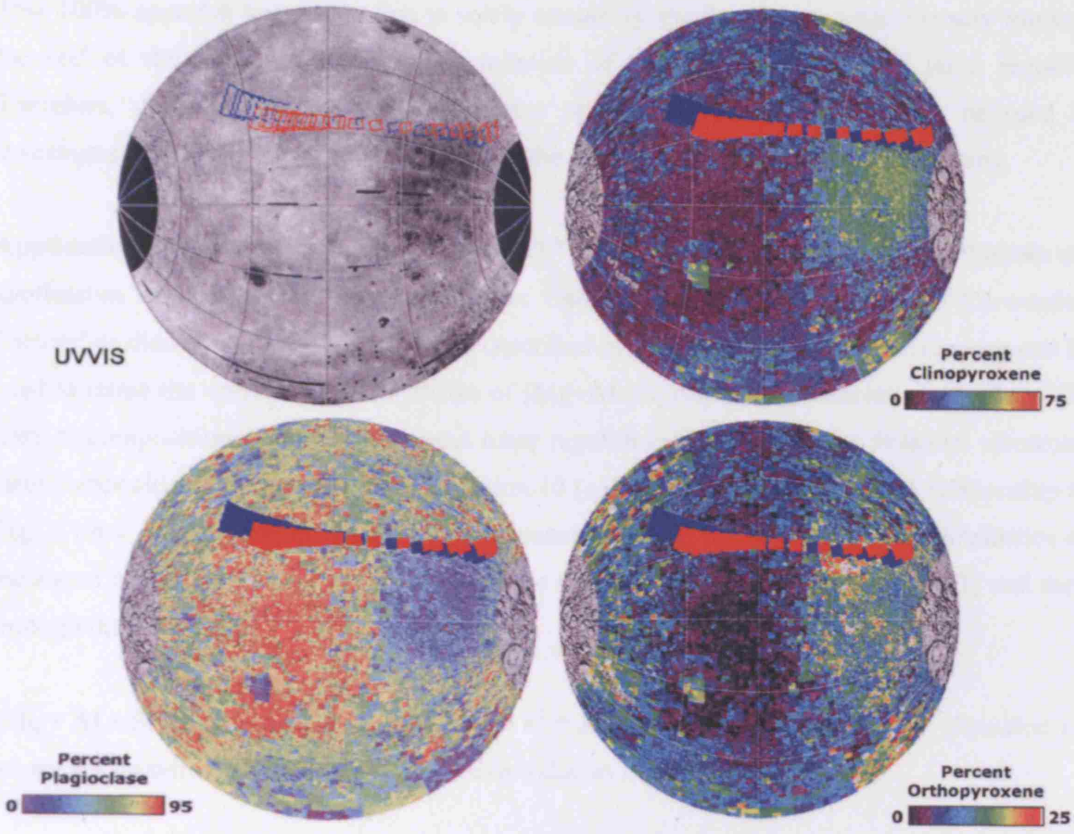

Fig. 6.33. D-CIXS ground-tracks for the 27th July flare observation compared with lunar far-side Clementine UVVIS albedo map and mineral distribution maps as published by Lucey et al. (2006). Note that the Moon has been rotated 90° anti-clockwise so that the North Pole now lies on the left, the South Pole on the right.

The intensity of Mg-flux also decreases between the two geological terranes by ~22-27% (Det. 0 and Det. 18 respectively: Table 6.3), probably as a result of the decrease in flare intensity which lowered the XRF flux rate from the lunar surface. However, the ratio of $Mg_{Det.0}/Si_{Det.0}$ does increase between the two terrains from 0.95 to 2.44, implying that despite the change in solar conditions there is actually a marked change in lithology from Mg/Si-poor regolith (i.e. plagioclase-rich) to regolith that is enriched in more Mg-rich (and Fe-rich?) compositions. This compositional variation is also consistent with the mapping by Lucey et al. (2006) of localised outcrops of orthopyroxene rich (norite) deposits that outcrop in the eastern rim of the SPA Basin (Fig. 6.33). (n.b. If D-CIXS had been observing the centre of the SPA basin, rather than the eastern-rim, this observation would also be consistent with clinopyroxene-rich regoliths that are associated with the outcropping of small gabbroic mare basalts pond deposits: Fig. 6.33).

Ca-Flux Variation. Ca-flux rate is observed to be significantly different between the two observation periods (fig. 6.32) as there is no statistically viable Gaussian fit to counts associated with a Ca-line in the second observation, while D-CIXS was flying over the SPA (Fig. 6.32b,d).

This 100% apparent loss of Ca-flux is solely caused by the decrease in solar intensity towards the end of the flare, preventing the excitation of heavier elements in the lunar regolith. Therefore, unfortunately for this flare event observation Ca-flux rate cannot be used to investigate the variability of Ca-abundance in the lunar regolith between the two terrains.

Application of Conversion Factors to July 27th Flare Data. Equations 11 and 12 illustrate the application of theoretically calculated 'Flux Intensity to Elemental Abundance Conversion Factors' as discussed in Section 6.2.3 and described by Equations 5-9. These conversions can be used to relate the variation in XRF fluxes of [Mg+Al+Si]/Mg during observations the July 27th flare to compositional information about lunar regolith in the two terrains. Potential elemental ratio compositions are derived using Equation 10 (calculated using the modelled relationship in Fig. 6.19b), where compositional ratios are generated from the [Mg+Al+Si]/Mg intensities as measured by Det. 0 in observations through the Feldspathic Highlands Terrane (FHT) and then through the SPA-Basin:

$$(Mg + Al + Si)/Mg_{Abundance} = -0.000463 * x^2 + 3.159179 * x - 1.755408 \quad \textit{Equation 10}$$

where x = modelled intensity ratio: i.e. x-axis value in Figure 6.19

$$HIGHLANDS\ Det.0\ (Mg + Al + Si)/Mg_{Intensity} = 3.103 \pm 0.146 = x$$

$$HIGHLANDS\ Det.0\ (Mg + Al + Si)/Mg_{Abundance} = -0.000463 * 3.103^2 + 3.159179 * 3.103 - 1.755408$$

$$= 8.053\ (\text{with a range of } 7.590 - 8.515) \quad \textit{Equation 11}$$

$$SPA\ BASIN\ Det.\ 0\ (Mg + Al + Si)/Mg_{Intensity} = 2.113 \pm 0.135 = x$$

$$SPA\ BASIN\ Det.\ 0\ (Mg + Al + Si)/Mg_{Abundance} = -0.000463 * 2.113^2 + 3.159179 * 2.113 - 1.755408$$

$$= 4.921\ (\text{with a range of } 4.493 - 5.349) \quad \textit{Equation 12}$$

These two theoretically calculated D-CIXS elemental abundance ratios of [Mg+Al+Si]/Mg measured in the far-side Highlands (FHT) and the SPA-Basin (SPA) are compared with the compositional range of the lunar sample, meteorite and average landing site soils in Figure 6.34. (n.b. X-axis Mg+Al+Si elemental wt. % cannot be modelled, and no conversion factors have been calculated, as line strength flux is very dependent on solar input intensity. For the 27th July flare event discussed here we do not currently have an accurate record of the concurrent solar spectrum, and so, the lunar XRF flux cannot be accurately be related back to a surface abundance.).

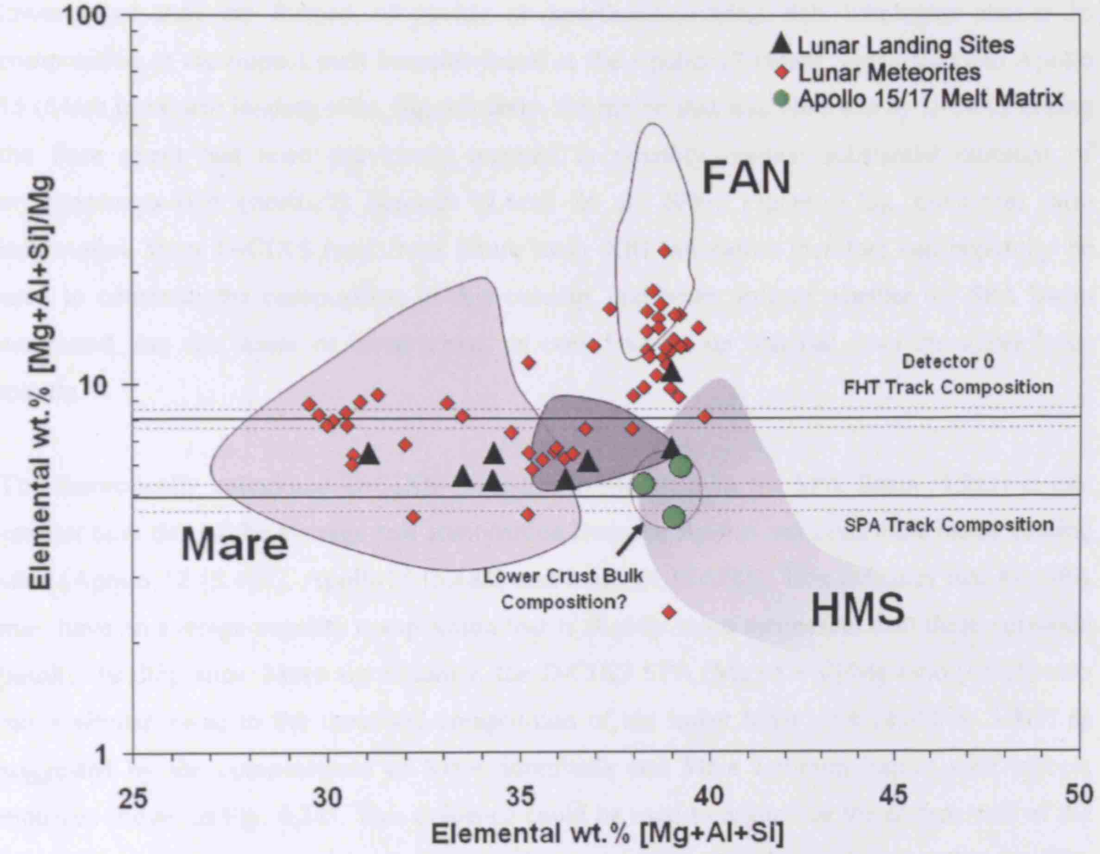

Fig. 6.34. Theoretically calculated lunar surface composition derived from of the [Mg+Al+Si]/Mg intensities measured by detector 0 during the 27th July Flare event through the Feldspathic Highlands Terrane (FHT) and the SPA-Basin. Minimum and maximum grey-dashed lines mark the error range propagated through from individual line flux energies. Major lunar lithologies are outlined and original data taken from references described in Fig. 6.21. Green circles show three average compositions of the matrix components of Apollo 17 (Mare Serenitatis) and Apollo 15 (Mare Imbrium) impact melt breccias. Ryder and Wood (1977) and Spudis and Davis (1986) advocate these to best represent the lower-crust composition on the lunar near-side. Our SPA [Mg+Al+Si]/Mg ratio is remarkably similar to these compositions.

The Feldspathic Highlands Terrane Composition. The theoretically calculated D-CIXS Det. 0 [Mg+Al+Si]/Mg ratio in the FHT (8.053) is lower (i.e. more magnesian) than the average soil composition from the Apollo 16 'Highlands' landing site (10.782). It is also Mg-poorer than any of the other average landing site soil compositions. By this interference, and assuming that the region is highly feldspathic rather than basaltic (e.g. as suggested by Clementine FeO map: Fig. 1.25), I conclude that the FHT may have an average XRF-flux measured [Mg+Al+Si]/Mg ratio (8.053) very similar to that of the feldspathic lunar meteorite ALH 85001 (8.091).

The South Pole-Aitkin Basin Composition. The impact that formed the SPA Basin is large enough that it may have excavated down into the lower crust (e.g. Wieczorek and Philips, 1999). It has been theorised by Ryder and Wood (1977) and Spudis and Davis (1985) that the

lower crust may be formed of noritic or anorthositic-noritic rich lithologies similar in composition to the impact melt breccias found at the Apollo 17 (Mare Serenitatis) and Apollo 15 (Mare Imbrium) landing sites. Significantly, the region that was observed by D-CIXS during the flare event has been previously mapped to possibly contain substantial outcrops of orthopyroxene-rich (noritic?) deposits (Lucey et al. 2006; Figure 6.33). Elemental ratio information from D-CIXS (and from future lunar XRF missions) therefore can hopefully be used to constrain the composition of this outcrop, and better inform whether the SPA Basin excavated into the upper or lower crust, or even brought up material from the upper lunar mantle.

The theoretically calculated D-CIXS [Mg+Al+Si]/Mg ratio in the SPA Basin (4.921) is just smaller than that of the average soil composition from the Apollo and Luna mare basalt landing sites (Apollo 12 [5.459], Apollo15 [5.488] and Luna 24 [5.628]). This indicates that the SPA may have an average regolith composition that is slightly more magnesian than these near-side basaltic landing sites. More significantly, the D-CIXS SPA [Mg+Al+Si]/Mg ratio (4.921) also has a similar value to the theorised composition of the lower lunar crust (4.320 to 5.917: as suggested by the compositions of Mare Serenitatis and Mare Imbrium impact melt breccia matrices shown in Fig. 6.34). This evidence could be used to argue that the eastern wall of the SPA indeed does expose magnesian, noritic lower crustal material, and therefore that the SPA does provides a stratigraphic view into the lunar crustal interior.

To fully qualify this interpretation, a much better understanding is needed of the line strength of the individual low-energy lines (i.e. recovering the surface Mg+Al+Si concentration, and thus the x-axis values in Fig 6.34). Therefore it is not yet possible to theorise whether this magnesian component originates from mixing of a noritic-regolith with a composition akin to that proposed for the lower-crust (higher Mg+Al+Si values) or if the instrument is recording a mixture of noritic deposits and clinopyroxene-rich mare basalt deposits (lower Mg+Al+Si values). (n.b. If D-CIXS had provided a resolvable Ca-peak for this flare it may have been possible to discriminate between clinopyroxene-rich (Ca-richer), and orthopyroxene-rich (Ca-poorer) SPA Basin outcrops.).

6.4 Future Work on the Interpretation of D-CIXS and C1XS Data

A great deal more work is required to fully exploit the D-CIXS XRF dataset and to understand the relationship between solar spectrum input and resultant observed lunar XRF fluxes. From working with the D-CIXS datasets I do not anticipate that the mapping of lunar absolute elemental abundances will ever be achieved because of a loss of elemental line resolution, double peaking spectral issues, interfering low-energy noise in many of the individual detectors, and the inoperability of the accompanying solar monitor during solar flare events. I do expect however that data from the flare events described in this thesis and from those studied by co-workers (Grande et al. 2007b) should be able to provide elemental ratio information from localised geological terrains or specific ground tracks. Some key scientific issues that still need to be addressed are outlined below:

- Identification of individual D-CIXS detectors that are operating well (i.e. have no noise peak interference) during flare periods. Data reduction and analysis can then focus on specific detector responses from these periods.
- A thorough development is needed of the Swinyard XRF prediction code in order to consider a range of likely solar input spectra (derived from spectra obtained by the X-ray Solar monitor instrument or the RHESSI or GOES satellites). A range of theoretically derived 'conversion factors' then need to be derived from varying solar conditions so that D-CIXS flux data can be converted to abundance ratios.
- A better understanding is needed of the influence of solar-surface scattering phase angle and particle size effects (e.g. Okada et al. 1998). It is hoped that some of these considerations will be addressed from the completion of a range of laboratory experiments (See Section 6.2.2). The results of these also need to be added to the Swinyard modelling code and 'conversion factors' derived for a range of known lunar phase angle observations.

After the issues relating to XRF modelling have been addressed, the Swinyard code needs to then be compared with other existing planetary XRF codes (i.e. designed for deconvolution of the NEAR and SELENE datasets) using a series of benchmark instrumental response and external factor tests. Thus, an international consensus can hopefully be reached in understanding the complexities of planetary X-ray fluorescence spectroscopic data deconvolution. This improved understanding will be vital for the success of future lunar and planetary XRF instruments such as those flying to the Moon on Selene and Chandrayaan-1 and those going Mercury aboard NASA's MESSENGER and ESA's Bepi-Columbo missions.

Appendix.6.1 Data summarised in relation to time from the flare event 14th January 2006. (a) Flare event 1. (b) Flare event 2. Output generated from B.J. Kellett's *D-CIXS_moon_sum_facet_new.pro* programme. Top panel illustrates abundance of counts in facet 1. Second panel down illustrates abundance of counts in facet 3. In both cases the upper red arrow indicates location of Ca-line enhancement (~channel 50), lower red arrow indicated location of low-energy elemental lines (~channel 10-25). The middle panel contains information about detector count rates. It also contains information about the flare strength (heavy red and blue line are taken from GOES solar activity monitor). The two lower panels illustrate the latitude and longitudinal ground-track location on the lunar surface (blue = facet 1 and red = facet 3) and the phase angle (lime green line) of the observation.

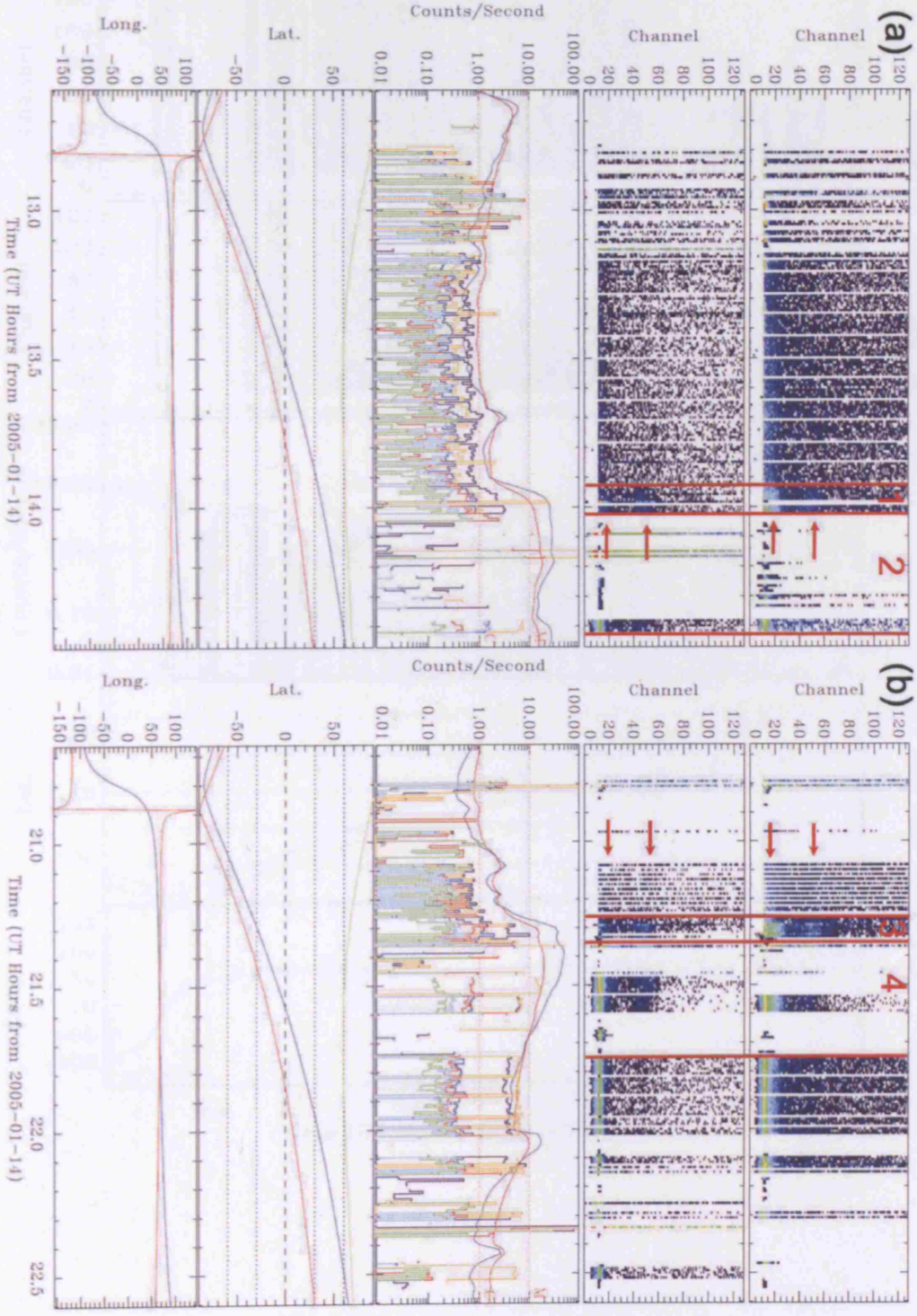

Appendix. 6.2. Data summarised in relation to time from the flare event 15th January 2006. Output generated from B.J. Kellett's *D-CIXS_moon_sum_facet_new.pro* programme. Top panel illustrates abundance of counts in facet 1. Second panel down illustrates abundance of counts in facet 3. The middle panel contains information about detector count rates. It also contains information about the flare strength (heavy red and blue lines are taken from GOES solar activity monitor). The two lower panels illustrate the latitude and longitudinal ground-track location on the lunar surface (blue = facet 1 and red = facet 3) and the phase angle (lime green line) of the observation.

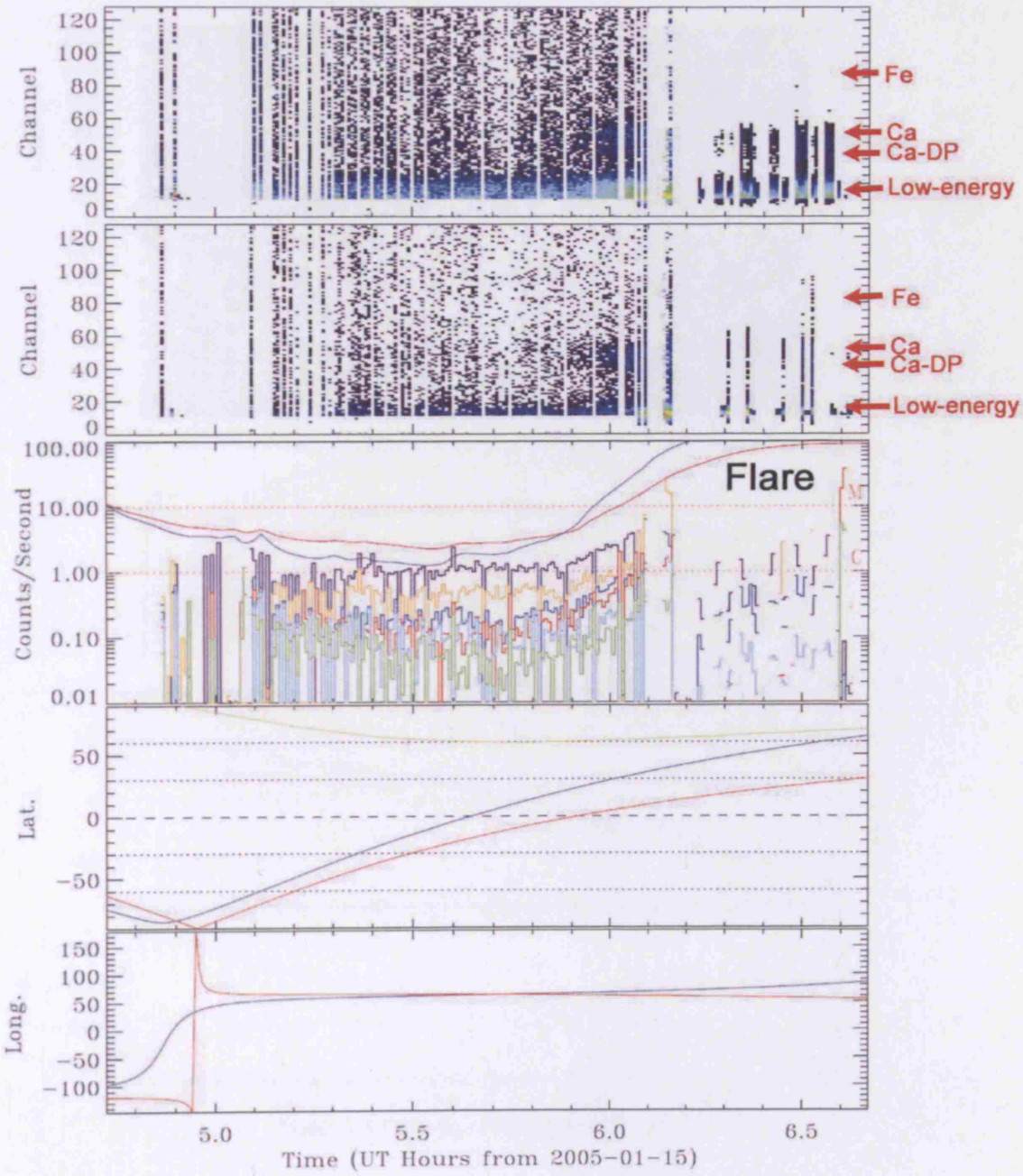

Appendix. 6.3. Data summarised in relation to time from the flare event 27th July 2006. Output generated from B.J. Kellett's *D-CIXS_moon_sum_facet_new.pro* programme. Top panel illustrates abundance of counts in facet 1. Second panel down illustrates abundance of counts in facet 3. Note no double peaking is occurring throughout the observation so only single line features observed. The middle panel contains information about detector count rates. It also contains information about the flare strength (heavy red and blue lines are taken from GOES solar activity monitor). The two lower panels illustrate the latitude and longitudinal ground-track location on the lunar surface (blue = facet 1 and red = facet 3) and the phase angle (lime green line) of the observation.

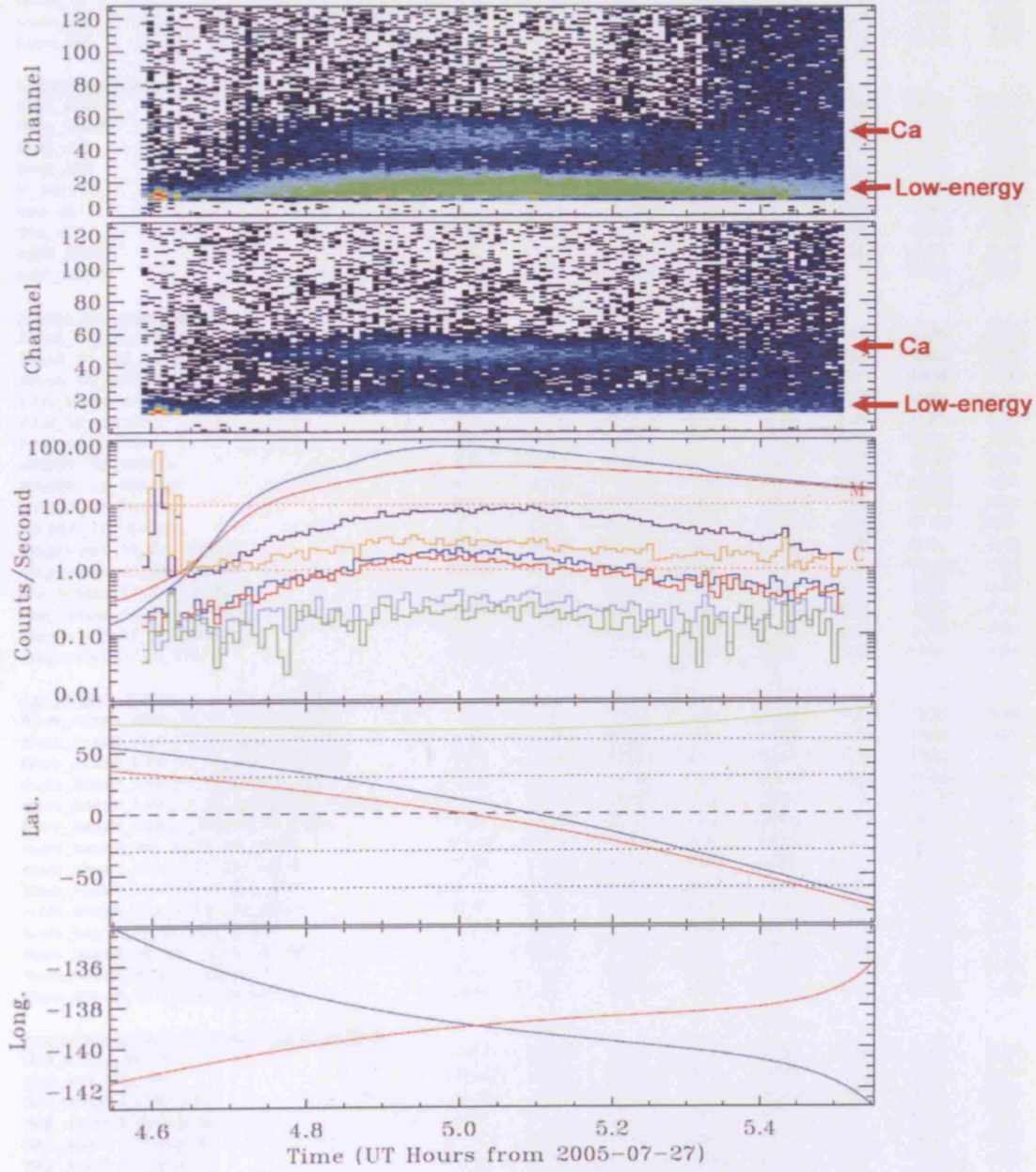

Appendix.6.4. List of element oxide wt.% for Apollo, Luna and lunar meteorite compositions used in X-ray Modelling.

	MgO	Al_2O_3	SiO_2	S	CaO	TiO_2	FeO	C
Apollo Bulk Soils								
Apoll11	7.93	12.58	41.99	0.00	11.74	7.94	16.40	0.00
Apoll12	10.42	12.13	46.21	0.00	9.85	2.61	17.19	0.00
Apoll15	10.95	14.32	47.19	0.00	10.47	1.46	14.98	0.00
Apoll16	6.00	27.23	44.89	0.00	14.56	0.53	4.98	0.00
Apoll17	9.95	18.93	44.47	0.00	12.29	2.84	10.29	0.00
Luna_16	8.78	15.68	44.37	0.00	11.50	3.30	16.75	0.00
Luna_20	9.69	22.75	45.20	0.00	14.70	0.50	7.46	0.00
Luna_24	9.87	11.95	45.40	0.00	11.07	1.04	19.55	0.00
Lunar Meteorites								
MET_01210	6.20	16.60	44.03	0.00	12.96	1.55	16.46	0.00
PCA_02007	6.80	25.71	43.41	0.00	15.19	0.28	6.31	0.00
DaG_400	4.84	27.76	41.42	0.00	17.27	0.17	3.61	0.00
DaG_262	5.21	27.50	44.24	0.00	16.45	0.22	4.40	0.00
Y_981031	8.12	19.65	45.90	0.00	13.32	0.56	11.36	0.00
Dhf_081	2.82	30.50	44.90	0.00	16.80	0.15	2.93	0.00
Dhf_025	7.10	26.90	45.10	0.00	16.20	0.29	4.90	0.00
QUE_93069	4.45	28.90	44.20	0.00	16.49	0.25	4.44	0.00
LAP_02005	5.58	10.13	44.53	0.00	11.23	3.43	21.69	0.00
Apollo Non-mare rocks								
Alkali_14_MG_14161	2.68	12.60	53.60	0.00	9.00	2.40	13.99	0.00
Alkali_14_MG_14161a	6.30	8.50	44.90	0.00	12.90	1.80	16.05	0.00
Alkali_15_QMD_15434	5.50	9.80	56.00	0.00	10.50	1.11	14.60	0.00
FAN_16_60015a	0.53	35.00	43.90	0.00	19.00	0.02	0.33	0.00
FAN_16_60015b	0.35	35.60	44.20	0.00	19.65	0.06	0.31	0.00
FAN_16_65315	0.25	34.90	44.30	0.00	19.10	0.01	0.31	0.00
KREEP_15_15386a	9.34	15.00	50.80	0.00	9.60	2.06	10.40	0.00
KREEP_15_15386b	8.17	14.77	50.83	0.00	9.71	2.23	10.55	0.00
KREEP_17_72275a	6.80	14.50	51.49	0.00	10.80	1.54	13.90	0.00
KREEP_17_72275b	9.30	13.30	48.14	0.00	11.10	1.48	15.50	0.00
Magnesian_16_GN_61224	12.77	13.20	50.70	0.00	11.60	0.40	9.91	0.00
Magnesian_16_GN_67667	26.40	7.56	42.40	0.00	5.32	1.03	17.10	0.00
Magnesian_17_TR_76335	10.28	27.58	43.40	0.00	14.97	0.07	2.97	0.00
Magnesian_17_TR_76535	19.10	20.70	42.90	0.00	11.40	0.05	4.99	0.00
Magnesian_17_N_77035	1.90	19.10	50.30	0.00	11.80	0.20	5.79	0.00
Magnesian_17_N_77075	12.90	14.97	51.10	0.00	8.82	0.34	10.67	0.00
Apollo Mare Rocks								
Mare_basalt_High_Ti_11_Highk_10049	7.03	9.50	41.00	0.00	11.00	11.30	18.70	0.00
Mare_basalt_High_Ti_11_Lowk_10003	6.70	10.40	39.80	0.00	11.10	10.50	19.80	0.00
Mare_basalt_Low_Ti_12_ilmenite_12051	7.00	10.00	45.30	0.00	11.40	4.70	20.20	0.00
mare_basalt_Low_Ti_12_olivine_12006	14.67	7.67	44.23	0.00	8.13	2.59	20.94	0.00
mare_basalt_Low_Ti_12_pidgeonite_12017	7.63	10.00	47.27	0.00	10.97	3.37	19.72	0.00
Mare_basalt_Low_ti_HighAl_14_14053	8.50	13.60	46.40	0.00	11.20	2.60	16.80	0.00
mare_basalt_low_ti_15_ON_15256	9.08	8.89	44.93	0.00	10.27	2.54	22.21	0.00
mare_basalt_low_ti_15_ON_15545	10.36	8.77	45.02	0.00	9.89	2.33	22.02	0.00
Mare_basalt_Low_Ti_15_Pig_15597	8.70	9.40	48.00	0.00	10.40	1.80	20.20	0.00
mare_basalt_low_ti_15_QN_15499	8.94	9.27	47.62	0.00	10.40	1.81	20.26	0.00
mare_basalt_lti_15_QN_15058	9.01	8.87	47.81	0.00	10.32	1.77	19.97	0.00
Mare_basalt_highAL_Luna_16_303	2.32	20.20	46.30	0.00	14.80	1.02	11.10	0.00
Mare_basalt_highAL_Luna_16_301	5.20	14.50	44.10	0.00	14.20	3.70	16.60	0.00
Mare_basalt_VLT_luna_24_24174	6.00	12.10	46.00	0.00	11.60	1.10	22.10	0.00
Apollo Impact Melt Breccia Group Averages								
IMB_A17_aphanitic	10.17	20.87	46.83	0.00	12.38	0.78	8.26	0.00
IMB_A17_ITE_rich	10.98	17.24	47.12	0.00	10.88	1.63	9.53	0.00
IMB_Apoll14_ITE_rich	10.10	16.60	48.80	0.00	9.90	1.70	10.30	0.00
IMB_Apoll15_Group_A	9.81	16.17	49.83	0.00	10.86	1.85	10.04	0.00
IMB_Apoll15_Group_B	13.75	15.77	48.50	0.00	10.18	1.21	9.27	0.00
IMB_Apoll15_Group_C	11.02	19.96	46.77	0.00	11.94	0.91	7.34	0.00
IMB_Apoll15_Group_D	15.80	16.40	44.60	0.00	10.20	1.45	10.00	0.00
IMB_Apoll16_Group_1M	13.35	17.10	46.70	0.00	10.65	1.37	9.72	0.00
IMB_Apoll16_Group_1F	9.90	19.25	47.00	0.00	11.85	1.20	8.00	0.00
IMB_Apoll16_Group_2DB	10.90	22.00	45.70	0.00	12.50	0.93	8.00	0.00
IMB_Apoll16_Group_2NR	11.10	21.20	45.30	0.00	12.90	1.00	7.70	0.00
IMB_Apoll17_Poikilitic	12.67	18.06	46.47	0.00	11.07	1.51	9.06	0.00
Apollo Fragmental Breccia Averages								
Fragmental_breccia_14063(ii)	10.70	21.60	45.00	0.00	12.60	1.64	6.90	0.00
Fragmental_breccia_67015(i)	5.10	29.00	44.80	0.00	15.70	0.51	4.26	0.00

Fragmental_breccia_67015(ii)	3.90	29.50	46.00	0.00	15.40	0.50	3.65	0.00
Fragmental_breccia_67016(i)	3.50	30.01	45.30	0.00	16.90	0.44	3.57	0.00
Fragmental_breccia_67016(ii)	4.40	28.20	44.80	0.00	16.70	0.35	3.94	0.00
Fragmental_breccia_67115	3.00	31.20	44.80	0.00	17.80	0.24	2.60	0.00
Fragmental_breccia_67455(i)	2.83	30.80	44.50	0.00	17.10	0.21	3.58	0.00
Fragmental_breccia_67455(ii)	3.40	30.60	45.20	0.00	18.10	0.20	4.37	0.00

Chapter 7: Summary

7.1 Introduction

This chapter summarises the discussions and conclusions from the previous chapters, and makes recommendations for future research opportunities.

7.2 Summary of Lunar Meteorite Research

In this thesis I have performed geochemical and petrological studies of the three lunar meteorites:

DaG 400 is a feldspathic regolith breccia. It is highly consolidated and contains lithic clasts and mineral fragments that are fused together in a glassy, fine grained matrix. The lithic clast portion includes rock fragments from the anorthositic-ferroan ferroan-anorthosite (AF-FAN) suite (Al_2O_3-rich, REE-poor), the mafic-magnesian-FAN suite (Mg-rich, REE-rich), and impact melt breccias. Trace element investigations of the impact melt breccia clasts suggest that the majority of clasts probably originated from a single impact event. They are texturally diverse as they have experienced different post-excavation cooling regimes.

DaG 400 has a bulk composition typical of many of the other feldspathic lunar meteorites and it is likely that the stone was launched from the far-side of the Moon, probably from somewhere in the Feldspathic Highlands Terrane. These feldspathic meteorites are therefore the best representation we have of the geochemistry of the most ancient lunar terrane, and our best insight into early lunar crustal evolution processes.

MET 01210 is a complex, immature, heterogeneous regolith breccia that is dominated by lithic and mineral fragments from a low-Ti mare basalt bedrock deposit. It contains an additional lithic component of feldspathic impact melt breccias and feldspathic rock fragments (granulites, meta-clastic rocks, norites, troctolite) that have originated from non-mare basalts lithologies. Impact melt breccia clasts have a trace element content suggestive of formation in a 'highlands' environment, rather than a mare basalt environment, suggesting that they may have been introduced to the regolith setting by lateral transport from surrounding FAN-rich terrains. Mare basalt rocklets within the breccia are texturally diverse and are likely to have come from a petrologically related low-Ti, ferroan lava flow (possibly from the same flow as sampled by

lunar meteorite Yamoto-793169). Monomineralic grains are large and are sampled from a slowly cooled, coarse grained basalt/gabbro deposit (possibly from the same flow as sampled by lunar meteorite MIL 05035/Asuka-881757). The four lunar meteorites Yamoto-793169, Asuka-881757, MIL 05035 and MET 01210 are considered to be paired stones that represent a stratigraphic sequence from regolith, into an underlying lava flow deposit. MET 01210 has been radiometrically dated to 3.95 Ga (Terada et al. 2007), representing one of the oldest samples of low-Ti sourced mare basalt in the lunar rock collection.

Regolith breccias like MET 01210 and DaG 400 are important as they can provide a remote sensing calibration 'ground-truth' for the composition of the upper regolith. In particular lunar feldspathic regolith breccia meteorites are useful for being able to calibrate remote sensing information from the lunar highlands on the far-side of the Moon.

The LAP paired stones (LAP 02205/02224/02226/02436/03632), are holocrystalline mare basalts. They have been radiometrically dated to being crystallised at 2.9-3.15 Ga (Nyquist et al. 2005; Rankenburg et al. 2005; Anand et al. 2006) and are some of the youngest mare basalts samples in the lunar rock collection. The stones are likely launch-paired with the hot desert meteorites NWA 032 / NWA 479.

These stones consist mainly of zoned pyroxene and plagioclase grains, with minor ilmenite, spinel and mesostasis regions. Large, possibly xenocrystic, forsteritic olivine grains contain small trapped multiphase melt inclusions. Accessory mineral and mesostasis composition shows that the samples have experienced residual melt crystallization with silica over-saturation and late stage liquid immiscibility.

The lunar basalt flow represented by the LAP meteorite is the product of fractional crystallization from a parental source melt, similar in composition to the low-Ti source region that produced the Apollo 12 and Apollo 15 low-Ti basalts and low-Ti volcanic glasses. However, the stones cannot be directly classed with any site-specific mare basalt group as they are REE-rich, have systematically different major element compositions, and lower Mg# numbers than characterized Apollo and Luna basalt samples. Therefore the LAP stones appear to represent part of a previously unsampled, young, low-Al, low-Ti mare basalt suite that crystallized from a relatively evolved lunar melt.

It is most probable that LAP was launched from the Moon's near-side, and it is possible that the stones were ejected from a lava flow within the PKT region, which is known to be an area of relatively young basaltic emplacement

7.2.1 Future Lunar Meteorite Studies

My future lunar meteorite research will be focused around a group of hot and cold desert feldspathic regolith breccias that have been provided by the Meteorite Working Group and by research colleagues. Some of this material is shown in Figure 7.1 and includes the Antarctic feldspathic lunar meteorites PCA 02007 and MAC 88105 / 88104, and the hot desert lunar meteorites Dhofar 1428, NEA 001, NWA 2200, NWA 2995, NWA 2998, NWA 3163, NWA 482 and Dhofar 908.

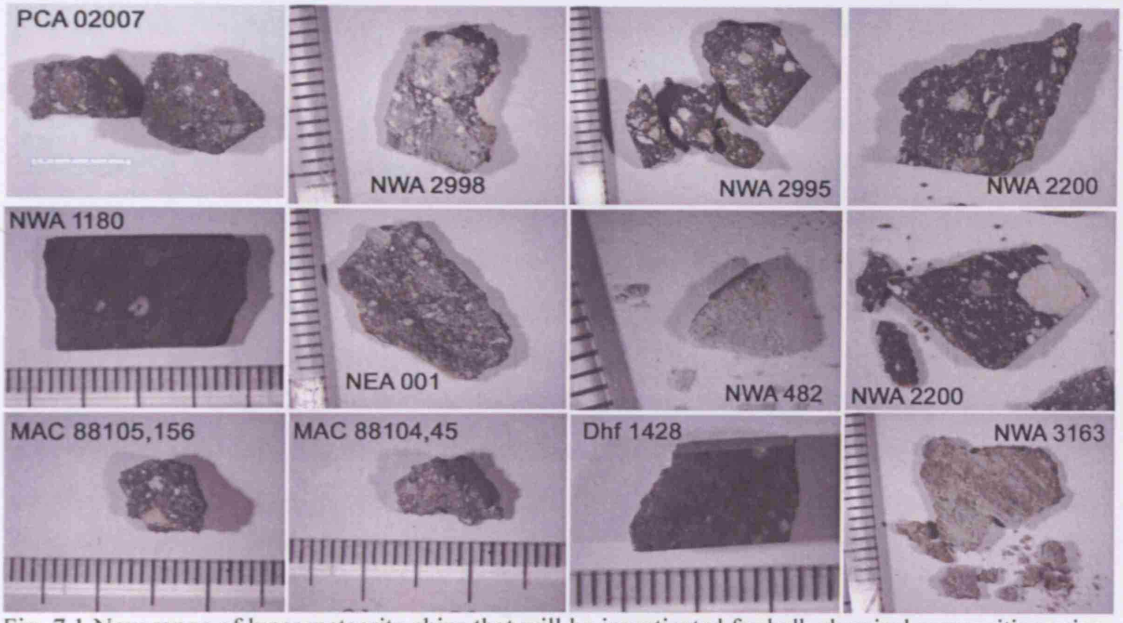

Fig. 7.1 New range of lunar meteorite chips that will be investigated for bulk chemical composition using ICP-AES / ICP-MS and/or for petrographic analysis. Ruler tick marks where shown = 1 mm.

These meteorites will be petrographically examined for the purpose of investigating the geological heterogeneity of the lunar highlands. I will assess the variability of lithic clast and mineral chemistry and discuss the effects of modification by impact related metamorphism. In situ mineral and bulk clast LA-ICP-MS studies will be conducted and a detailed survey made of minor and trace element concentration in impact melt clast material. It is hoped that through new collaborations with the University of Manchester I will partake in Ar-Ar radiometric dating of impact melt material to provide a link between the timing of impact events on the Moon and the geochemistry of target bedrock that was being melted to produce large melt deposits.

It is hoped that these investigations will provide a better understanding of models of early lunar crustal formation and magma ocean heterogeneity. I also hope to understand the role of ancient

impact processes and ask whether new radiometric dating of feldspathic impact melt material provides a new constraint on whether there was a late heavy bombardment event at ~3.85 Ga.

7.3 Summary of D-CIXS Research

D-CIXS was a technology demonstrator of a planetary X-ray spectrometer that flew on ESA's SMART-1 mission to the Moon. The 18 month cruise stage slowly spiralled SMART-1 through the Earth's radiation belts, causing damage to D-CIXS's Swept Charge Device (SCD) detector arrays. This damage resulted in the degradation of energy resolution, causing X-ray counts recorded in the low-energy Mg, Al and Si lines to become blended into single feature.

Planetary X-ray fluorescence spectroscopy is a very complicated process and requires a thorough understanding of the observational conditions: i.e. a careful record of the incoming solar spectrum and galactic backgrounds, a record of the observation phase angle, instrumental efficiency and individual detector calibration. I have used an XRF modelling code to investigate the modelled response from a range of typical lunar rock, meteorite and soil composition inputs from given physical and observational parameters. This work has developed a theoretical method of recovering lunar surface compositions from their recorded X-ray flux: i.e. calculating a library of 'conversion factors' from modelled / real lunar flux back to the original input / observed elemental composition. This modelling work is still in its preliminary stages and needs to be completed for a wide range of possible phase angle and solar input variations.

D-CIXS recorded more than 18 months of lunar XRF observations. The best data achieved in this time are those taken during solar flare events, when high solar photon intensity caused large amounts of secondary generated X-rays to be produced from the lunar surface. Three of the observations made during these flare events have been discussed in this thesis, focusing in particular on the flare event that occurred on the 27th July 2005 whilst SMART-1 was orbiting over the far-side feldspathic highlands and the eastern rim of the South Pole-Aitkin Basin (Fig. 6.33).

Preliminary analysis of this flare event suggests that there is a marked change in X-ray flux between the two lithological terrains (Fig. 6.31). Whilst some of this effect is probably caused by the evolution of the solar flare event (i.e. the reduction of solar photon flux caused less excitation of characteristic Ca-lines), elemental line ratios between the low-energy lines (Mg, Al and Si) do differ between the terrains suggesting a change in observed compositional conditions. Analysis of these XRF fluxes shows that summed spectra from the Feldspathic Highlands

Terrane are notably enriched in an Al-line feature compared to the SPA Basin. This is consistent with the highlands being formed of abundant Al-rich plagioclase deposits (Fig. 6.33). Gaussian fit profiling of summed spectra has made a first order attempt to deconvolve the low-energy blended line feature into three individual line energies (Fig. 6.32, Table 6.3). These fits indicate that the ratio of Mg/Si increased and [Mg+Al+Si]/Mg decreased (Fig. 6.34) as ground-tracks moved from the highlands into the SPA basin, corresponding to an underlying change in composition from an Mg-poor regolith (e.g. feldspathic) to a moderately Mg-rich regolith (e.g. mafic element rich). During this observation D-CIXS was orbiting over the eastern rim of the SPA (Fig. 6.33) that is thought on the basis of Clementine observations (Lucey et al. 2006) to contain noritic-rich regolith (possibly indicative of excavated lower-crustal deposits) rather than the gabbroic-rich regolith associated with the central SPA basin (associated with small outcrops of mare basalts ponds). It is therefore possible that the compositional variation recorded by D-CIXS's XRF flux is directly related to the compositional variation between the upper crustal anorthositic highlands, and the underlying noritic lower crust (as exposed in the wall of SPA). This SPA noritic-rich outcrop is shown by this study to have [Mg+Al+Si]/ratios similar to those of the Apollo 15 and Apollo 17 impact melt breccias that have been proposed to represent the composition of the near-side lunar lower crust.

7.3.1 Future D-CIXS / C1XS Data Analysis

XRF Theoretical Modelling Research. An in-depth exercise needs to be completed into simulating a wide-range of lunar XRF spectra, and calculating a look-up table of appropriate 'conversion factors' to allow the interpretation of lunar XRF datasets. Initial investigations must focus on attempting to quantify the effects of a range of solar spectra inputs, with a range of known energy scales (from A-class to X-class) and with variable spectral elemental line features (similar to the range observed by SMART-1's XSM and by RHESSI). Other variables that need to be explored include varying viewing geometry to understand effects of large phase angles, and the effects of viewing the lunar surface close to the terminator.

D-CIXS Data Analysis. A continued assessment of D-CIXS data will be made to see whether there are any other significant flare events that provide interesting, and interpretable, data from the lunar surface. Further deconvolution work will be carried out on existing flare observations so that in the future we can report geochemical variation studies for localised regions of the Moon.

Chandrayaan-1 X-ray Spectrometer. All of this work will help to lay the groundwork for understanding and interpreting data from the new C1XS instrument, which will fly to the Moon in 2008 aboard the Indian Chandrayaan-1 mission. It is anticipated that C1XS will conduct science operations during a more favourable part of the solar cycle so that statistically valuable data will be collected from a large potion of the lunar surface and provide new maps into global and localised composition variability.

7.4 Future Lunar Exploration

It is an exciting time to be involved with lunar research. NASA's plan to return human beings to the Moon by c. 2018 (Fig. 7.2g,h,i) has motivated the international community to compete for a stake in this exploration adventure. New space-faring nations such as China, Japan and India are all reaching for the Moon through a range of satellite obiter (Fig. 7.2a: Change-1, Fig. 7.2b: Selene and Fig. 7.2c: Chandrayaan-1) and lander (Change-2, Selene-2, Chandrayaan-2) missions that are due to launch in the next 5 years. NASA is planning on launching its own series of new lunar probes including the eagerly anticipated Lunar Reconnaissance Orbiter (LRO: Fig 7.2d) which is due to launch in 2008. This satellite will carry with it a suite of instrumentation designed to complete global lunar photographic and topographic mapping, and to take extremely high resolution (~25 cm/pixel) images of potential new landing sites. The European community is currently still defining its future lunar exploration programme, and UK lunar robotic hopes are currently riding on two recently proposed missions: the MoonLITE orbiter / penetrometer mission (Fig. 7.2f), and the MoonRaker lander (Fig. 7.2e) planned to contain a geochemical and seismology package.

As well as being scientifically interesting endeavours, these missions are promoting the international collaboration and technology innovation that will be necessary for the successful return of astronauts to the lunar surface. Moreover, a human presence will in return provide a new variety of scientific opportunities that will hopefully contribute to a better understanding of the structure, formation and geological history of the Moon, and a better understanding of the history of the whole of the inner solar system. For example, the distribution of new surface science experiments such as heat-flow and seismic packages will help to constrain models of the lunar interior, helping to refine our understanding of the Moon's structure and physical evolution. Sample return from new regions of the lunar surface will help us to understand the global distribution of lunar lithological groups and will shed new light on lunar geological history. Samples from ancient lunar basins and young impact craters will accurately date the cratering history of the inner solar system from the last 4.5 billion years, helping us to

understand the probability of future impacts hazards happening on Earth. Samples from the South-Pole Aitkin basin may well provide a new view into the composition of the lower crust, giving lunar scientists a real sense of the Moon's stratigraphy and differentiation history.

The future possibilities for scientific discovery are endless and I hope that I will be involved in the new adventure of better understanding the geological history of the Moon.

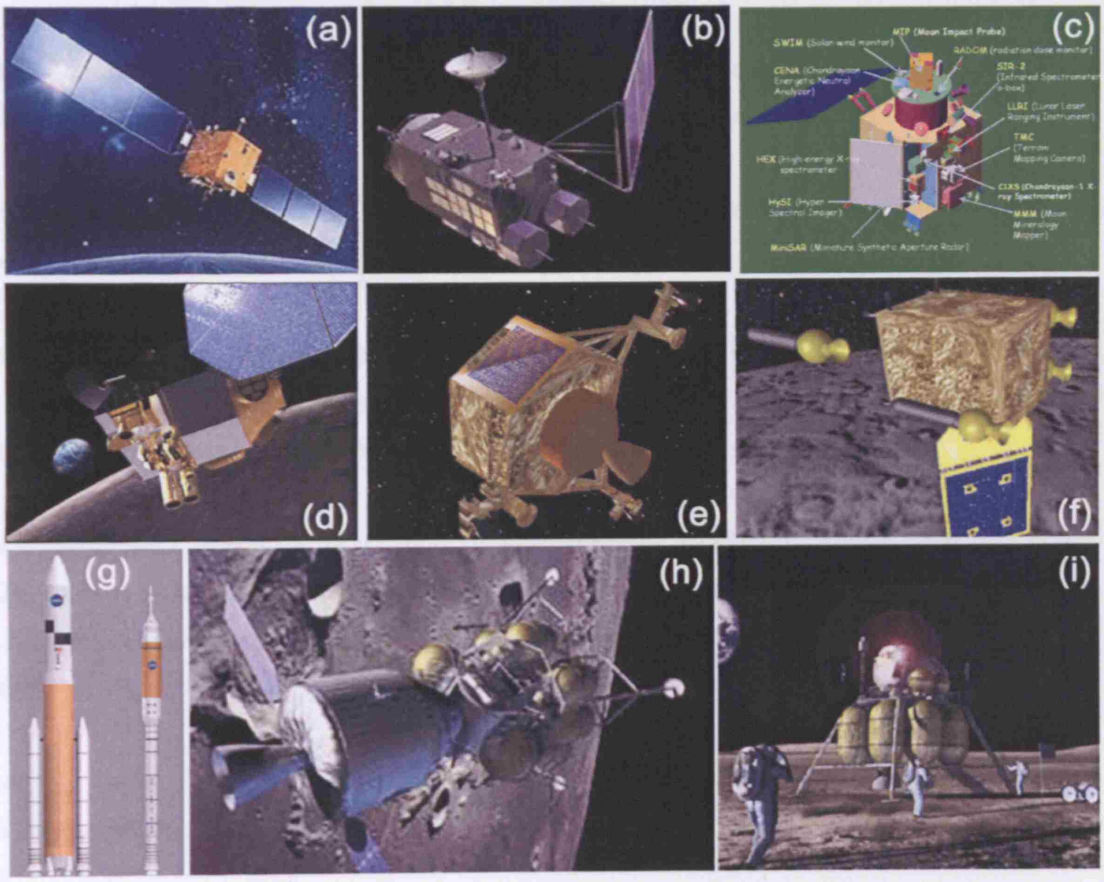

Fig. 7.2. Upcoming missions to the Moon. (a) The Chinese Change-1 satellite due to launch in 2007 (b) The Japanese Selene satellite also due to launch in 2007. (c) Design plan for the Chandrayaan-1 Indian mission, due to launch in 2008. (d) LRO, also due to be launched in 2008. (e) Artists impression (credit SSTL) of the UK-proposed MoonRaker lander and (f) MoonLITE mission. (g) Artist impressions of the new NASA ARES launch vehicles, (h) lunar transfer capsule and (i) lunar lander vehicle. (Website 1.10).

References

Adler I., Trombka J. et al. 1971. X-ray Fluorescence Experiment. In *Apollo 15 Preliminary Science Report*, NASA SP-289. Chap 17.

Adler I., Trombka et al. 1972a. Apollo 15 Geochemical X-ray Fluorescence Experiment: Preliminary Report. *Science*. Vol. 175. pp. 436-440.

Adler I., Gerard J. 1972b. The Apollo 15 X-ray fluorescence experiment. Proceedings of third Lunar Science Conferenc. *Supplement 3, Geochimica et Cosmochimica Acta*, 3. pp.2157-2178.

Adler I., Trombka et al. 1972c. Apollo 16 Geochemical X-ray Fluorescence Experiment: Preliminary Report. *Science*, 177. pp. 256-259.

Adler I., Trombka J.I.., Schmadebeck R., Blodget H., Eller E., Yin L., Lamothe R., Osswakd G., Gorenstein P., Bjorkhom P., Gursky H., Harris B., Arnold J., Metzer A., Reedy. R. 1972d. Apollo 15 and 16 Results of the integrated Geochemical Experiment. *Moon*, 7. pp. 487-503.

Adler I., Trombka J., Gerard J., Lowman P., Schmadebeck R., Blodget H., Eller E., Yin L., Lamothe R., Osswakd G., Gorenstein P., Bjorkhom P., Gursky H., Harris B., Golub L., Harden F.R. Jn. 1972e. X-ray Fluorescence Experiment. *In Apollo 16 Preliminary Science Report, NASA SP-315*, Chap 19.

Anand M., Taylor L. A., Neal C. R., Snyder G. A., Patchen A., Sano Y., and Terada K. 2003a. Petrogenesis of lunar meteorite EET 96008, *Geochimica et Cosmochimica Acta*. Vol. 67. pp. 3499 – 3518.

Anand M., Taylor L.A/. Misra K.C. Deminova S.I., and Nazarovi M.A. 2003b. KREEPy lunar meteorite Dhofar 287a: A new lunar mare basalt. *Meteorit. Planet. Sci.* Vol. 38. pp. 485-499.

Anand M., Taylor L. A. , Nazarov M.A., Shu J., Mao H.-K., and Hemley R. J. 2004. Space weathering on airless planetary bodies: Clues from the lunar mineral hapkeite. *PNAS* 101. pp. 6847-6851

Anand M., Taylor L. A., Floss C., Neal C., Terada K., and Tanikawa S. 2006. Petrology and geochemistry of LaPaz Icefield 02205: A new unique low-Ti mare-basalt meteorite. *Geochimica et Cosmochimica Acta*, Vol. 70. Issue 1. pp. 246 - 264.

Anders E. and Grevesse N. 1989. Abundances of the elements: Meteoritic and solar. *Geochimica et Cosmochimica Acta.* Vol. 53. pp. 97 – 214.

Andre C.G., Bielefield M.J., Eliason E., Adler I., Philpotts J.A. 1977. Lunar Surface Chemistry: A New Imaging Technique. *Science* 197. pp. 986 – 989.

Arai T., Takeda H. and Warren P.H. 1996. Four lunar mare meteorites: crystallization trends of pyroxenes and spinels. *Meteorit. Planet. Sci.* Vol. 33. pp. 877 - 892.

Arai T. and Warren P. H. (1999) Lunar meteorite Queen Alexandra Range 94281: Glass compositions and other evidence for launch pairing with Yamato 793274, *Meteorit. Planet. Sci.* Vol 34. pp. 209 - 234.

Arai T., Ishi T. and Otsuki M. 2002 Mineralogical study of new lunar meteorite Yamato 981031 (abstract). In *33rd Lunar Planet. Sci. Conf.*, abstract no. #2064, Lunar and Planetary Institute, Houston.

Arai T., Misawa K. and Kojima H. (2005) A new lunar meteorite MET 01210: Mare breccia with a low-Ti ferrobasalt (abstract). In *Lunar and Planetary Science XXXVI*, abstract no. 2361, Lunar and Planetary Institute, Houston.

Aramovich C.J., Head C.D.K, and Papike J.J. 2001. Possible causes for late-stage reaction textures associated with pyroxferroite and metastable pyroxenes in the basaltic Martian meteorites. *32nd Lunar Planet. Sci. Conf.*, abstract no. #1003. Lunar and Planetary Institute, Houston.

Asimow P.D., Ghiorso M.S. 1998. Algorithmic Modifications Extending MELTS to Calculate Subsolidus Phase Relations. *American Mineralogist* Vol. 83. pp.1127 - 1131

Basaltic Volcanism Study Project.1981. Basaltic Volcanism on the Terrestrial Planets. Pergamon Press, Inc., New York. Chapter 1.2.9 Lunar Mare Basalts. pp. 236 - 266.

Beatty, D.W., Hill, S.M.R., Albee, A.L., Ma, M.-S., Schmitt, R.A. 1979. The petrology and chemistry of basaltic fragments from the Apollo 11 soil, part I. *Proc. 10th Lunar Planet. Sci. Conf.* pp. 41 - 75.

Basilevsky, A. T.; Keller, H. U.; Nathues, A.; Mall, U.; Hiesinger, H.; Rosiek, M. 2004. Scientific objectives and selection of targets for the SMART-1 Infrared Spectrometer (SIR). *Planetary and Space Science*, Vol. 52, Issue 14. pp. 1261 - 1285.

Bischoff A., Weber D., Clayton R. N., Faestermann T., Franchi I. A., Herpers U., Knie K., Korschinek G., Kubik P. W., Mayeda T. K., Merchel S., Michel R., Neumann S., Palme H., Pillinger C. T., Schultz L., Sexton A. S., Spettel B., Verchovsky A. B., Weber H. W., Weckwerth G., and Wolf D. 1998. Petrology, chemistry, and isotopic compositions of the lunar highland regolith breccia Dar al Gani 262, *Meteorit. Planet. Sci.* Vol. 33. pp. 1243 - 1257.

Blewett D.T.; Lucey P.G.; Hawke B.R. and Jolliff B.L. 1997. Clementine images of the lunar sample return stations: Refinement of FeO and TiO2 mapping techniques. *J. Geophy. Res.* 102 (E7). pp. 16319 - 16325.

Borg, L. E; Shearer, C. K; Asmerom, Y.; Papike, J. J. 2004. Prolonged KREEP magmatism on the Moon indicated by the youngest dated lunar igneous rock. *Nature.* Vol. 432. no. 7014. pp. 209 - 211.

Bugiolacchi, R.; Spudis, P. D.; Guest, J. E. 2006. Stratigraphy and composition of lava flows in Mare Nubium and Mare Cognitum *Meteorit. Planet. Sci.* Vol. 41. Issue 2. pp.285 - 304

Bukovanska M., Dobosi G., Brandstätter F., and Kurat G. (1999) Dar al Gani 400: Petrology and geochemistry of some major lithologies. *Meteorit. Planet. Sci.* Vol. 34. A21.

Cahill J. T., Floss C., Anand M., Taylor L. A., Nazarov M. A., and Cohen B. A. 2004. Petrogenesis of lunar highlands meteorites: Dhofar 025, Dhofar 081; Dar al Gani 262, and Dar al Gani 400. *Meteorit. Planet. Sci.* Vol. 39. pp. 503 – 530.

Cahill, J. T.; Lucey, P. G.; Steutel, D.; Gillis, J. J. 2005, Analysis of the Lunar Surface with Global Mineral and Mg-Number *Meteorit. Planet. Sci. . 36th Lunar Planet. Sci. Conf.*. Abstract no.2186

Canup R.C. and Agnor C.B. 2000. Accretion of the Terrestrial Planets and the Earth-Moon System. R.C. Canup and K. Righter, editors (2000). *Origin of the Earth and Moon.* University of Arizona Press, Tuscon. pp. 113

Clark P.E. and Ray Hawke B. 1991. The Lunar Farside: the nature of the highlands east of mare Smythii. *Earth, Moon and Planets.* Vol. 53. pp. 93-107.

Clark P.E. and Trombka J.I 1997. Remote X-ray Spectrometry for NEAR and future missions: Modeling and Analyzing X-ray production from source to target. *Journal of Geophysical Research.* Vol. 102. No. E7. pp. 16631-16384.

Cohen B.A., Kring D.A. Swindlw T.D. 1999. Impact melt clasts in lunar meteorites Dar al Gani 262 and Dar al Gani 400 (abstract) *Meteoritics Society Meeting 62*, #5220.

Cohen B.A., James O.B., Taylor L.A., Nazarove M.A. Barsukova L.D. 2004. Lunar highland meteorite Dhofar 026 and Apollo sample 15418: Two Strongly shocked, partially melted, granulitic breccias. *Meteorit. Planet. Sci.* . Vol. 39. No. 9. pp. 1419.

Cohen, B.A., T.D. Swindle, and D.A. Kring. 2005. Geochemistry and ^{40}Ar-^{39}Ar geochronology of lunar highland meteorite impact melt clasts. *Meteorit. Planet. Sci.* 40. pp.755-777.

Consolmagno G. J., Russell S. S., and Jeffries T. E. (2004) An in–situ study of REE abundances in three anorthositic impact melt lunar highland meteorites (abstract). *Lunar Planet. Sci. Conf XXXV*, abstract no. 1370, Lunar and Planetary Institute, Houston.

Crozaz G., Floss C., Wadhwa M. 2003. Chemical Alteration and REE mobilization in meteorites from hot and cold deserts. *Geochim. Cosmchim. Acta.* Vol. 67. pp. 4727-4741.

Cushing, Janet A.; Taylor, G. Jeffrey; Norman, Marc D.; Keil, Klaus 1999. The granulitic impactite suite: Impact melts and metamorphic breccias of the early lunar crust. *Meteorit. Planet. Sci.* Vol. 34. no. 2. pp. 185-195

Day J. M. D., Pearson D. G., Taylor L. A. (2005). ^{187}Re-^{187}Os isotope disturbance in La Paz mare basalt meteorites (abstract). In *Lunar Planet. Sci. Conf. XXXVI*, abstract no. 1424, 36th Lunar and Planetary Science Conference, Houston.

Day J. M. D., Taylor L. A., Floss C., Patchen A. D., Schnare D. W., Pearson D. G. (2006) Comparative petrology, geochemistry and petrogenesis of eVolved, low-Ti lunar mare basalt meteorites from the La Paz icefield, Antarctica. *Geochim. Cosmochim. Acta* Vol. 70. pp. 1581 - 1600.

Day J. M. D., Taylor L.A., Hill E., Liu Y. (2005) Textural analysis and crystallization histories of the LaPaz mare basalt meteorites (abstract). *Meteorit. Planet. Sci.* 40, A37.

Day J. M. D., Floss C., Taylor L. A., Anand M. and Patchen A. D. (2006) Evolved mare basalt magmatism, high Mg/Fe feldspathic crust, chondritic impactors, and the petrogenesis of Antarctic lunar breccia meteorites Meteorite Hills 01210 and Pecora Escarpment 02007. *Geochim. Cosmochim. Acta.* Vol. 70. pp. 5957 – 5989.

Delano, J. W. 1986. Pristine lunar glasses - Criteria, data, and implications. Lunar *Lunar Planet. Sci. Conf.*. , 16th, Houston, TX, Mar. 11-15, 1985) *Journal of Geophysical Research*, Vol. 91, March 30, 1986., pp. D201-D213.

Dunkin S. K., Grande M., Casanova I., Fernandes V., Heather D. J., Kellett B., Muinonen K., Russell S. S., Browning R., Waltham N., Parker D., Kent B., Perry C. H., Swinyard B., Perry A., Feraday J., Howe C., Phillips K., McBride G., Huovelin J., Muhli P.,. Hakala P. J, Vilhu O., Thomas N., Hughes D., Alleyne H., Grady M., Lundin R., Barabash S., Baker D., Clark P. E., Murray C. D., Guest J., d'Uston L. C., Maurice S., Foing B., Christou A., Owen C., Charles P., Laukkanen J., Koskinen H., Kato M., Sipila K., Nenonen S., Holmstrom M., Bhandari N., Elphic R. and Lawrence D. 2003. Scientific rationale for the D-CIXS X-ray spectrometer on board ESA's SMART-1 mission to the Moon. *Planetary and Space Science*. Vol. 51. pp. 435 - 442.

Dymek R. F., Albee A. L., Chodos A. A. and Wasserburg G. J. 1976. Petrography of isotopically-dated clasts in the Kapoeta howardite and petrologic constraints on the evolution of its parent body *Geochimica et Cosmochimica Acta*, Vol. 40. pp. 1115 - 1116

El Goresy A., Prinz M., and Ramdohr P. 1976. Zoning in spinels as an indicator of the crystallization histories of mare basalts. *Proceedings of the 7th Lunar Planet. Sci. Conf.*. pp 1261-1279. Lunar and Planetary Institute, Houston.

Elkins-Tanton L.T., Chatterjee N., Grove T.L. 2003. Magmatic processes that produced lunar fire fountains Geophys. Res. Lett. Vol. 30. No. 10. pp. 1513.

Elphic, R. C.; Lawrence, D. J.; Feldman, W. C.; Barraclough, B. L.; Maurice, S.; Binder, A. B.; Lucey, P. G. Lunar Fe and Ti abundances: Comparison of Lunar Prospector and Clementine Data, *Science*. Vol. 281, pp. 1493 - 96.

Fagan T. J., Taylor G. J., Keil K., Bunch T. E., Wittke J. H., Korotev R. L., Jolliff B. L., Gillis J. J., Haskin L. A., Jarosewich E., Clayton R. N., Mayeda T. K., Fernandes V. A., Burgess R., Turner G., Eugster O., and Lorenzetti S. 2002. Northwest Africa 032: Product of lunar Volcanism. *Meteorit. Planet. Sci.* Vol.37. pp. 371 - 394.

Feldman W. C., B. L. Barraclough, K. R. Fuller, D. J. Lawrence, S. Maurice, M. C. Miller, T. H. Prettyman, and A. B. Binder. 1999. The Lunar Prospector Gamma-Ray and Neutron Spectrometers, *Nuclear Instruments and Methods in Physics Research A, 422*. pp.562-566.

Fernandes, V.A., Burgess, R.., and Turner, G. 2003. ^{40}Ar-^{39}Ar chronology of lunar meteorites NWA 032 and 773. *Meteorit. Planet. Sci.*, Vol. 38. pp. 555 - 564.

Fitton G. 1997. X-ray fluorescence spectrometry. In *Modern Analytical Geochemistry: An Introduction to quantitative Chemical Analysis Techniques for Earth, Environmental and Material Scientists*. Ed. Robin Gill. Longman Ltd. ISBN 0 582 09944 7. pp. 87 - 115.

Floran R.J. Phinney W.C. Blanchard D.P. Warner J.L.Simonds C.H. Brown R.W. Brannon J.C. Korotev R.L. 1976. A comparison between the geochemistry and petrology of Apollo 16 – terrestrial impact melt analogs. *Lunar Planet. Sci. Conf.* VII, 263-265 (abstr.).

Floss C. A. James A.B. McGee J.J. Crozaz G. 1998. Lunar ferroan anorthosite petrogenesis: Clues from trace element distributions in FAN subgroups. Geochim. Cosmo. Acta. Vol. 62. Issue 7. pp. 1255 -1283

Foing, B. H.; Racca, G. D.; Marini, A.; Heather, D. J.; Koschny, D.; Grande, M.; Huovelin, J.; Keller, H. U.; Nathues, A.; Josset, J. L.; Malkki, A.; Schmidt, W.; Noci, G.; Birkl, R.; Iess, L.; Sodnik, Z.; McManamon, P. 2003. SMART-1 mission to the moon: Technology and science goals. *Advances in Space Research*. Vol. 31. Issue 11. pp. 2323-2333.

French, B. M. 1998. Traces of Catastrophe: A Handbook of Shock-Metamorphic Effects in Terrestrial Meteorite Impact Structures. Technical Report, LPI-Contrib-954.

Ghiorso, M.S., and Sack, R.O. (1995) Chemical Mass Transfer in Magmatic Processes. IV. A Revised and Internally Consistent Thermodynamic Model for the Interpolation and Extrapolation of Liquid-Solid Equilibria in Magmatic Systems at Elevated Temperatures and Pressures. Contributions to *Mineralogy and Petrology*, Vol. 119. pp.197 – 212.

Gault, D. E., Hoerz, F., Brownlee, D. E., & Hartung, J. B. 1974. Mixing of the lunar regolith. *Proc. Lunar Planet. Sci. Conf.* 5th. Vol. 3.pp. 2365 - 2386.

Gillis J.J., Jolliff B.L., Korotev R.L., Lawerence D.J. 2000. An empirical relation between the Lunar Prospector gamma-ray and soil sample Th abundances. *31st Lunar Planet. Sci. Conf.* abstract #2058.

Gillis J. J., Jolliff B. L., Korotev R. L. 2004. Lunar surface geochemistry: Global concentrations of Th, K, and FeO as derived from lunar prospector and Clementine data. *Geochimica et Cosmochimica Acta*. Vol. 68. No. 18. pp. 3791 – 3805.

Goodrich C.A., Taylor G. J., Keil K., Boynton W. V., and Hill D. H. (1984) Petrology and chemistry of hyperferroan anorthosites and other clasts from lunar meteorite ALHA81005. *Proc. Lunar Planet. Sci. Conf. 15th*, in *J. Geophys. Res.* 89. C87-C94.

Grande, M.; Dunkin, S. K. 2003. CIXS: An X-ray spectrometer for ESA's Bepicolombo mission to Mercury *EGS - AGU - EUG Joint Assembly*, abstract #11508

Grande, M.; Browning, R.; Waltham, N.; Parker, D.; Dunkin, S. K.; Kent, B.; Kellett, B.; Perry, C. H.; Swinyard, B.; Perry, A.; Feraday, J.; Howe, C.; McBride, G.; Phillips, K.; Huovelin, J.; Muhli, P.; Hakala, P. J.; Vilhu, O.; Laukkanen, J.; Thomas, N.; Hughes, D.; Alleyne, H.; Grady, M.; Lundin, R.; Barabash, S.; Baker, D.; Clark, P. E.; Murray, C. D.; Guest, J.; Casanova, I.; D'Uston, L. C.; Maurice, S.; Foing, B.; Heather, D. J.; Fernandes, V.; Muinonen, K.; Russell, S. S.; Christou, A.; Owen, C.; Charles, P.; Koskinen, H.; Kato, M.; Sipila, K.; Nenonen, S.; Holmstrom, M.; Bhandari, N.; Elphic, R.; Lawrence, D. 2003. The D-CIXS X-ray mapping spectrometer on SMART-1. *Planetary and Space Scienc.* Vol. 51. Issue 6. pp. 427 - 433.

Grande M., Maddison B, Kellett B.J., Sreekumar P. and the C1XS Team. 2006. The C1XS X-ray Spectrometer on Chandrayaan-1.

Grande M., B.J. Kellett, C. Howe, C.H. Perry, B. Swinyard, S. Dunkin, J. Huovelin, L. Alha, L.C. D'Uston, S. Maurice, O. Gasnault, S. Couturier-Doux, S. Barabash, K.H. Joy, I.A. Crawford, D. Lawrence, V. Fernandes, I. Casanova M. Wieczorek, N. Thomas, U. Mall, B. Foing, D. Hughes, H. Alleyne, S. Russell, M. Grady, R. Lundin, D. Baker, C.D. Murray, J. Guest and A. Christou. 2007a. The D-CIXS X-ray spectrometer on the SMART-1 mission to the Moon—First results Planetary and Space Science.

Grande M. * Kellett B. J. Howe C. Perry C. H. Swinyard B. Dunkin S. Huovelin J. Alha L. D'Uston L. C. Maurice S. Gasnault O. Barabash S. Joy K. H. Crawford I. A. Lawrence D. Fernandes V. Casanova I. Wieczorek M. Thomas N. Mall U. Foing B. Hughes D. Alleyne H. Russell S. Grady M. Lundin R. Baker D. Murray C. D. Guest J. Christou A. 2007b. Observations of Past Lunar Landing Sites by the D-CIXS X-Ray Spectrometer on SMART-1 Abstract #1154.

Grossman J.M. 1998. The Meteoritical Bulletin, No. 82, *Meteorit. Planet. Sci.* Vol. 33. A221-A240

Hapke B.; Danielson G..E.; Klaasen K.; Wilson L. 1975. Photometric observations of Mercury from mariner 10. *J. Geophy. Res.*, 80 (17). pp. 2431-2443.

Hackwill T.; Guest J.; Spudis P. 2006. Stratigraphy and evolution of basalts in Mare Humorum and south eastern Procellarum. *Meteorit. Planet. Sci.* Vol. 41. Issue 3. pp. 479 - 488

Halliday A.N. and Lee. D-C.1999. Tungsten isotopes and the early development of the Earth and Moon *Geochimica et Cosmochimica Acta*, Vol. 63. No. 23/24. pp. 4157 – 4179.

Hartmann W. K. and Davis D. R.1975. Satellite-sized planetesimals and lunar origin. *Icarus*. Vol. 24. pp. 504-515

Haskin L., Warren P. 1991. Lunar Chemistry. In *Lunar sourcebook: A user's guide to the moon*: Edited by Grant H. Heiken David Vaniman and Bevan M. French. Cambridge University Press, 1991. (ISBN 0-521-33444-6).

Head, J. W., III; Wilson, L. 1992. Lunar mare Volcanism - Stratigraphy, eruption conditions, and the evolution of secondary crusts. *Geochimica et Cosmochimica Acta* (ISSN 0016-7037), Vol. 56, no. 6, pp. 2155-2175.

Head, J. W., III; Wilson, L. 2002. Dark ring in southwestern Orientale Basin: Origin as a single pyroclastic eruption. *Journal Of Geophysical Research*, Vol. 107. No. E1. pp.5001

Heather, D. J.; Dunkin, S. K. 2002. A stratigraphic study of southern Oceanus Procellarum using Clementine multispectral data. *Planetary and Space Science*. Vol. 50. Issue 14-15. pp. 1299-1309.

Hess, P. C. 1994. Petrogenesis of lunar troctolites. *Journal of Geophysical Research*. Vol. 99. no. E9. pp. 19,083-19,093

Hess, P. C.; Parmentier, E. M. 1995. A model for the thermal and chemical evolution of the Moon's interior: implications for the onset of mare Volcanism. *Earth and Planetary Science Letters*. Vol. 134, Issue 3-4. pp.501-514

Herzberg, C. T.; Baker, M. B. 1979. The Cordierite- to Spinel-Cataclasite Transition in the Moon, and its Bearing on the Structure of the Crust and Mantle. Abstracts of Papers *Presented to the Conference on The Lunar Highlands Crust*. Sponsored by the Lunar Science Institute. TX. LPI Contribution 394, edited by P. C. Robertson, published by the Lunar and Planetary Institute. pp.63.

Hiesinger, H.; Jaumann, R.; Neukum, G.; Head, J. W.1998. On the Relation of Age and Titanium Content of Lunar Mare Basalts. *29th Annual Lunar Planet. Sci. Conf.*, abstract no. 1243

Hiesinger, H.; Head, J. W., III; Jaumann, R.; Neukum, G. 1999. Lunar Mare Volcanism. *30th Annual Lunar Planet. Sci. Conf.* Abstract no. 1199

Hiesinger, H.; Jaumann, R ; Neukum, G. Head, J. W. 2000a. Ages of mare basalts on the lunar nearside. *J. Geophys. Res,* Vol 105. NO. E12. pp. 29,239 – 29,276.

Hiesinger, H.; Head, J. W., III; Wolf, U.; Neukum, G. 2000b. Lunar Mare Basalts in Oceanus Procellarum: Initial Results on Age and Composition. *31st Annual Lunar Planet. Sci. Conf.* Abstract no. 1278

Hiesinger H.H., Head J.W. Head III, Wolf U., Jaumann R., Neukum G. 2003. Ages and stratigraphy of mare basalts in Oceanus Procellarum, Mare Nubium, Mare Cognitum, and Mare Insularum. *Journal of Geophysical Research.* Vol. 108. pp. 5065.

Hiesinger, H.; Head, J. W., III. 2006. New Views of Lunar Geoscience: An Introduction and Overview Reviews in Mineralogy and Geochemistry. In *New Views on the Moon. Reviews in Mineralogy.* January 2006. Vol. 60. pp.1-81.

Holland A. D., Hutchinson I. B., Smith D. R., Pool P. 2004. Proton damage in the E2V swept charge device. Nuclear instruments & methods in physics research. Vol. 521. No. 2-3. pp. 393 - 398.

Hörz F, Grieve R, Heiken G, Spudis P, Binder A (1991) Lunar surface processes. In: *Lunar Sourcebook – A Users Guide to the Moon* .Heiken G, Vaniman D, French B (eds) Cambridge University Press. pp. 1-120

Howarth I D, J Murray, D Mills & D S Berry. 2003. Starlink User Note 50.24 (CCLRC)

Howe C.J. 2006. Summary Of EEPROM Corruption Events. CCLRC SMART-1 Technical Doc No: S1-CIX-RAL-TN-3032

Huovelin, J.; Alha, L.; Andersson, H.; Andersson, T.; Browning, R.; Drummond, D.; Foing, B.; Grande, M.; Hämäläinen, K.; Laukkanen, J.; Lämsä, V.; Muinonen, K.; Murray, M.; Nenonen, S.; Salminen, A.; Sipilä, H.; Taylor, I.; Vilhu, O.; Waltham, N.; Lopez-Jorkama, M.2002. The SMART-1 X-ray solar monitor (XSM): calibrations for D-CIXS and independent coronal science *Planetary and Space Science.* Vol. 50. Issue 14-15. pp. 1345 - 1353.

Huber H. and Warren P. H. (2005) MET01210: Another lunar mare meteorite (regolith breccia) with extensive pyroxene exsolution, and not part of the YQ launch pair (abstract). In *Lunar and Planetary Science XXXVI*, abstract no. 2401, Lunar and Planetary Institute, Houston.

James O.B., Lindstron M.M., and Flohr M.K. (1989). Ferroan anorthosite from lunar breccia 64435: Implications for the origin and history of lunar ferroan anorthosites. *Proc. 19th Lunar Planet. Sci. Conf.* pp. 219 - 243.

Jolliff B.L.; Haskin L.A. 1995. Cogenetic rock fragments from a lunar soil: Evidence of a ferroan noritic-anorthosite pluton on the Moon. *Geochimica et Cosmochimica Acta*, Volume 59, Number 11, June 1995. pp. 2345 - 2374.

Jolliff B. L., Rockow K. M., and Korotev R. L. (1998) Geochemistry and petrology of lunar meteorite Queen Alexandra Range 94281, a mixed mare and highland regolith breccia, with special emphasis on very-low-Ti mafic components. *Meteorit. Planet. Sci.*. Vol. 33. pp. 581 - 601.

Jolliff B.L., Gillis J.J., Haskin L.A., Korotev R.L., Wieczorek M.A. 2000. Major lunar crustal terranes: Surface expressions and crust-mantle origins. *J.Geophys. Res.* 105. pp. 4197 - 4216.

Jolliff B. L., Korotev R. L., Zeigler R. A., and Floss C. 2003. Northwest Africa 773: Lunar mare breccia with a shallow-formed olivine-cumulate component, inferred very-low-Ti (VLT) heritage, and a KREEP connection, *Geochimica et Cosmochimica Acta*. Vol. 67. pp. 4857 – 4879.

Josset, J. L. 1999. AMIE: Micro-Imaging System for SMART-1 Mission American Astronomical Society, *DPS meeting* #31, #21.08

Joy K.H., Crawford I.A., Russell S.S., Kearsley A.T. 2005a. LAP 02205, LAP 02224 and LAP 02226 - Lunar Mare Basaltic Meteorites. Part 1: Petrography and Mineral Chemistry. In *36th Lunar Planet. Sci. Conf.*, abstract no. 1697, Lunar and Planetary Institute, Houston.

Joy K.H., Crawford I.A., Russell S.S., Kearsley A.T. 2005b.LAP 02205, LAP 02224 and LAP 02226 - Lunar Mare Basaltic Meteorites. Part 2: Geochemistry and Crystallisation. In *36th Lunar Planet. Sci. Conf.*, abstract no.#1701, Lunar and Planetary Institute, Houston.

Joy K. H., Crawford I. A., Russell S. S., Swinyard B., Kellett B., and Grande M. 2006a. Lunar regolith breccias MET 01210, PCA 02007 and DAG 400: Their importance in understanding the

lunar surface and implications for the scientific analysis of D-CIXS data (abstract). In *Lunar Planet. Sci. Conf* XXXVII, abstract no. 1274, Lunar and Planetary Institute, Houston.

Joy K. H., Crawford I. A., Downes H., Russell S. S., and Kearsley A. T. 2006b. A petrological, mineralogical, and chemical analysis of lunar mare basalt meteorite LaPaz Icefield 02205, 02224, and 02226. *Meteorit. Planet. Sci.* Vol. 41. pp. 1003 – 1025.

Joy K. H., Anand, M. Crawford I. A., Russell S. S. 2007. Petrography and Bulk Composition of Miller Range 050535: a new lunar VLT gabbro In *Lunar Planet. Sci. Conf*. XXXVIII.

Kaiden, H.; Kojima, H. 2002. Yamato 983885: A New Lunar Meteorite Found in Antarctica. *33rd Annual Lunar Planet. Sci. Conf*, abstract no.1958

Kempa, M. J.; Papike, J. J. 1980. The Apollo 16 regolith - Comparative petrology of the greater than 20 micron and 20-10 micron soil fractions, lateral transport and differential Volatilization Lunar and Planetary Science Conference, 11th, Houston, TX, March 17-21, 1980, Proceedings. Vol. 2. (A82-22296 09-91) New York, Pergamon Press. pp. 1635-1661

Koeberl C., Kurat G., and Brandstätter F. (1993) Gabbroic lunar mare meteorites Asuka-881757 (Asuka-31) and Yamato 793169: Geochemical and mineralogical study, *Proc. NIPR Symp. Antarct. Meteorites* 6, 14–34. Nat. Inst. Polar Res., Tokyo.

Koizumi E., Chokai J., Mikouchi M., Makishima J., and Miyamoto M. 2005. Crystallisation of lunar mare meteorite LAP 02205 (abstract). *68th Meeting of the Meteorit. Planet. Sci.* Abstract no. #5152.

Korotev R. L., 1991. Apollo 16 Impact Melt Breccias 1: Intrasample Compositional Variations and Their Causes (abstract). In *22nd Lunar and Planetary Science Conference*. Vol. 22. pp743.

Korotev R.L. 1994. Compositional variation in the Apollo 16 impact-melt breccias and inferences for the geology and bombardment history of the Central Highlands of the Moon. Geochem. Cosmo. Acta. Vol. 58. No. 18. pp.3931 - 3969.

Korotev R.L. 1996. On the relationship between the Apollo 16 ancient regolith breccias and feldspathic fragmental breccias, and the composition of the prebasin crust in the Central highlands of the Moon. *Meteorit. Planet. Sci.* Vol. 31. pp. 403 - 412.

Korotev R.L. 1997. Invited review: Some things we can infer from the Moon from the composition of the Apollo 16 regolith. *Meteorit. Planet. Sci.* Vol. 32. pp. 447 - 478.

Korotev R. L. 2005. Lunar geochemistry as told by lunar meteorites. *Chemie der Erde* Vol. 65, pp. 297 – 346.

Korotev R. L., Zeigler R. A., Jolliff B. L., and Haskin L. A. (2002) Northwest Africa 773 – An unusual rock from the lunar maria, *65th Meteoritical Society Meeting*, no. 5259.

Korotev, R. L.; Jolliff, B. L.; Zeigler, R. A.; Gillis, J. J.; Haskin, L. A. 2003a. Feldspathic lunar meteorites and their implications for compositional remote sensing of the lunar surface and the composition of the lunar crust. *Geochimica et Cosmochimica Acta.* Vol. 67. Iss. 24 pp. 4895 – 492.3

Korotev R. L., Jolliff B. L., Zeigler R. A., and Haskin L. A. 2003b. Compositional constraints on the launch pairing of three brecciated lunar meteorites of basaltic composition, *Antarctic Meteorite Research* Vol. 16. pp. 152 – 175.

Korotev R. L., Jolliff B. L., Zeigler R. A., and Haskin L. A. 2003c. Compositional evidence for launch pairing of the YQ and Elephant Moraine lunar meteorites, *Lunar Planet. Sci. Conf.* 34, CD-ROM #1357, Lunar and Planetary Institute, Houston.

Lang J, C M Brown, J E Magraw, J Payne. 1993. The Laboratory calibration of the Yohkoh Bragg crystal spectrometer RAL-93-035. CCLRC.

Lawrence D. J., * Feldman W. C., Barraclough B. L, Binder A. B, R Elphic R. C, Maurice S., Thomsen D. R.. 1998. Global Elemental *Meteorit. Planet. Sci.* of the Moon: The Lunar Prospector Gamma-Ray Spectrometer *Science* . Vol. 281. no. 5382, pp. 1484 – 1489.

Lawrence, D. J., Feldman W. C., Barraclough B. L., Elphic R. C, Maurice S., Binder A. B., Miller M. C., and Prettyman T. H.. 1999. High resolution measurements of absolute thorium abundances on the lunar surface, *Geophys. Res. Lett.*, Vol. 26(17)., pp.2681 – 2684.

Lawrence, D. J., Feldman W. C., Barraclough B. L., Elphic R. C., Prettyman T. H., Maurice S., Binder A. B., and Miller M. C. 2000. Thorium abundances on the lunar surface, *J. Geophys. Res.*, Vol. 105(E8). pp. 20,307 – 20,331.

Lawrence, D. J.; Elphic, R. C.; Feldman, W. C.; Gasnault, O.; Genetay, I.; Maurice, S.; 2002a. Small-Area Thorium Enhancements on the Lunar Surface. *33rd Annual Lunar Planet. Sci. Conf.* Abstract no.1970

Lawrence, D. J., R. C. Elphic, W. C. Feldman, O. Gasnault, I. Genetay, S. Maurice, and T. H. Prettyman, 2002b. Optimizing the spatial resolution for gamma-ray measurements of thorium abundances on the lunar surface, *New Views of the Moon, Europe.*

Lawrence, D. J., Feldman W. C., Elphic R. C., Little R. C., Prettyman T. H., Maurice S., Lucey P. G., and Binder A. B. 2002c. Iron abundances on the lunar surface as measured by the Lunar Prospector gamma-ray and neutron spectrometers. *J. Geophys. Res.*, Vol. 107(E12). pp. 5130.

Lawrence, D. J., Elphic R. C., Feldman W. C., Prettyman T. H., Gasnault O., and Maurice S. 2003. Small area thorium features on the lunar surface. *J. Geophys. Res.*, Vol. 108(E9). pp.5102.

Lawrence, D. J., Maurice S., Feldman W. C. 2004. Gamma-ray measurements from Lunar Prospector: Time series data reduction for the gamma-ray spectrometer, *J. Geophys. Res.– Planets*, Vol. 109. No. E7. pp. E07S05.

Lin R. P. , K. A. Anderson, S. Ashford, C. Carlson, D. Curtis, R. Ergun, D. Larson, J. McFadden, M. McCarthy, G. K. Parks, H. Rème, J. M. Bosqued, J. Coutelier, F. Cotin, C. D'Uston, K. -P. Wenzel, T. R. Sanderson, J. Henrion, J. C. Ronnet and G. Paschmann. 1995. A three-dimensional plasma and energetic particle investigation for the wind spacecraft. Space Science Reviews. Volume 71, Numbers 1 - 4.

Lindstrom M.M. and Haskin L.A. 1978. Caused of compositional variations within mare basalt suites. *Proceedings of the 9th Lunar Planet. Sci. Conf.* pp 465. Lunar and Planetary Institute, Houston.

Lindstrom, M. M. & Lindstrom, D. J. 1986. Lunar Granulites and Their Precursor Anorthositic Norites of the Early Lunar Crust. *Lunar Planet. Sci. Conf.* 16th, Journal of Geophysical Research Vol. 91, March 30, 1986. pp. D263-D276

Longhi, J. 2003. A new view of lunar ferroan anorthosites: Postmagma ocean petrogenesis. *Journal of Geophysical Research*, Vol. 108. Issue E8. pp. 2-1

Longhi, J.; Ashwal, L. D. 1984. A Two-Stage Model for Lunar Anorthosites: an Alternative to the Magma Ocean Hypothesis. *Lunar Planet. Sci. Conf.*, XV, Abstract. pp. 491-492.

Lowe, B. G.; Holland, A. D.; Hutchinson, I. B.; Burt, D. J.; Pool, P. J. 2001. The swept charge device, a novel CCD-based EDX detector: first results. Nuclear Instruments and Methods in Physics Research Section A, Vol. 458. Issue 1-2. pp. 568-579.

Lucey, P. 2004. Mineral Meteorit. Planet. Sci. of the Moon. *Geophys. Res. Lett.* Vol. 3. L08701.

Lucey P. and Cahill J. 2006. Magnesian Rock Types In The Lunar Highlands: Remote Sensing Using Data from Lunar Prospector And Clementine. *Lunar Planet. Sci. Conf.*, XXXVII

Lucey P.; Taylor G.J.; and Maleret E. 1995. Abundance and distribution of iron on the Moon, *Science* Vol. 268. pp.1150-1153.

Lucey, Paul G.; Blewett, David T.; Hawke, B. Ray. 1998. Mapping the FeO and TiO2 content of the lunar surface with multispectral imagery. *J. Geophys. Res.* Vol. 103. no. E2. pp. 3679-3699.

Lucey, P. G., D. T. Blewett, B. L. Jolliff. 2000. Lunar iron and titanium abundance algorithms based on final processing of Clementine ultraviolet-visible images, *J. Geophys. Res.* Vol. 105(E8). pp. 20297-20306

Lucey, P. G.; Gillis, J. J.; Steutel, D. 2004 Global Images of Mg-Number Derived from Clementine Data. *35th Lunar Planet. Sci. Conf.* Abstract no.1717

Lucey, P., Korotev R.L., Gillis J.J., Taylor L.A., Lawrence D., Campbell B.A., Elphic R., Feldmann B., Hood L.L., Hunten D., Mendillo M., Noble S., Papike J.J., Reedy R.C., Lawson S., Prettyman T., Gasault O., Maurice S. 2006a. Understanding the Lunar Surface and Space-Moon Interactions in *New Views of the Moon, Rev. Mineral. Geochem.* Vol. 60. pp. 83 - 219.

Maddison, B., Crawford, I.A., Joy, K.H. 2006. "C1XS Science Requirements Document". RAL Document: C1-C1X-RAL-RS-0003.

Markowicz, A.A. 2002. X-ray Physics. In *Handbook of X-ray Spectrometry (Second Edition, Revised and Expanded).* Edited by Van Grieken R.E. and Markowicz, A.A. Marcel Dekker,Inc. New York. ISBN 0 8247 0600 5. pp. 1 - 94.

Maxwell T.A. Straun P.L. El-Baz F. 1977. Mare Crisium: Compositional inferences from low-altitude X-ray fluorescence data. *Proceedings of 8th Lunar Planet. Sci. Conf.* pp. 933 - 944

McBride G. and Castiglione D.C. R&D Of The Manufacturing Of A Micro-Machined Collimator For A Compact X-Ray Spectrometer For Planetary Missions. RAL Documentation.

McCoy et al. (2004). The Meteoritical Bulletin, No. 88, *Meteorit. Planet. Sci.* Vol. 39. A215-A272

McGee J.J. 1989. Granulitic Breccia Clasts and Feldspathic Melt Breccia Clasts from North Ray Crater Breccia 67975: Precursors and Petrogenesis. Proceedings of the 19th Planetary Science Conference. *Cambridge University Press and the Lunar and Planetary Institute.* pp.73-84

McKay D.S., Bogard D.D, Morris R.V., Korotex R.L., Johnson P., Wentworth S.J. (1986) Apollo 16 Regolith Breccias: Characterization and Evidence for Early Formation in the Mega-Regolith. *Lunar Planet. Sci. Conf. 16th* in *J.Geophys. Res.* 91, D277-D303.

McKinley J. P. Taylor, G. J. Keil, K. Ma M-S. Schmitt R. A. 1984. Apollo 16: Impact melt sheets, contrasting nature of the Caylay Plains and Descartes Mountains, and geologic history. JGR. Vol. 89. Issue B1. pp. B513 - B524.

Metzger A.E., Trombka J.I., Peterson L.E., Reedy R.C., Arnold J.R. 1973. Lunar Surface Radioactivity: Preliminary Results of the Apollo 15 and Apollo 16 Gamma-Ray Spectrometer Experiments. *Science.* Vol. 179. No. 4075. pp. 800 - 803

Milliken, R.E., and Basu, A. (2000) A Modified CIPW Norm Calculation of Lunar Mare Basalts. (abstract), in *Lunar Planet. Sci. Conf. 31*, #1427

Morgan Z., Liang Y., Hess P. 2006. An experimental study of anorthosite dissolution in lunar picritic magmas: Implications for crustal assimilation processes .*Geochimica et Cosmochimica Acta*, Vol. 70, Issue 13. pp. 3477 - 3491.

Morris R. V. 1978. In situ reworking /gardening/ of the lunar surface - Evidence from the Apollo cores. *Lunar Planet. Sci. Conf.*, 9th, Houston, Tex., Proceedings. Volume 2. New York, Pergamon Press, Inc. pp.1801 - 1811.

Naney, M. T.; Crowl, D. M.; Papike, J. J. 1976. The Apollo 16 drill core - Statistical analysis of glass chemistry and the characterization of a high alumina-silica poor /HASP/ glass. Lunar Science Conference, 7th, Houston, Tex., March 15-19, 1976, Proceedings. Volume 1. (A77-34651 15-91) New York, Pergamon Press, Inc. 1976. pp. 155 - 184

Neal C.R., and Taylor L.A. 1989. Metasomatic products of the lunar magma ocean: The role of KREEP dissemination. *Geochimica et Cosmochimica Acta.* Vol. 53. pp. 529 - 541.

Neal C.R. and Taylor L.A. 1992. Petrogenesis of mare basalts: A record of lunar Volcanism. *Geochimica et Cosmochimica Acta.* Vol. 56. pp 2177-2211.

Neal C.R., Hacker M.D., Snyder G.A., Taylor L.A., Lui Y-G., Schmitt R.A. 1994 (a). Basalt Generation at the Apollo 12 site, Part 1: New data, classification, and re-evaluation. *Meteorit. Planet. Sci.* Vol.29. pp. 334 - 348.

Neal C.R., Hacker M.D., Snyder G.A., Taylor L.A., Lui Y-G., Schmitt R.A. 1994 (b). Basalt Generation at the Apollo 12 site, Part 2: Source heterogeneity, multiple melts, and crustal contamination. *Meteorit. Planet. Sci.* Vol. 29. pp. 349 - 361.

Nielsen R.J. and Drake M.J. 1978. The case for at least three mare basalt magmags at the Luna 24 site. In *Mare Crisium: The View from Luna 24.* Edited by Merrill R.B. and Papike J.J. pp. 419 - 428. Pergamon, New York.

Nishiizumi K., Okazaki R., Park J., Nagao K., Masarik J. and Finkel R.C. 2002. Exposure and terrestrial histories of Dhofar 019 Martian meteorite (abstract), in *Lunar and Planetary Science 33*, #1366.

Nishiizumi K., Hillegonds D. J., and Welten K. C. 2006. Exposure and terrestrial histories of lunar meteorites LAP 02205/02224/02226/02436, MET 01210, and PCA 02007 (abstract), *In 37th Lunar Planet. Sci. Conf.*, abstract no. #2369.

Nittler, L. R.; Starr, R. D.; Lim, L.; McCoy, T. J.; Burbine, T. H.; Reedy, R. C.; Trombka, J. I.; Gorenstein, P.; Squyres, S. W.; Boynton, W. V.; McClanahan, T. P.; Bhangoo, J. S.; Clark, P. E.; Murphy, M. E.; Killen, R 2001. .X-ray fluorescence measurements of the surface elemental composition of asteroid 433 Eros. *Meteorit. Planet. Sci.* Vol. 36. no. 12. pp. 1673 – 1695.

Nyquist, L.E., and Shih, C.-Y.:1992, 'The Isotopic Record of Lunar Volcanism', *Geochimica et Cosmochimica Acta* Vol. 56. pp. 2,213 - 2,234.

Nyquist L.E., Shih C.-Y., Reese Y., and Bogard D.D. 2005. Age of lunar meteorite LAP02205 and implications for impact-sampling of planetary surfaces (abstract). In *36th Lunar Planet. Sci. Conf.* abstract no.1374, Lunar and Planetary Institute, Houston.

Nyquist L. E., Shih C-Y., and Reese Y. D. (2007) Sm-Nd and Rb-Sr ages for MIL 05035: Implications for surface and mantle sources (abstract). In *Lunar and Planetary Science XXXVIII*, abstract no. 1702, 38th Lunar and Planetary Science Conference, Houston.

Oba, T. and Kobayashi, Y. 2001. The mineral assemblage of symplectites in lunar meteorite Asuka-881757. Antarctic Meteorite Research. Vol. 14. pp.21

O'Hara M. J. 2000a. Flood Basalts, Basalt Floods or Topless Bushvelds? Lunar Petrogenesis Revisited. *Journal of Petrology* Vol. 41. No. 11. pp.1545 - 1651

O'Hara M. J. 2000b. Flood Basalts and Lunar Petrogenesis *Journal of Petrology* Vol. 41 Number 11. pp. 1121-1125

Okada. T. 2004. Particle Size Effect In X-Ray Fluorescence At A Large Phase Angle: Importance On Elemental Analysis Of Asteroid EROS(433) . *Lunar Planet. Sci. Conf.* XXXVI Abstract no. 1174

Okada T., Kuwada Y., and Mizutani H.. 1998. Particle Size Effects In X-Ray Fluorescence: Implications For Planetary Missions. *Lunar Planet. Sci. Conf.* XXIX. Abstract No# 1597.

Okada T., M. Kato, A. Fujimura, H. Tsunemi and S. Kitamoto. 1999. X-ray fluorescence spectrometry with the SELENE orbiter. *Adv. Spac. Res.* Vol. 23. pp. 1833 – 1836

Okada T.; Kato M.; Yamashita Y.; Shirai K.; Yamamoto Y.; Matsuda T.; Tsunemi H.; Kitamoto S. 2002. Lunar X-ray spectrometer experiment on the SELENE mission. *Adv. Spac. Res.* Vol. 30, No.8, October 2002. pp. 1909 - 1914

Okada, Tatsuaki; Shirai, Kei; Yamamoto, Yukio; Arai, Takehiko; Ogawa, Kazunori; Hosono, Kozue; Kato, Manabu. 2006a. X-ray Fluorescence Spectrometry of Asteroid Itokawa by Hayabusa. *Science*, Vol. 312. Issue 5778. pp. 1338 - 1341.

Ogawa, K.; Okada, T.; Shirai, K.; Yamamoto, Y.; Arai, T.; Shiraishi, H.; Hosono, K.; Inoue, T.; Inoue, T.; Maruyama, Y.; Arakawa, M.; Kato, M. 2006. Development of X-Ray Fluorescence Spectrometer Onboard SELENE. *37th Annual Lunar Planet. Sci. Conf.*, Abstract no.2244.

Palme H., Spettel B., Jochum K.H. Dreibus G., Weber H., Weckwerth G., Wänke H., Birschoff A., Stöffler D. (1991) Lunar highland meteorites and the composition of the lunar crust. *Geochim. Cosmchim. Acta.* Vol. 55. pp. 3105 - 3122.

Papike J. J., 1998. Comparative planetary mineralogy: Chemistry of melt-derived pyroxene, feldspar, and olivine. In *Planetary Materials*. Edited by Papike J. J. Mineralogical Society of America. Washington D.C. pp. 7-1– 7-11.

Papike J. J., Taylor L., Simon S. 1991. Lunar Minerals. In *Lunar sourcebook: A user's guide to the moon*: Edited by Grant H. Heiken David Vaniman and Bevan M. French. Cambridge University Press, 1991. (ISBN 0-521-33444-6).

Papike J. J., Ryder G., Shearer C.K. 1998. Lunar Samples. In *Planetary Materials*, Edited by Papike J. J. Mineralogical Society of America. Washington D.C. pp. 5-1– 5-234.

Papike J. J., Karner J. M., and Shearer C. K. 2003. Determination of planetary basalt parentage: A simple technique using the electron microprobe. *American Mineralogist.* Vol.88. pp. 469-472.

Pearce N.J.G., Perkins W.T., Westgate J.A., Gorton M.P., Jackson S.E., Neal C.R., and Chenery S. P. 1997. New data for the National Institute of Standards and Technology 610 and 612 glass reference materials. Geostandards Newsletter 21. pp.115-144.

Pieters, C.; Shkuratov, Y.; Kaydash, V.; Stankevich, D.; Taylor, L. 2006. Lunar soil characterization consortium analyses: Pyroxene and maturity estimates derived from Clementine image data. *Icarus*, Vol. 184, Issue 1, pp. 83-101

Potts P.J., Bowles J.F.W., Reed S.J.B., Cave M.R. 1995. *Microprobe Techniques in the Earth Science.* The Mineralogical Society Series 6. Chapman & Hall. London.

Powell B.N, Dungan M.A. and Weiblen P.W. 1975. Apollo 16 feldspathic melt rocks: Clues to the magmatic history of the lunar crust. *Lunar Planet. Sci. Conf.* 6th, Houston, Tex., March 17-21, 1975, Proceedings. Volume 1. (A78-46603 21-91) New York, Pergamon Press, Inc. 1975. pp. 415-433.

Prettyman, T. H., Feldman W. C., Lawrence D. J., McKinney G. W., Binder A. B., Elphic R C., Gasnault O. M., Maurice S., and Moore K. R. 2002a. Library least squares analysis of Lunar Prospector gamma-ray spectra, *Proc. Lunar Planet. Sci. Conf.*33rd, abstract 2012.

Prettyman, T. H., Lawrence D. J., Vaniman D. T., Elphic R. C., and Feldman W. C. 2002b. Classification of regolith materials from lunar prospector data reveals a magnesium-rich highland province, paper presented at *The Moon Beyond 2002: Next Steps in Lunar Science and Exploration*, Lunar and Planet. Inst..

Prettyman T. H., Hagerty J. J., Elphic R. C., Feldman W. C., Lawrence D. J., McKinney G. W., Vaniman D. T. 2006. Elemental Composition of the Lunar Surface: Analysis of Gamma Ray Spectroscopy Data from Lunar Prospector. ***Journal of Geophysical Research – Planets***. Vol. 111, E12007.

Racca G.D.:, A. Marini, L. Stagnaro, J. van Dooren, L. di Napoli, B.H. Foing, R. Lumb, J. Volp, J. Brinkmann, R . Grlunagel, D. Estublier, E. Tremolizzo, M. McKay, O. Camino,J. Schoemaekers, M. Hechler, M. Khan, P. Rathsman, G. Andersson, K. An8o, S. Berge,P. Bodine, A. Edfors, A. Hussain, J. Kugelberg, N. Larsson, B. Ljung, L. Meijer, A. Mlortsell, T. Nordeblack, S. Persson, F. Sjloberg. 2002. SMART-1 mission description and development status. *Planetary and Space Science*. Vol. 50. pp.1323 – 1337

RAL report: Filter Specification. Doc. No. S1-CIX-3007. Issue 2. 2001.

Rankenburg K., Brandon A., Norman M., and Righter K. 2005 LAP 02 205: An evolved member of the Apollo 12 olivine basalt suite? (abstract). *68th Annual Meeting of the Meteoritical Society*, number #5294.

Rankenburg K., Brandon A. D., Neal C. R. 2006. Neodymium Isotope Evidence for a Chondritic Composition of the Moon. *Science*. Vol. 312. no. 5778, pp. 1369 – 1372

Raymond K. N. and Wenk H. R. 1971. Lunar ilmenite (Refinement of the crystal structure). Contributions to Mineralogy and Petrology. Volume 30.

Rhodes J.M. and Hubbard N.J. 1973. Chemistry, classification, and petrogenesis of Apollo 15 mare basalts. *Proceedings of the Lunar Planet. Sci. Conf.*. pp 1127. Lunar and Planetary Institute, Houston.

Rhodes, J. M., Brannon, J. C., Rodgers, K. V., Blanchard, D. P., Dungan, M. A. 1977. Chemistry of Apollo 12 mare basalts - Magma types and fractionation processes. *Proceedings of the 8th Lunar Planet. Sci. Conf.*. Vol.2. pp 1305-1338. Lunar and Planetary Institute, Houston.

Riner M.A.; Robinson M. S.; Tangeman J.A. and Elphic R. C. 2005. Is Ilmenite Always The Dominant Carrier Of Titanium In Lunar Mare Basalts? *Lunar Planet. Sci. Conf.* XXXVI

Riner M. A., Robinson M. S., Lucey P. G., Ebel D. S. 2006. Variations in Lunar Opaque Phase and Grain Size: Implications for Remote Sensing of TiO2 . Meteoritics & Planetary Science, Vol. 41, Supplement, *Proceedings of 69th Annual Meeting of the Meteoritical Society*, held August 6-11, 2006 in Zurich, Switzerland., pp.5339

Righter K., Brandon A.D., and Norman M.D. 2004 Mineralogy and petrology of unbrecciated lunar basaltic meteorite LAP 02205 (abstract). In *35th Lunar Planet. Sci. Conf.*, abstract no.1667, Lunar and Planetary Institute, Houston.

Righter K., Collins S.J., and Brandon A.D. (2005) Mineralogy and petrology of the LaPaz Icefield lunar mare basaltic meteorites. *Meteoritics & Planetary Science.* **Vol. 40. pp. 1703–1722.**

Robinson M. and Riner M. 2005. Advances in lunar science from the Clementine mission: A Decadal perspective. *J. Earth System Sci.* **114, No. 6, pp. 669–686.**

Roedder E., Weiblen P.W. 1977. Compositional variation in late-stage differentiates in mare lavas, as indicated by silicate melt inclusions. *Proceedings of the 8th Lunar Planet. Sci. Conf.* Vol.2. pp 1767-1783.

Rubin. A. E., Scott E. R. D., and Keil K. 1997. Shock metamorphism of enstatite chondrites. *Geochimica et Cosmochimica Acta*, Vol. 61. pp. 847-858.

Russell S.S. 2005. The Meteoritical Bulletin, no. 89. *Meteorit. Planet. Sci.* 40, A201-A263.

Ryder G. 1985. Catalog of Apollo 15 Rocks. *Curatorial Branch Publication 72.* JSC 20787. Lunar and Planetary Science Institute; Northrop Services Inc.

Ryder, G. & Wood. 1977. J. A. Serenitatis and Imbrium impact melts - Implications for large-scale layering in the lunar crust. Lunar Science Conference, 8th, Vol.1. pp.655-668.

Ryder G. and D. Norman. 1980. Catalog of Apollo 16 Rocks. JSC Publ. No. 16904, Curational Branch Publ. 52, NASA Johnson Space Center, Houston.

Saal A. E., Hauri E. H., Rutherford M. J., and Cooper R. F., 2007. The Volatile Contents (CO2, H2O, F, S, Cl) Of The Lunar Picritic Glasses. In *38th Lunar Planet. Sci. Conf.*, abstract no.1338, Lunar and Planetary Institute, Houston.

Satterwhite C.E. 2003. *Antarctic Meteorite Newsletter*, Vol. 26(2)

Satterwhite C.E. 2004a. *Antarctic Meteorite Newsletter*, Vol. 27(1)

Satterwhite C.E. 2004b. *Antarctic Meteorite Newsletter*, Vol. 27(3)

Scherer P., Pätsch M., and Schultz L. (1998) Noble-Gas study of the new lunar highland meteorite Dar al Gani 400. *Meteorit. Planet. Sci.* 33. A135-A136.

Schwartz J. M. and McCallum I. S. 1999. Inferred Depths Of Formation Of Spinel Cataclasites And Troctolitic Granulite, 76535 Using New Thermodynamic Data For Cr-Spinel. *Lunar Planet. Sci. Conf.* XXX. Abstract #1308

Semenova A. S., Nazarov M. A., Kononkova N. N., Patchen A., Taylor L. A. (2000) Mineral chemistry of lunar meteorite Dar al Gani 400 (abstract), in *Lunar Planet. Sci. Conf. 31*, #1252.

Shearer, C. K.; Papike, J. J. 1993. Basaltic magmatism on the moon - A perspective from Volcanic picritic glass beads. *Geochimica et Cosmochimica Acta*, Vol. 57., pp. 4785.

Shearer C.K., Papike J.J. 1999. Magmatic evolution of the Moon. *American Mineralogist*. Vol. 84, pp. 1469–1494

Shearer, C. K.; Floss, C. 2000. Evolution of the Moon's Mantle and Crust as Reflected in Trace-Element Microbeam Studies of Lunar Magmatism. In *Origin of the Earth and Moon*, edited by R.M. Canup and K. Righter and 69 collaborating authors. Tucson: University of Arizona Press. pp.339-359

Shearer, C. K., P. C. Hess, M. A. Wieczorek, M. E. Pritchard, E. M. Parmentier, L. Borg, J. Longhi, L. T. Elkins-Tanton, C. R. Neal, I. Antonenko, R. M. Canup, A. N. Halliday, T. L. Grove, B. H. Hager, D.-C. Less, and U. Wiechert (2006) Thermal and magmatic evolution of the Moon, in *New Views of the Moon*, eds. B. L. Jolliff, M. A. Wieczorek, C. K. Shearer, and C. R. Neal, , in *New Views of the Moon, Rev. Mineral. Geochem.* Vol. 60, pp. 365-518.

Shervais, J.W. and McGee, J.J., 1998, Ion & electron microprobe study of Mg suite troctolites, norite, and anorthosites from Apollo 14: Evidence for urKREEP assimilation during Petrogenesis of Apollo 14 Mg-suite rocks. *Geochimica Cosmochimica Acta*, 62/17. pp.3009-3023.

Shervais J. W., McGee J. J. *1999.* KREEP cumulates in the western lunar highlands: Ion and electron microprobe study of alkali-suite anorthosites and norites from Apollo 12 and 14. *American Mineralogist.* Vol. 84, pp. 806–820

Shinsuke K., Yasushi. Y. 2003.Lunar mare Volcanism in the eastern nearside region derived from Clementine UV/VIS data. *Meteoritics & Planetary Science*, Vol. 38, Issue 10. pp.1423-1548

Shkuratov, Yu. G.; Kreslavsky, M. A.; Stankevich, D. G.; Kaydash, V. G.; Pinet, P.; Shevchenko, V. V.; Foing, B. H.; Josset, J.-L. 2003. The SMART-1 Mission: Photometric Studies of the Moon with the AMIE Camera. *Solar System Research*, Vol. 37. Issue 4 pp. 251-259.

Simonds C.H. 1973. Petrology of Apollo 16 poikilitic rocks. Proceedings of the Forth KLunar Science Conference. Supplement 4, Geochim. Cosmo. Acta. Vol. 1. pp.613-632.

Shultz, P. H.; Spudis, P. D. 1983. Beginning and end of lunar mare Volcanism. *Nature.* Vol. 302. pp. 233-236.

Smith, J.V., Anderson, A.T., Newton R.C., Olsen, E.J., Wyllie, P.J., Crewe, A., Issachson, M.S., Johnson, D. 1970. Petrologic history of the Moon inferred from petrography, mineralogy, and petrogenesis of Apollo 11 rocks, *Proc. Lunar Planet. Sci. Conf.* Vol. 2. pp. 897-925.

Snyder G.A., Taylor L.A., Neal C.R. 1992.A chemical model for generating the sources of mare basalts - Combined equilibrium and fractional crystallization of the lunar magmasphere. Geochimica et Cosmochimica Acta. Vol. 56, no. 10, pp. 3809-3823

Snyder G.A. Taylor L.A. Halliday A.N. 1995. Chronology and petrogenesis of the lunar highlands suite: Cumulates from KREEP basalt crystallization. *Geochimica Cosmochimica Acta.* Vol 59 No. 6 . pp. 1185-1203.

Spudis, P. D. 1993. The Geology of Multi-Ring Impact Basins: The Moon and Other Planets. *Cambridge University Press.* Cambridge. ISBN 052162103. Chapter 8 pp. 165-190.

Spudis, P. D.; Davis, P. A. 1986. A Chemical and Petrological Model of the Lunar Crust and Implications for Lunar Crustal Origin. *Proceedings Of The 17th Lunar Planet. Sci. Conf.*,. Part 1. *Journal of Geophysical Research.* Vol. 91, No. B13, E84-E90.

Spudis P.D., Hawke B.R., Taylor G.J., McCormick K.A., Keil K., and Grieve R.A.F. 1991. Sources of mineral fragments in impact melts 15445 and 15455: Toward the origin of low-K Fra Mauro basalt. *Proc. Lunar Planet. Sci. Conf. 21*, pp. 151-165.

Spudis, P. D.; Shoemaker, E.; Acton, C.; Burratti, B.; Duxbury, T.; Baker, D.; Smith, D.; Blamont, J.; Davies, M.; Eliason, E., McEwen A.; Lucey P.; Pieters C. 1994. The Clementine Mission Initial Results from lunar mapping . *NASA report NASA-TM-110555.* Goddard Space Flight Center; Jet Propulsion Laboratory.

Spudis, P. D.; Bussey, D. B. J.; Gillis, J. J. 2000. Petrologic Mapping of the Moon from Clementine and Lunar Prospector Data: Incorporation of New Thorium Data. *31st Annual Lunar Planet. Sci. Conf.*. Abstract no. 1414

Spudis, P. D.; Zellner, N. E. B.; Delano, J. W.; Whittet, D. C. B.; Fessler, B. Petrologic Mapping of the Moon: A New Approach. 2002. *33rd Annual Lunar Planet. Sci. Conf.* Abstract no.1104

Starr, R. D.; Ho, G. C.; Schlemm, C.; Gold, R. E.; Goldsten, J. O.; Boynton, W. V.; Trombka, J. I. 2001. The X-Ray Spectrometer for Mercury Messenger. *Proceedings of Workshop on Mercury: Space Environment, Surface, and Interior.* LPI Contribution No. 1097. Houston, TX: Lunar and Planetary Science Institute, 2001. pp.102

Stöffler, D., Knoll H-D., Marvin U.B., Simonds C.H. and Warren P.H. 1980. Recommended classification and nomenclature of lunar highland rocks - a committee report. In *Proceedings of the Conference on the Lunar Highlands Crust* (eds. J.J. Papike and R.B. Merrill), pp. 51-70. Pergamon Press, New York, USA.

Stöffler D. and Grieve R.A.F. 1994. Classification and the nomenclature of Impact Metamorphic Rocks: A Proposal to the IUGS Sub-commission on the Systematics of Metamorphic Rocks. *Lunar Planet. Sci. Conf.*, 25. abstract 1347.

Stöffler, D. and Ryder, G. 2001. Stratigraphy and Isotope Ages of Lunar Geologic Units: Chronological Standard for the Inner Solar System. *Space Science Reviews*, v. 96, Issue 1/4, pp. 9-54.

Stöffler, D.; Knoell, H.-D.; Maerz, U. 1979. Terrestrial and lunar impact breccias and the classification of lunar highland rocks. In: *Lunar Planet. Sci. Conf.*, 10th. Proceedings. Vol. 1. (A80-23557 08-91) New York, Pergamon Press, Inc., 1979, pp. 639-675

Stöffler D., Keil K., and Scott E. R. D. (1991) Shock metamorphism of ordinary chondrites. *Geochimica et Cosmochimica Acta. Vol.* 55. pp. 3845- 3867.

Stöffler D., Ryder G., Ivanov B. A., Artemieva N. A., Cintala M. J., Grieve R. A. F. 2006. Cratering history and lunar chronology (*in* New views of the Moon) *Reviews in Mineralogy and Geochemistry* (2006), Vol. 60. pp. 519-596.

Swinyard B.M. 1999. How to Calculate the Minimum Detectable Flux for D-CIXS. *CCLRC Document number: S1-CIX-RAL-TN-3029.* Issue/Rev.No: 1

Taylor G. J. (1991) Impact melts in the MAC88105 lunar meteorite: Inferences for the lunar magma ocean hypothesis and the diversity of basaltic impact melts, *Geochim. Cosmochim. Acta* Vol. 55. pp. 3031-3036.

Taylor, G.J., Warren, P., Ryder, G., Delano, J., Pieters, C. and Lofgren, G. (1991) Lunar rocks. In *The Lunar sourcebook: A user's guide to the moon.* (G. Heiken, D. Vaniman, and B. French, editors), Chapter 6. pp.183-284 Cambridge University Press.

Taylor L.A., Misra K.C. 1975. Pyroxene-phyric basalt 15075: Petrography and petrogenesis. *Proceedings of the 6th Lunar Planet. Sci. Conf.*, pp 165-179. Lunar and Planetary Institute, Houston.

Taylor L. A and Day J. M. D. (2005). FeNi metal grains in La Paz mare basalt meteorites and Apollo 12 basalts (abstract). In *36th Lunar Planet. Sci. Conf.*, abstract no. #1417, Lunar and Planetary Institute, Houston.

Taylor, S. R. 1982a. *Planetary Science: A Lunar Perspective.* Houston: Lunar Planet. Inst.

Terada K., Sasaki Y., and Sano Y. 2006a. In-situ U-Pb dating of phosphates in lunar basaltic breccia Yamato 981031 (abstract). In *Lunar Planet. Sci. Conf. XXXVII*, abstract no. 1665, Lunar and Planetary Institute, Houston.

Terada, K., Sasaki, Y., Anand, M., Joy, K.H., Sano, Y. 2007. Uranium-lead systematics of phosphates in lunar basaltic regolith breccia, Meteorite Hills 01210, EPSL, doi: 10.1016/j.epsl.2007.04.029

Terada K., Sasaki Y., and Sano Y. (2006b) Ion microprobe U-Pb dating of phosphates in very-low-Ti basaltic breccia (abstract). *69th Annual Meeting of the Meteoritical Society*, abstract no. 5129. Lunar and Planetary Institute, Houston

Thompson, M. and Walsh, JN. 2003 Handbook *of Inductively Coupled Plasma Atomic Emission Spectrometry*. Viridian Publishing.

Tompkins, S; Pieters, C. M. 1999. Mineralogy of the lunar crust: Results from Clementine. *Meteorit. Planet. Sci.* . Vol. 34. no. 1. pp. 25-41

Trombka JI, Squyres SW, Bruckner J, Boynton WV, Reedy RC, McCoy TJ, Gorenstein P, Evans LG, Arnold JR, Starr RD, Nittler LR, Murphy ME, Mikheeva I, McNutt RL, McClanahan TP, McCartney E, Goldsten JO, Gold RE, Floyd SR, Clark PE, Burbine TH, Bhangoo JS, Bailey SH, Petaev M. 2000. The elemental composition of asteroid 433 Eros Results of the NEAR-Shoemaker x-ray spectrometer. *Science*. Vol. 289. pp. 2101-2105

Trombka, J. I.; Nittler, L. R.; Starr, R. D.; Evans, L. G.; McCoy, T. J.; Boynton, W. V.; Burbine, T. H.; Brückner, J.; Gorenstein, P.; Squyres, S. W.; Reedy, R. C.; Goldsten, J. O.; Lim, L.; Hurley, K.; Clark, P. E.; Floyd, S. R.; McClanahan, T. P.; McCartney, E.; Branscomb, J.; Bhangoo, J. S.; Mikheeva, I.; Murphy, M. E. 2001. The NEAR-Shoemaker x-ray/gamma-ray spectrometer experiment: Overview and lessons learned. *Meteorit. Planet. Sci.* Vol. 36. no. 12. pp. 1605-1616

Vaniman D., Dietrich J., Taylor G.J., Heiken G. Exploration, samples, and recent concepts of the Moon. 1991. In *Lunar sourcebook: A user's guide to the moon*: Edited by Grant H. Heiken David Vaniman and Bevan M. French. Cambridge University Press, 1991. (ISBN 0-521-33444-6).

Walker, D. 1983. Lunar and terrestrial crust formation *Lunar Planet. Sci. Conf.* 14th, Houston, TX, Mar. 14-18, 1983) *Journal of Geophysical Research*, Supplement, Vol. 88.

Warren. P. H. 1985. The Magma Ocean Concept and Lunar Evolution. *Annual Review of Earth and Planetary Sciences*. Vol. 13. pp. 201-240

Warren. P. H. 1990. Lunar anorthosites and the magma-ocean plagioclase-floation hypothesis: Importance of FeO enrichment in the parent magma. *American Mineralogist*. Vol. 75. pp. 46-58.

Warren. P. H. 1993. A concise compilation of petrologic information on possibly pristine non mare Moon rocks *American Mineralogist*; April 1993. Vol. 78. no. 3-4; pp. 360-376

Warren, P.H., 1994. Lunar and Martian meteorite delivery systems. *Icarus*. Vol. 111 pp. 338–363.

Warren, P. H. 2005. "New" lunar meteorites: Implications for composition of the global lunar surface, lunar crust, and the bulk Moon, *Meteoritics & Planetary Science*. Vol. 40. No. 3. pp. 477–506.

Warren P. H. and Kallemeyn G. W. (1993) Geochemical investigations of two lunar mare meteorites: Yamato-793169 and Asuka-881757. Proc. NIPR Symp. *Antarct. Meteorites* Vol. 6. pp. 35-57. Nat. Inst. Polar Res., Tokyo.

Warren P.H., Jerde E.A. Kallemeyn G.W. (1989) Lunar meteorites: Siderophile element contents. And implications for the composition and origin of the Moon. *Earth Planet Sci. Lett.* Vol. 91. pp. 245-260

Warren, P. H.; Ulff-Møller, F.; Kallemeyn, G. W. 2005. New" lunar meteorites: Impact melt and regolith breccias and large-scale heterogeneities of the upper lunar crust. *Meteorit. Planet. Sci.* Vol. 40. pp.989

Weiblen P. W. Examination of the liquid line of descent of mare basalts in light of data from melt inclusions in olivine. 1977. *Proceedings of the 8th Lunar Planet. Sci. Conf.* pp. 1751-1765.

Wiechert, U.; Halliday, A. N.; Lee, D.-C.; Snyder, G. A.; Taylor, L. A.; Rumble, D. 2001. Oxygen Isotopes and the Moon-Forming Giant Impact. *Science*, Vol.294, Issue 5541, pp. 345-348

Wilhelms D.E. 1982. General Features in *The Geologic History of the Moon*. U.S. Geological Survey, United States Government Printing Office, Washington. Chapter 1. pp.3.

Wieczorek, M. A; Phillips, R. J. 2000. The 'Procellarum KREEP Terrane' - Implications for mare Volcanism and lunar evolution. *Journal of Geophysical Research*. Vol. 105. no. E8, pp. 20, 417-20, 430.

Wieczorek, M. A and Zuber M.T. 2001.The composition and origin of the lunar crust: Constraints from central peaks and crustal thickness modelling. *Geophys. Res. Lett.* Vol. 28, No. 21. pp. 4023–4026.

Wieczorek, M. A., B. L. Jolliff, A. Khan, M. E. Pritchard, B. P. Weiss, J. G. Williams, L. L. Hood, K. Righter, C. R. Neal, C. K. Shearer, I. S. McCallum, S. Tompkins, B. R. Hawke, C. Peterson, J. J. Gillis, and B. Bussey. 2006. The constitution and structure of the lunar interior. In *New Views of the Moon, Rev. Mineral. Geochem.* Vol. 60. pp. 221-364.

Wetherill, G. W. 1975. Possible Slow Accretion of the Moon and its Thermal and Petrological Consequences. Abstracts of Papers Presented to the Conference on Origins of Mare Basalts and their Implications for Lunar Evolution. LPI Contribution number 234 from the conference held November 17-19, 1975. Sponsored by the Lunar Science Institute. LPI Contribution number 234, published by the Lunar Science Institute, 3303 Nasa Road 1, Houston, TX 77058. pp.184

Wood, J. A.; Dickey, J. S., Jr.; Marvin, Ursula B.; Powell, B. N. 1970 Lunar anorthosites and a geophysical model of the moon Geochimica et Cosmochimica Acta Supplement, Volume 1. Proceedings of the Apollo 11 Lunar Science Conference held 5-8 January 1970 in Houston, TX. Volume 1: Mineraolgy and Petrology. Edited by A. A. Levinson. New York: Pergammon Press, ., p.965-988

Vaniman D., Dietrich J., Taylor G.J., Heiken G. Exploration, samples, and recent concepts of the Moon. 1991. In *Lunar sourcebook: A user's guide to the moon*: Edited by Grant H. Heiken David Vaniman and Bevan M. French. Cambridge University Press, 1991. (ISBN 0-521-33444-6).

Yin L. I., Trombka J.I., Adler I., Bielefield M. 1993. X-ray remote sensing techniques for geochemical analysis of planetary surfaces. In: Pieters C.M., Englert P.A. (Eds), *Remote Geochemical Analysis: Elemental and Mineralogical Composition.* Cambridge University Press, Cambridge.

Zeigler R. A., Korotev R. L., Jolliff B. L., and Haskin L. A. (2005a Petrology and geochemistry of the LaPaz Icefield basaltic lunar meteorite and source-crater pairing with Northwest Africa 032. *Meteorit. Planet. Sci.* Vol. 40. pp.1073–1102.

Zeigler R. A., Korotev R. L., Jolliff B. J., and Haskin L. A. (2005b Petrography of lunar meteorite MET 01210, a new basaltic regolith breccia (abstract). In *Lunar and Planetary Science XXXVI*, abstract no. 2385, Lunar and Planetary Institute, Houston.

Zeigler R. A., Korotev R. L., Haskin L. A., Jolliff B. L., and Gillis J. J. (2006) Petrology and geochemistry of five new Apollo 16 mare basalts and evidence for post-basin deposition of basaltic material at the site. *Meteorit. Planet. Sci.* Vol. 41. pp. 263-284.

Zipfel J., Spettel B., Palme H., Wolf D., Franchi I., Sexton A. S., Pillinger C. T., and Bischoff A. (1998) Dar al Gani 400: Chemistry and petrology of the largest lunar meteorite. *Meteorit. Planet. Sci.* Vol. 33. A171.

Website References

WEBSITE 1.1: http://www.mentallandscape.com/C_CatalogMoon.htm (Last accessed: Jan. 2007)

WEBSITE 1.2: http://epsc.wustl.edu/admin/resources/meteorites/moon_meteorites_list.html (March. 2007)

WEBSITE 1.3: http://www.amptek.com/xrf.html (Nov. 2007)

WEBSITE 1.4: http://www.lpi.usra.edu/expmoon/Apollo16/A16_Orbital_xray.html (Nov. 2007)

WEBSITE 1.5 http://lunar.lanl.gov/pages/documentation.html (Nov. 2007)

WEBSITE 1.6: http://sci.esa.int/science-e/www/area/index.cfm?fareaid=10

WEBSITE 1.7: http://www.sstd.rl.ac.uk/SMART-1/X-ray.html (Nov. 2007)

WEBSITE 1.8: http://www.sec.noaa.gov/sxi/index.html (March 2007)

WEBSITE 1.9: http://hesperia.gsfc.nasa.gov/rhessidatacenter/ (March 2007)

WEBSITE 1.10: http://www.nasa.gov/mission_pages/constellation/ares/aresV.html (March 2007)